

1997 0314 078

The Pennsylvania State University  
**APPLIED RESEARCH LABORATORY**  
P.O. Box 30  
State College, PA 16804

A PHYSICS-BASED MEANS OF COMPUTING THE FLOW  
AROUND A MANEUVERING UNDERWATER VEHICLE

edited by

W. C. Zierke

written and performed by

D. A. Boger  
F. Davoudzadeh  
J. J. Dreyer  
H. McDonald  
C. G. Schott  
W. C. Zierke

Applied Research Laboratory  
The Pennsylvania State University

A. Arabshahi  
W. R. Briley  
J. A. Busby  
J. P. Chen  
M. Y. Jiang  
R. Jonnalagadda  
J. McGinley  
R. Panajakshan  
C. Sheng  
M. L. Stokes  
L. K. Taylor  
D. L. Whitfield

Engineering Research Center  
Mississippi State University

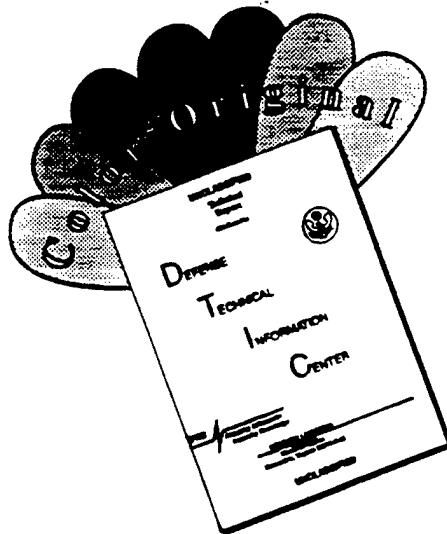
Technical Report No. TR 97-002  
January 1997

Supported by:  
Office of Naval Research

L. R. Hettche, Director  
Applied Research Laboratory

Approved for public release; distribution unlimited

# **DISCLAIMER NOTICE**



**THIS DOCUMENT IS BEST  
QUALITY AVAILABLE. THE COPY  
FURNISHED TO DTIC CONTAINED  
A SIGNIFICANT NUMBER OF  
COLOR PAGES WHICH DO NOT  
REPRODUCE LEGIBLY ON BLACK  
AND WHITE MICROFICHE.**

## REF ID: D0001 DOCUMENTATION PAGE

OMB NO. 0704-0188

Public reporting burden for this collection of information is estimated to average 1 hour per response, including the time for reviewing instructions, searching existing data sources, gathering and maintaining the data needed, and completing and reviewing the collection of information. Send comments regarding this burden estimate or any other aspect of the collection of information, including suggestions for reducing this burden, to Washington Headquarters Services, Directorate for Information Operations and Reports, 1215 Jefferson Davis Highway, Suite 1204, Arlington, VA 22202-4382, and to the Office of Management and Budget, Paperwork Reduction Project 0704-0188, Washington, DC 20503.

1. AGENCY USE ONLY (Leave blank)		2. REPORT DATE	3. REPORT TYPE AND DATES COVERED
		January 1997	
4. TITLE AND SUBTITLE		5. FUNDING NUMBERS	
A Physics-Based Means of Computing the Flow Around a Maneuvering Underwater Vehicle		N00039-92-C-0100	
6. AUTHOR(S)			
William C. Zierke, et.al.			
7. PERFORMING ORGANIZATION NAME(S) AND ADDRESS(ES)		8. PERFORMING ORGANIZATION REPORT NUMBER	
Applied Research Laboratory P.O. Box 30 State College, PA 16804		Engineering Research Center Mississippi State University P.O. Box 6176 Mississippi, MS 39762	
9. SPONSORING/MONITORING AGENCY NAME(S) AND ADDRESS(ES)		10. SPONSORING/MONITORING AGENCY REPORT NUMBER	
Office of Naval Research 800 North Quincy Street Arlington, VA 22217-5000		97-002	
11. SUPPLEMENTARY NOTES			
12a. DISTRIBUTION/AVAILABILITY STATEMENT		12b. DISTRIBUTION CODE	
Unlimited			
13. ABSTRACT (Maximum 200 words) A team of researchers from the Engineering Research Center at Mississippi State University and the Applied Research Laboratory at The Pennsylvania State University have developed a physics-based method that will lead to a means of accurately predicting the forces and moments acting on a maneuvering, self-propelled, appended, underwater vehicle and the resulting vehicle motion. This methodology has been developed in order to supplement and, eventually, replace the traditional correlation-based means of "predicting" the maneuvering characteristics of a submerged vehicle. One primary difference exists between this new physics-based method and traditional correlation-based methods. While the traditional methods use empirical correlations from model-scale experiments to determine the hydrodynamic forces and moments acting on a vehicle during a maneuver, this new method numerically solves for the fluid dynamics using the three-dimensional, time-dependent Reynolds-averaged Navier-Stokes equations on time-dependent curvilinear coordinates. Considering that large-scale simulations of a maneuvering vehicle at high Reynolds number will require large amounts of floating-point arithmetic and considerable storage capacity, the research team also investigated the use of high-performance parallel computing for making these types of large computations. In addition, while the baseline code used			
14. SUBJECT TERMS		15. NUMBER OF PAGES 276	
Vehicle, Maneuvering, Computational Fluid Dynamics		16. PRICE CODE	
17. SECURITY CLASSIFICATION OF REPORT	18. SECURITY CLASSIFICATION OF THIS PAGE	19. SECURITY CLASSIFICATION OF ABSTRACT	20. LIMITATION OF ABSTRACT
Unclassified	Unclassified	Unclassified	Unlimited

(Cont.)

an algebraic turbulence model, the team also investigated the use of two-equation turbulence models. Finally, the team coupled the fluid dynamics and vehicle dynamics together with a subroutine that solves for the vehicle dynamics at each time step using the six vector equations of Newton's laws of motion and seven additional kinematic relations.

The research team performed a substantial number of steady and unsteady computations to validate various elements of the prediction method, improve confidence in the use of the method, and check the feasibility of using the method to calculate flow fields of increasing complexity. For test cases where experimental data or analytical solutions exist, the quality of agreement with the computations has been considered reasonable to excellent. The steady-flow test cases concentrate on the ability of the code to compute boundary layers, three-dimensional separation, and vortical flows-including the flow over an appended vehicle. The unsteady-flow cases focus on prescribed maneuvers, rotating propulsors, and an initial investigation of moving control surfaces. Although no experimental data exists for the last few test cases, these cases give examples of how this new method can compute unsteady maneuvers, including crashback, with the fluid and vehicle dynamic coupled together.

## Abstract

A team of researchers from the Engineering Research Center at Mississippi State University and the Applied Research Laboratory at The Pennsylvania State University have developed a physics-based method that will lead to a means of accurately predicting the forces and moments acting on a maneuvering, self-propelled, appended, underwater vehicle and the resulting vehicle motion. This methodology has been developed in order to supplement and, eventually, replace the traditional correlation-based means of "predicting" the maneuvering characteristics of a submerged vehicle. One primary difference exists between this new physics-based method and traditional correlation-based methods. While the traditional methods use empirical correlations from model-scale experiments to determine the hydrodynamic forces and moments acting on a vehicle during a maneuver, this new method numerically solves for the fluid dynamics using the three-dimensional, time-dependent Reynolds-averaged Navier-Stokes equations on time-dependent curvilinear coordinates. Considering that large-scale simulations of a maneuvering vehicle at high Reynolds number will require large amounts of floating-point arithmetic and considerable storage capacity, the research team also investigated the use of high-performance parallel computing for making these types of large computations. In addition, while the baseline code used an algebraic turbulence model, the team also investigated the use of two-equation turbulence models. Finally, the team coupled the fluid dynamics and vehicle dynamics together with a subroutine that solves for the vehicle dynamics at each time step using the six vector equations of Newton's laws of motion and seven additional kinematic relations.

The research team performed a substantial number of steady and unsteady computations to validate various elements of the prediction method, improve confidence in the use of the method, and check the feasibility of using the method to calculate flow fields of increasing complexity. For test cases where experimental data or analytical solutions exist, the quality of agreement with the computations has been considered reasonable to excellent. The steady-flow test cases concentrate on the ability of the code to compute boundary layers, three-dimensional separation, and vortical flows--including the flow over an appended vehicle. The unsteady-flow cases focus on prescribed maneuvers, rotating propulsors, and an initial investigation of moving control surfaces. Although no experimental data exists for the last few test cases, these cases give examples of how this new method can compute unsteady maneuvers, including crashback, with the fluid and vehicle dynamics coupled together.

## Acknowledgments

We would like to extend our appreciation to the Office of Naval Research for supporting this program under their Advanced Technology Initiative on Maneuvering Underwater Vehicles. Our special thanks go to Mr. James A. Fein, who had the vision to initiate and support this program at a time when very few others thought that the development of a physics-based means of predicting vehicle maneuvers should be supported. His advocacy and ideas were paramount to the success of this program. We would also like to thank Dr. L Patrick Purtell who continued to support this program during its later stages.

The essential element that led to the success of this program was the performance of the entire team of researchers working together. The authors are indebted to Dr. Michael L. Billet at the Applied Research Laboratory of The Pennsylvania State University and to Dr. Joe F. Thompson and Dr. J. Donald Trotter at the Engineering Research Center of the Mississippi State University for their overall support. In addition, the authors would like to thank Vehicle Control Technologies, Inc. for their help with our use of the six-degree-of-freedom equation solver within their vehicle trajectory code TRAJv. Finally, we extend our appreciation to Dr. Ray L. Shoaff, who used his considerable maneuvering expertise to help review this document.

# Table of Contents

	<u>Page</u>
List of Tables . . . . .	vii
List of Figures . . . . .	viii
Nomenclature . . . . .	xxii
1. Introduction . . . . .	1
1.1 Maneuvering . . . . .	1
1.2 Vehicle Motion . . . . .	2
1.3 Forces and Moments on a Vehicle . . . . .	2
1.4 Physics-Based Means of Predicting Vehicle Maneuvers . . . . .	5
2. Numerical Approach . . . . .	7
2.1 Reynolds-Averaged Navier-Stokes Equations . . . . .	7
2.2 Numerical Flux Vector . . . . .	9
2.3 Solution Algorithm . . . . .	10
2.4 Grid Generation . . . . .	11
3. Parallel Computing Methodology . . . . .	13
3.1 Parallel Algorithm . . . . .	13
3.2 Parallel Algorithmic Performance . . . . .	14
3.3 Problem Definition and Parallel Efficiency . . . . .	14
3.4 Parallel Performance Estimate . . . . .	15
3.4.1 Storage and CPU Requirements . . . . .	15
3.4.2 Communication Requirements . . . . .	15
3.5 Parallel Implementation . . . . .	16
3.6 Parallel Solution for Configurations with a Rotating Propulsor . . . . .	17

4. Turbulence Modeling . . . . .	18
4.1 Algebraic Turbulence Model . . . . .	18
4.2 Two-Equation Turbulence Models . . . . .	20
4.2.1 Low-Reynolds-Number $k-\epsilon$ Model . . . . .	21
4.2.2 Low-Reynolds-Number $q-\omega$ Model . . . . .	22
4.2.3 Adaptation of the $q-\omega$ Model to the UNCLE Flow Solver . . . . .	24
4.2.4 Solution of the Turbulence Equations . . . . .	25
4.3 Nonlinear Modeling of Anisotropy . . . . .	26
4.3.1 The Nonlinear $k-\epsilon$ Models . . . . .	27
4.3.2 Selection of a Nonlinear Model . . . . .	28
4.3.3 Implementation of the Nonlinear Model into the $q-\omega$ Model . . . . .	29
4.3.4 Calibration of the Model Constants . . . . .	29
4.3.5 Numerical Implementation . . . . .	30
5. Coupling with a Vehicle Dynamics Solver . . . . .	31
6. Propulsor Treatments . . . . .	35
6.1 Body-Force Propulsor Model . . . . .	35
6.2 Actual Rotating Propulsor . . . . .	36
7. Results with the Baseline Flow Solver . . . . .	37
7.1 Flat-Plate Boundary Layers . . . . .	37
7.2 SUBOFF Barebody . . . . .	37
7.3 Prolate Spheroid . . . . .	39
7.4 Appendage Junction Flow . . . . .	40
7.5 Vortex Preservation . . . . .	41
7.6 SUBOFF with Appendages . . . . .	42
7.6.1 Flow Field . . . . .	42
7.6.2 Hydrodynamic Forces and Moments . . . . .	44
7.7 Flapping Foil . . . . .	46
7.8 Prolate Spheroid (Unsteady) . . . . .	47
7.9 SUBOFF with a Body-Force Propeller Model . . . . .	49
7.10 Freestream Propeller . . . . .	50
7.11 SUBOFF with a Rotating Propeller . . . . .	50
7.12 High Reynolds Number Pump . . . . .	52
7.12.1 IGV Flow Field . . . . .	53
7.12.2 Rotor Blade Flow Field . . . . .	53
7.13 Moving Appendages . . . . .	54
8. Results Using Parallel Processing . . . . .	56

9. Results Using Two-Equation Turbulence Models . . . . .	59
9.1 Turbulence Decay . . . . .	59
9.2 Fully-Developed Channel Flow (Linear Model) . . . . .	60
9.3 Fully-Developed Channel Flow (Nonlinear Model) . . . . .	61
9.4 Flat-Plate Boundary Layers . . . . .	62
9.5 SUBOFF Barebody . . . . .	62
9.6 Prolate Spheroid (Nonlinear Model) . . . . .	63
10. Results Including Vehicle Dynamics . . . . .	64
10.1 Free-Falling Sphere . . . . .	64
10.2 Free-Falling Prolate Spheroid . . . . .	66
10.3 SUBOFF with a Body-Force Propeller Model . . . . .	68
10.3.1 Phase I: Accelerating Vehicle . . . . .	69
10.3.2 Phase II: Positive Buoyancy . . . . .	69
10.3.3 Phase III: Neutral Buoyancy . . . . .	70
10.3.4 Phase IV: Thrust Reduction . . . . .	70
10.4 Unconstrained Motion of SUBOFF with a Rotating Propeller . . . . .	71
10.5 Roll and Yaw Moments Applied to SUBOFF with a Rotating Propeller . . . . .	74
10.6 SUBOFF with a Propeller Rotating in Reverse . . . . .	75
10.6.1 Generation of a Ring Vortex . . . . .	76
10.6.2 Characteristics of the Ring Vortex . . . . .	77
10.6.3 Dynamic Response of the Vehicle . . . . .	77
10.6.4 Vehicle Trajectory . . . . .	79
11. Summary and Conclusions . . . . .	81
12. Future Work . . . . .	87
13. Bibliography . . . . .	90

## List of Tables

<u>Table</u>		<u>Page</u>
1	A Comparison of Nonlinear $k-\epsilon$ Models . . . . .	28
2	Fluctuating Velocities in the Logarithmic Layer of Fully-Developed Channel Flow . . . . .	30
3	SUBOFF Hull with a Sail and Four Stern Appendages ( $Re = 12,000,000$ , 600,000 Grid Points, and 500 Steps) . . . . .	57
4	SUBOFF Hull with a Sail, Sail Planes, and Four Stern Appendages ( $Re = 12,000,000$ and 500 Steps) . . . . .	57
5	SUBOFF Barebody ( $Re = 12,000,000$ , $18.115^\circ$ Incidence, 800,000 Grid Points, and 200 Steps) . . . . .	58
6	SUBOFF Hull with a Rotating Propeller ( $Re = 12,000,000$ , $0^\circ$ Incidence, 360,000 Grid Points, and 1 Revolution = 160 Steps) . . . . .	58
7	Key Properties for the Free-Falling Sphere Test Case . . . . .	64
8	Key Properties for the Free-Falling 6:1 Prolate-Spheroid Test Case . . . . .	66
9	Different Phases of the SUBOFF Maneuver with a Body-Force Propeller Model . . . . .	68
10	Key Properties for the Fully-Appended SUBOFF with a Rotating Propeller . . . . .	72
11	Key Computational Parameters for the Fully-Appended SUBOFF with a Rotating Propeller . . . . .	72

# List of Figures

<u>Figure</u>		<u>Page</u>
1	Iterations for 0(3) Residual Reduction . . . . .	100
2	Complexity for 0(3) Residual Reduction . . . . .	101
3	Effect of Subiterations on Convergence . . . . .	102
4	Approach for Flow Simulation on Parallel Machines . . . . .	103
5	Run Time for 500 Steps of SUBOFF on 1/4/8 Nodes of the IBM SP2 . . . . .	104
6	Run Time for 500 steps of 602,700-Grid-Point Case on 12 Nodes of the IBM SP2 . .	105
7	Run Time for 500 Steps of 3,363,360-Grid-Point Case on 32 Nodes of the IBM SP2 .	106
8	Calibration of the Nonlinear $q$ - $\omega$ Turbulence Model . . . . .	107
9	Schematic of the Coordinate Systems Used for Trajectory Prediction . . . . .	108
10	Velocity Profile for Laminar Flow Past a Flat Plate at $Re = 10,000$ . . . . .	109
11	Velocity Profile for Turbulent Flow Past a Flat Plate at $Re = 5,000,000$ . . . . .	110
12	Aspect Ratios of First Cells on the Surface for the Three SUBOFF Barebody Grids .	111
13	Convergence Histories of Multigrid and Single-Grid Solutions on the SUBOFF Barebody Grid I at $\alpha = 0^\circ$ and $Re = 12,000,000$ . . . . .	112
14	CPU Times of Multigrid and Single-Grid Solutions on the SUBOFF Barebody Grid I at $\alpha = 0^\circ$ and $Re = 12,000,000$ . . . . .	113
15	Convergence Histories of Multigrid and Single-Grid Solutions on the SUBOFF Barebody Grid II at $\alpha = 0^\circ$ and $Re = 12,000,000$ . . . . .	114
16	CPU Times of Multigrid and Single-Grid Solutions on the SUBOFF Barebody Grid II at $\alpha = 0^\circ$ and $Re = 12,000,000$ . . . . .	115
17	Convergence Histories of Multigrid and Single-Grid Solutions on the SUBOFF Barebody Grid III at $\alpha = 0^\circ$ and $Re = 12,000,000$ . . . . .	116

## List of Figures (continued)

<u>Figure</u>		<u>Page</u>
18	CPU Times of Multigrid and Single-Grid Solutions on the SUBOFF Barebody Grid III at $\alpha = 0^\circ$ and $Re = 12,000,000$ . . . . .	117
19	Computed and Measured Surface-Pressure Distributions on the SUBOFF Barebody Grid III at $\alpha = 0^\circ$ and $Re = 12,000,000$ . . . . .	118
20	Computed and Measured Skin-Friction Distributions on the SUBOFF Barebody Grid III at $\alpha = 0^\circ$ and $Re = 12,000,000$ . . . . .	119
21	Comparison of Computed Skin-Friction Distributions at Different Residual Levels about the SUBOFF Barebody at $\alpha = 0^\circ$ and $Re = 12,000,000$ . . . . .	120
22	Convergence Histories of Multigrid and Single-Grid Solutions on the SUBOFF Barebody Grid III at $\alpha = 0^\circ$ and $Re = 1,200,000,000$ . . . . .	121
23	CPU Times of Multigrid and Single-Grid Solutions on the SUBOFF Barebody Grid III at $\alpha = 0^\circ$ and $Re = 1,200,000,000$ . . . . .	122
24	Comparisons of Surface-Pressure Distributions on the SUBOFF Barebody and $Re = 12,000,000$ and $Re = 1,200,000,000$ (for $\alpha = 0^\circ$ ) . . . . .	123
25	Comparisons of Skin-Friction Distributions on the SUBOFF Barebody and $Re = 12,000,000$ and $Re = 1,200,000,000$ (for $\alpha = 0^\circ$ ) . . . . .	124
26	Convergence Histories of Multigrid and Single-Grid Solutions on the 6:1 Prolate Spheroid at $\alpha = 10^\circ$ and $Re = 4,200,000$ . . . . .	125
27	CPU Times of Multigrid and Single-Grid Solutions on the 6:1 Prolate Spheroid at $\alpha = 10^\circ$ and $Re = 4,200,000$ . . . . .	126
28	Computed and Measured Surface-Pressure Distributions on the 6:1 Prolate Spheroid at Different Circumferential Locations (for $\alpha = 10^\circ$ and $Re = 4,200,000$ ) . . . . .	127
29	Computed and Measured Profiles of the $u$ -Component of Velocity on the 6:1 Prolate Spheroid at $x/L = 0.4$ (for $\alpha = 10^\circ$ and $Re = 4,200,000$ ) . . . . .	128
30	Computed and Measured Profiles of the $u$ -Component of Velocity on the 6:1 Prolate Spheroid at $x/L = 0.6$ (for $\alpha = 10^\circ$ and $Re = 4,200,000$ ) . . . . .	129
31	Computed and Measured Profiles of the $u$ -Component of Velocity on the 6:1 Prolate Spheroid at $x/L = 0.772$ (for $\alpha = 10^\circ$ and $Re = 4,200,000$ ) . . . . .	130

## List of Figures (continued)

<u>Figure</u>	<u>Page</u>
32 NACA 0020 Wing Mounted on a Flat Plate . . . . .	131
33 Convergence Histories of Multigrid and Single-Grid Solutions for the Wing-Body Junction Flow at $\alpha = 0^\circ$ and $Re = 500,000$ . . . . .	132
34 CPU Times of Multigrid and Single-Grid Solutions for the Wing-Body Junction Flow at $\alpha = 0^\circ$ and $Re = 500,000$ . . . . .	133
35 Computed and Measured Surface-Pressure Distributions on the Wing Surface for the Wing-Body Junction Flow at $\alpha = 0^\circ$ and $Re = 500,000$ . . . . .	134
36 Computed and Measured Surface-Pressure Contours on the Flat-Plate Surface for the Wing-Body Junction Flow at $\alpha = 0^\circ$ and $Re = 500,000$ . . . . .	135
37 Computed Particle Traces and Measured Skin-Friction Lines on the Flat-Plate Surface for the Wing-Body Junction Flow at $\alpha = 0^\circ$ and $Re = 500,000$ . . . . .	136
38 Computed and Measured Profiles of the $u$ -Component of Velocity for the Wing-Body Junction Flow at $x/L = -0.157$ (for $\alpha = 0^\circ$ and $Re = 500,000$ ) . . . . .	137
39 Computed and Measured Profiles of the $u$ -Component of Velocity for the Wing-Body Junction Flow at $x/L = 0.003$ (for $\alpha = 0^\circ$ and $Re = 500,000$ ) . . . . .	138
40 Computed and Measured Profiles of the $u$ -Component of Velocity for the Wing-Body Junction Flow at $x/L = 0.167$ (for $\alpha = 0^\circ$ and $Re = 500,000$ ) . . . . .	139
41 Computed and Measured Profiles of the $u$ -Component of Velocity for the Wing-Body Junction Flow at $x/L = 1.048$ (for $\alpha = 0^\circ$ and $Re = 500,000$ ) . . . . .	140
42 Vortex Core Pressure History for a Coarse 211x31 (6,541 Point) Grid . . . . .	141
43 Initial Distribution of $p$ , $u$ , and $v$ for an Idealized Thomson-Rankine Vortex . . . . .	142
44 Distribution of $p$ , $u$ , and $v$ for a Vortex That Has Traveled 45 Core Radii, as Computed on a Coarse 211x31 (6,541 Point) Grid . . . . .	143
45 Vortex Core Pressure History for a Medium 421x61 (25,681 Point) Grid . . . . .	144
46 Comparison of Temporal Accuracy for the Vortex Core Pressure Computed on a Medium 421x61 (25,681 Point) Grid . . . . .	145

## List of Figures (continued)

<u>Figure</u>		<u>Page</u>
47	Vortex Core Pressure History for a Fine 841x121 (101,761 Point) Grid . . . . .	146
48	Aft Region of the 8-Block Grid for SUBOFF with Four Stern Appendages . . . . .	147
49	Convergence Histories of Multigrid Solutions for SUBOFF with Four Stern Appendages at 0° and 2° Angles of Attack and $Re = 12,000,000$ . . . . .	148
50	Computed and Measured Static-Pressure Distributions on the Hull of SUBOFF with Four Stern Appendages at a 0° Angle of Attack and $Re = 12,000,000$ . . . . .	149
51	Computed and Measured Static-Pressure Distributions on the Hull of SUBOFF with Four Stern Appendages at 2° Angle of Attack and $Re = 12,000,000$ . . . . .	150
52	Computed and Measured Static-Pressure Distributions on the Upper Fin Surface of SUBOFF with Four Stern Appendages at 0° Angle of Attack and $Re = 12,000,000$ .	151
53	Computed and Measured Static-Pressure Distributions on the Upper Fin Surface of SUBOFF with Four Stern Appendages at 2° Angle of Attack and $Re = 12,000,000$ .	152
54	Computed and Measured Contours of the $u$ -Component of Velocity at $x/L = 0.978$ of SUBOFF with Four Stern Appendages at 0° Angle of Attack and $Re = 12,000,000$ .	153
55	Side View of the 12-Block, Fine Grid for SUBOFF with a Sail and Four Stern Appendages . . . . .	154
56	Convergence Histories of Multigrid Solutions for SUBOFF with a Sail and Four Stern Appendages on Three Grids at 0° and 2° Angles of Attack and $Re = 12,000,000$ .	155
57	Computed and Measured Static-Pressure Distributions on the Hull of SUBOFF with a Sail and Four Stern Appendages at a 0° Angle of Attack and $Re = 12,000,000$ .	156
58	Computed and Measured Static-Pressure Distributions on the Sail Surface of SUBOFF with a Sail and Four Stern Appendages at a 0° Angle of Attack and $Re = 12,000,000$ .	157
59	Computed and Measured Static-Pressure Distributions on the Sail Surface of SUBOFF with a Sail and Four Stern Appendages at a 2° Angle of Attack and $Re = 12,000,000$ .	158
60	Computed and Measured Static-Pressure Distributions on the Upper Fin Surface of SUBOFF with a Sail and Four Stern Appendages at a 0° Angle of Attack and $Re = 12,000,000$ . . . . .	159

## List of Figures (continued)

<u>Figure</u>		<u>Page</u>
61	Computed and Measured Static-Pressure Distributions on the Upper Fin Surface of SUBOFF with a Sail and Four Stern Appendages at a $2^\circ$ Angle of Attack and $Re = 12,000,000$ . . . . .	160
62	Computed and Measured Contours of the $u$ -Component of Velocity at $x/L = 0.978$ of SUBOFF with a Sail and Four Stern Appendages at $0^\circ$ Angle of Attack and $Re = 12,000,000$ . . . . .	161
63	Comparisons of Crossflow Velocity Vectors at $x/L = 0.978$ of SUBOFF with a Sail and Four Stern Appendages on Three Different Grids at a $0^\circ$ Angle of Attack and $Re = 12,000,000$ . . . . .	162
64	Computed and Measured Axial Force, Lateral Force, and Yawing Moment for the SUBOFF Barebody at Various Angles of Drift and $Re = 14,000,000$ . . . . .	163
65	Convergence Histories of the Computed Axial Force, Lateral Force, and Yawing Moment for the SUBOFF Barebody at a $10.05^\circ$ Angle of Drift and $Re = 14,000,000$ . . . . .	164
66	Computed and Measured Axial Force, Lateral Force, and Yawing Moment for SUBOFF with Four Stern Appendages at Various Angles of Drift and $Re = 14,000,000$ . . . . .	165
67	Convergence Histories of the Computed Axial Force, Lateral Force, and Yawing Moment for SUBOFF with Four Stern Appendages at an $8^\circ$ Angle of Drift and $Re = 14,000,000$ . . . . .	166
68	Computed and Measured Axial Force, Lateral Force, and Yawing Moment for SUBOFF with Four Stern Appendages on Three Different Grids at Various Angles of Drift and $Re = 14,000,000$ . . . . .	167
69	Computed and Measured Axial Force, Lateral Force, and Yawing Moment for SUBOFF with a Sail at Various Angles of Drift and $Re = 14,000,000$ . . . . .	168
70	Computed and Measured Normal Force, Rolling Moment, and Pitching Moment for SUBOFF with a Sail at Various Angles of Drift and $Re = 14,000,000$ . . . . .	169
71	Convergence Histories of the Computed Axial Force, Lateral Force, and Yawing Moment for SUBOFF with a Sail at an $8^\circ$ Angle of Drift and $Re = 14,000,000$ . . . . .	170
72	Schematic of the Flapping Foil Experiment . . . . .	171

## List of Figures (continued)

<u>Figure</u>		<u>Page</u>
73	Computed Velocity Magnitude for the Flapping Foil Experiment at $Re = 3,780,000$ after Five Complete Periods of Motion of the Two, Small NACA 0025 Hydrofoils . . . . .	172
74	Schematic of the Prescribed Unsteady Plunge, Turning, and Pitch-Up Maneuvers for a 6:1 Prolate Spheroid . . . . .	173
75	Computed and Measured Surface-Pressure Distributions for the Plunge Maneuver of a 6:1 Prolate Spheroid at $Re = 4,200,000$ : (a) Displacement of Six Inches . . . . . (b) Displacement of Twelve Inches . . . . .	174 175
76	Computed and Measured Surface-Pressure Distributions for the Turning Maneuver of a 6:1 Prolate Spheroid at $Re = 4,200,000$ : (a) 2° of Motion . . . . . (b) 4° of Motion . . . . . (c) 6° of Motion . . . . . (d) 8° of Motion . . . . . (e) 10° of Motion . . . . .	176 177 178 179 180
77	Computed and Measured Surface-Pressure Distributions for the Pitch-Up Maneuver of a 6:1 Prolate Spheroid at $Re = 4,200,000$ : (a) 5° of Motion . . . . . (b) 10° of Motion . . . . . (c) 15° of Motion . . . . . (d) 20° of Motion . . . . . (e) 25° of Motion . . . . . (f) 30° of Motion . . . . .	181 182 183 184 185 186
78	Steady-State Computed Contours of Surface Pressure on a Fully-Appended SUBOFF at $Re = 12,000,000$ with Contours of Axial Velocity on the Plane Where the Body-Force Propeller Model is Located . . . . .	187
79	Steady-State Computed Contours of the $u$ -Component of Velocity at the Plane of Symmetry on a Fully-Appended SUBOFF at $Re = 12,000,000$ . . . . .	188
80	Snapshots of the Computed Contours of the $u$ -Component of Velocity at the Plane of Symmetry for the Prescribed 15° Pitch-Up Maneuver of a Fully-Appended SUBOFF at $Re = 12,000,000$ . . . . .	189

## List of Figures (continued)

<u>Figure</u>	<u>Page</u>
81 Snapshots of the Computed Contours of the $u$ -Component of Velocity at the Plane of Symmetry for the Prescribed $15^\circ$ Pitch, $5^\circ$ Yaw, and $5^\circ$ Roll Maneuver of a Fully-Appended SUBOFF at $Re = 12,000,000$ . . . . .	190
82 3-Block Grid for Marine Propeller 4119 Tested in a Uniform Freestream . . . . .	191
83 Computed Contours of the $u$ -Component of Velocity for Two Different Multigrid Cycles of Marine Propeller 4119 Tested in a Uniform Freestream at $Re = 576,000$ (Where the Top Contour Plot Refers to One Multigrid Cycle Per Time Step and the Bottom Contour Plot Refers to Two Multigrid Cycles Per Time Step) . . . . .	192
84 Computed and Measured Static-Pressure Distributions on the Blade Surfaces and Thrust and Torque Coefficients of Marine Propeller 4119 Tested in a Uniform Freestream at $Re = 576,000$ . . . . .	193
85 Solid-Body Model of the Appended SUBOFF with a Rotating Propeller, Including a Portion of the Surface Grid for the 13-Block Grid . . . . .	194
86 Blade Pressure History, Using Local Time Stepping in the Beginning, for the Appended SUBOFF with a Rotating Propeller at $0^\circ$ Angle of Attack and $Re = 12,000,000$ . . . . .	195
87 Blade Pressure History, Without Using Local Time Stepping in the Beginning, for the Appended SUBOFF with a Rotating Propeller at $0^\circ$ Angle of Attack and $Re = 12,000,000$ . . . . .	196
88 Computed Contours of the Axial Velocity in the Aft Region for the Periodic Solution of the Appended SUBOFF with a Rotating Propeller at $0^\circ$ Angle of Attack and $Re = 12,000,000$ . . . . .	197
89 Solid-Body Model of the Fully-Appended SUBOFF with a Rotating Propeller, Including a Portion of the 51-Block Grid . . . . .	198
90 Computed Contours of Surface Pressure for the Periodic Solution of the Fully-Appended SUBOFF with a Rotating Propeller at $0^\circ$ Angle of Attack and $Re = 12,000,000$ . . . . .	199

## List of Figures (continued)

<u>Figure</u>		<u>Page</u>
91	Solid-Body Model and Computational Grid for HIREP: (a) Downstream View . . . . . (b) Inboard View . . . . . (c) Computational Grid . . . . . (d) Enlarged View of Interface . . . . .	200 200 200 200
92	Computed and Measured Static-Pressure Distributions on the Inlet Guide Vanes of HIREP at $Re = 2,300,000$ . . . . .	201
93	Computed and Measured Velocity Distributions Between the Inlet Guide Vanes and the Rotor Blades of HIREP at $Re = 2,300,000$ : (a) Circumferentially Averaged . . . . . (b) Circumferential Variation . . . . .	202 202
94	Computed and Measured Static-Pressure Distributions on the Rotor Blades of HIREP at $Re = 5,500,000$ (Using the Inlet Relative Velocity at 90% Span) . . . . .	203
95	Experimentally Observed Skin-Friction Lines and Computed Particle Traces on the Rotor Blades of HIREP at $Re = 5,500,000$ (Using the Inlet Relative Velocity at 90% Span): (a) Observed Experimental Skin-Friction Lines . . . . . (b) Computed Particle Traces . . . . .	204 204
96	Computed and Measured Velocity Distributions Downstream of the Rotor Blades of HIREP at $Re = 5,500,000$ (Using the Inlet Relative Velocity at 90% Span): (a) Circumferentially Averaged . . . . . (b) Circumferential Variation . . . . .	205 205
97	Computed and Measured Velocity Contours Downstream of the Rotor Blades of HIREP at $Re = 5,500,000$ (Using the Inlet Relative Velocity at 90% Span) . . . . .	206
98	SUBOFF Stern Appendage on a Flat Plate, with a Small Gap and the Corresponding Grid Existing Between the Two Surfaces . . . . .	207
99	Snapshot of the Computed The u-Component of Velocity at $10^\circ$ Deflection of a SUBOFF Stern Appendage Moving Over a Flat Plate at $Re = 12,000,000$ . . . . .	208
100	Snapshot of the Particle Traces Looking Up Towards the Bottom of the Appendage at $10^\circ$ Deflection of a SUBOFF Stern Appendage Moving Over a Flat Plate at $Re = 12,000,000$ . . . . .	209

## List of Figures (continued)

<u>Figure</u>		<u>Page</u>
101	Convergence Behavior of the Parallel Algorithm for the Lateral Force Coefficient at an Angle of Drift of $18.11^\circ$ . . . . .	210
102	Spatial Decay of $q$ and $\omega$ in Homogeneous Turbulence . . . . .	211
103	Unsteady Decay of $q$ and $\omega$ in Homogeneous Turbulence . . . . .	212
104	Velocity Profile in a Two-Dimensional Channel . . . . .	213
105	Turbulence Profiles in a Two-Dimensional Channel . . . . .	214
106	Average Velocity Fluctuations in a Two-Dimensional Channel . . . . .	215
107	Shear Stress in a Two-Dimensional Channel . . . . .	216
108	Secondary Velocity Profiles in a Square Duct . . . . .	217
109	Skin-Friction Coefficient for a Turbulent Flat Plate Boundary Layer . . . . .	218
110	Surface Pressure for a Turbulent Flat Plate Boundary Layer . . . . .	219
111	Velocity Profile for a Flat Plate Boundary Layer at $Re_x = 4,000,000$ . . . . .	220
112	Pressure Distribution on the SUBOFF Barebody . . . . .	221
113	Skin-Friction Distribution on the SUBOFF Barebody . . . . .	222
114	Boundary Layer Velocity Profiles on a 6:1 Prolate Spheroid Using the Anisotropic Turbulence Model ( $x/L = 0.4$ , $\phi = 100^\circ$ , $\alpha = 10^\circ$ , and $Re = 4,200,000$ ) . . . . .	223
115	Surface Flow Angles on a 6:1 Prolate Spheroid Using the Anisotropic Turbulence Model ( $x/L = 0.4$ , $\phi = 100^\circ$ , $\alpha = 10^\circ$ , and $Re = 4,200,000$ ) . . . . .	224
116	Boundary Layer Normal-Stress Profiles on a 6:1 Prolate Spheroid Using the Anisotropic Turbulence Model ( $x/L = 0.4$ , $\phi = 100^\circ$ , $\alpha = 10^\circ$ , and $Re = 4,200,000$ ) . . . . .	225
117	Boundary Layer Shear-Stress Profiles on a 6:1 Prolate Spheroid Using the Anisotropic Turbulence Model ( $x/L = 0.4$ , $\phi = 100^\circ$ , $\alpha = 10^\circ$ , and $Re = 4,200,000$ ) . . . . .	226
118	Schematic of the Free-Falling Sphere Calculation . . . . .	227

## List of Figures (continued)

<u>Figure</u>	<u>Page</u>
119 Body-Fixed Velocity and Rotation Rate Histories for the Free-Falling Sphere Obtained from Integration of the 6DOF Equations:	
(a) Velocities . . . . .	228
(b) Rotation Rates . . . . .	228
120 Inertial Trajectory for the Free-Falling Sphere Obtained from Integration of the Kinematic Equations:	
(a) Orientation . . . . .	229
(b) Position . . . . .	229
121 Particle Traces in the Relative Velocity Field for the Free-Falling Sphere Showing the Location of the Lee-Side Ring Vortex . . . . .	230
122 Schematic of the Free-Falling Ellipsoid Calculation . . . . .	231
123 Body-Fixed Velocity and Rotation Rate Histories for the Free-Falling 6:1 Prolate Spheroid Obtained from Integration of the 6DOF Equations:	
(a) Velocities . . . . .	232
(b) Rotation Rates . . . . .	232
124 Inertial Trajectory for the Free-Falling 6:1 Prolate Spheroid Obtained from Integration of the Kinematic Equations:	
(a) Orientation . . . . .	233
(b) Position . . . . .	233
125 Particle Traces in the Relative Velocity Field for the Free-Falling 6:1 Prolate Spheroid Showing the Location of the Lee-Side Ring Vortex . . . . .	234
126 Schematic of the Initial Condition for the Actuator Disc-Propelled SUBOFF Calculation Showing the Relative Locations of the Inertial and Body-Fixed Coordinate Systems . . . . .	235
127 Body-Fixed Velocity and Rotation Rate Histories for the Propelled SUBOFF Obtained from Integration of the 6DOF Equations:	
(a) Velocities . . . . .	236
(b) Rotation Rates . . . . .	236

## List of Figures (continued)

<u>Figure</u>		<u>Page</u>
128	Inertial Trajectory for the Propelled SUBOFF Obtained from Integration of the Kinematic Equations:	
(a)	Orientation . . . . .	237
(b)	Position . . . . .	237
129	Contours of Relative Velocity in the Geometric Symmetry Plane for the Propelled SUBOFF, $t = 0.02$ (Beginning of Phase I) . . . . .	238
130	Contours of Relative Velocity in the Geometric Symmetry Plane for the Propelled SUBOFF, $t = 2.52$ (Between Phases I and II) . . . . .	239
131	Contours of Relative Velocity in the Geometric Symmetry Plane for the Propelled SUBOFF, $t = 5.02$ (End of the Simulation) . . . . .	240
132	Contours of the $u$ -Component of Velocity at $t = 0.0$ for the Fully-Appended SUBOFF with a Rotating Propeller at $Re = 12,800,000$ . . . . .	241
133	Unsteady Pressure Signature on a Blade at $t = 0.0$ for the Fully-Appended SUBOFF with a Rotating Propeller at $Re = 12,800,000$ . . . . .	242
134	Surface Pressure Distribution on the Pressure Surface (Left) and Suction Surface (Right) of the Rotating Propeller Blades at $t = 0.0$ for the Fully-Appended SUBOFF at $Re = 12,800,000$ . . . . .	243
135	Definitions of the Force, Moment, and Velocity Components in the Body-Fixed Coordinate System . . . . .	244
136	Time History of the Forces, the $u$ -Component of the Vehicle Velocity, and the Propeller Angular Velocity for the Unconstrained Motion of the Fully-Appended SUBOFF with a Rotating Propeller . . . . .	245
137	Time History of the Moments, the $u$ -Component of the Vehicle Velocity, and the Propeller Angular Velocity for the Unconstrained Motion of the Fully-Appended SUBOFF with a Rotating Propeller . . . . .	246
138	Time History of the Angular Rates, the $u$ -Component of the Vehicle Velocity, and the Propeller Angular Velocity for the Unconstrained Motion of the Fully-Appended SUBOFF with a Rotating Propeller . . . . .	247

## List of Figures (continued)

<u>Figure</u>		<u>Page</u>
139	Time History of the Vehicle's Orientation, the $u$ -Component of the Vehicle Velocity, and the Propeller Angular Velocity for the Unconstrained Motion of the Fully-Appended SUBOFF with a Rotating Propeller . . . . .	248
140	Time History of the Forces and the $v$ -Component of the Vehicle Velocity (Sideslip) for the Roll and Yaw Moments Applied to the Fully-Appended SUBOFF with a Rotating Propeller . . . . .	249
141	Time History of the Moments for the Roll and Yaw Moments Applied to the Fully-Appended SUBOFF with a Rotating Propeller . . . . .	250
142	Time History of the Angular Rates and the $v$ -Component of the Vehicle Velocity (Sideslip) for the Roll and Yaw Moments Applied to the Fully-Appended SUBOFF with a Rotating Propeller . . . . .	251
143	Time History of the Vehicle's Orientation and the $v$ -Component of the Vehicle Velocity (Sideslip) for the Roll and Yaw Moments Applied to the Fully-Appended SUBOFF with a Rotating Propeller . . . . .	252
144	Starboard View of Surface-Pressure Distribution for the Roll and Yaw Moments Applied to the Fully-Appended SUBOFF with a Rotating Propeller . . . . .	253
145	Stern View of Surface-Pressure Distribution for the Roll and Yaw Moments Applied to the Fully-Appended SUBOFF with a Rotating Propeller . . . . .	254
146	Particle Traces Showing a Rotor Blade Tip Vortex for the Roll and Yaw Moments Applied to the Fully-Appended SUBOFF with a Rotating Propeller . . . . .	255
147	Time History of the Vehicle's Path and the $u$ -Component of the Vehicle Velocity for the Roll and Yaw Moments Applied to the Fully-Appended SUBOFF with a Rotating Propeller . . . . .	256
148	Time History of the Forces, the $u$ -Component of the Vehicle Velocity, and the Propeller Angular Velocity for the Fully-Appended SUBOFF with a Propeller Rotating in Reverse . . . . .	257
149	Ring Vortex Formation at $t = 2.01$ (with the Propeller Colored by Surface Pressure and the Particle Traces Colored by the Velocity Magnitude) . . . . .	258
150	Side View of the Ring Vortex at $t = 2.01$ (with the Propeller Colored by Surface Pressure and the Particle Traces Colored by the Velocity Magnitude) . . . . .	259

## List of Figures (continued)

<u>Figure</u>	<u>Page</u>
151 Asymmetric Structure of the Ring Vortex at $t = 2.01$ (with the Propeller Colored by Surface Pressure and the Particle Traces Colored by the Velocity Magnitude) . . . . .	260
152 Ring Vortex Position at $t = 2.33$ (with the Propeller Colored by Surface Pressure and the Particle Traces Colored by the Velocity Magnitude) . . . . .	261
153 Contour Lines of Static Pressure Showing the Varying Strength of the Vortex Ring Along Its Core (with the Propeller Colored by the Surface Pressure) . . . . .	262
154 Ring Vortex Becoming Weaker and More Symmetric as Vehicle Decelerates to Time $t = 5.15$ (with the Propeller Colored by Surface Pressure and the Particle Traces Colored by the Velocity Magnitude) . . . . .	263
155 Side View of the Ring Vortex at $t = 5.15$ (with the Propeller Colored by Surface Pressure and the Particle Traces Colored by the Velocity Magnitude) . . . . .	264
156 Low-Pressure Region of Ring Vortex Image Rotating in the Opposite Direction of Blade Rotation:	
(a) $t = 1.86$ . . . . .	265
(b) $t = 2.01$ . . . . .	265
(c) $t = 2.17$ . . . . .	265
(d) $t = 2.33$ . . . . .	265
(e) $t = 2.48$ . . . . .	266
(f) $t = 2.64$ . . . . .	266
(g) $t = 2.80$ . . . . .	266
(h) $t = 2.96$ . . . . .	266
(i) $t = 3.11$ . . . . .	267
(j) $t = 3.27$ . . . . .	267
(k) $t = 3.43$ . . . . .	267
(l) $t = 3.74$ . . . . .	267
(m) $t = 3.90$ . . . . .	268
(n) $t = 4.06$ . . . . .	268
(o) $t = 4.21$ . . . . .	268
(p) $t = 4.37$ . . . . .	268
(q) $t = 4.53$ . . . . .	269
(r) $t = 4.68$ . . . . .	269
(s) $t = 5.15$ . . . . .	269
157 Time History of the Forces, the Location of the Ring Vortex Image, the $u$ -Component of the Vehicle Velocity, and the Propeller Angular Velocity for the Fully-Appended SUBOFF with a Propeller Rotating in Reverse . . . . .	270

## List of Figures (continued)

<u>Figure</u>		<u>Page</u>
158	Large-Amplitude, Low-Frequency and Low-Amplitude, High-Frequency Force Oscillations for the Fully-Appended SUBOFF with a Propeller Rotating in Reverse . . .	271
159	Time History of the Angular Rates, the $u$ -Component of the Vehicle Velocity, and the Propeller Angular Velocity for the Fully-Appended SUBOFF with a Propeller Rotating in Reverse . . . . .	272
160	Time History of the Moments, the $u$ -Component of the Vehicle Velocity, and the Propeller Angular Velocity for the Fully-Appended SUBOFF with a Propeller Rotating in Reverse . . . . .	273
161	Time History of the Vehicle's Orientation, the $u$ -Component of the Vehicle Velocity, and the Propeller Angular Velocity for the Fully-Appended SUBOFF with a Propeller Rotating in Reverse . . . . .	274
162	Time History of the Vehicle's Linear Velocity Components and the Propeller Angular Velocity for the Fully-Appended SUBOFF with a Propeller Rotating in Reverse . . . .	275
163	Vehicle's Path for the Fully-Appended SUBOFF with a Propeller Rotating in Reverse	276

## Nomenclature

6DOF	six-degree-of-freedom (equations)
$A$	annular area through the propulsor
$\mathbf{A}$	matrix = $\partial \mathbf{F} / \partial \mathbf{Q}$ ; “mass” matrix
$\bar{\mathbf{A}}$	Roe matrix, containing the negative eigenvalues of $\bar{\mathbf{A}}$
$\mathbf{b}$	inertial coupling vector
$B$	vehicle buoyancy
$c$	chord length
$C_{1,2}$	empirical constants associated with $\omega$
$C_{1,2,3}$	empirical constants associated with the nonlinear turbulence model ( $C_\beta$ , with $\beta = 1, 2, 3$ )
$C_{CP}$	empirical constant in the algebraic turbulence model = 1.6
$C_f$	skin-friction coefficient = $\frac{\tau_w}{\frac{1}{2} \rho V_\infty^2}$
$C_{kleb}$	empirical constant in the algebraic turbulence model = 0.3
$C_p$	static-pressure coefficient = $\frac{p - p_\infty}{\frac{1}{2} \rho V_\infty^2}$
$C_T$	thrust coefficient = $\frac{Thrust}{\frac{1}{2} \rho V_\infty^2 A}$
$C_Q$	torque coefficient = $\frac{Torque}{\frac{1}{2} \rho V_\infty^2 A r_{tip}}$
$C_{wk}$	empirical constant in the algebraic turbulence model = 1.0

## Nomenclature (continued)

$C_\beta$	empirical constants associated with the nonlinear turbulence model ( $C_\beta$ , with $\beta = 1, 2, 3$ )
$C_{\epsilon 1}$	empirical constant associated with the production of $\epsilon = 1.44$
$C_{\epsilon 2}$	empirical constant associated with the destruction of $\epsilon = 1.92$
$C_\mu$	empirical constant associated with the eddy viscosity = 0.09
CFL	nondimensional time step or the Courant-Fredrichs-Lowy stability condition
CPU	central processing unit
$D$	dissipation rate of turbulence at the wall
$e_i$	quaternions (vehicle inertial orientation), where $i = 0, 1, 2$ , or 3
$E$	low-Reynolds number term associated with the $\epsilon$ -equation
$E_{ij}$	mean strain rate tensor
EAGLEView	an interactive surface and grid-generation software package based on a previously-developed grid-generation code called EAGLE
$f_\mu$	damping function associated with the eddy viscosity
$f$	vector of forces and moments
$F(x)$	function
$F(y)$	function used in the algebraic turbulence model
$F$	forces acting on the vehicle;
	flux vector associated with the $\xi$ -coordinate direction
$F_{B_x}(r)$	axial body force per unit volume as a function of $r$
$F_{B_0}(r)$	circumferential body force per unit volume as a function of $r$
$F_{kleb}$	Klebanoff intermittency factor in the algebraic turbulence model
$F_{max}$	maximum value of $F(y)$ that occurs in the boundary layer or wake profile

## Nomenclature (continued)

$F_{wake}$	empirical function in the algebraic turbulence model (boundary layer wake region)
$F_x$	hydrodynamically-induced force in the $x$ -direction (body-fixed frame of reference)
$F_y$	hydrodynamically-induced force in the $y$ -direction (body-fixed frame of reference)
$F_z$	hydrodynamically-induced force in the $z$ -direction (body-fixed frame of reference)
$F_{ij}$	second-order tensor associated with the nonlinear turbulence model
$Fr$	Froude number
$\mathcal{F}(x)$	vector function
$g$	acceleration due to gravity
$g(r)$	propulsor blade circulation distribution as a function of $r$
$g_i$	buoyancy
$G$	flux vector associated with the $\eta$ -coordinate direction
$Gr$	Grashof number
<b>GUM_B</b>	General Unstructured Multi-Block Structured Grid Generator
$h$	angular momentum vector of the vehicle
$H$	flux vector associated with the $\xi$ -coordinate direction
<b>HIREP</b>	high Reynolds number pump
$i$	index
$I$	identity matrix
$I_a$	identity matrix, except that the first diagonal element is zero
$I_J$	number of time steps before updating the flux Jacobian linearizations
$I_S$	number of subiterations
$I_x$	moment of inertia about the $x$ -axis (body-fixed frame of reference)

## Nomenclature (continued)

$I_{xy}$	product of inertia with respect to the $x$ - and $y$ -axes (body-fixed frame of reference)
$I_{xz}$	product of inertia with respect to the $x$ - and $z$ -axes (body-fixed frame of reference)
$I_y$	moment of inertia about the $y$ -axis (body-fixed frame of reference)
$I_{yz}$	product of inertia with respect to the $y$ - and $z$ -axes (body-fixed frame of reference)
$I_z$	moment of inertia about the $z$ -axis (body-fixed frame of reference)
IGES	initial graphics exchange specification
IGV	inlet guide vane
I/O	input/output
$J$	metric Jacobian
$k$	turbulent kinetic energy
$k_i$	transformation metric quantities ( $k = \xi, \eta$ , or $\zeta$ ) with differentiation with respect to $i$ (where $i = x, y, z$ , or $t$ )
K	Clauser constant used in the algebraic turbulence model = 0.0168
$\mathbf{K}$	flux vector (equal to $\mathbf{F}$ , $\mathbf{G}$ , or $\mathbf{H}$ )
$K_p$	static-pressure coefficient = $\frac{p - p_\infty}{\frac{1}{2} \rho U_{tip}^2}$
$l$	turbulence mixing length
$L$	vehicle length
$L_m$	message length for a single data surface (Mb)
LGD	localized grid distortion
LU	lower-upper matrix decomposition
$m$	vehicle mass

## Nomenclature (continued)

$M$	moments acting on the vehicle
$M_x$	hydrodynamically-induced moment in the $x$ -direction (body-fixed frame of reference)
$M_y$	hydrodynamically-induced moment in the $y$ -direction (body-fixed frame of reference)
$M_z$	hydrodynamically-induced moment in the $z$ -direction (body-fixed frame of reference)
Mflops	million floating point operations
MPI	Message Passing Interface
MUSCL	monotone upstream-centered scheme for conservation laws
$n_i$	number of grid points in the $i^{\text{th}}$ direction (where $i = \xi, \eta$ , or $\zeta$ )
$N$	number of finite-volume cells
$N_b$	number of blocks
$N_m$	number of block interfaces exchanging messages
NURBS	non-uniform rational B-spline
$p$	(roll) rotation rate about the $x$ -axis (body-fixed frame of reference); static pressure
$p_\infty$	reference static pressure
$P$	number of computing processors
$P_T$	turbulent pressure
PLOT3D	flow visualization code with a specific data format
$q$	(pitch) rotation rate about the $y$ -axis (body-fixed frame of reference); square root of the turbulent kinetic energy; integer such that $P > 2^{q-1}$

## Nomenclature (continued)

$q^+$	dimensionless value of $q$ in the inner boundary layer = $q/u_\tau$
$Q$	vector of dependent variables
$\Delta Q$	change in $Q$ during one solution time increment
$r$	(yaw) rotation rate about the $z$ -axis (body-fixed frame of reference); propulsor radius; normal distance from the surface of a prolate spheroid
$r_{hub}$	representative radius of the propulsor blade hub
$r_{tip}$	representative radius of the propulsor blade tip
$R_{CPU}$	effective processor speed in Mflops
$R_\xi$	similarity matrix (having the right eigenvectors of $\bar{A}$ as columns)
RAM	random-access memory
RANS	Reynolds-averaged Navier-Stokes (equations)
RANS/6DOF	coupled RANS and 6DOF (equations)
$Re$	Reynolds number
$Re_x$	Reynolds number with respect to $x$
$R_T$	turbulent Reynolds number
$s$	vector of velocities and rotation rates
$S$	vector of source terms associated with the two-equation turbulence model
$S_{\beta ij}$	tensor of quadratic terms associated with the nonlinear model
SGS	symmetric Gauss-Seidel iteration method
SOE	submerged operating envelope
SUBOFF	submarine-type model and code validation experimental project

## Nomenclature (continued)

$t$	time
$t_{comm}$	estimated total time required for message passing
$T$	mean temperature
$T_{k_i}$	viscous flux components in curvilinear coordinates
TRAJv	vehicle trajectory code by Smith and Watkinson [1994]
$u$	linear (surge or streamwise) vehicle velocity in the $x$ -direction (body-fixed frame of reference);  flow velocity in the $x$ -direction
$u^+$	dimensionless velocity in the inner boundary layer = $u/u_\tau$
$u_i$	$i^{th}$ component of the fluctuating velocity
$u_\tau$	shear or friction velocity = $\sqrt{\tau_w/\rho}$
$U$	contravariant flow velocity component in the $\xi$ -coordinate direction
$U_{diff}$	difference between the maximum and minimum total velocity in the boundary layer or wake profile, used in the algebraic turbulence model
$U_i$	$i^{th}$ component of the mean velocity
$U_{tip}$	rotor blade tip speed
UNCLE	<u>un</u> steady <u>computation of field</u> <u>equations</u> (flow solver computer code)
$v$	linear (sway or sideslip) vehicle velocity in the $y$ -direction (body-fixed frame of reference);  flow velocity in the $y$ -direction
$v$	velocity vector of the vehicle
$V$	contravariant flow velocity component in the $\eta$ -coordinate direction

## Nomenclature (continued)

$V_\infty$	vehicle speed; reference velocity
$w$	linear (heave or plunge) vehicle velocity in the $z$ -direction (body-fixed frame of reference);  flow velocity in the $z$ -direction
$W$	contravariant flow velocity component in the $\xi$ -coordinate direction;
	vehicle weight
$x$	axial body-fixed Cartesian coordinate
$x_B$	location of the vehicle center of buoyancy in the $x$ -direction (body-fixed frame of reference)
$x_G$	location of the vehicle center of gravity in the $x$ -direction (body-fixed frame of reference)
$x_j$	$j^{th}$ Cartesian coordinate
$\Delta x$	axial thickness of the body-force propulsor model (actuator disc or actuator duct)
$X$	first inertial Cartesian coordinate
$y$	horizontal body-fixed Cartesian coordinate;  normal distance to the wall
$y^+$	dimensionless distance normal to a surface in the inner boundary layer = $yu_\tau/v$
$y_B$	location of the vehicle center of buoyancy in the $y$ -direction (body-fixed frame of reference)
$y_G$	location of the vehicle center of gravity in the $y$ -direction (body-fixed frame of reference)
$y_{max}$	value of $y$ at which $F_{max}$ occurs
$Y$	second inertial Cartesian coordinate
$z$	vertical body-fixed Cartesian coordinate

## Nomenclature (continued)

$z_B$	location of the vehicle center of buoyancy in the $z$ -direction (body-fixed frame of reference)
$z_G$	location of the vehicle center of gravity in the $z$ -direction (body-fixed frame of reference)
$Z$	third inertial Cartesian coordinate
$\alpha$	empirical constant associated with the $q$ - $\omega$ damping function; angle of attack
$\beta$	pseudo- or artificial-compressibility parameter; MPI software bandwidth (Mb/s)
$\gamma$	thermal expansion coefficient
$\delta$	fin deflection
$\delta_i$	central-difference operator associated with the $i^{\text{th}}$ curvilinear coordinate
$\delta_{ij}$	Kronecker delta
$\epsilon$	turbulent energy dissipation rate
$\xi$	third curvilinear coordinate
$\eta$	second curvilinear coordinate
$\theta$	contravariant velocity component (equal to $U$ , $V$ , or $W$ ); Euler angle (inertial frame of reference), rotation about the $Y$ -axis
$\kappa$	scalar parameter associated with high-resolution (MUSCL) flux scheme; von Karman constant = 0.41
$\Lambda_{\xi}^-$	eigenvalue diagonal matrix (containing only the nonpositive eigenvalues of $\bar{A}$ )
$\mu$	laminar or molecular viscosity
$\mu_T$	turbulent or eddy viscosity

## Nomenclature (continued)

$\nu$	laminar or molecular kinematic viscosity
$\nu_T$	turbulent or eddy kinematic viscosity
$\xi$	first curvilinear coordinate
$\rho$	fluid density
$\sigma$	MPI software latency (seconds); Prandtl number
$\tau$	computational time
$\Delta\tau$	computational time step
$\tau_w$	wall or surface shear stress
$\tau_{ij}$	laminar stress tensor
$\phi$	parameter associated with high-resolution (MUSCL) flux scheme; Euler angle (inertial frame of reference), rotation about the X-axis; circumferential angle on a prolate spheroid
$\Phi$	strain rate invariant
$\chi$	distance from the trailing edge
$\psi$	Euler angle (inertial frame of reference), rotation about the Z-axis
$\omega$	turbulent rate of decay = $\epsilon / k$
$\omega$	angular velocity vector of the vehicle
$ \omega $	absolute magnitude of the vorticity
$\omega^+$	dimensionless value of $\omega$ in the inner boundary layer = $\omega v/u_\tau^2$
$\Omega$	rotation matrix

## Nomenclature (continued)

### Subscripts

<i>i</i>	index corresponding to a cell center
$i \pm \frac{1}{2}$	indices corresponding to cell faces
<i>inner</i>	inner region of the boundary layer
<i>k</i>	curvilinear coordinate index (referring to $\xi$ , $\eta$ , or $\zeta$ ); associated with the <i>k</i> -equation
<i>L</i>	left of cell face
<i>outer</i>	outer region of the boundary layer
<i>q</i>	associated with the <i>q</i> -equation
<i>R</i>	right of cell face
<i>t</i>	differentiation with respect to <i>t</i>
<i>TE</i>	trailing edge
<i>v</i>	flux associated with viscous effects
<i>x</i>	differentiation with respect to <i>x</i>
<i>y</i>	differentiation with respect to <i>y</i>
<i>z</i>	differentiation with respect to <i>z</i>
$\epsilon$	associated with the $\epsilon$ -equation
$\omega$	associated with the $\omega$ -equation

## Nomenclature (continued)

### Superscripts

-1	inverse
<i>L</i>	left of cell face
<i>m</i>	Newton iteration
<i>n</i>	time step level
<i>R</i>	right of cell face
-	average value
/	Jacobian with respect to the dependent variable vector
.	time derivative
..	second time derivative

### Note

Bold variables are either vector or matrix quantities.

# **1. Introduction**

The purpose of any underwater vehicle is to be able to maneuver through the water in order to accomplish some specified mission. Unfortunately, current methods to "predict" the maneuvering characteristics of underwater vehicles require a number of expensive tests with model-scale hardware. Even with this current methodology, most extreme maneuvers cannot be predicted. Also, modifications to the vehicle can result in severe changes in the maneuvering characteristics--changes that these current methods cannot confidently predict. This report describes the development of a new methodology for predicting the maneuvering characteristics of underwater vehicles. However, some background information on the current status of maneuvering "predictions" is necessary to show precisely why this new methodology is required.

## **1.1 Maneuvering**

Any controlled change or retention of the heading, depth, or speed of an underwater vehicle is classified as a maneuver. These maneuvers can be identified as path keeping, path changing, or speed changing--with path keeping being primarily related to the stability of the vehicle.

Path changing maneuvers include changes in heading or depth, as well as tactical and uncontrolled turns. Various vehicles respond differently to changes in heading or depth, with differences occurring in the time to perform the change and the amount of overshoot. As with all maneuvers, the response of the vehicle varies with speed, control surface angles, and the time required to activate the maneuvering order. Some vehicles are relatively benign with respect to out-of-plane forces and moments, but some vehicles are quite sensitive. For instance, vehicles intending to turn in the horizontal plane may or may not have significant motion in the vertical plane. Depending on the stability and response of the vehicle, tactical turns use prescribed settings of the control surfaces during different phases of the turn. During the turn, the vehicle will undergo a loss in speed and a certain amount of roll, while establishing a particular position after the specified new heading has been reached. In fact, large rudder angles can lead some vehicles to experience a large roll, called a snap roll. The vehicle requires the use of sternplanes, fairwater planes (sail planes), or bow planes in order to prevent an uncontrolled turn with changes in depth, pitch, and roll.

Speed changing maneuvers involve the acceleration and deceleration of the vehicle by changing the horsepower and, thus, the angular velocity of the propulsor. Again, knowledge of the stability and response of the vehicle allows one to prescribe settings of the control surfaces in order to maintain course and depth. The acceleration and deceleration characteristics of the vehicle include the time to attain the specified speed and the distance the vehicle has moved during this amount of time. Deceleration can involve decreasing the angular velocity of the propulsor and allowing the vehicle to coast, or it can involve a crashback maneuver--where the angular velocity of the propulsor changes from rotating in its design direction to rotating in the reverse direction. Reversing the direction of propulsor rotation is also used during backing. Further complications occur since the vehicle decelerates during most path changing maneuvers.

Other maneuvers involve the recovery from emergencies. These emergencies can involve casualties where the rudder jams or where the sternplane jams in either the dive or rise position. When scheduled recovery measures are taken, the vehicle can experience excursions in depth and

pitch, as well as roll--excursions that depend on the speed and the jam angles. Other emergencies may require a crashback maneuver while the vehicle is at some angle of attack.

## 1.2 Vehicle Motion

The motion of a vehicle can be described by Newton's laws of motion, with the coordinate system fixed to the vehicle. These general Euler equations of unsteady motion can be written as

$$m \frac{dv}{dt} + \omega \times mv = \sum \mathbf{F}$$

and

$$\frac{d\mathbf{h}}{dt} + \omega \times \mathbf{h} = \sum \mathbf{M}.$$

These six vector equations represent motion with six degrees of freedom (6DOF). In translation, the vehicle can surge ( $u$ ) in the axial direction ( $x$ ), sway ( $v$ ) in the horizontal direction ( $y$ ), and heave ( $w$ ) in the vertical direction ( $z$ ); while in rotation, the vehicle can roll ( $p$ ) about the  $x$ -axis, pitch ( $q$ ) about the  $y$ -axis, and yaw ( $r$ ) about the  $z$ -axis. Essentially, the inertial terms on the left-hand side of these equations remain the same for most vehicles. If the origin of the coordinate system does not coincide with the center of gravity, or if the vehicle has a variable mass or a variable position of the center of gravity, the equations of motion will require additional inertial terms.

## 1.3 Forces and Moments on a Vehicle

The maneuvering characteristics of a vehicle depend on the external forces and moments, as well as the response of the vehicle to those forces and moments. In order to determine these maneuvering characteristics, one must compute these external forces and then determine the moments that these forces create about the center of gravity of the vehicle. First, one must compute the vertical forces resulting from weight and buoyancy. The weight acts vertically downward through the center of gravity, which can be altered somewhat by changing the ballast. Through Archimedes' Law, a buoyancy force will act vertically upward through the center of buoyancy, with the buoyancy force being equal and opposite to the weight of the water displaced by the vehicle. Imlay [1964] developed expressions of the weight and buoyancy terms within the right-hand side of the equations of motion. For positive stability, the center of gravity must be lower than the center of buoyancy. Any difference in the longitudinal position of the centers of gravity and buoyancy will result in a longitudinal inclination or trim, while any difference in the magnitude of weight and buoyancy will result in positive or negative buoyancy (with a lighter weight giving positive buoyancy). A vehicle in equilibrium will have neutral buoyancy and zero trim.

The action of the propulsor will also greatly affect the maneuvering characteristics of a vehicle, both directly and indirectly. First, the propulsor will directly generate forces and moments on the vehicle. For straight-and-level flight, one designs the propulsor to generate only time-average values of thrust and torque, with these magnitudes changing with advance ratio. However, changes in

the angle of the inflow or the existence of nonuniformities in the inflow can result in forces in the horizontal or vertical planes. Even very small side forces can have a great impact on the maneuvering characteristics since the moment arm--the distance between the propulsor and the center of gravity--is large. Second, the propulsor can indirectly affect maneuvering by inducing changes in the flow over the stern of the vehicle.

The primary forces and moments experienced by a maneuvering vehicle result from the static pressures and shear stresses on the hull and on any appendages. Integration of the entire pressure and shear-stress fields gives a resultant hydrodynamic force, and the location of where this force acts relative to the center of gravity of the vehicle gives the resultant hydrodynamic moment. Traditionally, the components of the hydrodynamic forces and moments acting on the hull and on each appendage are treated as a function of the motion state variables. For example, the axial external force would be

$$F_x = F(u, v, w, p, q, r, \dot{u}, \dot{v}, \dot{w}, \dot{p}, \dot{q}, \dot{r}) ,$$

where the dot indicates a time derivative. In addition, the hydrodynamic forces and moments on the control surfaces are treated as a function of the control state variables, such as fin deflection,  $\delta$ , or

$$F_x = F(\delta, \dot{\delta}, \ddot{\delta}) .$$

Propulsor forces are treated as a function of angular velocity, advance ratio, efficiency, or other characteristic variables. At this point, the traditional approach allows one to represent these functional expressions with a truncated Taylor series. If one were to neglect derivatives higher than first-order derivatives, one could obtain the linearized equations of motion--assuming the inertial terms were also linearized. However, this assumption allows for only small changes in the motion state variables and in the control state variables.

Most of the techniques currently being used to compute the hydrodynamic forces and moments for a maneuvering vehicle represent the forces and moments with a truncated Taylor series that includes some second- and third-order derivatives, including cross derivatives that model the cross-coupling effect of some of the variables. Originally introduced in aerodynamics, this approach uses empirical correlations for the "derivatives" in the truncated Taylor series. Derivatives of the forces and moments with respect to motion state variables are often called stability derivatives, while derivatives with respect to control state variables are often called control derivatives. The difficulty occurs when one wants to determine time-dependent coefficients that represent these hydrodynamic derivatives during various unsteady maneuvers. In the past, experiments have been used to obtain empirical coefficients, although some theoretical results have also been incorporated.

Much of the determination of empirical hydrodynamic coefficients has involved captive-model tests. One can perform these tests with either a fully-appended model or with a systematic addition of the appendages--in order to evaluate the contribution of each appendage to the total forces and moments. Straight-line tests within a towing tank using a model at angles of yaw and/or pitch (with and without fin deflection) have been used for many years to obtain hydrodynamic coefficients. Additional coefficients result from towing tank tests using a planar motion mechanism, where the model oscillates during the test. Other oscillator techniques have also been employed. Many coefficients involving rotation have been obtained from a rotating-arm facility. Again, the model can be set at various yaw and pitch angles--as well as various fin deflections--during the rotating test.

Finally, the determination of some control derivatives involves the operation of control surfaces in a water tunnel, separate from the hull.

While these types of captive-model tests have been used for many years, several problems do exist. First, for the case of very large vehicles such as submarines, the model experiments are run with a much smaller Reynolds number than exists at full scale. Differences in Reynolds number can change the location of transition zones and separation lines--which, in turn, can change the distribution of static pressures and shear stresses and, thus, the resulting hydrodynamic forces. The location of separation lines can also be affected by the crossflow over the model in straight-line tests. During these tests, the crossflow shows little variation over the length of the model, while this crossflow varies significantly during an actual vehicle maneuver. The effects of bounding walls, free surfaces, and support struts can also change the pressure distribution from what one might obtain using a free-running model. Because of the strong influence of the propulsor on hydrodynamic derivatives, one should acquire all hydrodynamic force measurements with the propulsor operating--at some specified advance ratio. In addition, for rotating-arm tests, one must accelerate the model to the proper test speed and acquire all the data within a single revolution. Otherwise, the model will run through its own wake. Also, rotation data will be limited by the radius of the turn available within the facility. For control surfaces tested in water tunnels, the lack of a hull and any gaps adjacent to moving parts of the control surface can adversely affect the hydrodynamic force measurements.

Even if all of these problems are satisfactorily resolved, one might still question whether the measured hydrodynamic coefficients and the coupling between different coefficients correctly represents the characteristics of a time-dependent vehicle maneuver. For this reason, recent experiments have involved a free-running, radio-controlled model. While one must still account for the effects of bounding walls and free surfaces, operation of this model during a specific maneuver can lead to better measurements of hydrodynamic forces. However, actual modeling of the maneuvering characteristics of a vehicle requires dynamic similitude, where the vehicle and the model have the same Froude number and Reynolds number,

$$Fr = \frac{V_\infty}{\sqrt{gL}} \quad \text{and} \quad Re = \frac{V_\infty L}{v}$$

For underwater vehicle maneuvers, the Froude number is often referred to as a modified Froude number, since no free-surface effects exist. The ratio of  $Re$  to  $Fr$  can be interpreted as the ratio of the hydrostatic forces and moments, from the effects of weight and buoyancy, to the hydrodynamic forces and moments. Except at full scale, this dynamic similitude is impossible; and while some full-scale submarine data does exist, the costs to acquire such data is extremely high, and the installation of proper instrumentation on an actual submarine provides difficult problems. Radio-controlled model tests are run with the full-scale Froude number, while the effects of the Reynolds number are modeled using an equivalent flat-plate resistance. Unfortunately, for the very low Reynolds numbers used in radio-controlled model tests, the three-dimensional locations of transition zones and separation lines will differ considerably from the full-scale vehicle, and flat-plate correlations will not account for these differences. Strakes and surface roughness (grit) are often added in an *ad hoc* manner in an attempt to force the model-scale trajectory data to better match full-scale trajectory data. These additions to the model will tend to fix transition and separation, but these effects are contrary to what occurs naturally during a time-dependent maneuver.

## 1.4 Physics-Based Means of Predicting Vehicle Maneuvers

The traditional correlation-based means of “predicting” the maneuvering characteristics of a submerged vehicle have worked fairly well for vehicles with slender sterns and for simple and some moderate maneuvers. However, for vehicles with full sterns, for nonaxisymmetric hulls, and for any vehicle operating under an extreme maneuver, these traditional methods have not proven adequate. For new vehicle designs, the determination of a submerged operating envelope (SOE) requires a large number of expensive tests in order to obtain correlations for the stability and control derivatives; and yet, uncertainties remain because the methodology has major difficulties with extreme maneuvers. Small changes in a design require many expensive tests to be run again. These traditional methods are also severely hampered by their inability to model the effects of the propulsor. Finally, these “predictions” treat time-dependent maneuvers in a quasi-steady manner--a series of steady-state calculations. Accurate predictions of the trajectory of a maneuvering vehicle will require unsteady calculations.

Accurate predictions of maneuvering characteristics also require the ability to compute the generation of vorticity within the hull and appendage boundary layers; the three-dimensional separation of these boundary layers that leads to vortical structures leaving the surface and entering the flow field; the correct diffusion of these vortices as they convect downstream; and the interaction of these vortices with the hull, the appendages, and the propulsor. This interaction of a vortex with a downstream surface will change the static pressure and shear stress on the surface and can result in significant changes in the resulting hydrodynamic forces and moments on the maneuvering vehicle. Traditional correlation-based methods cannot directly address these very important issues for a time-dependent maneuver.

As a result of the limitations of the traditional correlation-based means of “predicting” the maneuvering characteristics of a submerged vehicle, a team of researchers from the Engineering Research Center at Mississippi State University and the Applied Research Laboratory at The Pennsylvania State University completed a three-and-a-half-year project to develop a physics-based means of accurately predicting the forces and moments acting on a maneuvering, self-propelled, appended, underwater vehicle and the resulting vehicle motion. This report discusses various elements within the development of this *a priori* prediction method.

The next section of the report describes the numerical approach to solving the Reynolds-averaged Navier-Stokes (RANS) equations. The resulting computer code solves for the unsteady flow field around the maneuvering vehicle at each instance of time--including the static pressures and shear stresses on each surface and the effects of vortices within the flow field. The computation of flow past a maneuvering vehicle at high Reynolds number is a large-scale simulation requiring large amounts of floating-point arithmetic and considerable storage capacity. Therefore, the report next describes the ability to exploit high-performance parallel computing in solving these flows. Following this section, the report discusses the issues concerning turbulence modeling for these unsteady, three-dimensional, high Reynolds number flows. After computing the flow field at each time step, the code must integrate the pressure and shear-stress fields on all of the surfaces to obtain the hydrodynamic forces and moments acting on the vehicle. With this information, the report describes how the code solves for the new velocity and location of the vehicle using the 6DOF vehicle dynamics equations. In the final section describing the prediction method, the report focuses on the treatment of the propulsor.

After the description of each element within the maneuvering prediction methodology, the rest of the report describes the results from applying this method. These results include two types of computations. First, the code was run for many cases--both simple and complex--where experimental data or analytical solutions exist. Comparisons between the computational and experimental results provide verification of various elements of the prediction method and improve confidence in the use of the method--at least to the extent practical. Extensive code validation for a maneuvering vehicle was not expected at this time. Second, the code was run for many cases where experimental data did not exist. These computations were performed to check the feasibility of the method to calculate flow fields of varying complexity--leading up to the computation of a maneuvering, self-propelled, appended, underwater vehicle. Finally, the report concludes by summarizing the current state of the computational method and its ability to predict maneuvering. The report also suggests what future work is still necessary to accurately predict vehicle maneuvering characteristics.

## 2. Numerical Approach

To develop a physics-based means of making maneuvering predictions of self-propelled underwater vehicles, the research team first needed to solve the unsteady Reynolds-averaged Navier-Stokes (RANS) equations in order to compute the necessary three-dimensional, time-dependent, incompressible, turbulent flow fields. The resulting computer code is referred to as UNCLE, an acronym for the unsteady computation of field equations. Because of the magnitude of the problem size with regard to resolving fully-configured vehicles that include appendages and a rotating propulsor, the numerical solution of the RANS equations is carried out on dynamic, relative-motion, multiblock, structured grids. The Reynolds numbers of these flows are extremely large, and the viscous regions must be resolved within the near-wall region of the turbulent boundary layers (minimum  $y^+$  values near one). This resolution places severe demands on the numerical solution scheme in terms of stability and accuracy. Moreover, the flow is both three-dimensional and unsteady in the sense of the Reynolds-averaged mean flow. To make the computation of these high Reynolds number, unsteady flow problems practical in terms of the total computational (CPU) time required, one must restrict the computational time-step needs by the physics of the problem being solved and not by the numerics of the scheme used to solve the equations. This section discusses the equations, numerical flux formulation, solution algorithm, and computational grids used to solve the equations and achieve the physics-based time restriction.

### 2.1 Reynolds-Averaged Navier-Stokes Equations

The three-dimensional, time-dependent Reynolds-averaged Navier-Stokes equations are first transformed to a time-dependent curvilinear coordinate system. The artificial (or pseudo) compressibility idea of Chorin [1967] is then introduced, as done previously by Pan and Chakravarthy [1989], Rogers and Kwak [1990], and Taylor [1991]. The use of artificial compressibility permits the experience gained in the numerical solution of compressible flow problems to be exploited in the numerical solution of incompressible flow problems--as shown, for example, by Whitfield [1995]. The artificial compressibility form of the three-dimensional, time-dependent RANS equations in general curvilinear coordinates is

$$\frac{\partial \mathbf{Q}}{\partial \tau} + \frac{\partial \mathbf{F}}{\partial \xi} + \frac{\partial \mathbf{G}}{\partial \eta} + \frac{\partial \mathbf{H}}{\partial \zeta} = 0 , \quad (1)$$

where

$$\mathbf{Q} = J \begin{bmatrix} p \\ u \\ v \\ w \end{bmatrix} ,$$

$$\mathbf{K} = J \begin{bmatrix} \beta(\theta_k - k_t) \\ u\theta_k + k_x p - T_{k_x} \\ v\theta_k + k_y p - T_{k_y} \\ w\theta_k + k_z p - T_{k_z} \end{bmatrix},$$

and

$$\theta_k = k_t + k_x u + k_y v + k_z w$$

$$\mathbf{K} = \mathbf{F}, \quad \theta_k = U \text{ for } k = \xi$$

$$\mathbf{K} = \mathbf{G}, \quad \theta_k = V \text{ for } k = \eta$$

$$\mathbf{K} = \mathbf{H}, \quad \theta_k = W \text{ for } k = \zeta.$$

In these equations,  $\beta$  is the artificial compressibility coefficient, with a typical value of  $5 \sim 10$ ;  $p$  is the static pressure;  $u$ ,  $v$ , and  $w$  are the velocity components in Cartesian coordinates  $x$ ,  $y$ , and  $z$ .  $U$ ,  $V$ , and  $W$  are the contravariant velocity components in curvilinear coordinate directions  $\xi$ ,  $\eta$ , and  $\zeta$ , respectively. The terms  $T_{k_x}$ ,  $T_{k_y}$ , and  $T_{k_z}$ --where  $k = \xi$ ,  $\eta$ , and  $\zeta$ --are the viscous flux components in curvilinear coordinates.  $J$  is the Jacobian of the inverse transformation and  $k_x$ ,  $k_y$ ,  $k_z$ , and  $k_t$ --with  $k = \xi$ ,  $\eta$ , and  $\zeta$ --are the transformation metric quantities, as described by Taylor [1991], where a subscript denotes differentiation.

In this work, the thin-layer approximation is introduced to simplify the full RANS equations. To satisfy closure for turbulent flow computations, the code incorporated turbulence models, as will be discussed in a later section. Gatlin [1987] described the details of treating the viscous terms, while Chen [1991] made improvements with regard to the computation of the wall shear stress by using better computations of the tangential velocity derivatives normal to a solid surface. He showed that this improvement is simple to implement and works extremely well on grids that may be highly skewed.

## 2.2 Numerical Flux Vector

Equation 1 is discretized into a cell-centered finite-volume form which for one-dimensional flow, for example, can be written as

$$\frac{\mathbf{Q}_i^{n+1} - \mathbf{Q}_i^n}{\Delta t} + \left( \bar{\mathbf{F}}_{i+\frac{1}{2}}^{n+1} - \bar{\mathbf{F}}_{i-\frac{1}{2}}^{n+1} \right) = 0 , \quad (2)$$

where the index  $i$  corresponds to a cell center and indices  $i \pm \frac{1}{2}$  correspond to cell faces. In this expression, the dependent variable vector  $\mathbf{Q}$  is considered to be constant throughout the cell, whereas the flux  $\mathbf{F}$  is assumed to be uniform over each surface of the cell. A flux vector is therefore needed at each cell face.

There are numerous ways of developing this flux vector, and early on in this maneuvering program, the formulation presented by Taylor [1991] was used. He incorporated the flux-difference-split scheme of Roe [1981] for the first-order contribution and a hybrid numerical flux vector for the higher-order contribution that was patterned after the flux vector developed for compressible flow by Whitfield, Janus, and Simpson [1988]. An advantage of this hybrid flux is that the formulation leads more or less naturally to the limiting of characteristic variables, which is important for compressible flows with discontinuities. However, perhaps because two of the eigenvalues never change sign in this artificial-compressibility formulation, Whitfield and Taylor [1994] showed that limiting the characteristic variables for these incompressible flow computations has not been required. Therefore, after some considerable time following the first version of this incompressible code, Whitfield and Taylor [1994] began to investigate the sort of results that could be obtained for second- and third-order flux vectors by the more classical MUSCL-type of numerical flux-vector formulation originally developed by van Leer [1979]. Whitfield and Taylor [1994] found that the nonlimited form of the dependent variable extrapolation method of Anderson, Thomas, and van Leer [1986] worked well for this incompressible formulation and that the numerical results were extremely close to the results provided by the hybrid numerical flux vector. For the currently used numerical flux, Whitfield and Taylor [1994] decided on a formulation based on the approximate Riemann solver of Roe [1981], which in the interest of a reduced floating-point-operation count is written for this one-dimensional example (Equation 2) in the form:

$$\bar{\mathbf{F}}_{i+\frac{1}{2}} = \left[ \mathbf{F} \left( \mathbf{Q}_{i+\frac{1}{2}}^L \right) \right]_{i+\frac{1}{2}} + \bar{\mathbf{A}} \left( \mathbf{Q}_{i+\frac{1}{2}}^L, \mathbf{Q}_{i+\frac{1}{2}}^R \right) \left( \mathbf{Q}_{i+\frac{1}{2}}^R - \mathbf{Q}_{i+\frac{1}{2}}^L \right) , \quad (3)$$

where  $\bar{\mathbf{A}}$  is the Roe matrix given by

$$\bar{\mathbf{A}} = \mathbf{R}_\xi \Lambda_\xi^- \mathbf{R}_\xi^{-1} . \quad (4)$$

The eigenvalue diagonal matrix,  $\Lambda_\xi^-$ , contains only the nonpositive eigenvalues of  $\bar{\mathbf{A}}$ , and the

similarity matrix,  $\mathbf{R}_\xi$ , has the right eigenvectors of  $\bar{\mathbf{A}}$  as columns. Whitfield and Taylor [1994] showed that the matrix  $\bar{\mathbf{A}}$  consists of the Roe-averaged variables, and all metric quantities occurring in Equation 3 are evaluated at the cell face  $i+1/2$ .

The numerical scheme is made higher order by using the MUSCL approach of van Leer [1979]. Anderson, Thomas, and van Leer [1986] used a MUSCL-type approach in flux-vector-split schemes. Following their approach, the dependent variables just to the right of the cell face,  $\mathbf{Q}^R$ , located at  $i+1/2$  and just to the left of the same cell face,  $\mathbf{Q}^L$ , are written as

$$\mathbf{Q}_{i+\frac{1}{2}}^R = \mathbf{Q}_{i+1} - \frac{\phi}{4} [(1 - \kappa)(\mathbf{Q}_{i+2} - \mathbf{Q}_{i+1}) + (1 + \kappa)(\mathbf{Q}_{i+1} - \mathbf{Q}_i)] \quad (5a)$$

and

$$\mathbf{Q}_{i+\frac{1}{2}}^L = \mathbf{Q}_i + \frac{\phi}{4} [(1 - \kappa)(\mathbf{Q}_i - \mathbf{Q}_{i-1}) + (1 + \kappa)(\mathbf{Q}_{i+1} - \mathbf{Q}_i)]. \quad (5b)$$

For  $\phi = 0$  in Equations 5a and 5b, the numerical scheme would be first order in space. For higher-order schemes,  $\phi = 1$ . With  $\kappa = -1$ , only points to the right of the cell face are used for  $\mathbf{Q}^R$  and only points to the left of the cell face are used for  $\mathbf{Q}^L$ --and a second-order upwind scheme results. With  $\kappa = 1/3$ , two points to the right and one point to the left of the cell face are used for  $\mathbf{Q}^R$ , and two points to the left and one point to the right of the cell face are used for  $\mathbf{Q}^L$ . Anderson, Thomas, and van Leer [1986] referred to the resulting scheme as a third-order upwind-biased scheme. Note that the third-order upwind-biased scheme depends on information from the same number of points as the second-order scheme. All numerical results presented here were obtained with  $\kappa = 1/3$ .

## 2.3 Solution Algorithm

The normal procedure for the solution of Equation 2 would be to linearize the spatial-difference terms, move the terms not containing  $\Delta\mathbf{Q}^n$  to the right-hand side of the equations, and solve for  $\Delta\mathbf{Q}^n$ . This procedure is particularly true for problems expected to have steady-state solutions, because the sum of the spatial-difference operator terms and  $\Delta\mathbf{Q}^n$  would both go to zero. However, for unsteady flow, the ideal situation would be to find  $\mathbf{Q}^{n+1}$  such that Equation 2 is satisfied. That is, find  $\mathbf{Q}^{n+1}$  such that

$$\mathcal{F}(\mathbf{Q}^{n+1}) = \frac{\Delta\mathbf{Q}^n}{\Delta\tau} + \delta_i \bar{\mathbf{F}}(\mathbf{Q}^{n+1}) = 0, \quad (6)$$

as suggested by Whitfield [1990].

One way of attempting to solve this problem is to use Newton's method. Ortega and Rheinboldt [1970] showed that Newton's method for the function  $\mathcal{F}(\mathbf{x})$  would be

$$\mathcal{F}'(\mathbf{Q}^{n+1,m})(\mathbf{Q}^{n+1,m+1} - \mathbf{Q}^{n+1,m}) = \mathcal{F}'(\mathbf{Q}^{n+1,m})\Delta\mathbf{Q}^{n+1,m} = -\mathcal{F}(\mathbf{Q}^{n+1,m}), \quad (7)$$

where  $m = 1, 2, 3, \dots$  and  $\mathcal{F}'(\mathbf{x})$  is the Jacobian matrix of the vector  $\mathcal{F}(\mathbf{x})$ . In principle, the generated sequence  $\mathbf{Q}^{n+1,m+1}$  converges to  $\mathbf{Q}^{n+1}$  and, hence, Equation 6 is satisfied. For the one-dimensional example,

$$\begin{aligned} & -\bar{\mathbf{F}}'_{i-\frac{1}{2}, i-1} \Delta\mathbf{Q}_{i-1}^{n+1,m} + \left( \frac{\mathbf{I}}{\Delta\tau} + \bar{\mathbf{F}}'_{i+\frac{1}{2}, i} - \bar{\mathbf{F}}'_{i-\frac{1}{2}, i} \right) \Delta\mathbf{Q}_i^{n+1,m} + \bar{\mathbf{F}}'_{i+\frac{1}{2}, i+1} \Delta\mathbf{Q}_{i+1}^{n+1,m} \\ &= -\left\{ \mathbf{I}_a \frac{\mathbf{Q}_i^{n+1,m} - \mathbf{Q}_i^n}{\Delta\tau} + \left[ \bar{\mathbf{F}}'_{i+\frac{1}{2}}(\mathbf{Q}^{n+1,m}) - \bar{\mathbf{F}}'_{i-\frac{1}{2}}(\mathbf{Q}^{n+1,m}) \right] \right\}. \end{aligned} \quad (8)$$

In this expression,  $\bar{\mathbf{F}}'$  is the Jacobian of the numerical flux vector, with the first subscript representing the position of the cell face of the numerical flux vector and the second subscript representing the position of the dependent variable vector with which the numerical flux vector is differentiated.  $\mathbf{I}_a$  is an identity matrix, except that the first diagonal element is zero in order to satisfy the true incompressible continuity equation.

A linear system of equations must be solved at each iteration of Newton's method. For three-dimensional problems, Vanden and Whitfield [1995] showed that a direct solution seems to be impractical and, in this work, symmetric Gauss-Seidel relaxation is used. Whitfield and Taylor [1991] suggested that the flux Jacobian should be obtained numerically since this technique is simple compared to the difficult task of analytically obtaining the flux Jacobian of the flux vector based on Roe's formulation in three dimensions. Ortega and Rheinboldt [1970] referred to this solution scheme as discretized Newton-relaxation, while Vanden and Whitfield [1995] abbreviated it as the DNR scheme. Sheng, Taylor, and Whitfield [1995c, 1995a, 1995b] added a multigrid scheme to accelerate the convergence of the numerical solutions, extended it for use with the multiblock code, and used it for unsteady flow computations.

## 2.4 Grid Generation

While the application of any flow solver requires a well-constructed grid, many of the applications in this maneuvering program required the use of the multigrid UNCLE code on dynamic, relative-motion, multiblock, structured grids. The multiblock topology allows one to divide the domain into smaller regions for detailed gridding which, in turn, allows for a better quality grid--especially for complex geometry. Just as important, multiblock topology allows one to obtain a numerical solution using much less memory than would be required for a single-block topology. The current working grid-generation package has no difficulty in subdividing the grid into blocks. For the

UNCLE code, the grid within each block requires point-to-point continuity across block interfaces. Users of the UNCLE code need to compromise between the number of blocks and the size of each block. Most of the applications of the multigrid version of the UNCLE code used grids constructed to have at least three levels of multigrid. Because of this constraint, at least nine grid points had to be added or deleted to existing grid blocks in order for the number of points in each block to conform to the use of multigrid. While multigrid is certainly very efficient for the computations, one must be careful with the placement of points since the requirement for multigrid affects the overall grid arrangement and the number of grid points.

This maneuvering program has included test cases with several different geometries, including various vehicle configurations. The mixture of C-type grids and H-type grids were used in the domain, where C-grids were applied to the region around the front section of a vehicle hull, and H-grids were applied to the remaining regions. A few cases also include O-type grids. As shown later, the most complex grid included a submarine-type vehicle that included a hull, a sail with sail planes, four stern appendages, and a five-bladed propeller. This grid was constructed with 51 blocks and the total number of grid points was 1,642,659. A buffer zone between the stern appendages and the propeller was created to ensure the matching between the rotating section--which included the propeller and regions downstream--and the fixed section--which included the regions upstream of the propeller.

Most of the grids in the program were generated using the software package EAGLEView, a package discussed in detail by Soni, Thompson, Stokes, and Shih [1992] and Remotigue, Hart, and Stokes [1992]. EAGLEView is an interactive surface and grid-generation software package developed to reduce the amount of time spent on the surface definition and the grid refinement for computational field simulation problems. The user can define his geometry, construct the volume grid, visualize the results, and make changes without having to execute a different program. Geometries are constructed in EAGLEView in a fashion: Points are used to create curves, which are used to create surfaces, which are used to create volumetric grids. Embedded in EAGLEView is a point-and-click interface in which every point, vector, axis, curve, surface, or grid may be accessed and/or queried using a mouse. A streamlined version of the previously-developed EAGLE grid-generation code, easyEAGLE, has been developed to handle the smoothness of the grids from EAGLEView. During later stages of the maneuvering program, some grids were generated using the new software package GUM\_B. GUM\_B is an acronym for the General Unstructured Multi-Block Structured Grid Generator, and it was used primarily to generate grids for the test case involving the high Reynolds number pump (HIREP). The quality of the resulting grid looked very promising for such a difficult geometry.

### **3. Parallel Computing Methodology**

Future use of UNCLE for large-scale simulations of a maneuvering vehicle at high Reynolds number will require large amounts of floating-point arithmetic and considerable storage capacity. This section describes a version of UNCLE that encompasses a methodology for solving these flows using high-performance parallel computing. This code is written in FORTRAN-77 and uses the Message Passing Interface (MPI) for interprocessor communications on distributed-memory parallel computing systems. MPI provides portability across a wide range of multiprocessor computers. In this parallel code, the linearized implicit solution algorithm is modified to run in parallel by using a block-decoupled subiterative strategy. A heuristic performance estimate is used for guiding the parallel problem definition.

#### **3.1 Parallel Algorithm**

The symmetric Gauss-Seidel (SGS) subiterations in the sequential algorithm are associated with good stability, convergence properties, and efficiency--but they are not easily parallelized. The approach followed in the parallel code is to implement this algorithm on spatially decomposed grid blocks assigned to separate processes in a context such that the subiterations are effectively decoupled, so that each block can be done in parallel. This decoupling tends to give good parallel performance, but the decoupling of subiterations in blocks can degrade the performance of this otherwise implicit algorithm.

In designing this parallel algorithm, an effort was made to identify a procedure that keeps the total number of arithmetic operations required for a converged solution as close as possible to that for the sequential algorithm, and then to achieve good parallel efficiency through high concurrency and minimal communications overhead. This strategy requires that the parallel algorithm has stability and convergence properties close to that of the sequential algorithm. It is demonstrated here that the convergence rate of the sequential algorithm can be recovered at reasonable cost in the parallel algorithm by using a sufficient number of (inexpensive) subiterations.

The parallel implementation employs an overlapping spatial domain decomposition of the grid into blocks which are assigned to separate processes and, then, distributed across multiple processors. During each SGS subiteration, the solution increments are exchanged for two rows (or surfaces) of points adjacent to each block interface. The decoupling is accomplished by starting each sweep of the subiteration within each block using boundary conditions from the previous subiteration sweep instead of waiting for values from the current subiteration. This algorithm uses Gauss-Seidel relaxation sweeps within each process but is effectively explicit across block boundaries, allowing for a parallel solution for all blocks. The solution increments are updated by message passing following completion of the forward sweep of the subiteration and, then, again following the backward sweep. In addition, an algebraic eddy viscosity turbulence model is used which requires global line searches that traverse block boundaries. As discussed in the next section, the turbulence model is a modified version of the one proposed by Baldwin and Lomax [1978]. The turbulence model is updated before each time step. Key elements of the parallel solution methodology are summarized here; Pankajakshan and Briley [1995] provide further details.

### **3.2 Parallel Algorithmic Performance**

Numerical experiments were conducted to study the impact of some of the key algorithmic parameters on efficiency in solving for the flow over underwater vehicles. The initial test case was an axisymmetric submarine-type hull configuration known as SUBOFF--a test case that will be examined further in the results sections of this report. A 131x51x2 (13,362 point) grid was used, and this grid is highly stretched to resolve the very thin shear layer occurring at the high Reynolds number (12,000,000 based on hull length) for this case. For this grid, the ratio of maximum to minimum mesh spacing is 1,600,000 for the radial direction and 90 for the circumferential direction. The maximum cell aspect ratio is 12,778. The most important algorithm parameters are the nondimensional time step (or CFL number, defined by Briley, Neerarambam, and Whitfield [1995]) and the number of subiterations ( $I_s$ ). The frequency of updating flux Jacobian linearizations was found to have only a weak influence on stability and iterative convergence rate. The number of iterations required to reduce the maximum residual by a factor of 0.001 are plotted in Figure 1 as a function of CFL and  $I_s$ . The results in Figure 1 are re-plotted in Figure 2 to convert the number of iterations to arithmetic complexity (defined later using the CPU requirements from the performance estimate for this solution algorithm). Note that the minimum arithmetic complexity occurs for  $I_s$  of 3 to 5 and CFL of about 40 to 50, indicating that further subiteration is less efficient in CPU time even though fewer time step iterations are required. The optimal CFL number is expected to vary somewhat for other flow problems.

Figure 3 gives results which suggest guidelines for selecting the number of subiterations for the decoupled parallel algorithm to maintain the convergence rate of the sequential algorithm. In a series of cases with different numbers of processors and subiterations and with one- and two-dimensional decompositions, it appears that the sequential convergence rate is maintained--provided there is one subiteration for every two grid blocks in the direction of the longest block decomposition. This result implies that a balanced higher-dimensional decomposition will show the least amount of algorithmic degradation. It is significant that the additional subiterations required are inexpensive for this algorithm because flux Jacobians are saved and reused.

### **3.3 Problem Definition and Parallel Efficiency**

Another objective of this study is to identify a spatial domain decomposition that leads to good parallel efficiency on the available computing platform. To accomplish this decomposition, one can choose a minimum number of processors having sufficient global memory for the case to be run, arrange for a grid block structure with small a surface-to-volume ratio (ratio of the number of surface grid points to the number of volume grid points) to reduce communication, and use equal block sizes for load balance on homogeneous processors.

Figure 4 illustrates this procedure for making flow simulations on parallel processors. Once the computational problem to be solved is defined, the problem size determines the global memory required, and this memory determines the minimum number of processors required on the available computing platform. The run time is then estimated using a heuristic performance estimate (defined later) based on both solution algorithm and architectural parameters. Communication/computation ratios are reduced by keeping the granularity as coarse as available memory allows (to give a large volume of data for the CPU) and by choosing a decomposition with

small surface-to-volume ratio to reduce the size of messages. If the estimated run time is too large, it can be reduced by changing the number of processors,  $P$ , with guidance from the performance estimate. The final step is to generate a grid having  $P$  blocks.

In effect, the parallel decomposition and load balancing issues are introduced as constraints in the grid generation process. These constraints are easily dealt with by experienced grid generators with good grid generation programs and, at some point, the constrained grid generation may be automated. If an existing grid must be used, it can often be reblocked according to these guidelines. This constrained grid generation process yields a multi-block grid with blocks sized appropriately for the flow solver and computer configuration. A uniform grid block size provides static load balancing. The approach is well suited for problems that can be addressed by multi-block dynamic grids generated at the start of the flow calculation.

### 3.4 Parallel Performance Estimate

A heuristic means of estimating the parallel performance, given key parameters for the solution algorithm and parallel computing platform, is outlined next.

#### 3.4.1 Storage and CPU Requirements

Assuming an  $n_x \times n_y \times n_z$  grid with  $N$  finite-volume cells, the storage required for large arrays is approximately  $248 N$  64-bit words. Thus, a 50,000-point grid needs 109 Mb.

The floating point operations required by the solution algorithm during one step include three basic components of the calculation: (a) residual evaluation, (b) LU subiteration sweeps, and (c) numerical flux Jacobian linearizations. These components were determined by a sequence of calibration runs on a Cray YMP and are summarized here in Mflops (million floating point operations) as (a) residual: 0.001230  $N$  Mflops, (b) subiteration: 0.0003305  $N$  Mflops, and (c) Jacobian: 0.0052843  $N$  Mflops. If  $I_s$  denotes the number of LU subiterations, if the flux Jacobian linearizations are updated every  $I_j$  time steps, and if  $R_{CPU}$  is the effective processor speed in Mflops, then the total CPU time in seconds for an average step is given by

$$CPU \text{ (seconds)} = \frac{\left[ Residual + I_s \times Subiteration + \frac{Jacobian}{I_j} \right]}{R_{CPU}}$$

#### 3.4.2 Communication Requirements

Three basic components of the interprocessor communication requirement are considered: (a) exchange of data adjacent to block interfaces during subiteration, (b) global operations required by the algebraic eddy viscosity turbulence model, and (c) loading and unloading of buffer arrays used in

message passing (a slightly different MPI implementation with user-defined datatypes would avoid this explicit buffer loading, but has not yet been implemented).

The communications estimate is expressed in terms of the following parameters: number of processors,  $P$ ; number of block interfaces exchanging messages,  $N_m$ ; message length for a single data surface (Mb),  $L_m$ ; MPI software latency (seconds),  $\sigma$ , and; MPI software bandwidth (Mb/s),  $\beta$ . During each of the  $I_S$  subiterations, the solution time increment of  $\Delta Q$  must be exchanged twice (once for the forward sweep and once for the backward sweep) for each of the  $N_m$  block interfaces on each process. The overlapping domain decomposition is such that data is duplicated and exchanged for two surfaces of points adjacent to each block interface. In addition, the block decoupled solution algorithm is synchronized such that all messages are sent at approximately the same time. Consequently, an estimate for bisection width is needed to account for self contention in message passing. A factor of  $\sqrt{P}$  is a suitable estimate and is exact for a two-dimensional mesh. The estimated total time required for message passing is given by

$$t_{comm} = 2 I_S N_m \left( \sigma + \frac{2L_m}{\beta} \sqrt{P} \right) + 2 \left( q \sigma + \frac{2L_m}{\beta} \sqrt{P} \right) + 2 I_S N_m \left( \frac{2L_m}{9.71} \right),$$

Point-to-Point

Global

Bufferng

where  $q$  is such that  $P > 2^{q-1}$ .

For the architectural parameters, the effective processor speed  $R_{CPU}$  was calibrated for an IBM SP-2 processor as approximately 49 Mflops, while the MPI software latency and bandwidth were obtained from Saphir and Fineberg [1995] for an IBM SP-2 as  $\sigma = 62 \mu s$  and  $\beta = 34 \text{ Mb/s}$  (the asymptotic rate for large messages).

Figure 5 compares the parallel performance estimates with actual run times for these one-, four-, and eight-processor cases on an IBM SP-2 and, in general, the run-time estimates are in reasonable agreement with the actual trend. The reason for dividing the shorter direction (having 51 points) is that this direction cuts across the turbulent boundary layer. This demonstrates the ability of this particular algorithm to handle arbitrary domain decompositions.

In Figures 6 and 7, estimated and actual/calibrated run times are compared for two larger cases of flow past the SUBOFF hull with a sail and stern appendages, having grids with 12 blocks of 49x41x25 points (that is, 602,700 total grid points) and with 32 blocks of 49x65x33 points (that is, 3,363,360 total grid points), and having two-dimensional decompositions. Estimated times are given for both one- and two-dimensional decompositions.

### 3.5 Parallel Implementation

The grid in PLOT3D multiblock format is split into multiple files for parallel I/O if the MPI implementation permits it. The boundary conditions are specified by means of an input file. The block-to-block interfaces are also specified using a map which is generally automatically generated from the grid. Each block is tagged using an ordered triplet that defines a Cartesian grid.

The boundary conditions are applied using a library of subroutines with a uniform calling interface. New boundary conditions can be added by modifying a standard template. The block-to-block map is used to set up communications among neighboring blocks. Non-blocking MPI *send* and *receive* operations, with globally defined tags, are used for all messages.

Communication contexts are defined along the principal axes in the computational space using the Cartesian processor grid. The algebraic turbulence model uses MPI collective operations within these contexts to calculate the eddy viscosity. Pankajakshan and Briley [1995] provide further implementation details.

### 3.6 Parallel Solution for Configurations with a Rotating Propulsor

The parallel code for configurations with propulsors differs from the parallel implementation just described in that it has additional routines for handling grid interfaces associated with the rotating propulsor. The grid rotation and distortion routines are also modified to work in parallel using data replication and updating to handle access to non-local data. Algorithm and grid details associated with a rotating propulsor can be found in a later section of this report.

A unique feature of the propulsor version of the code is that each grid block having a rotating interface requires access to data from a set of blocks which varies over time as the propulsor rotates. Both the number and identity of elements in this interface set depend on the time step. As noted previously, the parallel code runs in a loosely-coupled mode—with each domain exchanging information after each forward and backward sweep of the symmetric Gauss-Seidel iteration. In the propulsor version of the parallel code, the same treatment is applied to the rotating interfaces. The parallel propulsor code uses a modified version of the ring-buffer concept developed by Janus [1989] to handle the time-variable dataset associated with the rotating interface.

In the ring-buffer concept, each process independently calculates the grid rotation and grid distortion within its own domain. The ring-buffer data is replicated across all processes which have a rotating interface. Each process writes data into its copy of the buffer. The buffer data is then consolidated across all the processes by an MPI global *all-reduce* operation. These processes then use appropriate offsets to locate and read the data they need. This implies that the static and dynamic faces of the interface need to have the same number of grid points, but each can be subdivided into unequal sub-blocks.

## 4. Turbulence Modeling

The ensemble or Reynolds averaging of the Navier-Stokes equations yields stress-like terms, and the solution of the resulting Reynolds-averaged Navier-Stokes equations requires modeling of these apparent or “Reynolds” stresses. For computing the flow past a maneuvering vehicle, prediction of the location of the forebody vortex lift-off will be important in determining the vehicle dynamics and, for at least that reason, a good turbulence model is essential. Also, because the vortex lift-off will be a function of the near-wall flow—and because no simple analytic expression can accurately or generally describe three-dimensional near-wall flow—the chosen turbulence model must be capable of predicting the near-wall, or low-Reynolds-number, region. In addition to the three-dimensional separation that leads to vortex lift-off, large separation regions will accompany the large control surface angles that occur during extreme maneuvers, and computing these separation regions will challenge the turbulence model. Finally, these turbulent flows will contain length scales and time scales which might vary dramatically from one situation to another. For this reason, two-equation models represent the minimum acceptable level of generalized closure since the need to empirically specify either the length scale or the time scale is removed.

This section will first describe the algebraic turbulence model that was developed for use with the baseline UNCLE code. In parallel to the development of this baseline code, work proceeded on two-equation turbulence models, initially with a stand-alone model that could be tested without interfering with the code development work on the numerical algorithm. Later, a two-equation turbulence model was installed as a module within the UNCLE code.

### 4.1 Algebraic Turbulence Model

The initial turbulence model used within the UNCLE code is based on the algebraic or zero-equation model of Baldwin and Lomax [1978]. Taylor [1991] and Chen [1991] modified this algebraic model for their applications with three-dimensional, turbulent, separated flows. An attractive feature of the Baldwin-Lomax model is that it avoids the necessity of finding the edge of the boundary layer. Taylor [1991] used the modified model for incompressible flows, while Chen [1991] used the model for compressible flows, including the calculation of the wall stress for non-orthogonal grids—a technique that has carried over to this maneuvering program.

In this method, the turbulence is modeled through the use of a turbulent or “eddy” viscosity coefficient,  $\mu_T$ . As a result, in the expressions for the stress tensors in the RANS equations, the molecular coefficient of viscosity,  $\mu$ , is replaced by  $\mu + \mu_T$ . A two-region model is used for computing  $\mu_T$ . The inner region is the region closest to the wall, where the flow equations are expected to match fundamental, universal behaviors. Here, the distribution of eddy viscosity follows the Prandtl-van Driest distribution described by Warsi [1993]. In both the inner and outer formulations, the distribution of vorticity is used to determine the length scales, avoiding the necessity to determine the outer edge of the boundary layer. For the inner region,

$$(\mu_T)_{inner} = l^2 |\omega| ,$$

where

$$l = \kappa y (1 - e^{-y^*/26})$$

and

$$y^+ = \frac{y \sqrt{\tau_w / \rho}}{v};$$

$y$  is the normal distance from the wall,  $|\omega|$  is the absolute magnitude of vorticity,  $\tau_w$  is the shear stress at the surface (wall) of the body, and  $\kappa = 0.41$  is the von Karman constant. The outer region is the region far from the wall, where universal near-wall behaviors break down completely. The eddy viscosity for the outer region is given by

$$(\mu_T)_{outer} = K C_{cp} F_{wake} F_{Kleb}(y),$$

where

$$F_{wake} = \min \left[ y_{max} F_{max}, C_{wk} y_{max} \frac{(U_{diff})^2}{F_{max}} \right].$$

The quantities  $y_{max}$  and  $F_{max}$  are determined from the function

$$F(y) = y |\omega| (1 - e^{-y^*/26}),$$

where  $F_{max}$  is the maximum value of  $F(y)$  and  $y_{max}$  is the value of  $y$  at which  $F_{max}$  occurs. The function  $F_{Kleb}(y)$  is the Klebanoff intermittency factor determined from

$$F_{Kleb}(y) = \left[ 1 + 5.5 \left( \frac{C_{Kleb}}{y_{max}} \right)^6 \right].$$

The quantity  $U_{diff}$  is the difference between the maximum and minimum values of total velocity in the profile and, for boundary layers, this minimum is defined as zero. The following constants are used in the above equations:

$$C_{cp} = 1.6, \quad C_{Kleb} = 0.3, \quad C_{wk} = 1.0, \quad \text{and} \quad K = 0.0168.$$

Multiple peaks in the  $F_{max}$  function typically occur in flows at incidence due to the presence of leeward vortical structures. Degani and Schiff [1986] proposed a method to choose the first peak, which corresponds to the attached boundary layer. However, their methodology requires a knowledge of the location of the windward side of the geometry, a restriction which would greatly increase the coding complexity for the general case of a maneuvering vehicle. A much simpler approach was taken in this work in that multiple peaks in the  $F_{max}$  function were avoided by stopping the search when the first maximum was found. Another modification to the turbulence model was made for flows at incidence to account for the thick stern boundary layer. Sung, Griffin, Tsai, Huang [1993, 1995] have developed a procedure to prevent the eddy viscosity from being overpredicted in this region. The expression for the outer eddy viscosity is altered to account for the experimental observation that the characteristic length scale in the stern boundary layer "is more closely related to the length scale of the annulus between the body surface and the edge of the boundary layer than the distance between the two." In this work, rather than modify the outer eddy viscosity formulation, the search for  $F_{max}$  was further restricted by a specified constant (or search parameter).

In all the results presented here, the turbulent eddy viscosity was calculated independently in each coordinate direction. For example, for the hull configuration with stern appendages, the eddy viscosity coefficient is calculated along the computational direction going away from the hull surface,  $\eta$ , and along the computational direction going away from the stern appendages,  $\zeta$ . Since  $\eta$ -lines run perpendicular to the hull, only the hull surface is considered when the eddy viscosity is calculated for stresses which rely on  $\eta$ -derivatives. On the other hand, eddy viscosities for stresses which rely on  $\zeta$ -derivatives are a function of only the appendage surfaces, since  $\zeta$ -lines run perpendicular to the appendage. No modifications to these computed values were made in the vicinity of the hull-appendage junctions.

In wakes, the mixing-length formulation is modified in a manner suggested by Mehta, Chang, and Cebeci [1985] so that the turbulence mixing length depends upon the distance from the trailing edge instead of the distance from the wake cut of the grid. This modified damping length is given by

$$l = \kappa y \left[ 1 - e^{-(y^+ + x^+)/26} \right],$$

where

$$\chi = (x - x_{TE}).$$

## 4.2 Two-Equation Turbulence Models

During this research, two different two-equation models were implemented in conjunction with the UNCLE flow solver---the  $k-\epsilon$  model of Launder and Sharma [1974] and the  $q-\omega$  model of Coakley [1983]. Both models and their implementation are described here.

#### 4.2.1 Low-Reynolds-Number $k$ - $\epsilon$ Model

Initial investigations into two-equation turbulence modeling used the low-Reynolds-number  $k$ - $\epsilon$  model of Launder and Sharma [1974]—that is, a  $k$ - $\epsilon$  model which can be used to integrate through the “low-Reynolds-number,” or near-wall, region. The model was chosen because of its long history of success and wide-spread use in the engineering community, and because Briley and McDonald [1977] had previously coded a stand-alone module.

Here, the effects of turbulence on momentum are represented by adding the laminar viscosity to an eddy viscosity defined by

$$\mu_T = \rho C_\mu f_\mu \frac{k^2}{\epsilon},$$

where  $k$ , the turbulent kinetic energy, and  $\epsilon$ , the turbulent energy dissipation rate, are supplied by two transport equations.

The modeled forms of the transport equations for  $k$  and  $\epsilon$  have been covered extensively elsewhere. Here, it suffices to show their form. The turbulent kinetic energy equation is

$$\rho \frac{Dk}{Dt} = \frac{\partial}{\partial x_j} \left[ \left( \mu + \frac{\mu_T}{\sigma_k} \right) \frac{\partial k}{\partial x_j} \right] - \rho \bar{u}_i \bar{u}_j \frac{\partial U_i}{\partial x_j} - \rho \epsilon - D$$

and the equation for the transport of the dissipation rate is

$$\rho \frac{D\epsilon}{Dt} = \frac{\partial}{\partial x_j} \left[ \left( \mu + \frac{\mu_T}{\sigma_\epsilon} \right) \frac{\partial \epsilon}{\partial x_j} \right] - \rho \bar{u}_i \bar{u}_j \frac{\partial U_i}{\partial x_j} C_{\epsilon I} \frac{\epsilon}{k} - C_{\epsilon 2} \rho \frac{\epsilon^2}{k} + E.$$

The terms  $D$  and  $E$  arise in the low-Reynolds-number modifications. For the Launder and Sharma [1974] model,

$$D = 2\mu \frac{\partial k^{1/2}}{\partial x_j} \frac{\partial k^{1/2}}{\partial x_j},$$

which represents the value of the dissipation rate at the wall, allowing the boundary condition on  $\epsilon$  to be zero. The term denoted by  $E$ , on the other hand, is an *ad hoc* term needed to attain the correct peak of  $k$  in the logarithmic region. It takes the form

$$E = \frac{2\mu \mu_T}{\rho} \frac{\partial^2 U_i}{\partial x_j \partial x_k} \frac{\partial^2 U_i}{\partial x_j \partial x_k}.$$

These general tensor forms for  $D$  and  $E$  were given by Launder and Li [1992]. As shown, they strictly obey the Einstein summation convention and should leave no room for confusion.

Five empirical constants--and damping functions to model low-Reynolds-number effects--are needed to complete the model. For the constants, the values

$$\sigma_k = 1.0, \quad \sigma_\epsilon = 1.3, \quad C_\mu = 0.09, \quad C_{\epsilon 1} = 1.44, \quad \text{and} \quad C_{\epsilon 2} = 1.92$$

are used as specified by Launder and Sharma [1974]. The damping functions

$$f_\mu = \exp[-3.4 / (1 + R_T / 50)^2]$$

and

$$f_2 = 1 - 0.3 \exp(-R_T^2)$$

multiply the constants  $C_\mu$  and  $C_{\epsilon 2}$ , respectively. Their dependence on the turbulent Reynolds number, defined by  $R_T = \rho k^2 / \mu \epsilon$ , alleviates the need to calculate a normal distance to the wall.

Initially, the stand-alone  $k-\epsilon$  model was coupled externally to the UNCLE flow solver. At each iteration, the flow solver would write the grid and velocity field to a file. A separate code would convert this output file to a restart file for the turbulence equation solver and, then, the turbulence equation code would take the restart file as input to the two-equation model. The stand-alone code would update the turbulence parameters, calculate the eddy viscosity, and pass the eddy viscosity back to the flow solver. Even though it was rather cumbersome, this system allowed work on the turbulence model to progress independently of modifications being made to the flow solver. Based on experience with this system, work was then begun to implement a two-equation turbulence model directly into the UNCLE code.

#### 4.2.2 Low-Reynolds-Number $q-\omega$ Model

At the Applied Research Laboratory of The Pennsylvania State University, Knight and Zajaczkowski [1995] had previously installed a two-equation turbulence model into a code with a similar algorithm as used in the UNCLE code. They had successfully demonstrated the use of this model for incompressible flows over representative axisymmetric bodies. In this case, the turbulence transport equations governed the velocity scale,  $q = k^{1/2}$ , and the inverse time scale of decay,  $\omega = \epsilon / k$ . Clearly, the  $q-\omega$  model is largely determined by a straight-forward change of variables from the  $k-\epsilon$  model. As will be seen, the transport equations share a nearly identical form so that, once one set is coded, interchanging between the two is trivial. Therefore, the  $q-\omega$  model was selected for initial installation into the UNCLE code.

Transport equations are needed for the two variables. The equation for  $q$  can be derived by an exact change of variables in the equation for the turbulent kinetic energy,  $k$ . The resulting

equation can be written as

$$\rho \frac{Dq}{Dt} = \frac{\partial}{\partial x_j} \left[ \mu + \frac{\mu_T}{\sigma_q} \right] \frac{\partial q}{\partial x_j} + \frac{\rho q}{2} \left( \frac{C_\mu f_\mu \Phi}{\omega} - \omega \right), \quad (9)$$

where  $\rho$  is the density,  $\mu$  is the laminar viscosity and,  $\mu_T$  is the turbulent viscosity. The strain-rate invariant,  $\Phi$ , is defined as

$$\Phi = \left( \frac{\partial U_i}{\partial x_j} + \frac{\partial U_j}{\partial x_i} \right) \frac{\partial U_i}{\partial x_j},$$

using the solution for the mean flow from the previous time step. Also, the damping function,  $D$ , is specified as

$$f_\mu = 1 - \exp(-\alpha \rho q y / \mu). \quad (10)$$

The normal distance to the wall is represented by  $y$ , while  $\alpha$ ,  $C_\mu$ , and  $\sigma_q$  are empirical constants.

The equation for  $\omega$  is also derived by a change of variables from the  $k$  and  $\epsilon$  equations, with some simplification of terms arising from diffusion. The result in this case is

$$\rho \frac{D\omega}{Dt} = \frac{\partial}{\partial x_j} \left[ \left( \mu + \frac{\mu_T}{\sigma_\omega} \right) \frac{\partial \omega}{\partial x_j} \right] + \rho C_1 C_\mu \Phi - C_2 \omega^2, \quad (11)$$

where  $C_1$ ,  $C_2$ , and  $\sigma_\omega$  are empirical constants.

Continuing with the change of variables, the eddy viscosity, as determined by  $q$  and  $\omega$ , is

$$\mu_T = \rho C_\mu f_\mu \frac{q^2}{\omega}. \quad (12)$$

Finally, the empirical constants are given as

$$\alpha = 0.020, \quad C_1 = 0.055 + 0.500 f_\mu, \quad C_2 = 0.833, \quad C_\mu = 0.09, \quad \text{and} \quad \sigma_q = \sigma_\omega = 2.0. \quad (13)$$

Note that while the damping function,  $f_\mu$ , is still needed to model the near-wall effects, the additional low-Reynolds-number source terms (denoted as  $f_\mu$  and  $E$  in the formulation of the  $k-\epsilon$  model) have vanished or been removed. Also, while the damping function in Equation 10 now relies on a normal distance to the wall, Coakley [1983] provided an alternative form,

$$f_\mu = 1 - \exp[-\alpha \rho q^2 / (\omega \mu)] = 1 - \exp(\alpha R_T),$$

where  $R_T = \frac{pq^2}{\omega\mu}$ , that is available if needed.

#### 4.2.3 Adaptation of the $q$ - $\omega$ Model to the UNCLE Flow Solver

The turbulence model represented by Equations 9 through 13 is a closed system once the velocity field has been specified. Thus, it can be solved separately from the momentum equations, but using an identical method. In this case, the method is that which has been developed for the UNCLE flow solver, and both the method and the notation are copied here. Toward that end, the governing Equations 9 and 11 can be written as

$$\frac{\partial \mathbf{Q}}{\partial \tau} + \frac{\partial \mathbf{F}}{\partial \xi} + \frac{\partial (\mathbf{G} - \mathbf{G}_v)}{\partial \eta} + \frac{\partial (\mathbf{H} - \mathbf{H}_v)}{\partial \zeta} = \mathbf{S}, \quad (14)$$

where

$$\mathbf{Q} = J(q \ \omega)^T$$

and  $\mathbf{F}$ ,  $\mathbf{G}$ ,  $\mathbf{G}_v$ ,  $\mathbf{H}$ , and  $\mathbf{H}_v$  are the viscous and inviscid fluxes as defined for the momentum equations, but with  $q$  and  $\omega$  as the transported variables. For instance,

$$\mathbf{G} = J \begin{pmatrix} q V \\ \omega V \end{pmatrix}$$

represents the inviscid flux in the  $y$ -direction where  $V$  is the transporting contravariant velocity. Similarly, the viscous fluxes take the form

$$\mathbf{G}_v = J \begin{bmatrix} \left( \mathbf{v} + \frac{\mathbf{v}_T}{\sigma_q} \right) \left( \eta_x \frac{\partial}{\partial x} + \eta_y \frac{\partial}{\partial y} + \eta_z \frac{\partial}{\partial z} \right) q \\ \left( \mathbf{v} + \frac{\mathbf{v}_T}{\sigma_\omega} \right) \left( \eta_x \frac{\partial}{\partial x} + \eta_y \frac{\partial}{\partial y} + \eta_z \frac{\partial}{\partial z} \right) \omega \end{bmatrix},$$

where  $\nu$  and  $\nu_T$  are the laminar and turbulent kinematic viscosities. A thin-layer approximation is applied to the turbulent viscous fluxes in the same way that it was applied to the viscous fluxes of the momentum equations.

Relative to the momentum equations, the source term on the right-hand side of Equation 14 is new. For the  $q$ - $\omega$  model, it takes the form

$$\mathbf{S} = J \begin{bmatrix} q(C_\mu f_\mu \Phi/\omega - \omega)/2 \\ C_\mu C_I \Phi - C_2 \omega^2 \end{bmatrix}.$$

#### 4.2.4 Solution of the Turbulence Equations

Once the system of turbulence equations has been cast in the form of the momentum equations, it is convenient to apply the same method of solution used for the momentum equations. For demonstration purposes, Equation 14 is simplified to the form

$$\frac{\partial \underline{Q}}{\partial \tau} + \frac{\partial \underline{F}}{\partial \xi} - \underline{S} = 0.$$

Next, an implicit, central-difference scheme is implemented such that

$$\mathcal{F}(\underline{Q}^{n+1}) = \frac{\Delta \underline{Q}_i^n}{\Delta \tau} + \delta_i \bar{\underline{F}}(\underline{Q}^{n+1}) - \underline{S}^{n+1} = 0, \quad (15)$$

where  $\mathcal{F}$  simply denotes a function,  $n$  denotes a time step, and  $\delta_i$  is the central-difference operator. The form of Equation 15 lends itself to solution by Newton's method, wherein

$$\mathcal{F}'(\underline{Q}^{n+1,m}) \Delta \underline{Q}^{n+1,m} = -\mathcal{F}(\underline{Q}^{n+1,m});$$

$\mathcal{F}'$  denotes the Jacobian of  $\mathcal{F}$  with respect to  $\underline{Q}$ , and  $m$  denotes a Newton iteration. In this case, the resulting system of equations can be written as

$$-\bar{\underline{F}}_{i-1/2,i-1}^{n+1,m} \Delta \underline{Q}_{i-1} + \left( \frac{1}{\Delta \tau} + \bar{\underline{F}}_{i+1/2,i}^{n+1,m} - \bar{\underline{F}}_{i-1/2,i}^{n+1,m} - \underline{S}_{i,i}^{n+1,m} \right) \Delta \underline{Q}_i +$$

$$\bar{\underline{F}}_{i+1/2,i+1}^{n+1,m} \Delta \underline{Q}_{i+1} = - \left( \frac{\underline{Q}_i^{n+1,m} - \underline{Q}_i^n}{\Delta \tau} + \bar{\underline{F}}_{i+1/2}^{n+1,m} - \bar{\underline{F}}_{i-1/2}^{n+1,m} - \underline{S}_i^{n+1,m} \right),$$

where  $I$  is the identity matrix. From this system of equations, one can see that the Jacobian of the source term with respect to  $\underline{Q}$  is needed on the left-hand side of the matrix system. The source term itself constitutes a part of the residual calculation on the right-hand side of the matrix system.

The flux Jacobians are computed numerically in keeping with the formulation of the momentum equations; however, the Jacobian of the source term has been computed analytically since it is trivial to do so. Each Newton iteration is solved iteratively using a symmetric Gauss-Seidel solver.

This formulation of the  $q$ - $\omega$  model was added to the UNCLE flow solver and was used successfully in a number of test cases. Currently, the CPU time for the two-equation solver is approximately 30% of the time needed to solve the momentum equations alone. That cost is expected to go down once more attention is directed toward improving efficiency.

### 4.3 Nonlinear Modeling of Anisotropy

Two-equation turbulence models have become a popular choice for use in modern engineering applications of computational fluid dynamics. They represent a more general model than the rather limiting algebraic or mixing-length models and are much simpler and less computationally expensive than full Reynolds stress models (that is, models that solve each component of the Reynolds stress tensor separately). One drawback, however, is the assumption of an isotropic eddy viscosity, which causes the normal Reynolds stresses in most cases to be roughly but erroneously equal. Chen [1995] showed that the absence of these normal Reynolds stress differences is detrimental in predicting the formation and evolution of primary and secondary horseshoe vortices shed from appendage-hull intersections, an important aspect of the current study.

Early on, Rivlin [1957] had noted the potential importance of normal Reynolds stress differences. Rivlin [1957] compared turbulent flows with non-Newtonian, visco-elastic flows in a non-circular straight duct where both were characterized by secondary velocities in a plane normal to the primary flow direction. Noting that the secondary flow in the non-Newtonian fluid was generated by differences in normal stress, Rivlin [1957] suggested that differences in the normal Reynolds stresses might explain the secondary motion in turbulent flow. Several years later, Gessner and Jones [1965] showed experimentally that this was indeed the case. Building on this work, researchers such as Lumley [1970] suggested that a nonlinear constitutive relation for the Reynolds stresses, comparable to that used for non-Newtonian fluids, might be appropriate. These suggestions gave rise to two schools of nonlinear turbulence modeling in which researchers hoped to capture anisotropic effects with a nonlinear, or “anisotropic,” eddy viscosity without resorting to the solution of six second-order, nonlinear, partial differential closure equations.

The first class of models, the “algebraic Reynolds stress models,” such as that developed by Rodi [1976], are typically derived from the Reynolds stress equations by relating the transport of the Reynolds stress to the transport of the turbulent kinetic energy. The result is an implicit, nonlinear, algebraic relation for the Reynolds stresses which is also a function of  $k$  and  $\epsilon$ . The model gives improved results for the square duct problem, where turbulence-driven secondary flow is induced, but Speziale [1994] noted that the model “can give rise to divergent solutions when applied to non-equilibrium turbulent flows.”

A second school, which developed a decade later partially in response to these problems, has been termed the “nonlinear  $k$ - $\epsilon$  models.” These models, though they have been derived in different ways by different investigators, all assume that the relationship between the Reynolds stress and the mean strain rate tensor is not linear but includes terms which are quadratic in the mean strain rate tensor as well. This idea is not new, but instead has been applied before in visco-elastic fluid dynamics and rarefied gas dynamics modeling.

Nonlinear  $k$ - $\epsilon$  models, such as those proposed by Yoshizawa [1984] and Speziale [1987], have become an attractive option to users of the  $k$ - $\epsilon$  model. Reasons for their popularity may be the ease with which they can be implemented into an existing  $k$ - $\epsilon$  code and their inherent lack of assumptions concerning flow conditions or geometry. Additionally, Gatski and Speziale [1993] showed that these models represent a limiting form of the exact explicit solution of the implicit algebraic Reynolds stress models, such as the model developed by Rodi [1976]. Thus, they can be derived either by series expansion arguments or directly from the full Reynolds stress equations.

#### 4.3.1 The Nonlinear $k-\epsilon$ Models

All of the nonlinear  $k-\epsilon$  models bear a striking similarity which allows them to be represented in large part by a single set of equations. To begin, each model is intended for use with the RANS equations,

$$\rho \frac{DU_i}{Dt} = \frac{\partial}{\partial x_j} (\tau_{ij} - \rho \bar{u}_i \bar{u}_j), \quad (16)$$

where  $-\rho \bar{u}_i \bar{u}_j$  represents the Reynolds stress tensor. Each model proposes that the Reynolds stress be modeled as

$$-\rho \bar{u}_i \bar{u}_j = -P_T \delta_{ij} + 2\mu_T E_{ij} - \frac{\mu_T^2}{P_T} C_\beta \left( S_{\beta ij} - \frac{1}{3} S_{\beta mm} \delta_{ij} \right) + \frac{\mu_T^2}{P_T} F_{ij}, \quad (17)$$

where  $P_T = \frac{2}{3} \rho k$  and

$$E_{ij} = \frac{1}{2} \left( \frac{\partial U_i}{\partial x_j} + \frac{\partial U_j}{\partial x_i} \right)$$

is the mean strain rate tensor. Summation is performed over  $\beta$ , resulting in constants  $C_1$ ,  $C_2$ , and  $C_3$  and three forms of  $S_{\beta ij}$ :

$$S_{1ij} = \frac{\partial U_i}{\partial x_k} \frac{\partial U_j}{\partial x_k}, \quad S_{2ij} = \frac{1}{2} \left( \frac{\partial U_i}{\partial x_k} \frac{\partial U_k}{\partial x_j} + \frac{\partial U_j}{\partial x_k} \frac{\partial U_k}{\partial x_i} \right), \quad \text{and} \quad S_{3ij} = \frac{\partial U_k}{\partial x_i} \frac{\partial U_k}{\partial x_j}.$$

The conventional linear  $k-\epsilon$  model is obtained when  $C_\beta$  and  $F_{ij}$  are zero.

The major differences in the models can be confined to the trailing term,  $F_{ij}$ . Referring to Table 1, the models of Yoshizawa [1984] and Speziale [1987] both include a material derivative of the mean strain rate tensor. The derivation by Yoshizawa [1984] included a material derivative and a third-order second-derivative term, but they were never recommended for use. The material derivative in the Speziale [1987] model, on the other hand, arises from an Oldroyd derivative of the mean strain rate tensor and was felt to be significant in his calculation of the flow over a backward facing step. The model developed by Myong and Kasagi [1990] includes a term for modeling the near-wall effects in a two-dimensional channel. For that term,  $m$  and  $n$  represent the streamwise and normal directions in the two-dimensional channel, and no summation is performed over them. As a result, the term is *not* frame-invariant and is not generally applicable. Finally, the second model by Yoshizawa [1986] includes a term to model thermal buoyancy effects. That term was used by Sada and Ichikawa [1993] where they obtained good results for the flow over a heated flat plate, but it seems to be frequently overlooked by other researchers.

The constants in Equation 17 are empirical. They are listed in Table 1 but have been modified to suit the form in which they are used here. Speziale [1987], for example, had only one empirical constant in his original work which he arrived at experimentally, and all four constants

which appear in Table 1 are factors of it. The constants of Nisizima and Yoshizawa [1987] and Myong and Kasagi [1990] were arrived at through computer optimization.

Table 1. A Comparison of Nonlinear  $k-\epsilon$  Models

Model	$C_1$	$C_2$	$C_3$	$F_{ij}$
Yoshizawa [1984]	2.37	-0.393	1.98	$-5.14 \frac{DE_{ij}}{Dt} + 7.43 \frac{\mu_T}{\rho} \frac{\partial^2 E_{ij}}{\partial x_k \partial x_k}$
Speziale [1987]	3.36	2.24	-1.12	$4.48 \frac{DE_{ij}}{Dt}$
Nisizima and Yoshizawa [1987]	5.76	?	-1.23	0
Yoshizawa [1986]	5.76	-16.5	-1.23	$-2.47 \gamma \left( g_i \frac{\partial T}{\partial x_j} + g_j \frac{\partial T}{\partial x_i} - \frac{2}{3} g_k \frac{\partial T}{\partial x_k} \delta_{ij} \right)$
Nisizima [1989]	4.69	-27.2	-.551	0
Rubinstein and Barton [1990]	2.80	17.1	-1.15	0
Myong and Kasagi [1990]	5.93	3.33	-1.11	$4.94 \frac{\mu}{\mu_t} (\delta_{ij} + \delta_{in} \delta_{jn} - 4 \delta_{im} \delta_{jm}) \left( \frac{\partial \sqrt{k}}{\partial x_n} \right)^2$
Sada and Ichikawa [1993]	4.69	-27.2	-.551	$2.47 \frac{Gr}{Re^2} \left( \delta_{i3} \frac{\partial T}{\partial x_j} + \delta_{j3} \frac{\partial T}{\partial x_i} - \frac{2}{3} \delta_{k3} \frac{\partial T}{\partial x_k} \delta_{ij} \right)$

Excluding the constants for the first model by Yoshizawa [1984], which were not really advocated for use, it can be seen that agreement among the various investigators for  $C_1$  and  $C_3$  is fairly good. This may be attributed to the fact that Yoshizawa [1986], Speziale [1987], and Myong and Kasagi [1990] calibrated their models, either experimentally or computationally, with two-dimensional channel flows in which  $C_2$  does not appear. The agreement on  $C_2$  is very poor, apparently due to the relative lack of effort spent on its calibration.

#### 4.3.2 Selection of a Nonlinear Model

Initial work with the Speziale [1987] model was plagued by numerical difficulties which were traced to the material derivative in  $F_{ij}$ . Speziale [1987] had observed similar problems in his own studies and suggested that the trouble might be alleviated by numerical smoothing. It was decided for the present work that the artificial dissipation introduced by filtering was unacceptable, and instead, encouraged by the lead of Nisizima and Yoshizawa [1987], the term was dropped altogether. Recent observations by Yakhot and his colleagues [1992] and by Speziale [1995] seem to

indicate that the Speziale [1987] model, in practice, no longer includes this term. Nevertheless, with  $F_{ij}$  dropped from the Speziale [1987] model for numerical reasons, dropped from the Myong and Kasagi [1990] model for generality, and dropped from the Yoshizawa [1986] model when thermal buoyancy effects are neglected, all of the models reduce to that proposed by Nisizima and Yoshizawa [1987]. At this point, only a set of constants needs to be selected; those suggested by Myong and Kasagi [1990] were chosen since they were complete and closely resembled those offered by Nisizima and Yoshizawa [1987].

#### 4.3.3 Implementation of the Nonlinear Model into the $q$ - $\omega$ Model

The nonlinear model has traditionally been reserved for work with the  $k$ - $\epsilon$  model but can be easily adapted for the  $q$ - $\omega$  model by substituting Equations 10 and 12 and the relations  $q = k^{1/2}$  and  $\omega = \epsilon / k$  into Equation 17. Thus, the nonlinear  $q$ - $\omega$  model can be written as

$$-\rho \overline{u_i u_j} = -\frac{2}{3} \rho q^2 \delta_{ij} + 2\mu_T E_{ij} - \mu_T \frac{1}{\omega} C_\beta \left( S_{\beta ij} - \frac{1}{3} S_{\beta kk} \delta_{ij} \right), \quad (18)$$

where a summation is again performed over  $\beta$ . This form includes a regrouping of constants which is easy to conduct analytically. Beyond that, there is no reason to expect that the values of the empirical constants should be effected by the change in variables; however, the calibration is easy to check.

#### 4.3.4 Calibration of the Model Constants

For fully-developed, two-dimensional turbulent flows in equilibrium, Equation 9 reduces to

$$\frac{dU}{dy} = \frac{\omega}{\sqrt{C_\mu}},$$

which allows the normal stresses from Equation 18 to be written as

$$\begin{pmatrix} \overline{u_1 u_1} / k - 2/3 \\ \overline{u_2 u_2} / k - 2/3 \\ \overline{u_3 u_3} / k - 2/3 \end{pmatrix} = \frac{1}{3} \begin{pmatrix} 2C_1 - C_3 \\ -C_1 + 2C_3 \\ -C_1 - C_3 \end{pmatrix}, \quad (19)$$

where  $C_1$  and  $C_3$  are empirical constants of the nonlinear model, Equation 18. This equation, according to the model, is equally valid in the logarithmic region of a fully-developed channel flow or for homogeneous shear flow, both of which have available experimental data. It should be noted that Equation 19 represents a system of three equations in two unknowns; however, since the equations represent measures of anisotropy and must add to zero, only two of the equations are independent.

Experiments can help to determine the constants for the nonlinear model. Champagne, Harris, and Corrsin [1970] acquired experimental data from a nearly homogeneous shear flow, while

Kreplin and Eckelmann [1979] acquired data from a two-dimensional fully-developed channel flow at  $y^+ \approx 40$ . In fact, two sets of data were taken for nearly homogeneous shear flow experiments since Harris, Graham, and Corrsin [1977] thought that the first experiment was contaminated by convective effects. Figure 8 shows the calibrated constants  $C_1$  and  $C_3$  based on these experimental samplings, as well as the values for the constants suggested by various authors. Here, the scatter in the suggested constants falls within the range dictated by a combination of the validity of the model and the experimental error.

Unfortunately,  $C_2$  does not appear in this study, and it is frequently not clear how investigators have arrived at its value. In fact, suggested values of  $C_2$  vary drastically, and its calibration should be the focus of future research. In the meantime, the moderate values by Myong and Kasagi [1990] were chosen. Table 2 shows the improvement in the fluctuating velocities of a two-dimensional channel flow provided by the chosen model against experimental data at  $y^+ \approx 40$ .

Table 2. Fluctuating Velocities in the Logarithmic Layer of Fully-Developed Channel Flow

	Linear Model	Nonlinear Model <sup>1</sup>	Experimental Data <sup>2</sup>
$\tilde{u}_1 / u_\tau$	1.50	2.04	2.10
$\tilde{u}_2 / u_\tau$	1.50	1.00	1.02
$\tilde{u}_3 / u_\tau$	1.50	1.22	1.14

<sup>1</sup> Myong and Kasagi [1990]

<sup>2</sup> Kreplin and Eckelmann [1979]

#### 4.3.5 Numerical Implementation

As mentioned previously, the nonlinear model in Equation 18 simply adds new terms to the traditional linear model. Thus, if the Reynolds stress tensor is written

$$-\rho \bar{u}_i \bar{u}_j = (-\rho \bar{u}_i \bar{u}_j)_{\text{linear}} + (-\rho \bar{u}_i \bar{u}_j)_{\text{nonlinear}},$$

then Equation 16 becomes

$$\rho \frac{DU_i}{Dt} = \frac{\partial}{\partial x_j} \left[ \tau_{ij} + (-\rho \bar{u}_i \bar{u}_j)_{\text{linear}} \right] + \frac{\partial}{\partial x_j} (-\rho \bar{u}_i \bar{u}_j)_{\text{nonlinear}}. \quad (20)$$

The nonlinear term also enters into the turbulence equation production terms; however, the terms can be shown to be identically zero in two-dimensional flows and are dropped in three-dimensional problems as a simplification. The additional terms in Equation 20 can be considered correction terms and are expected to be small. Thus, the additional terms were treated explicitly and added with a minimum of coding changes since the implicit solver was left intact.

## 5. Coupling with a Vehicle Dynamics Solver

Prediction of a vehicle's trajectory requires coupling the fluid dynamics and the vehicle dynamics. The equations governing the fluid dynamics are the Navier-Stokes equations; Newton's Second Law governs the vehicle's motion, resulting in the six-degree-of-freedom (6DOF) equations. These equations describe the acceleration of a body at an instant in time, given the totality of forces and moments acting on the body. Integration of these equations yields the time history of the body's velocity and rotation rate. From this information, the trajectory (that is, the orientation and position of the vehicle) can be deduced using purely kinematical relations.

There are two relevant coordinate systems involved in the determination of the trajectory. First, there is a body-fixed system ( $x$ ,  $y$ ,  $z$ ) that is rigidly attached to the moving vehicle. It is this system to which the 6DOF equations are referenced. Additionally, there is an inertial or "earth"-fixed system ( $X$ ,  $Y$ ,  $Z$ ) to which the position and orientation of the vehicle are referenced (it is also in this system that the RANS equations are solved). By convention, this system is defined with  $X$  pointing North,  $Y$  pointing East, and  $Z$  pointing toward the center of the Earth (that is, gravitational acceleration points in the positive  $Z$ -direction). As this is taken to be an inertial system, the rotation of the Earth is neglected. Figure 9 shows a schematic of these frames of reference.

The fluid dynamic/vehicle dynamic coupling procedure is as follows. The flow solution about the vehicle is advanced in time by integrating the Reynolds-averaged Navier-Stokes equations--by the procedure described in the numerical approach section--over an increment of time from  $t$  to  $t + \Delta t$ . The hydrodynamic forces and moments are then updated by integration of the pressure and shear stresses over the vehicle surface. With these forces and moments, the 6DOF equations and the kinematic relations are integrated over the same  $\Delta t$  to yield the position and velocity of each point in the computational grid at  $t + \Delta t$ . This process is then repeated for the next time interval. The solution procedure for the RANS equations has been discussed previously; the solution procedure for the equations governing the vehicle's trajectory is described in this section. It should be noted that the code for the assembly and solution of the 6DOF and kinematical equations utilized in this work is derived directly from the vehicle trajectory code TRJv by Smith and Watkinson [1994].

The 6DOF equations as described by Gertler and Hagen [1967] for a submarine configuration can be simplified and rewritten in the following form

$$\frac{ds}{dt} = A^{-1}(f - b), \quad (21)$$

where  $A$  is the "mass" matrix,  $s$  is the vector of velocities and rotation rates,  $b$  is the inertial coupling vector, and  $f$  is the vector of forces and moments (due to gravity, buoyancy, and hydrodynamic

phenomena). The "mass" matrix is given by

$$\mathbf{A} = \begin{bmatrix} m & 0 & 0 & 0 & mz_G & -my_G \\ 0 & m & 0 & -mz_G & 0 & mx_G \\ 0 & 0 & m & my_G & -mx_G & 0 \\ 0 & -mz_G & my_G & I_x & -I_{xy} & -I_{xz} \\ mz_G & 0 & -mx_G & -I_{xy} & I_y & -I_{yz} \\ -my_G & mx_G & 0 & -I_{xz} & -I_{yz} & I_z \end{bmatrix},$$

where  $m$  is the vehicle mass,  $(x_G, y_G, z_G)$  is the location of the center of gravity,  $(I_x, I_y, I_z)$  are the moments of inertia of the vehicle, and  $(I_{xy}, I_{xz}, I_{yz})$  are the products of inertia of the vehicle--all of which are measured in the body-fixed frame-of-reference. The vector of velocities and rotation rates is given by

$$\mathbf{s} = \begin{bmatrix} u \\ v \\ w \\ p \\ q \\ r \end{bmatrix},$$

where  $(u, v, w)$  are the linear velocities and  $(p, q, r)$  are the rotational velocities in the body-fixed frame of reference. The inertial coupling vector is defined as

$$\mathbf{b} = \begin{bmatrix} m[wq - vr - x_G(q^2 + r^2) + y_Gpq + z_Gpr] \\ m[ur - wp - y_G(r^2 + p^2) + z_Gqr + x_Gqp] \\ m[vp - uq - z_G(p^2 + q^2) + x_Grp + y_Grq] \\ (I_z - I_y)qr - I_{xz}pq + I_{yz}(r^2 - q^2) + I_{xy}pr + m[y_G(vp - uq) - z_G(ur - wp)] \\ (I_x - I_z)rp - I_{xy}qr + I_{xz}(p^2 - r^2) + I_{yz}qp + m[z_G(wq - vr) - x_G(vp - uq)] \\ (I_y - I_x)pq - I_{yz}rp + I_{xy}(q^2 - p^2) + I_{xz}rq + m[x_G(ur - wp) - y_G(wq - vr)] \end{bmatrix}$$

Finally, the applied forces and moments appear in the following form:

$$\mathbf{f} = \begin{bmatrix} -(W-B) \sin(\theta) + F_x \\ (W-B) \cos(\theta) \sin(\phi) + F_y \\ (W-B) \cos(\theta) \cos(\phi) + F_z \\ (y_G W - y_B B) \cos(\theta) \cos(\phi) - (z_G W - z_B B) \cos(\theta) \sin(\phi) + M_x \\ -(x_G W - x_B B) \cos(\theta) \cos(\phi) - (z_G W - z_B B) \sin(\theta) + M_y \\ (x_G W - x_B B) \cos(\theta) \sin(\phi) + (y_G W - y_B B) \sin(\theta) + M_z \end{bmatrix},$$

where  $W$  is the vehicle weight,  $B$  is the vehicle buoyancy,  $(x_B, y_B, z_B)$  is the location of the center of buoyancy in the body-fixed frame of reference,  $(\phi, \theta)$  are the Euler angles about the inertial  $X$  and  $Y$  axes, and  $(F_x, F_y, F_z, M_x, M_y, M_z)$  are the hydrodynamic forces and moments in the body-fixed frame of reference. It is these forces and moments that are computed from integration of the fluid stresses over the vehicle surface. Clearly, it is through these terms that the fluid dynamic/vehicle dynamic coupling occurs. Jonnalagadda [1996] describes the force and moment calculation procedure.

To deduce the inertial orientation and position of the vehicle from the above relations, seven additional kinematic relations are required: four for the orientation and three for the position. The inertial orientation is described by quaternions whose evolution equations may be written in the following form:

$$\frac{d\mathbf{e}}{dt} = \boldsymbol{\Omega}\mathbf{e}, \quad (22)$$

where  $\mathbf{e} = [e_0, e_1, e_2, e_3]^T$  and

$$\boldsymbol{\Omega} = \frac{1}{2} \begin{bmatrix} 0 & -p & -q & -r \\ p & 0 & r & -q \\ q & -r & 0 & p \\ r & q & -p & 0 \end{bmatrix}.$$

The more familiar Euler angles  $(\phi, \theta, \psi)$  are related to the quaternions by the following equations:

$$\tan(\phi) = \frac{2(e_0 e_1 + e_2 e_3)}{(e_0^2 - e_1^2 - e_2^2 + e_3^2)},$$

$$\tan(\theta) = \frac{2(e_0e_2 - e_1e_3)}{2\sin(\phi)(e_0e_1 + e_2e_3) + \cos(\phi)(e_0^2 - e_1^2 - e_2^2 + e_3^2)},$$

and

$$\tan(\psi) = \frac{2(e_1e_2 + e_0e_3)}{(e_0^2 + e_1^2 - e_2^2 - e_3^2)}.$$

The Euler angles ( $\phi$ ,  $\theta$ ,  $\psi$ ) represent right-hand rotations about the inertial ( $X$ ,  $Y$ ,  $Z$ ) axes respectively. Finally, the inertial position is given by the solution to the following system:

$$\frac{d\mathbf{r}}{dt} = \mathbf{h}, \quad (23)$$

where  $\mathbf{r} = [X, Y, Z]^T$  and

$$\mathbf{h} = \begin{bmatrix} u[(e_0^2 + e_1^2) - (e_2^2 + e_3^2)] + v[2(e_1e_2 - e_0e_3)] + w[2(e_1e_3 - e_0e_2)] \\ u[2(e_1e_2 + e_0e_3)] + v[(e_0^2 + e_2^2) - (e_1^2 + e_3^2)] + w[2(e_2e_3 - e_0e_1)] \\ u[2(e_1e_3 - e_0e_2)] + v[2(e_0e_1 + e_2e_3)] + w[(e_0^2 + e_3^2) - (e_2^2 + e_1^2)] \end{bmatrix}.$$

In theory, Equation 21 can be integrated for the body-fixed velocities and rotation rates independently of Equations 22 and 23. Using these time-dependent velocities and rotation rates, Equation 22 can then be integrated for the vehicle orientation. Finally, with everything on the right hand side of Equation 23 known, it is a simple matter to integrate Equation 23 for the inertial position of the vehicle. In practice, however, Equations 21 through 23 are combined into a single system of 13 evolution equations. This system is then numerically integrated in time using a fourth-order accurate Runge-Kutta-Merson scheme.

Like the RANS equations, the 6DOF equations are actually solved in nondimensional form. When the RANS equations are nondimensionalized, the Reynolds number is naturally introduced. For a given geometry, this lone nondimensional parameter dictates the behavior of the resultant flow field. In other words, with everything else constant, different Reynolds numbers can potentially yield vastly different flow fields. When the RANS equations are coupled with the 6DOF equations and nondimensionalized, in addition to the Reynolds number, there are 14 new, independent nondimensional parameters. These include: nondimensional weight, buoyancy, moments of inertia, products of inertia, as well as the normalized locations of the centers of gravity and buoyancy. A change in any one of these 15 parameters has the potential to substantially impact the resultant vehicle trajectory. This dependency highlights the sensitivity in predicting the maneuvering characteristics of an underwater vehicle.

## 6. Propulsor Treatments

The simplest way of incorporating the primary function of the propulsor is to model the propulsor within UNCLE using body forces. A body-force propulsor model that is applied at a single plane is often called an actuator disc, while a model that is applied over a region more representative of the actual propulsor region is sometimes referred to as an actuator duct. However, as the rotating blades within a propulsor interact with time-dependent flow structures shed from upstream surfaces on a maneuvering vehicle, the simple body-force model will prove to be inadequate, especially for moderate and extreme maneuvers. Within this maneuvering program, the research team developed both types of propulsor treatments.

### 6.1 Body-Force Propulsor Model

The research team selected a body-force model because of its simplicity, its computational efficiency, and their experience with the model for similar simulations. For instance, Whitfield and Jameson [1984] used a body-force model for an open propeller, while Pankajakshan, Arabshahi, and Whitfield [1993] used one for a ducted fan. As explained by Whitfield and Jameson [1984], the basic approach consists of including body forces in Equation 1, such that the model operates on the fluid in a manner similar to the way that an actual propulsor operates on the fluid.

The model requires data from either measured databases or conventional propulsor design tools. Yang, Hartwich, and Sundram [1990] showed how to use this type of data for a body-force propulsor model. Specifically, the prescribed body forces were based upon known parameters of thrust and torque coefficients ( $C_T$  and  $C_Q$ ) and an assumed circulation distribution,  $g(r)$ . The radial distribution of the axial and circumferential body forces per unit volume were obtained from

$$F_{B_x}(r) = \frac{C_T r_{tip} g(r)}{4 \Delta x \int_{r_{hub}}^{r_{tip}} g(r) r dr}$$

and

$$F_{B_\theta}(r) = \frac{C_Q r_{tip}^3 g(r)}{2 \Delta x \int_{r_{hub}}^{r_{tip}} g(r) r dr} ,$$

where  $r_{hub}$  and  $r_{tip}$  are some reference radii of the propulsor blade hub and blade tip, respectively, and  $\Delta x$  is the thickness of the actuator disc (or duct). The circulation  $g(r)$  was assumed to be

$$g(r) = r \sqrt{1 - r} ,$$

where

$$r = \frac{r - r_{hub}}{r_{tip} - r_{hub}} .$$

These resulting components of the body force vector were then distributed to the center of the appropriate cells in this cell-centered finite-volume scheme within the region where the propulsor was located.

## 6.2 Actual Rotating Propulsor

For maneuvers in which the body-force model proves inadequate, the research team needed to develop the capability to compute the complicated unsteady interaction between a marine propulsor and stern appendages. Past researchers in the computational turbomachinery community have previously developed technologies to treat the problem of transferring data between grid blocks in relative motion. For instance, Rai [1985] developed a zonal method, in which the blocks slide against one another--and, consequently, grid lines become discontinuous across a block interface. This method requires complicated interpolation to maintain flux conservation at this interface. Another method proposed by McDonald [1985] maintains grid continuity by continuously distorting the grid lines as the blocks moved relative to one another, resulting in a highly-stretched grid.

This work adopts the method used in the compressible versions of the UNCLE code for turbomachinery, called localized grid distortion (LGD). Whitfield and his colleagues [1987] performed much of the early work, with Janus [1989] and Janus and Whitfield [1989, 1990] completing the development of LGD. Janus, Whitfield, Horstman, and Mansfield [1990], Janus, Horstman, and Whitfield [1992], and Chen and Whitfield [1993] have provided further experience for compressible flow problems. The LGD method insures continuous grid lines across block interfaces with relative motion and also minimizes grid stretching. The data communication between blocks is accomplished without interpolation. Flux conservation across block boundaries is maintained to preserve the conservation property of the finite-volume scheme.

Briefly, LGD calls for distortion of grid cells in the vicinity of the relative motion block interface in order to maintain continuity of grid lines across the interface. During this process, the adjacent blocks must continuously switch communication partners (referred to as "clicking") to minimize the grid stretching. A simple bookkeeping procedure insures a correct match between the communication partners so that information can be exchanged between the two blocks. Numerical temporal error can be introduced when switching communication partners; however, this error is minimized by using multiple Newton subiterations and/or multigrid cycles. Since the cell volumes in the vicinity of block interface change in time, Thomas and Lombard [1978] maintain that the geometric conservation law must be satisfied.

## 7. Results with the Baseline Flow Solver

Using the UNCLE code described previously, the research team proceeded with the application of this baseline solver to various flow problems. The ultimate objective of this work, which was the prediction of the trajectory of fully-appended, self-propelled, maneuvering vehicles, involved more complicated flow fields and configurations than those corresponding to the experiments for which measured data were available. Nevertheless, the team took the approach to perform rather critical comparisons with either analytical solutions or experimental data that were available. In this manner, computations could be carried out in order to validate the code to the extent possible, as each additional capability and improvement was added.

This section includes both steady and unsteady computations using the baseline UNCLE code with the algebraic turbulence model. Later sections will include results using the parallel version of the code, using two-equation turbulence models, and incorporating the coupling between the fluid dynamics and the vehicle dynamics. The quality of agreement for all of the steady and unsteady flow computations with experimental data and analytical solutions has been considered reasonable to excellent. It should be noted that all computations were carried out on several different computer workstations; such as an IBM RS6000 Model 560 (512 Mb RAM), an IBM RS6000 Model 590 (1536 Mb RAM), and a SGI Power Challenge R4400 and R8000 (2048 Mb RAM).

### 7.1 Flat-Plate Boundary Layers

The ability of the flow solver to correctly compute the flow over a maneuvering vehicle depends strongly on its ability to resolve boundary layers. Obtaining the proper boundary layer velocity profiles will provide the correct skin-friction distribution and generate the proper amount of vorticity. Therefore, while the computation of flat-plate boundary layers hardly seems ambitious, it is prudent that the numerical scheme being used can predict the appropriate velocity profile. The present computational approach has an advantage in computing these profiles since the Roe approximate Riemann solver was constructed in such a way that discontinuous surfaces, such as slip lines and contact discontinuities, can be captured exactly on grids that are properly aligned. Consequently, viscous regions can be captured accurately with a modest number of grid points. Figure 10 gives a comparison of the numerically-obtained boundary layer velocity profile to the Blasius velocity profile for laminar flow past a flat plate at a Reynolds number of 10,000 (based on plate length). While the agreement is not exact, it is considered to be good, especially in light of the fact that there are less than ten grid points in the viscous region. For turbulent flow, Figure 11 shows comparisons between the computed velocity profile and the law of the wall for a Reynolds number of 5,000,000 (based on plate length). Once again the velocity profile has been quite accurately predicted with less than fifteen grid points in the viscous region.

### 7.2 SUBOFF Barebody

Next, the research team moved to a test case where they could apply the UNCLE code to the computation of turbulent axisymmetric flow over a body typical of an actual underwater vehicle. This barebody represents the simplest form of a geometry that was used throughout this maneuvering program. Taylor [1991] also used the UNCLE code to make comparisons between computations and

experimental data obtained by Huang, Groves, and Belt [1980] for a similar axisymmetric body with an inflected stern.

In an effort to obtain code validation data on a submarine-type vehicle, Groves, Huang, and Chang [1989] designed an axisymmetric hull model that could be used with and without typical appendage components, such as a fairwater (or sail) and four identical stern appendages. They referred to the model and the subsequent experimental project as SUBOFF. Initially, the project was established as a competitive, blind test case for the evaluation of several computational codes. Huang and his colleagues [1992] conducted experiments by installing SUBOFF within a wind tunnel using two support struts. The model included a large number of static-pressure taps and some small obstacle blocks that stagnate the flow very close to the surface to produce a pressure rise that is approximately proportional to the shear stress. They also used various hot-film probes to measure the mean velocities and Reynolds stresses in the aft region of the model, close to where the propeller would exist. Using a viscous-inviscid interaction procedure, they computed the blockage effects within the tunnel and corrected the data. Using an identical model (except for the locations of static-pressure taps), Roddy [1990] reported experimental results using two support struts to tow the model in a towing tank. Aside from acquiring additional static-pressure measurements, he installed strain-gauge force cells within the support struts to obtain force and moment coefficients. All of the experiments were conducted at different angles of attack or drift at a Reynolds number of 12,000,000 (based on model length) for the wind tunnel tests and 14,000,000 for the towing tank tests.

The computation of the barebody SUBOFF at zero angle of attack was the first application of the multigrid algorithm to high Reynolds number turbulent flow. As a consequence of the relatively high Reynolds number of 12,000,000, grid lines must be located very close to the surface of the geometry in order to resolve the boundary layer. Three grids, indicated by Grids I, II, and III, were built with the same overall number of points ( $129 \times 65 \times 2 = 16,770$ ), but with different grid spacings near the surface (where the normal distance to first grid cell equals 0.00001, 0.000001, and 0.0000001 of the body length--with an average  $y^+$  value of 3.67, 0.363, and 0.036, respectively). The minimum value of  $y^+$  is an important measure for the resolution of the turbulent boundary layer. Figure 12 shows that these grids result in extremely high aspect ratios of grid cells on the surface. The three different grids in this study provided the opportunity to investigate the grid sensitivity of the multigrid scheme and to examine the efficiency and accuracy of the solution using such high aspect ratios and stretched grids--which are essential for simulation of high Reynolds number flows. Figures 13 through 18 show the convergence histories and CPU times of both the multigrid and single-grid solutions on the three different grids. Very fast convergence rates were obtained in multigrid solutions for all cases. The residuals were reduced to machine accuracy within 150 to 250 multigrid cycles, which resulted in a 45-60% savings in CPU time over single-grid solutions. These figures also demonstrate that the convergence property of the multigrid scheme was not sensitive to the grid spacing for up to 0.000001 of the body length and that this algorithm was robust in handling extremely high aspect ratio grids. Even though the convergence rate is a little bit slower on Grid III, which had the closest first grid point to the surface, it was still quite satisfactory. For the multigrid solutions using Grid III, Figures 19 and 20 show the surface-pressure coefficient,  $C_p$ , and the skin-friction coefficient,  $C_f$ , respectively. These solutions match reasonably well with the experimental data of Huang and his colleagues [1992], with little difference found between the multigrid and single-grid solutions.

Figure 21 demonstrates an interesting feature associated with the multigrid scheme. The final skin-friction coefficient distribution for the multigrid algorithm was reached at an earlier stage of

convergence than for the single-grid scheme. The  $C_f$  distribution does not change for the multigrid solution once the residual is dropped nearly 3 orders of magnitude from the initial -2.37 to -5.11. But for the single-grid solution, a reduction of 5 orders of magnitude in residual (from the initial -2.37 to -7.41) is required to reach the final solution. Note that skin friction is a very sensitive parameter since it involves the gradient of velocity near the surface. Once this parameter is converged, it is safe to say that all other variables are also converged. The implication of this result is that the actual savings in CPU time of the multigrid solution over the single-grid solution should be higher than indicated by the previous figures.

A solution at a very high Reynolds number of 1,200,000,000 was also obtained on Grid III, which resulted in an average  $y^+$  value of 2.62 for the first grid cell off the surface. This  $y^+$  value is small enough to resolve the viscous sublayer at this high Reynolds number. Figures 22 and 23 show the convergence histories and CPU times of both multigrid and single-grid solutions. Although the convergence rates of both multigrid and single-grid solutions at this Reynolds number are slower than those at the previous Reynolds number, a 65% savings in CPU time is still achieved with the multigrid solution over the single-grid solution. Figures 24 and 25 show the computed  $C_p$  and  $C_f$  distributions along the hull surface. Since no experimental data was available for this geometry at this Reynolds number, a correlative comparison was made on the  $C_f$  curve at Reynolds numbers of 12,000,000 and 1,200,000,000 using the formula given by Schlichting [1979]. It is apparent that a reasonable skin-friction distribution was obtained at this Reynolds number.

### 7.3 Prolate Spheroid

During a maneuver, vehicles operate at an angle of attack, creating a cross flow along the hull and a subsequent three-dimensional separation. A physics-based means of predicting a vehicle maneuver must be able to compute this three-dimensional separation in order to obtain the correct static-pressure and skin-friction distributions, as well as to correctly calculate where vortical structures leave the surface and enter the flow field. As part of a continuing experimental research program, Chesnakas, Simpson, and Madden [1994] acquired data for a 6:1 prolate spheroid at 10° angle of attack, and this experiment provided an excellent test case to show how well UNCLE could predict flow over a body with cross-flow separation.

The UNCLE simulation of the turbulent flow over a 6:1 prolate spheroid at 10° angle of attack was conducted at a Reynolds number of 4,200,000 (based on the model length and the freestream velocity). Symmetry of the geometry was exploited to reduce the total number of grid points used in the O-type grid of size 81x41x41 (136,161 points). The average  $y^+$  value of the first grid line near the body was 2.56. Numerical solutions were obtained for the single grid, for a 4-level multigrid with full-coarsening, and with semi-coarsening in the axial and radial computational directions. Figures 26 and 27 show the residual histories and CPU times. These results indicate that semi-coarsening has the best convergence rate, with 56% savings in CPU time over the single-grid solution, while full-coarsening saves 28.6% in CPU time compared to the single-grid solution.

Figure 28 provides comparisons between the numerical results and the experimental data for the static-pressure distributions along the prolate spheroid at different circumferential locations along the body. Next, Figures 29 through 31 show the profiles of the  $u$ -component of velocity at sections  $x/L = 0.4, 0.6$ , and  $0.772$ , where  $r$  is the normal distance from the surface. These particular

sections were chosen for comparison because the primary separation is not yet developed at  $x/L = 0.4$ , is incipient at  $x/L = 0.6$ , and is well developed at  $x/L = 0.772$ --according to Chesnakas, Simpson, and Madden [1994]. Note that the measured  $u$  velocity component is in the local freestream direction, whereas the computed  $u$  velocity component is in the axial direction of the body. It was assumed that the difference between these quantities was not significant since the angle of attack is not large. Computational results show good agreement with the experiment at most locations, except for the last section at  $x/L=0.772$  for circumferential locations corresponding to values of  $\phi$  greater than  $115^\circ$ , which may be due to the algebraic turbulence model used for these computations.

## 7.4 Appendage Junction Flow

An actual maneuvering underwater vehicle can include a number of appendages. In the junction region where the appendage is attached to the hull, the flow undergoes a three-dimensional separation and develops a "horseshoe" or "necklace" vortex. For the same reason as with the three-dimensional cross-flow separation on the hull, a physics-based means of predicting a vehicle maneuver must be able to compute this three-dimensional flow field. To investigate this type of flow, Devenport and Simpson [1990] conducted a comprehensive experiment, where they mounted a modified NACA 0020 airfoil on a flat plate in their wind tunnel. The Reynolds number was 500,000 (based on the airfoil chord length).

The research team performed a simulation of this appendage junction flow using the baseline UNCLE code. The experimental data selected for comparison are the distributions of the static-pressure coefficient,  $C_p$ , on both the wing and the flat plate, and the  $u$  (axial) component of velocity at the various stations shown in Figure 32. These stations correspond approximately to the separation (or saddle) point upstream of the leading edge, the leading edge, the maximum wing thickness, and the trailing edge. The computational grid used is an H-type grid (129x33x33 = 140,481 points) with spacings off solid surfaces which resulted in average minimum  $y^+$  values on the wing and flat plate of 2.74 and 1.61, respectively. Figures 33 and 34 show the residual histories and CPU times for the single-grid and multigrid solutions. The final residual for both solutions could not be reduced to machine accuracy, which probably is a consequence of the complicated behavior of this flow. Nevertheless, about a 50% savings in CPU time has been achieved for the multigrid solution over the single-grid solution.

Comparisons of the  $C_p$  distribution between the experiment and the computation on the wing and flat plate are given in Figures 35 and 36, respectively. The computed results agree reasonably well with the experiment. Figure 37 shows the computed flow particle traces on the flat plate around the wing compared to skin-friction lines obtained from flow visualization. Good agreement is obtained in both the overall shape and the size of the horseshoe vortex system. The primary separation lines starting from the leading-edge separation point wrap around the wing, and trail-off downstream. The primary separation point is located at  $x/L = -0.120$  in the experiment and  $x/L = -0.115$  in the computation. Another region of separation near the trailing edge can also be found in both the experiment and the computation. At the various stations shown in Figure 32, Figures 38 through 41 present both the computed and measured streamwise velocity components. Again, good agreement between the computation and the experiment was obtained at all computed stations.

## 7.5 Vortex Preservation

Three-dimensional cross-flow separation and appendage junction separation create vortical structures that leave the surface of a maneuvering vehicle and enter the flow field. Since the interaction of these vortices with downstream surfaces can significantly change the hydrodynamic forces and moments on the vehicle, a physics-based prediction method must preserve these vortices as they convect downstream. In order to test the UNCLE code's ability to handle this vortex preservation, the research team used a test case that involved the convection of an idealized vortex immersed in a uniform flow. Several other researchers have used a similar vortex preservation test to assess the temporal accuracy and dissipative nature of different numerical schemes. These researchers include Rai [1987], Liu, Davoudzadeh, Briley, and Shamroth [1990], Wake and Choi [1995], and Davoudzadeh, McDonald, and Thompson [1995].

This test case typically consists of either a Thomson-Rankine vortex (as given by Ogawa [1993]) or a Lamb-Oseen vortex (as given by Batchelor [1967]) immersed in a uniform freestream flow. The pressure distribution for this flow field has a minimum value at the center of the vortex, which increases asymptotically to the freestream value with increasing distance from the vortex core. In the absence of physical viscosity (as governed by the Euler equations), the value of the minimum pressure at the center of the vortex should remain constant as the vortex is convected in the uniform flow. Any deviation in the pressure at the center of the vortex can then be attributed to the numerical scheme and can be viewed as numerically-induced decay. Thus, monitoring the core pressure as the vortex is convected is a good indicator of a numerical scheme's capability to preserve the vortex.

All of the computations have been performed using the Thomson-Rankine vortex model provided by Ogawa [1993]. This model had an idealized velocity profile that varied linearly with distance within the core and inversely with distance outside of the core. This distribution proved to be a very severe test for the flow solver since at the radius of the core, where the maximum tangential velocity occurs, the velocity distribution was not continuous. Analytical expressions for the axial velocity, the azimuthal velocity, and the pressure can be prescribed as a function of the distance from the center of the vortex. The strength of the vortex was chosen such that the maximum tangential velocity at the radius of the core was 0.4 and the nondimensional pressure at the core was 0.84. All the results contained herein were obtained on a H-type rectangular grid measuring 52.5 x 7.5 radii (the core radius of the vortex being 1.0) and with equal spacing in the axial- and azimuthal-coordinate directions. Three different grid densities were used: a coarse grid of size 211x31 (6,541 points), a medium grid of size 421x61 (25,681 points), and a fine grid of size 841x121 (101,761 points). The computations were initialized by simply adding a uniform axial flow ( $u = 1$ ) to the previously mentioned analytical expressions for the velocity. The inviscid flow was then allowed to evolve in time. Since the vortex was embedded in a uniform flow, the position of the vortex was known at all times and the boundary conditions were updated accordingly to the exact solution at each time step. A nondimensional time step of 0.025 was used, and the vortex was allowed to travel 45 radii downstream.

For the coarse grid, Figure 42 shows the computed variation of core pressure versus radii traveled. Four unsteady Euler solutions with different numbers of Newton iterations per time step are presented. Once again, both first- and second-order temporal discretizations were tried and the solutions were virtually indistinguishable. Each calculation was terminated after the vortex traveled

twenty core radii due to the unacceptable rise in the core pressure. This grid was found to be too coarse to accurately model this problem. In Figure 43, the initial contours of pressure,  $u$ -component of velocity, and  $v$ -component of velocity are shown along with an outline of the grid. The calculation with three Newton iterations was carried out for a full forty-five radii of travel and the core pressure increased to approximately 0.9, over seven percent of its original value. Figure 44 contains the contours for the same quantities as Figure 43 at this point. It is interesting to note that although the vortex has lost a significant amount of its strength, the structure of the vortex is essentially unaltered.

For the next set of calculations on the medium size grid, Figure 45 contains the comparison of core pressure versus distance traveled for various iterations. The core pressure was preserved rather well, with the final value being within about one percent of the original value for 12 and 24 iterations. However, Figure 45 also shows that the vortex will continue to dissipate as it convects further downstream. For this medium size grid, Figure 46 demonstrates the importance of the second-order accurate temporal discretization for these vortex preservation tests. Even on the fine mesh, a second-order temporal discretization was necessary to obtain good results. The final computation on this fine grid used only three Newton iterations. Here, Figure 47 shows that the difference in the final and initial core pressure differs by less than one percent and, even more importantly, the dissipation is not increasing with distance traveled. While it is important that these results require less Newton iterations to achieve the desired accuracy, this fine grid includes 16 grid points within the vortex core—a number too fine for most practical maneuvering problems.

## 7.6 SUBOFF with Appendages

In the previous test cases, the research team isolated important physical phenomena and compared the numerical simulations using the baseline UNCLE code with experimental data and analytical solutions. Next, the team moved closer to the more complex geometry of an actual underwater vehicle, where several of these physical phenomena occur simultaneously and result in forces and moments acting on the body. Therefore, for the next set of test cases, the team selected the SUBOFF body with appendages. This appended body provided the first application of the multiblock capability, as used with the multigrid algorithm.

### 7.6.1 Flow Field

The first appended-body test case involved the turbulent flow about SUBOFF with four stern appendages (without the sail) at a Reynolds number of 12,000,000 (based on total body length) and at  $0^\circ$  and  $2^\circ$  angles of attack. To exploit symmetry, an 8-block O-type grid was built around  $180^\circ$  of the body with a total number of  $65 \times 33 \times 132$  ( $= 283,140$ ) grid points. The grid was split into two parts in the  $i$ -direction from the leading edge of the fins, and four parts in the  $k$ -direction. No blocking was made in the  $j$ -direction. Figure 48 shows the 8-block grid for this configuration. Each fin surface has 17 grid points in both the  $i$ - and  $j$ -directions. The average minimum  $y^+$  value is 0.380 on the body, and 0.409 on the fin surface.

Figure 49 presents the convergence histories of the blocked vertical multigrid solutions for both the  $0^\circ$  and  $2^\circ$  angles of attack. The figure shows that for both 3-level multigrid solutions, the total residual for all blocks is reduced by 3 orders of magnitude within 250 multigrid cycles. In fact,

no change was found in the flow variables (both velocity and pressure) after the residual was reduced by 2.5 orders of magnitude, which is about 200 multigrid cycles. The solution at this stage is referred to as the engineering answer. Huang and his colleagues [1992] presented experimental data that included the distributions of pressure coefficient on the body and fin surfaces, as well as the velocity profiles close to where the propeller would exist ( $x/L = 0.978$ ), which are used to compare with the computed results. Comparisons of the computed and measured pressure coefficients on the hull, at both  $0^\circ$  and  $2^\circ$  angles of attack, are presented in Figures 50 and 51, respectively. The computations show good agreement with the experiment at both angles of attack. Figures 52 and 53 show the computed and measured pressure coefficients on the upper fin surface at both  $0^\circ$  and  $2^\circ$  angles of attack, where the flow separated near the trailing edge of the fin--which made the flow structure in this region very complicated. Excellent agreement between the computation and the experiment is obtained at both  $0^\circ$  and  $2^\circ$  angles of attack. Note that there were only 17 grid points in both the  $i$ - and  $j$ -direction on the fin surface. Although Figure 54 shows that the comparison of computed and measured  $u$ -velocity distributions at the potential propeller location of  $x/L = 0.978$  was not very satisfactory, the overall shape is matched qualitatively. The reason for this discrepancy may have been due to several factors, including the algebraic turbulence model, especially the wake model used to handle such a complex flow. There is also some uncertainty in the SUBOFF experimental data at this location since the velocity data do not conform to an inner-variable plot ( $u^+$  versus  $y^+$ ).

The next test case involved the flow around the SUBOFF body with both a sail and the four stern appendages, at both  $0^\circ$  and  $2^\circ$  angles of attack. Again, symmetry was exploited in order to build grids around  $180^\circ$  of the body. Three C-type grids were used in the computations--a coarse grid of size  $145 \times 41 \times 97$  (576,665 points), a medium grid of size  $193 \times 65 \times 97$  (1,216,865 points), and a fine grid of size  $289 \times 65 \times 132$  (2,479,620 points). All grids were split into 12 blocks, with 3 blocks in the  $i$ -direction and 4 blocks in the  $k$ -direction. Note that the block boundaries are located in the critical regions of the trailing edge of the sail and the leading edges of the stern appendages. Each block has the same grid size. In the fine grid,  $41 \times 41$  (1,681) grid points are placed on the sail surface and  $25 \times 25$  (625) grid points on each of the fin surfaces. Figure 55 shows the 12-block fine grid for this geometry. In this grid, the average of the minimum  $y^+$  values are 1.5 on the hull surface, 0.3 on the sail surface, and 0.4 on the fin surfaces. The reasons for choosing different grid sizes in this case are, first, to study the convergence property of the current multiblock, multigrid method as the grid size increases and, second, to compare the quality of the results on these different size grids--which hopefully may provide some guideline in selecting grid sizes for simulating real maneuvering problems. Figure 56 presents the convergence histories on these three grids, with the fine-grid solution including both  $0^\circ$  and  $2^\circ$  angles of attack. The figure shows that the convergence rates obtained on the three grids are about the same. This indicates that the current multiblock, multigrid code is not sensitive to the grid size, and a nearly grid-independent convergence rate is achieved in all the cases. For all three grids, a converged solution is reached within 250 to 300 multigrid cycles--when the residual is reduced by 3 orders of magnitude--and an engineering solution (with the residual reduced by 2.5 orders of magnitude) is obtained in about 200 multigrid cycles.

The results obtained on the fine grid at both  $0^\circ$  and  $2^\circ$  angles of attack are compared with the experimental data acquired by Huang and his colleagues [1992]. Figure 57 shows the pressure-coefficient distributions on the hull surface obtained by the computation and the experiment at  $0^\circ$  angle of attack. The overall comparison is favorable except for the region of the sail-body junction, where a pair of horseshoe vortices were generated near the leading edge of the sail and where the flow separated at the trailing edge of the sail. Figures 58 and 59 show the computed and measured

pressure coefficient distributions on the sail surface at  $0^\circ$  and  $2^\circ$  angles of attack, where the experimental data was taken from the wind tunnel results for SUBOFF with the sail only, due to a lack of experimental data when the four stern appendages were included. Figures 60 and 61 show computed and measured pressure coefficient distributions on the upper fin surfaces at both  $0^\circ$  and  $2^\circ$  angles of attack. Comparisons of pressure coefficients on both the sail and fin surfaces show excellent agreement between the computation and experiment at  $0^\circ$  angle of attack, and reasonably good agreement at  $2^\circ$  angle of attack in this very complicated flow region. The computed  $u$ -velocity profiles at the potential propeller location ( $x/L = 0.978$ ) at  $0^\circ$  angle of attack qualitatively match well with the experiment, as shown in Figure 62.

As mentioned previously, one of the objectives in this case was to investigate the influences of the grid size on the solution; that is, how many grid points are required in order to resolve this flow without losing any important details. To this end, a comparison is made among the solutions at  $0^\circ$  angle of attack obtained on all three grids. Figure 63 shows the computed crossflow velocity vectors at the potential propeller location of  $x/L = 0.978$  for the three grids. It is seen that a pair of tip vortices generated by the stern appendages can be observed on the medium and fine grids, but not on the coarse grid. This observation suggests that a minimum of about one million grid points are needed for this configuration in order to resolve the vortical flow structures.

### 7.6.2 Hydrodynamic Forces and Moments

The previous validation comparisons for the SUBOFF computations have involved flow variables such as static pressure, velocity, and skin friction. Since the trajectory of a vehicle depends on the forces and moments produced by the flow over the vehicle, further validation comparisons are required in order to use the UNCLE code for maneuvering predictions. Roddy [1990] has reported experiments that include measurements of forces and moments acting on the SUBOFF body, with and without appendages. These data were used in what might be considered "component form"--that is, with various appendage combinations--to determine how accurately the forces and moments on the body with these isolated appendages could be predicted. While it is well known that one can obtain excellent agreement between computational and experimental results by "tuning" a turbulence model for each data point, this type of comparison is not appropriate for verifying a code's capability of computing a general problem. Therefore, all these computations were performed with the same algebraic turbulence model defined in the turbulence modeling section of this report.

Three different configurations of the SUBOFF model have been considered to validate the forces and moments acting on the body surface at different angles of drift. These three configurations included the SUBOFF barebody, the SUBOFF hull with the four stern appendages, and the SUBOFF hull with a sail. All experiments were carried out at a Reynolds number of 14,000,000 (based on total body length).

In order to give the reader a better idea of how well the computed results match with the experimental data, the next figures include error bars that represent the uncertainty in the measurements acquired by Roddy [1990]. Although Roddy [1990] did not report the data uncertainty, one can infer the size of the error bars from other computational comparisons reported by Sung, Griffen, Fu, and Huang [1995]. The axial-force coefficients are more difficult to measure accurately than the other coefficients, and the experimental axial-force coefficients have 10% error bars. On the other experimental coefficients (lateral force, normal force, pitching moment, rolling moment, and

yawing moment), 5% error bars exist. Also, the experimental data available for all SUBOFF configurations reported by Roddy [1990] are asymmetric about the negative and positive angles of drift, especially for the axial-force coefficients. One has to take this into account when viewing the comparisons of computed results with the experimental data.

The SUBOFF barebody computation included a C-type multiblock grid with 4 blocks and 161x73x17 (199,801) grid points per block--giving a total of 799,204 grid points. Figure 64 shows how both the computations and measurements of the axial-force coefficient, lateral-force coefficient, and yawing-moment coefficient vary with angle of drift. The force and moment coefficients were computed using two different strategies for the search parameter described in the section on turbulence modeling. In the first approach, an optimized search parameter was obtained for each angle of drift by varying its value, typically in the range of 300-1200, and taking the result which is in best overall agreement with the experimental data. The other approach is to simply use a constant value for the search parameter (750 ) for the various angles of drift, as was done for all the other configurations. All of the comparisons show excellent agreement, even though the axial-force measurements show considerable asymmetry. Figure 65 shows the convergence history of these computations for a sample angle of drift of 10.05°. All these coefficients have converged within 100 multigrid cycles, and a similar convergence rate existed up to 18° angle of drift.

Next, the research team computed forces and moments on the SUBOFF hull with the four stern appendages. Exploiting symmetry to generate a grid for only half of the geometry, they used a C-type grid with 8 blocks and 81x73x33 (195,129) grid points per block--giving a total of 1,561,032 grid points. The grid was split into two parts in the axial direction from the bow to the leading edge of the fins and into four parts in the circumferential direction. No blocking was made in the radial direction. Each fin surface had 17 grid points in the axial direction and 33 grid points in the radial direction. In the first four blocks, the wall surface existed only in the radial direction; therefore, the algebraic turbulence model is applied in this direction only.

Although the experimental normal force should be zero at angles of drift (if the body and the flow field are symmetrical), the experimental data show a small value of normal force. The computed normal force is zero for all angles of drift since the flow is solved for half of the geometry and symmetry is assumed for the other half. Hence, the normal force computed is not plotted against the experimental normal force. Furthermore, the computed pitching and rolling moments cannot be compared with the available experimental data since the computed pitching and rolling moments take into consideration the computed normal force. Only the results comparing the axial- and lateral-force coefficients and the yawing moment coefficient with the experimental data are shown for this configuration. Figure 66 shows the computations of the axial-force coefficient, lateral-force coefficient, and yawing-moment coefficient at various angles of drift as compared with the experimental data. The computed results for the axial-force coefficient lie within the error bars at lower angles (< 10°). At higher angles, the results lie outside the error bars for negative angles of drift, but they are within the error bars for positive angles of drift. This discrepancy is because the experimental data for the axial-force coefficient are not symmetrical for positive and negative angles of drift, while the computations assume symmetry. As observed from the figure, the axial-force coefficient increases with angle of drift within the computed range of 4° to 18°. Both the lateral-force and yawing-moment coefficients show good agreement with the experimental data and their magnitude increases with increasing angle of drift. Figure 67 shows the convergence history of the various force and moment coefficients for this configuration, for a sample angle of drift of 8°. The

axial-force, lateral-force, and yawing-moment coefficients converge rather quickly--typically taking less than 100 cycles even for angles of drift up to  $18^\circ$ .

In order to investigate the influence of grid density on the accuracy of these force and moment computations, the team constructed two additional grids: A fine grid with 12 blocks and  $81 \times 89 \times 41$  (295,569) grid points per block--giving a total of 3,546,828 grid points--and a coarse grid with 8 blocks and  $41 \times 37 \times 17$  (25,789) grid points per block--giving a total of 206,312 grid points. The force and moment coefficients were recomputed using these grids. The results obtained with these two grids and from the previous medium fine grid can be seen in Figure 68. Considering only the variation of the axial-force coefficient with angle of drift for all three grids, this figure shows that only slight differences exist between the fine and medium grids. Computations using the coarse grid under-predict the axial-force coefficient for positive angles of drift. The generally good agreement of the computed axial-force coefficient with the experimental data using the coarse grid may be because of the asymmetrical nature of the experimental data for positive and negative angles. The results obtained for the lateral-force and yawing-moment coefficient on the coarse grid show nearly as good agreement as the results obtained with the medium and fine grids. This agreement illustrates the point that the lateral-force coefficient and the yawing-moment coefficient are not as sensitive to grid density as the axial-force coefficient.

Finally, the research team computed forces and moments on the SUBOFF hull with a sail. The C-type grid included 12 blocks and  $89 \times 73 \times 33$  (214,401) grid points per block--giving a total of 2,572,812 grid points around the entire circumference of the body. The grid was split into three parts in the axial direction from the bow to the stern and into four parts in the circumferential direction. Again, no blocking was made in the radial direction. The sail surface has 41 grid points in both the axial and radial directions. Since the flow about this configuration is asymmetric about both the  $x$ - $z$  and  $y$ - $z$  planes, the grid was generated for the whole geometry under consideration. As a result, this case requires more CPU time compared to the earlier configurations. However, all three force coefficients and all three moment coefficients can be computed and compared with the experimental data.

Figures 69 and 70 summarize the results obtained for the various force and moment coefficients for this configuration. All the results show very good agreement with the experimental data, with the exception of the axial-force coefficient and the pitching-moment coefficient. Perhaps the agreement with the axial-force coefficient could be improved using an even finer grid, as demonstrated in the stern-appendage case. Figure 71 shows the convergence history of the various force and moment coefficients for this configuration, for a sample angle of drift of  $8^\circ$ . The axial-force, lateral-force, and yawing-moment coefficients converge rather quickly, taking approximately 150 time steps for this angle of drift. Even at an angle twice this large, all force and moment coefficients were converged in roughly 200 time steps.

## 7.7 Flapping Foil

Except for the vortex preservation case, all of the test cases thus far have been steady-state computations. Since the flow over a maneuvering vehicle is unsteady, the research team needed to perform validation cases in which computations using UNCLE were compared to time-dependent experimental data. In one case, Sheng, Taylor, and Whitfield [1995b] compared unsteady

computations with measurements made by Bouard and Coutanceau [1980] for an impulsively started cylinder. Another test case involved the flapping foil experiment conducted by Rice [1991], Delpero [1992], and Horwich-Lurie [1993]. The experiment was designed to study the flow about a two-dimensional hydrofoil undergoing high-reduced-frequency gust loading. The gust was created by two NACA 0025 hydrofoils oscillating sinusoidally in phase, upstream of the stationary foil.

Figure 72 shows a schematic of the experimental setup. Experimental data were taken in the flow field near the stationary foil, as well as on the foil itself.

The two-dimensional numerical computations were performed on the entire experimental domain, including the flapping foils. For these multiblock computations, the entire physical domain was divided into 4 blocks. Each block consists of an H-type grid comprised of 326x65 (21,190) grid points (giving a total of 84,760 grid points), with the minimum  $y^+$  values of approximately 1.0. This particular blocking arrangement allowed the multiblock solutions to correspond exactly to a single-block solution, even for unsteady flow. That is, there were no approximations at block boundary interfaces. A steady-state solution was first obtained and then motion of the flapping foils was initiated by boundary-conforming dynamic grids that moved in pitch with the flapping foils at a reduced frequency of 3.62 based on the half-chord of the stationary foil. All computations were for a Reynolds number of 3,780,000 (based on the stationary foil chord). The boundary layer on the stationary foil (both the suction and pressure sides) was tripped at a distance of 0.105 chord length from the leading edge, while the boundary layer on the flapping foils and tunnel walls was treated as completely turbulent. Figure 73 shows the computed velocity magnitude after five complete periods of motion of the two NACA 0025 hydrofoils upstream of the stationary foil. A comparison of the experimental and computed pressures and velocities on the bounding box and surface of the stationary foil were carried out for the steady case, as well as time histories and an harmonic analysis at the same locations for the unsteady case.

Taylor and his colleagues [1993] presented a complete comparison of the flapping-foil computations with experimental data. However, due to space limitations, only a summary of the results is given here. For the steady case, the agreement between the numerical and experimental bounding box data is good, and for the most part extremely good. The agreement between the numerical and experimental foil surface pressure data is not as good as would be expected for this type problem--while the boundary layer velocity profiles on the pressure side are in good agreement, but not so good on the suction surface for  $x/c > 0.90$ . For the unsteady case, the agreement for the bounding box varies from reasonable to excellent. Considering the foil surface pressure data, the mean pressure distribution has about the same discrepancy as the steady-state case. The amplitude is predicted reasonably well for both the pressure and suction sides; however, the phase is quantitatively not as good as the amplitude, but it is qualitatively correct. The agreement for the mean boundary layer profiles is good on the pressure side and had about the same discrepancy as the steady-state case for the suction side. The amplitude for both the pressure and suction sides was reasonable, as was the phase for the pressure side--while the phase for the suction side was quantitatively not good for  $x/c > 0.90$ , but qualitatively correct for all  $x/c$ .

## 7.8 Prolate Spheroid (Unsteady)

The next unsteady-flow test case returns to a geometry that more closely resembles a maneuvering vehicle. As part of the same experimental research program in which Chesnakas,

Simpson, and Madden [1994] acquired data for a 6:1 prolate spheroid at  $10^\circ$  angle of attack, Hoang, Wetzel, and Simpson [1994a,1994b] acquired measurements of flow about an identical 6:1 prolate spheroid undergoing time-dependent maneuvers. This test case included unsteady numerical simulations with a vertical plunge of one foot in 0.33 seconds, a turning maneuver of approximately  $10^\circ$  in 0.25 seconds about  $L/2$ , and a pitch-up maneuver of  $30^\circ$  in 0.33 seconds about  $L/2$ . Hoang, Wetzel, and Simpson [1994a,1994b] provided experimental surface pressure data for several axial and azimuthal locations. In order to compare with these measurements, the research team computed these prescribed maneuvers at a Reynolds number of 4,200,000 (based on total body length) using a  $111 \times 47 \times 61$  (318,237 point) O-type grid--with an average minimum  $y^+$  value of 1.0 (for a steady,  $0^\circ$  angle-of-attack case). All unsteady computations used a steady-state solution at  $\alpha = 0^\circ$  as an initial condition. The various maneuvers were initiated by prescribing a trajectory for the boundary-conforming dynamic grid. Minimum time stepping, as well as three Newton iterations and five symmetric Gauss-Seidel passes per time step, were used to insure time accuracy in the computations. Figure 74 shows a schematic of the plunge, turning, and pitch-up maneuvers.

Measurements for the plunge maneuver were made at various axial locations and at vertical displacements of six and twelve inches. The twelve-inch displacement occurred in 0.33 seconds, so the constant nondimensional plunge rate based on the freestream velocity was 0.02. Figure 75 shows the comparison between the computed and experimental surface pressure distributions for the six- and twelve-inch locations. The experimental data indicate that this motion seems to have little effect on the surface-pressure distribution, except at the bow and stern. Hoang, Wetzel, and Simpson [1994b] reported that the unsteadiness in the pressure distribution in these regions would produce a pitch-up moment. Inspection of the computed results on an exaggerated scale also confirm this to be the case; however, the magnitude of the computed pressure differential at the bow, as the maneuver is performed, is not as large as that shown in the experimental data.

In order to perform the turning maneuver, the relationship between the yaw angle and nondimensional time must be known. This information was obtained directly from the experiment itself. Figure 76 presents the computed and experimental values of surface-pressure coefficient for every two degrees of motion. The agreement is considered good, with the largest differences being toward the windward side at the forward axial stations for the first eight degrees of motion and at the suction peaks at ten degrees. However, a comparison on a considerably expanded scale with the steady case at ten degrees and  $x/L = 0.56$  indicates that the suction peaks for the turning maneuver are greater than those for the steady case and that the location of the minimum pressure is shifted leeward by approximately twenty degrees, just as in the experimental data.

The motion of the prolate spheroid for the pitch-up maneuver was initiated by a solid body rotation of the entire grid about the  $L/2$  position of the geometry. The  $30^\circ$  pitch-up was performed in 0.33 seconds, so the nondimensional pitch rate based on the freestream velocity was 0.047. A constant pitch rate was used instead of a prescribed trajectory since there was only a slight variance in the experimental rate for the entire motion. The computed and experimental surface pressures for each  $5^\circ$  of the pitch-up maneuver are shown in Figure 77. At axial locations of greater than  $x/L = 0.44$  and incidence angles greater than  $15^\circ$ , the pressure variation on the leeward side of the model indicates the presence of the leeward vortices. The largest discrepancies between the computations and the experiment occur in these regions, as well as near the windward side for  $30^\circ$  angle of attack. The algebraic turbulence model used in these computations does not exactly predict the location and magnitude of the suction peaks in the pressure profiles; however, the overall agreement and trend of the computed results compares favorably with the experimental data. Once again, a comparison with

a steady case at 30° angle of attack indicates that the behavior of the pressure distribution is similar to that of the turning maneuver in that the suction peaks for the pitch-up maneuver are greater than those for the steady case and the location of the minimum pressure is shifted leeward by approximately 5°. In addition, the location of the primary separation is also displaced by approximately the same amount. The shift in the computed results for these quantities is less than 5° and the position of the minimum pressure is almost the same for both the steady and pitch-up maneuver at 30°.

Overall, the comparison with experimental data is favorable even though there are some discrepancies for all of the maneuvers considered, mainly at higher angles of attack. Also, the comparison with available steady data at selected angles of attack demonstrates that the differences in the steady and unsteady data have been captured. Clearly, quasi-steady solutions would not be adequate to simulate these unsteady maneuvers.

## 7.9 SUBOFF with a Body-Force Propeller Model

Unfortunately, no experimental data is available for a propelled SUBOFF configuration. However, as a precursor to a fully-appended SUBOFF calculation in which the fluid and vehicle dynamics are coupled together, the research team computed two prescribed maneuvers using a body-force model for the propeller. First, the team computed a pure pitch-up maneuver, with an angle of attack up to 15° and a dimensional pitch rate of 10° per second. Second, the team computed a prescribed maneuver that include pitch, yaw, and roll, with the maximum values for the angle of attack, drift, and roll being 15°, 5°, and 5°, respectively. Both of these test cases included the fully-appended SUBOFF vehicle with a sail, four stern appendages, and a sail plane (a sail plane fabricated by this research team and not by the original SUBOFF designers). Inputs to the body-force propeller model came from propeller characteristics given by Yang, Hartwich, and Sundram [1990].

The grid for this fully-appended SUBOFF vehicle was composed of equal dimensioned blocks. For the pitch-up case, symmetry was used and resulted in an 18-block, 734,706-point grid for one half of the geometry. The pitch, yaw, and roll computation required the complete geometry, which meant that 36 blocks and 1,469,412 points were used. The Reynolds number for both computations was 12,000,000 (based on body length), and the body-force propeller model was located at  $x/L = 0.978$ . As in the previous cases, the grid lines were clustered to solid surfaces in such a manner that the resulting  $y^+$  values for the first cell off the surface were about 1.0.

Each of the prescribed maneuvers used a steady-state solution as the initial condition. Figure 78 shows the surface of the vehicle with contours of pressure, as well as contours of axial velocity on the body-force propeller plane. On the plane of symmetry, Figure 79 shows contours of the  $u$ -component of velocity for the same steady-state solution. Using this initial condition, the prescribed 15° pitch-up maneuver resulted in the  $u$  velocities shown in Figure 80 for the starting, half-way, and ending points of the maneuver. Figure 81 shows the same snapshots of the  $u$ -component of velocity for the prescribed 15° pitch, 5° yaw, and 5° roll maneuver. The effect of the maneuvers on the body-force propeller and the sail-plane wakes are evident in all of these contour plots.

## 7.10 Freestream Propeller

During a maneuver, a vehicle's propulsor ingests a nonuniform flow and generates forces in the horizontal or vertical planes--which, in turn, create a moment on the vehicle that can greatly affect its maneuvering characteristics. Therefore, for many cases, a body-force representation of the propulsor will prove to be inadequate, and the physics-based prediction method will have to include the actual propulsor with its rotating blades. As a first case to test the capability of the UNCLE code to handle rotating blades, the research team simulated the flow through the marine Propeller 4119 tested in a uniform freestream by Jessup [1989]. This freestream propeller provided the first application of the unsteady multigrid multiblock code.

For this numerical simulation, the computational grid consists of three blocks with a total of 279,825 points, as shown in Figure 82. The surface grids on both the streamwise and spanwise direction of the blade contain 41 points. The Reynolds number is 576,000, based on the freestream velocity and the diameter of the blades. The initial solution of the unsteady flow was obtained by running the unsteady code using local time stepping for the flow field, while the computational grid was rotated a minimum time step corresponding to a rate of 200 cycles per revolution of the propeller. After 200 time steps, the time-accurate calculation was started using a minimum time step of 0.004165, which is equivalent to 200 time steps per revolution. Multigrid cycles are employed to ensure the convergence of the solution at each time step. Figure 83 shows computed  $u$ -velocity contours obtained with different numbers of multigrid cycles. It was found that the final solution with one multigrid cycle at each time step is close to that with two multigrid cycles at each time step. Next, Figure 84 gives the pressure coefficient distributions on the blade surface, where  $r$  is the radial distance from the measured point on the blade to the hull axis, and  $R$  is the radius of the blade tip. Favorable agreement was obtained between the computation and experiment, except for the location  $r/R = 0.3$ . Also, Figure 84 shows good agreement between the experimental and computational results for both the thrust and torque coefficients.

## 7.11 SUBOFF with a Rotating Propeller

Having computed the flow through a freestream propeller, the research team next selected an appended SUBOFF configuration with a rotating propeller in order to test the unsteady multigrid, multiblock code for its dynamic relative motion grid capability, as well as its efficiency and robustness to simulate complex unsteady flows. However, as noted previously, no experimental data is available for a propelled SUBOFF configuration. Therefore, the team first needed to select an open propeller for these SUBOFF computations.

Although a propeller could have been designed specifically for this application, this approach provides little opportunity for performing diagnostic calculations in the event that unrealistic predictions were developed by the body/propeller flow calculations. Therefore a "stock" open propeller was selected for this application. The principal criteria used in selecting a propeller was that sufficient performance data be presently available to (1) allow accurate sizing of the propeller for the SUBOFF body and (2) provide for diagnostic "propeller-only" calculations to help assess the accuracy of propeller flow predictions. Boswell [1971] and Nelka [1974] have evaluated a skewed propeller series in several experimental facilities and extensively documented the performance. Since these propellers form a systematic series and have been shown to have uniform open-water powering

performance, they provide an opportunity to examine the effects of a few primary propeller design variables, especially skew, on maneuvering performance.

Three propellers from the series were chosen as candidates for this application. These included Propeller 4381 (no skew), Propeller 4497 ( $36^\circ$  warp), and Propeller 4498 ( $72^\circ$  warp). Propeller sizing was done on the basis of SUBOFF body resistance data provided by Crook [1990]. The relatively close agreement of open-water data among these three propellers allowed a common diameter to be chosen for this application. This was chosen so as to allow the propeller to operate at the effective advance ratio for peak open-water efficiency in the behind condition for the design hull resistance. The final diameter chosen was 10.5 inches for the 20-inch diameter SUBOFF body. After selection of a diameter, IGES NURBS spline surfaces were generated for the blade surfaces, and these surfaces were used for generating grids in the final flow solutions.

As shown in Figure 85, the geometry consists of the SUBOFF hull, a sail, four stern appendages, and a rotating propeller with five blades. For this computation and all subsequent computations on SUBOFF with a propeller, the team selected Propeller 4381 (no skew). The grid contained 13 blocks and had 1,153,901 points. The localized grid distortion technique mentioned previously was used to treat the relative motion between the SUBOFF body grid and the rotating propulsor grid. Three levels of multigrid with full coarsening were used to ensure that the solution converged at each time step. At each time step, only one multigrid cycle and one Newton iteration was implemented. The computation was first carried out using local time stepping--while rotating the propeller grid for two revolutions (240 time steps)--and, then, switching to minimum time stepping for the true time-dependent simulation. The minimum time step used was 0.0005087, which is about 160 time steps per revolution. Figure 86 shows that a periodic flow field in the region of the rotating blades is obtained after a total of five to six revolutions of the propeller (720 ~ 880 time iterations). Alternatively, Figure 87 shows that a periodic solution is achieved in about 2200 time iterations, if the calculation is performed using only minimum time stepping (320 time steps per revolution) from the beginning of the computation. This indicates that using local time stepping in the beginning of the computation can significantly improve the convergence of the solution process, since the wake behind the sail is developed more quickly than using minimum time stepping. Special attention should be paid to the pattern of the periodicity. One peak differs from the other three because the wake from the top fin mixes with the wake from the sail, so that the propeller blades encounter a different upstream wake as they pass the top fin position.

Figure 88 shows contour lines of axial velocity in the propeller region. The continuity of the contour lines across the interface not only indicates the proper treatment of data communication between the moving blocks but also serves to demonstrate the unsteady interaction between the appendage wakes and the propeller blades.

The research team performed similar computations for a fully-configured geometry, after adding fabricated sail planes to the previous appended SUBOFF geometry--the same sail planes used for the SUBOFF computations with a body-force propeller model. The addition of these sail planes resulted in the development of a radial blocking scheme. The final grid included 51 blocks and 1,642,659 grid points. Figure 89 shows the geometry and a portion of the grid, while Figure 90 displays the surface-pressure distribution for the periodic solution.

## 7.12 High Reynolds Number Pump

As stated previously, the action of the propulsor will greatly affect the maneuvering characteristics of a vehicle. Thus far, the results have shown how well the UNCLE code can compute the flow through open propellers, operating both in a freestream flow and on the stern of a vehicle. However, Wislicenus [1960], for example, showed that submerged vehicles can operate with a ducted propulsor with more than one blade row, using both rotating and stationary blades. He described these propulsors as "propulsion pumps" or "pumpjets" and it is widely known that these types of propulsors have been used on torpedoes and other types of unmanned undersea vehicles. In order to verify how well the UNCLE code can compute this type of flow field, one can compare numerical computations with experimental data acquired within an axial-flow pump. In performing an experiment to obtain precisely this type of code validation data, Zierke, Straka, and Taylor [1993,1995] utilized the high Reynolds number pump (HIREP) facility at the Applied Research Laboratory of The Pennsylvania State University.

HIREP consists of a pump stage driven by a downstream turbine. The pump and turbine rotor blades rotate together on a common shaft in the test section of the 48-inch diameter Garfield Thomas Water Tunnel, such that the main drive impeller of the tunnel overcomes the energy loss within HIREP. Zierke, Straka, and Taylor [1993,1995] acquired all of the data in the pump stage, which includes a row of 13 inlet guide vanes, a row of 7 rotating blades, and three downstream support struts. The experimental techniques included flow visualization, static-pressure measurements, laser Doppler velocimetry, and both slow- and fast-response pressure probes. Subsequent to these measurements, Weyer [1995] acquired unsteady static-pressure measurements on inlet guide vanes and on rotor blades.

Recently, Dreyer and Zierke [1994], Yang [1994], and Lee, Hah, and Loellbach [1996] all performed numerical analyses of HIREP using a variety of RANS codes. However, all of these three-dimensional simulations were performed as steady-state computations. Dreyer and Zierke [1994] accounted for the effects of one blade row on another using the average-passage equations originally developed by Adamczyk [1985], while Lee, Hah, and Loellbach [1996] used the mixing-plane approach. Yang [1994] treated the blade rows independently. For this maneuvering program, the research team performed a time-dependent computation using the unsteady UNCLE code, including the use of periodic boundary conditions.

In order to reduce the computational time and storage, the team modeled the 13:7 blade count (ratio of inlet guide vanes to rotor blades) with a 14:7 blade count, which allowed for a 2:1 computational blade count. Figure 91 shows the HIREP geometry and the corresponding computational grid. The computational geometry used a constant hub upstream of the inlet guide vane instead of the actual inlet used in the experiment, which included a nose, the tunnel walls, and a tunnel liner. The computational grid consists of three blocks--one for each inlet guide vane (IGV) passage and one for the rotor blade passage. Each IGV block had 89x49x33 (143,913) grid points, while the rotor block had 89x49x65 (283,465) grid points--for a total of 571,291 points. Great care was taken in the gridding process to maintain the fillets and rounded tip on the pressure surface of the rotor blades. Figure 91d displays the fillets, tip gridding, and the interface region between the two blade rows.

Computations for HIREP were run on various platforms--a Cray YMP, an SGI R8000, and an SGI R10000. These final results computed on an SGI R10000 using two time steps per click, no Newton subiterations, and one multigrid cycle. It takes approximately two revolutions to reach this periodic state, requiring about 98 CPU hours on the SGI R10000 (0.000345 seconds/grid point/time step). No-slip boundary conditions were used on all solid surfaces. The uniform inlet core flow was used with endwall boundary layers based on a 1/7-power-law velocity profile, while characteristic variable boundary conditions were used for the outflow.

### 7.12.1 IGV Flow Field

Figure 92 presents the static-pressure distribution on the inlet guide vanes. Both the measured and computed values are the time-averaged pressures on the blade. The measured and computed distributions in this figure compare quite favorably, which indicates that the simulation gives the proper vane loading and subsequent flow turning before entering the rotor blades. To model transition, the computed solution is "tripped" at 18 percent chord on both the suction and pressure surfaces.

The velocity distribution is presented in Figure 93, along with a schematic of the geometry that shows the location of the measurement plane (represented by a line between the two blade rows). The circumferentially-averaged velocities in Figure 93a again show that the computations of the flow turning compare very well with the measurements, as shown by the agreement in the plot of  $V_\theta$ . The agreement between the computed and measured axial velocities is very good. Figure 93b shows the circumferential variation of all three components of the velocity (over two IGV pitches). While the computed and measured values of the tangential and radial velocity profiles compare quite favorably, the predicted axial-velocity wakes are wider and deeper than the measured wakes. Two reasons may explain this discrepancy. First, the finite measurement volume of the five-hole pressure probes used in the experiment will lead to some spatial averaging and result in measured wakes that are too shallow. Second, the grid used for the computations may be too coarse downstream of the inlet guide vanes.

### 7.12.2 Rotor Blade Flow Field

Similar to Figure 92 for the inlet guide vanes, Figure 94 presents the static-pressure distribution on the rotor blades. The computed results compare quite well with the measured data, with just a slight overprediction of the suction side pressure near the leading edge. The computed solution is "tripped" at 10 percent chord on the suction surface of the rotor and at the leading edge on the pressure surface.

Figure 95 shows the observed experimental skin-friction lines and the computed surface particle traces on the suction side of a rotor blade. Both the measurements and the computations show the same overall two-dimensional behavior of the flow in the midspan region. The predictions also capture the experimentally observed corner separation near the hub; however, it appears that the predicted corner separation and the predicted outboard separation along the trailing edge occur closer to the trailing edge than those viewed in the experiment. Since the trailing-edge pressure distributions shown in Figure 94 compare so well, it is believed that the difference in the locations of the separation regions may be due to the three-dimensionality of the view in Figure 95b.

Figure 96 presents the velocity profiles downstream of the rotor blades, along with the axial location of the measurement plane. Unlike the velocity measurements downstream of the inlet guide vanes that were acquired with five-hole pressure probes (see Figure 93), the velocity measurements in Figure 96 were acquired using a two-component laser Doppler velocimeter. Thus, only the axial and tangential components of the velocity were measured. The comparisons of the circumferentially-averaged velocity components are shown in Figure 96a. The good agreement between the computed and measured axial velocity indicates that the computations maintained the proper mass flow rate through the rotor. The rotor blades were designed to remove the swirl imparted to the flow by the inlet guide vanes, except near the hub where the rotor blades provided additional turning. The experimental values of the tangential velocity show this design intent, with negligible tangential velocity over most of the span and a small amount of tangential velocity near the hub. Meanwhile, the simulation indicates that the rotor blades have overturned the flow, resulting in negative values of the tangential velocity across the span. The computed pressure distribution at 90% span in Figure 94 shows more loading than the measurements near midchord, which is consistent with overturning of the flow. Near the leading edge, however, the computations show less loading than the measurements, which indicates underturning.

Figure 96b shows the circumferential variation of the axial and tangential velocities at various spanwise locations. The agreement between the computed and measured data is reasonable in the midspan region. Near the hub, the computed wakes have the correct depth, but they are slightly wider than the measured wakes. Near the shroud, the computed wakes are very shallow. This discrepancy in wake depth could be due to poor gridding in this region and the influence of the tip leakage vortex.

One important point should be noted. The computed data is collected in the same manner as the measured data. That is, a “probe” is inserted into the flow field at a given circumferential location. Data is then extracted from the computed solution at that location as the rotor block sweeps past the “probe.” Thus, the circumferential variation of the velocity can also be thought of as a time history of the velocity, as opposed to a spatial variation of the velocity. Although this difference may seem subtle, it is the fundamental difference between the solutions obtained by a time-dependent code and a steady-state code.

Presenting the velocities of Figure 96 in a different manner, Figure 97 presents contour plots of the axial and tangential velocity, both for the measurements and for the computations. The contours show both the skewed wakes exiting the rotor blades and the vortical structures shed from the blade tips. For the experimental data near midspan, Zierke, Straka, and Taylor [1993] showed that the spanwise varying contours within the rotor blade wakes occur from coarsely-spaced, discrete measurement locations. These spanwise varying contours do not indicate any physical phenomenon. The computations show similar spanwise varying contours because of the coarseness of the grid well away from the solid surfaces.

## 7.13 Moving Appendages

Recall that a maneuver of an underwater vehicle is defined as a controlled change or retention of the heading or speed. While changes in the angular velocity of the propulsor or changes in ballast provide some control over the maneuver, the primary control mechanism is changing the

settings of various appendages. Therefore, a physics-based means of predicting a vehicle maneuver must include the capability of handling moving appendages.

Previous test cases have focused on either stationary appendages or appendages that rotate, as in the case of the rotating blades of the propulsor. This test case focuses on the computational capability to dynamically change the settings of an appendage. Towards this end, the research team created a geometry where a SUBOFF stern appendage stands on a flat plate. Figure 98 shows this setup, where a small gap exists between the bottom of the appendage and the plate in order to allow for movement of the appendage. The vertical distance between the plate and the bottom of the appendage was approximately 5% of the total span of the appendage. Here, the appendage motion is accomplished by performing a solid body rotation of the appendage about the quarter-chord location, while the grid about and underneath the appendage was allowed to distort to follow the motion. These computations with UNCLE used a Reynolds number of 12,000,000 (based on the length of the plate) and the total number of grid points for this configuration was 366,439--with 25 grid points running axially through the gap region and 13 points running radially across the gap.

For this initial moving-appendage test case, the appendage was rotated in a time-accurate manner to a total deflection of  $10^\circ$ . The constant rate of rotation was  $10^\circ$  in 0.2 seconds. Similar to previous test cases, this unsteady motion used a steady-state solution for the configuration at  $0^\circ$  of deflection as an initial condition. The movement of the appendage was then initiated through the use of a dynamic grid and allowed to continue to a final deflection of  $10^\circ$ . Figure 99 shows a snapshot in time at  $10^\circ$  of deflection, showing the axial component of velocity around and under the appendage. Looking closer at the flow field at this same instance of time, up towards the bottom surface of the appendage, Figure 100 displays particle traces that indicate a migration of the fluid under the gap--from the "pressure" surface to the "suction" surface--and a roll-up into a root leakage vortex. In situations where an appendage lies on a vehicle hull, this root leakage vortex could interact with downstream surfaces, such as the vehicle propulsor.

## 8. Results Using Parallel Processing

In the previous section, the research team started with test cases that used few grid points and moved toward test cases that used a large number of grid points. Real maneuvering vehicle predictions will require even more grid points (on the order of 5,000,000 to perhaps even 10,000,000 points), as well as an enormous amount of CPU time using the baseline UNCLE code. In an effort to reduce the run time of these large computations, the team utilized the parallel version of UNCLE to compute the flow over the fully-appended SUBOFF body, with and without a rotating propeller.

The overall objective of the parallel computing effort in this study has been to develop a portable, scalable parallel capability that would allow one to perform these large-scale maneuvering simulations and to reduce their run times. This effort included the development of a suitable adaptation of the RANS solution algorithm, based on a block-decoupled subiteration, and the development of a parallel version of the UNCLE code. The parallel code was designed and constructed in a modular form that maintains as much familiarity as possible to developers of the single-processor code. A high degree of portability has been achieved across different computing platforms through the use of the MPI message-passing library, which is widely available and rapidly becoming a *defacto* standard. The parallel code has been routinely used on the IBM SP-1 and SP-2, the SGI Power Challenge, Sun and SGI workstations, and the Super MSPARC--a testbed of 32 processors with hybrid performance monitoring capabilities constructed by the Engineering Research Center at Mississippi State University. No effort has yet been made to tune these calculations to the machines, other than the selection of compiler optimization options.

The parallel development initially focused on a simple, unappended hull requiring only a single-block grid of 13,362 points. The parallel code was then extended to include capabilities developed in the evolving single-processor code, including capabilities for multiblock grids, MUSCL fluxes, general turbulent stresses, a multigrid solution algorithm, and unsteady flow with a rotating propulsor. These capabilities were demonstrated and validated on some of the same flow cases evaluated with the single-processor code, by comparing with both experiments and computed results obtained with the single-processor code. The configurations tested included the SUBOFF hull/sail/stern-appendage configuration with and without a propeller. The parallel code was also used to compute many of the sequence of cases used to validate the prediction of axial force, lateral force, and yawing moment coefficients by comparison with measurements.

The run times for various parallel cases are summarized in Tables 3 through 6. Table 3 gives results for steady flow past a hull/sail/stern-appendage configuration requiring about 600,000 grid points. Although the three different computers used in these calculations have widely different performance, in each case there is good parallel efficiency as indicated by CPU utilizations of 92%, 72%, and 85%. Table 4 gives timing results for the IBM SP-2 (wide nodes) for a similar configuration, but including sail planes. These two cases (for resolutions of about 600,000 and 3,300,000 grid points) illustrate the scalability of the present approach. Good parallel efficiency is obtained in each case by using the heuristic performance estimate (compared with Figures 6 and 7) to match each flow case to the computing resources used.

The parallel code (with the multigrid algorithm) was used for production running of validation cases for axial force, lateral force, and yawing moment coefficients--with Table 5 giving run time comparisons. A considerable reduction in run time was realized through parallel computing.

Although the parallel and sequential algorithms are somewhat different, their convergence behavior is very similar, as illustrated for this case in Figure 101. Finally, the propulsor capability of the parallel code is demonstrated by a re-computation for a SUBOFF hull with rotating propeller, using about 360,000 grid points. Table 6 shows that good efficiency (74%) was achieved, despite a 19% load imbalance due to unequal grid block sizes. This load imbalance could be reduced considerably by a relatively minor re-partitioning of the grid.

Table 3. SUBOFF Hull with a Sail and Four Stern Appendages  
( $Re=12,000,000$ , 600,000 Grid Points, and 500 Steps)

Machine	Processors	Memory	Run Time	CPU %	Mflops
Parallel Code without Multigrid					
SGI R8000	12	12 x 101 Mb	6 Hours	92 %	84
SP-1	12	12 x 101 Mb	6 Hours	72 %	84
SP-2	12	12 x 101 Mb	0.66 Hours	85 %	480

Table 4. SUBOFF Hull with a Sail, Sail Planes, and Four Stern Appendages  
( $Re=12,000,000$  and 500 Steps)

Machine	Processors	Memory	Run Time	CPU %	Mflops
600,000 Grid Points					
SP-2	12		40 Minutes	85 %	480
3,300,000 Grid Points					
SP-2	32		80 Minutes	81 %	1,200

Table 5. SUBOFF Barebody  
 $(Re = 12,000,000, 18.115^\circ$  Incidence, 800,000 Grid Points, and 200 Steps)

Machine	Processors	Memory	Run Time	CPU %	Mflops
Sequential Code: Vertical Multigrid					
IBM-590	1	400 Mb	~ 12 Hours	100%	
SGI R8000	1	400 Mb	~ 24 Hours	100%	
Parallel Code: Horizontal Multigrid					
SP-2	8	8 x 200 Mb	1.55 Hours		
SP-2	16	16 x 100 Mb	0.85 Hours		
SGI R10000	8	8 x 200 Mb	2.28 Hours	94%	
S-Msparc	16	16 x 100 Mb	4.43 Hours		

Table 6. SUBOFF Hull with a Rotating Propeller  
 $(Re = 12,000,000, 0^\circ$  Incidence, 360,000 Grid Points, and 1 Revolution = 160 Steps)

Machine	Processors	Memory	Run Time	CPU %	Mflops
Sequential Code without Multigrid					
IBM-590	1		4.00 Hours	100%	
Parallel Code without Multigrid (Note: This Decomposition has a 19% Load Imbalance)					
SP-2	15		0.47 Hours	74%	

The overall impact of the parallel capability developed and demonstrated here is that it enables the solution of problems too large or computationally intensive for solution using a single processor, and it can also reduce the run time to achieve timely turn-around of solutions needed in a design environment.

## 9. Results Using Two-Equation Turbulence Models

The two-equation  $q$ - $\omega$  turbulence model, as described previously, was implemented directly into the UNCLE flow solver and tested with and without the nonlinear model for a range of validation cases. The specifics of these tests and the results are given in this section. Included are both very fundamental problems to test the integrity of the coding, as well as more relevant problems which begin to show the capability to make maneuvering predictions for underwater vehicles.

### 9.1 Turbulence Decay

The first step in analyzing any computational model is to verify the integrity of the computer code. In this respect, the decay of turbulence is probably the single most attractive problem for the validation of two-equation turbulence models for two reasons. First, the problem can be described with a single, independent variable---either time or a single spatial coordinate. Second, the physics of the flow are governed by only a small number of the terms in the model, providing an easily obtained analytical solution with which the numerical results may be compared.

The spatial decay of turbulence is often referred to as the decay of grid-generated turbulence. In this case, a uniform mean flow passes through a fine, turbulence-generating grid. Sufficiently far downstream, the flow is governed by a balance between convection and dissipation only. This will be the case, for instance, downstream of a turbulence-generating appendage on a maneuvering vehicle. In the absence of any velocity gradients, an analytical solution to Equations 9 and 11 is attainable and can be written as

$$\omega = \frac{\omega_i}{(\omega_i C_2 t + 1)} \quad \text{and} \quad q = \frac{q_i}{(\omega_i C_2 t + 1)^{1/2C_2}} ,$$

where  $C_2$  is the empirical constant from the  $q$ - $\omega$  model,  $t$  is the transit time of a particle, and the subscript  $i$  denotes the initial value of the turbulence.

The temporal decay of turbulence can be isolated by stirring fluid in a large container. After a period of time, the mean flow decreases to zero, and the remaining turbulence dissipates over time. In this case, the two-equation model simplifies to a balance between the unsteady term and the dissipation term. The analytical solution has the same form as that for the spatial decay listed previously, but with the independent variable  $t$  now denoting time.

The turbulence decay problems were solved using the UNCLE flow solver with the  $q$ - $\omega$  turbulence model in two different ways. To model spatial decay, which checks the convection and dissipation terms within the code, 100 cubic control volumes were aligned in a row in the  $x$ -direction and symmetry was enforced in both the  $y$ - and  $z$ -directions. Initial values at the inlet were fixed as  $u = 1$ ,  $v = w = 0$ ,  $q_i = 0.01$ , and  $\omega_i = 0.10$ . A CFL number of 10 was used, and the turbulence solution converged quickly to its single precision limit. Figure 102 shows that the spatial decay of  $q$  and  $\omega$  match the analytical solutions very closely, demonstrating that the convection and dissipation terms in the  $q$  and  $\omega$  equations are coded properly.

The unsteady decay of homogeneous turbulence was solved using a single cubic control volume with zero average velocity and symmetry boundary conditions in all directions. Arbitrary levels of initial turbulence were specified as  $q_i = 0.006$  and  $\omega_i = 0.05$ . The resulting decay of the turbulence was solved in a time-accurate manner using time step sizes which varied from 0.01 to 1.0. Just like the case for spatial decay, Figure 103 shows that the time decay of  $q$  and  $\omega$  match the analytical decay very closely, demonstrating that the unsteady term was coded properly.

## 9.2 Fully-Developed Channel Flow (Linear Model)

Two terms from the turbulence model---namely, the diffusion and production terms---were absent in the calculations of turbulence decay and needed to be tested. Steady, fully-developed, two-dimensional channel flow provides an excellent opportunity to study these effects for several reasons. First, this flow eliminates convective and unsteady effects, which have already been inspected in the previous calculations. Next, researchers have studied this flow extensively and have established empirical and analytical curves for each of the dependent variables. Finally, the effect of a solid, turbulence-producing boundary is introduced, which will be a characteristic feature of the maneuvering vehicle predictions.

Fully-developed channel flow was modeled on a  $10 \times 49 \times 2$  grid (980 points) in the streamwise, normal, and spanwise directions, respectively. Symmetry was enforced in the normal direction so that the solution only spanned half of the channel height. The solution was integrated all the way to the wall, where the grid was clustered. The streamwise and spanwise spacings were each constant and equal to 1% of the channel height. Inlet profiles were copied from the exit at each iteration for all variables except pressure, which was linearly extrapolated from the interior nodes. Characteristic variable boundary conditions were used at the exit, and the exit pressure was specified as constant. The Reynolds number was 150,000 based on the bulk velocity of the fluid and the channel height. The convergence rate is especially poor for this case since errors which would normally be allowed to pass through the exit boundary are now being re-introduced at the inlet. For this reason, the CFL number was ramped gradually from 0.1 to 1000 once the solution had been started with the modified Baldwin-Lomax turbulence model.

The solution was compared to well-established profiles in the near-wall region for  $u^+$ ,  $q^+$ , and  $\omega^+$  versus the normalized wall distance  $y^+$ . In all three comparisons, a log-linear scale is used, with  $y^+$  on the logarithmic scale to magnify the various turbulence layers. As usual, the viscous sublayer is the region below  $y^+ = 10$  where the viscous or "laminar" shear stress dominates and turbulence production is negligible, and the "log-layer" is the region beyond  $y^+ = 30$  or so where turbulence production dominates. In this latter region, the turbulence is roughly in "equilibrium," since diffusion is negligible, leaving production and dissipation nearly equal.

These physical considerations can be used in deriving analytical expressions for  $u$ ,  $q$ , and  $\omega$  in the near-wall regions. Figures 104 and 105 shows comparisons of these expressions with the numerical solutions. Clearly, the numerical solution matches the analytical expressions very closely, indicating that the diffusion and production terms have been coded properly.

### 9.3 Fully-Developed Channel Flow (Nonlinear Model)

As stated previously, the traditional form of the two-equation turbulence models makes it impossible to predict any significant anisotropy of the normal Reynolds stresses. The nonlinear model addresses this problem. Fully-developed two-dimensional channel flow provides an excellent opportunity to test the construction and coding of the nonlinear model. Analytically, one can show that the nonlinear model only modifies the normal Reynolds stresses in this case, but not the Reynolds shear stresses. One can also show that only the Reynolds shear stresses are coupled to the flow. As a result, the addition of the nonlinear effects should achieve the same answer as was obtained with the linear model, but with an improved prediction of the normal Reynolds stresses.

The case of two-dimensional fully-developed channel flow, subject to all of the specifications listed in the previous discussion, was repeated using the nonlinear  $q$ - $\omega$  model with the constants of Myong and Kasagi [1990]. Figure 106 shows the improved prediction of the average velocity fluctuations compared to the experimental data of Laufer [1950]. It is important to remember that the linear model can only predict the three components to be equal everywhere; however, the nonlinear model clearly gives the desired anisotropy. Figure 107 shows that the shear stress is linear throughout most of the domain in accordance with the governing equations and has a slope which is proportional to the pressure gradient.

The nonlinear form of the  $q$ - $\omega$  turbulence model was next applied in solving for the flow through a three-dimensional square duct. This case is well-suited in validating the nonlinear model for application to appended vehicles. Primarily, the presence of secondary flow in a fully-developed, non-circular duct is due entirely to anisotropy, or differences in the normal Reynolds stresses. Thus, the linear model is completely incapable of predicting any secondary flow, but the nonlinear model should provide a reasonable prediction. This ability of the turbulence model may be an important enhancement in the prediction of juncture flows, as described by Chen [1995]. Chen [1995] showed that a nonlinear model was necessary to properly predict the formation of a primary and secondary horseshoe vortex in an appendage-hull junction flow.

The  $q$ - $\omega$  model was applied using  $3 \times 100 \times 100$  grid points (30,000 total) in the streamwise, spanwise, and normal directions, respectively, and at a Reynolds number of 150,000. In order to achieve fully-developed flow, the inlet flow profiles were copied from the exit after each iteration for every variable except pressure, which was linearly extrapolated from the interior nodes. Characteristic variable boundary conditions were applied at the exit, and symmetry was applied at two boundaries so that only a quarter of the square duct needed to be solved. The model was applied with both the linear and nonlinear models. While secondary flow was absent in the former case, a distinct pattern of secondary flow emerged in the latter case with a behavior which qualitatively matches that seen in experiments. Again, convergence for this case is quite slow since errors which would normally be convected through the exit are re-introduced at the inlet. In fact, compared to experiments, the magnitude of the secondary velocities is too small, and so the results are not complete.

Previously, a solution for the same flow was obtained using the stand-alone form of the nonlinear  $k$ - $\epsilon$  model. In this case, the secondary flow profiles could be directly compared to the experimental data of Gessner and Jones [1965]. The results, shown in Figure 108, confirm that the

nonlinear model was well-suited for the prediction of turbulence-driven secondary flow, as both the magnitude and shape of the secondary profiles compare well with the experimental data.

## 9.4 Flat-Plate Boundary Layers

Although the fully-developed channel flows have helped to verify that the traditional  $q$ - $\omega$  turbulence model and nonlinear terms have been coded correctly, they describe internal fully-developed flows which differ substantially from the developing and sometimes transitioning external flows that occur during vehicle maneuvers.

To test the prediction of external boundary layer development, the two-dimensional flow over a flat plate was modeled. Again, a single spanwise control volume and symmetry conditions on both spanwise boundaries were employed. The grid size in the  $x$ - $y$  plane was 117x39 (4,563 points) and was four times as long as it was high. A constant grid-expansion ratio of 1.2 was used normal to the solid surface. Characteristic variable boundary conditions were enforced on the top and exit of the domain, where pressure was constant. The Reynolds number based on the domain height and freestream velocity was 1,000,000, so that the maximum Reynolds number based on  $x$  was 4,000,000. Freestream values given as  $q = 0.006$  and  $\omega = 0.05$ , which are representative values in ordinary wind tunnel tests. A uniform inlet velocity profile was specified at the start of the plate; this is something of a contradiction and causes a large pressure spike at the leading edge of the flat plate. The two-equation model was “cold-started” with a CFL number which was ramped from 0.1 to 1000 over the course of convergence.

White [1979] presented empirical curves for the behavior of the skin-friction coefficient with respect to the Reynolds number based on  $x$ . Figure 109 shows that the solution obtained with the linear  $q$ - $\omega$  model matches the curves closely, transitioning from laminar to turbulent behavior near  $Re_x = 100,000$ . Figure 110 shows the pressure gradient along the flat plate, where it can be seen to be near zero relative to the gradients caused by the inlet boundary condition and the transition to turbulence. Finally, Figure 111 shows that the velocity profile at  $Re_x = 4,000,000$  matches the expected near-wall behavior.

## 9.5 SUBOFF Barebody

At this point, having successfully isolated and tested the various terms of the linear and nonlinear model, the code can begin to address problems on geometries of interest. The first such case also introduces a curvilinear grid and a stagnation point to the model for the first time, so it is kept as simple as possible otherwise. On the other hand, the geometry has been tested experimentally, and experimental data are available for quantities such as skin friction and pressure on the hull.

The flow over the axisymmetric, bare SUBOFF body was solved using an O-type grid rotated through 90° with 131x51x11 grid points (73,491 total). Symmetry was enforced in the circumferential direction and along the body’s axis, and characteristic variable boundary conditions were specified for the far-field. Freestream turbulence levels of  $q = 0.006$  and  $\omega = 0.05$  were applied and nondimensionalized with respect to freestream velocity and the maximum body radius. The

Reynolds number based on body length was 12,000,000. The two-equation model was again cold-started with a CFL number of 0.1 and gradually increased to a CFL number of 40 over the course of convergence.

Experimental data are available for coefficients of pressure and skin friction along the surface of the body. Figure 112 compares experimental data for  $C_p$  with numerical solutions given by both the modified Baldwin-Lomax turbulence model and the linear  $q-\omega$  turbulence model, while Figure 113 compares experimental data for  $C_f$  with both solutions. The two-equation model matches the algebraic model closely for most of the body length but improves the prediction of the surface pressure and, especially, the skin friction toward the aft end of the body.

It is important in this case that special attention be paid to the two-equation model to prevent the over-prediction of turbulence at the stagnation point. Common to two-equation models, the problem is referred to as the stagnation point anomaly. Here, this anomaly was treated through the use of a limiter on  $\omega$  which arises from the realizability considerations shown by Durbin [1996]. This treatment is straight-forward and based on fundamental, mathematical requirements. As such, the use of a limiter is completely general in theory but will require further testing to ensure that it is successful in practice.

## 9.6 Prolate Spheroid (Nonlinear Model)

A wealth of experimental maneuvering data has been provided in a series of experiments, beginning with the work of Chesnakas, Simpson, and Madden [1994]. In the first several tests, the “vehicle” of interest is a 6:1 prolate spheroid which was tested first at an angle-of-incidence and later during pitching and plunging motions. These tests provide extensive measurements of the velocities and Reynolds stresses around a simple, curved body and a first step into the prediction of maneuvering underwater vehicles.

To begin, the stand-alone nonlinear  $k-\epsilon$  model was applied in solving for the flow over a 6:1 prolate spheroid at 10° angle of attack and a Reynolds number of 4,200,000, according to the experimental work of Chesnakas, Simpson, and Madden [1994]. A plane of symmetry was used so that only half of the flow needed to be examined, thus halving the grid size to 111x41x41 (186,591 points).

Computational results were compared to the experimental results in local freestream coordinates for all three components of velocity, for the flow angle, and for the six components of the Reynolds stress tensor at a number of different locations around the spheroid. These results are presented in Figures 114, 115, 116, and 117. It can be seen that, without *any* modifications to adjust for the new application, the nonlinear  $k-\epsilon$  model is able to closely capture the velocity profiles and flow angles and approximate most of the features of the Reynolds stress profiles. In particular, the anisotropy of the normal Reynolds stresses is greatly enhanced compared to the linear  $k-\epsilon$  predictions.

Calculations of this case using the embedded  $q-\omega$  coding are underway but were not completed at the time of this writing.

## 10. Results Including Vehicle Dynamics

All of the results to this point have demonstrated the capabilities of the UNCLE code. However, to compute the flow over an actual maneuvering vehicle, one must also include computations of the vehicle dynamics. In order to demonstrate the coupling between the vehicle dynamics and the fluid dynamics, the research team first performed simulations of two freely-falling bodies at moderate Reynolds numbers: a sphere and a 6:1 prolate spheroid. These cases were attractive for two reasons. First, by limiting the Reynolds numbers to regimes where the flow field is unsteady but not turbulent, one can remove the necessity of including the additional complication of a turbulence model. Second, by utilizing a weight/buoyancy imbalance to provide a net force, one does not require any arbitrary body forces to obtain vehicle motion. The remaining test cases involved the fully-appended SUBOFF geometry and the algebraic turbulence model. Initially, all appendages were rigidly attached to the hull and the propulsive force was provided by a body force in the region of the propeller. Later cases included a fully rotating five-bladed propeller.

### 10.1 Free-Falling Sphere

The first coupled simulation was a negatively buoyant sphere freely falling through a viscous fluid. While this case is primarily of academic interest, it does reveal the necessity of coupling the vehicle dynamics and the fluid dynamics. The test case was designed to yield a terminal condition corresponding to a Reynolds number (based on sphere diameter) of about 1,000. Table 7 gives the properties of the fluid and the 7-millimeter-diameter sphere, while Figure 118 shows a sketch of the simulation with the fluid at rest--that is, no far-field velocity.

Table 7. Key Properties for the Free-Falling Sphere Test Case

Kinematic Viscosity of the Fluid	0.000002795 m <sup>2</sup> /s
Density of the Fluid	1,085 kg/m <sup>3</sup>
Density of the Sphere	2,170 kg/m <sup>3</sup>

A “tethered condition” was used to provide the starting condition for the coupled computation, in which the sphere was held rigidly in place and the fluid was given a uniform far-field velocity. Initially, UNCLE was run using local time steps, corresponding to a CFL number of 10. The code was run this way for several hundred iterations, with the intention of quickly eliminating most of the large errors in the domain. From this solution, the case was restarted and run time-accurately for several thousand time steps with the nondimensional time step set to  $\Delta t = 0.01$  (which implies that it takes 100 time steps to traverse one body diameter at a nondimensional velocity of 1.0). After these time-accurate computations, the uniform far-field velocity was subtracted from the velocity at every point in the domain and the sphere was given an initial velocity equal to the negative of the far-field velocity. This velocity was the initial condition for the coupled Reynolds-averaged Navier-Stokes/six degree-of-freedom (RANS/6DOF) simulation. From this condition, the RANS/6DOF simulation was run with  $\Delta t = 0.01$  for 10,000 time steps. This computational test case

was started in this manner since most maneuvering vehicle simulations will begin from some sort of well-defined, uniform, non-stationary state (for example, "straight and level flight"). Also, this test case demonstrates that the UNCLE code has the capability to both generate the starting state and execute the coupled RANS/6DOF simulation.

The computational grid used for this simulation consisted of two blocks with 16x35x41 grid points each (45,920 total grid points). The case was run single-precision on an IBM RS6000 Model 590 workstation and required approximately 25 Mbytes of memory. Although the case was initially run using an early version of the UNCLE code, the results included here are from a run using the latest version. The total run time for the 10,000 time steps of the coupled RANS/6DOF simulation was about 35 hours, with only 9% of the run time devoted to the force and vehicle dynamics calculations.

Figure 119 shows the time histories of the body-fixed velocities and rotation rates for the sphere. These time histories result from integration of the vehicle dynamics equations (Equation 21). The time histories of the sphere's inertial orientation and position are shown in Figures 120a and 120b, respectively. These time histories are obtained from the solution of the kinematical relations (Equations 22 and 23). At  $t = 0$ , Figures 119 and 120 show that the sphere initially resided at the inertial origin, with zero orientation angles, no rotation, and an initial velocity of 1.0 in the positive z-direction (downward). From  $t = 0$ , the sphere began its untethered free fall. Figure 119 clearly shows the highly unsteady nature of the calculation.

Because of the large changes in sphere orientation indicated in Figure 120a, it is nearly impossible to describe heuristically what is happening to the sphere in Figures 119a and 119b in terms of "streamwise," "sideslip," and "plunge" velocities, or "roll," "pitch," and "yaw" rates. However, observing the sphere's inertial position in Figure 120b shows that the sphere does not fall in a straight line. In fact, by  $t = 100$ , the sphere attains rather appreciable offsets in the X and Y coordinates. Also, the speed at which the sphere falls (indicated by the slope of the Z-coordinate) changes at about  $t = 40$  and seems to oscillate about a smaller value than that with which it began. Interestingly, it is also at around  $t = 40$  that the sphere orientation began to experience large oscillations. It seems that the sphere, which began its free fall with only translational kinetic energy, acquires rotational kinetic energy as a result of the unsteady fluid dynamics. At around  $t = 40$ , some event occurred that caused a significant amount of energy to transfer to the rotational modes. The result is that by  $t = 100$ , the sphere is falling not only appreciably slower (Figure 120b), but with significant rotation rates about all three axes (Figure 119b).

From examination of the flow field, it appears that the primary contributor to these unsteady forces and moments is the presence of a ring vortex on the leeward side of the sphere. Figure 121 shows particle traces in the relative velocity field on a slice of the flow field through this vortex. The asymmetric orientation of this vortex appears to give rise to transverse forces and moments, and its presence on the back side of the sphere also generates a large pressure or form drag. Based on tethered results, it is believed that this vortex exhibits a sort of random precession. In tethered calculations, where the trajectory of the sphere is prescribed as a straight line at constant speed, the unsteady transverse forces appear to oscillate in a plane parallel to the sphere's velocity vector. This plane rotates about the velocity vector with a frequency and direction that varies in time in an apparently random fashion. It is believed that a related phenomenon is present in the untethered simulation.

## 10.2 Free-Falling Prolate Spheroid

The second test case for the coupling between the vehicle and fluid dynamics involved a freely-falling 6:1 prolate spheroid. This case represents a step closer, physically, to the ultimate goal of computing the coupled vehicle and fluid dynamics of a submerged, streamlined body. This case is different from the sphere case, not only in the use of a more streamlined geometry, but also due to the fact that the stability of the body was augmented by an assumed density distribution of the prolate spheroid.

Specifically, the prolate spheroid was assumed to be constructed of two different materials, one light and one heavy, with the interface at the minor-axis plane of symmetry. Table 8 provides properties of the prolate spheroid and the fluid. The effect of the disparate densities of this 1.2-meter long prolate spheroid was to move the center of gravity 0.2 meters away from the geometric centroid (and center of buoyancy), along the axis of rotational symmetry. With the heavy side pointed down (positive Z-direction), this offset provided a natural restoring moment and helped the prolate spheroid maintain its initial orientation.

Table 8. Key Properties for the Free-Falling Prolate-Spheroid Test Case

Kinematic Viscosity of the Fluid	0.001182 m <sup>2</sup> /s
Density of the Fluid	0.001261 kg/m <sup>3</sup>
Density of the Downward Portion of the Prolate Spheroid	5,774 kg/m <sup>3</sup>
Density of the Upward Portion of the Prolate Spheroid	200 kg/m <sup>3</sup>

The properties in Table 8 were not arrived at arbitrarily; they came from an attempt to limit the terminal Reynolds number to a value that would allow for a laminar flow solution, here  $Re_{term} = 7,500$ . The terminal condition was estimated by determining the time-averaged drag of the prolate spheroid before it was "released" (that is, coupled with the 6DOF solver). Knowing the time-averaged drag and choosing a length, fluid, and terminal Reynolds number allows one to fix the required weight and, hence, the average density of the vehicle. Of course, as was made clear by the sphere case, the untethered behavior can be very different from the tethered behavior; nevertheless, this drag calculation is the only *a priori* estimate available. Figure 122 shows a schematic of this simulation.

The computational grid used was a single-block, O-type grid with 31x35x41 (44,485) grid points. The case was run in single precision on an IBM RS6000 Model 3AT workstation. The results shown here were obtained from a run using an earlier version of the UNCLE code, a version that did not possess multiblock nor unsteady multigrid capability. Because the required memory and CPU time do not represent the current code capabilities, they are not quoted for this case (as they

were for the free-falling sphere). This prolate-spheroid calculation was also started somewhat differently than the sphere calculation. No local time-stepping was used as in the sphere initialization. Here, the calculation was started from scratch in a time-accurate, tethered mode. Also, the time step was not explicitly set; rather, the maximum CFL number in the domain was specified to be 10. Unfortunately, this specification resulted in an overly-conservative time step of  $\Delta t \approx 0.001$ . The prolate spheroid was run tethered for about 6,000 time steps before it was released and, then, run untethered for an additional 11,000 time steps. It should be noted that, unlike the sphere calculation, the time variable was not reset to zero upon release; here,  $t = 0$  corresponds to the beginning of the entire calculation.

Figure 123 contains the body-fixed velocities and rotation rates of the prolate spheroid. The 6DOF results begin at  $t = 6.47$ . The rate of descent is constant,  $w = 1.0$ , and small oscillations occur in  $u$  and  $v$  about 0.0, with  $v$  having the larger amplitude. Figure 123b shows  $p$  and  $q$  both oscillating about 0.0, with  $p$  displaying the larger amplitude. This shows that the prolate spheroid exhibits more motion in the  $y$ - $z$  plane than in the  $x$ - $z$  plane as it falls untethered. This preferential direction of the “wobble” is due to the asymmetric state of the flow field at the moment of release ( $t = 6.47$ ). A nonzero transverse force at release (likely from the leewardside unsteady ring vortex) gave the prolate spheroid an initial “kick” in the  $y$ - $z$  plane that is reflected in its subsequent behavior.

Figure 124 presents the time histories of the inertial orientation and position of the prolate spheroid. This figure shows that, like the sphere (except to a far lesser degree), the prolate spheroid veers from a straight path. Figure 124a shows that the orientation angle  $\phi$  oscillates not about 0.0, but about an angle that becomes increasingly negative with time. The angle  $\theta$  exhibits this same behavior, though less noticeably. The angle  $\psi$  remains 0.0, indicating that the prolate spheroid does not roll as it falls. Figure 124b shows that, by the time the calculation was terminated at  $t \approx 18$ , the prolate spheroid achieved nonzero values for  $X$  and  $Y$  (although amounting to only a fraction of the prolate-spheroid length). The constant slope of the  $Z$  trace demonstrates the achievement of a true terminal condition.

For completeness, Figure 125 includes particle traces in the relative velocity field of the prolate spheroid. In analogy with the free-falling sphere (Figure 121), a ring vortex is apparent near the tail of the prolate spheroid. Clearly, this vortex is of a scale that is markedly smaller than the scale of the prolate spheroid. This was not the case for the sphere, where the scales were comparable.

Finally, it is interesting to compare the overall results from the sphere and prolate-spheroid calculations. Both cases were normalized in essentially the same way, using the predicted terminal velocity and the diameter for the sphere and the length for the prolate spheroid. Yet, consistently, the forces and moments and subsequent motion of the prolate spheroid were an order of magnitude (or more) smaller than those for the sphere. The prolate spheroid does indeed appear to be a significantly more stable body than the sphere, although its absolute stability has yet to be determined (pending a much longer run).

### 10.3 SUBOFF with a Body-Force Propeller Model

After testing coupled RANS/6DOF simulations of freely falling bodies, the research team next proceeded to compute a coupled simulation of the previously described fully-appended SUBOFF vehicle performing very simple maneuvers. For this first coupled SUBOFF computation, the team modeled the propeller with body forces (or an actuator disc), as described previously. Roddy [1990] gives the physical characteristics of the vehicle (length, mass, moments of inertia, locations of centers of gravity and buoyancy, *et cetera*) for the tow-tank model of SUBOFF. The medium was taken to be fresh water at 68° F. To achieve the starting condition of straight-and-level flight at a velocity of 10.97 ft/sec and a Reynolds number of 12,800,000 (based on vehicle length), the team ran UNCLE for 300 iterations with local time steps (CFL = 10) and 3 levels of multigrid at each iteration. The code was then run time-accurately for an additional 150 time steps at a nondimensional time step of 0.005, also using three levels of multigrid. The resulting flow field was taken to be the initial condition for the coupled RANS/6DOF simulation. Figure 126 shows a schematic of the initial positions of the vehicle, the body-fixed origin, and the inertial origin. (Note that the relative positions of the centers of gravity and buoyancy in Figure 126 are exaggerated for clarity.)

The computational grid for the coupled RANS/6DOF calculation consisted of 36 blocks and a total of 1,469,412 grid points. The code was run using double precision accuracy on an IBM RS6000 Model 590 workstation. Using three levels of multigrid, the simulation required 360 Mbytes of memory and 414 CPU seconds per time step. The time step for this calculation was fixed at  $\Delta t = 0.005$ . In more meaningful terms, this means that at a nondimensional vehicle velocity of 1.0, it required approximately 23 CPU hours to move the vehicle one body length. As with the free-fall calculations, the 6DOF coupling made up about 8% of the total run time. For the results shown here, the entire coupled calculation, start to finish, required about 115 CPU hours.

The version of the code utilized for this calculation did not have rotating-propeller capability nor moving-control surface capability. Starting from straight-and-level flight, the only means available to affect the trajectory of the vehicle was to alter the thrust provided by the actuator disc or alter the weight/buoyancy ratio of the vehicle--that is, mimic some sort of ballast tank manipulation. Table 9 provides details of the different phases of the simulated maneuver. Figure 127 shows the vehicle velocities and rotation rates in the body-fixed frame of reference, and Figure 128 shows the time history of the vehicle's orientation and position (that is, its trajectory).

Table 9. Different Phases of the SUBOFF Maneuver with a Body-Force Propeller Model

Phase of Maneuver	Starting Time, $t$	Ending Time, $t$	Comments
Phase I: Accelerating Vehicle	0.00	1.52	Neutrally Buoyant; Net Thrust
Phase II: Positive Buoyancy	1.52	2.52	20% Weight Reduction
Phase III: Neutral Buoyancy	2.52	4.27	Original Weight Restored
Phase IV: Thrust Reduction	4.27	5.02	95% Thrust Reduction

### 10.3.1 Phase I: Accelerating Vehicle

Phase I of the maneuver is essentially straight-and-level flight (heading due north), with the vehicle neutrally buoyant, and with the actuator disc generating a net thrust. Figure 127 shows that the net thrust accelerates the vehicle during this phase (increasing  $u$ ), with no discernable sideslip ( $v$ ) or plunge ( $w$ ) velocities. Figure 127b, however, does indicate the development of a small roll rate ( $p$ ), as well as pitch rate ( $q$ ), over this interval. Consistent with these roll and pitch rates, Figure 128a indicates that by  $t = 1.52$ , the vehicle exhibits a slightly rolled and nose-up attitude (that is,  $\phi$  and  $\theta$  are both  $< 1^\circ$  each).

Figure 129 shows contours of relative velocity magnitude on the geometric symmetry plane at  $t = 0.02$ --very shortly after the initiation of the coupled RANS/6DOF calculation. The position of the inertial axes near the nose of the vehicle shows that at this time, the vehicle has moved forward a distance equal to about 2% of its length. At this time, the sail wake appears to be divided into two parts by the wakes from the sail planes. The propeller disc appears to ingest the lower portion of this sail wake, as well as most of the rudder wakes. Finally, the significant flow acceleration through the actuator disc (which is responsible for the net thrust) is readily apparent just downstream of the stern appendages.

### 10.3.2 Phase II: Positive Buoyancy

Phase II of the maneuver begins with an instantaneous weight reduction of 20%. This reduction imparts an instantaneous net upward force at the center of gravity, which causes an upward acceleration of the center of gravity, which, when combined with its forward velocity, induces a negative flow incidence on the vehicle. This negative flow incidence results in a significant downward hydrodynamic force and nose-down pitching moment on the vehicle.

Figure 127a shows a slow down in the rate of acceleration of the vehicle in this phase, with the  $u$ -velocity approaching a constant by  $t = 2.52$ . The appearance of the negative  $w$ -velocity over the interval is a direct result of the sudden buoyant force; it too, appears to level off by  $t = 2.52$ . There is no sideslip ( $v$ ) velocity apparent during this portion of the maneuver. The most striking feature of Phase II of the maneuver, in Figure 127b, is the rapid development of a significant nose-down pitch rate (negative  $q$ )--with the pitch rate reaching  $20^\circ$  per unit time by the end of the phase. Also in Figure 127b, the small roll rate continues to increase and a very small, positive yaw rate develops.

During this positive buoyancy phase, Figure 128a shows that the vehicle rolls approximately  $1^\circ$  and pitches nose-down approximately  $9^\circ$ . Figure 128b shows that the vehicle continues to maintain its due-north heading, although its depth decreases by about 10% of the vehicle length by the end of the phase. The net result of instantaneously decreasing the vehicle's weight by 20% at a significant forward speed is a rather small decrease in depth accompanied by an extreme nose-down pitch.

Figure 130 shows contours of relative velocity magnitude on the geometric symmetry plane at the end of this second phase ( $t = 2.52$ ). The contours away from the body and almost parallel to it are due to the rapid nose-down pitch rate that the vehicle is experiencing. The horizontal line running

through the center of the figure (and intersecting the nose of the vehicle just above the stagnation point) is the inertial X-axis. The center of gravity of the vehicle is located roughly midway between the nose and the tail along the pressure hull symmetry axis. The figure demonstrates that the center of gravity lies just a small fraction of the hull length above the X-axis. Also clearly evident is the 9° nose-down attitude of the vehicle. As in Figure 129, Figure 130 shows a significant flow acceleration through the propeller disc. Unlike Figure 129, however, Figure 130 shows the entire sail wake being ingested by the propeller disc.

### 10.3.3 Phase III: Neutral Buoyancy

Phase III of the maneuver is initiated by an instantaneous return to neutral buoyancy at  $t = 2.52$ ; with the intention of stopping the rapid nose-down pitching of the vehicle. Figure 127a shows that the vehicle begins to accelerate again through Phase III of the maneuver. The plunge velocity ( $w$ ) appears to overshoot zero at about  $t = 3.0$  and eventually relaxes back toward zero by  $t = 4.27$ , while the sideslip velocity ( $v$ ) is negligible. Figure 127b shows some oscillations in the roll rate ( $p$ ) during this portion of the maneuver indicating some relatively low amplitude rocking motion about the roll axis. The yaw rate ( $r$ ) exhibits a similar behavior, though with much smaller amplitude. The most important aspect of this neutral buoyancy phase is the rapid reduction in the magnitude of the pitch rate ( $q$ ) upon removal of the buoyant force at  $t = 2.52$ . In fact, by  $t \approx 3.45$ , the pitch rate overshoots zero and becomes positive, indicating a nose-up pitch rate; the vehicle appears to be righting itself. At  $t \approx 3.85$  the positive pitch rate reaches a maximum and, then, begins to relax toward zero once again.

Figure 128a shows oscillations in both roll ( $\phi$ ) and yaw ( $\psi$ ) angles during this phase of the maneuver. They both appear to vary with approximately the same temporal period, though  $\phi$  seems to oscillate about an angle that becomes increasingly positive over the interval, while  $\psi$  oscillates about an increasingly negative angle. Even so, both angles remain relatively small over the interval (that is, less than 1.5°). Because of rotational inertia, the nose-down pitch angle ( $-\theta$ ) continues to increase until  $t \approx 3.45$  when the vehicle reaches a maximum nose-down attitude of almost 20°. From  $t \approx 3.45$  to  $t = 4.27$ , the vehicle begins to right itself, though at a slower and slower rate. By  $t = 4.27$ , the vehicle is oriented nose-down just over 17°. Figure 128b shows that the vehicle continues on its northerly course (that is,  $Y$  remains  $\approx 0$ ). The upward curvature in  $X$  from the continued acceleration is almost indiscernible in this figure. The interesting aspect of this third phase of the maneuver is the relatively rapid *increase* in depth of the vehicle, from  $Z \approx -0.1$  at  $t = 2.52$  to  $Z \approx 0.6$  at  $t = 4.27$ . The vehicle is reaching a new equilibrium flight path that has a *downward* component. In other words, once the vehicle is orientated nose down and the buoyant force removed, the only remaining force acting on the vehicle is from the propulsor. This propulsor force acts in the direction of positive  $x$ -which, in this case, happens to be pointing approximately 17° downward. The tendency of the vehicle will be to stay on this path and accelerate until a terminal condition is achieved.

### 10.3.4 Phase IV: Thrust Reduction

The final phase of the maneuver begins with a sudden 95% reduction in the propeller thrust. Figure 127a clearly shows the reduction in the vehicle's velocity ( $u$ ) during this last phase of the

maneuver. The propeller has almost been “turned off” and the result is a rapid slow down due to the hull drag force. The sideslip and plunge velocities ( $v$  and  $w$ , respectively) are negligible over Phase IV. In Figure 127b, it appears as though the pitch rate ( $q$ ) is asymptoting to zero as the vehicle settles on a new straight (but descending) trajectory. In this figure, the roll and yaw rates ( $p$  and  $r$ , respectively) continue their growing oscillatory behavior. Based on the apparent diverging behavior of  $p$  and  $r$  as far back as the second phase of the maneuver, it appears entirely conceivable that there is some sort of coupled roll/yaw instability in this hull. In fact, Roddy [1990] determined, based on captive-model tests, that the appended SUBOFF hull (without sail planes) is unstable in both the vertical and horizontal planes of motion.

The continued increase in the roll and yaw angles is evident in Figure 128a, where by  $t = 5.02$ , the vehicle is rolled ( $\phi = +2.0^\circ$ ) and yawed about ( $\psi = -0.5^\circ$ ). The pitch angle appears to be approaching a new equilibrium value of approximately  $-17^\circ$ . Figure 128b shows the vehicle steadfastly continuing on its northerly course with no discernable east/west excursions. The vehicle also continues to increase its depth. In fact, the net result of this maneuver is that at  $t = 5.02$ , the vehicle has traveled  $\sim 5.6$  body lengths north and  $\sim 1$  body length down. Also, the vehicle has pitched  $\sim 17^\circ$  nose-down, rolled  $\sim 2^\circ$ , and yawed  $\sim 0.5^\circ$ , while heading straight ahead (relative to the nose of the vehicle) at a velocity of  $\sim 1.3$  and decelerating.

Figure 131 shows contours of relative velocity magnitude on the geometric symmetry plane at the end of the maneuver. The horizontal line at the extreme top of this figure is the inertial  $X$ -axis. The lack of far-field contours in Figure 131, like those that appear in Figure 130, is due to the fact that the pitch rate is negligible at  $t = 5.02$ . The lack of significant propeller thrust in Figure 131 is evident by the lack of flow acceleration through the propeller disc. In fact, other than the lack of propeller thrust, the  $17^\circ$  nose-down inclination of the trajectory, and the slightly larger range in velocity, the flow fields in Figures 129 and 131 are quite similar.

## 10.4 Unconstrained Motion of SUBOFF with a Rotating Propeller

The previous test case provided the first simulation--albeit, a very simple simulation-- of a maneuvering underwater vehicle with the fluid dynamics and the vehicle dynamics coupled together. The last three test cases expand on this first maneuvering SUBOFF vehicle by looking at more complex situations. These cases involve SUBOFF with an actual rotating propeller, instead of a propeller modeled with body forces. Here, the vehicle is free to react to the forces and moments applied to it by the fluid, with the only control coming from changes in the angular velocity of the propeller. Table 10 gives key properties for all three of the test cases involving the fully-appended SUBOFF with a rotating propeller, while Table 11 provides the key computational parameters.

The magnitude of the time step, given in the Table 11, is based on the nondimensional angular velocity of the propeller and the number of time steps chosen to make a complete revolution. The nondimensional angular velocity of the propeller is defined as

$$\hat{\omega} = \omega t_{ref}$$

The reference time  $t_{ref}$  is defined as

$$t_{ref} = \frac{L_{ref}}{V_{ref}},$$

where  $L_{ref}$  is the reference length ( $= 14.2917$  ft) and  $V_{ref}$  is the reference velocity ( $= 10.97$  ft/s). Most of the calculations involving SUBOFF with a rotating propeller used 120 time steps per revolution and  $\Delta t = 0.00074$ . With this time scale, it will take the vehicle approximately 137 hours of CPU time to move one body length forward. For the last test case with the propeller rotating in reverse, the number of time steps per revolution is taken as 160 with  $\Delta t = 0.0005$ .

Table 10. Key Properties for the Fully-Appended SUBOFF with a Rotating Propeller

SUBOFF Body Length	14.2917 ft
SUBOFF Initial Velocity	10.97 ft/sec
Initial Reynolds Number	12,800,000
Body Weight	1557 lb <sub>f</sub>
Fluid Density	1.937 slugs/ft <sup>3</sup>
Location of the Center of Gravity	(-0.01327 ft, 0.0, 0.0)
Location of the Center of Bouyancy	(-0.01327 ft, 0.0, -0.0067 ft)
Propeller Rotation Rate	515.6 rpm

Table 11. Key Computational Parameters for the Fully-Appended SUBOFF with a Rotating Propeller

Computer	IBM RS6000 Model 590
RAM	555 Mb
Number of Blocks	51
Number of Grid Points Per Block	Blocks 1-24: 49x17x41 (= 34,153 Points) Blocks 25-36: 33x17x41 (= 23,001 Points) Blocks 37-51: 65x17x33 (= 36,465 Points)
Total Number of Grid Points	1,642,659
Levels of Multigrid	3
Magnitude of the Time Step, $\Delta t$	0.00074
CPU/Time Step/Grid Point	223 $\mu$ sec

As with the simulation of the SUBOFF motion using an actuator disc, the simulation of SUBOFF with a rotating propeller requires an initial condition of the flow over SUBOFF using only the UNCLE code, without any coupling to the 6DOF equations. Instead of reaching a steady-state solution, however, this initial solution of the RANS equations reaches a periodic solution, since the propeller ingests a circumferentially nonuniform inflow as it rotates through the wakes of the sail and stern appendages. Figure 132 shows the contour lines of the  $u$ -component of velocity on a plane between the stern appendages and the propeller. Note that the wakes and vortices from the sail, the sail planes, and the four stern appendages are evident in this plot, resulting in a nonuniform inflow to the propeller. Figure 133 shows the time history of the static pressure, registered at a grid point located on the pressure surface of a blade, close to the leading edge and near the hub. The initial condition is achieved once the flow about the rotating propeller establishes a periodic flow pattern. Recall that this initial condition matches the test case shown in Figure 90. Looking at the entire vehicle, Figure 90 shows contour plots of static pressure for this periodic initial solution of the flow over SUBOFF, while Figure 134 shows more details of this periodic flow on the pressure and suction surfaces of the propeller. These plots indicate that the pressure distribution on the blades are not steady as the blades rotate through the appendage wakes.

For this test case, the propeller rotational velocity was varied during the calculation to either increase or decrease the vehicle speed. Before investigating the effect of changes in the propeller rotational velocity on the vehicle motion, Figure 135 reviews the definitions of the force, moment, and velocity components in the body-fixed coordinate system. Using these definitions, Figure 136 demonstrates the variation, in nondimensional time, of the vehicle forward velocity ( $u$ )—as well as the integrated forces acting on the vehicle. This graph also shows the variation of the propeller speed (in red) plotted versus time. Using an initial nondimensional propeller speed of 77.2 obtained from the vehicle’s self-propulsion point, the vehicle starts to decelerate. This deceleration is consistent with the negative net axial force acting on the vehicle, also shown in Figure 136. Recall that the advance ratio of the propeller at self-propulsion was obtained from towing-tank resistance tests, without any sail planes. The additional drag created by adding sail planes results in the propeller needing more angular velocity to generate the additional thrust required for self-propulsion.

From  $t = 0.08$  to  $t = 0.132$ , the propeller speed is linearly increased from 77.2 to 115.8. This time interval corresponds to one full revolution of the propeller. Responding to the increase in the propeller speed, the net axial force (the  $x$ -component of the force in Figure 136) starts to increase from a negative value to a positive value and, after a small overshoot, it drops to a constant positive value—corresponding to the constant propeller speed of 115.8. As the propeller speed increases, the forward velocity of the vehicle increases. This increase continues, even as the propeller speed is kept at the constant value of 115.8, since a net thrust acts on this over-propelled vehicle (see Figure 136). To slow the vehicle, the propeller speed was decreased from 115.8 to 100.0 and, then, kept constant from  $t = 0.63$  to  $t = 0.8$ . The dynamic response of the vehicle to the propeller speed is immediate and consistent with the physical expectations. The net axial force acting on the vehicle decreases, and the vehicle forward velocity responds by also decreasing. The variation of the vehicle forces in the  $y$ - and  $z$ -directions is also shown in Figure 136. These transient out-of-plane forces include a periodic waveform created by the five-bladed propeller ingesting a nonuniform inflow. Also note that changes in the out-of-plane forces are an order of magnitude less than changes in the in-plane or axial force.

Figure 137 shows the variation of the moments acting on the vehicle. For reference, this figure also shows the variation of the propeller speed and the forward velocity of the vehicle.

Because of the propeller's sense of rotation, it exerts a positive moment on the fluid and the fluid, in turn, exerts a negative rolling moment (the  $x$ -component of the moment) on the vehicle. The rate of change of the rolling moment is consistent with the variation in the propeller speed. Examination of the moments in the other two directions (that is, the  $y$ - and  $z$ -components) again demonstrates the underlying unsteadiness associated with the nonuniform forces acting on the propeller.

Finally, Figure 138 shows the variation of the vehicle rotation rates (degrees per unit of nondimensional time) with respect to time. The maximum change in the rotation rates occurs in roll, with no significant changes occurring for either the pitch or yaw rate. Since no control is applied to the vehicle, it is obliged to roll in the direction opposite to the direction of propeller rotation. In this case, since the sense of rotation of the propeller is positive, the roll rate has a negative value. Figure 138 demonstrates that the vehicle response to the increase in the propeller speed dictates the change in the roll rate. The roll rate stabilizes to a constant value once the propeller speed is kept constant at 100.0. The actual values of the roll, pitch, and the yaw angles versus time are shown in Figure 139.

## 10.5 Roll and Yaw Moments Applied to SUBOFF with a Rotating Propeller

The next test case also involves the fully-appended SUBOFF vehicle with a rotating propeller. Without the complication of actually having moving control surfaces, the research team controlled the maneuvering vehicle in this case by applying two "external" controls. First, as shown in the previous test case, the vehicle will roll in the direction opposite of the propeller rotation. To counteract this tendency in actual underwater vehicles, the rudders are differentially splayed--that is, the upper and lower rudders are offset by some pre-set angle. This practice is called "splitting the rudders." Another means to create this counteractive roll moment is to increase the distance between the center of buoyancy and the center of gravity. However, for this test case, the team has directly applied an external rolling moment into the 6DOF equations in order to counteract the roll produced by the propeller torque. A second external control was used in order to turn the vehicle without using moving control surfaces. Here, the team directly applied an external yawing moment about the center of gravity into the 6DOF equations to simulate a turn.

Based on the experience gained from the first coupled computation of SUBOFF with a rotating propeller, the team increased the propeller speed from 77.2 to 95.0 to stop the vehicle from decelerating. This increase occurred within one revolution of the propeller, or for the time period from 0.0 through 0.073. Figure 140 shows that this increase in propeller speed does, in fact, increase the net axial force--such that the vehicle experiences a small net thrust. From this point in time onward, the propeller speed was kept at the constant value of 95.0.

Figure 141 shows the time history of the yawing moment (the  $z$ -component of the moment) in the inertial frame of reference and in the body-fixed frame of reference. The prescribed yawing moment is applied in the inertial frame. Starting at time  $t = 0.4656$ , the moment is gradually increased from approximately zero to the nondimensional value of 0.0001. The moment is kept at this constant value for the rest of the computation. Correspondingly, Figure 140 shows that the sway or sideslip velocity ( $v$ -component of the velocity in the  $y$ -direction) also increases. Transformation of the rolling moment from the inertial frame of reference to the body-fixed frame indicates an increasing rolling moment in the body-fixed frame of reference, as seen in Figure 141. This is due to

the coupling of the motion. As the vehicle experiences the turn, the rolling moment (the  $x$ -component of the moment) takes on increasingly negative values, indicating a tendency of the vehicle to roll during the turn. Considering the fact that the externally applied rolling moment has compensated for the rolling moment created by the propeller, the turning motion accounts for the rolling moment seen in Figure 141. This roll can be attributed to the lift generated by the sail during the turn; the sense is such that the sail rolls away from the center of curvature of the turn. The rate of increase of the yawing moment, in the body-fixed frame, is proportional to the rate of roll of the vehicle.

Figure 142 shows the roll rate, while Figure 143 shows the actual roll angle. A similar behavior, but with less degree of severity, is shown about the pitch axis (that is, the  $y$ -axis). The pitching moment (the  $y$ -component of the moment) and the corresponding pitching rate and pitching angle are shown in Figures 141, 142, and 143, respectively.

For a given forward speed, the incidence angle that the fluid makes with any point on the vehicle is directly proportional to the distance from that point to the vehicle's center of gravity and the yaw rate. As this distance becomes larger, or as the yaw rate becomes larger, the drift angle becomes larger as well--where the drift angle is the angle that the fluid flow makes with the longitudinal axis of the vehicle. At a nondimensional time of 1.20, Figure 142 shows that the yaw rate is approximately  $35.0^\circ$  per nondimensional unit of time, and this yaw rate yields a  $15.8^\circ$  drift angle, as experienced by the nose of the vehicle. Figure 144 gives the surface distribution of static pressure on the vehicle, which demonstrates how the stagnation point has moved away from the vehicle nose as a result of this drift angle. The stagnation point on the sail moves in the same manner as the stagnation point on the vehicle nose, while the stagnation point on the upper stern appendage (or rudder) moves in the opposite direction. The movement of the stagnation point on the sail accounts for the pressure distribution that rolls the vehicle during the turn. Since the aft portion of the vehicle is downstream of the center of gravity, the drift angle--and, thus, the incidence angle on the upper stern appendage--has the opposite sign compared to portions of the vehicle forward of the center of gravity. Figure 145 shows more clearly that this change in drift angle moves the stagnation point in the opposite direction of the movement on the nose and sail. Looking upstream towards the propeller, Figure 146 also shows the surface distribution of static pressure at  $t = 1.20$ . Also, Figure 146 shows sample particle traces that indicate the presence of a tip vortex emanating from a propeller blade tip.

Figure 147 shows the trajectory of the vehicle with respect to time, with large excursions in the  $y$ - and  $x$ -directions and little movement in the  $z$ -direction. Note that the vehicle has traveled approximately 1.2 body lengths during a turn where the yaw angle has reached  $7.0^\circ$ . Even though a more thorough investigation of a turning maneuver should involve a complete turn, this preliminary investigation does demonstrate the applicability of the coupled RANS/6DOF solver to determine both the hydrodynamic forces and moments, as well as the resulting movement of the vehicle.

## 10.6 SUBOFF with a Propeller Rotating in Reverse

Under this maneuvering program, the final test case demonstrates how one can use this coupled RANS/6DOF solver to show how fluid flow phenomena can affect the behavior of the vehicle. Once again, the research team has selected the fully-appended SUBOFF vehicle with a rotating propeller. For this test case, the team did not directly apply an external rolling moment into

the 6DOF equations in order to counteract the roll produced by the propeller torque. Similar to the test case prior to the previous one where SUBOFF went through an unconstrained motion, the team used only changes in the propeller rotational velocity to affect the maneuver. Therefore, the vehicle is free to respond to the resulting hydrodynamic forces and moments. However, for a portion of this case, the propeller was allowed to rotate in a direction opposite to its design direction. With the vehicle still moving forward, this case represents the most severe off-design computation for flow through the propeller.

The coupled RANS/6DOF solution for this test case begins at the dimensionless time  $t = 0.462$  in the middle of the test case prior to the last one where SUBOFF went through an unconstrained motion. At this instant, the vehicle has traveled about 0.46 of a body length in the  $x$ -direction, has a nondimensional propeller speed of 115.0, and has already rolled approximately  $-5.0^\circ$ . The drift angle ( $0.1^\circ$ ) and incidence angle ( $0.07^\circ$ ) are both small. Figure 148 shows that the propeller speed is reduced from 115.0 to 0.0 in a dimensionless time increment of  $\Delta t = 0.2646$ . This portion of the maneuver requires 120 computational time steps, which is the time during which the propeller makes one revolution. Further, Figure 148 shows that the propeller was reversed until the rotational speed reached -80.0 at  $t = 1.27$ . Note that the rate of change of the propeller speed with respect to time is smaller during the increment when the propeller rotation increases in the negative direction. This was simply a precautionary measure to prevent a possible instability in the calculation when the propeller was reversed.

In addition, Figure 148 shows the effect of the rate of change of the propeller speed with respect to time. As the propeller speed is reduced and eventually reversed, the net axial force (the  $x$ -component of the force)--which has an initial positive value--drops and goes through a sudden change of sign in a short period of time. This change indicates that the drag force has become greater than the thrust, slowing the forward velocity of the vehicle. At  $t = 1.27$ , the propeller speed takes on the constant value of -80. This instance of the maneuver is marked by a rapid oscillation in the net axial force, which quickly stabilizes. Furthermore, Figure 148 shows that oscillations in the lateral and vertical forces also accompany alterations in the propeller speed.

### 10.6.1 Generation of a Ring Vortex

Deceleration of an underwater vehicle by means of reversing the angular velocity of the propeller is called a crashback maneuver. For this test case, the vehicle's velocity has dropped by more than 50% of its initial value by the end of the simulation at time  $t = 5.15$ . However, during this crashback maneuver, the vehicle continues to move in a forward direction. Relative to the vehicle itself, the fluid generally flows towards the stern, with pathlines passing outboard of the actual propeller. Within the propeller region, the reversed rotation of the blades moves the fluid upstream. These downstream and upstream fluid motions create a shear stress and, subsequently, generate a ring vortex located just outboard and just downstream of the propeller blade tips. Furthermore, the propeller blade tips tend to drag the vortex ring as they rotate, giving the vortex ring a helical structure. The unsteady motion and eventual decay of this ring vortex has a pronounced effect on the hydrodynamics of the vehicle.

Figure 149 shows the vortex ring at time  $t = 2.01$ . The flow traces are colored by the magnitude of the velocity, while the blades are colored by the magnitudes of the static pressure. The

arrows shown on the particle traces of the vortex ring demonstrate that the ring rotates in the same sense as the propeller. The vortex ring, however, is not symmetric about the axis of the propeller rotation. As will be shown later, asymmetric effects of the vortex ring appear to rotate around the propeller, in the opposite sense of blade rotation. Figure 149 shows that as the vortex ring rotates, part of the ring "touches" one or two blades, resulting in low static-pressure patches on the blade surfaces. These blade surface contours of static pressure lead to regions of adverse pressure gradients that can cause local separation of the blade boundary layers.

### 10.6.2 Characteristics of the Ring Vortex

An examination of Figure 149 shows that the vortex ring is not symmetric about the axis of symmetry of the propeller. The vortex ring has an unsteady motion both in and out of the propeller plane. In other words, the ring "wobbles" around the propeller blades, similar to the motion of an elastic ring dropped on a solid flat surface. At the same time  $t = 2.01$ , a side view of the vortex ring in Figure 150 shows the asymmetric structure of the vortex ring about the propeller's axis of symmetry. Figure 151 shows a view of the vortex ring looking upstream, at the same instance of time. Finally, Figure 152 shows how the structure of the vortex ring has changed from time  $t = 2.01$  to time  $t = 2.33$ , during which the propeller has rotated 4.07 times.

The strength of the vortex varies along its center line. At time  $t = 2.01$ , Figure 153 shows contours of static pressure on a plane cutting through the vortex ring. One of the characteristics of a vortex is that the pressure distribution is at a minimum in the vortex core and increases asymptotically--to the far-field pressure--with the inverse square of the radial distance from the vortex center. A stronger vortex will have a smaller value of the pressure in its core. Figure 153 shows that the vortex ring filament is much stronger near the top, in the vicinity of the upper blade. The image of the vortex is also depicted on the surface of the upper blade.

As the vehicle decelerates during this crashback maneuver, the  $u$ -component of the velocity flowing outboard of the propeller decreases. This reduction in forward velocity will decrease the shear stress in the mixing region between the forward and reverse velocities. Thus, the ring vortex will weaken--and eventually, once the vehicle stops, it will vanish. Figures 154 and 155 view the vortex ring at time  $t = 5.15$ . Comparing these figures with Figures 151 and 150 demonstrates the extent of the decay of the vortex ring.

### 10.6.3 Dynamic Response of the Vehicle

Referring back to Figure 148, random oscillations in the lateral and vertical forces occur during the early stages of crashback, especially when the slope of the propeller speed line changes (at the time when the propeller angular velocity is reduced to zero and begins to be reversed). Then, after the propeller rotational speed reaches a constant value of -80 and the drag stabilizes, the lateral and vertical forces undergo two distinct oscillatory patterns. First, Figure 148 shows large-amplitude, large-wavelength oscillations of both the lateral force (or the  $y$ -component of the force) and the vertical force (or the  $z$ -component of the force), with oscillations between positive and negative values. These oscillations are virtually identical between the two components, except for the expected 90° phase difference. Figure 148 also shows small-amplitude oscillations of the out-of-plane forces with a much higher frequency superimposed on the large oscillations.

Recall from Figure 149 and subsequent figures that the unsteady vortex ring rotates and actually "touches" one or two blades, resulting in low static-pressure patches on the blade surfaces and possible local boundary layer separation. Figure 156 shows the pressure contours on the suction surfaces of the propeller blades at different time intervals--with each image occurring at integral multiples of blade rotation. An examination of these contours shows a low-pressure region that moves circumferentially about the propeller axis of symmetry in the clockwise direction--in the opposite direction of blade rotation. Clearly, the tip portion of each propeller blade undergoes different loadings and, since the low-pressure region can lead to possible local separation, one might think of this phenomena as similar to the "rotating stall" phenomena that occurs in other types of turbomachinery flows. It also seems likely that the low pressure on the blade surfaces could initiate cavitation, resulting in a phenomenon similar to "rotating cavitation."

The time traces of Figure 148 are repeated in Figure 157, except that a new trace replaces the axial-force trace. This new trace represents the approximate location of the low-pressure region--or "rotating stall" cell--from Figure 156 as a function of time. In Figure 157, the angle,  $\theta$ , measures the approximate location of this low-pressure-region cell from the stern plane, in the clockwise direction looking upstream. Each symbol represents the approximate circumferential location of the cell on the blades at an instance of time. For clarity, these locations are plotted as a sine wave, with a line representing a least-squares polynomial fit.

At time  $t = 2.01$ , Figure 156a shows that the "rotating stall" cell is located at  $\theta \approx -270^\circ$ , which aligns the cell with the  $-z$ -axis. Therefore, the cell will change the loading on blades passing through this region and create an extreme in the vertical or  $z$ -component of the force, which is shown as a minimum in Figure 157. At this position, the effect of the "rotating stall" cell appears to be negligible on the lateral or  $y$ -component of the force. As the cell rotates to a position that aligns with the  $+y$ -axis, the cell will create an extreme in the lateral force, which is shown as a maximum in Figure 157. At this position, the effect on the vertical force is negligible. This process continues in time, although the force amplitudes decrease as the vehicle deceleration causes the vortex ring to decay. The frequency of the rotation of these cells matches the frequency of the oscillating forces and, since these cells rotate at a much slower rate than the propeller blades, the blades may pass through the stalled region many times before the stalled region completes one rotation. It should be noted that the low-pressure region rotates about the axis of symmetry of the propulsor approximately two times during which the amplitude of the "out-of-plane forces" becomes small. In conclusion, it seems evident that this "rotating stall"--and, thus, the unsteady vortex ring--generates the large oscillations in the lateral and vertical forces.

Both Figures 148 and 157 show small-amplitude, small-wavelength oscillations of the lateral and vertical forces superimposed on the large oscillations. For more detail, Figure 158 zooms in on a portion of the time trace for the vertical or  $z$ -component of the force. The vertical lines in this enlarged section separate the time intervals within which the propeller makes a complete rotation. There are five peaks within each time interval, each corresponding to a blade passing through a high-gradient flow region. Therefore, the frequency of these small oscillations corresponds to the propeller blade passing frequency. The existence of the out-of-plane forces oscillating at two distinct frequencies shows the capability of the coupled RANS/6DOF computations to handle multiple-time-scale problems.

The amplitude of the high-frequency oscillations is a function of the way in which the ring vortex interacts with the blades. As shown previously, the ring vortex “touches” one or more blades at different times. This interaction implies that the time period during which a blade passes through the low-pressure region varies, depending on both the proximity of the ring vortex core to the location of the blades and on the length of the vortex core that is close enough to the blades to make the low-pressure impressions on the blades. The longer the period, the more pronounced the effect. Furthermore, since the ring vortex moves unsteadily, both in and out of the propeller plane, the angle at which blades cut through the ring vortex domain can affect the amplitude of the high-frequency oscillations. These high-frequency oscillations are not unique to the crashback simulations. They are present in the cases where the propulsor is rotating in the design direction. Figure 136 demonstrates these oscillations in the unconstrained-motion case.

#### 10.6.4 Vehicle Trajectory

Figure 159 shows the time history of the roll, pitch, and yaw rates. These rates are induced on the vehicle as the direct effect of the moments, as shown in Figure 160. The rates are expressed as degrees per nondimensional unit of time. It should be noted that in this simulation, the only mechanism inhibiting roll of the vehicle is that introduced by the forces of the weight and the buoyancy. In the absence of any other force, the interaction of the forces of weight and buoyancy causes the vehicle to reach a stable equilibrium, in which the centers of buoyancy and gravity align vertically. Any rotation from this position will cause these forces to generate a moment tending to move the vehicle back to the stable position. However, the moment induced on the vehicle by the propeller causes the vehicle to rotate to a different state of stability than that defined by the weight and the buoyancy force. Considering Figure 159, starting at  $t = 0.46$ , as the propeller angular velocity is reduced, the absolute value of the roll rate decreases. At  $t = 0.73$ , when the propeller rotation is reversed, the roll rate becomes positive and continues to increase until it reaches a peak at  $t = 1.39$ . The vehicle continues to roll until it reaches an angle at which the moment developed by the forces of weight and buoyancy equals the moment developed by the rotation of the propulsor. As the roll angle approaches this limiting angle, the roll rate starts to decrease. The roll rate becomes zero once the roll angle reaches this limit and becomes negative as the roll angle passes this limit. Once the roll angle passes this limit, the righting moment produced by the weight and the buoyancy force becomes larger than the moment induced by the propeller and acts to move the vehicle toward the upright position, causing the roll rate to change direction. The vehicle will rotate in a pendulum type motion until it reaches the stable equilibrium at which the roll rate is zero and the vehicle has rolled to an angle at which the opposing moments are equal.

Figure 161 shows the time history of the values of the roll angle, the pitch angle, and the yaw angle. Note that the vehicle reaches a maximum roll angle of  $42.7^\circ$ . The small distance between the centers of gravity and buoyancy leads to this large roll angle before the righting moment reduces the amount of roll. Figure 162 shows the variation of the vehicle’s linear velocities. The oscillations in the  $v$ - and  $w$ -components of velocity, as well as the yaw and pitch rates in Figure 159 and the yaw and pitch angles in Figure 161, correlate with the large-amplitude, large-wavelength oscillations in the out-of-plane forces shown in Figures 148 and 157.

Figure 163 shows the path of the vehicle during the crashback simulation. The initial location of the vehicle on this figure is indicated by a bold X. The plot of Z-position versus Y-position

demonstrates that the center of gravity of the vehicle initially moves to a positive  $Y$ -position, then reverses back to zero, and finally moves to a negative  $Y$ -position. Simultaneously, the center of gravity of the vehicle moves upward. These changes in the position of the vehicle are associated with the changes in the vehicle's orientation as shown previously in the Figure 161.

## 11. Summary and Conclusions

A team of researchers from the Engineering Research Center at Mississippi State University and the Applied Research Laboratory at The Pennsylvania State University have developed a physics-based method that will lead to a means of accurately predicting the forces and moments acting on a maneuvering, self-propelled, appended, underwater vehicle and the resulting vehicle motion. This methodology has been developed in order to supplement and, eventually, replace the traditional correlation-based means of "predicting" the maneuvering characteristics of a submerged vehicle. These correlation-based methods have difficulty with extreme maneuvers, propulsor effects, non-traditional vehicle shapes, vehicle modifications, and the effects of vortical structures created by the flow over the vehicle. Also, these traditional methods require a large number of expensive model tests--tests that also have several flaws, including problems with Reynolds number scaling. The new method can address these problem areas and allow the hydrodynamicist to investigate the physics of a maneuvering vehicle. Thus, the new method will impact the hydrodynamic design of underwater vehicles.

One primary difference exists between this new physics-based means of making maneuvering predictions and the old correlation-based means. While the traditional methods use empirical correlations from model-scale experiments to determine the hydrodynamic forces and moments acting on a vehicle during a maneuver, this new method numerically solves for the fluid dynamics using the three-dimensional, time-dependent Reynolds-averaged Navier-Stokes equations. Since the Reynolds numbers of these flows are extremely large, the viscous regions must be resolved within the near-wall region of the turbulent boundary layers, and this resolution places severe demands on the numerical scheme in terms of stability and accuracy. To make the computation of these high Reynolds number, unsteady flow problems practical in terms of the total CPU time, one must restrict the computational time-step needs by the physics of the problem being solved and not by the numerics of the scheme used to solve the problem.

The UNCLE code developed here solves for the three-dimensional, time-dependent Reynolds-averaged Navier-Stokes equations on time-dependent curvilinear coordinates and uses artificial (or pseudo) compressibility to obtain the numerical solution for incompressible flow. This cell-centered finite-volume code uses a third-order upwind-biased scheme, with third-order flux vectors based on the classical MUSCL-type of numerical flux-vector formulation. Discretized Newton-relaxation is used for the solution algorithm. Here, the solution of the equations involves Newton's method, with symmetric Gauss-Seidel relaxation used at each Newton iteration and the flux Jacobian obtained numerically. A multigrid scheme has been added to accelerate the convergence of the numerical solution, including an extension for unsteady flow computations. The UNCLE code is solved on dynamic, relative-motion, multiblock, structured grids. The multiblock topology allows one to divide the domain into smaller regions for detailed gridding, allowing for high-quality grids on complex geometry. Also, by solving the equations one block at a time, the multiblock topology reduces the required computer memory.

The research team performed a number of steady and unsteady computations using this baseline UNCLE code. This baseline code included an algebraic turbulence model based on the model developed by Baldwin and Lomax [1978]. The team modified the search routines within the model to better handle flows with leeward vortical structures and flows with thick stern boundary layers. Initially, the validation test cases centered on the ability of UNCLE to compute simple

boundary layer flows, both on a flat plate and on a submarine-type vehicle called SUBOFF. Since the UNCLE code uses a Roe approximate Riemann solver, the boundary layer computations gave very good results with only a modest number of grid points--assuming that the closest point to the solid surface was within the viscous sublayer. Also, the algorithm proved to be robust in handling extremely high aspect ratio grids, and the multigrid scheme gave very fast convergence rates--with 45-60% savings in CPU time over single-grid solutions. In fact, the savings due to the multigrid scheme were actually higher, since this scheme gave good skin-friction results at an earlier stage of convergence.

Next, the research team tested the ability of the baseline UNCLE code to handle vortical structures created in the flow field. They obtained reasonable to excellent results in comparing with experimental measurements on a 6:1 prolate spheroid at an angle of attack that generated a three-dimensional cross-flow separation and for an appendage junction flow that generated a "horseshoe" or "necklace" vortex. The code's ability to preserve the vortex structure as it convected downstream was also tested by using the idealized Thomson-Rankine vortex model. Since the velocity distribution of the vortex was discontinuous at the edge of the vortex core, this test case proved to be severe. The basic structure of the vortex was preserved even on a relatively coarse grid, but a very fine grid was required to give accuracies within 1% for long convection distances. Finally, the research team tested the multiblock capability of the code using SUBOFF with appendages. The UNCLE code reached a nearly grid-independent convergence rate, even for coarse grids, and no change in the flow field was found after the residual was reduced by 2.5 orders of magnitude, which is about 200 multigrid cycles. The flow field computations gave excellent comparisons to all measured data when the grid contained at least a million points for an appended vehicle without a propulsor. Even more critical to future maneuvering computations, the UNCLE code gave excellent agreement with the force and moment data as a function of the angle of drift, with a larger number of grid points necessary to reach agreement with the axial-force data.

In order to verify the ability of UNCLE to handle unsteady flow, the research team compared computations with measured data for impulsively started cylinders, a hydrofoil undergoing high-reduced-frequency gust loading, and a 6:1 prolate spheroid undergoing three prescribed, time-dependent maneuvers. For a plunge maneuver with the prolate spheroid, the comparisons were good, with the computations giving a smaller pressure differential at the bow. For a turning maneuver, both the computational and the experimental results showed that the suction peaks toward the windward side were greater during the unsteady maneuver than the suction peaks that would be found from a quasi-steady maneuver. However, a small discrepancy existed in comparing the actual magnitude of the computed and measured suction peaks. Finally, for a pitch-up maneuver, the comparisons again gave good agreement, with the largest discrepancies occurring on the leeward side as the vortices from the cross-flow separation rolled-up and on the windward side at 30° angle of attack. Overall, these computations clearly showed that quasi-steady solutions would not be adequate to simulate unsteady maneuvers and that the UNCLE code does well in solving for the required unsteady flow.

The action of the propulsor can greatly affect the maneuvering characteristics of a vehicle, and the research team first modeled the propulsor with body forces or an actuator disc. They tested this capability by simulating two prescribed maneuvers with a fully-appended SUBOFF configuration. However, the importance of the out-of-plane forces generated by the propulsor on a real vehicle led the team to computing flows with an actual rotating propulsor. This capability was realized within UNCLE using localized grid distortion, which insures continuous grid lines across block interfaces with relative motion and also minimizes grid stretching. The numerical temporal error introduced as

grid lines on these adjacent blocks switch communication partners, or "click," is minimized by using Newton subiterations and/or multigrid cycles. The research team tested this capability by first comparing with data for a freestream propeller and, then, comparing with data for a high Reynolds number pump. Again, both test cases gave reasonable to excellent agreement with experimental data, with the axial-flow pump case providing numerous types of measurements in which to compare. The research team also tested the rotating-propulsor capability by making additional computations with the fully-appended SUBOFF body, using a five-bladed propeller. They found that local time stepping should be used for computing the start-up solution to significantly improve the convergence rate--before switching to minimum time stepping for the unsteady computation. Finally, the research team also performed initial computations with a SUBOFF appendage moving over a flat plate. This computation, which showed the expected root leakage vortex, will lead to the capability of handling moving control surfaces on an underwater vehicle.

Future use of UNCLE for large-scale simulations of a maneuvering vehicle at high Reynolds number will require large amounts of floating-point arithmetic and considerable storage capacity. Thus, from the beginning of this research program, the team investigated the use of high-performance parallel computing for making these types of large-scale computations using UNCLE. The primary objective was to develop a portable, scalable capability that would allow one to perform these large-scale maneuvering simulations and to reduce their run times.

Unfortunately, the symmetric Gauss-Seidel subiterations in the sequential algorithm of UNCLE, which give excellent stability, convergence, and efficiency, are not easily parallelized. The parallel code required spatially decomposed grid blocks assigned to separate processors, but the resulting decoupling of the subiterations can degrade the performance of this otherwise implicit algorithm. Therefore, the team had to use a sufficient number of inexpensive subiterations in order to recover the convergence rate of the sequential algorithm. The parallel algorithm uses Gauss-Seidel relaxation sweeps within each process but is effectively explicit across block boundaries. The additional subiterations are kept inexpensive because the flux Jacobians are saved and reused. To evaluate the performance of the code, the team developed a heuristic means of estimating the parallel performance. This technique gave heuristic performance estimates of the CPU time requirements and the total time required for message passing. The Message Passing Interface (MPI) supplies these interprocessor communications and allows for a high degree of portability across different computing platforms. Finally, for computations with the parallel code involving a rotating propulsor, the team used a modified ring-buffer concept to handle the time-variable dataset associated with the rotating interface.

The research team performed several computations using the parallel version of UNCLE that involved SUBOFF with various combinations of appendages, including a five-bladed propeller. All cases gave good parallel efficiency as indicated by CPU utilizations between 72% and 94%. This good efficiency was obtained by using the heuristic performance estimate to match each flow case to the computing resources used. Computations were run with different grid sizes and on several different platforms, illustrating the scalability and portability of the parallel code. The team also demonstrated a considerable reduction in run time compared to the sequential code--including a test case with the rotating propulsor capability. These results show the necessity of using parallel processing to achieve the timely turn-around of solutions needed in a design environment.

While the baseline UNCLE code included an algebraic turbulence model, the research team recognized that the flow over maneuvering vehicles would have time and length scales which

vary dramatically from one situation to another. Therefore, the team also investigated the use of two-equation turbulence models since these models avoid the need to empirically determine either type of scale. For these types of flow fields that include three-dimensional, separated flow, these two-equation turbulence models also have to describe the near-wall, or low Reynolds-number, region. In addition, the team investigated nonlinear models in order to avoid the assumption of an isotropic eddy viscosity. The absence of differences in the normal Reynolds stresses may be detrimental in computing flows such as the evolution of primary and secondary horseshoe vortices shed from appendage-hull intersections.

Initially, the research team concentrated their turbulence model investigation on a stand-alone  $k-\epsilon$  turbulence model and, then later, installed a  $q-\omega$  turbulence model directly into the UNCLE code. One can derive one model from the other one using a straight-forward change of variables, with the main difference being the damping function in the low-Reynolds-number modification. Within UNCLE, the two-equation turbulence model is "loosely coupled" in that these equations are solved as a separate system from the continuity and momentum equations by assuming that the velocities appearing in the turbulence transport equations are known at each iteration. The team also looked at several nonlinear anisotropic models that assume that the relationship between the Reynolds stress and the mean strain rate tensor is not linear but includes terms which are quadratic in the mean strain rate tensor as well. These detailed investigations resulted in the selection of a specific nonlinear model.

The first test cases for the two-equation turbulence models involved comparisons with analytical solutions for the spatial and temporal decay of turbulence. The excellent comparison for the spatial decay showed the expected balance between convection and dissipation, while the excellent comparison for the temporal decay showed the expected balance between the unsteady and dissipation terms. For fully-developed channel flow, the results for the two-equation turbulence model compared very well with empirical and analytical curves. Since the turbulence is roughly in "equilibrium" within the logarithmic region, the computations showed the expected balance between production and dissipation. These models also showed excellent agreement with experimental data for flat-plate boundary layers and for the SUBOFF barebody, with some improvement over results using the algebraic turbulence model.

The research team also used fully-developed channel flow as a test case for the nonlinear anisotropic turbulence model. Analytically, for two-dimensional flow, one can show that the nonlinear model only modifies the normal Reynolds stresses in this case, but not the Reynolds shear stresses--and the computations show that the prediction of the anisotropy of the normal stresses is greatly improved. In three dimensions, the agreement between the computations (for the stand-alone model) and the experimental data show that the nonlinear model is well-suited for the prediction of turbulence-driven secondary flow, a flow that linear models cannot predict. Comparisons were also made to measurements on a 6:1 prolate spheroid at an angle of incidence. Without any modifications, the nonlinear model closely captured the velocity profiles and flow angles and approximated most of the features of the Reynolds stress profiles. Thus, the anisotropy of the normal Reynolds stresses greatly enhanced the predictions with the linear two-equation turbulence model.

Prediction of a vehicle's trajectory requires coupling the fluid dynamics and the vehicle dynamics. The vehicle dynamics can be described by the six vector equations of Newton's laws of motion. These six-degree-of-freedom (6DOF) equations describe the acceleration of the vehicle at an instant in time, given the forces and moments due to weight and buoyancy and the hydrodynamic

forces and moments computed by the UNCLE code. From this information, the trajectory can be deduced using purely kinematic relations. For this research program, the UNCLE code provided these forces and moments at each time step to a subroutine that solved the 6DOF equations and seven additional kinematic relations using a fourth-order accurate Runge-Kutta-Merson scheme. This 6DOF solver then updates the position and velocity of the vehicle. After computing the new grid point velocities, the process repeats. Run in a decoupled fashion, the UNCLE code contains only one nondimensional parameter, the Reynolds number, that can dictate the behavior of the flow. However, when one runs UNCLE coupled with the 6DOF solver, there are 14 new, independent nondimensional parameters (such as nondimensional weight and buoyancy). A change in any one of these 15 parameters has the potential to impact the resultant vehicle trajectory--making the prediction of the maneuvering characteristics of an underwater vehicle very sensitive.

For the initial computations using the UNCLE code coupled with the 6DOF solver, the research team selected two freely-falling bodies at moderate Reynolds number: a sphere and a 6:1 prolate spheroid. These cases allowed the team to test the coupling without the additional complication of a turbulence model and without requiring arbitrary forces other than weight and buoyancy. Both cases were initiated from a well-defined, uniform, non-stationary state, as computed from running the UNCLE code decoupled from the 6DOF solver. Then, after computing with the coupled equations, a ring vortex on the leeward side of the free-falling sphere created large unsteady forces and moments that produced rotational kinetic energy, in addition to the initial translational kinetic energy. The free-falling prolate spheroid consisted of a heavy material near the nose and a lighter material near the tail, and this density distribution provided a natural restoring moment and helped the prolate spheroid maintain its initial orientation. The ring vortex on this body created unsteady forces that were an order of magnitude smaller than those on the sphere. Only 9% of the total run time was devoted to computing the forces and moments and performing the vehicle dynamics calculations.

The first vehicle maneuvers computed with the UNCLE code coupled with the 6DOF solver involved the fully-appended SUBOFF body performing very simple maneuvers. Initially, a body-force model was used to simulate the propeller. The maneuver consisted of only changes in the thrust provided by the actuator disc and the weight/buoyancy ratio. The vehicle responded as expected to changes in thrust, while a weight reduction produced a net upward force at the center of gravity. The resulting upward acceleration combined with the forward velocity of the vehicle induced a negative flow incidence, and this incidence, in turn, caused a significant downward hydrodynamic force and nose-down pitching moment on the vehicle. Again, this nose-down motion was the expected result. The next maneuvering test case used a rotating five-bladed propeller. The dynamic response to changes in propeller thrust, or rotational speed, was immediate and consistent with physical expectations. For instance, the propeller torque produced a rolling moment on the vehicle. For the next case, the research team applied an external roll moment to counteract the propeller torque and, also, applied an external yaw moment to simulate the beginning of a turn. These externally-applied moments allowed the team to determine how much roll could be attributed to the lift generated on the sail during the turn.

The final test case run during this research program illustrates the current status of the physics-based means of computing maneuvering characteristics and the potential utility of the code for maneuvering computations. Here, the vehicle decelerated by means of reversing the angular velocity of the propeller. This crashback maneuver represents the most severe off-design computation for flow through the propeller. The flow outboard of the propeller moves opposite to the flow through

the propeller blades, creating a shear stress that generates a ring vortex. This unsteady ring vortex is not symmetric, and it weakens as the vehicle decelerates. As the propeller rotates, the ring vortex "touches" one or two propeller blades, resulting in low static-pressure patches on the blade surfaces. These patches rotate in the opposite direction of the propeller (and with a much lower frequency), and produce large-amplitude, low-frequency oscillations in the out-of-plane forces. These oscillations combine with small-amplitude, high-frequency oscillations corresponding to the blade-passing frequency. As a result of these unsteady out-of-plane forces and the other forces and moments acting on the vehicle, the vehicle responds by rolling, pitching, and yawing--motions captured by the UNCLE code.

In summary, the research team has developed a physics-based method that will lead to a means of accurately predicting the forces and moments acting on a maneuvering, self-propelled, appended, underwater vehicle and the resulting vehicle motion. This physics-based method solves the unsteady Reynolds-averaged Navier-Stokes equations and includes the effects of using parallel processing and two-equation turbulence models, as well as the coupling between the fluid and vehicle dynamics. The method has been tested for several steady and unsteady flow problems that verify various elements of the code and check the feasibility of calculating flow fields of varying complexity--leading up to the computation of the flow over a maneuvering vehicle and the vehicle's response.

## 12. Future Work

The team of researchers from the Engineering Research Center at Mississippi State University and the Applied Research Laboratory at The Pennsylvania State University have made tremendous progress towards developing a physics-based method to predict the maneuvering characteristics of underwater vehicles, but many issues still exist. These issues are aimed at extending, improving, and exercising the method. Until now, this first-of-its-kind research has focused on the development and verification of various components of the code--with a concentration on Reynolds numbers for which useful experimental data could be obtained. However, for underwater vehicles such as submarines, the Reynolds numbers can be as much as two orders of magnitude greater than these model-scale experiments. Thus far, only the SUBOFF barebody has been computed at these very high Reynolds numbers.

As described in this report, the research team developed an excellent algorithm within UNCLE for solving the unsteady Reynolds-averaged Navier-Stokes (RANS) equations. Nevertheless, new algorithms may arise in the future that better handle these types of maneuvering problems. For instance, experience gained thus far in parallel computing for these types of problems indicates that it is easier to get access to processors than memory; consequently, one should try to reduce memory requirements as much as possible. All future algorithms need to be robust enough to withstand the burden placed on them by the requirements of solving complex flow problems with extremely high Reynolds numbers on highly-clustered grids.

Future applications of the parallel version of UNCLE for extremely high Reynolds numbers will require many more grid points and, in turn, more processors. Since computational efficiency is known to degrade as the number of processors increases, additional research will be required to produce an efficient and robust parallel computational capability for these high Reynolds numbers. Also, any future changes in the sequential algorithm for the flow solver will require work to develop a version for parallel processing. In addition, a few items still need to be considered for the existing parallel code. One example is a slightly different MPI implementation with user-defined datatypes that would avoid explicit buffer loading. Finally, the parallel code still needs to be utilized for an actual maneuvering computation, including the coupling with the vehicle dynamics.

The most pressing capability that the research team still needs to develop is the time-accurate motion of vehicle appendages. These computations include the solution of both the unsteady RANS equations and the 6DOF equations. Future computations that include complex propulsors with more than one blade row also need to be addressed. Since sufficiently gridding each blade passage in each blade row will result in a grid that is extremely large, the research team should investigate simplifications that would reduce the number of grid points and still allow for the correct blade interactions and, thus, the correct out-of-plane forces. Recent work by Chen, Celestina, and Adamczyk [1994] showed promise in modeling these aperiodic boundaries using a tangential time-shift approach. Using this approach, only one blade passage per blade row is required for the computational domain. The research team needs to investigate the use of this technique for the incompressible flow over a vehicle and through a propulsor with multiple blade rows.

In order to increase the capability of this physics-based method, the research team needs to address the maneuvering vehicles operating in shallow-water environments or operating near or on the water surface. These vehicles can operate at lower Reynolds numbers and must deal with unique

boundary conditions, such as free surfaces, cross currents, and solid or porous bottom surfaces. Surface winds and waves can also play roles--with mass, momentum, and energy exchanges.

With regards to turbulence modeling, the results using the UNCLE code with an algebraic turbulence model were surprisingly good. In the future, many of the test cases described in this report that the team ran with the algebraic model need to be repeated using the two-equation turbulence models that have also been investigated in this report--including the initial computations with the two-equation turbulence model using the multigrid, multiblock capability. These test cases should establish if these models offer significant improvements. In doing so, the research team needs to ensure that they can use these two-equation models in a robust manner. Furthermore, the team needs to address how well both algebraic and two-equation turbulence models work for extremely high Reynolds numbers. Certainly, the effect of wall roughness on the near-wall turbulence structure will be magnified at higher Reynolds numbers, and these effects will need to be included in the future. Flow fields for some maneuvers will have sufficiently small Reynolds numbers where the flow transitions from laminar to turbulent on the vehicle hull and/or the appendages. Therefore, the research team will need to address issues involving the modeling of this transition.

Specific issues on two-equation turbulence modeling also need to be addressed. Some of these issues address the robustness of the code, the effect of freestream turbulence, and the behavior of these models in the vicinity of stagnation points. For the low-Reynolds-number modifications of different two-equation turbulence models, the damping functions vary, and the research team needs to remove the dependency of these damping functions on the normal distance to the solid surface. The work discussed in this report uses a "loosely coupled" system, in that the two turbulence transport equations are solved as a separate system from the continuity equation and the three momentum equations by assuming that the velocities appearing in the turbulence transport equations are known at each iteration. The research team should also investigate a "strongly coupled" system, where all six equations are solved simultaneously. Both systems will require investigations into the algorithms in order to improve the efficiency of the solver and reduce the CPU time. Finally, the nonlinear model requires more testing, including a careful examination of its empirical constants. These further investigations might also consider the use of "explicit algebraic Reynolds stress models."

In order to couple the fluid and vehicle dynamics, the UNCLE code currently calls a subroutine that solves the 6DOF equations and seven additional kinematic relations. However, for a real life maneuvering scenario, this process needs improvement. Here, a main code must provide the executive commands to set the "state" of the vehicle, compute the response of the vehicle to these commands by solving the 6DOF and kinematic equations, and model the behavior of the ballast and other important aspects. This main code would call UNCLE as a subroutine to provide the hydrodynamic forces and moments--with a module in between that would accept arbitrary control-surface angles and propulsor shaft rotation rates and, then, regrid and compute the "distortion velocity" for each grid point in the regredded blocks. The flow solver requires the total grid point velocity as obtained by adding the "distortion velocity" to the grid point velocity from the gross motion of the vehicle.

Future computations of vehicle trajectories will require *a priori* prescription of the motion of control surfaces and, yet, this prescription does not ensure controlled motion of the vehicle or the execution of a precise maneuver. Vehicle maneuvers involve nonlinear dynamical systems where small errors in the initial conditions, including the *a priori* prescription of control surface motion, accumulate and could lead to large deviations in the anticipated trajectory and attitude of the vehicle.

In other words, the computational errors from UNCLE may be small at each stage of the maneuver, but the accumulated error in the trajectory at the end of the maneuver may be very large. Therefore, the main code requires additional systems of equations that represent the controller. These equations can be simplified to allow computations of experimental maneuvers and, also, lay the groundwork for the incorporation of more elaborate and sophisticated control systems.

The key ingredient in future work of all aspects of maneuvering computations is the execution of more and more test cases. Again, these test cases will be used to validate various elements of the prediction method, improve confidence in the use of the method, and check the feasibility of using the method to calculate flow fields of increasing complexity. Most importantly, the research team needs to run validation test cases with actual geometry for captive-model tests, free-running-model tests, and full-scale trials. Grid generation issues need to be addressed for these test cases. The flow fields must include a wide range of Reynolds numbers, including Reynolds numbers that are as much as two orders of magnitude greater than those tested so far. Successfully addressing these technical issues and applying them to these various test cases will result in a physics-based means of accurately predicting the forces and moments acting on a maneuvering, self-propelled, appended, underwater vehicle and the resulting vehicle motion.

## 13. Bibliography

- Adamczyk, J. J., "A Model Equation for Simulating Flows in Multistage Turbomachinery," ASME Paper 85-GT-226, 1985.
- Ahn, S., "An Experimental Study of Flow Over a 6 to 1 Prolate Spheroid at Incidence," Ph.D. Dissertation, Aerospace and Ocean Engineering Department, Virginia Polytechnic Institute and State University, October 1992.
- Anderson, W. K., Thomas, J. L., and van Leer, B., "Comparison of Finite Volume Flux Vector Splittings for the Euler Equations," *AIAA Journal*, Vol. 24, No. 9, pp. 1453-1460, September 1986.
- Arabshahi, A., Taylor, L. K., and Whitfield, D. L., "UNCLE: Toward a Comprehensive Time-Accurate Incompressible Navier-Stokes Flow Solver," AIAA Paper No. 95-0050, AIAA 33<sup>rd</sup> Aerospace Sciences Meeting and Exhibit, Reno, NV, January 9-12, 1995.
- Baldwin, B. S. and Lomax, H., "Thin-Layer Approximation and Algebraic Model for Separated Turbulent Flows," AIAA Paper 78-257, January 1978.
- Batchelor, G. K., *An Introduction to Fluid Dynamics*, Cambridge University Press, New York, NY, 1967.
- Boswell, R. J., "Design, Cavitation Performance, and Open-Water Performance of a Series of Research Skewed Propellers," David W. Taylor Naval Ship Research and Development Center, Report No. 3339, March 1971.
- Bouard, R. and Coutanceau, M., "The Early Stage of Development of the Wake Behind an Impulsively Started Cylinder for  $40 < Re < 104$ ," *Journal of Fluid Mechanics*, Vol. 101, Part 3, pp. 583-607, 11 December 1980.
- Briley, W. R. and McDonald, H., "Solution of the Multidimensional Compressible Navier-Stokes Equations by a Generalized Implicit Method," *Journal of Computational Physics*, Vol. 24, pp. 372-397, 1977.
- Briley, W. R., Neerarambam, S. S., and Whitfield, D. L., "Implicit Lower-Upper/Approximate-Factorization Algorithms for Viscous Incompressible Flows", AIAA Paper No. 95-1742-CP, 1995.
- Bushnell, P., "Measurement of the Steady Surface Pressure Distribution on A Single Rotation Large Scale Advanced Prop-Fan Blade at Mach Numbers from 0.03 to 0.78," NASA Contract Report 182124, July 1988.
- Champagne, F. H., Harris, V. G., and Corrsin, S., "Experiments on Nearly Homogeneous Turbulent Shear Flow," *Journal of Fluid Mechanics*, Vol. 41, Part 1, pp. 81-139, 26 March 1970.

- Chen, J. P., "Unsteady Three-Dimensional Thin-Layer Navier-Stokes Solutions for Turbomachinery in Transonic Flow," Ph.D. Dissertation, Mississippi State University, December 1991.
- Chen, J. P. and Whitfield, D. L., "Navier-Stokes Calculations for the Unsteady Flow Field of Turbomachinery," AIAA Paper No. 93-0676, 31<sup>st</sup> AIAA Aerospace Sciences Meeting and Exhibit, Reno, Nevada, January 1993.
- Chen, J. P., Celestina, M. L. and Adamczyk, J. J., "A New Procedure for Simulating Unsteady Flows Through Turbomachinery Blade Passages," ASME Paper 94-GT-151, 1994.
- Chen, H.-C., "Assessment of a Reynolds Stress Closure Model for Appendage-Hull Junction Flows," Transactions of the ASME, *Journal of Fluids Engineering*, Vol. 117, pp. 557-563, December 1995.
- Chesnakas, C. J., Simpson, R. L., and Madden, M M., "Three-Dimensional Velocity Measurements on a 6:1 Prolate Spheroid at 10° Angle of Attack," Department of Aerospace and Ocean Engineering, Virginia Polytechnic Institute and State University, Report VPI-AOE-202, January 18, 1994.
- Chorin, A. J., "A Numerical Method for Solving Incompressible Viscous Flow Problems," *Journal of Computational Physics*, Vol. 2, pp. 12-26, 1967.
- Coakley, T. J., "Turbulence Modeling Methods for the Compressible Navier-Stokes Equations," AIAA Paper 83-1693, 1983.
- Crook, L. B., "Resistance for DARPA SUBOFF as Represented by Model 5470," David Taylor Research Center, DTRC Ship Hydromechanics Department Report DTRC/SHD-1298-07, March 1990.
- Davoudzadeh, F. , McDonald, H., and Thompson, B. E., "Accuracy Evaluation of Unsteady CFD Numerical Schemes By Vortex Preservation," *Computers & Fluids*, Vol. 24, No. 8, Elsevier Science Ltd., pages 883-895, 1995.
- Degani, D. and Schiff, L.B., "Computation of Turbulent Supersonic Flows Around Pointed Bodies Having Crossflow Separation," *Journal of Computational Physics*, Vol.66, No.1, pp. 173-196, 1986.
- Delpero, P. M., "Investigation of Flows around a Two Dimensional Hydrofoil Subject to A High Reduced Frequency Gust Loading," M.S. Thesis, Massachusetts Institute of Technology, February 1992.
- Devenport, W. J. and Simpson, R. L., "An Experimental Investigation of the Flow Past an Idealized Wing-Body Junction: Final Report," Department of Aerospace and Ocean Engineering, Virginia Polytechnic Institute and State University, Report VPI-AOE-172, July 1990.

- Dreyer, J. J. and Zierke, W. C., "Solution of the Average-Passage Equations for the Incompressible Flow Through Multiple-Blade-Row Turbomachinery," ARL Penn State Technical Report TR 94-05, Applied Research Laboratory, The Pennsylvania State University, February 1994.
- Durbin, P., "On the  $k-\epsilon$  Stagnation Point Anomaly," *International Journal of Heat and Fluid Flow*, Vol. 17, No. 1, pp. 89-90, February 1996.
- Gatlin, B., "An Implicit, Upwind Method for Obtaining Symbiotic Solutions to the Thin-Layer Navier-Stokes Equations," Ph.D. Dissertation, Mississippi State University, August 1987.
- Gatski, T. B., and Speziale, C. G., "On Explicit Algebraic Stress Models for Complex Turbulent Flows," *Journal of Fluid Mechanics*, Vol. 254, pp. 59-78, September 1993.
- Gertler, M. And Hagen, G. R., "Standard Equations of Motion for Submarine Simulations," David W. Taylor Naval Ship Research and Development Center, DTNSRDC Report No. 2510, June 1967.
- Gessner, F. B., and Jones, J. B., "On Some Aspects of Fully-Developed Turbulent Flow in Rectangular Channels," *Journal of Fluid Mechanics*, Vol. 23, Part 4, pp. 689-713, 1965.
- Gropp, W., Lusk, E., and Skjellum, A., *Using MPI*, MIT Press, pp. 185-188, 1994.
- Groves, N., Huang, T., Chang, M., "Geometric Characteristics of DARPA SUBOFF Models (DTRC Models 5470 and 5471)," David Taylor Research Center Report SHD-1298-01, March 1989.
- Harris, V. G., Graham, J. A. H., and Corrsin, S., "Further Experiments in Nearly Homogeneous Turbulent Shear Flow," *Journal of Fluid Mechanics*, Vol. 81, Part 4, pp. 657-687, 5 August 1977.
- Hoang, N. T., Wetzel, T. G., and Simpson, R. L., "Unsteady Measurements Over a 6:1 Prolate Spheroid Undergoing a Pitch-Up Maneuver," AIAA Paper No. 94-0197, January 1994a.
- Hoang, N. T., Wetzel, T. G., and Simpson, R. L., "Surface Pressure Measurements Over a 6:1 Prolate Spheroid Undergoing Time-Dependent Maneuvers," AIAA Paper No. 94-1908, June 1994b.
- Horwich-Lurie, E., "Unsteady Response of a Two-Dimensional Hydrofoil Subject to High Reduced Frequency Gust Loading," M.S. Thesis, Massachusetts Institute of Technology, May 1993.
- Huang, T. T., Groves, N. C., and Belt, G., "Boundary-Layer Flow on An Axisymmetric Body with An Inflected Stern," David W. Taylor Naval Ship Research and Development Center, Report No. DTNSRDC-80/064, August 1980.

- Huang, T. T., Liu, H-L., Groves, N. C., Forlini, T. J., Blanton, J. N., and Gowing, S., "Measurement of Flows Over an Axisymmetric Body with Various Appendages (DARPA SUBOFF Experiments)," Nineteenth Symposium on Naval Hydrodynamics, Seoul, Korea, August 24-28, 1992.
- Imlay, F. H., "Complete Expressions for the Gravitational and Buoyancy Force Terms in the Equations of Motion of a Submerged Body," David Taylor Model Basin Report 1845, July 1964.
- Janus, J. M. and Whitfield, D. L., "A Simple Time-Accurate Turbomachinery Algorithm with Numerical Solutions of an Uneven Blade Count Configuration," AIAA Paper No. 89-0206, January 1989.
- Janus, J. M., "Advanced 3-D CFD Algorithm for Turbomachinery," Ph.D. Dissertation, Mississippi State University, May 1989.
- Janus, J. M., and Whitfield D. L., "Counterrotating Prop-Fan Simulations which Feature a Relative-Motion Multiblock Grid Decomposition Enabling Arbitrary Time Steps," AIAA Paper No. 90-0687, 28<sup>th</sup> Aerospace Science Meeting, January 8-11, 1990.
- Janus, J. M., Whitfield, D. L., Horstman, H., and Mansfield, F., "Computation of the Unsteady Flowfield About a Counter Rotating Propfan Cruise Missile," AIAA Paper No. 90-3093, August 1990.
- Janus, J. M., Horstman, H. Z., and Whitfield, D. L., "Unsteady Flowfield Simulation of Ducted Prop-Fan Configurations," AIAA Paper No. 92-0521, January 1992.
- Jessup, S. D., "An Experimental Investigation of Viscous Aspects of Propeller Blade Flow," Ph.D. Dissertation, The Catholic University of America, 1989.
- Jiang, M. Y., Remotigue, M. G., Stokes, M. L., and Thompson, J. F., "EAGLEView: Grid Enhancement and Applications," AIAA Paper No. 94-0316, January 1994.
- Jonnalagadda, R., "Reynolds Averaged Navier-Stokes Computation of Forces and Moments for Appended SUBOFF Configurations at Incidence," M. S. Thesis, Mississippi State University, May 1996.
- Knight, C. J. and Zajaczkowski, F. J., "Validation of a Viscous, Incompressible Throughflow Code," AIAA Paper 95-0864, 1995.
- Kreplin, H.-P. and Eckelmann, H., "Behavior of the Three Fluctuating Velocity Components in the Wall Region of a Turbulent Channel Flow," *Physics of Fluids*. Vol. 22, No. 7, pp. 1233-1239, July 1979.
- Laufer, J., "Investigation of Turbulent Flow in a Two-Dimensional Channel," NACA Technical Note 2123, 1950.

- Launder, B. E., and Li, S.-P., "The Prediction of Riblet Behaviour with a Low-Reynolds Number  $k-\epsilon$  Model," *Aeronautical Journal*, pp. 351-355, November 1992.
- Launder, B. E., and Sharma, B. I., "Application of the Energy-Dissipation Model of Turbulence to the Calculation of Flow Near A Spinning Disc," *Letters in Heat and Mass Transfer*, Vol. 1, pp. 131-138, 1974.
- Lee, Y.-T., Hah, C., and Loellbach, J., "Flow Analysis in a Single-Stage Propulsion Pump," Transactions of the ASME, *Journal of Turbomachinery*, Vol. 118, pp. 240-249, April 1996.
- Liu, N. S., Davoudzadeh, F., Briley, W. R., and Shamroth, S. J., "Navier-Stokes Simulation of Transonic Blade-Vortex Interactions," Transactions of the ASME, *Journal of Fluids Engineering*, Vol. 112, pp. 501-509, December 1990.
- Lumley, J. L., "Toward a Turbulent Constitutive Relation," *Journal of Fluid Mechanics*, Vol. 41, Part 2, pp. 413-434, 13 April 1970.
- McDonald, H., "Computational Aspects of Internal 3-D Viscous Flows," ASME Computational Fluid Dynamics Third Working Group Meeting, NASA Marshall Space Flight Center, Huntsville, AL, June 11-14, 1985.
- Myong, H. K., and Kasagi, N., "Prediction of Anisotropy of the Near-Wall Turbulence With an Anisotropic Low-Reynolds-Number  $k-\epsilon$  Turbulence Model," Transactions of the ASME, *Journal of Fluids Engineering*, Vol. 112, pp. 521-524, December 1990.
- Nelka, J. J., "Experimental Evaluation of a Series of Skewed Propellers with Forward Rake: Open-Water Performance, Cavitation Performance, Field Point Pressures, and Unsteady Loading," David W. Taylor Naval Ship Research and Development Center, Report No. 4113, July 1974.
- Nisizima, S., "Numerical Study of Turbulent Square-Duct Flow Using an Anisotropic  $k-\epsilon$  Model," *Nippon Kikai Gakkai Ronbunshu, B Hen / Transactions of the Japan Society of Mechanical Engineers*, Part B, Vol. 55, No. 512, pp. 991-998, April 1989.
- Nisizima, S., and Yoshizawa, A., "Turbulent Channel and Couette Flows Using an Anisotropic  $k-\epsilon$  Model," *AIAA Journal*, pp. 414-420, March 1987.
- Ogawa, O., *Vortex Flow*, CRC Press, Boca Raton, FL, 1993.
- Ortega, J. M. and Rheinboldt, W. C., *Iterative Solution of Nonlinear Equations in Several Variables*, Academic Press, Inc., New York, 1970.
- Pan, D. and Chakravarthy, S., "Unified Formulation for Incompressible Flows", AIAA Paper No. 89-0122, January 1989.

- Pankajakshan, R., Arabshahi, A., and Whitfield, D. L., "Turbofan Flowfield Simulation Using Euler Equations with Body Forces," AIAA Paper No. 93-1978, AIAA/SAE/ASME/ASEE 29<sup>th</sup> Joint Propulsion Conference and Exhibit, Monterey, CA, June 28-30, 1993.
- Pankajakshan, R. and Briley, W. R., "Parallel Solution of Viscous Incompressible Flow on Multi-Block Structured Grids Using MPI," *Parallel Computational Fluid Dynamics - Implementations and Results Using Parallel Computers*, Edited by A. Ecer, J. Periaux, and N. Satofuca, and S. Taylor, Elsevier Science B. V., Amsterdam, pp. 601-608, 1995.
- Rai, M. M., "An Implicit, Conservative, Zonal-Boundary Scheme for Euler Equation Calculations," NASA CR-3865, February 1985.
- Rai, M. M., "Navier-Stokes Simulations of Blade-Vortex Interaction Using High-Order Accurate Upwind Schemes," AIAA Paper No. 87-0543, January 1987.
- Remotigue, M. G., Hart, E. T., and Stokes, M. L., "EAGLEView: A Surface and Grid Generation Program and Its Data Management," Proceedings of the Workshop on Software Systems for Surface Modeling and Grid Generation, NASA CP-3143, pp. 243, April 1992.
- Rice, J. Q., "Investigation of A Two Dimensional Hydrofoil in Steady and Unsteady Flows," M.S. Thesis, Massachusetts Institute of Technology, June 1991.
- Rivlin, R. S., "The Relation Between the Flow of Non-Newtonian Fluids and Turbulent Newtonian Fluids," *Quarterly of Applied Mathematics*, Vol. 15, No. 2, pp. 212-215, 1957.
- Roddy, R. F., "Investigation of the Stability and Control Characteristics of Several Configurations of the DARPA SUBOFF Model (DTRC Model 5470) from Captive-Model Experiments," David Taylor Research Center Report DTRC/SHD-1298-08, September 1990.
- Rodi, W., "A New Algebraic Relation for Calculating the Reynolds Stresses," *ZAMM*, Vol. 56, T219-T221, 1976.
- Roe, P. L., "Approximate Riemann Solvers, Parameter Vector, and Difference Schemes," *Journal of Computational Physics*, Vol. 43, pp. 357-372, 1981.
- Rogers, S. E. and Kwak, D., "Upwind Differencing for the Time-Accurate Incompressible Navier-Stokes Equations," *AIAA Journal*, Vol. 28, No. 2, pp. 253-262, February 1990.
- Rubinstein, R., and Barton, J. M., "Nonlinear Reynolds Stress Models and the Renormalization Group," *Physics of Fluids A*, Vol. 2, No. 8, pp. 1472-1476, August 1990.
- Sada, K., and Ichikawa, Y., "Simulation of Air Flow over a Heated Flat Plate Using Anisotropic  $k-\epsilon$  Model," *Journal of Wind Engineering and Industrial Aerodynamics*, Vol. 46 & 47, pp. 697-704, 1993.
- Saphir, B. and Fineberg, S., <http://lovelace.nas.nasa.gov/Parallel/SP2/MPIPerf/report.html>, 1995.

Schlichting, H., *Boundary-Layer Theory*, Seventh Edition, McGraw-Hill, Inc., 1979.

Sheng, C., Taylor, L. K., and Whitfield, D. L., "An Efficient Multigrid Acceleration for Solving the 3-D Incompressible Navier-Stokes Equations in Generalized Curvilinear Coordinates," AIAA Paper No. 94-2335, 25<sup>th</sup> AIAA Fluid Dynamics Conference, Colorado Springs, CO, June 1994.

Sheng, C., Taylor, L. K., and Whitfield, D. L., "Multiblock Multigrid Solution of Three-Dimensional Incompressible Turbulent Flow About Appended Submarine Configurations," AIAA Paper No. 95-0203, AIAA 33<sup>rd</sup> Aerospace Sciences Meeting and Exhibit, Reno, NV, January 9-12, 1995a.

Sheng, C., Taylor, L. K., and Whitfield, D. L., "A Multigrid Algorithm for Unsteady Incompressible Euler and Navier-Stokes Flow Computations," Sixth International Symposium on Computational Fluid Dynamics, Lake Tahoe, Nevada, USA, September 4-8, 1995b.

Sheng, C., Taylor, L. K., and Whitfield, D. L., "Multigrid Algorithm for Three-Dimensional Incompressible High-Reynolds Number Turbulent Flows," *AIAA Journal*, Vol. 33, No. 11, pp. 2073-2079, November 1995c.

Smith, N. S. and Watkinson, K. W., "A Six-Degree-Of-Freedom Simulation Program For Underwater Vehicles With Significant Vortical Flow Effects," V.C.T. Report No. 3 (User's Manual for TRJv), Vehicle Control Technologies, Inc., August 1994.

Soni, B. K., Thompson, J. F., Stokes, M. L., and Shih M.-S., "GENIE++, EAGLEView, and TIGER: General and Special Purpose Graphically Interactive Grid Systems," AIAA Paper No. 92-0071, 1992.

Speziale, C. G., "On Nonlinear  $k-l$  and  $k-\epsilon$  Models of Turbulence," *Journal of Fluid Mechanics*, Vol. 178, pp. 459-475, May 1987.

Speziale, C. G., "A Review of Reynolds Stress Models for Turbulent Shear Flows," *20th Symposium on Naval Hydrodynamics*, University of California, Santa Barbara, Aug. 21-26, 1994.

Speziale, C. G., Private Communication, March 1995.

Sung, C.-H, Griffin, M. J., Tsai, J. F., and Huang, T. T., "Improvements in Incompressible Turbulent Horseshoe Vortex Juncture Flow Calculations," AIAA Paper 91-0022, January 1991.

Sung, C.-H, Griffin, M. J., Tsai, J. F., and Huang, T. T., "Incompressible Flow Computation of Forces and Moments On Bodies of Revolution at Incidence," AIAA Paper 93-0787, January 1993.

Sung, C.-H, Griffen, M. J., Fu, T. C., and Huang, T. T., "Validation of Incompressible Flow Computation of Forces and Moments on Axisymmetric Bodies at Incidence," AIAA Paper 95-0528, January 1995.

- Taylor, L. K., "Unsteady Three-Dimensional Incompressible Algorithm Based on Artificial Compressibility," Ph.D. Dissertation, Mississippi State University, May 1991.
- Taylor, L. K. and Whitfield, D. L., "Unsteady Three-Dimensional Incompressible Euler and Navier-Stokes Solver for Stationary and Dynamic Grids," AIAA Paper No. 91-1650, June 1991.
- Taylor, L. K., Busby, J. A., Jiang, M. Y., Arabshahi, A., Sreenivas, K. , and Whitfield, D. L., "Time Accurate Incompressible Navier-Stokes Simulation of the Flapping Foil Experiment," The Proceedings Sixth International Conference on Numerical Ship Hydrodynamics, Iowa City, Iowa, pp. 721-738, August 2-5, 1993.
- Taylor, L. K., Arabshahi, A., and Whitfield, D. L., "Unsteady Three-Dimensional Incompressible Navier-Stokes Computations for a 6:1 Prolate Spheroid Undergoing Time-Dependent Maneuvers," AIAA Paper No. 95-0313, AIAA 33<sup>rd</sup> Aerospace Sciences Meeting and Exhibit, Reno, NV, January 9-12, 1995.
- Thomas, P. D., and Lombard, C. K., "Geometric Conservation Law and Its Application to Flow Computations on Moving Grids," *AIAA Journal*, Vol. 17, No. 10, pp. 1030-1037, October 1978.
- van Leer, B., "Towards the Ultimate Conservative Difference Scheme. V. A Second-Order Sequel to Godunov's Method," *Journal of Computational Physics*, Vol. 32, pp. 101-136, 1979.
- Vanden, K. J. and Whitfield, D. L., "Direct and Iterative Algorithms for the Three-Dimensional Euler Equations," *AIAA Journal*, Vol. 33, No. 5, pp. 851-858, May 1995.
- Wake, B. E. and Choi, D., "Investigation of High-Order Upwinded Differencing for Vortex Convection," AIAA Paper No. 95-1719, June 1995.
- Warsi, Z. U. A., *Fluid Dynamics, Theoretical and Computational Approaches*, CRC Press, 1993.
- Webster, R. S., Chen, J. P., and Whitfield, D. L., "Numerical Simulation of a Helicopter Rotor in Hover and Forward Flight," AIAA Paper No. 95-0193, AIAA 33<sup>rd</sup> Aerospace Sciences Meeting and Exhibit, Reno, NV, January 9-12, 1995.
- Weyer, R. M., Unsteady Static-Pressure Measurements in the High Reynolds Number Pump Facility, Applied Research Laboratory, The Pennsylvania State University, Private Communication, August 1995.
- White, F. M., *Fluid Mechanics*, McGraw-Hill Book Company, New York, 1979.
- Whitfield, D. L. and Jameson, A., "Euler Equation Simulation of Propeller-Wing Interaction in Transonic Flow," *Journal of Aircraft*, Vol. 21, No. 11, pp. 835-839, November 1984.

- Whitfield, D. L., Swafford, T. W., Janus, J. M., Mulac, R.A., and Belk, D. M., "Three-Dimensional Unsteady Euler Solutions for Propfans and Counter-Rotating Propfans in Transonic Flow," AIAA Paper No. 87-1197, June 1987.
- Whitfield, D. L., Janus, J. M., and Simpson, L. B., "Implicit Finite Volume High Resolution Wave-Split Scheme for Solving the Unsteady Three-Dimensional Euler and Navier-Stokes Equations on Stationary or Dynamic Grids," Engineering and Industrial Research Station Report MSSU-EIRS-ASE-88-2, Mississippi State University, Mississippi State, MS, February 1988.
- Whitfield, D. L., "Newton-Relaxation Schemes for Nonlinear Hyperbolic Systems," Engineering and Industrial Research Station Report MSSU-EIRS-ASE-90-3, Mississippi State University, Mississippi State, MS, October 1990.
- Whitfield, D. L. and Taylor, L. K., "Discretized Newton-Relaxation Solution of High Resolution Flux-Difference Split Schemes," AIAA Paper No. 91-1539, June 1991.
- Whitfield, D. L. and Taylor, L. K., "Numerical Solution of the Two-Dimensional Time-Dependent Incompressible Euler Equations," MSSU-EIRS-ERC-93-14, April 1994.
- Whitfield, D. L., "Perspective on Applied CFD," AIAA Paper No. 95-0349, AIAA 33<sup>rd</sup> Aerospace Sciences Meeting and Exhibit, Reno, NV, January 9-12, 1995.
- Wislicenus, G. F., "Hydrodynamics and Propulsion of Submerged Bodies," American Rocket Society, *ARS Journal*, pp. 140-1148, December 1960.
- Yakhot, V., Orszag, S. A., Thangam, S., Gatski, T. B., and Speziale, C. G., "Development of Turbulence Models for Shear Flows by a Double Expansion Technique," *Physics of Fluids*, Vol. 4, No. 7, pp. 1510-1520, July 1992.
- Yang, C.-I., Hartwich, P. M., and Sundaram, P., "A Navier-Stokes Solution of Hull-Ring Wing-Thruster Interaction," Eighteenth Naval Hydrodynamics Symposium, University of Michigan, Ann Arbor, MI, August 1990.
- Yang, C.-I., "A Simulation of Viscous Incompressible Flow Through Multiple-Blade-Row Turbomachinery with a High-Resolution Upwind Finite-Differencing Scheme," Carderock Division, Naval Surface Warfare Center, Hydromechanics Directorate, Report CDRKNSWC/HD-1427-01, October 1994.
- Yoshizawa, A., "Statistical Analysis of the Deviation of the Reynolds Stress from its Eddy-Viscosity Representation," *Physics of Fluids*, Vol. 27, No. 6, pp. 1377-1387, June 1984.
- Yoshizawa, A., "Statistical Modeling of Turbulent Thermally Buoyant Flows," *Journal of the Physical Society of Japan*, Vol. 55, No. 9, pp. 3066-3072, 1986.

Zierke, W. C., Straka, W. A., and Taylor, P. D., "The High Reynolds Number Flow Through an Axial-Flow Pump," ARL Penn State Technical Report TR 93-12, Applied Research Laboratory, The Pennsylvania State University, November 1993.

Zierke, W. C., Straka, W. A., and Taylor, P. D., "An Experimental Investigation of the Flow Through an Axial-Flow Pump," Transactions of the ASME, *Journal of Fluids Engineering*, Vol. 117, No. 3, pp. 485-490, September 1995.

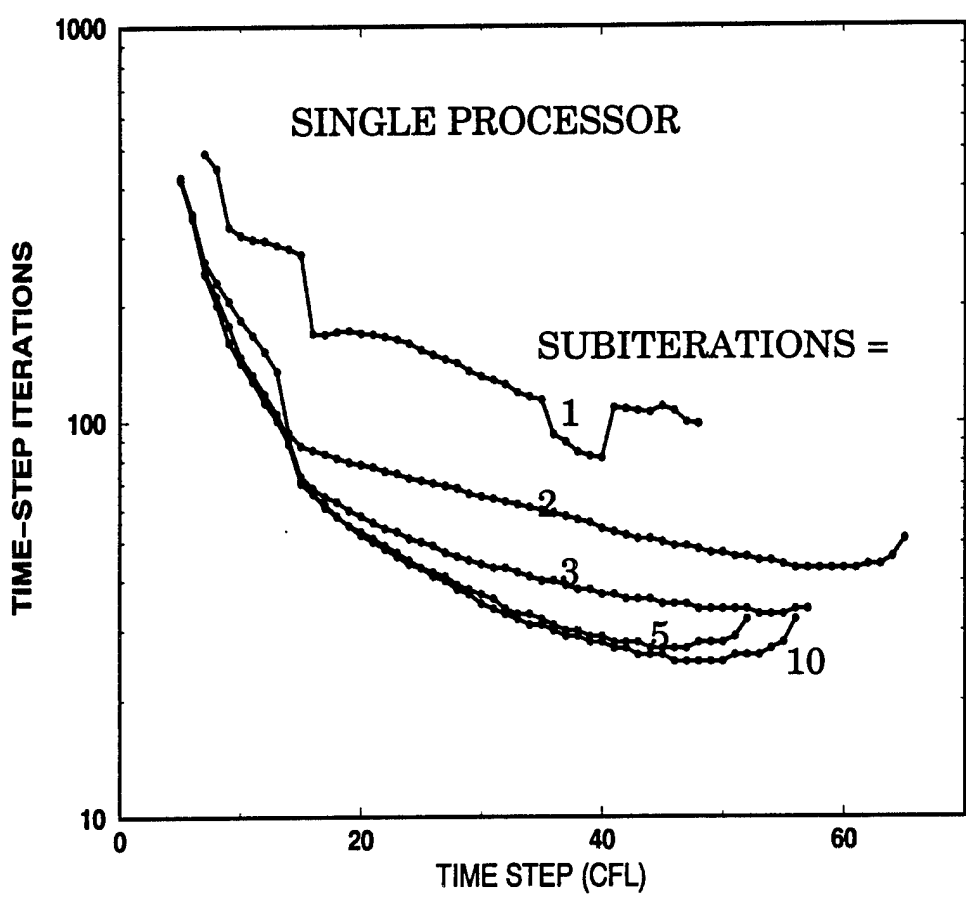


Figure 1. Iterations for 0(3) Residual Reduction

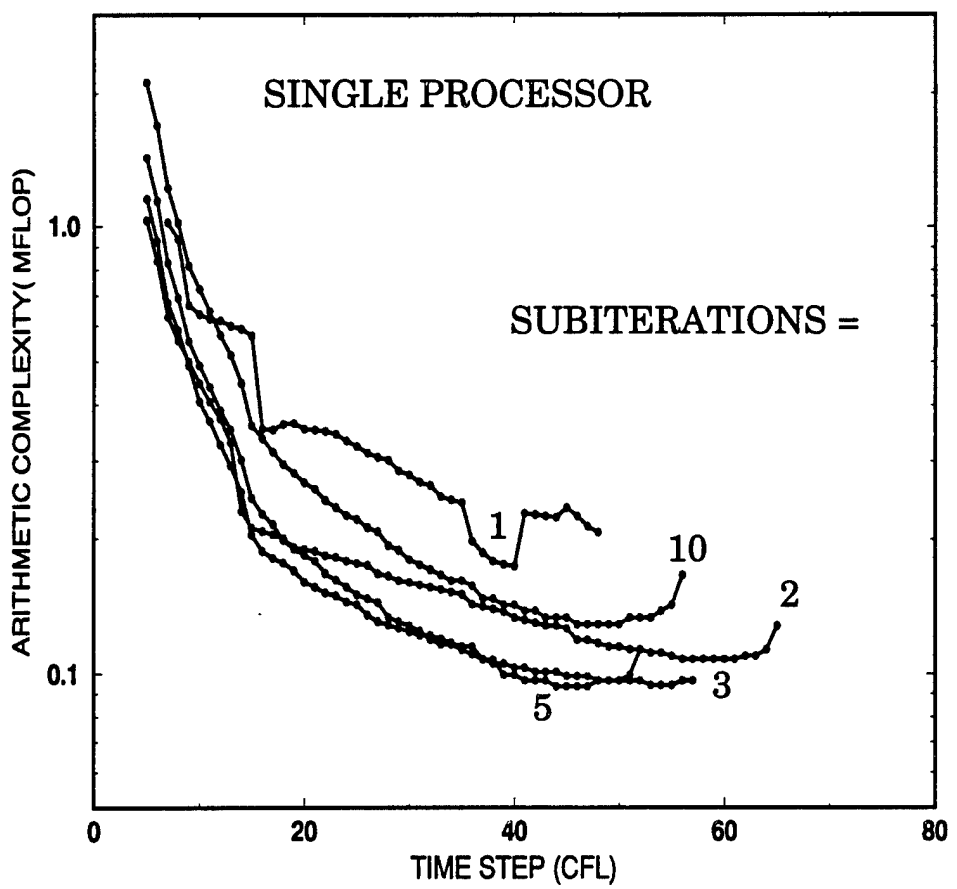


Figure 2. Complexity for 0(3) Residual Reduction

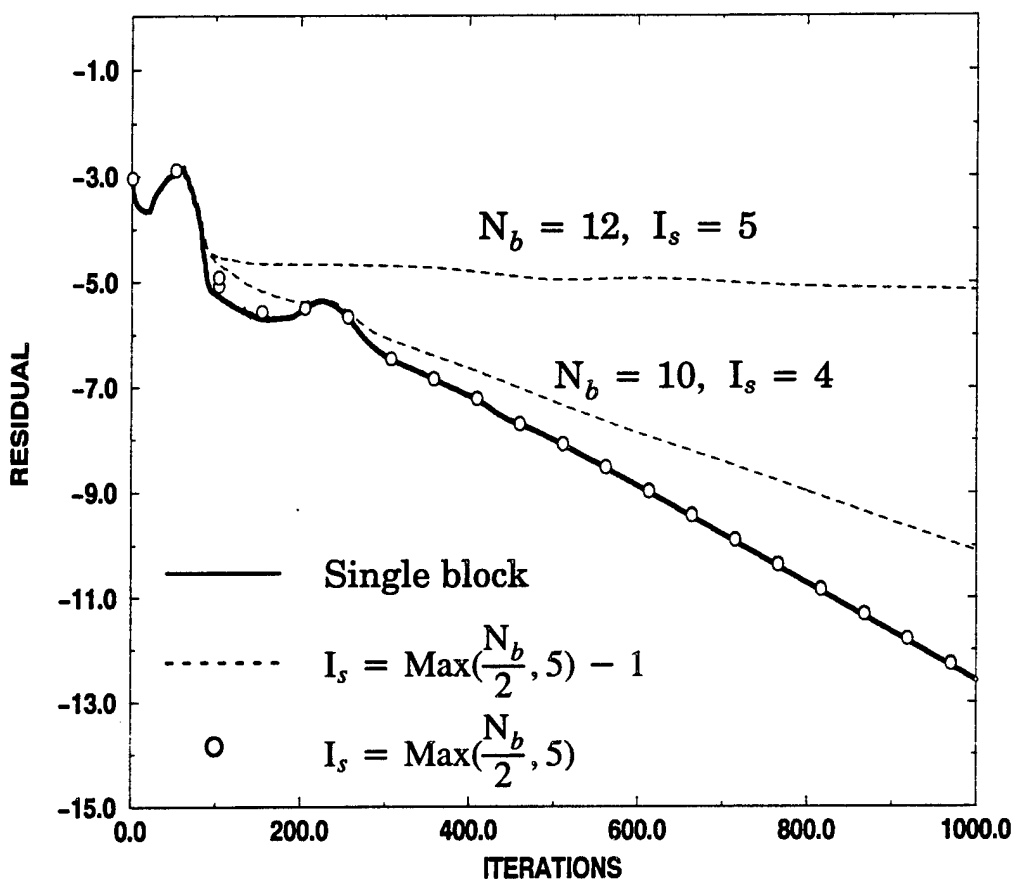


Figure 3. Effect of Subiterations on Convergence

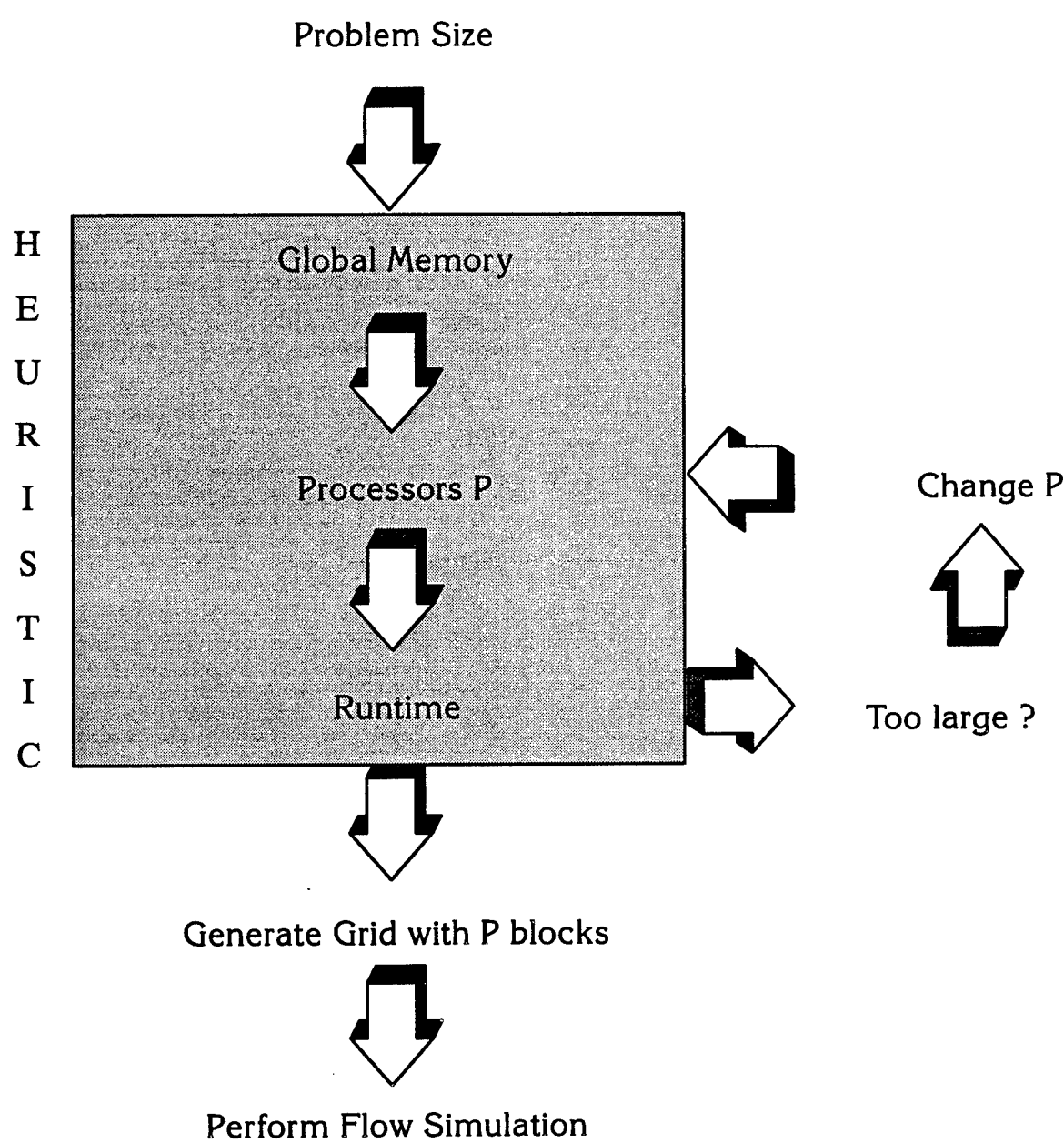


Figure 4. Approach for Flow Simulation on Parallel Machines

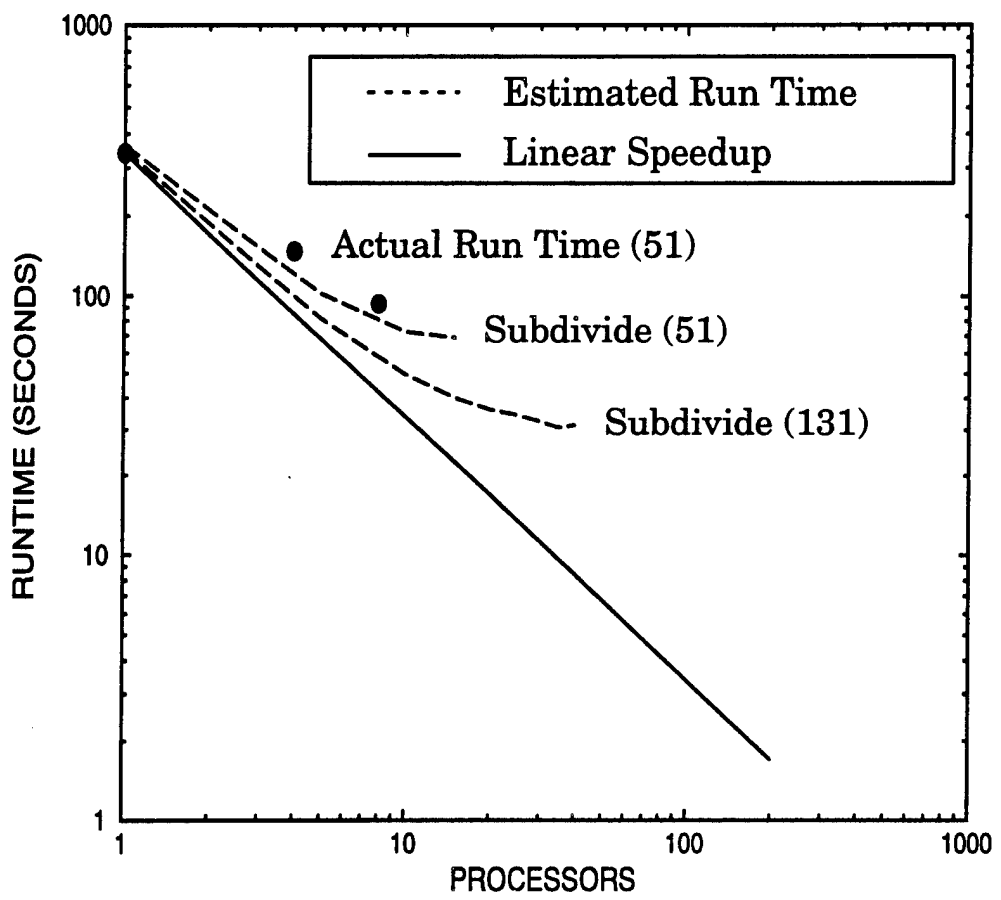


Figure 5. Run Time for 500 Steps of SUBOFF on 1/4/8 Nodes of the IBM SP2

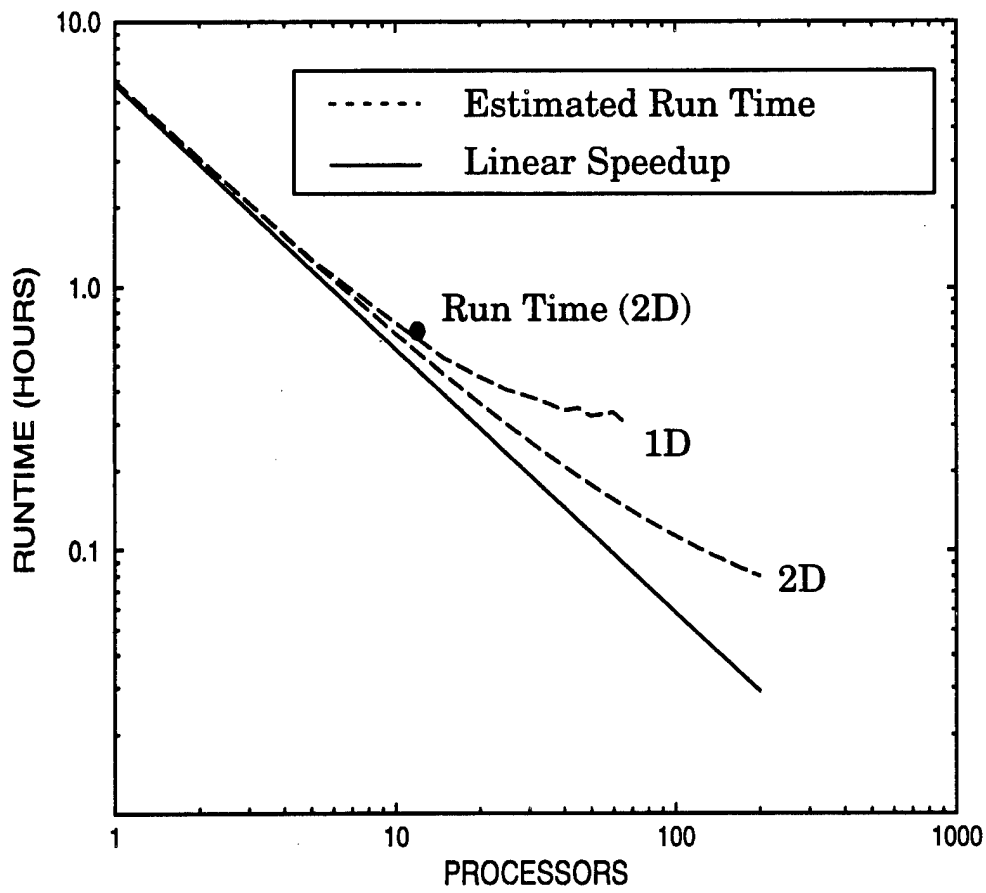


Figure 6. Run Time for 500 steps of 602,700-Grid-Point Case on 12 Nodes of the IBM SP2

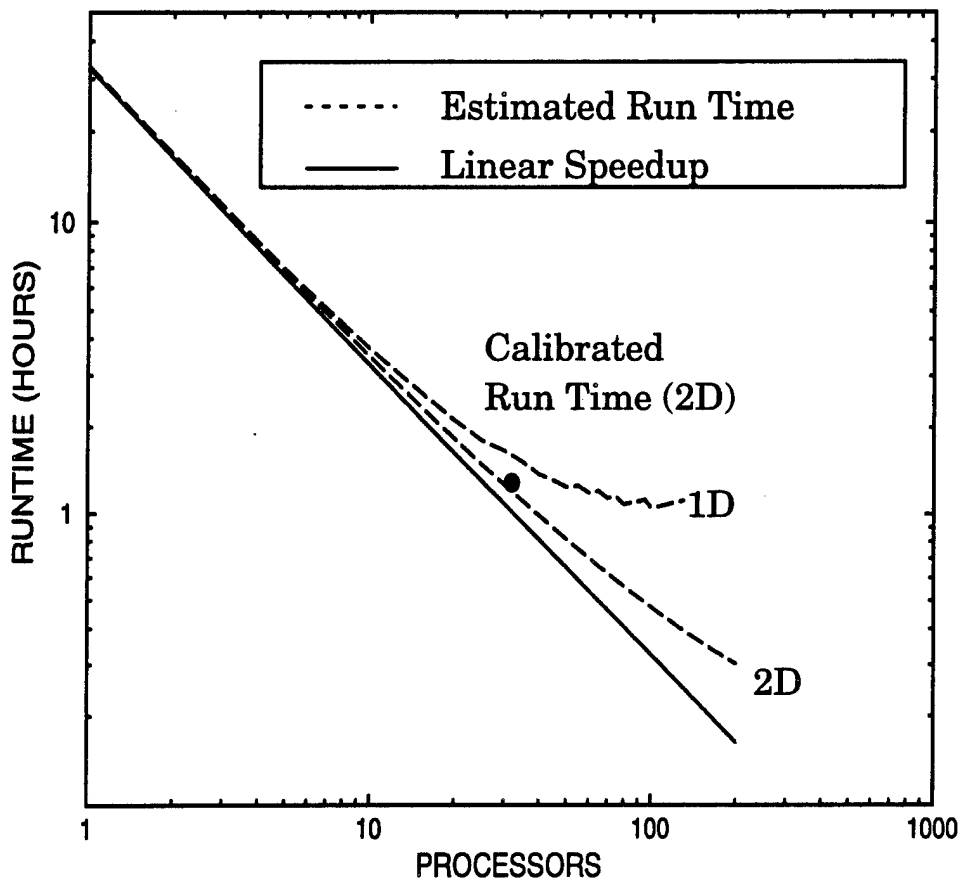


Figure 7. Run Time for 500 Steps of 3,363,360-Grid-Point Case on 32 Nodes of the IBM SP2

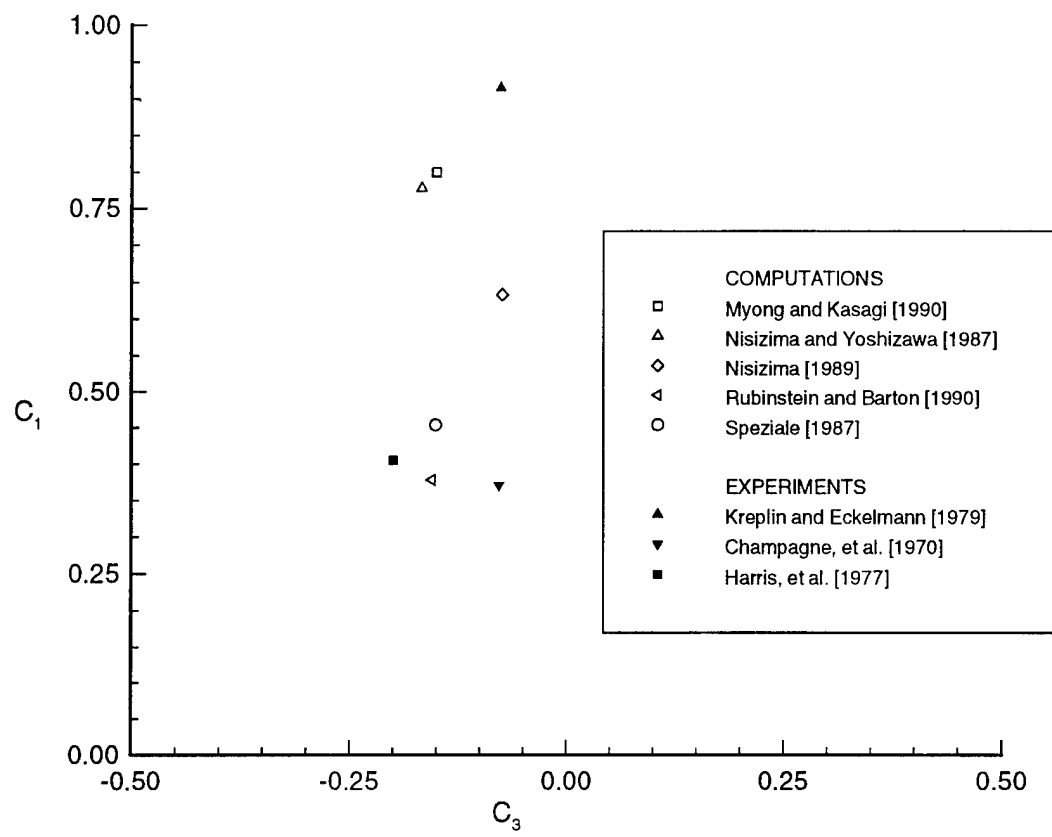


Figure 8. Calibration of the Nonlinear  $q$ - $\omega$  Turbulence Model

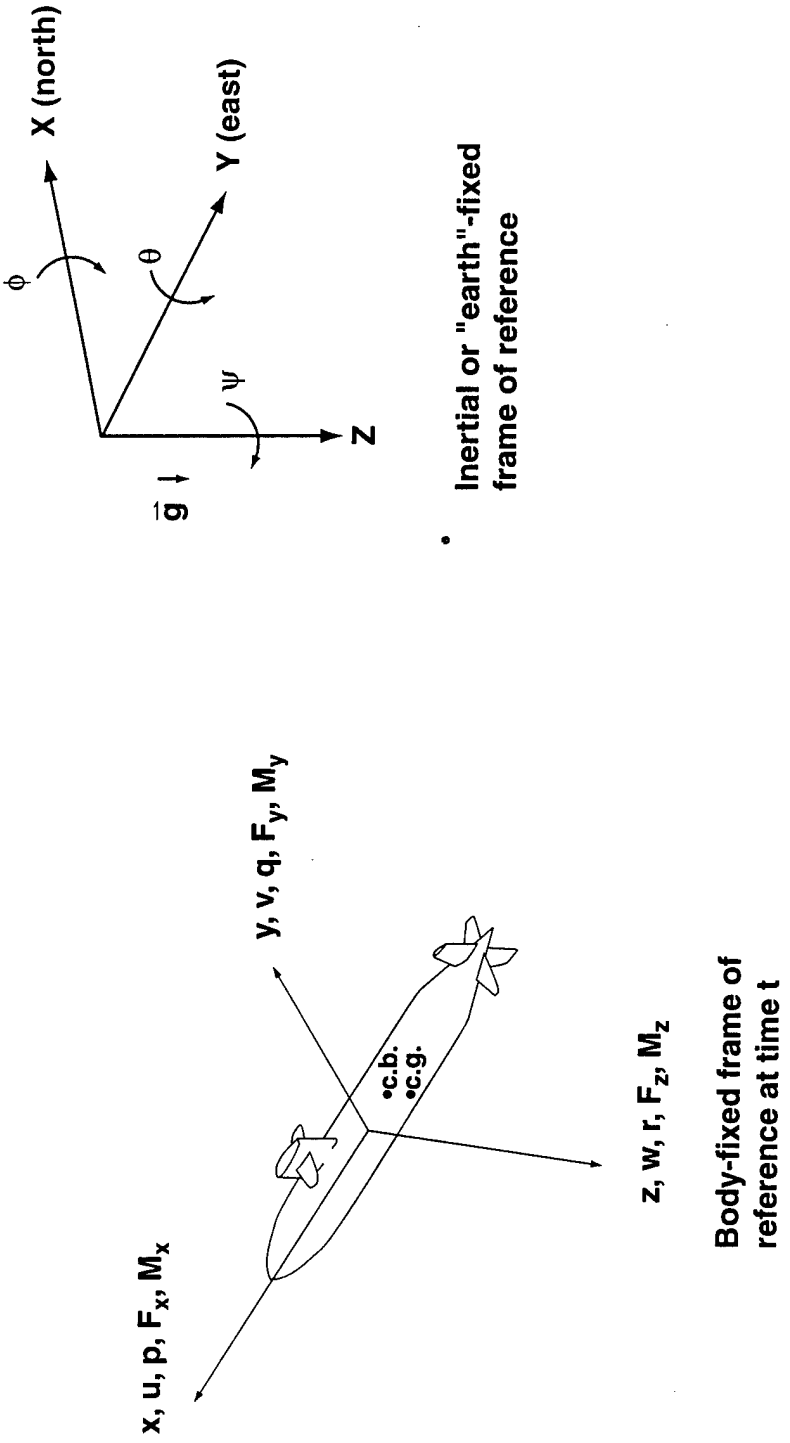


Figure 9. Schematic of the Coordinate Systems Used for Trajectory Prediction

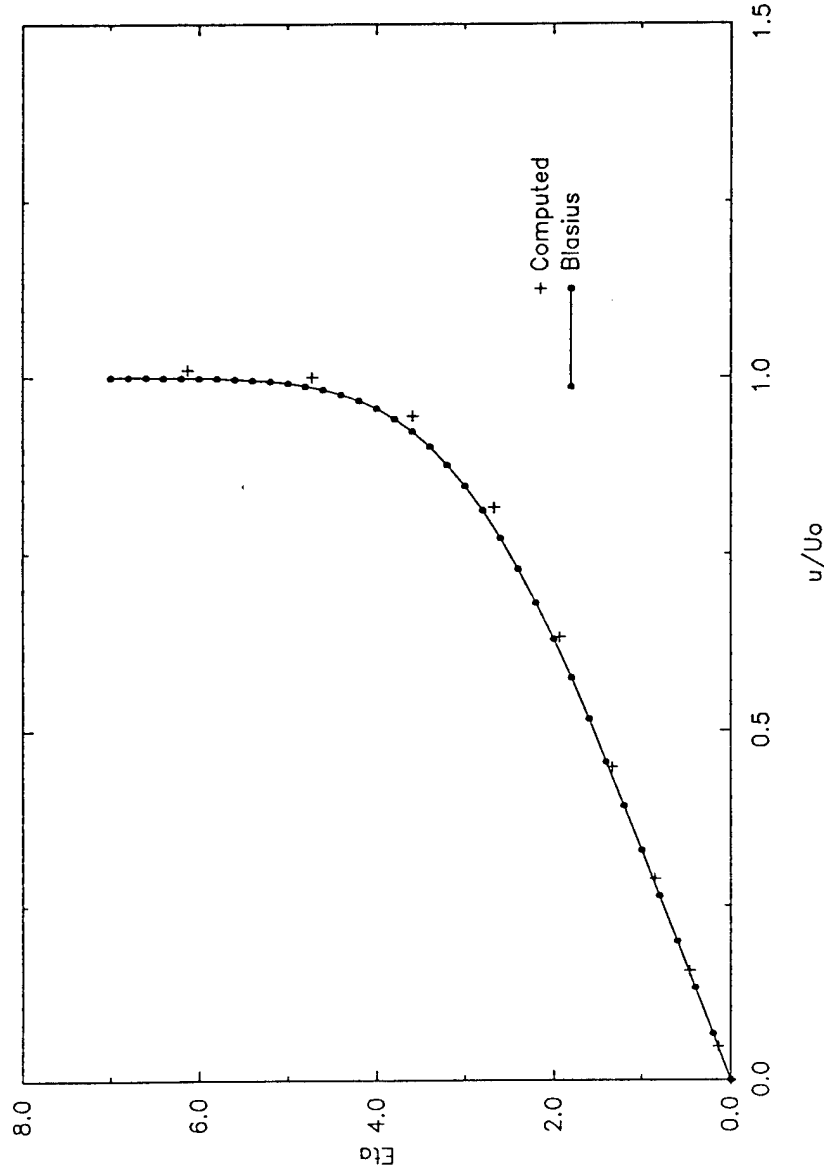


Figure 10. Velocity Profile for Laminar Flow Past a Flat Plate at  $Re = 10,000$

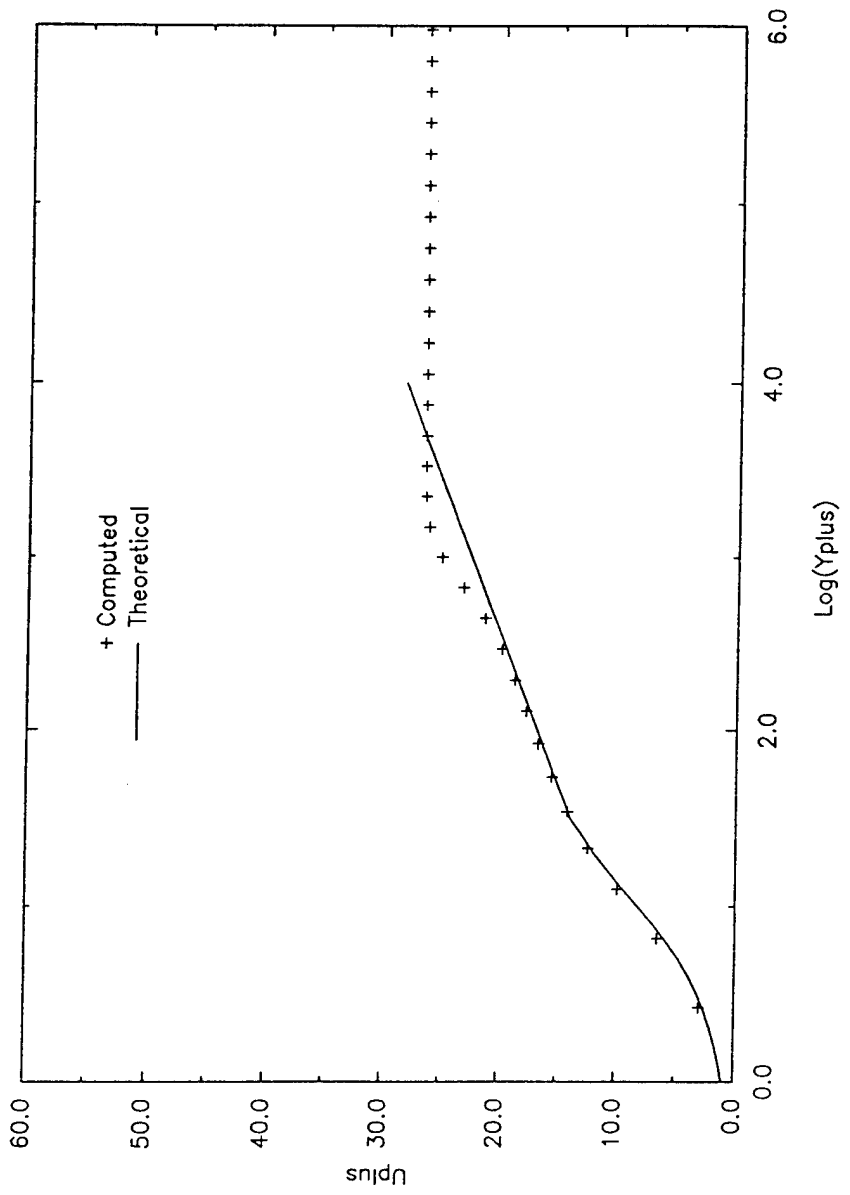


Figure 11. Velocity Profile for Turbulent Flow Past a Flat Plate at  $Re = 5,000,000$

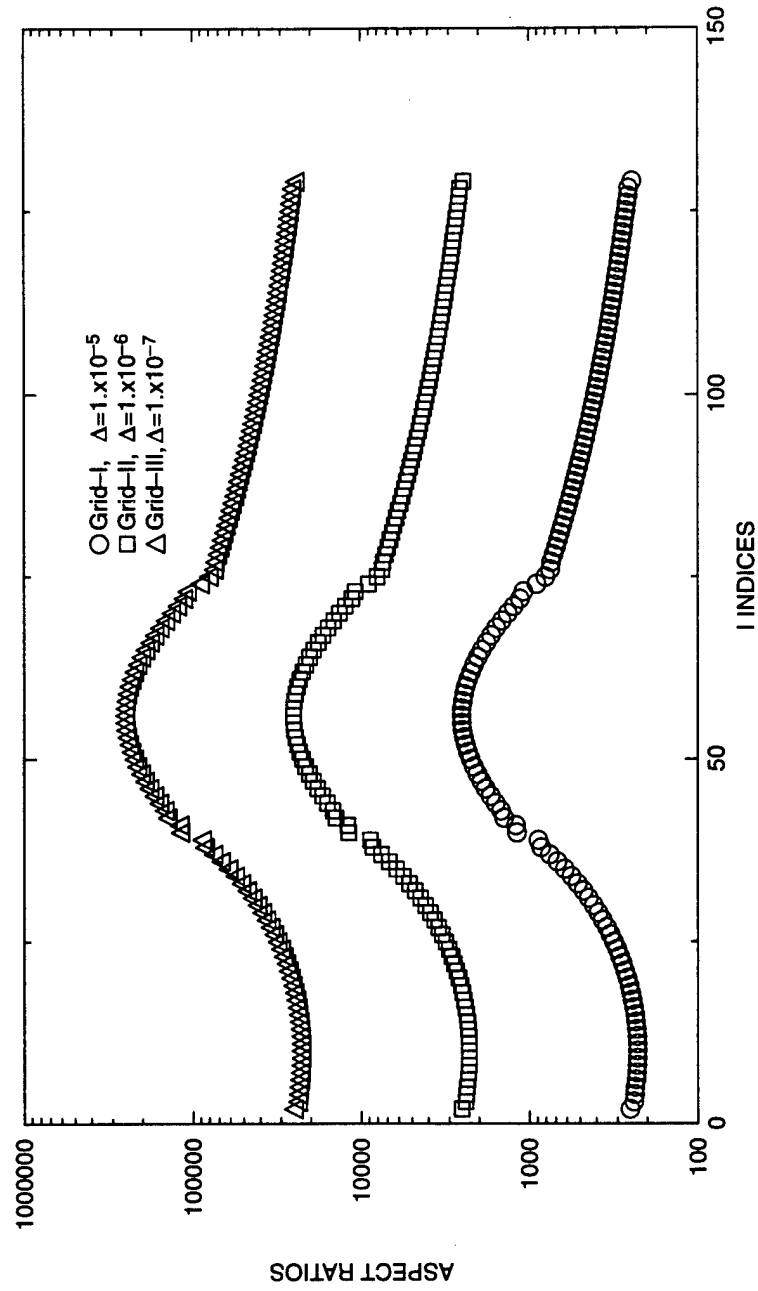


Figure 12. Aspect Ratios of First Cells on the Surface for the Three SUBOFF Barebody Grids

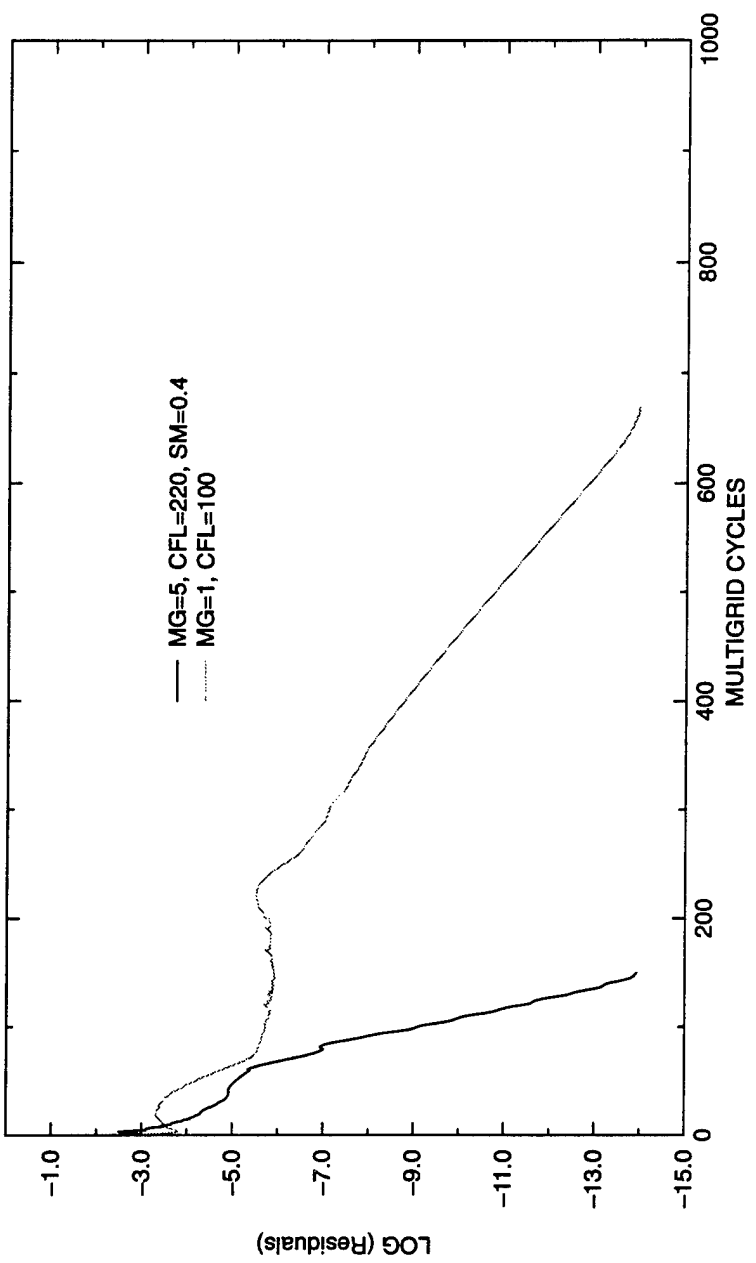


Figure 13. Convergence Histories of Multigrid and Single-Grid Solutions on the SUBOFF Barebody Grid I at  $\alpha = 0^\circ$  and  $Re = 12,000,000$

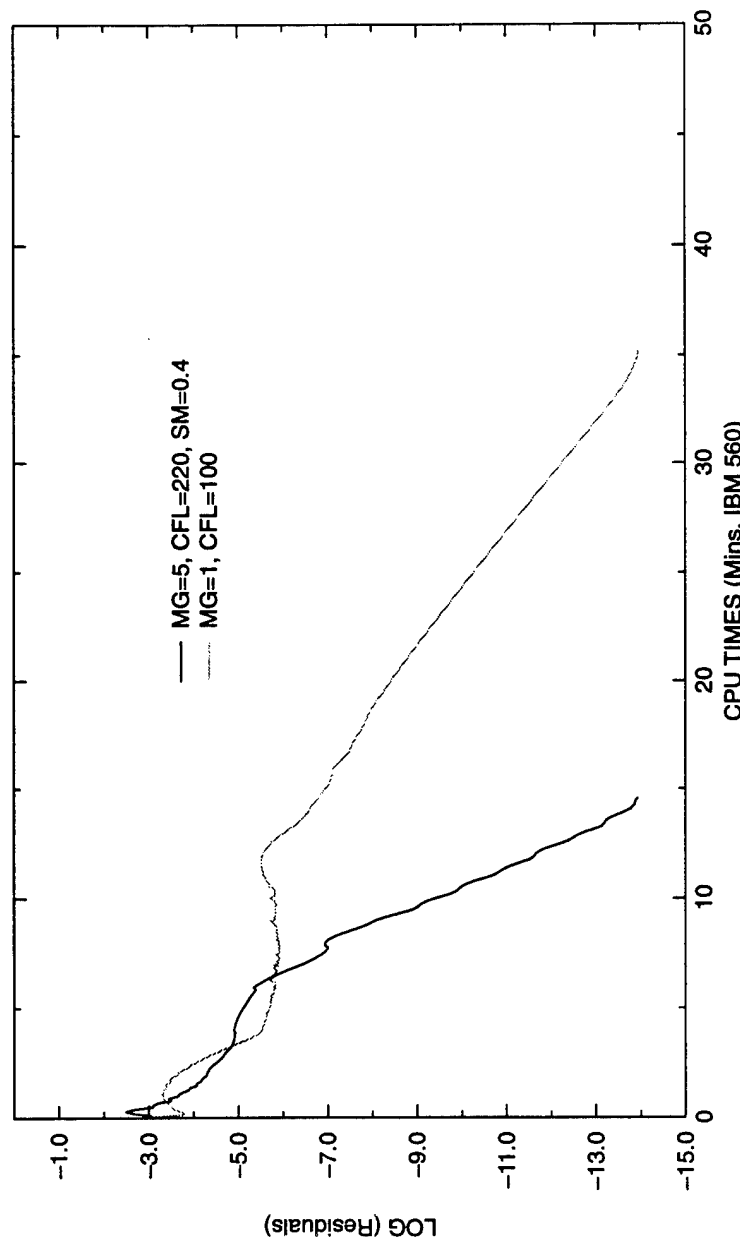


Figure 14. CPU Times of Multigrid and Single-Grid Solutions on the SUBOFF Barebody  
Grid I at  $\alpha = 0^\circ$  and  $Re = 12,000,000$

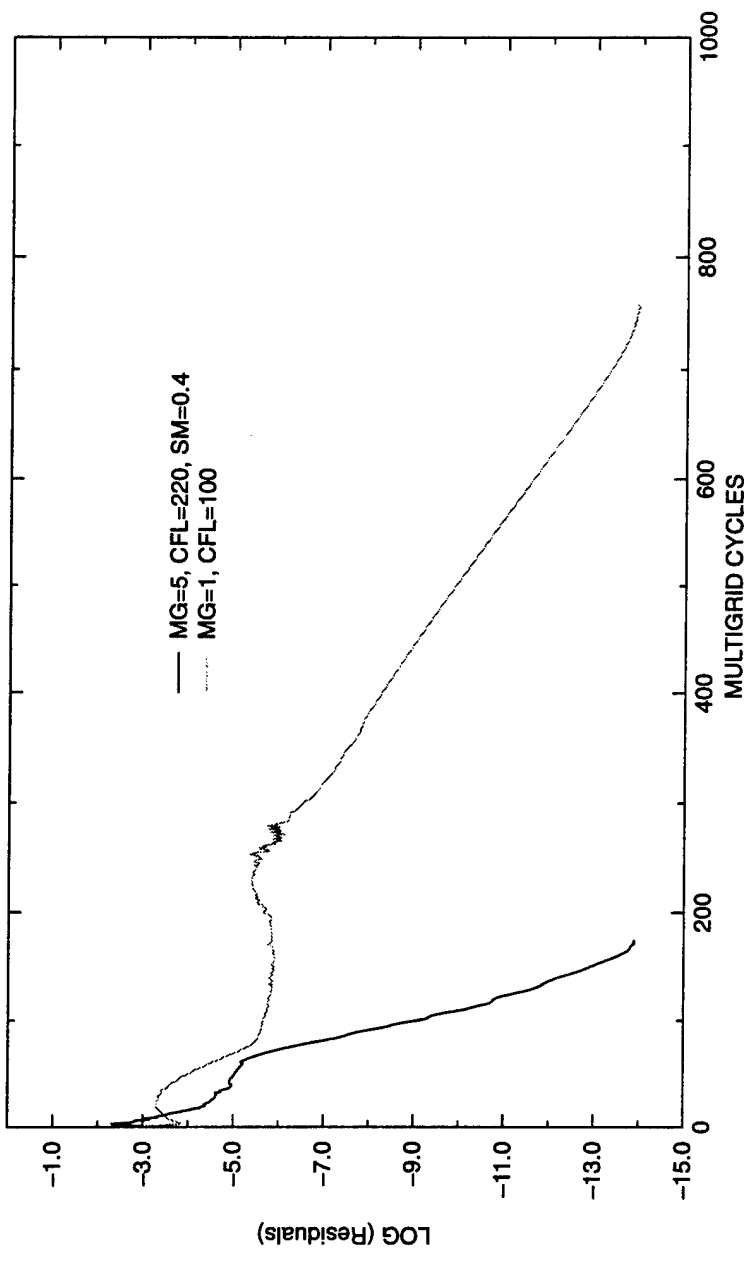


Figure 15. Convergence Histories of Multigrid and Single-Grid Solutions on the SUBOFF Barebody Grid II at  $\alpha = 0^\circ$  and  $Re = 12,000,000$

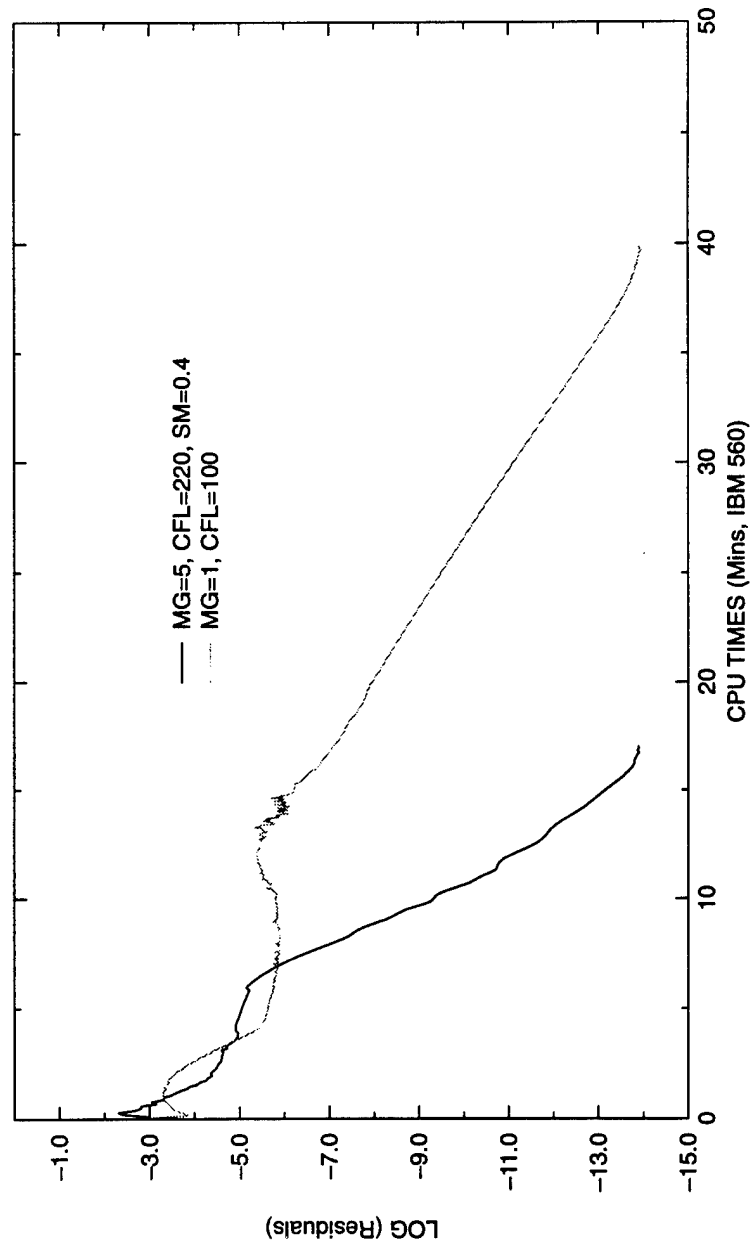


Figure 16. CPU Times of Multigrid and Single-Grid Solutions on the SUBOFF Barebody  
Grid II at  $\alpha = 0^\circ$  and  $Re = 12,000,000$

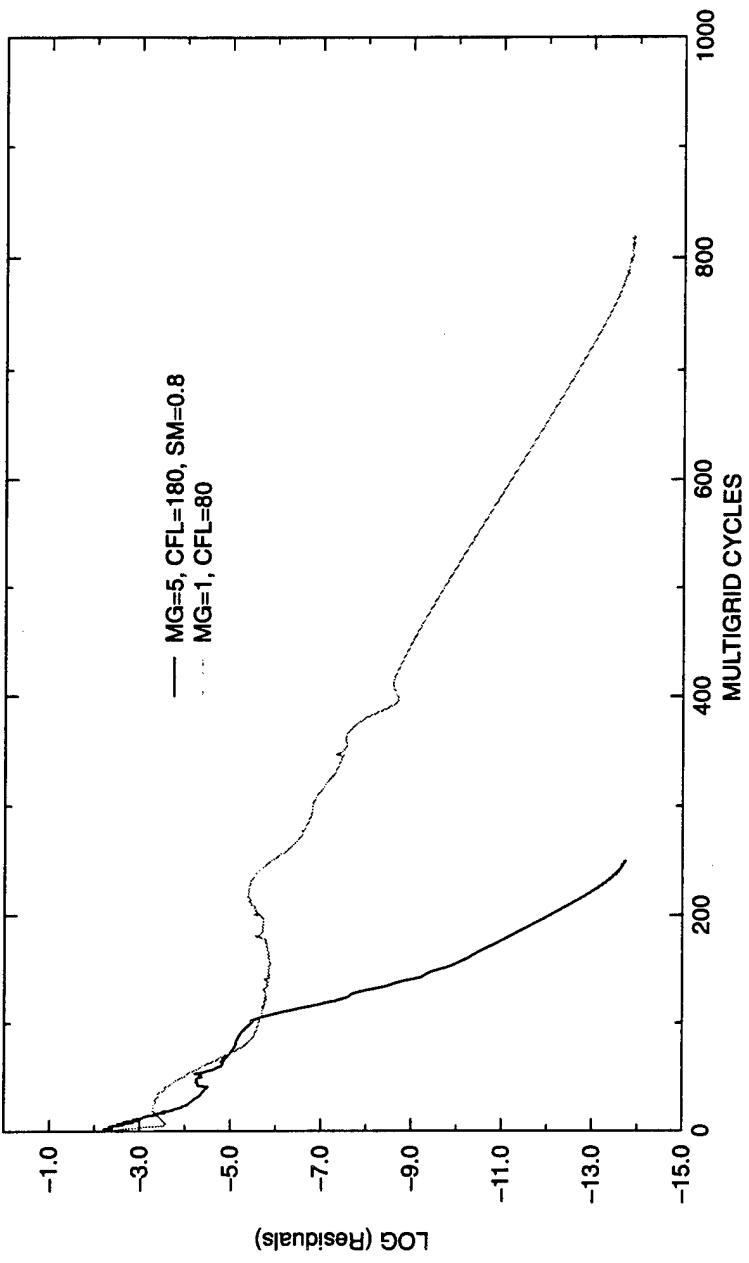


Figure 17. Convergence Histories of Multigrid and Single-Grid Solutions on the SUBOFF Barebody Grid III at  $\alpha = 0^\circ$  and  $Re = 12,000,000$

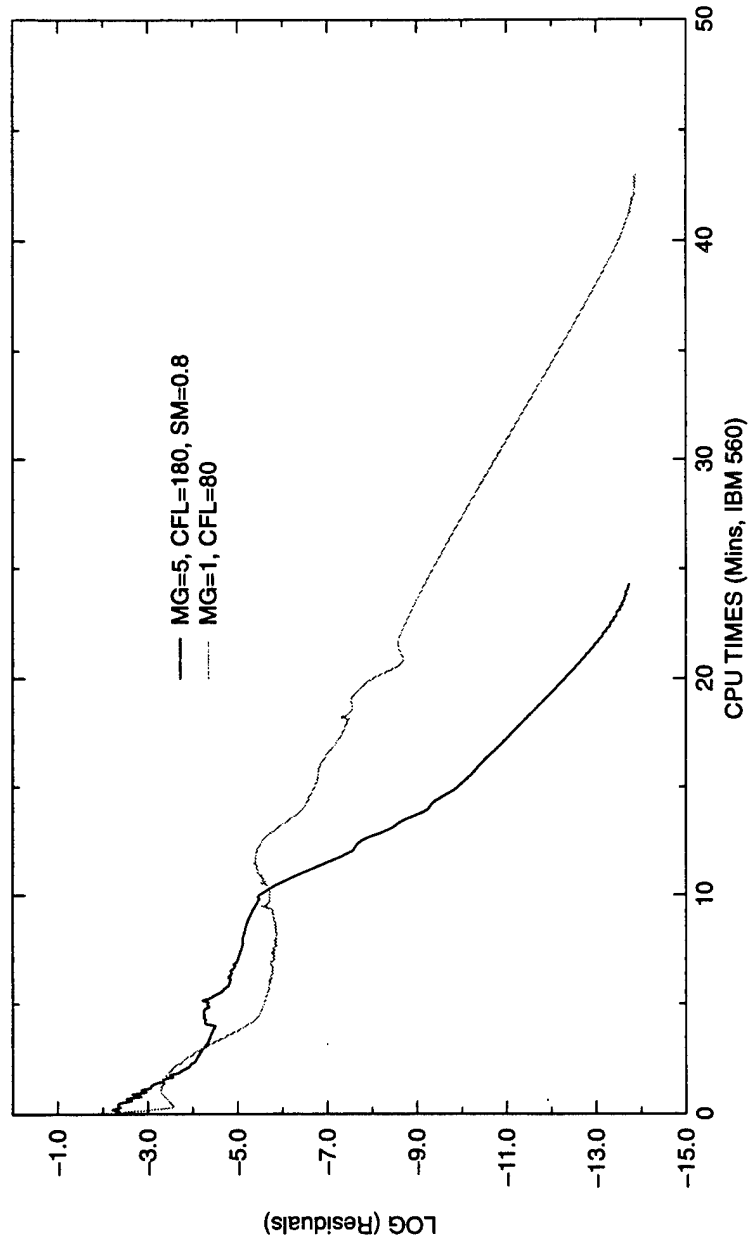


Figure 18. CPU Times of Multigrid and Single-Grid Solutions on the SUBOFF Barebody  
Grid III at  $\alpha = 0^\circ$  and  $Re = 12,000,000$

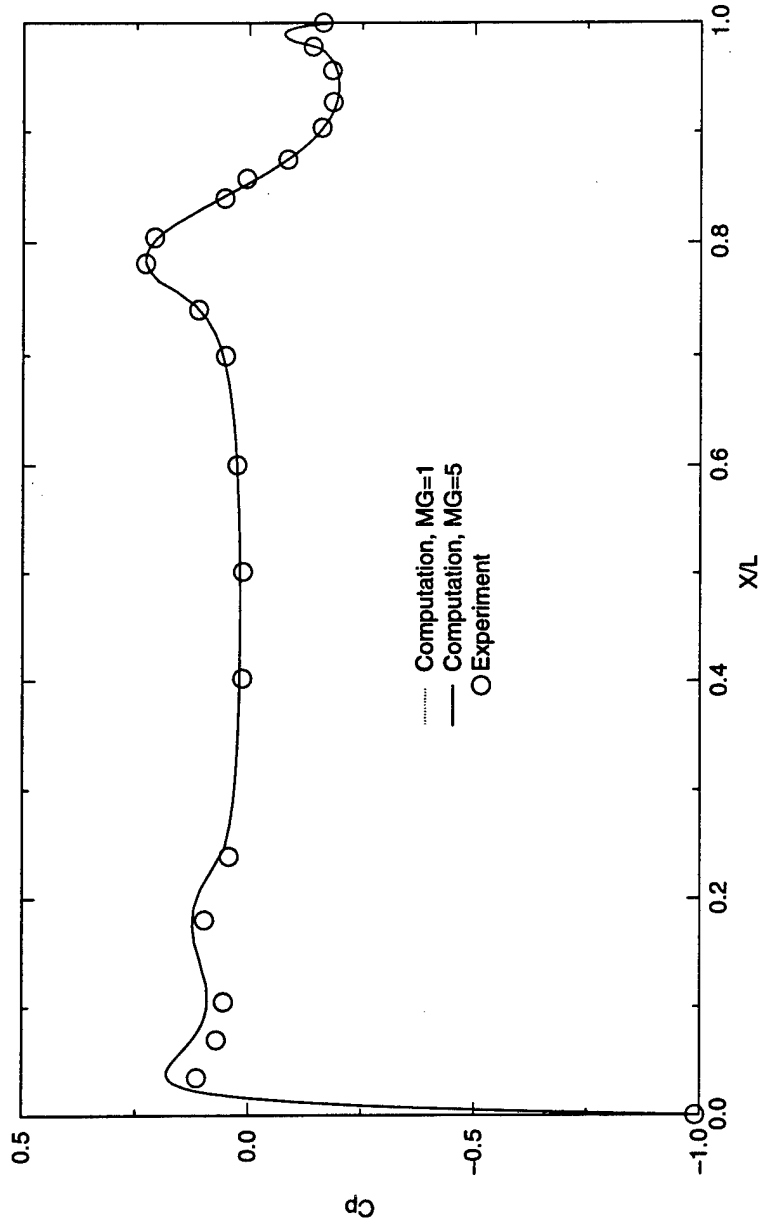


Figure 19. Computed and Measured Surface-Pressure Distributions on the SUBOFF Barebody Grid III at  $\alpha = 0^\circ$  and  $Re = 12,000,000$

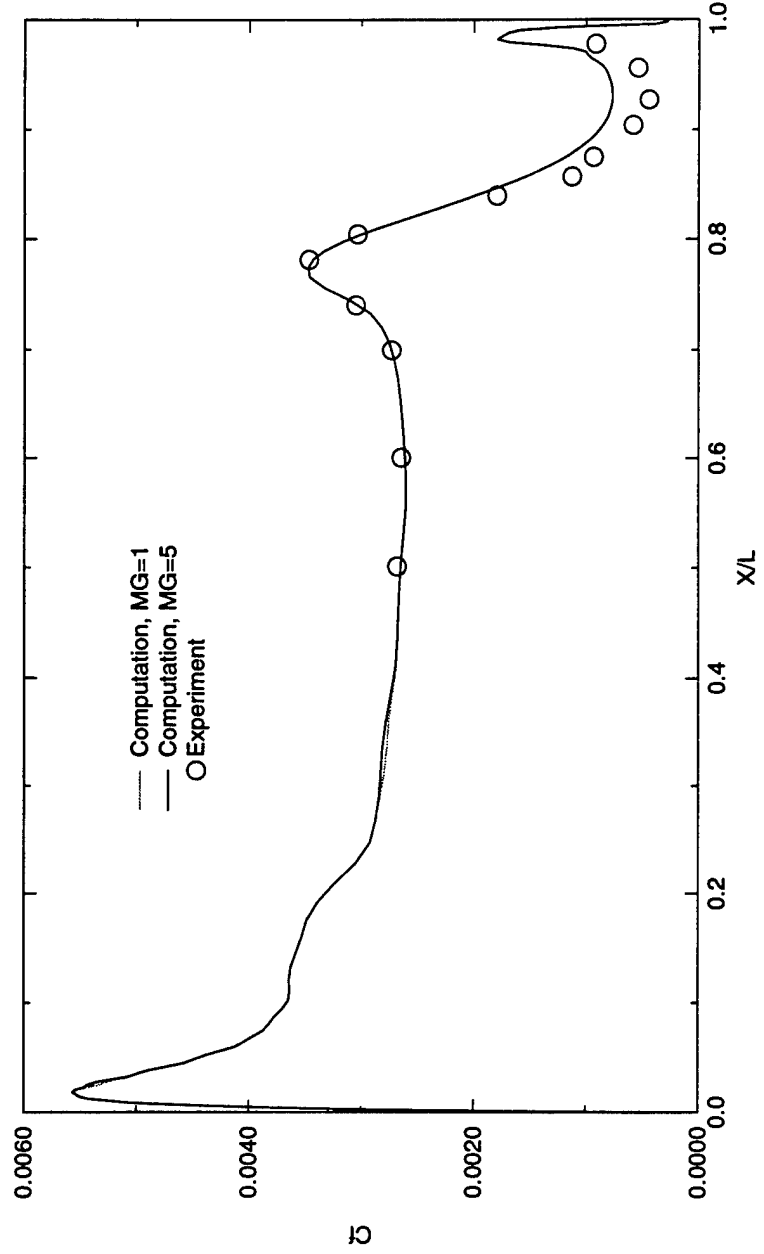


Figure 20. Computed and Measured Skin-Friction Distributions on the SUBOFF Barebody Grid III at  $\alpha = 0^\circ$  and  $Re = 12,000,000$

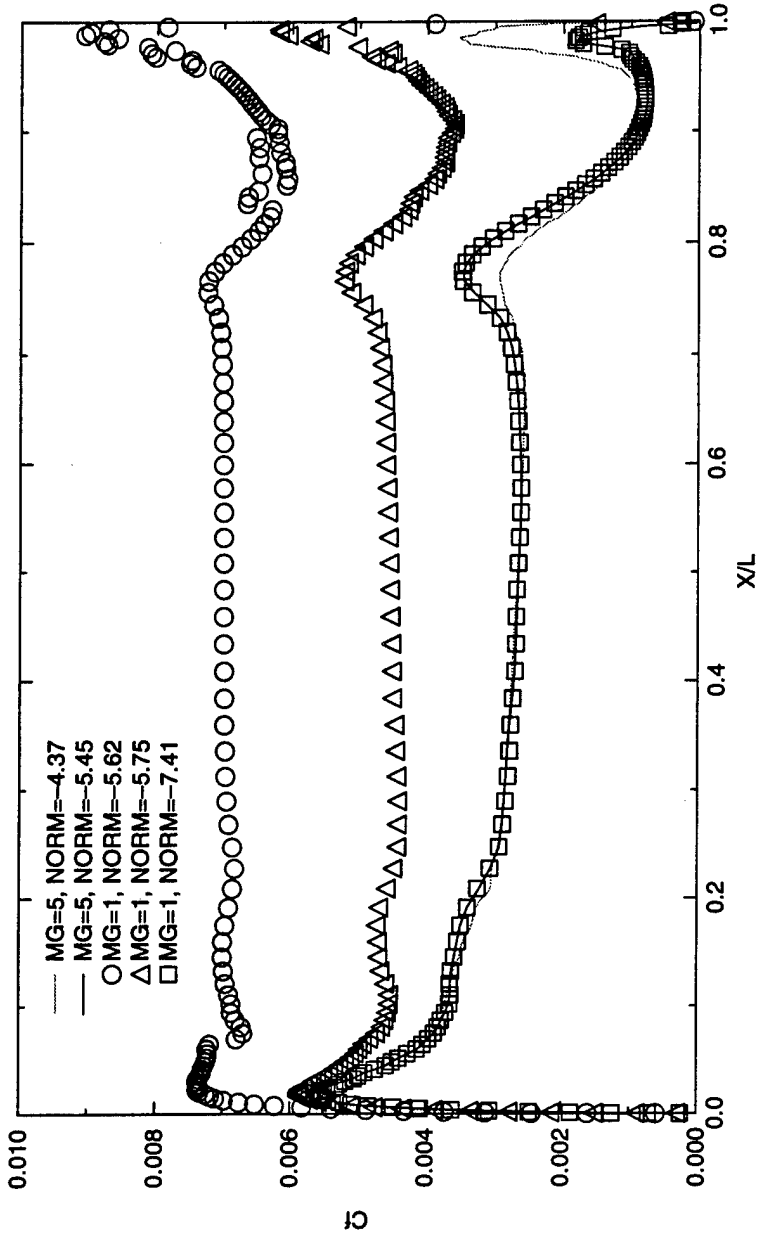


Figure 21. Comparison of Computed Skin-Friction Distributions at Different Residual Levels about the SUBOFF Barebody at  $\alpha = 0^\circ$  and  $Re = 12,000,000$

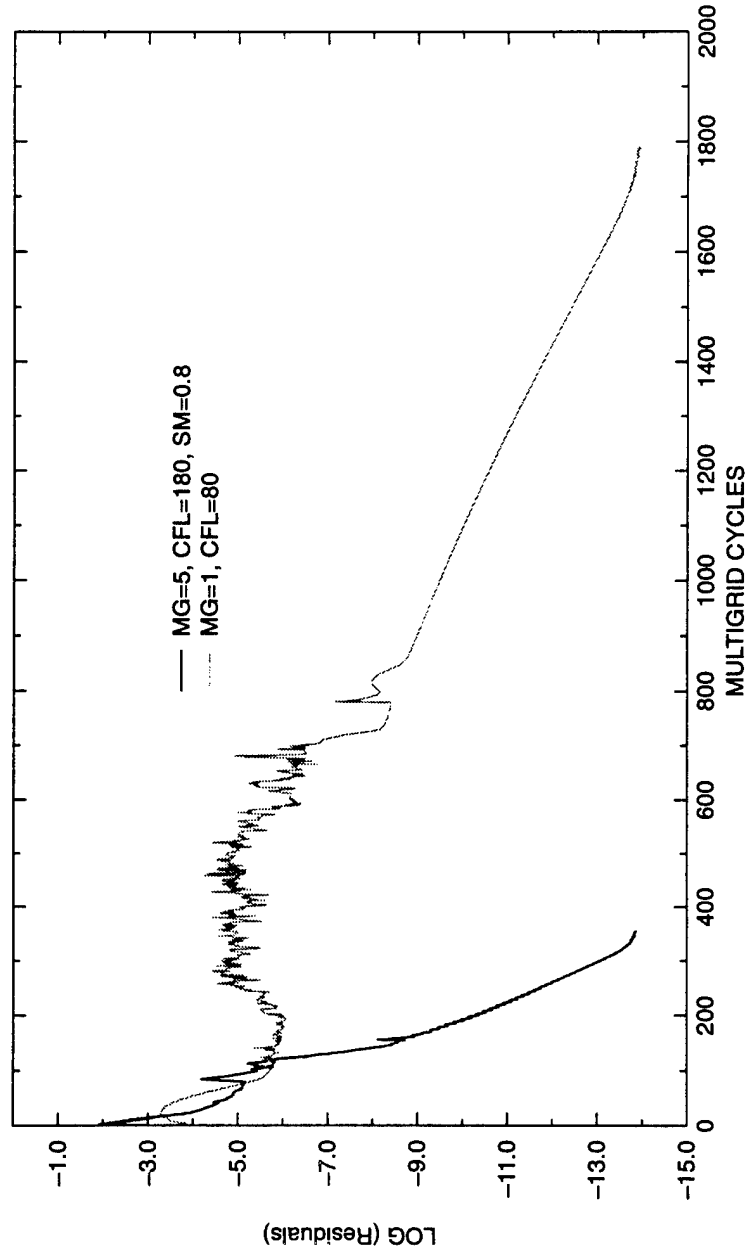


Figure 22. Convergence Histories of Multigrid and Single-Grid Solutions on the SUBOFF  
Barebody Grid III at  $\alpha = 0^\circ$  and  $Re = 1,200,000,000$

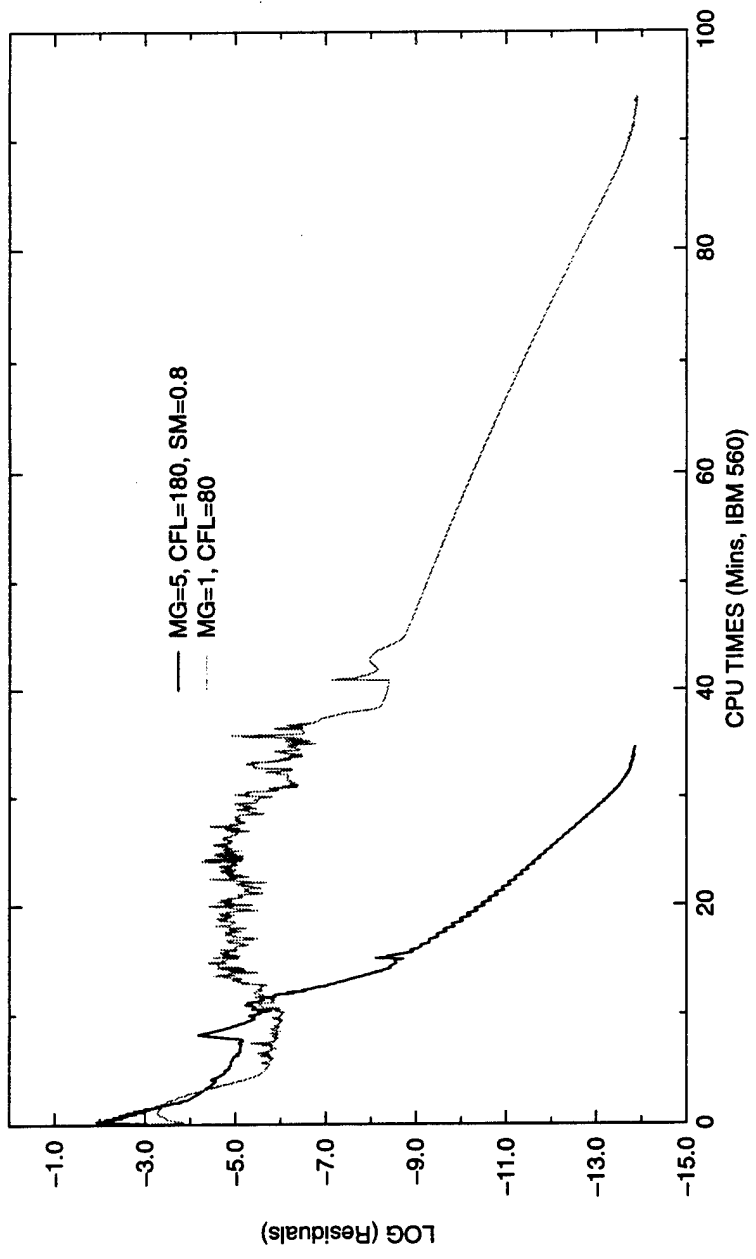


Figure 23. CPU Times of Multigrid and Single-Grid Solutions on the SUBOFF Barebody  
Grid III at  $\alpha = 0^\circ$  and  $Re = 1,200,000,000$

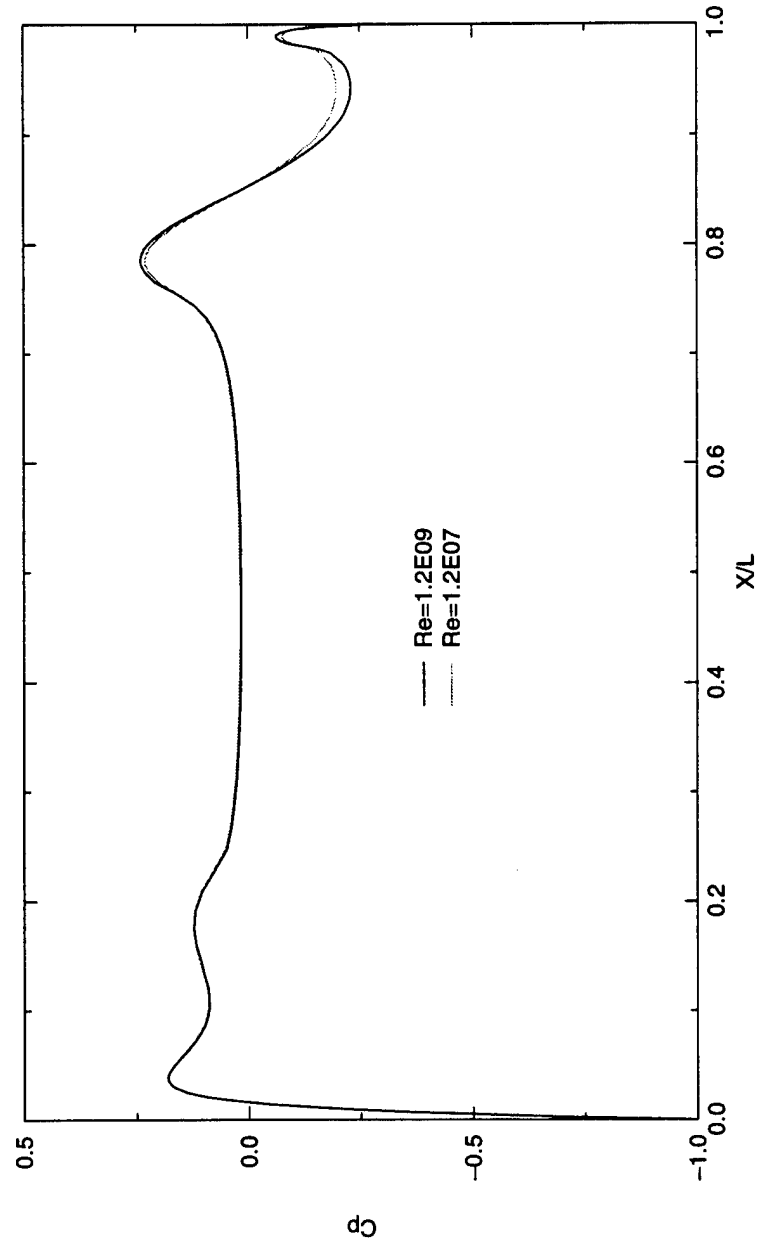


Figure 24. Comparisons of Surface-Pressure Distributions on the SUBOFF Barebody and  $Re = 12,000,000$  and  $Re = 1,200,000,000$  (for  $\alpha = 0^\circ$ )

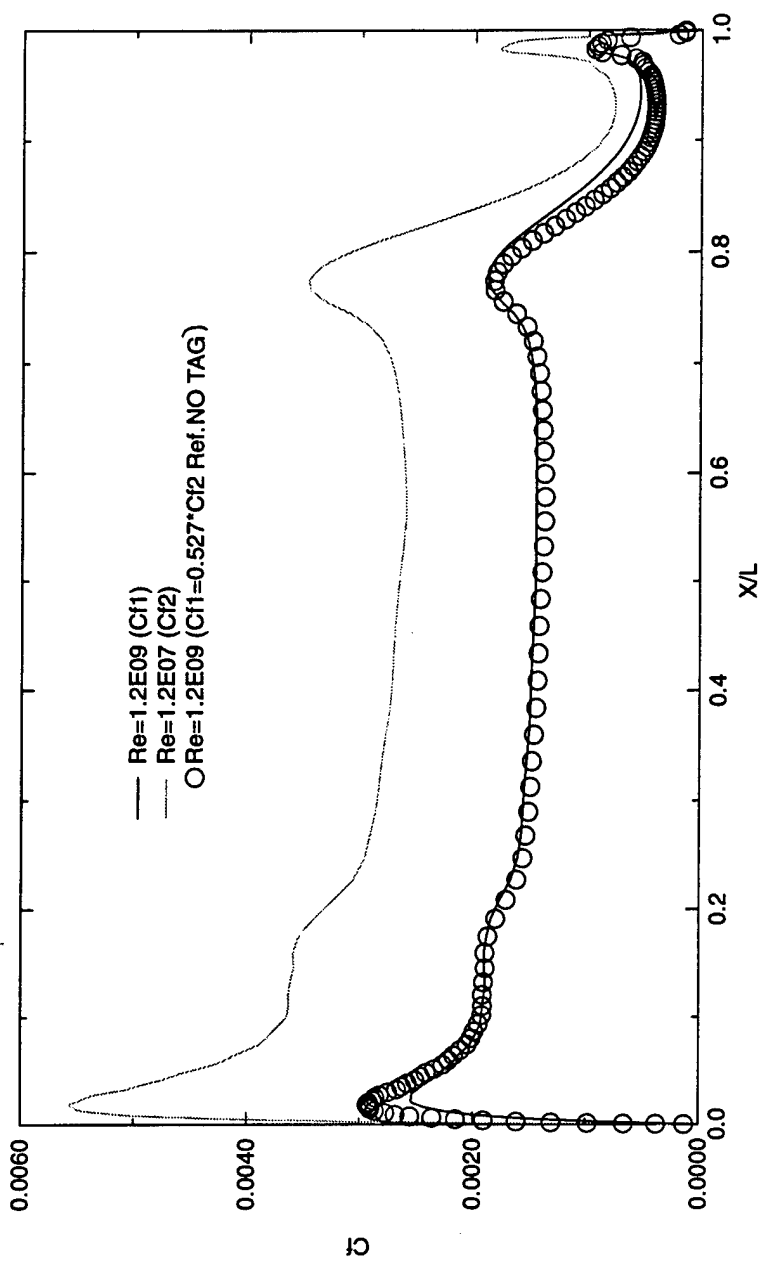


Figure 25. Comparisons of Skin-Friction Distributions on the SUBOFF Barebody and  
 $Re = 12,000,000$  and  $Re = 1,200,000,000$  (for  $\alpha = 0^\circ$ )

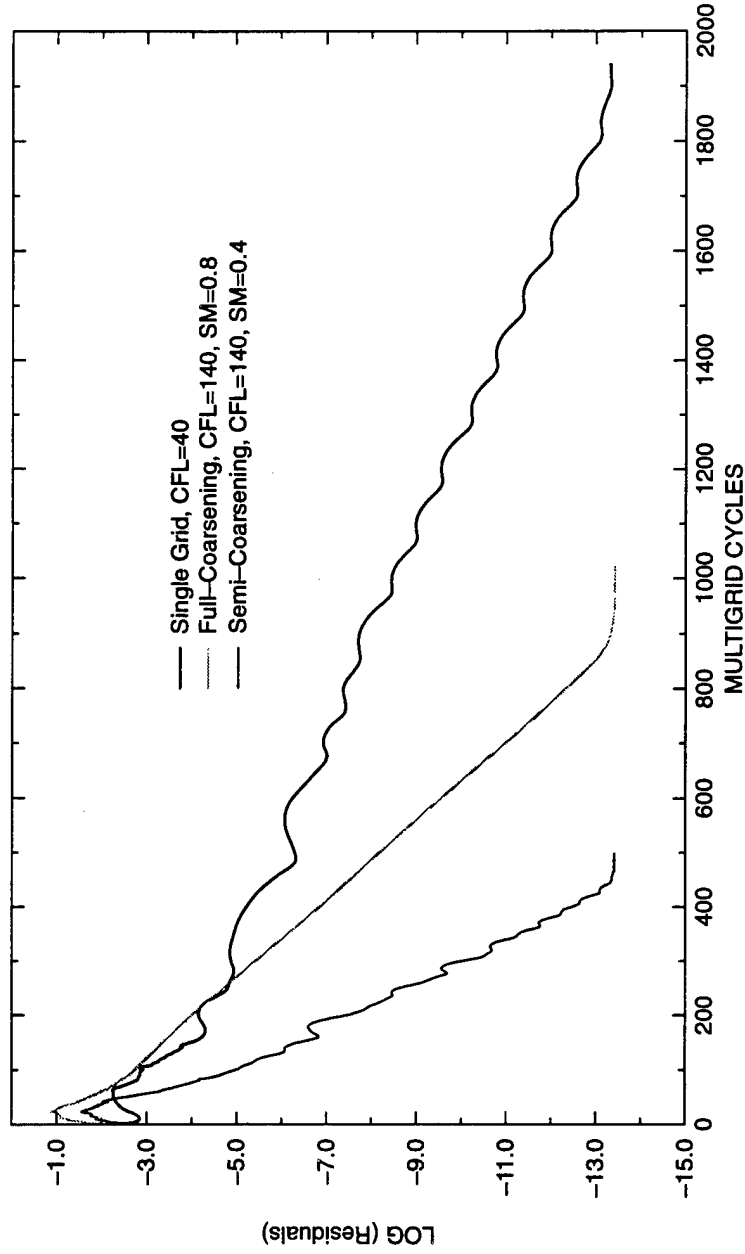


Figure 26. Convergence Histories of Multigrid and Single-Grid Solutions on the 6:1 Prolate Spheroid at  $\alpha = 10^\circ$  and  $Re = 4,200,000$

Figure 26.

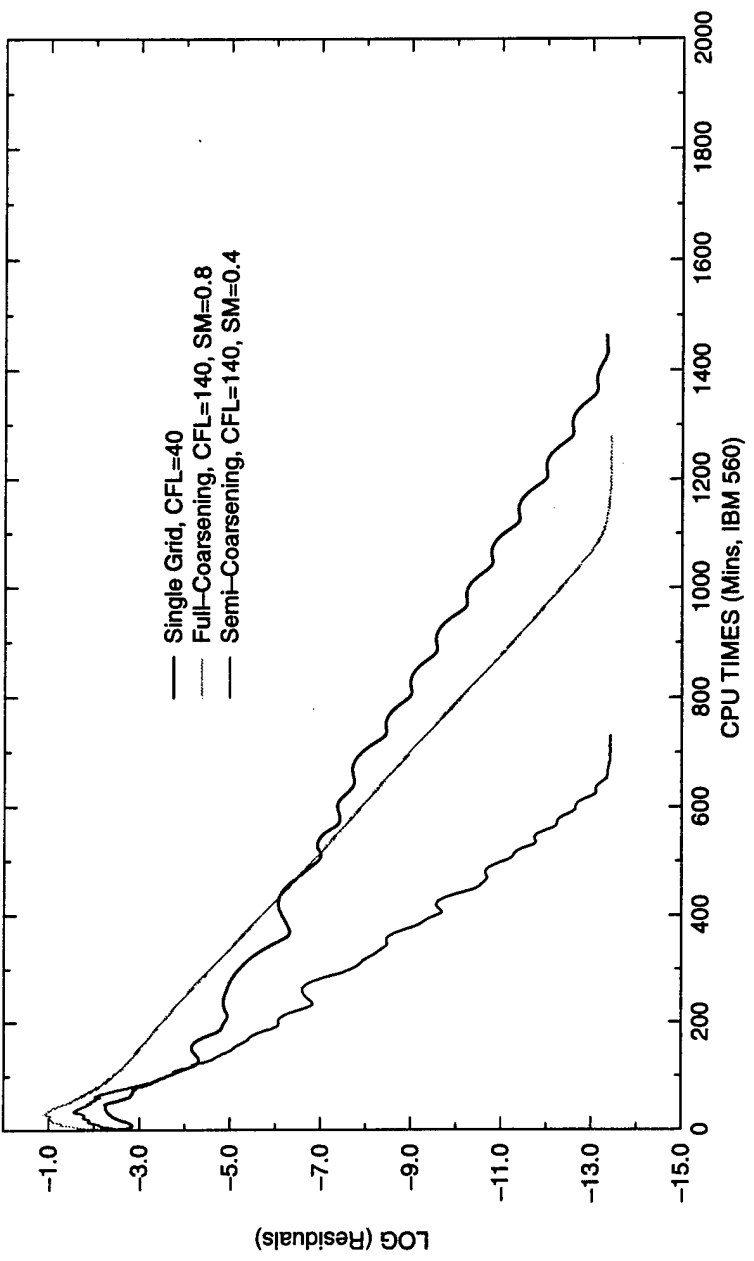


Figure 27. CPU Times of Multigrid and Single-Grid Solutions on the 6:1 Prolate Spheroid at  $\alpha = 10^\circ$  and  $Re = 4,200,000$

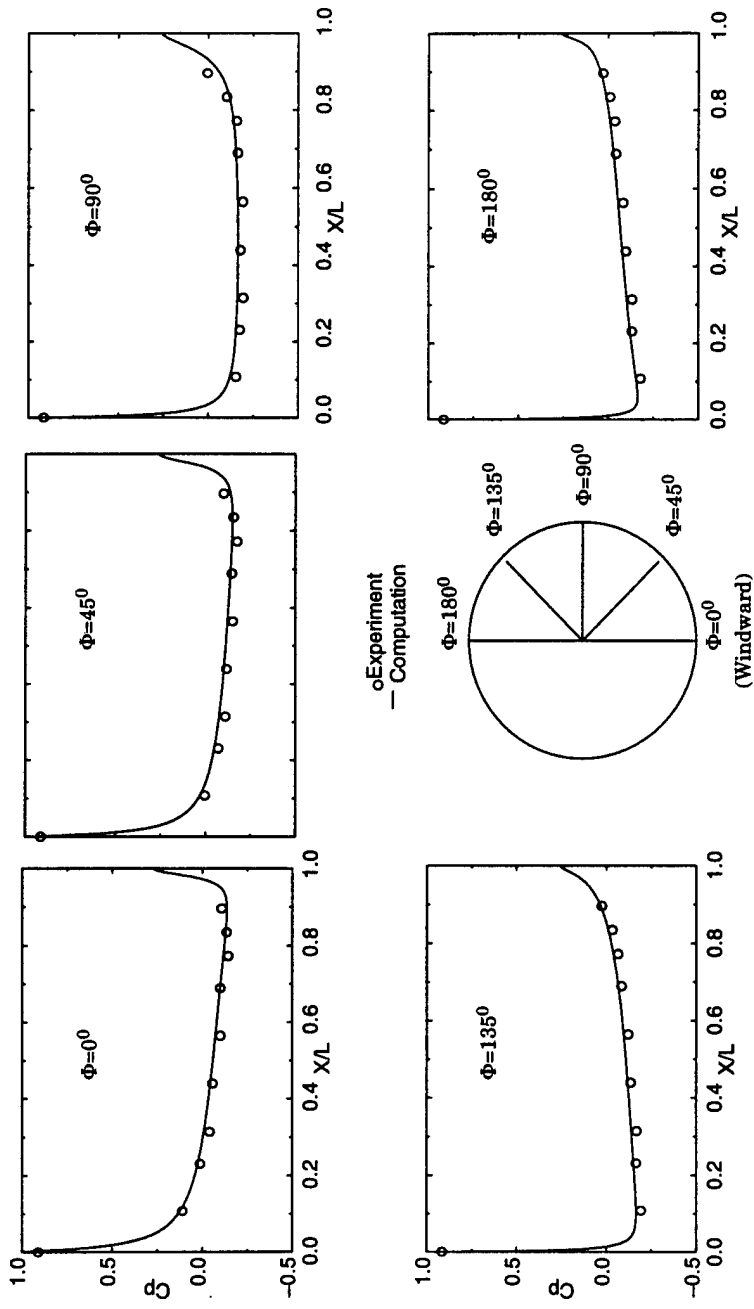


Figure 28. Computed and Measured Surface-Pressure Distributions on the 6:1 Prolate Spheroid at Different Circumferential Locations (for  $\alpha = 10^\circ$  and  $Re = 4,200,000$ )

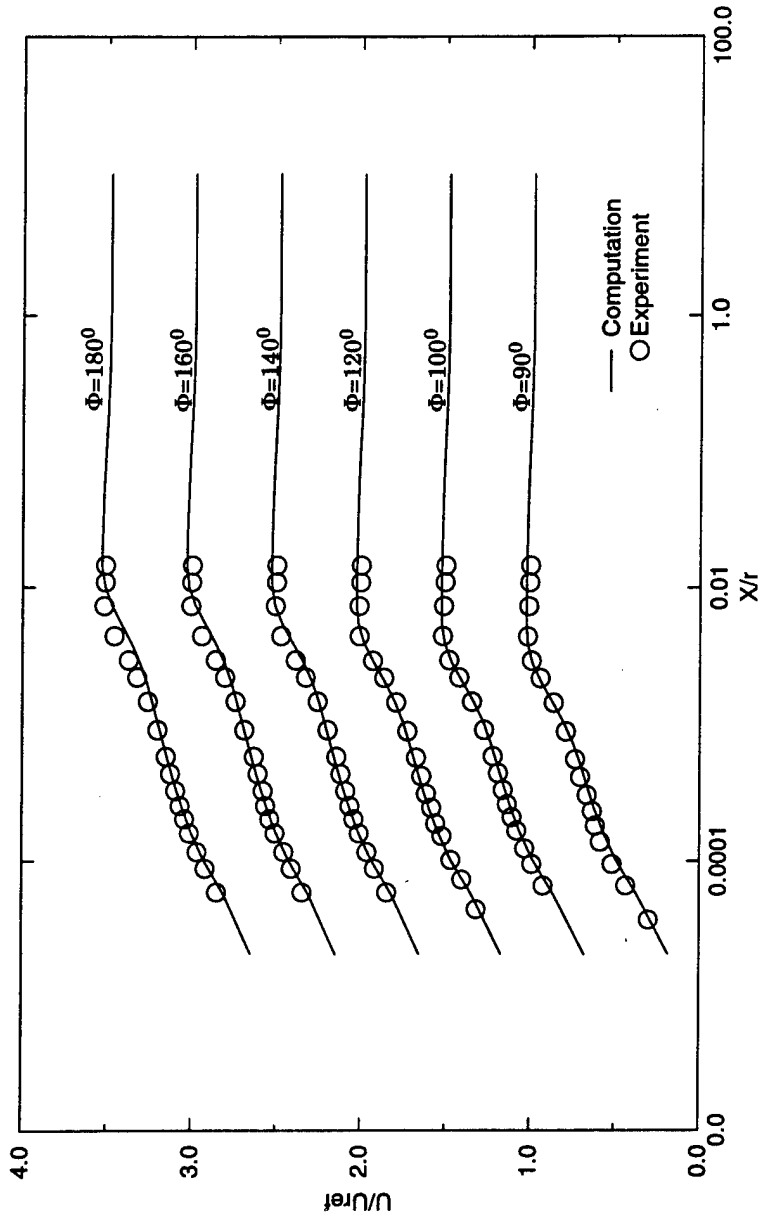


Figure 29. Computed and Measured Profiles of the  $u$ -Component of Velocity on the 6:1 Prolate Spheroid at  $x/L = 0.4$  (for  $\alpha = 10^\circ$  and  $Re = 4,200,000$ )

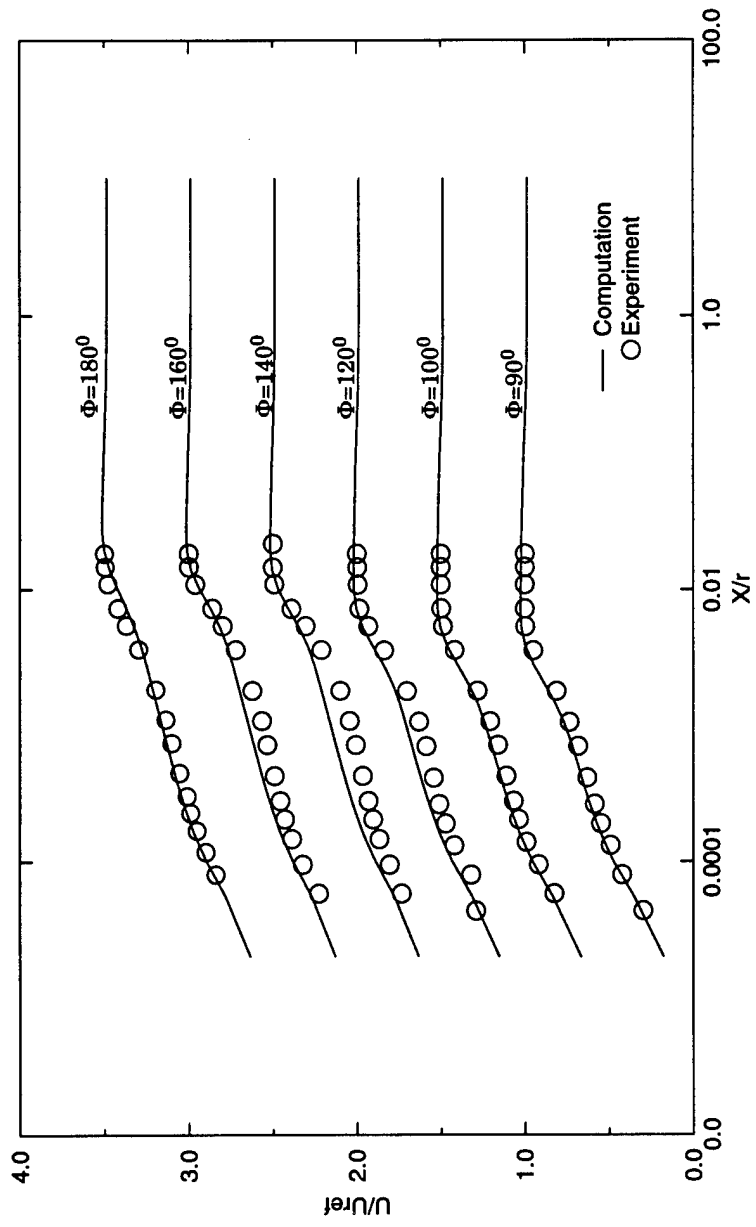


Figure 30. Computed and Measured Profiles of the  $u$ -Component of Velocity on the 6:1 Prolate Spheroid at  $x/L = 0.6$  (for  $\alpha = 10^\circ$  and  $Re = 4,200,000$ )

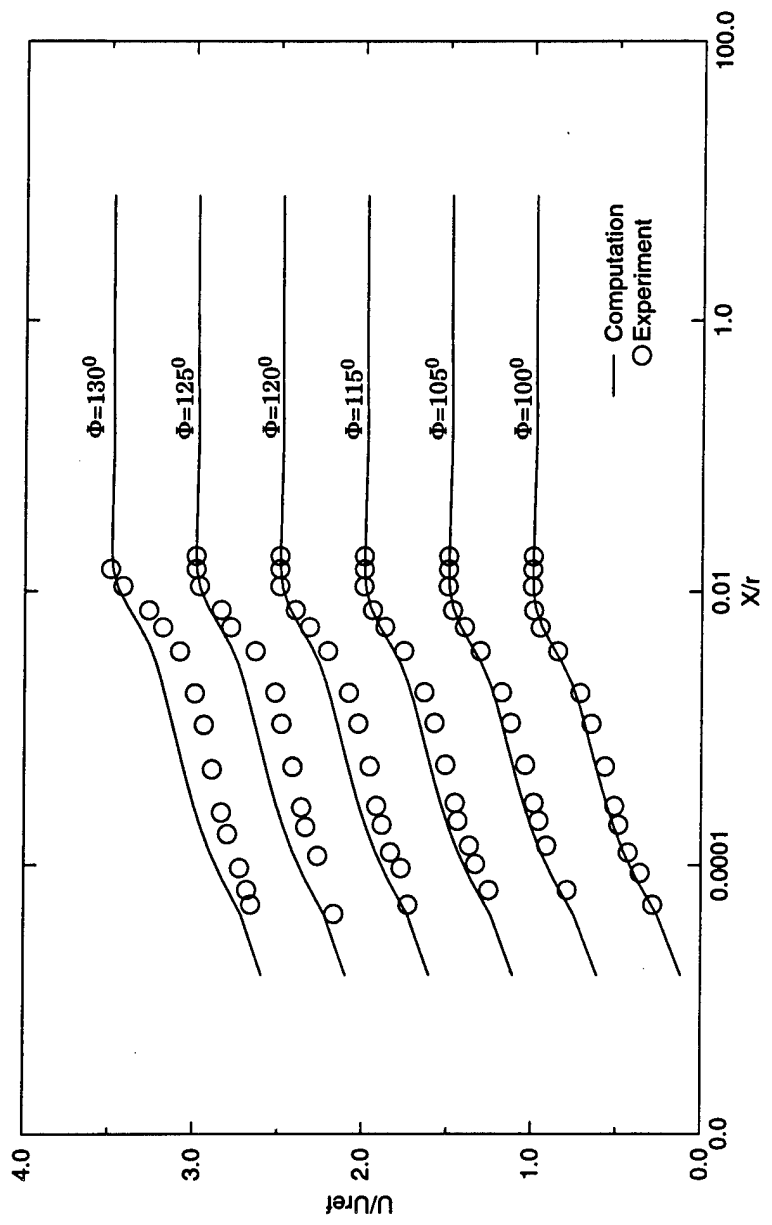


Figure 31. Computed and Measured Profiles of the  $u$ -Component of Velocity on the 6:1 Prolate Spheroid at  $x/L = 0.772$  (for  $\alpha = 10^\circ$  and  $Re = 4,200,000$ )

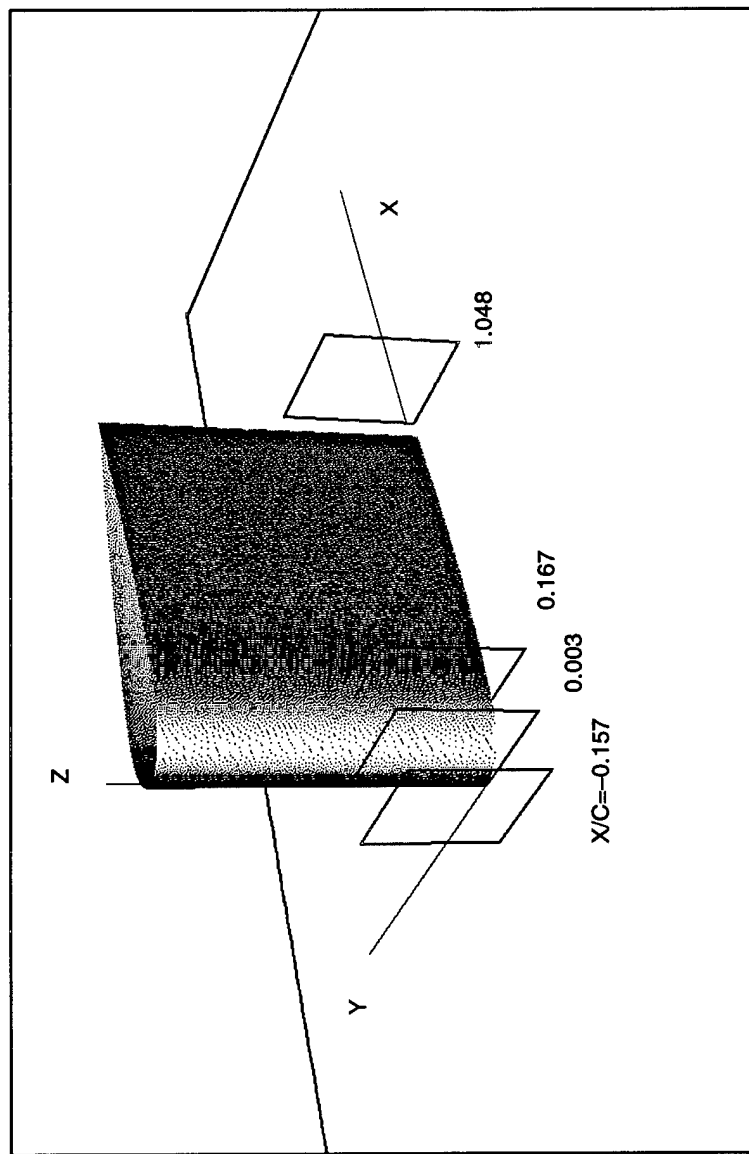


Figure 32. NACA 0020 Wing Mounted on a Flat Plate

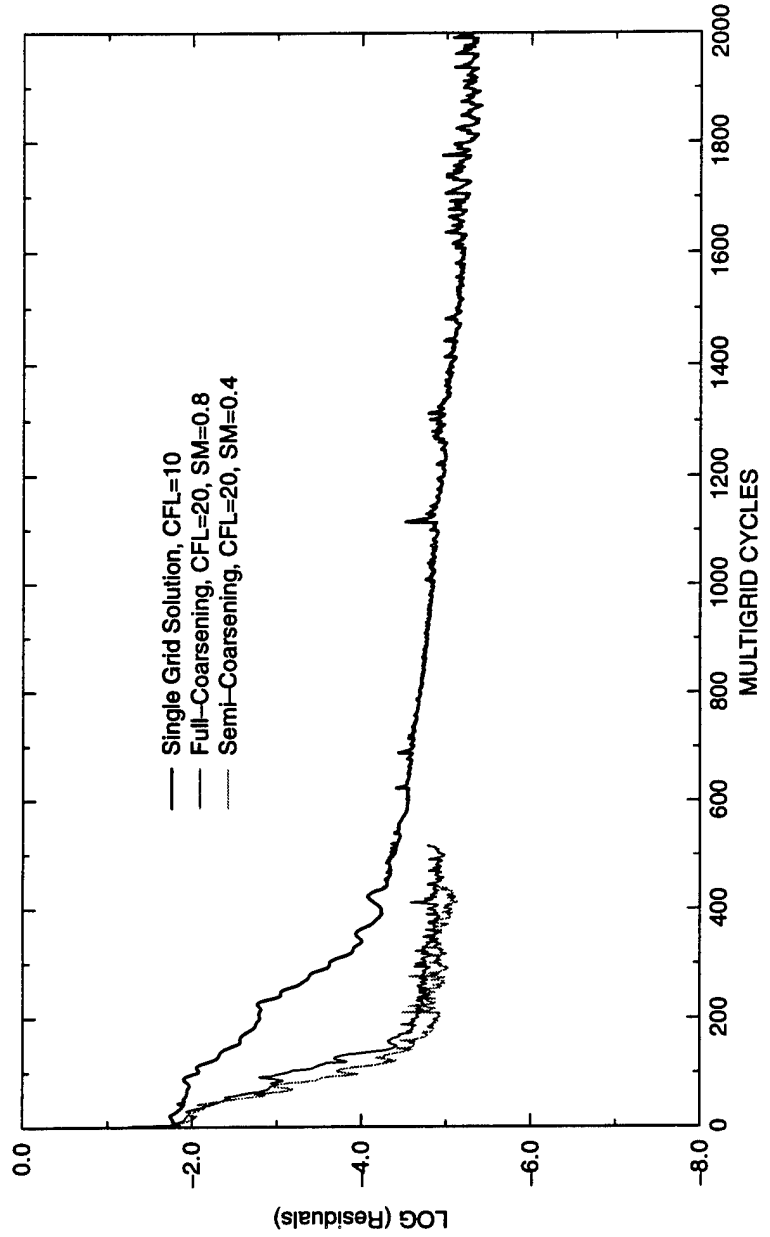


Figure 33. Convergence Histories of Multigrid and Single-Grid Solutions for the Wing-Body Junction Flow at  $\alpha = 0^\circ$  and  $Re = 500,000$

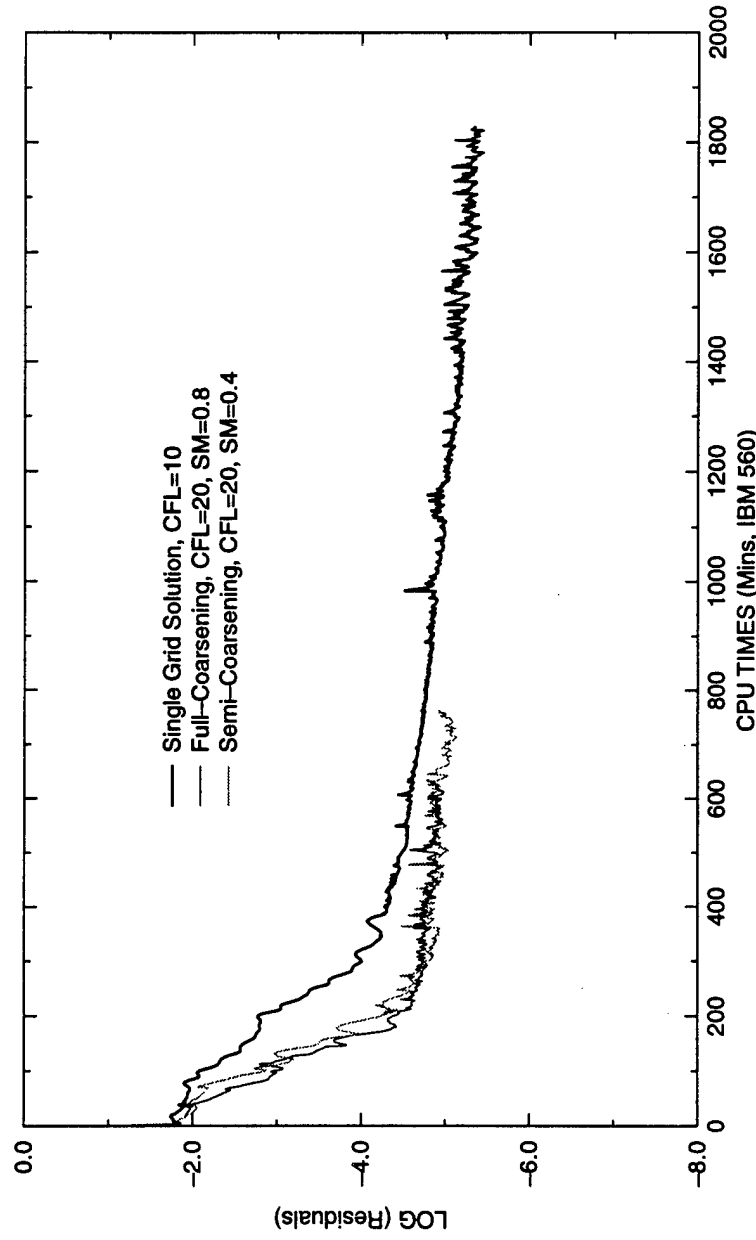


Figure 34. CPU Times of Multigrid and Single-Grid Solutions for the Wing-Body Junction  
Flow at  $\alpha = 0^\circ$  and  $Re = 500,000$

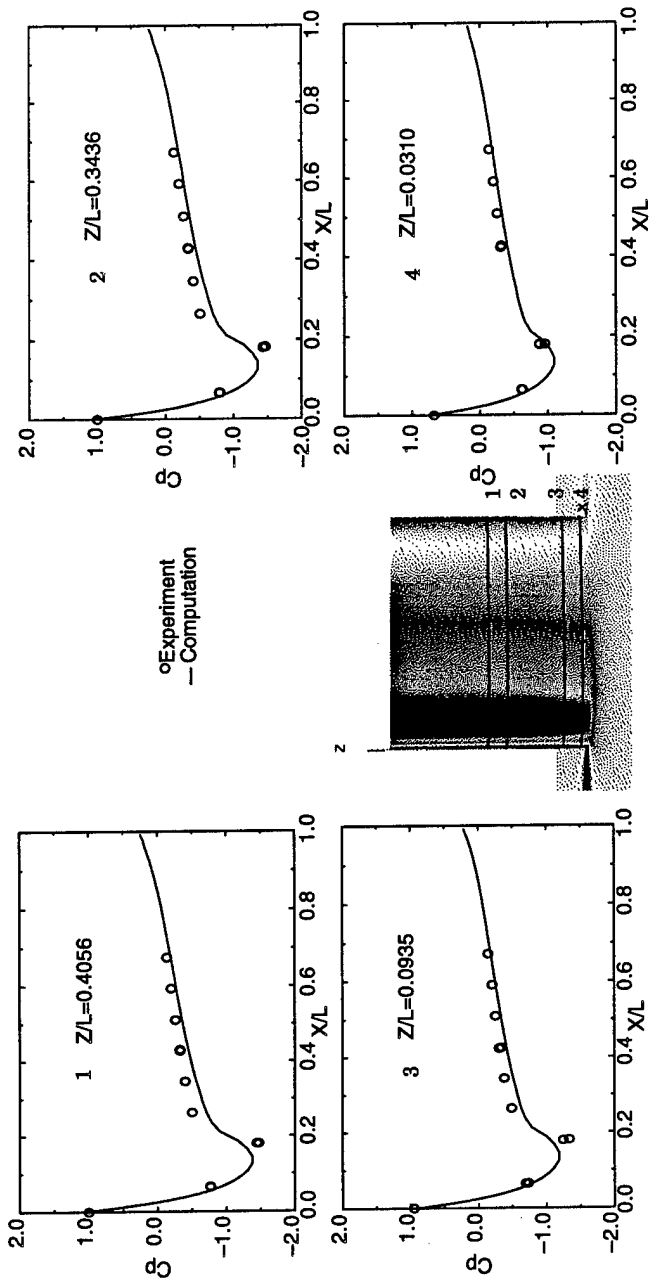


Figure 35. Computed and Measured Surface-Pressure Distributions on the Wing Surface for the Wing-Body Junction Flow at  $\alpha = 0^\circ$  and  $Re = 500,000$

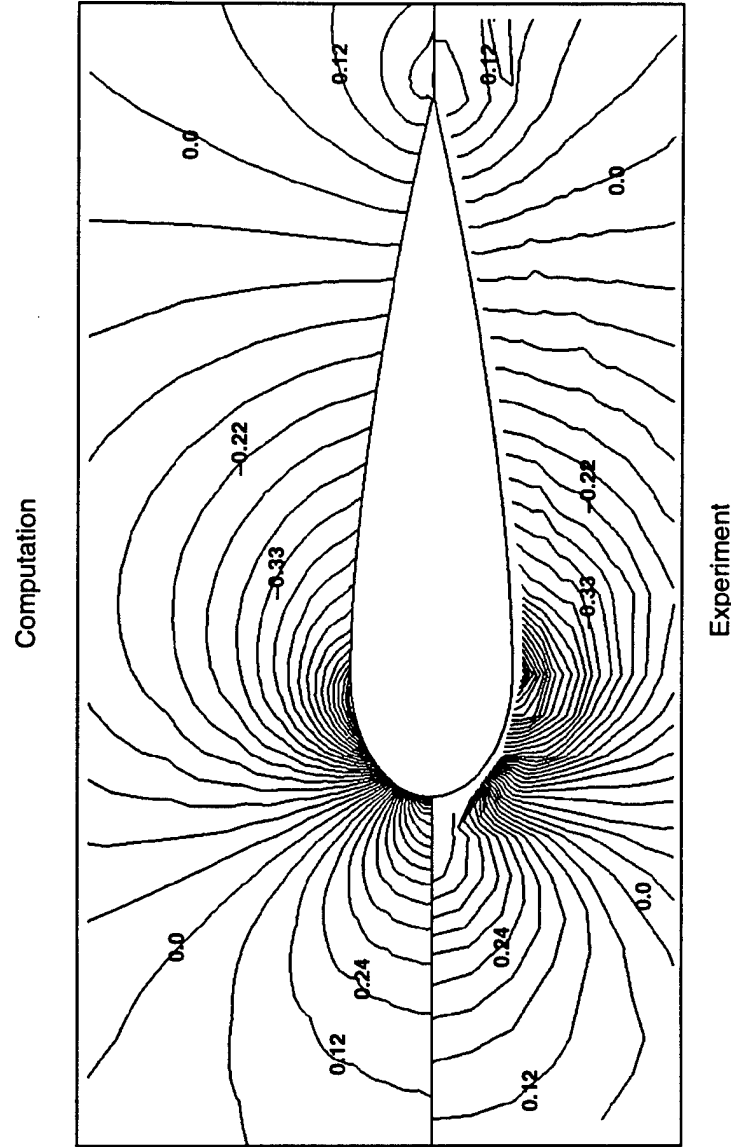
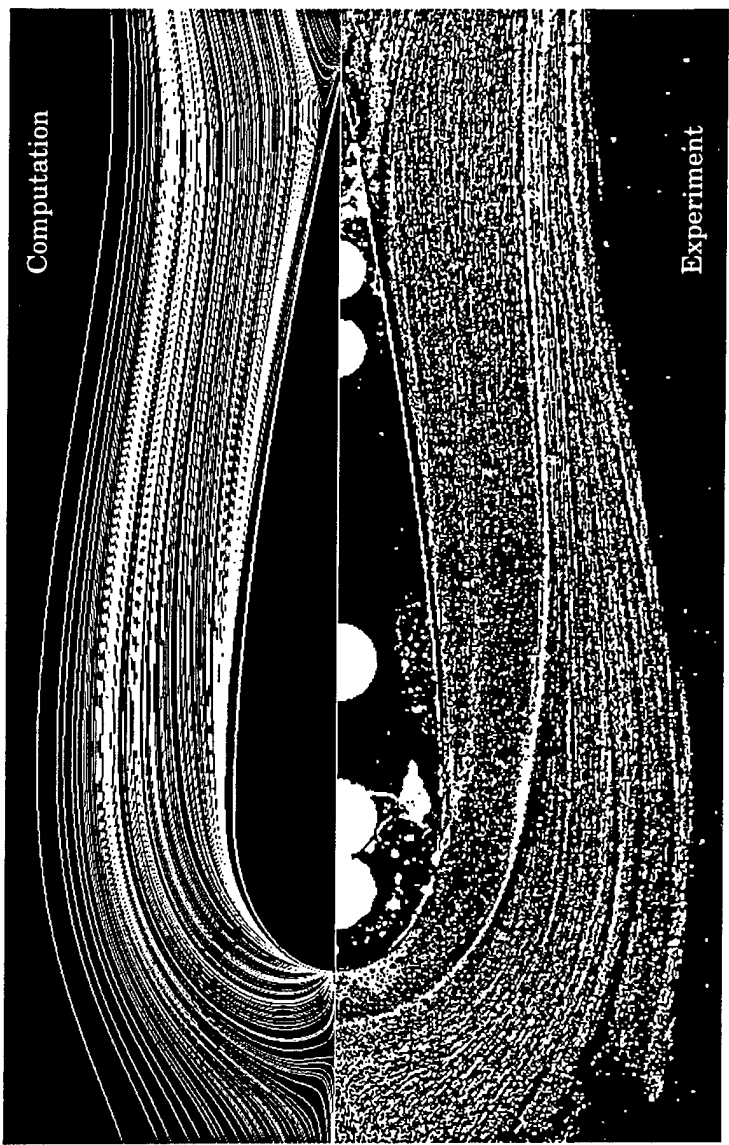


Figure 36. Computed and Measured Surface Pressure Contours on the Flat-Plate Surface for the Wing-Body Junction Flow at  $\alpha = 0^\circ$  and  $Re = 500,000$

Figure 37. Computed Particle Traces and Measured Skin-Friction Lines on the Flat-Plate Surface for the Wing-Body Junction Flow at  $\alpha = 0^\circ$  and  $Re = 500,000$



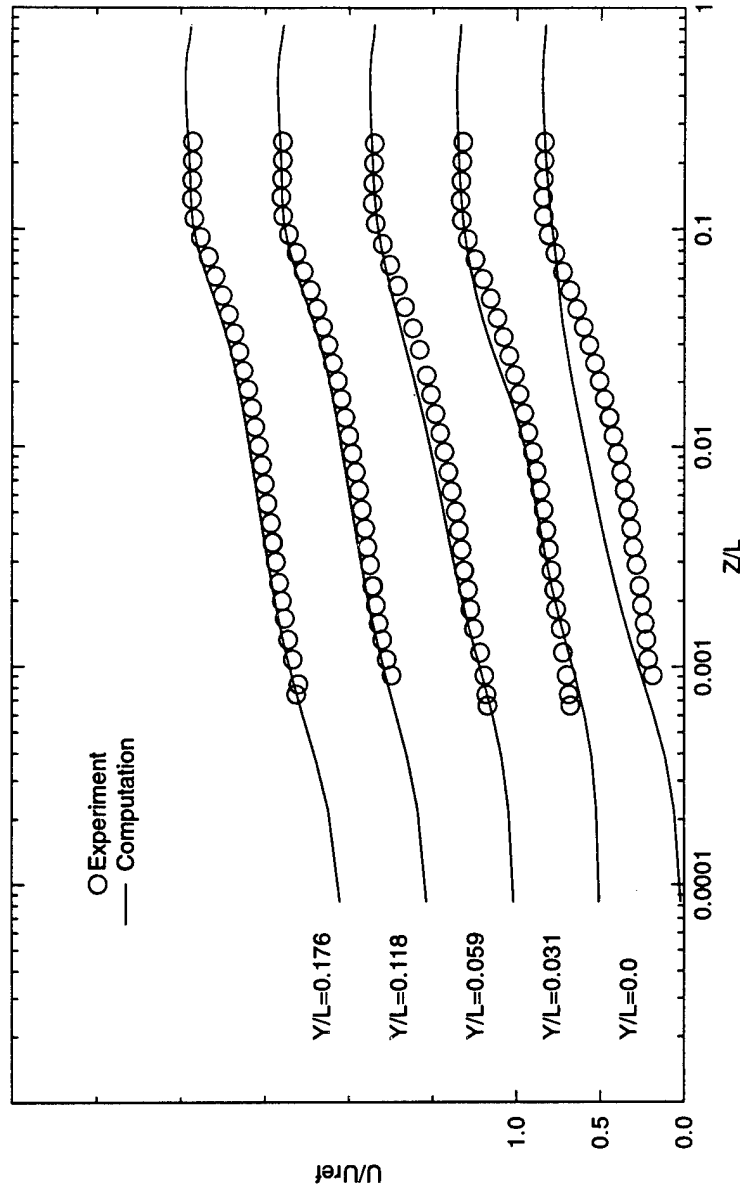


Figure 38. Computed and Measured Profiles of the  $u$ -Component of Velocity for the Wing-Body Junction Flow at  $x/L = -0.157$  (for  $\alpha = 0^\circ$  and  $Re = 500,000$ )

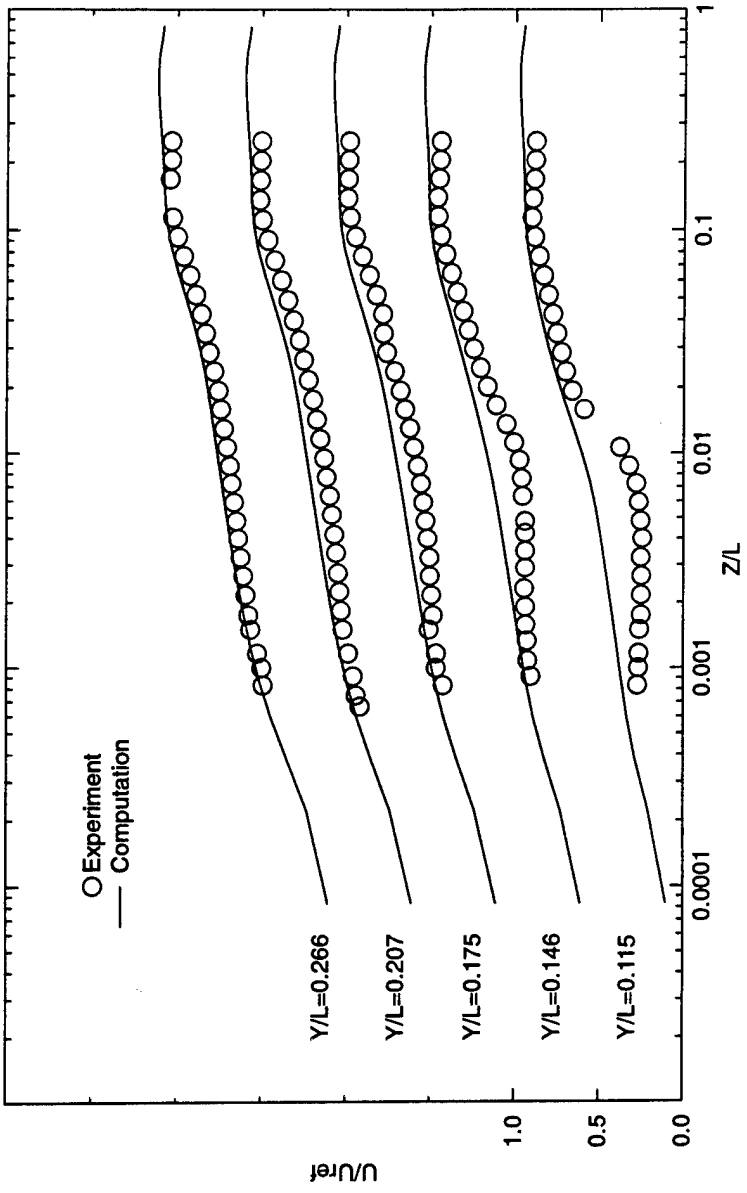


Figure 39. Computed and Measured Profiles of the  $u$ -Component of Velocity for the Wing-Body Junction Flow at  $x/L = 0.003$  (for  $\alpha = 0^\circ$  and  $Re = 500,000$ )

Figure 39.

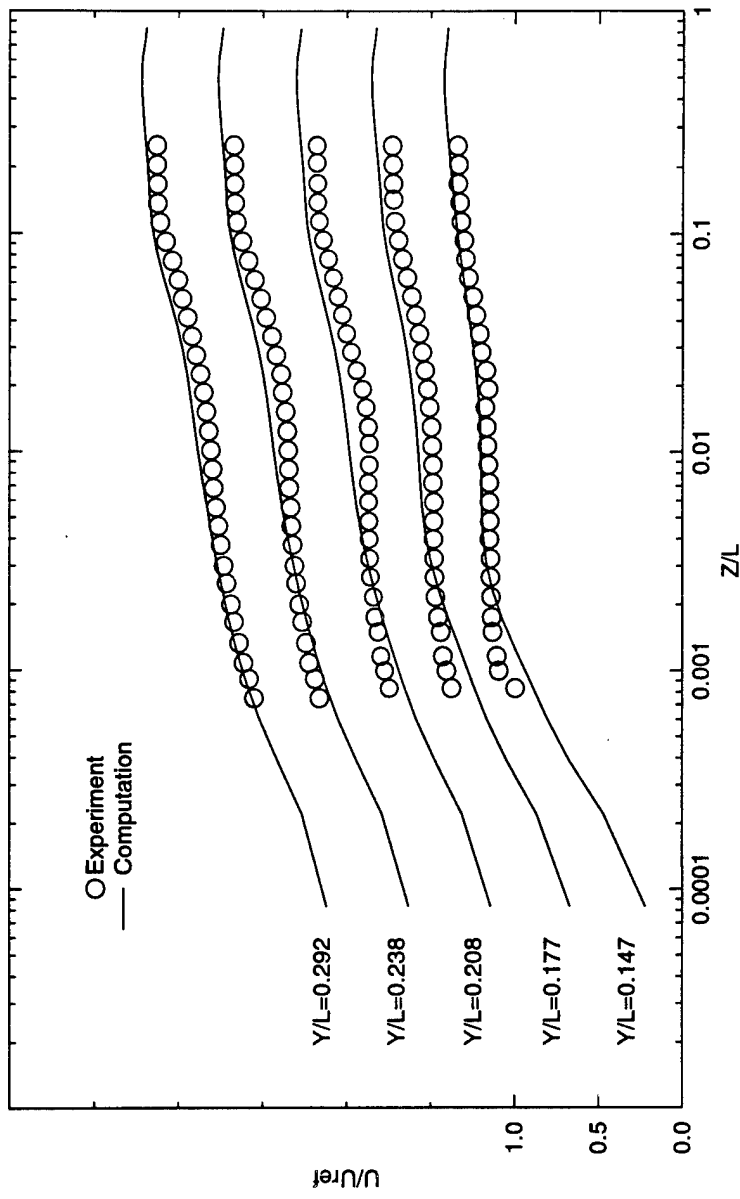


Figure 40. Computed and Measured Profiles of the  $u$ -Component of Velocity for the Wing-Body Junction Flow at  $x/L = 0.167$  (for  $\alpha = 0^\circ$  and  $Re = 500,000$ )

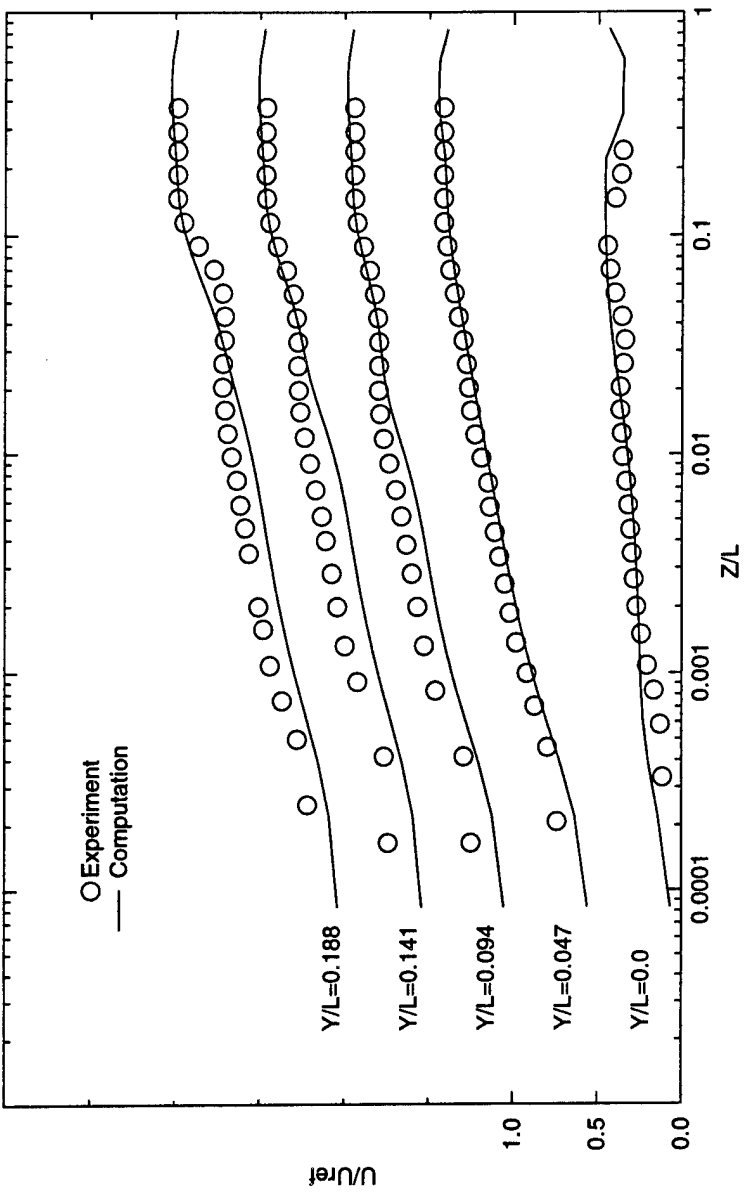


Figure 41. Computed and Measured Profiles of the  $u$ -Component of Velocity for the Wing-Body Junction Flow at  $x/L = 1.048$  (for  $\alpha = 0^\circ$  and  $Re = 500,000$ )

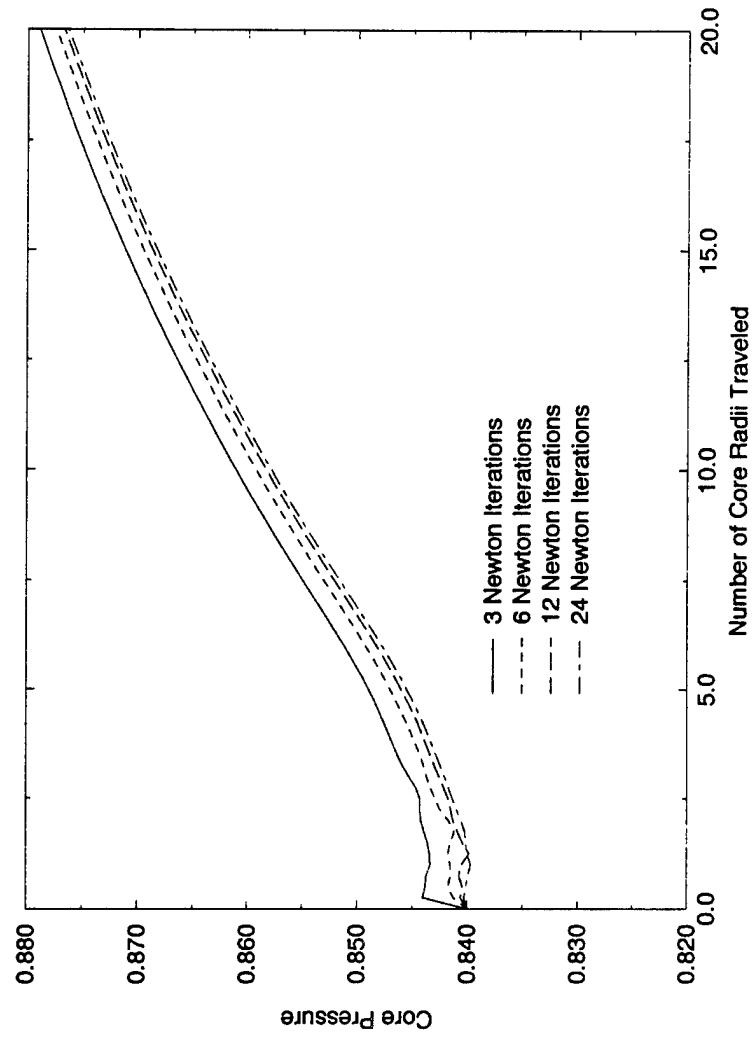


Figure 42.

Vortex Core Pressure History for a Coarse 211x31 (6,541 Point) Grid

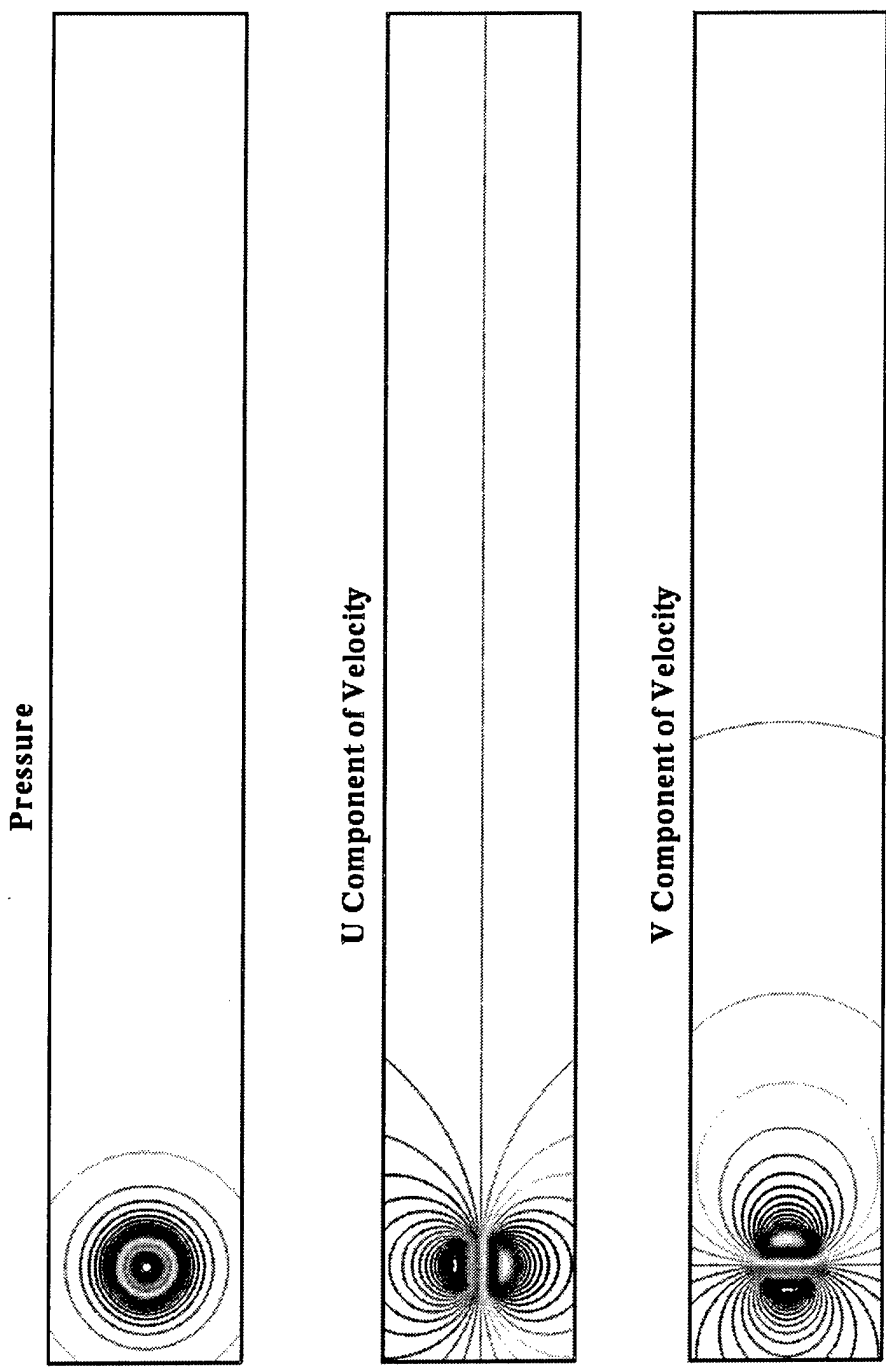


Figure 43. Initial Distribution of  $p$ ,  $u$ , and  $v$  for an Idealized Thomson-Rankine Vortex

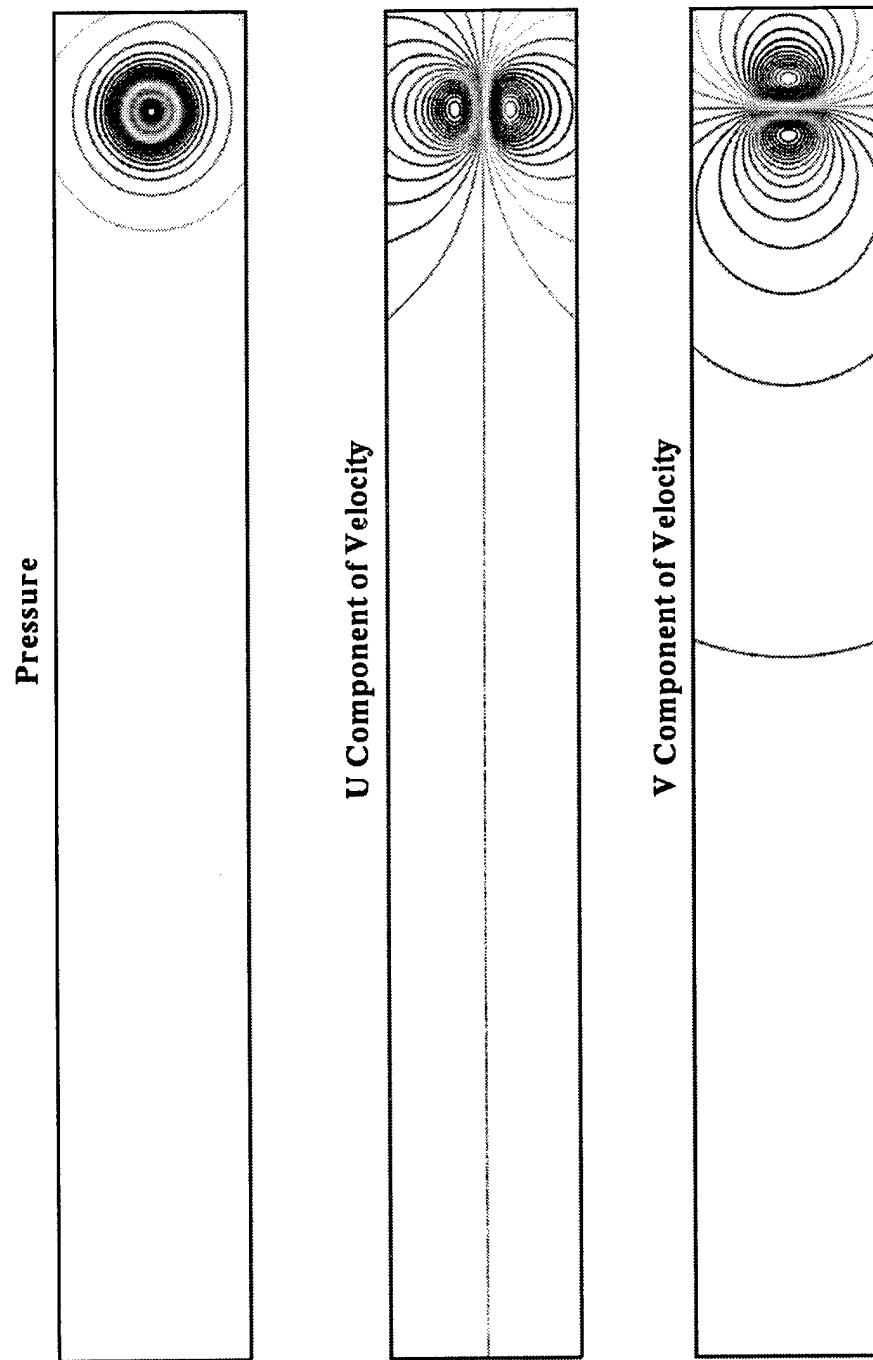


Figure 44. Distribution of  $p$ ,  $u$ , and  $v$  for a Vortex That Has Traveled 45 Core Radii, as Computed on a Coarse 211x31 (6,541 Point) Grid

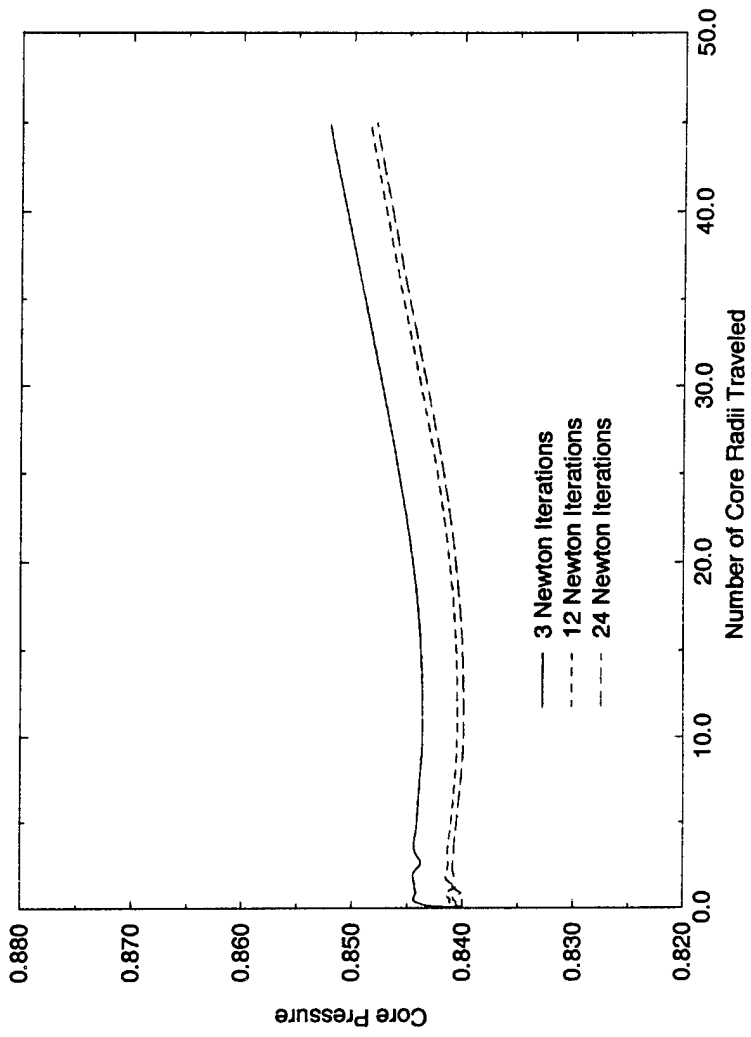


Figure 45. Vortex Core Pressure History for a Medium 421x61 (25,681 Point) Grid

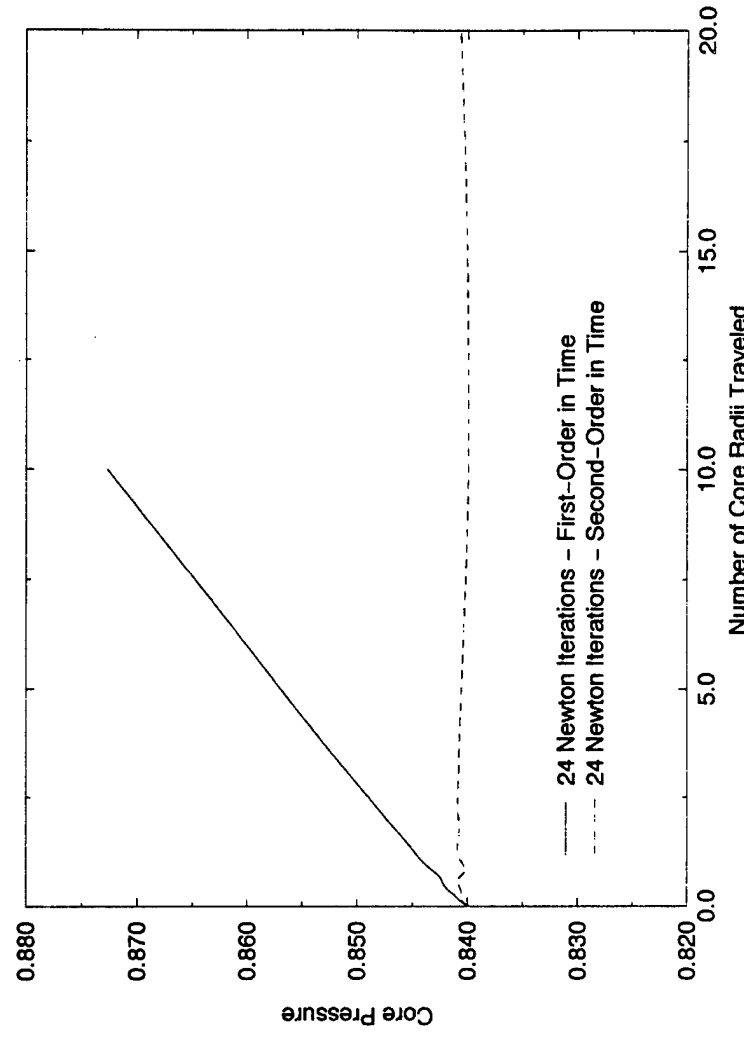


Figure 46. Comparison of Temporal Accuracy for the Vortex Core Pressure Computed on a Medium 421x61 (25,681 Point) Grid

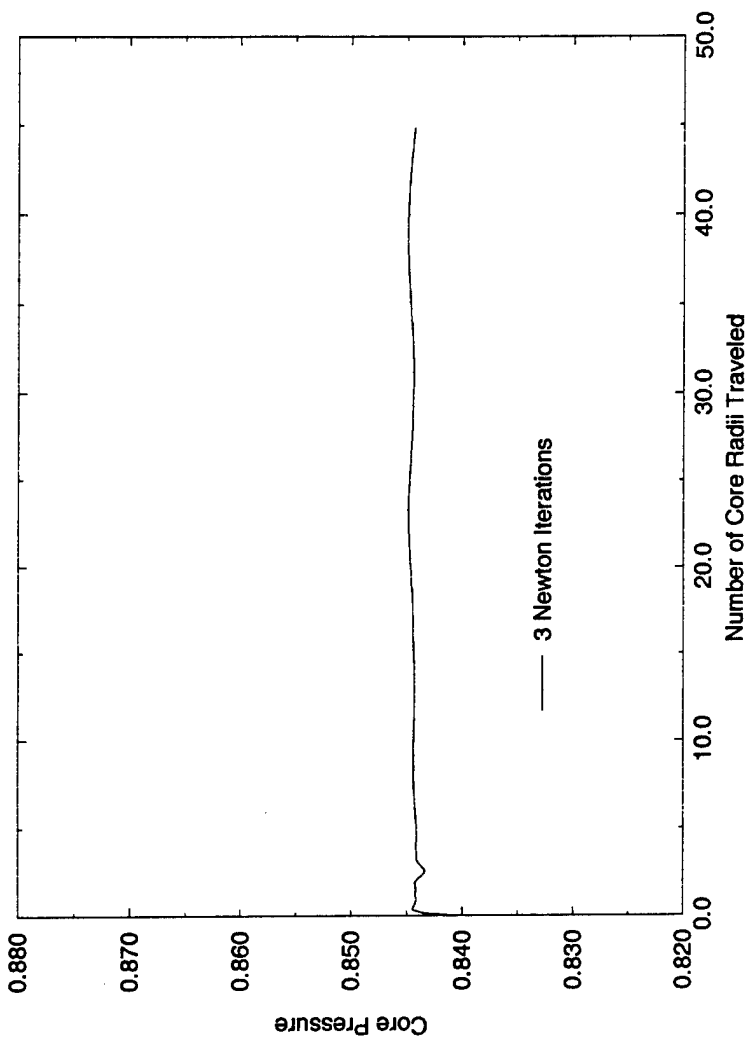


Figure 47.

Vortex Core Pressure History for a Fine 841x121 (101,761 Point) Grid

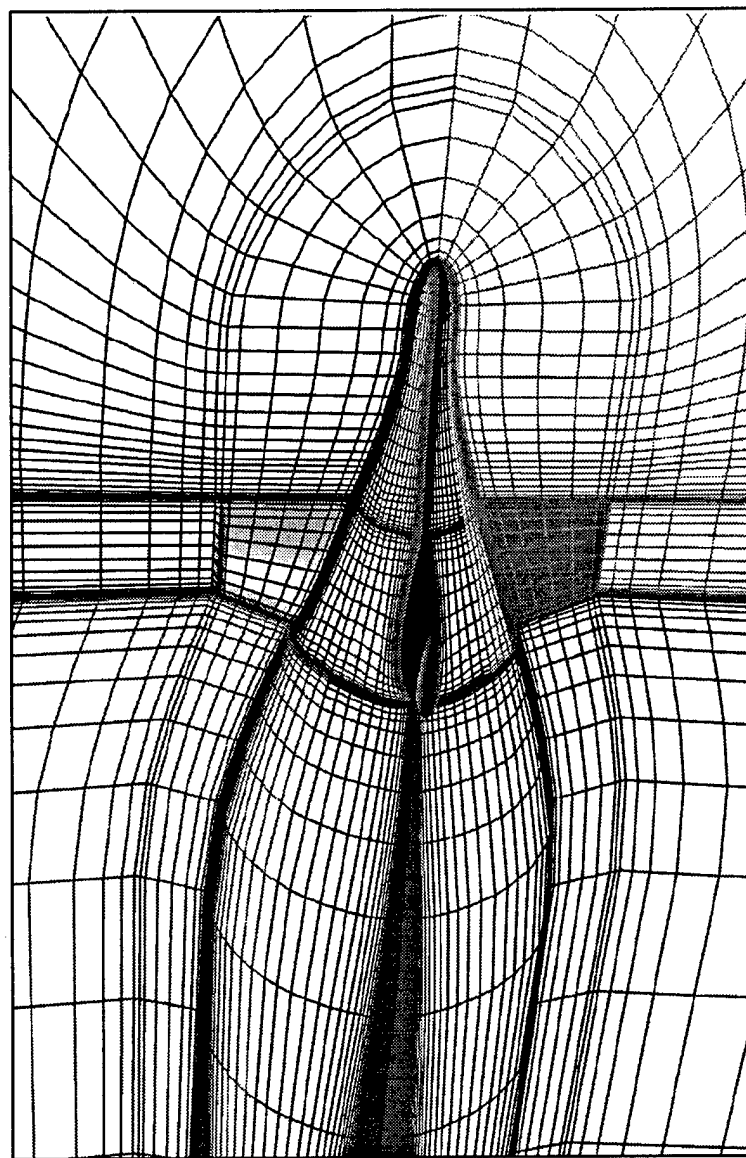


Figure 48. Aft Region of the 8-Block Grid for SUBOFF with Four Stern Appendages

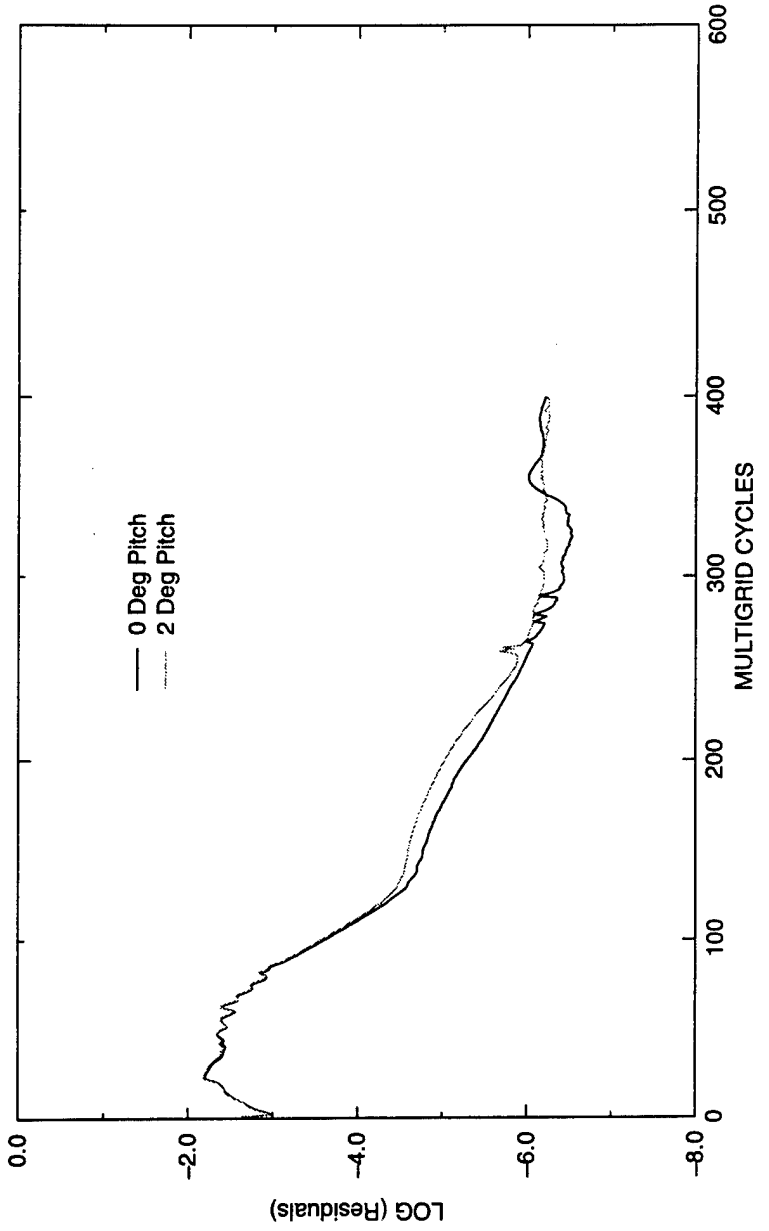


Figure 49. Convergence Histories of Multigrid Solutions for SUBOFF with Four Stern Appendages at  $0^\circ$  and  $2^\circ$  Angles of Attack and  $Re = 12,000,000$

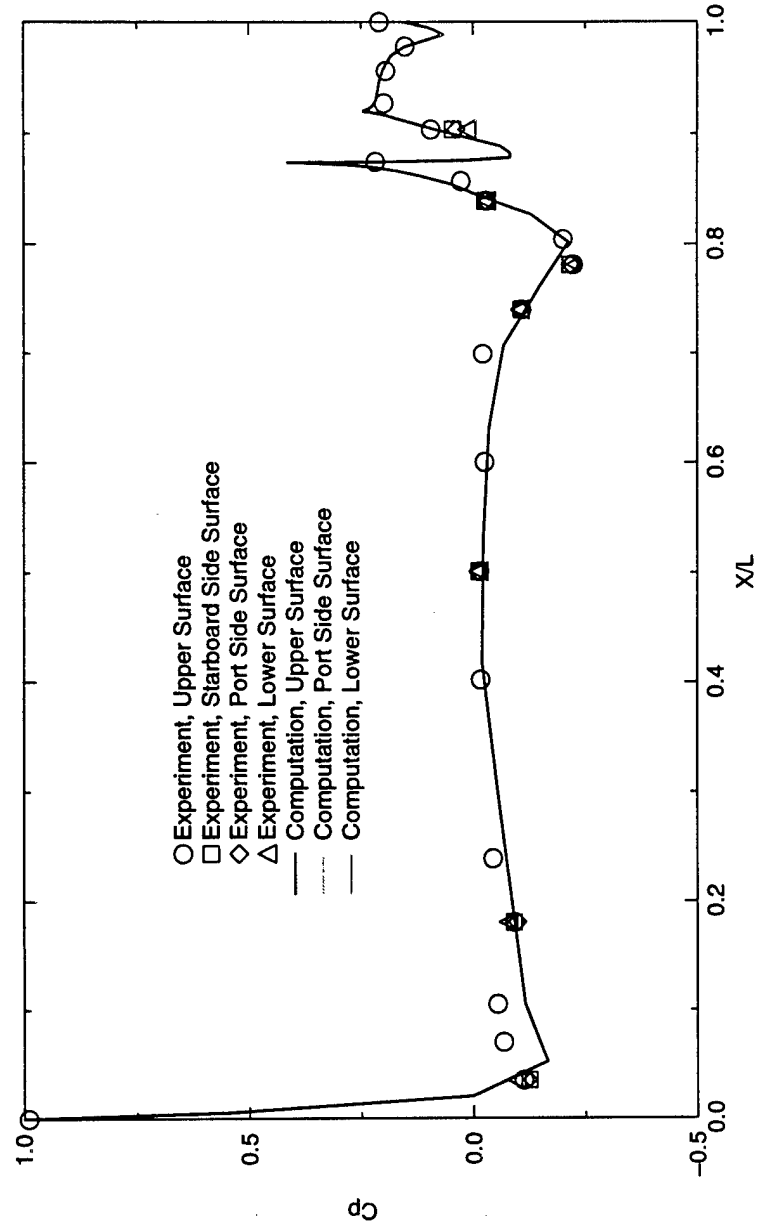


Figure 50. Computed and Measured Static-Pressure Distributions on the Hull of SUBOFF with Four Stern Appendages at a  $0^\circ$  Angle of Attack and  $Re = 12,000,000$

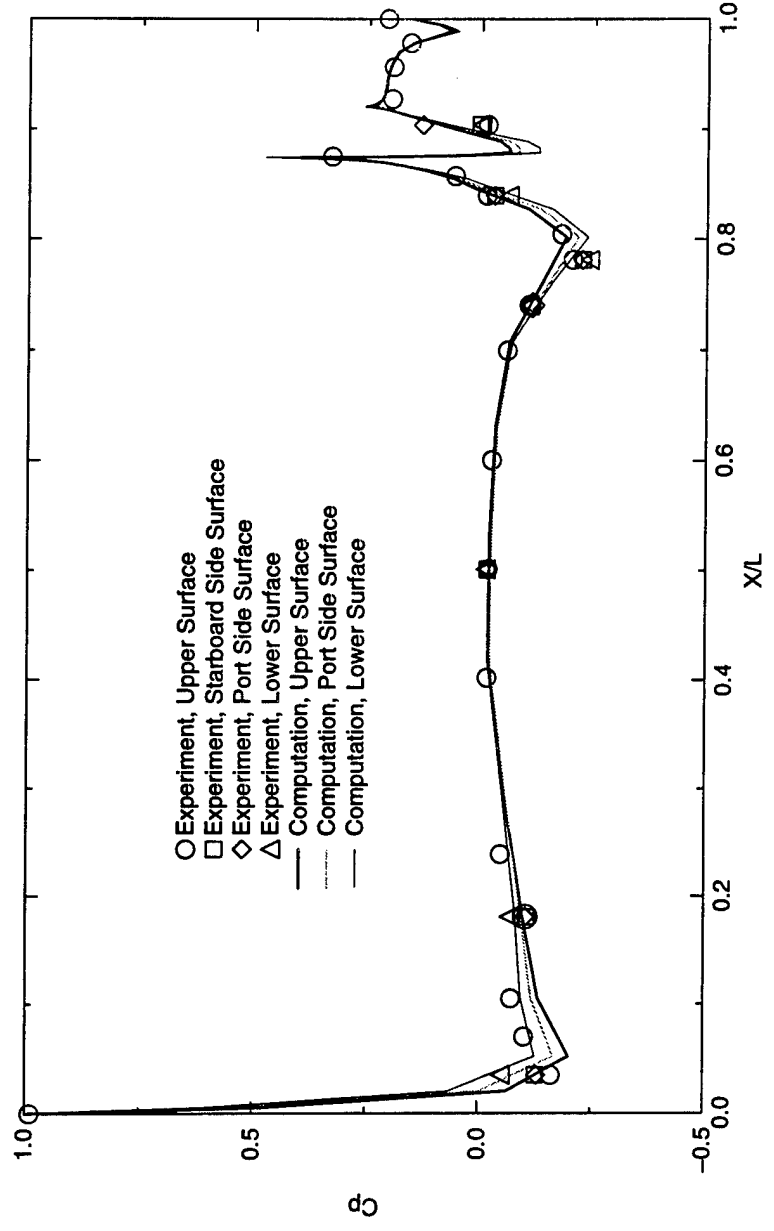


Figure 51. Computed and Measured Static-Pressure Distributions on the Hull of SUBOFF with Four Stern Appendages at  $2^\circ$  Angle of Attack and  $Re = 12,000,000$

Figure 51.

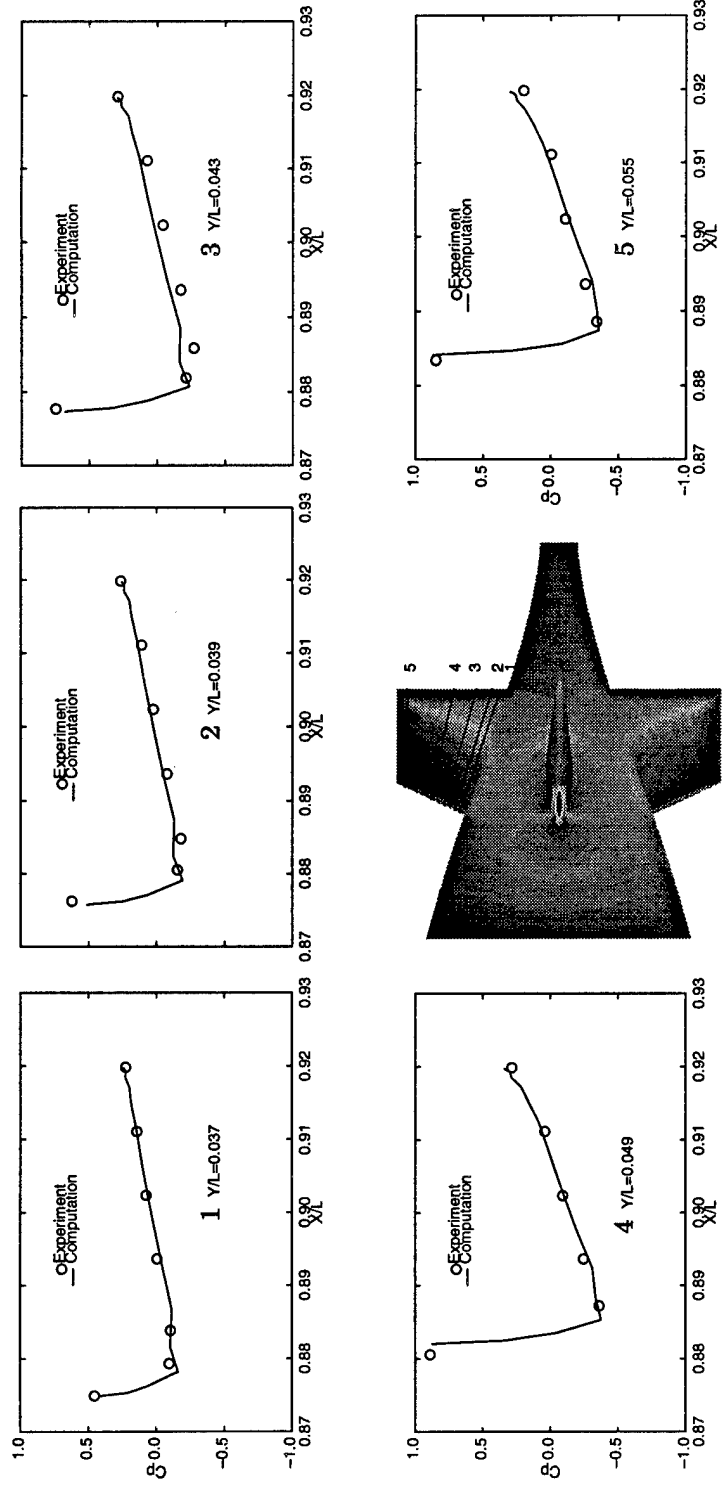


Figure 52. Computed and Measured Static-Pressure Distributions on the Upper Fin Surface of SUBOFF with Four Stern Appendages at 0° Angle of Attack and  $Re = 12,000,000$

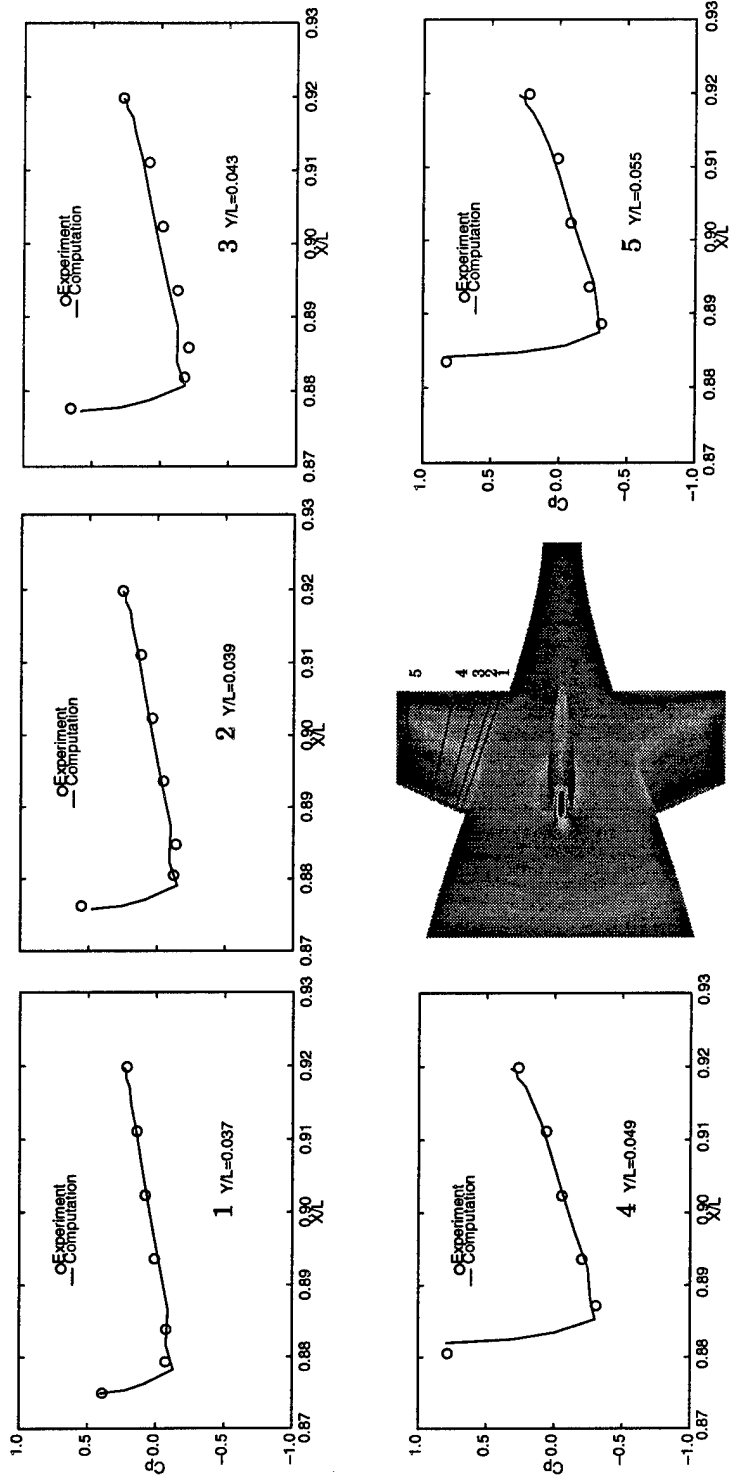


Figure 53. Computed and Measured Static-Pressure Distributions on the Upper Fin Surface of SUBOFF with Four Stern Appendages at  $2^\circ$  Angle of Attack and  $Re = 12,000,000$

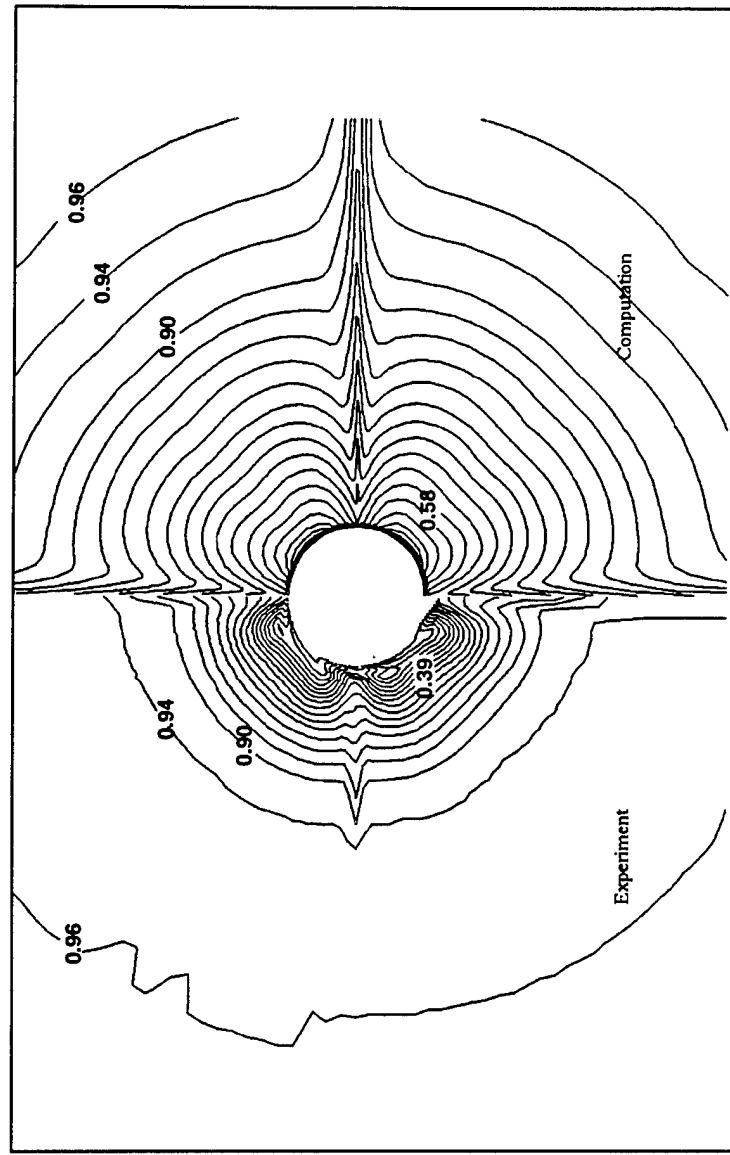
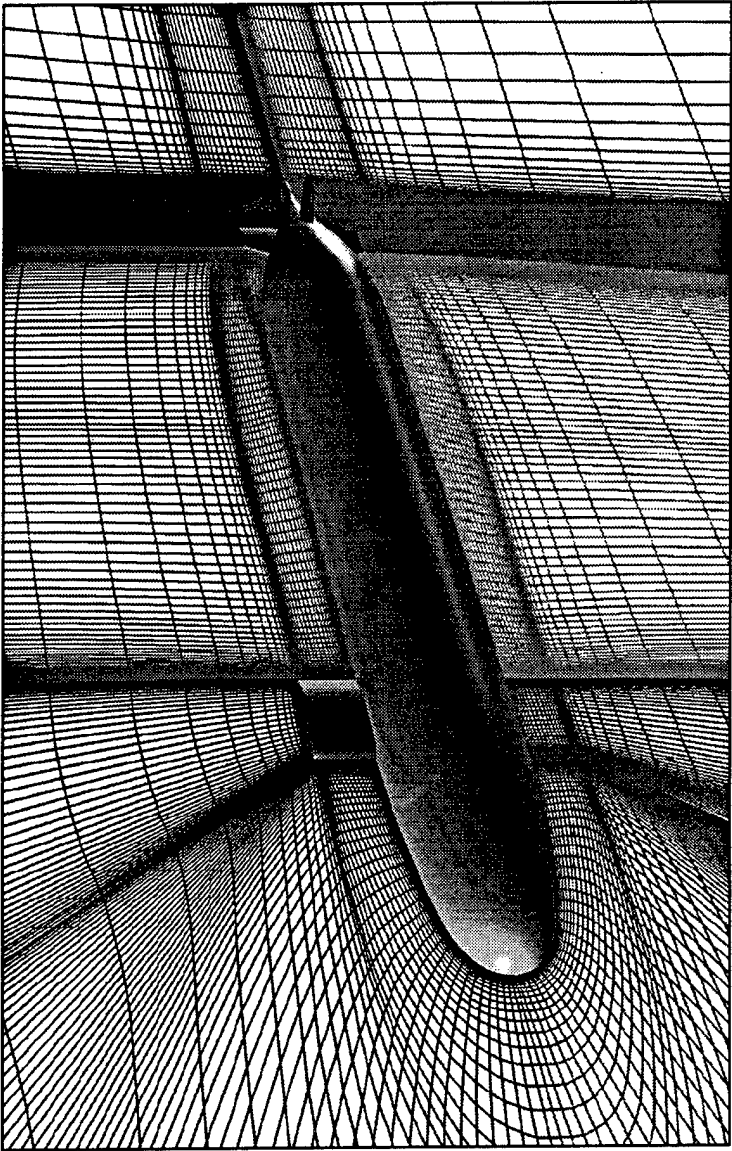


Figure 54.  
Computed and Measured Contours of the  $u$ -Component of Velocity at  $x/L = 0.978$   
of SUBOFF with Four Stern Appendages at  $0^\circ$  Angle of Attack and  
 $Re = 12,000,000$

Figure 55. Side View of the 12-Block, Fine Grid for SUBOFF with a Sail and Four Stern Appendages



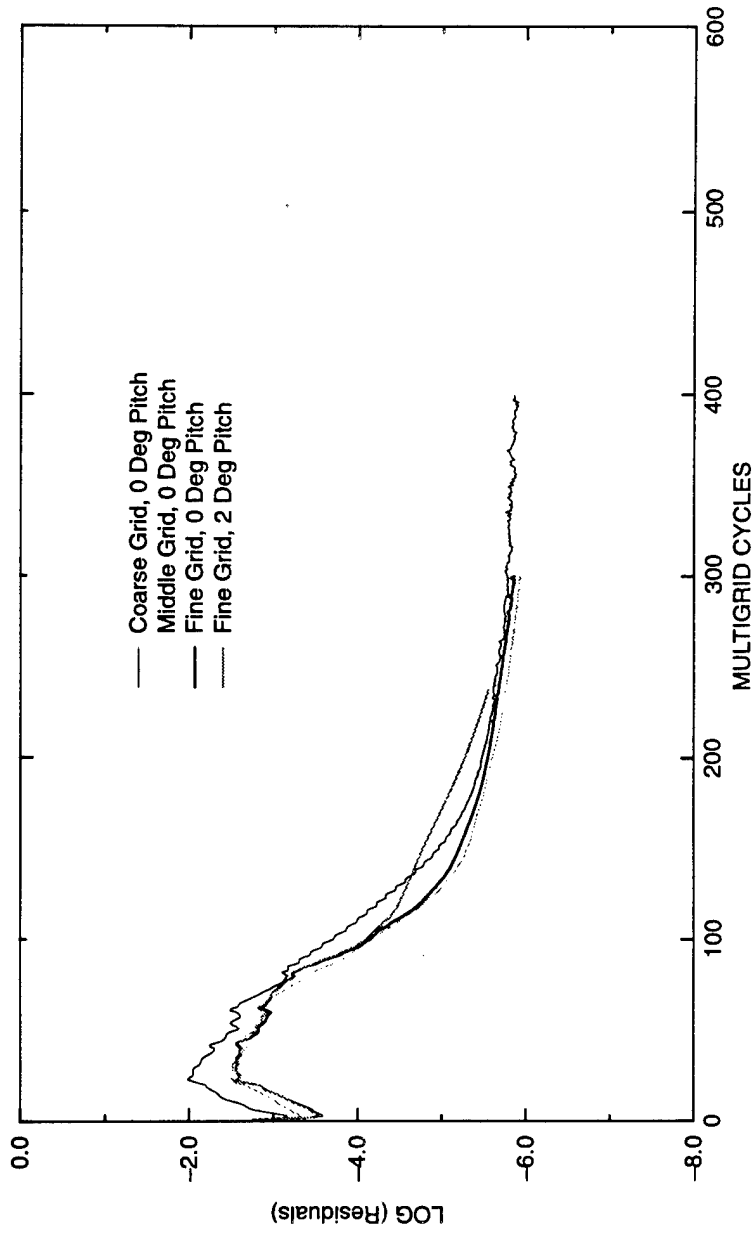


Figure 56. Convergence Histories of Multigrid Solutions for SUBOFF with a Sail and Four Stern Appendages on Three Grids at  $0^\circ$  and  $2^\circ$  Angles of Attack and  $Re = 12,000,000$

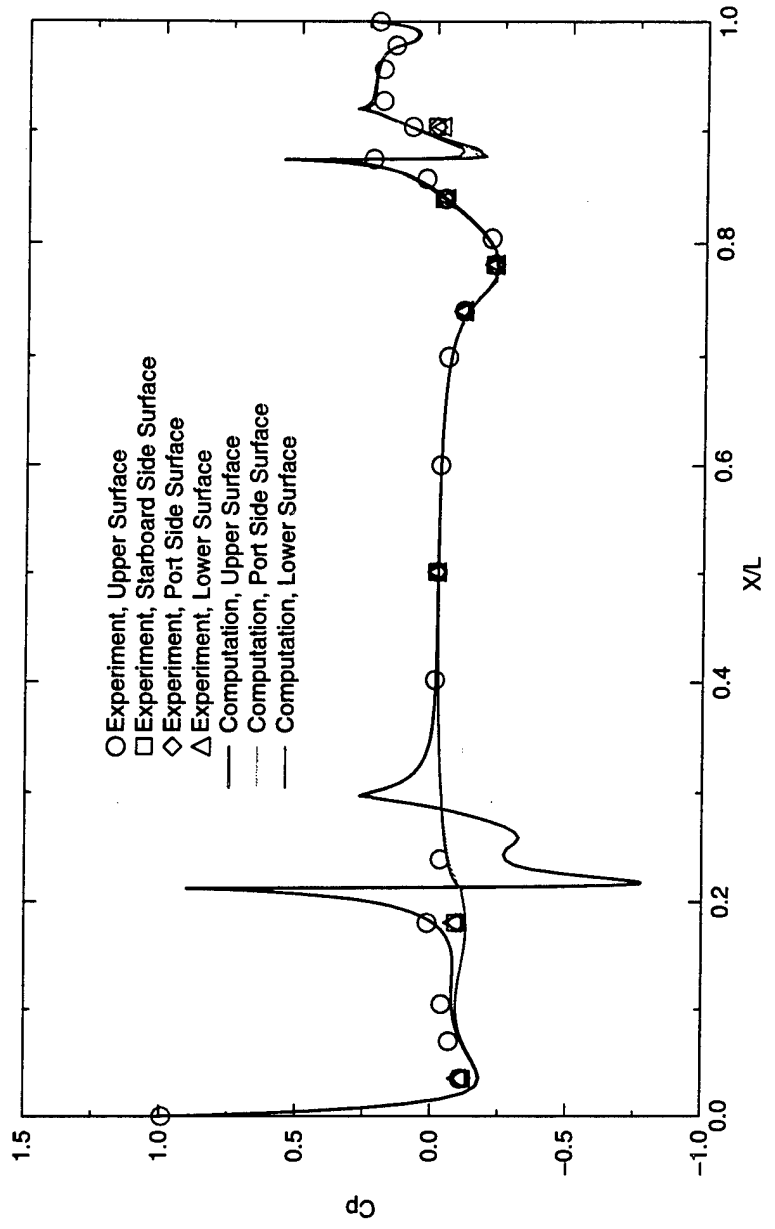


Figure 57. Computed and Measured Static-Pressure Distributions on the Hull of SUBOFF with a Sail and Four Stern Appendages at a  $0^\circ$  Angle of Attack and  $Re = 12,000,000$

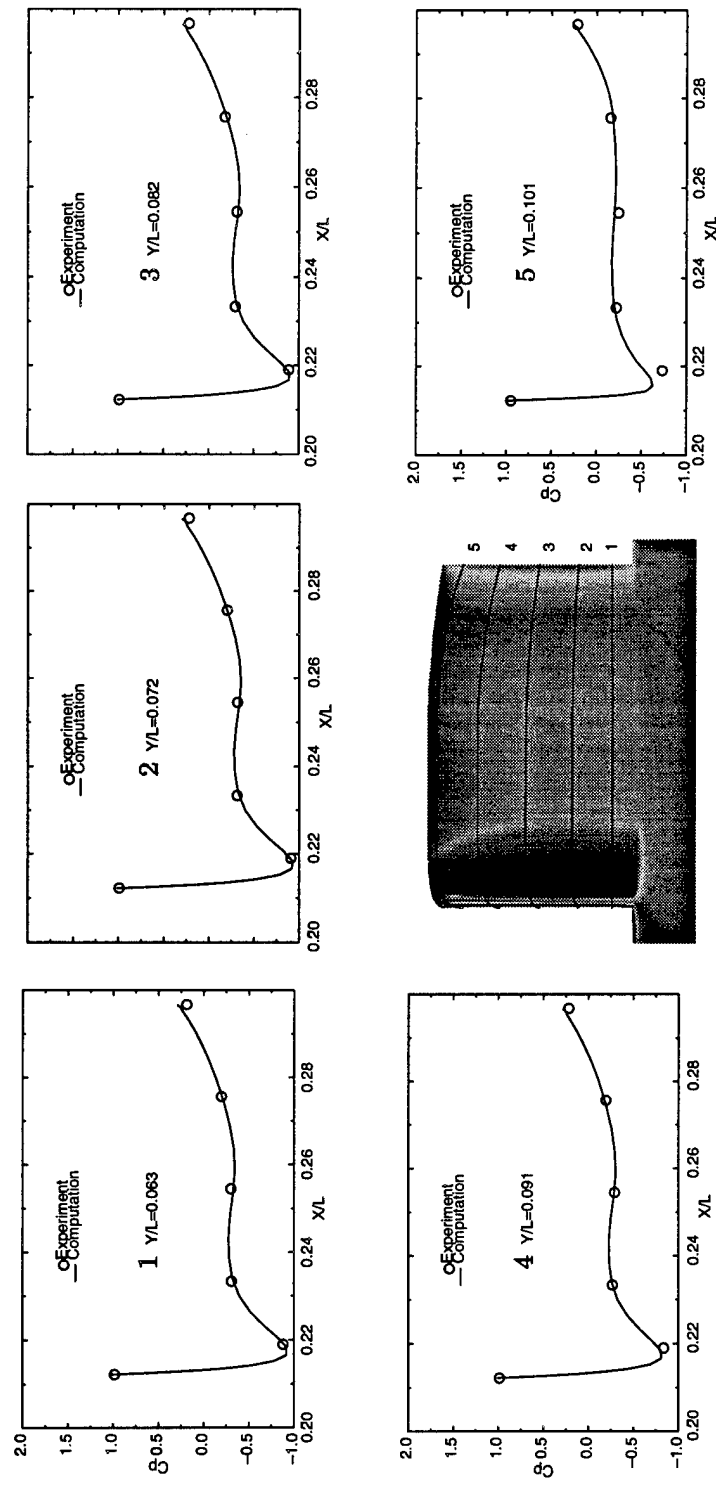


Figure 58. Computed and Measured Static-Pressure Distributions on the Sail Surface of SUBOFF with a Sail and Four Stern Appendages at a  $0^\circ$  Angle of Attack and  $Re = 12,000,000$

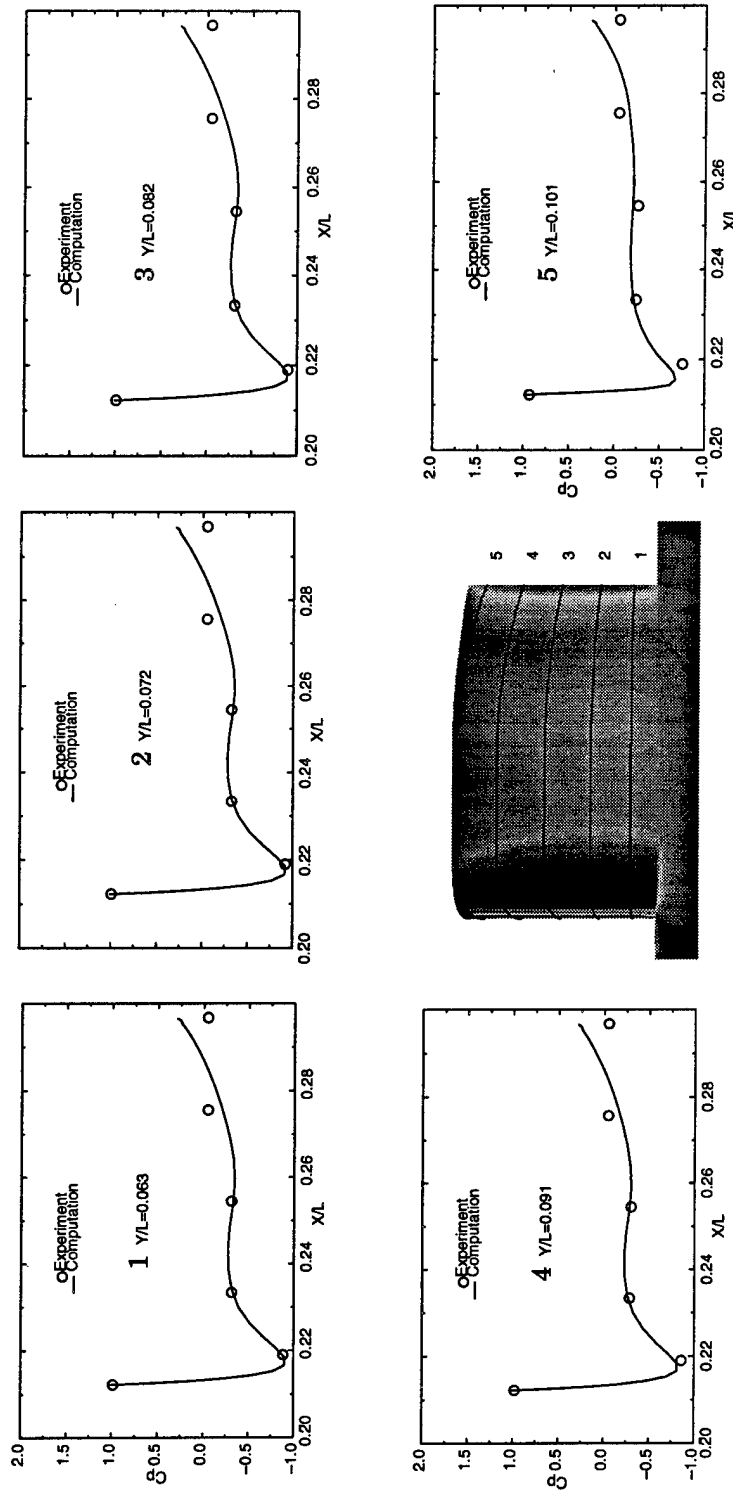


Figure 59. Computed and Measured Static-Pressure Distributions on the Sail Surface of SUBOFF with a Sail and Four Stern Appendages at a  $2^\circ$  Angle of Attack and  $Re = 12,000,000$

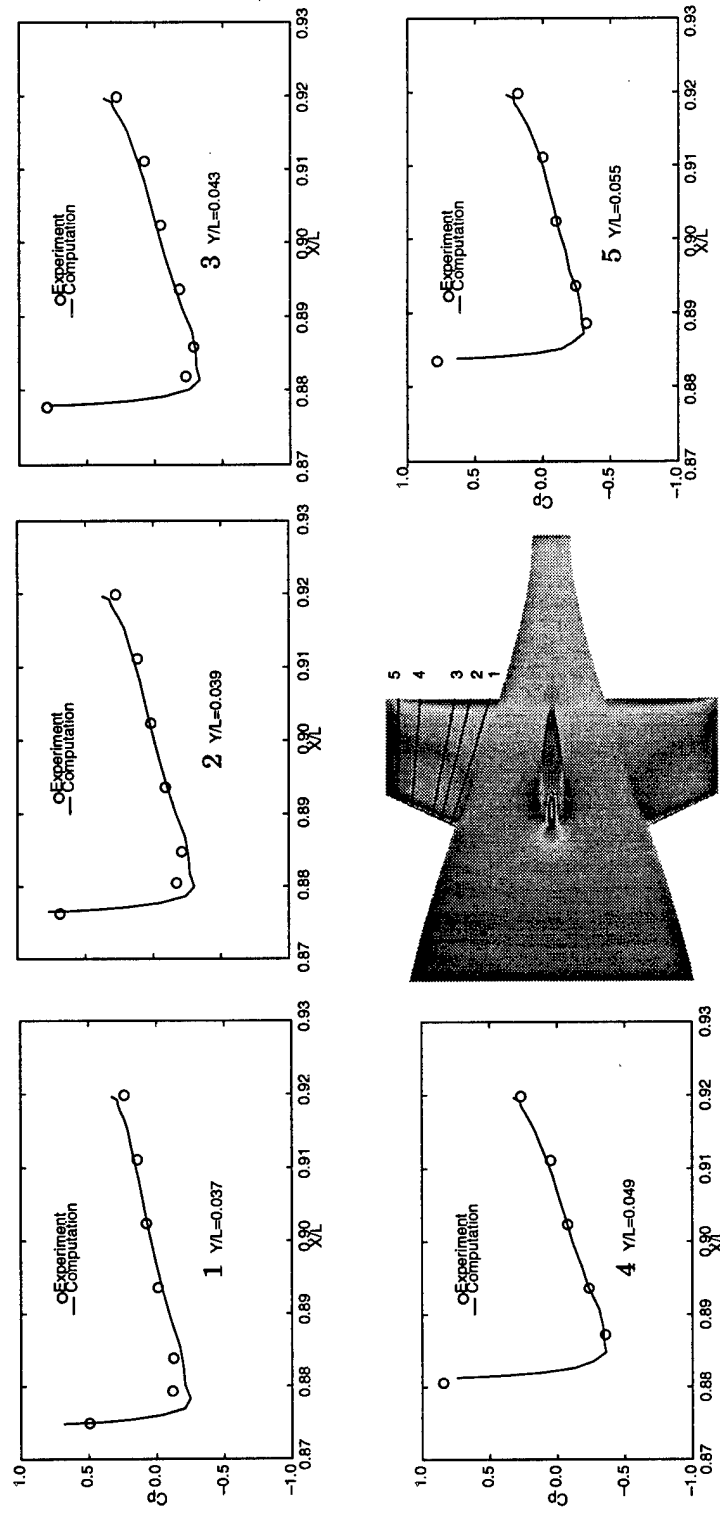


Figure 60. Computed and Measured Static-Pressure Distributions on the Upper Fin Surface of SUBOFF with a Sail and Four Stern Appendages at a 0° Angle of Attack and  $Re = 12,000,000$

Figure 60.

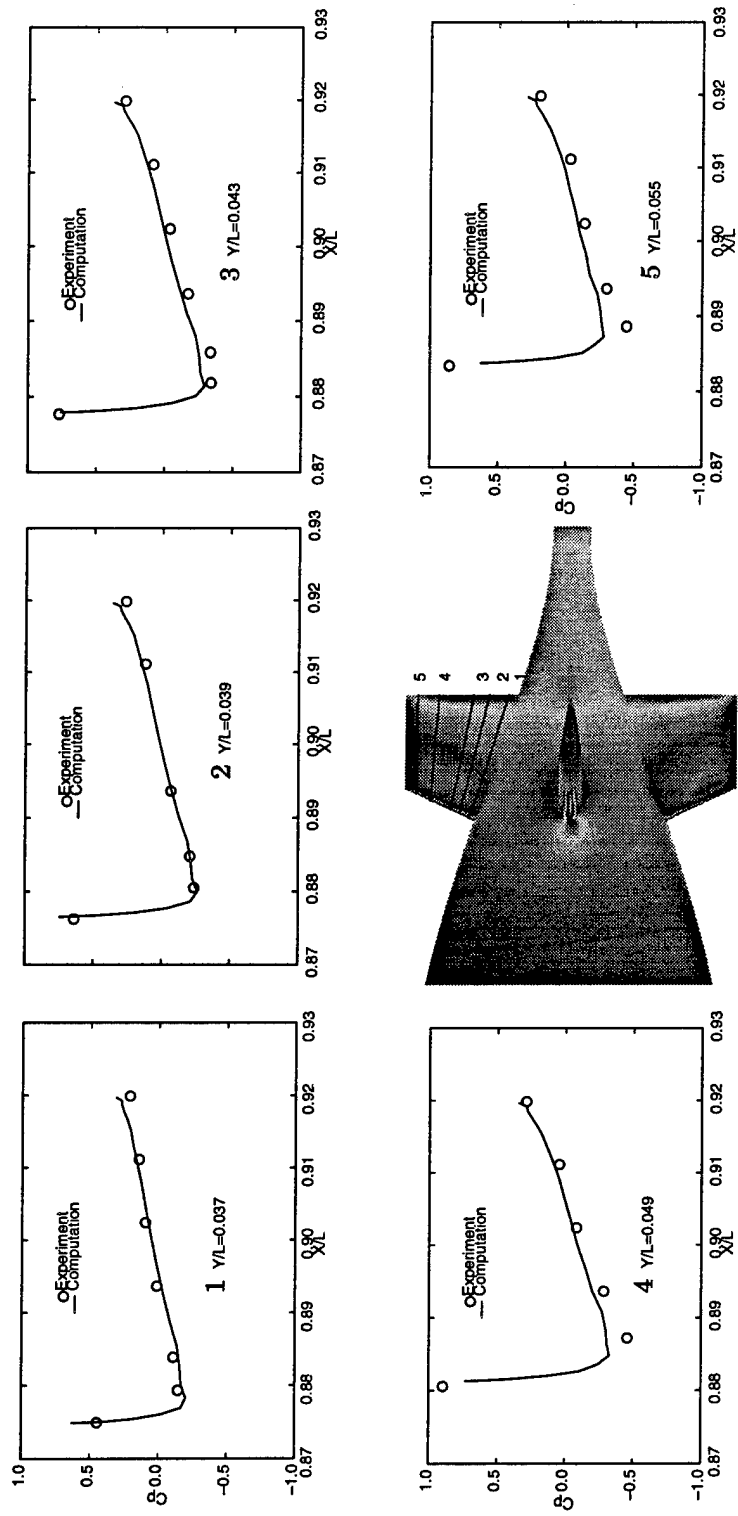


Figure 61. Computed and Measured Static-Pressure Distributions on the Upper Fin Surface of SUBOFF with a Sail and Four Stern Appendages at a  $2^\circ$  Angle of Attack and  $Re = 12,000,000$

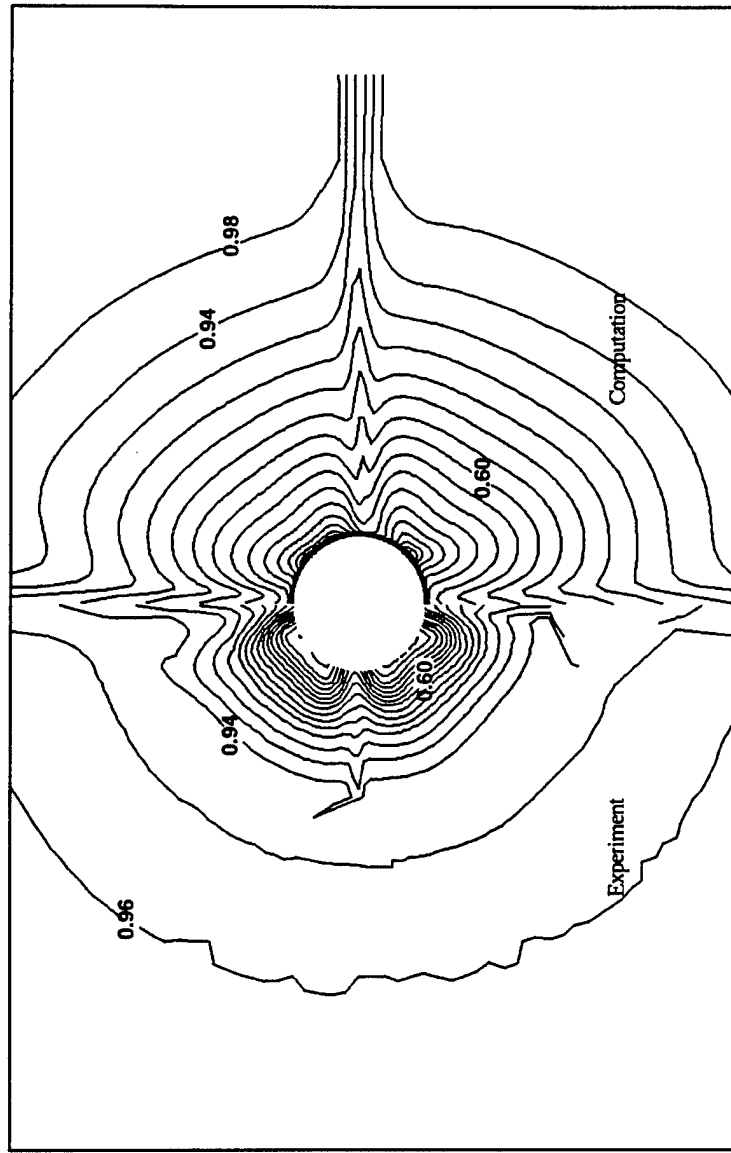


Figure 62. Computed and Measured Contours of the  $u$ -Component of Velocity at  $x/L = 0.978$  of SUBOFF with a Sail and Four Stern Appendages at  $0^\circ$  Angle of Attack and  $Re = 12,000,000$

Figure 62.

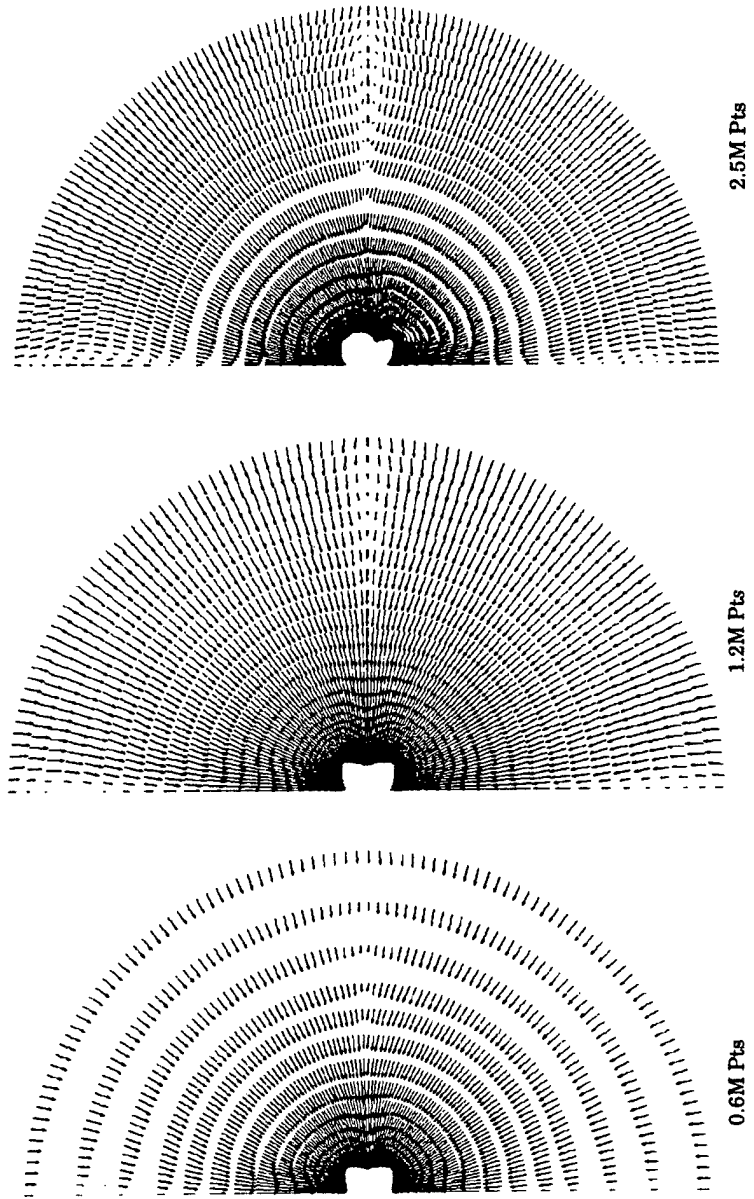


Figure 63. Comparisons of Crossflow Velocity Vectors at  $x/L = 0.978$  of SUBOFF with a Sail and Four Stern Appendages on Three Different Grids at a  $0^\circ$  Angle of Attack and  $Re = 12,000,000$

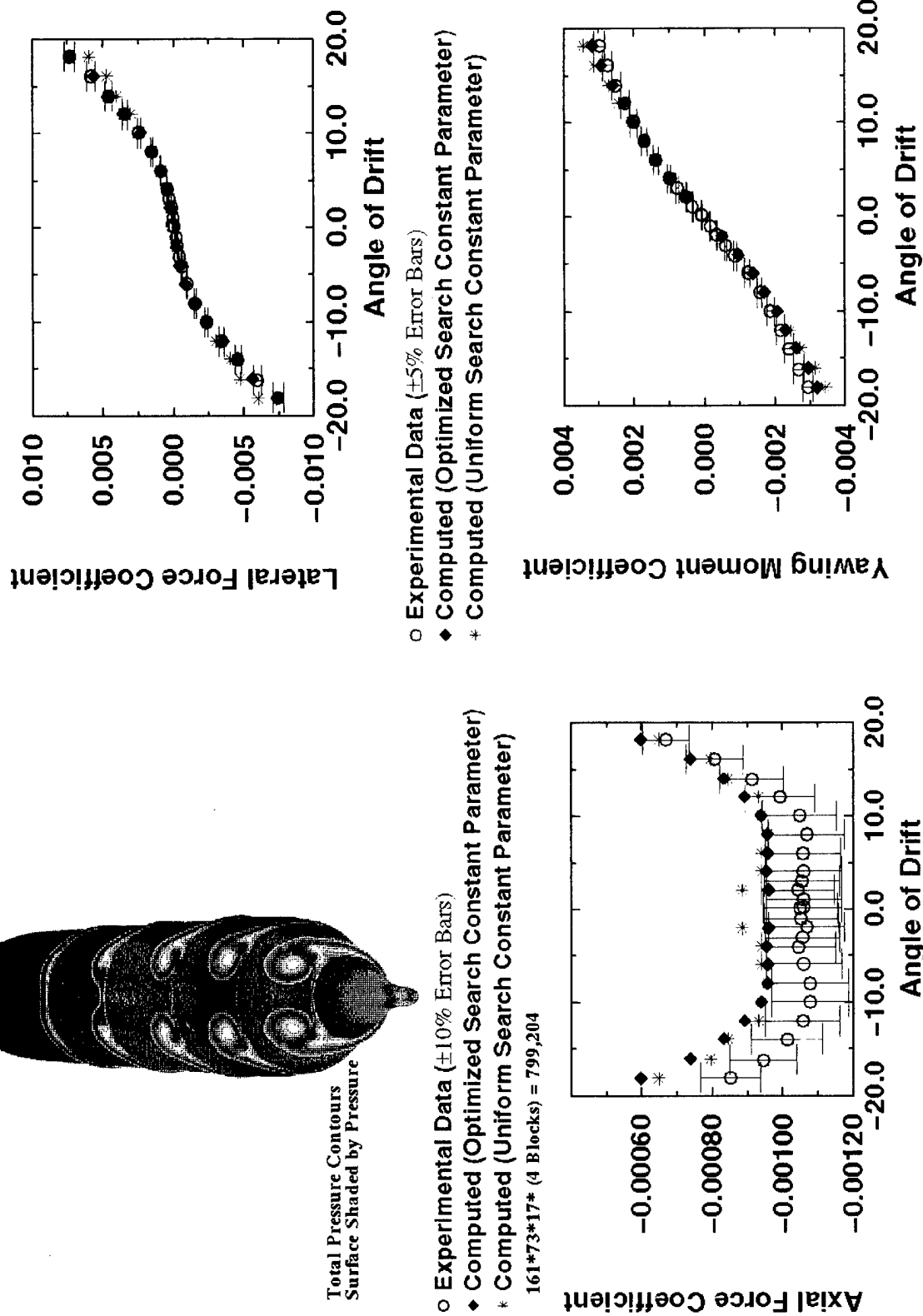
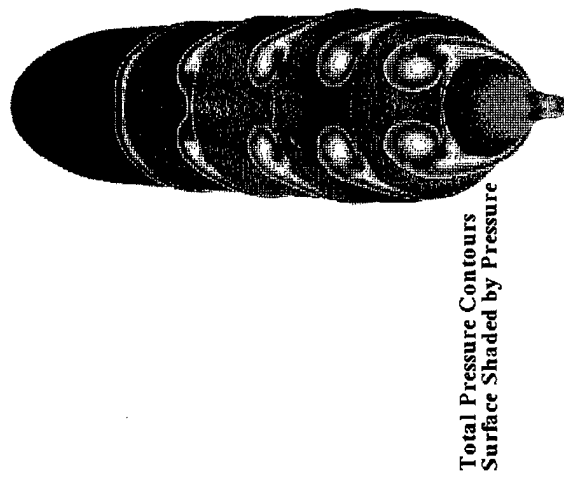
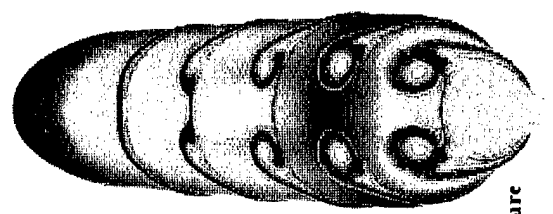
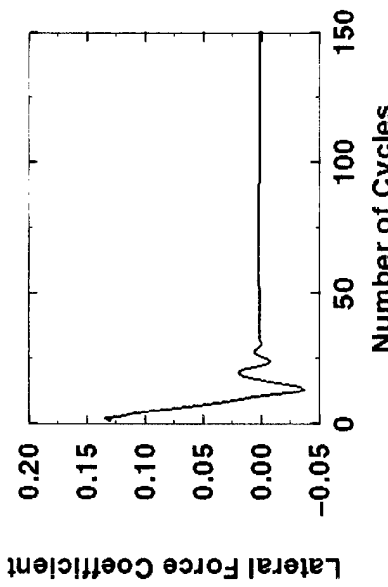


Figure 64.

Computed and Measured Axial Force, Lateral Force, and Yawing Moment for the SUBOFF Barebody at Various Angles of Drift and  $Re = 14,000,000$

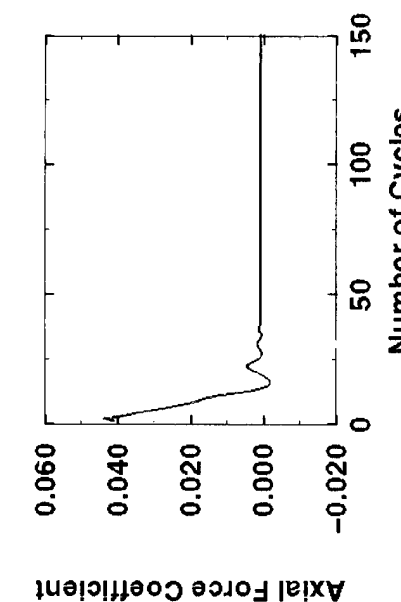


Total Pressure Contours  
Surface Shaded by Pressure

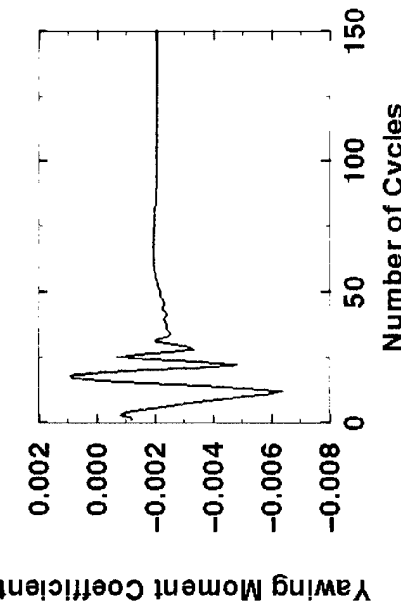


Lateral Force Coefficient

Convergence Histories  
Angle of Drift = 10.05 Degrees  
161\*73\*17\* (4 Blocks) = 799,204



Axial Force Coefficient



Yawning Moment Coefficient

Figure 65. Convergence Histories of the Computed Axial Force, Lateral Force, and Yawing Moment for the SUBOFF Barebody at a  $10.05^\circ$  Angle of Drift and  $Re = 14,000,000$

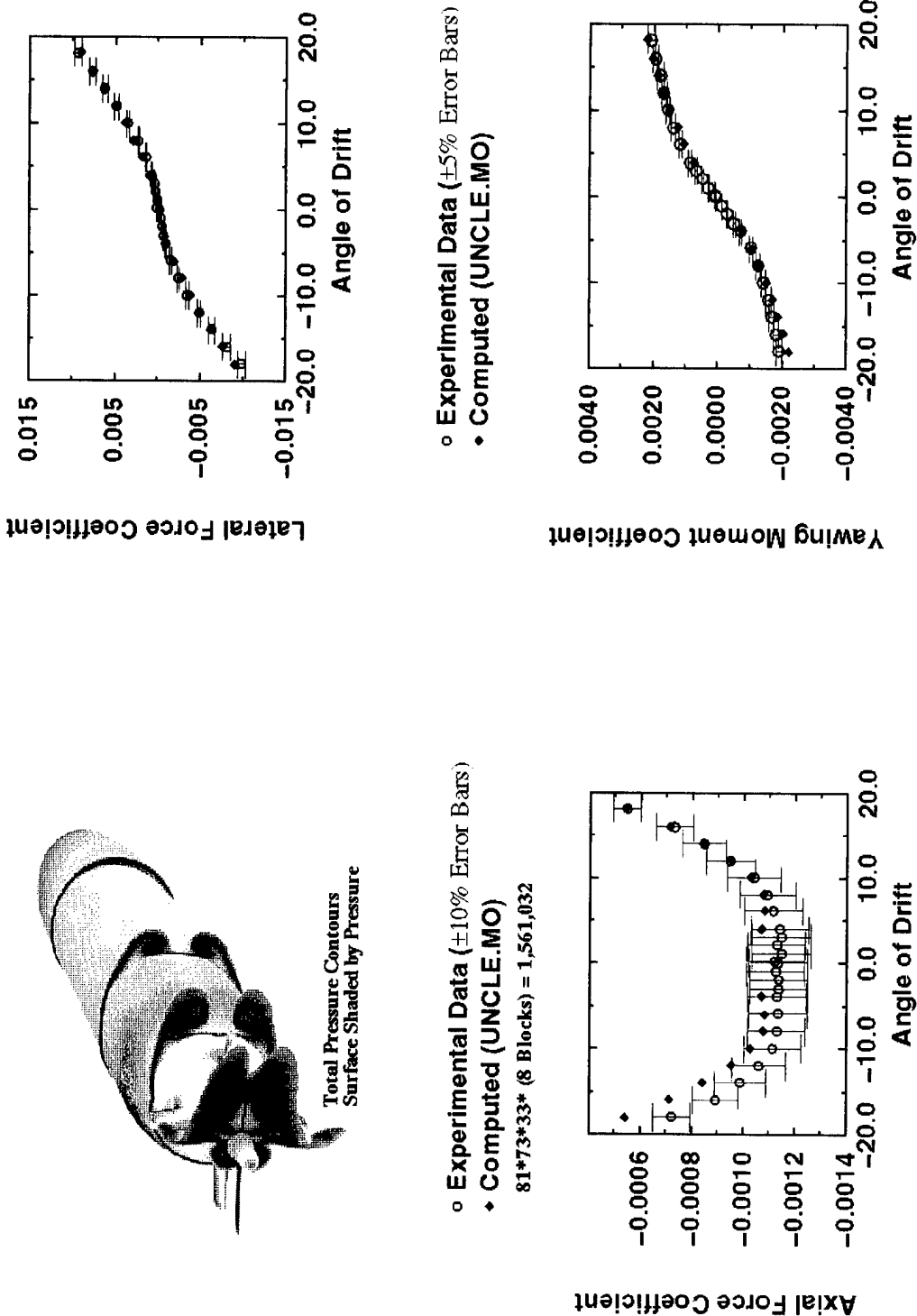


Figure 66. Computed and Measured Axial Force, Lateral Force, and Yawing Moment for SUBOFF with Four Stern Appendages at Various Angles of Drift and  $Re = 14,000,000$

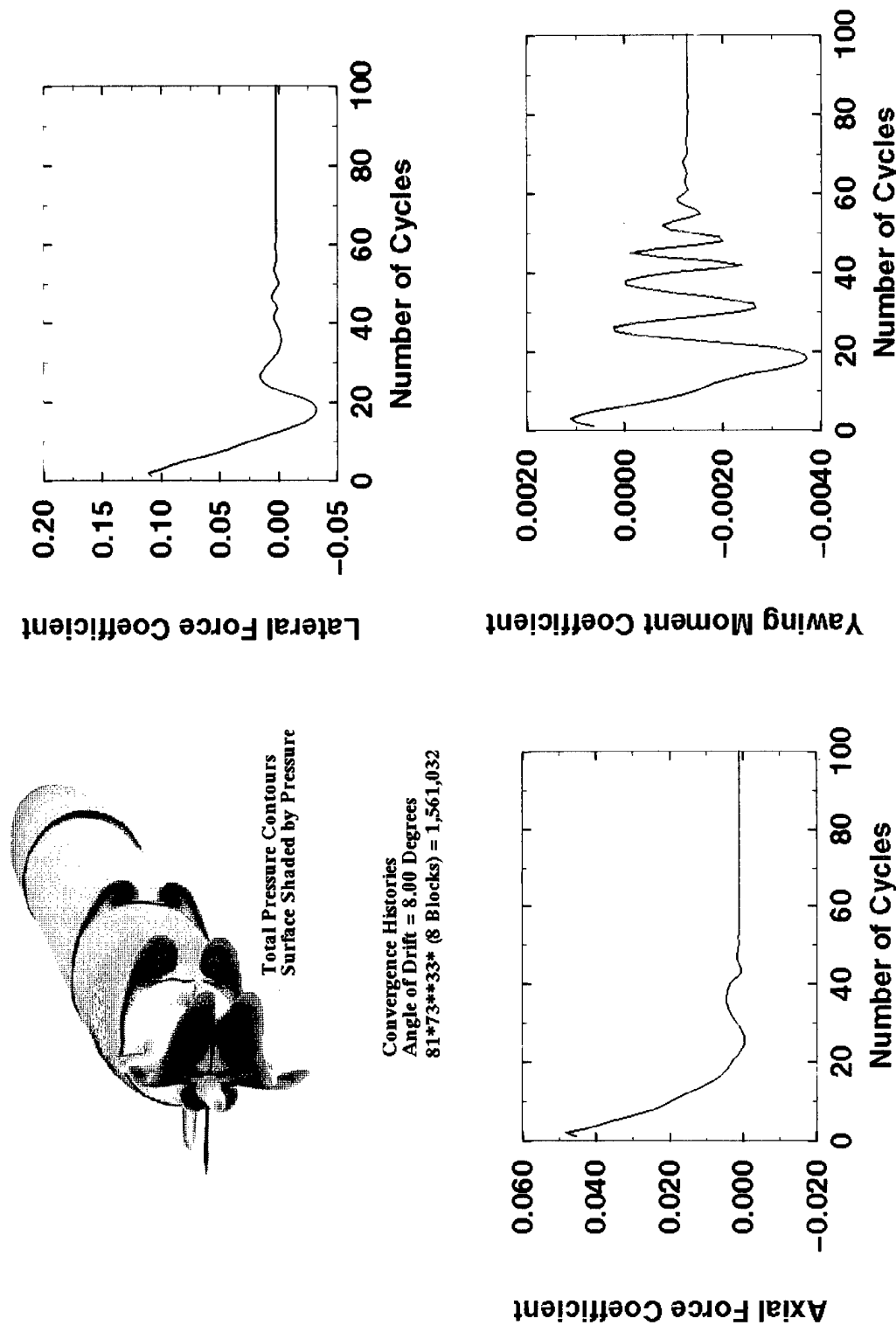


Figure 67. Convergence Histories of the Computed Axial Force, Lateral Force, and Yawing Moment for SUBOFF with Four Stern Appendages at an 8° Angle of Drift and  $Re = 14,000,000$

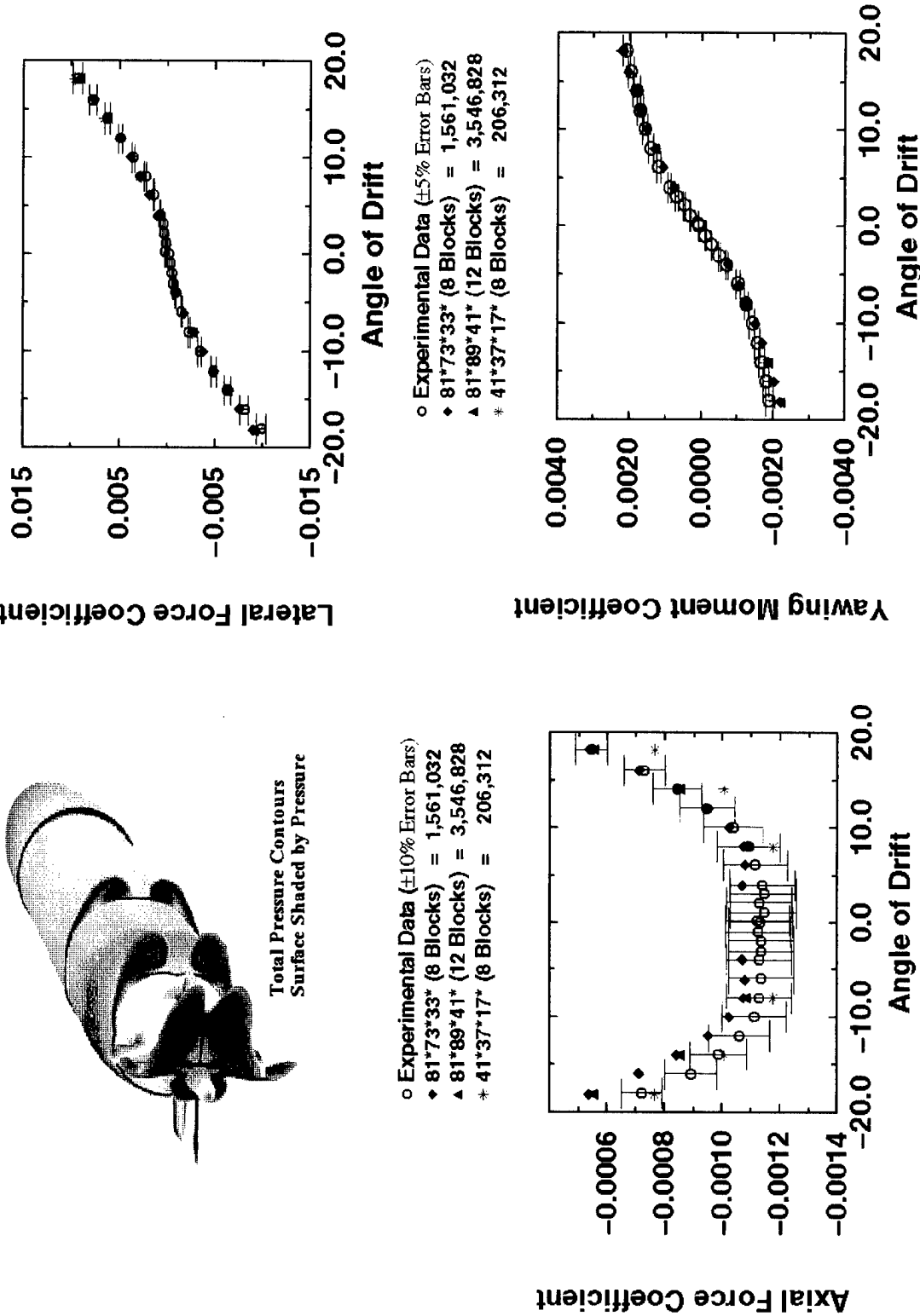


Figure 68. Computed and Measured Axial Force, Lateral Force, and Yawing Moment for SUBOFF with Four Stern Appendages on Three Different Grids at Various Angles of Drift and  $Re = 14,000,000$

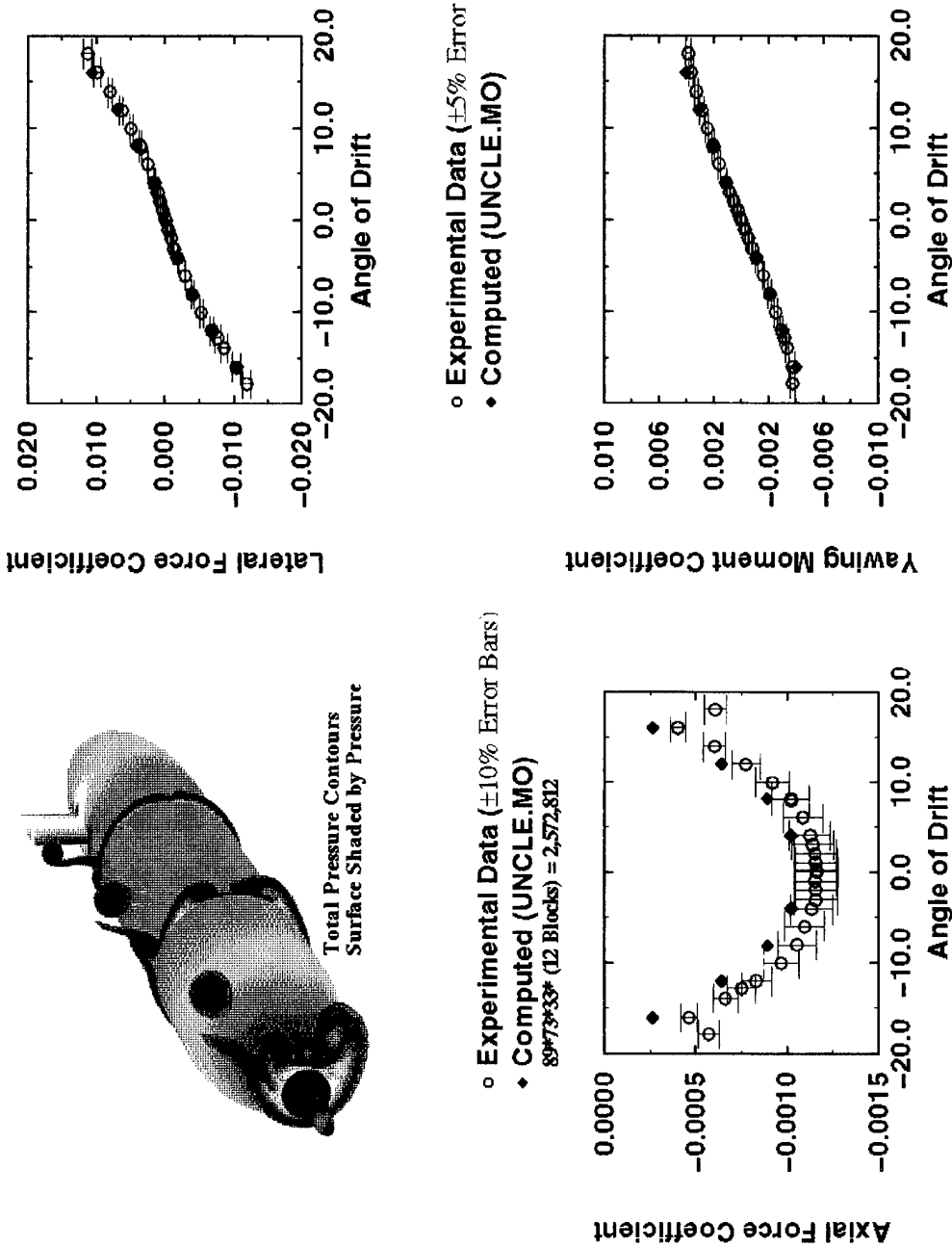


Figure 69. Computed and Measured Axial Force, Lateral Force, and Yawing Moment for SUBOFF with a Sail at Various Angles of Drift and  $Re = 14,000,000$

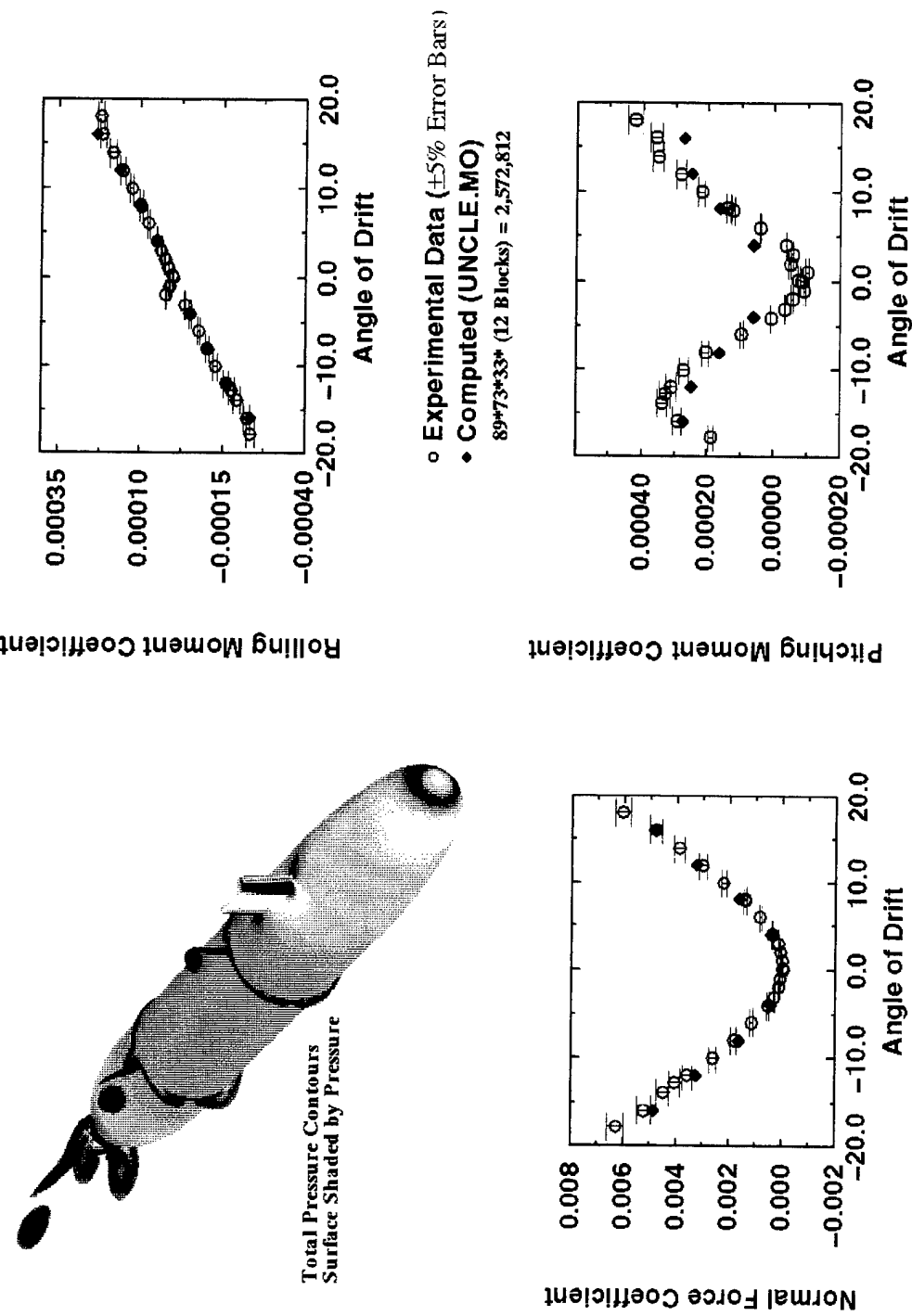


Figure 70. Computed and Measured Normal Force, Rolling Moment, and Pitching Moment for SUBOFF with a Sail at Various Angles of Drift and  $Re = 14,000,000$

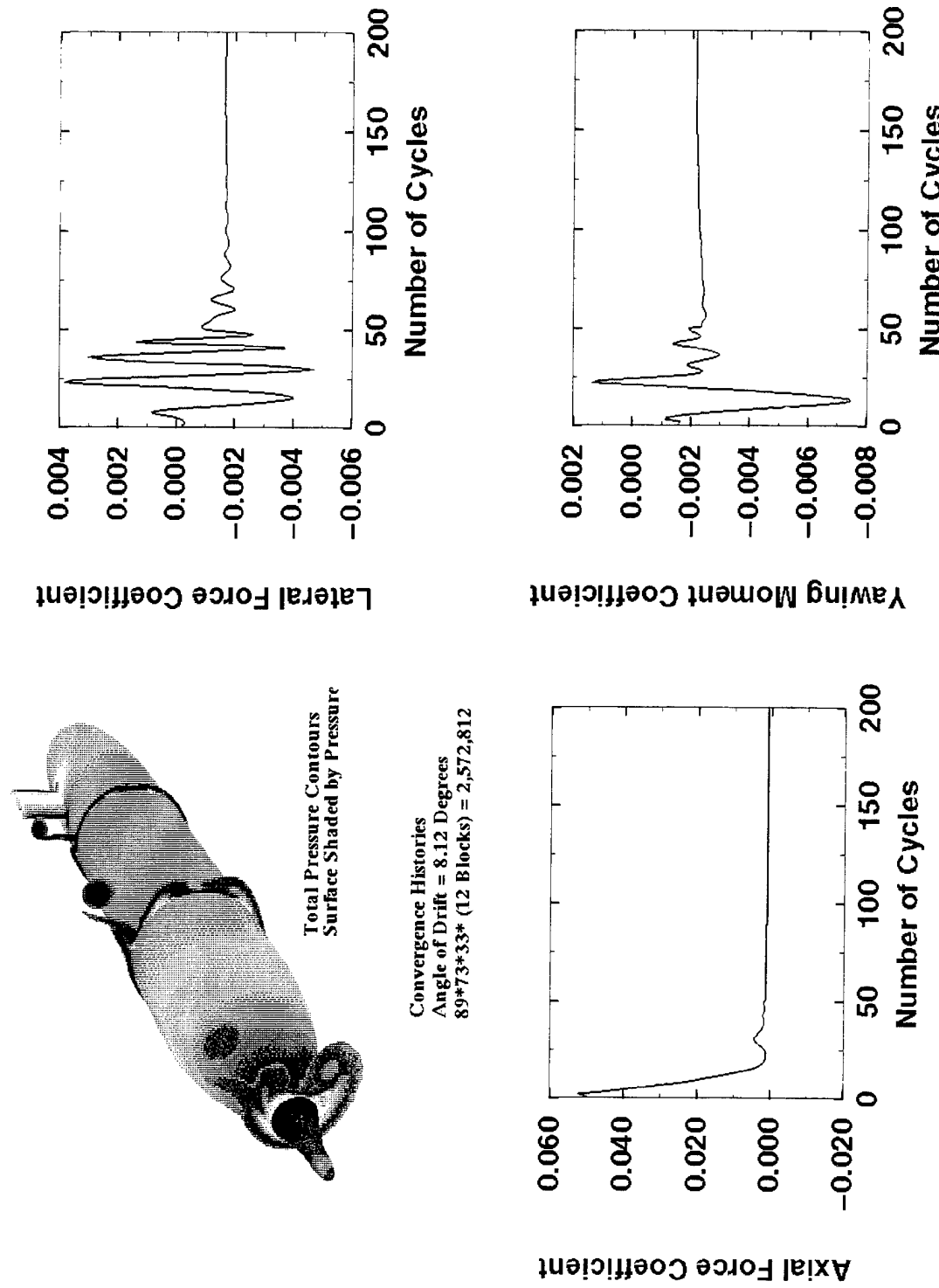


Figure 71. Convergence Histories of the Computed Axial Force, Lateral Force, and Yawing Moment for SUBOFF with a Sail at an 8° Angle of Drift and  $Re = 14,000,000$

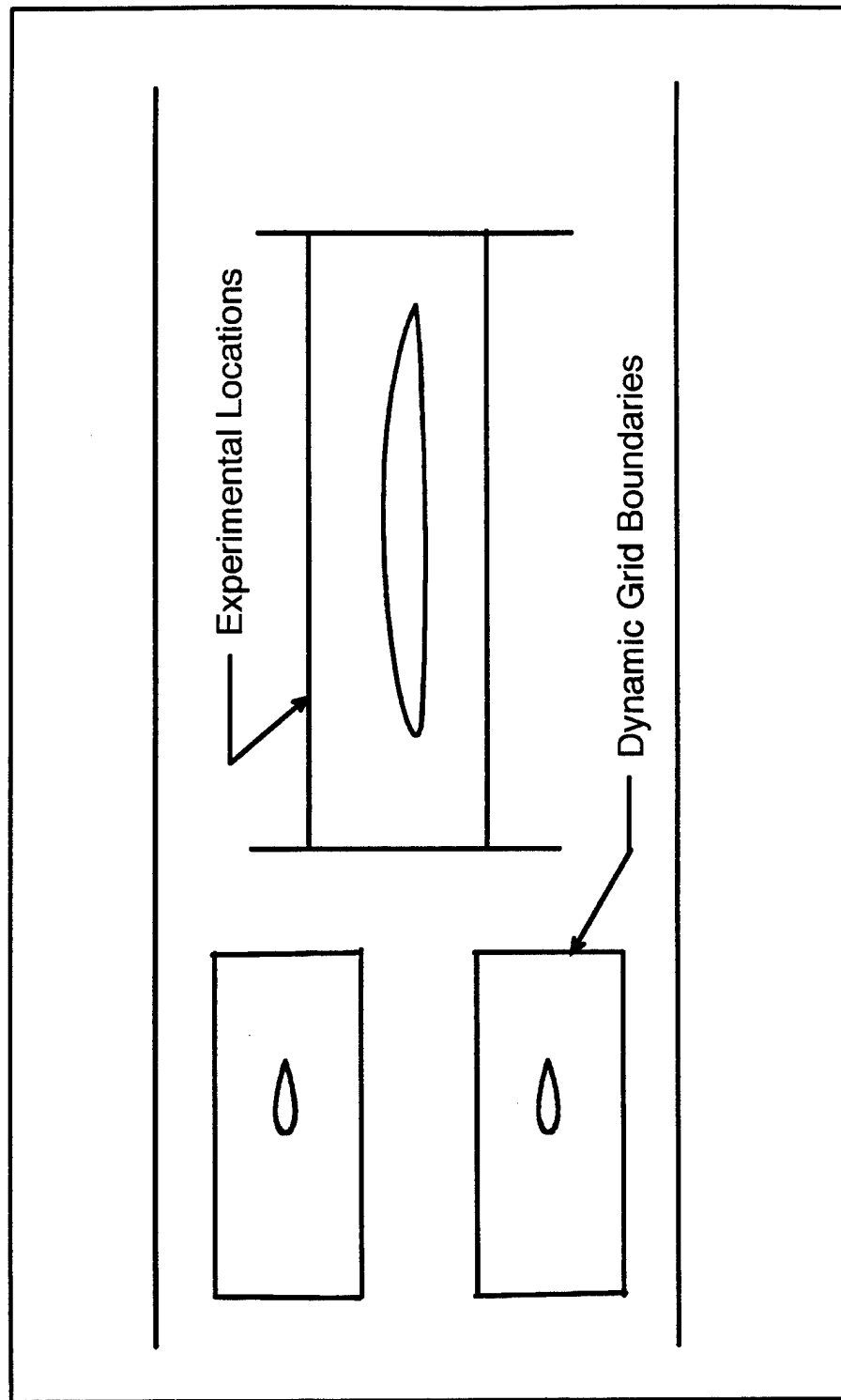


Figure 72. Schematic of the Flapping Foil Experiment

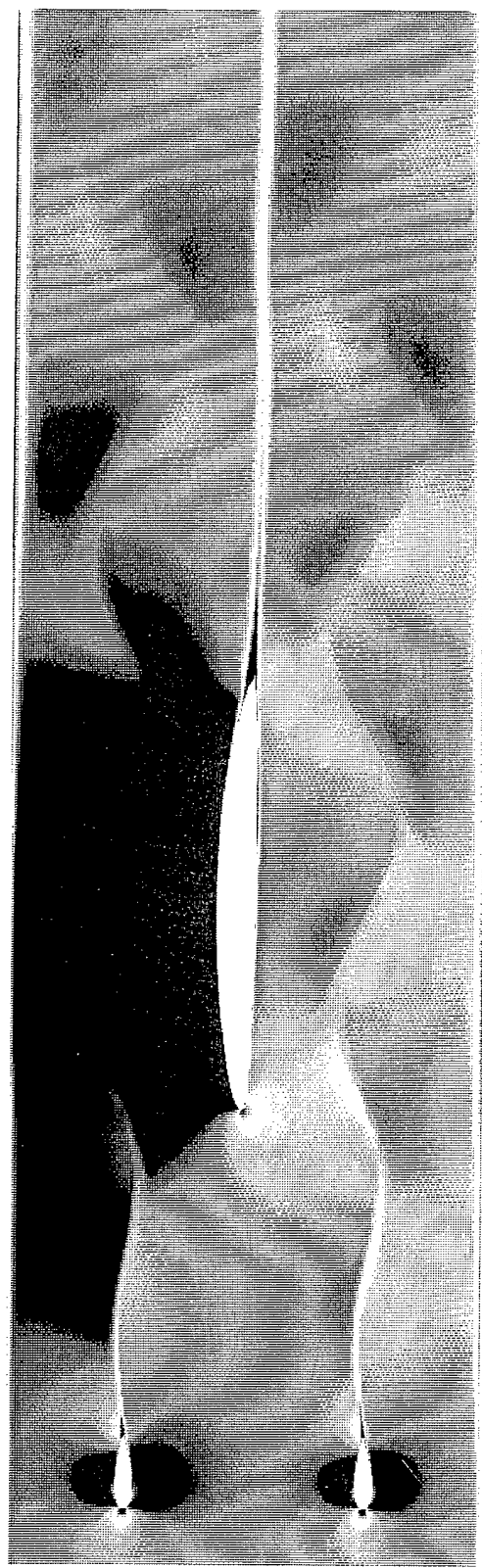


Figure 73.

Computed Velocity Magnitude for the Flapping Foil Experiment at  $Re = 3,780,000$   
after Five Complete Periods of Motion of the Two, Small NACA 0025 Hydrofoils

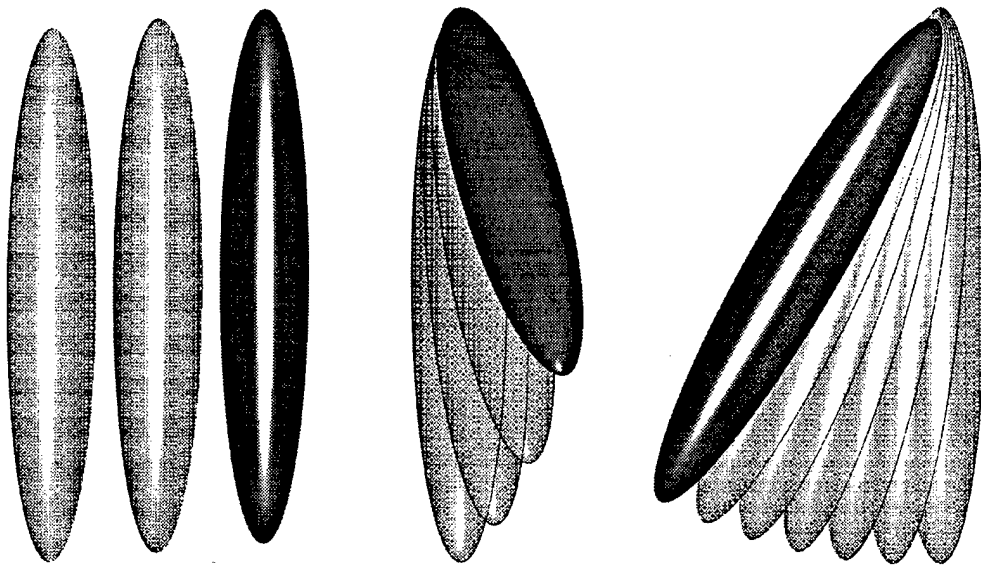


Figure 74.  
Schematic of the Prescribed Unsteady Plunge, Turning, and Pitch-Up Maneuvers  
for a 6:1 Prolate Spheroid

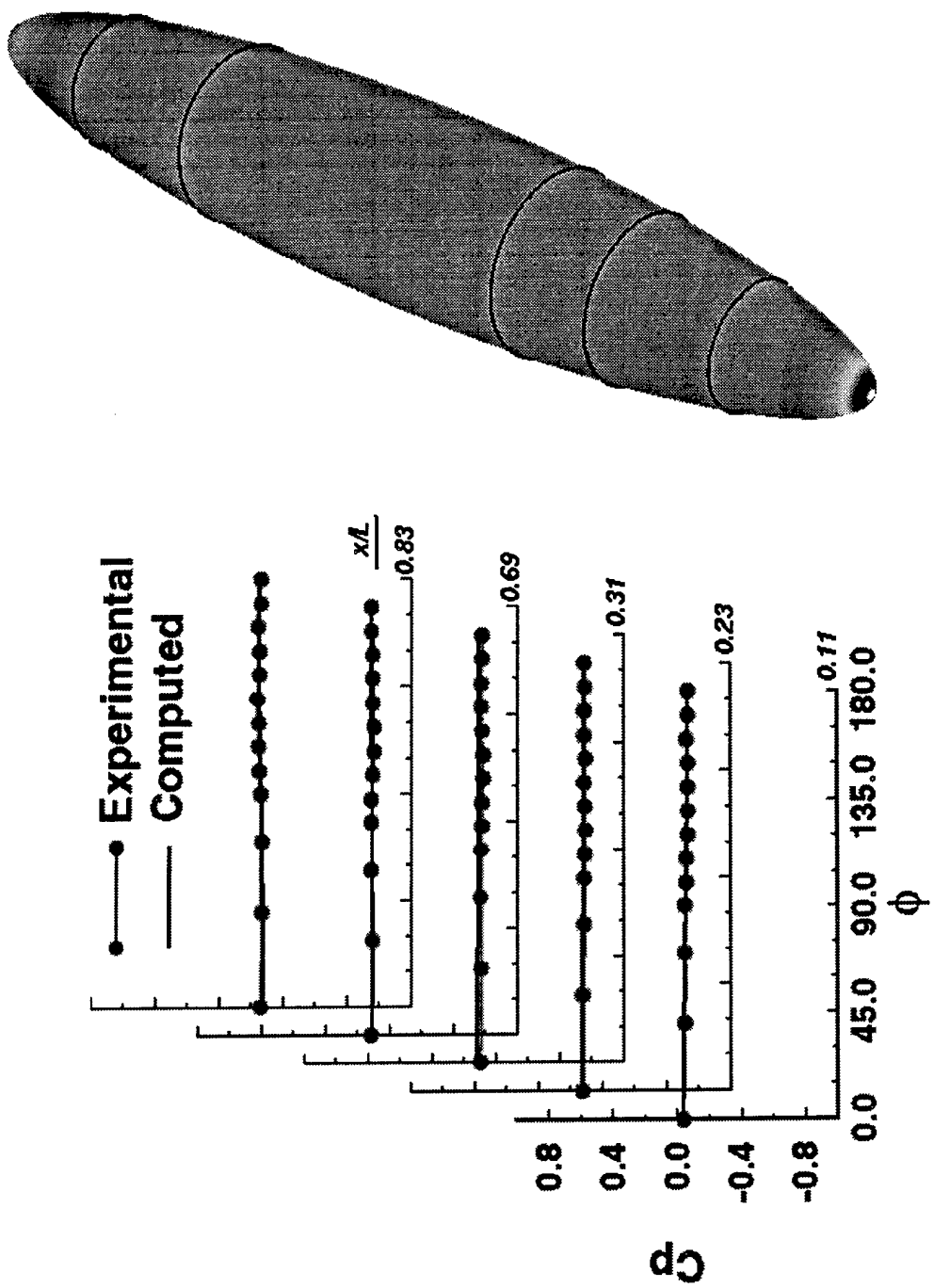


Figure 75a. Computed and Measured Surface-Pressure Distributions for the Plunge Maneuver of a 6:1 Prolate Spheroid at  $Re = 4,200,000$ :  
 (a) Displacement of Six Inches

Figure 75a.

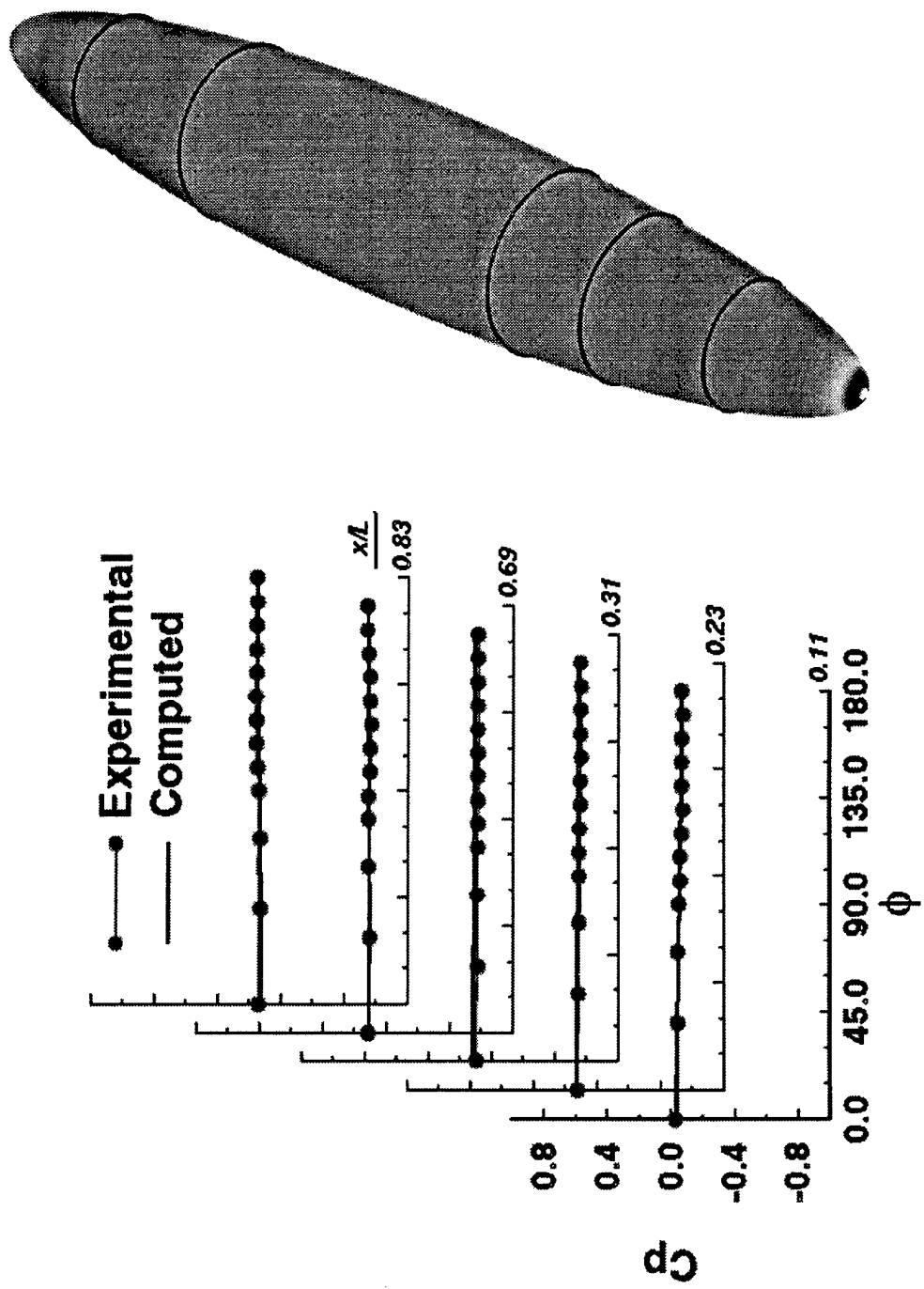


Figure 75b. Computed and Measured Surface-Pressure Distributions for the Plunge Maneuver of a 6:1 Prolate Spheroid at  $Re = 4,200,000$ :  
 (b) Displacement of Twelve Inche

Figure 75b.

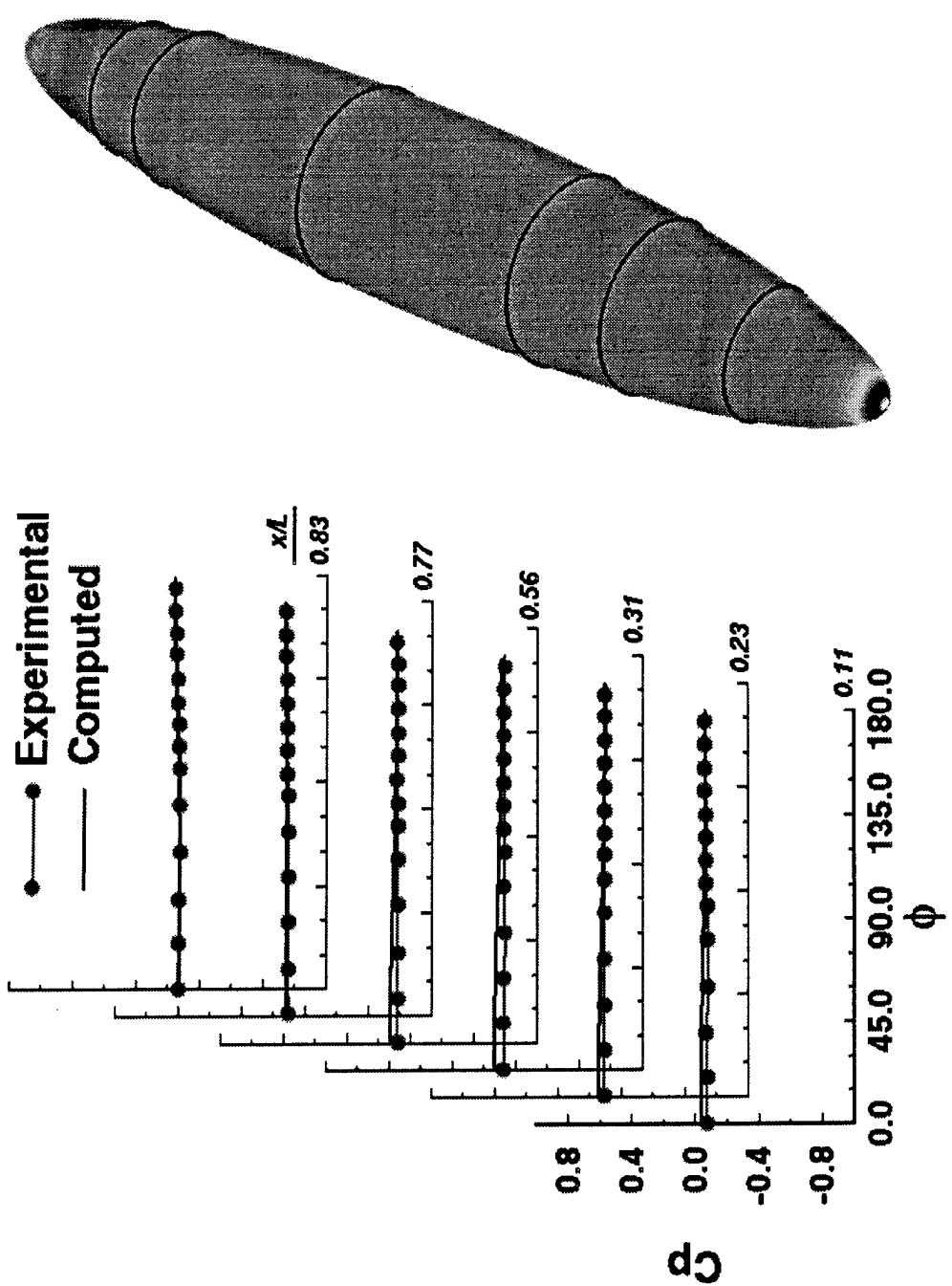


Figure 76a. Computed and Measured Surface-Pressure Distributions for the Turning Maneuver of a 6:1 Prolate Spheroid at  $Re = 4,200,000$ :  
 (a)  $2^\circ$  of Motion

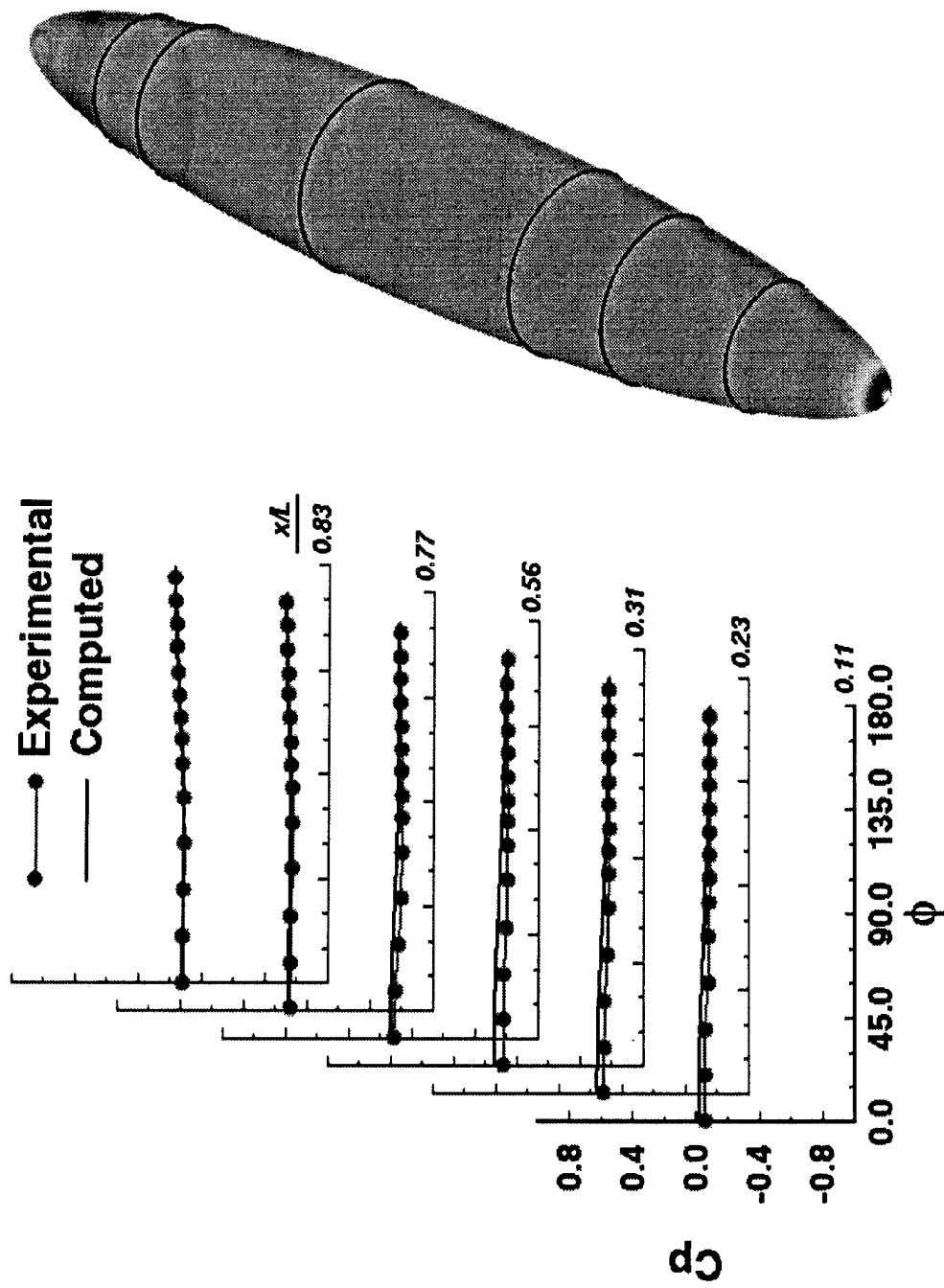


Figure 76b. Computed and Measured Surface-Pressure Distributions for the Turning Maneuver of a 6:1 Prolate Spheroid at  $Re = 4,200,000$ :  
 (b)  $4^\circ$  of Motion

Figure 76b.

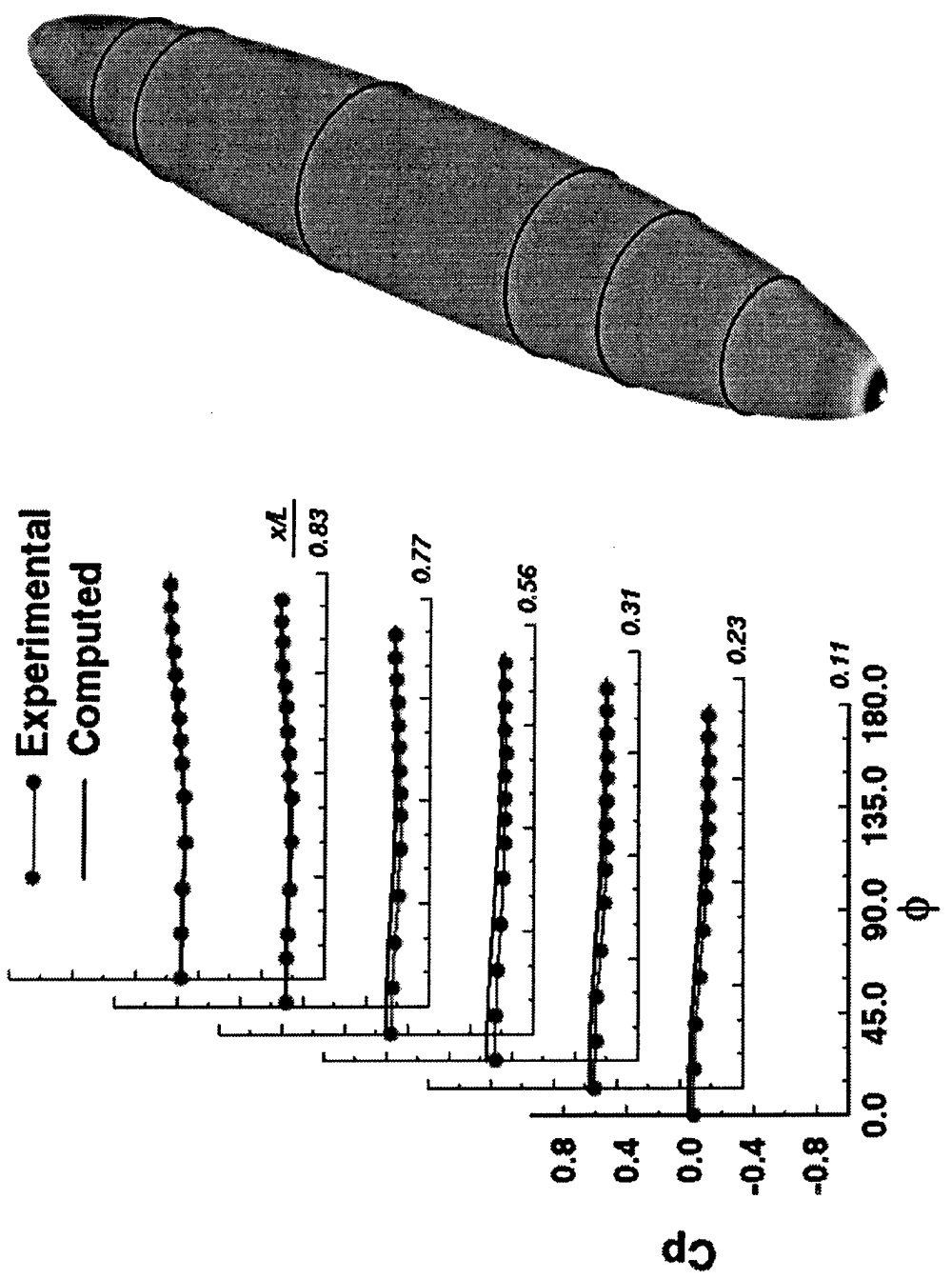


Figure 76c. Computed and Measured Surface-Pressure Distributions for the Turning Maneuver of a 6:1 Prolate Spheroid at  $Re = 4,200,000$ :  
(c)  $6^\circ$  of Motion

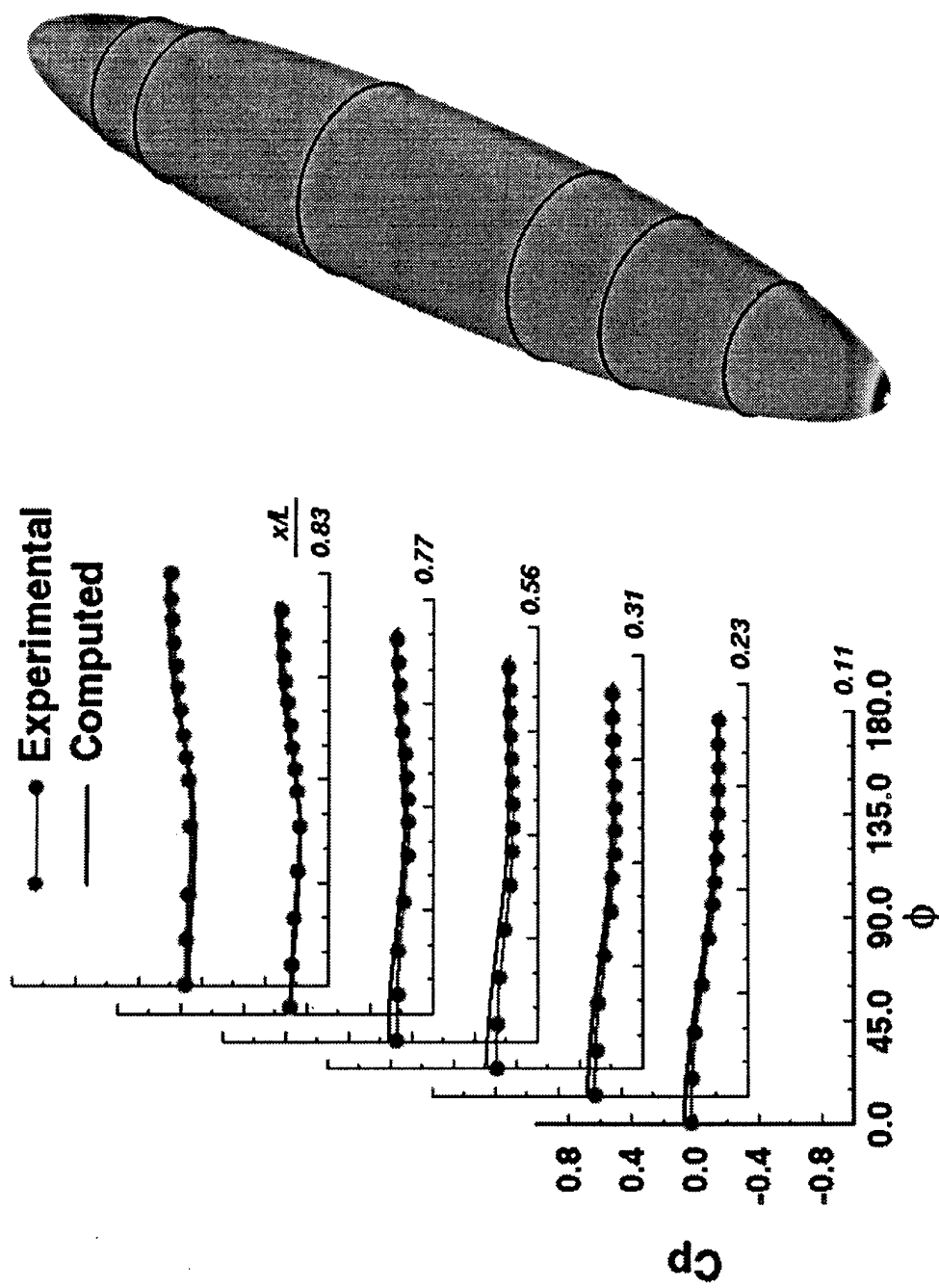


Figure 76d. Computed and Measured Surface Pressure Distributions for the Turning Maneuver of a 6:1 Prolate Spheroid at  $Re = 4,200,000$ :  
(d)  $8^\circ$  of Motion

Figure 76d.

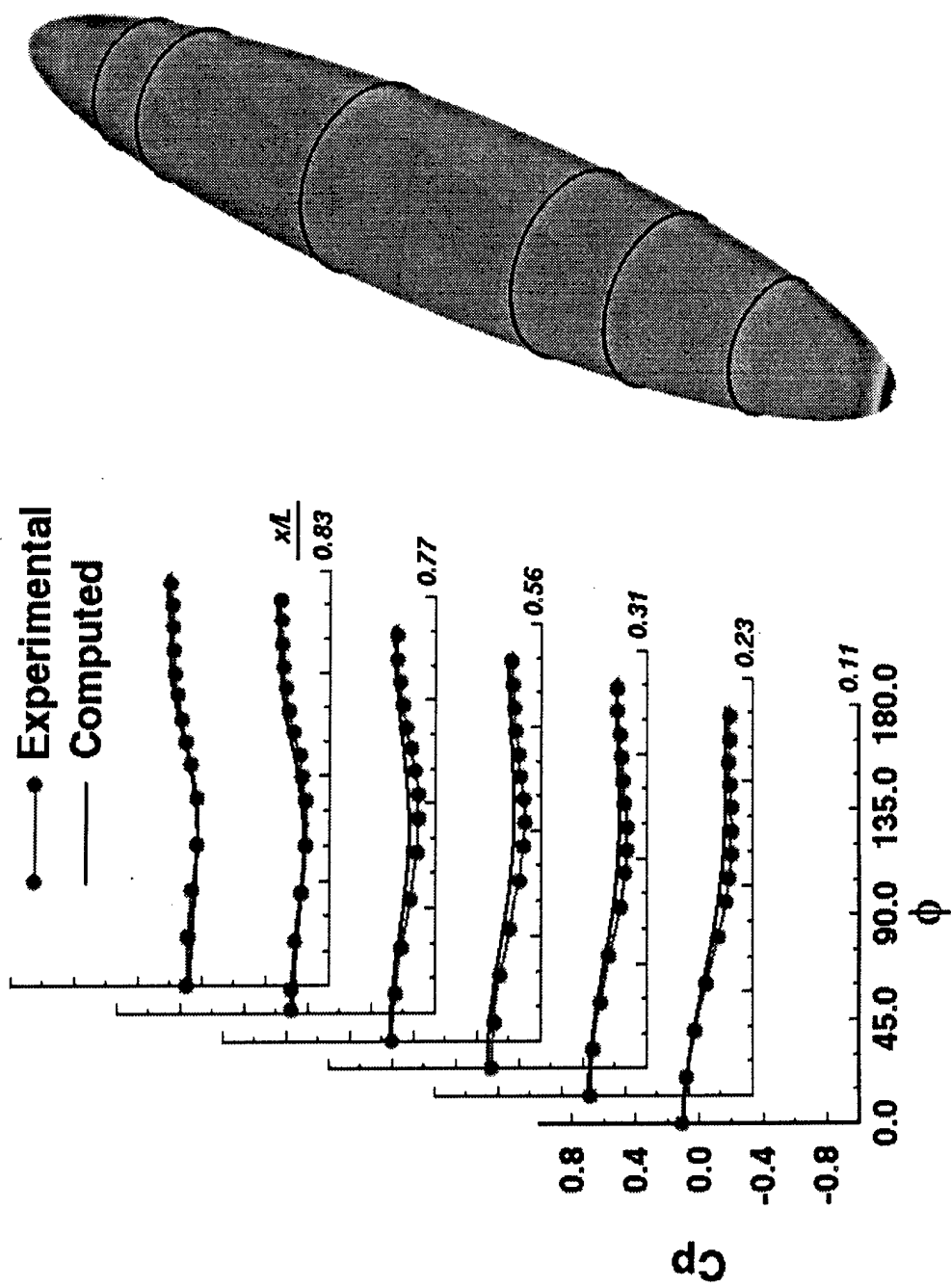


Figure 76e. Computed and Measured Surface-Pressure Distributions for the Turning Maneuver of a 6:1 Prolate Spheroid at  $Re = 4,200,000$ :  
(e)  $10^\circ$  of Motion

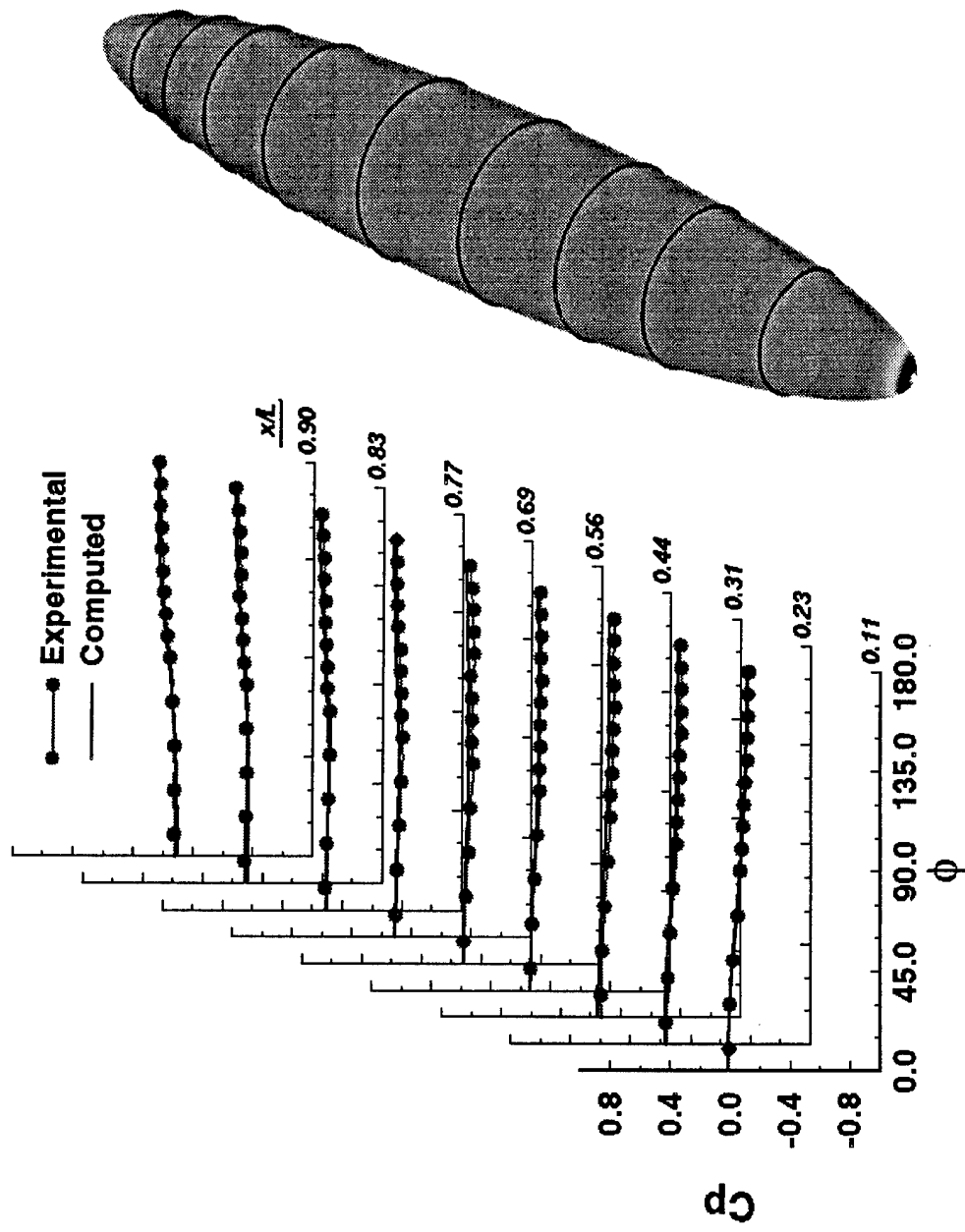


Figure 77a. Computed and Measured Surface-Pressure Distributions for the Pitch-Up Maneuver of a 6:1 Prolate Spheroid at  $Re = 4,200,000$ :  
 (a)  $5^\circ$  of Motion

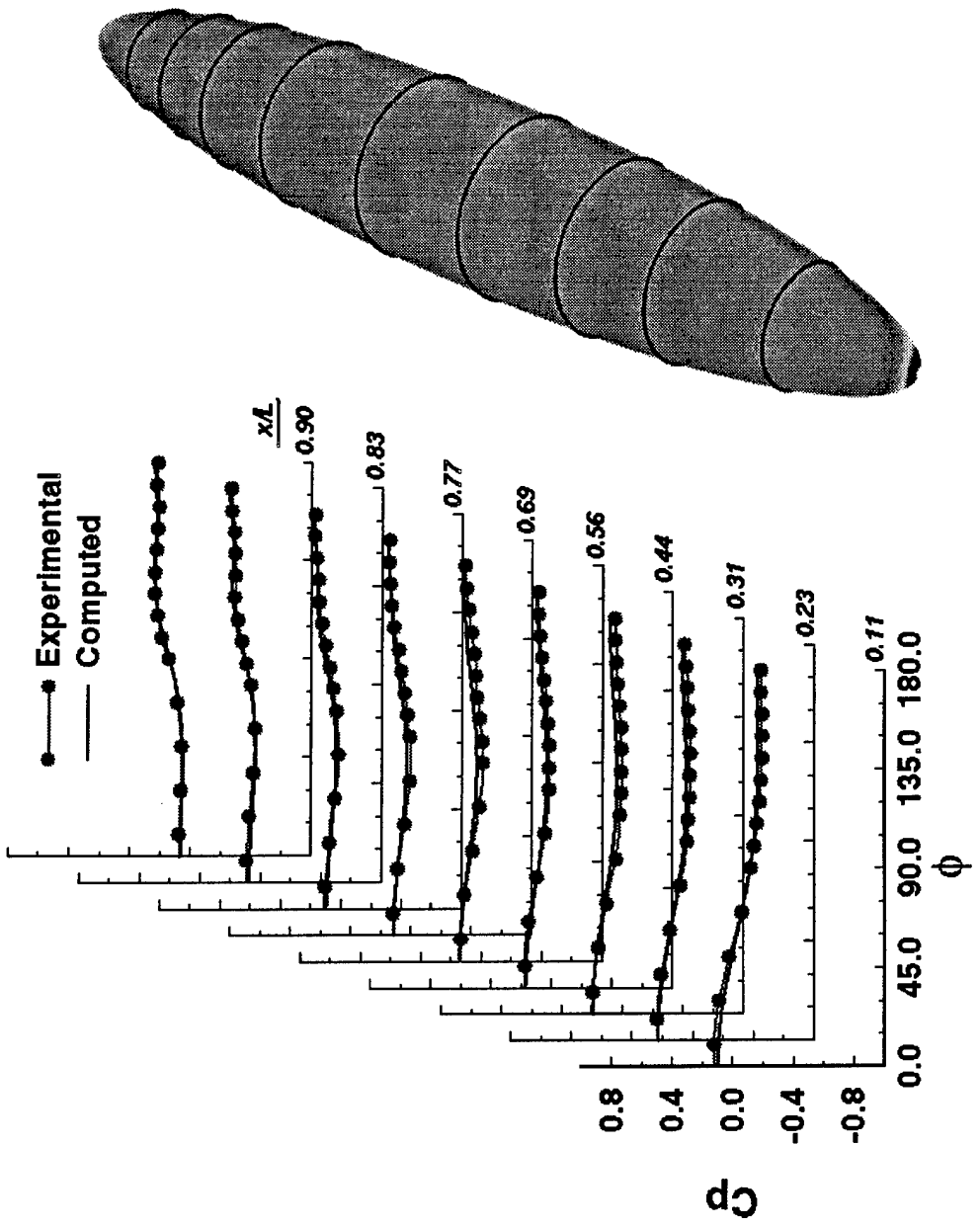


Figure 77b. Computed and Measured Surface-Pressure Distributions for the Pitch-Up Maneuver of a 6:1 Prolate Spheroid at  $Re = 4,200,000$ :  
 (b)  $10^\circ$  of Motion

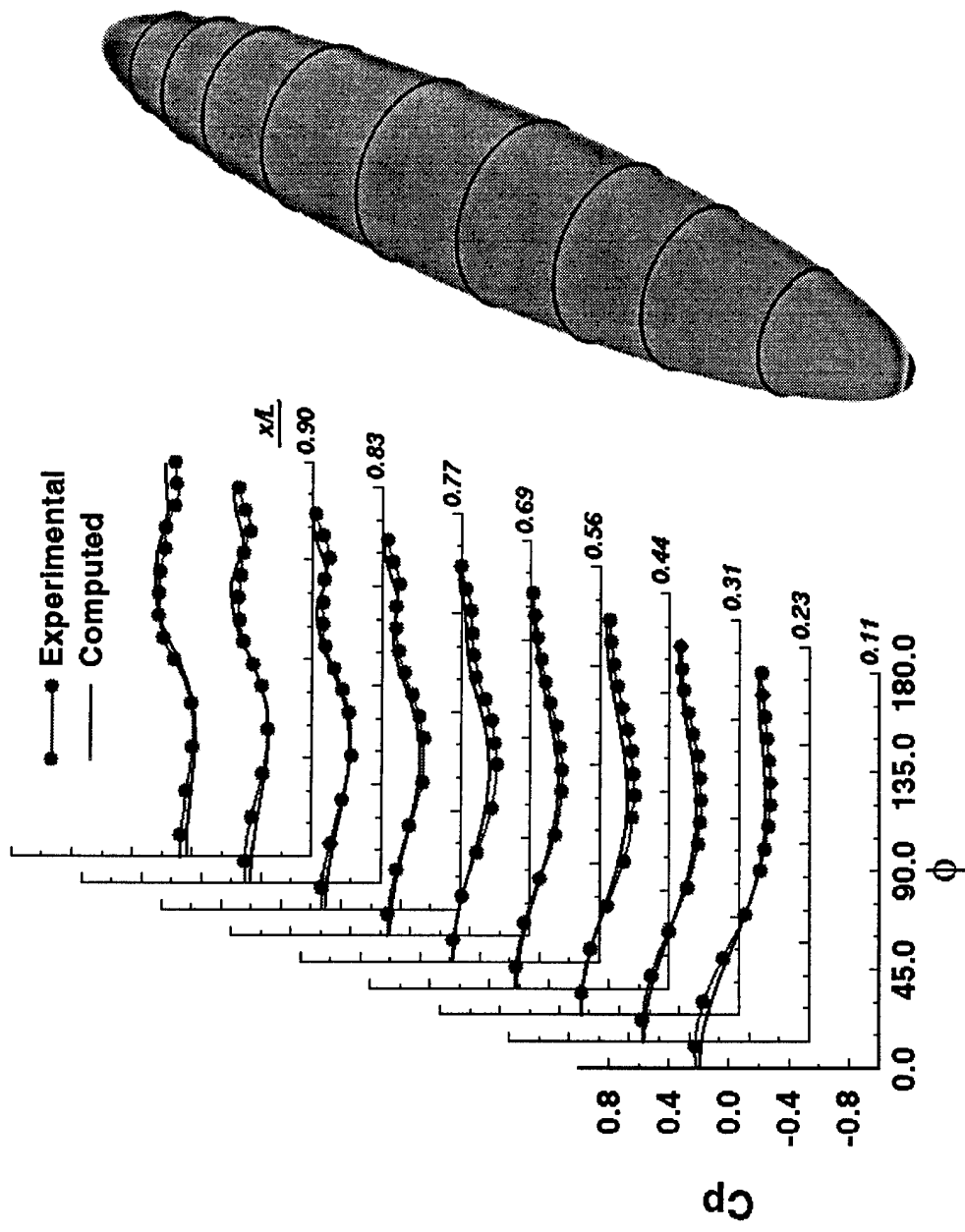


Figure 77c. Computed and Measured Surface-Pressure Distributions for the Pitch-Up Maneuver of a 6:1 Prolate Spheroid at  $Re = 4,200,000$ :  
(c)  $15^\circ$  of Motion

Figure 77c.

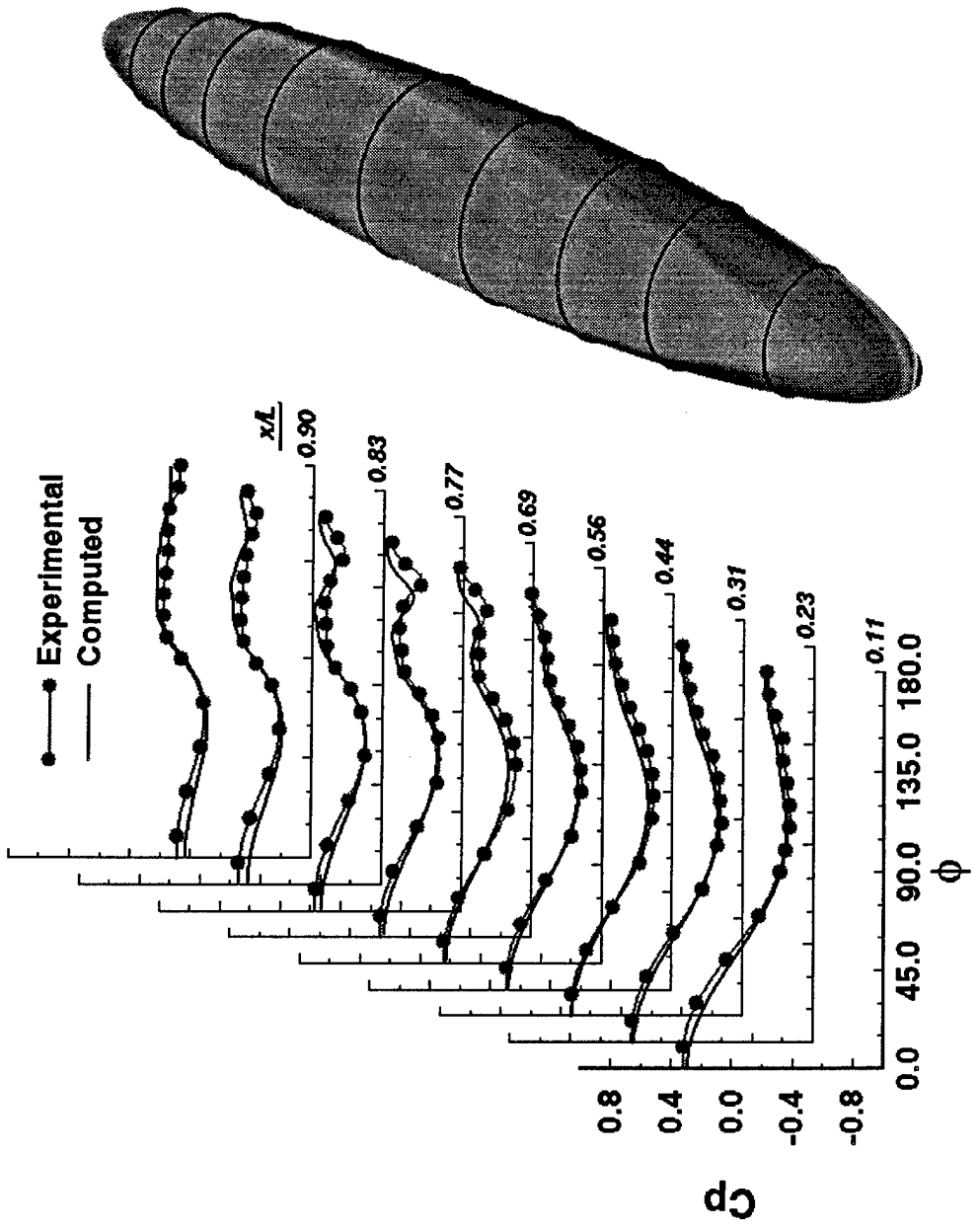


Figure 77d. Computed and Measured Surface-Pressure Distributions for the Pitch-Up Maneuver of a 6:1 Prolate Spheroid at  $Re = 4,200,000$ :  
(d)  $20^\circ$  of Motion

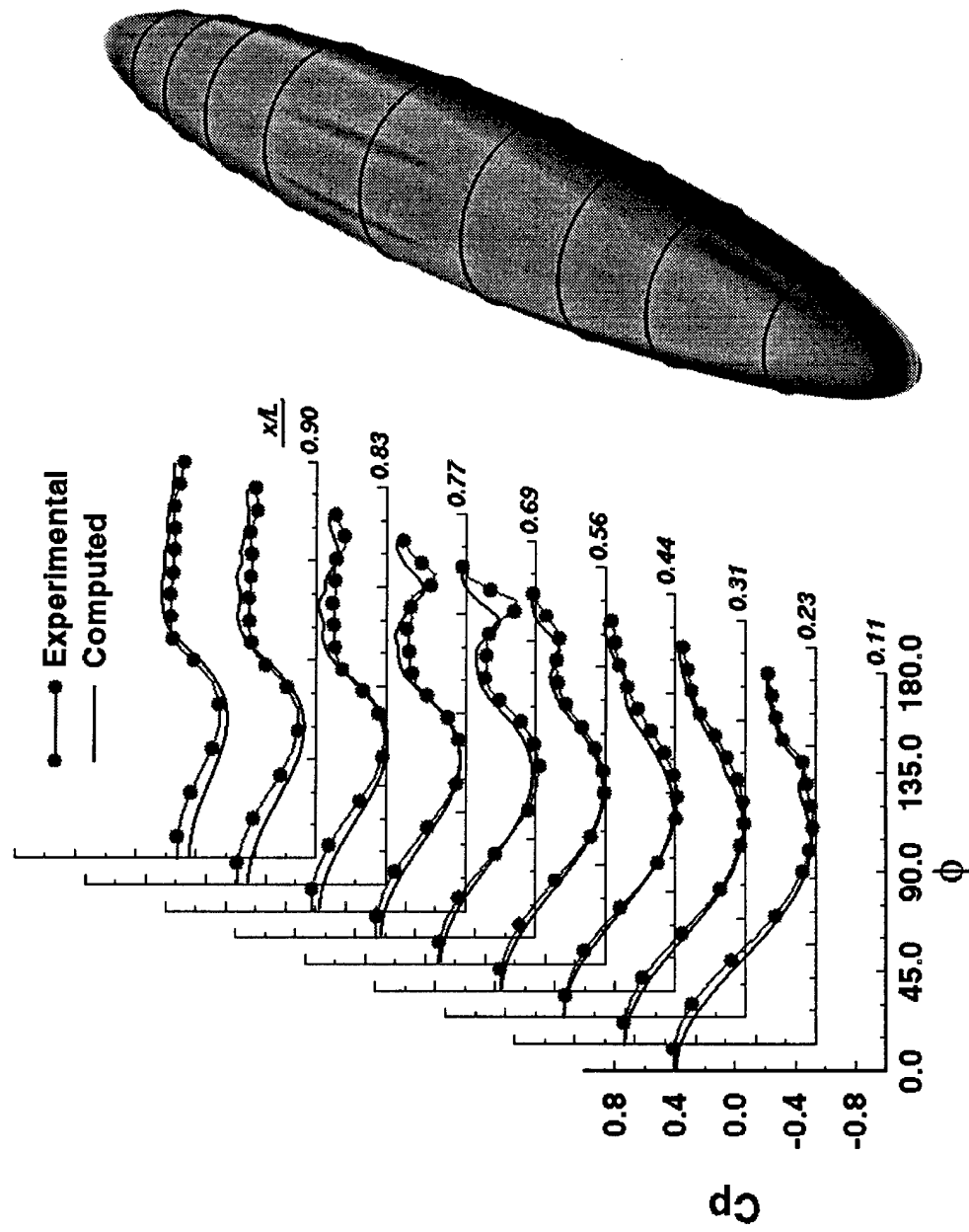


Figure 77e. Computed and Measured Surface-Pressure Distributions for the Pitch-Up Maneuver of a 6:1 Prolate Spheroid at  $Re = 4,200,000$ :  
(e)  $25^\circ$  of Motion

Figure 77e.

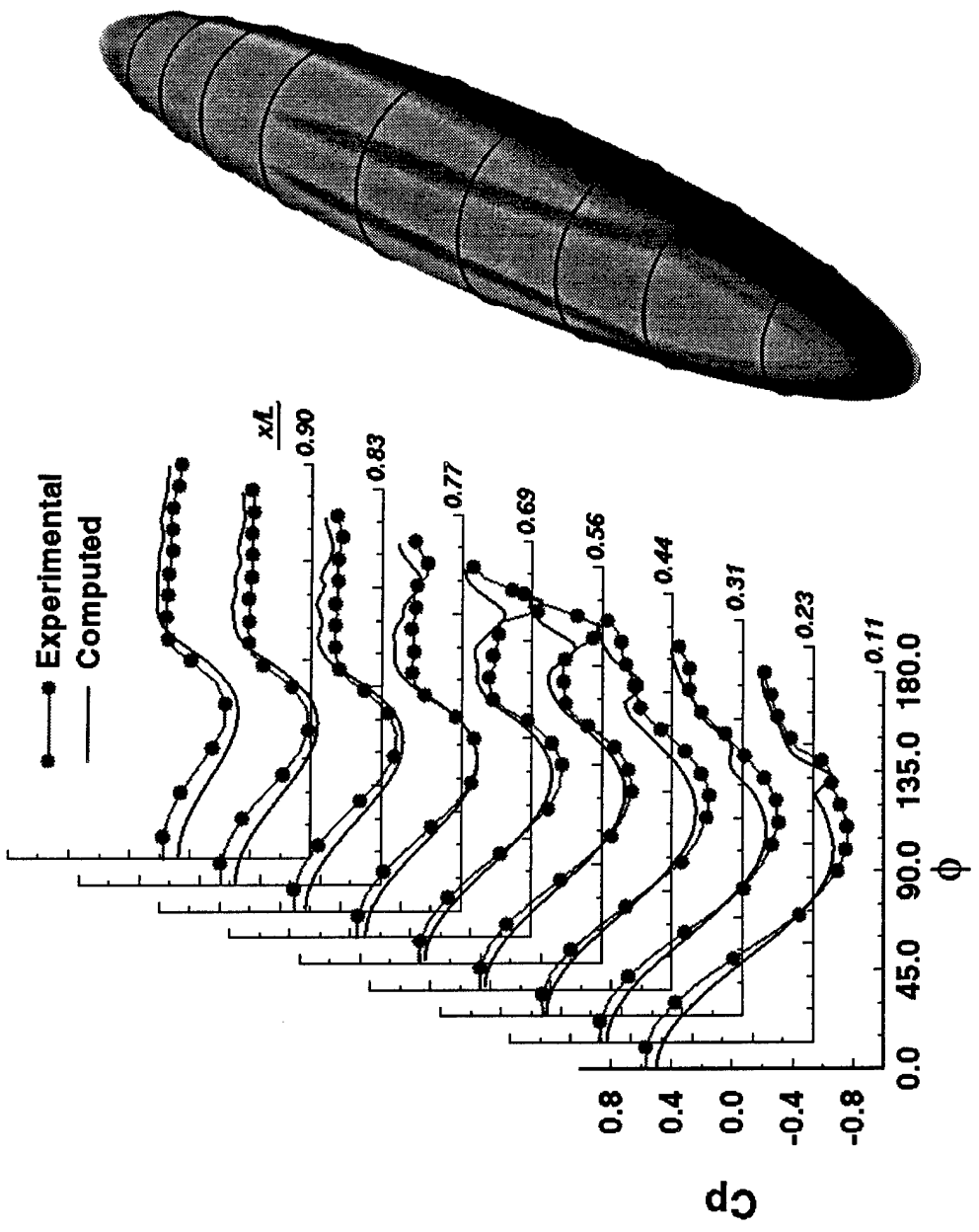


Figure 77f. Computed and Measured Surface-Pressure Distributions for the Pitch-Up Maneuver of a 6:1 Prolate Spheroid at  $Re = 4,200,000$ :  
(f)  $30^\circ$  of Motion

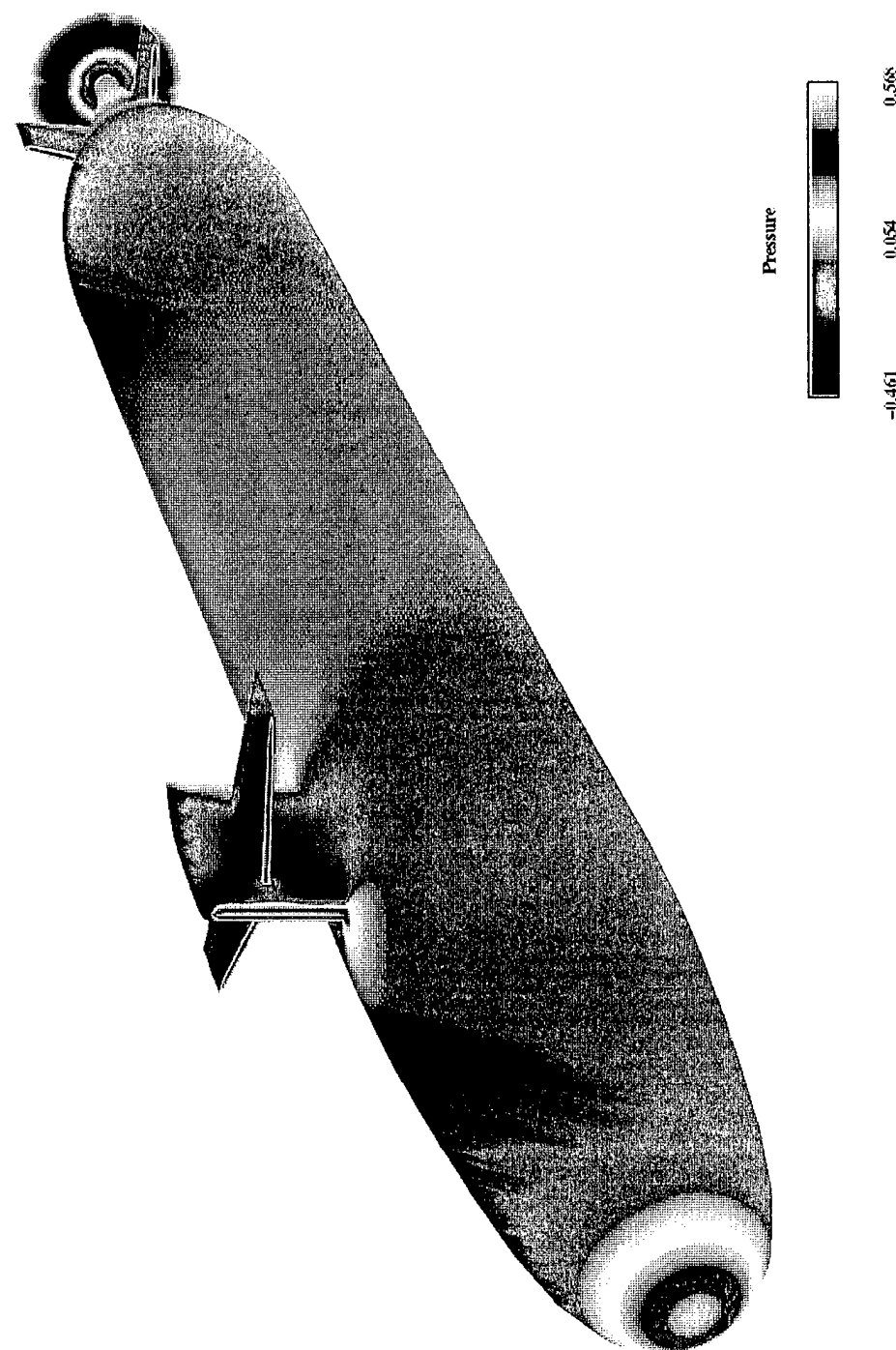


Figure 78.

Steady-State Computed Contours of Surface Pressure on a Fully-Appended SUBOFF at  $Re = 12,000,000$  with Contours of Axial Velocity on the Plane Where the Body-Force Propeller Model is Located

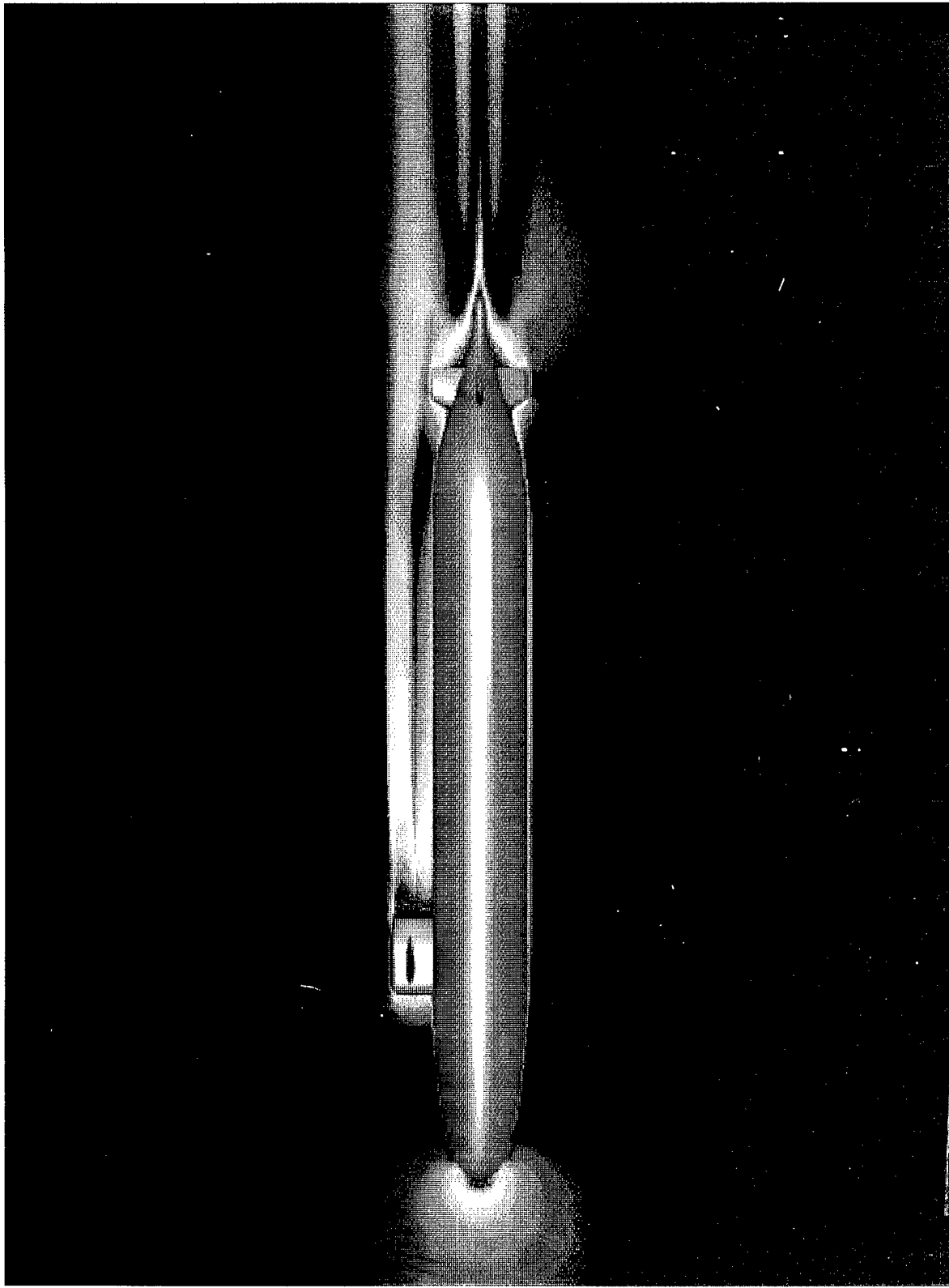


Figure 79.

Steady-State Computed Contours of the  $u$ -Component of Velocity at the Plane of Symmetry on a Fully-Appended SUBOFF at  $Re = 12,000,000$

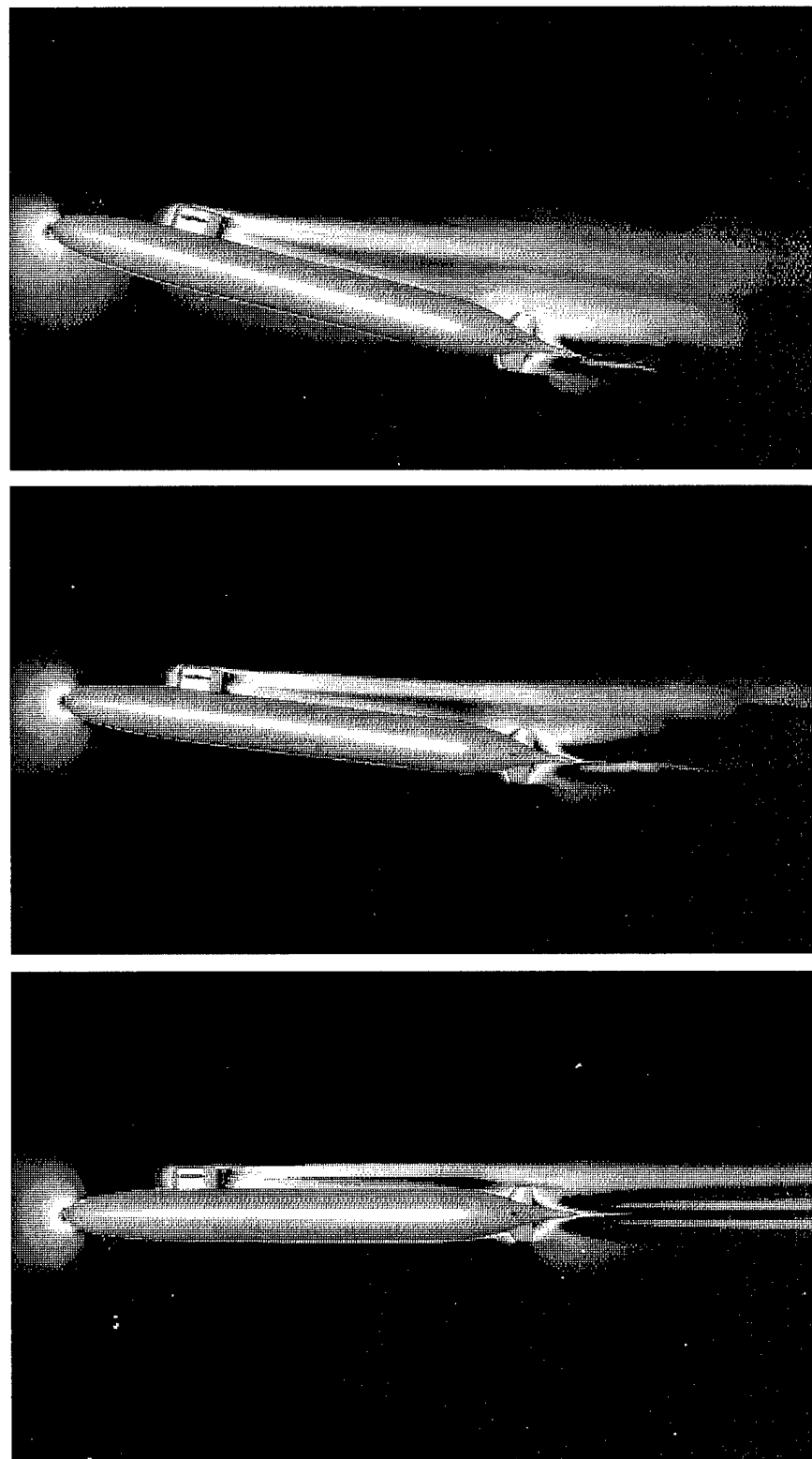


Figure 80.

Snapshots of the Computed Contours of the  $u$ -Component of Velocity at the Plane of Symmetry for the Prescribed  $15^\circ$  Pitch-Up Maneuver of a Fully-Appended SUBOFF at  $Re = 12,000,000$

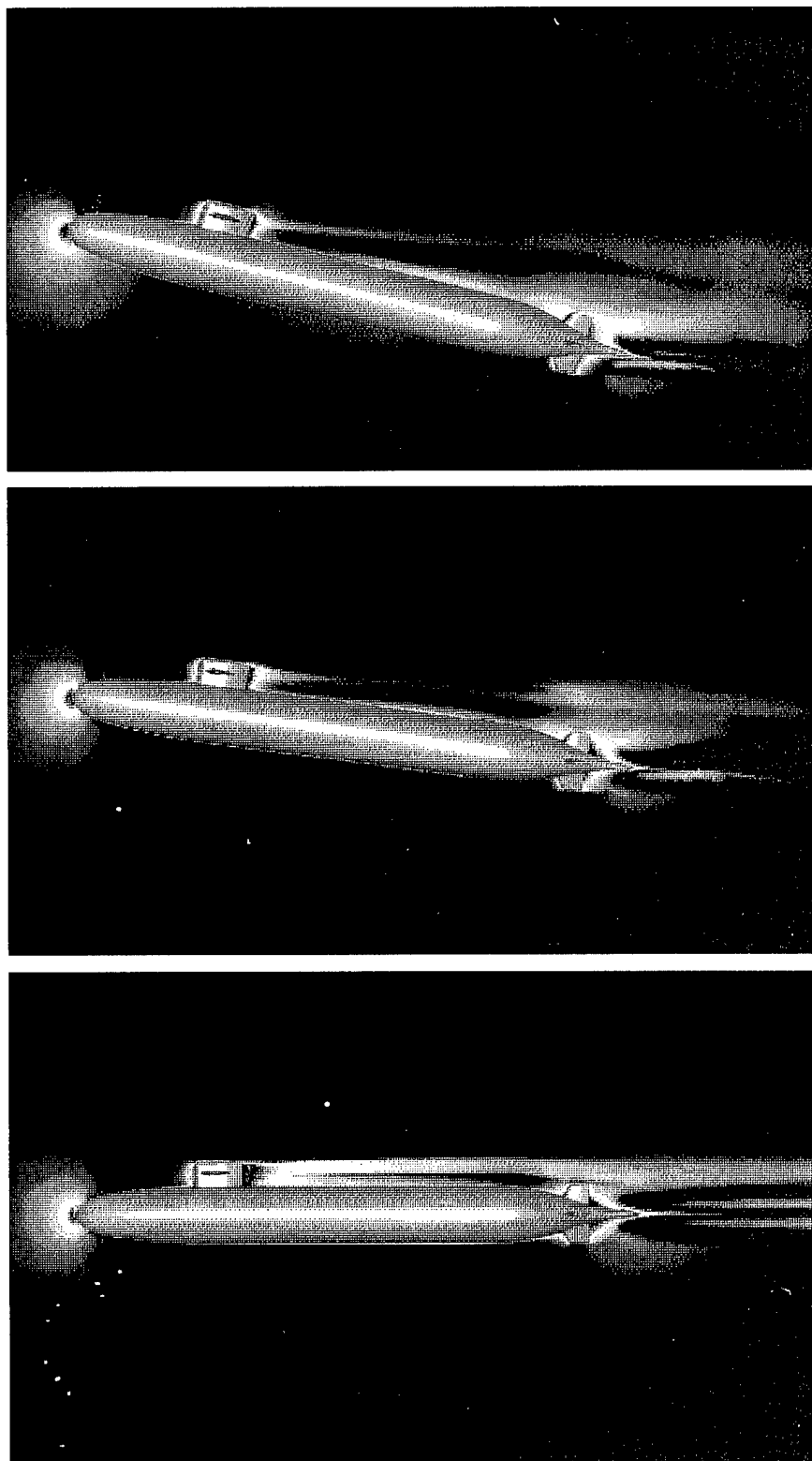
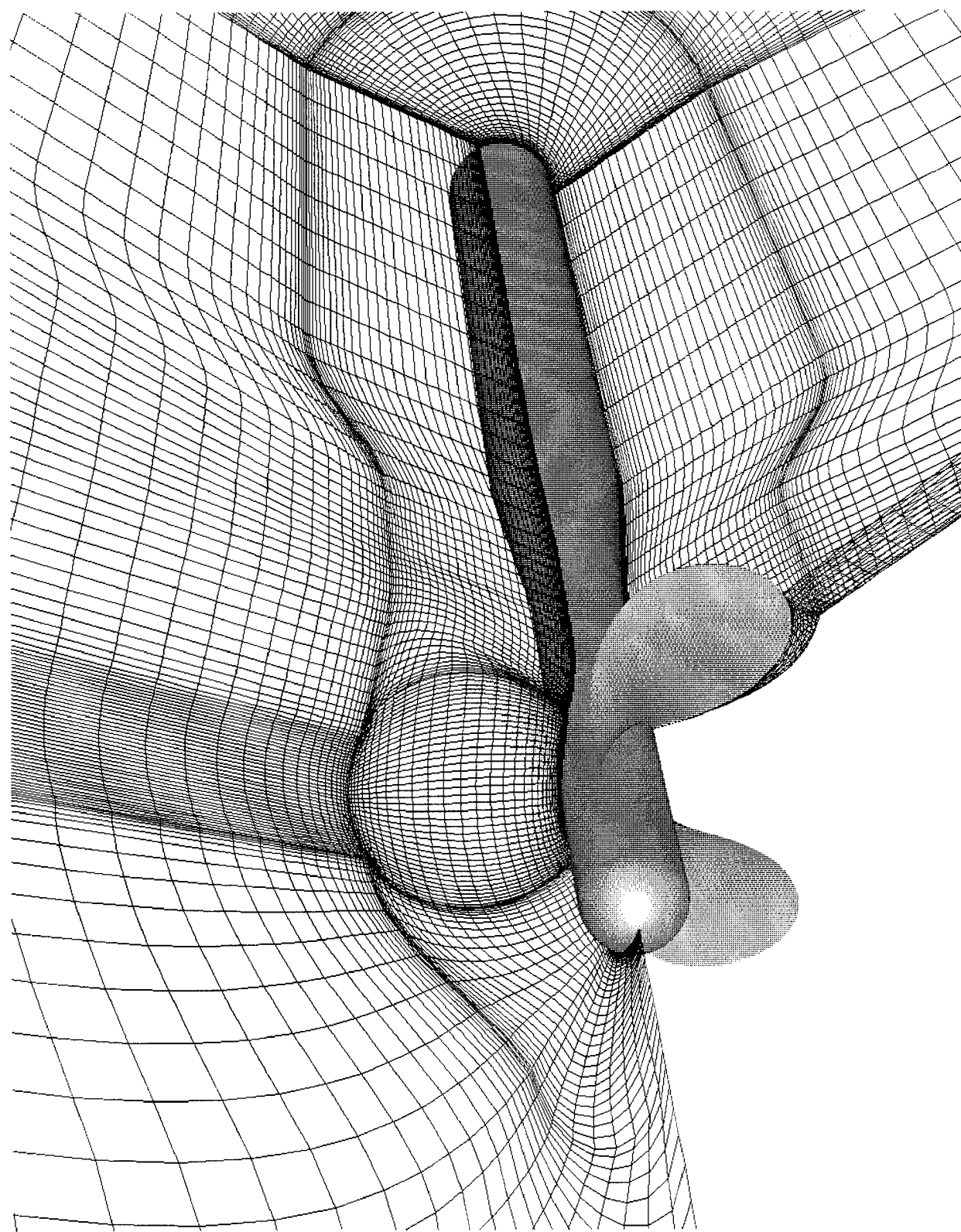
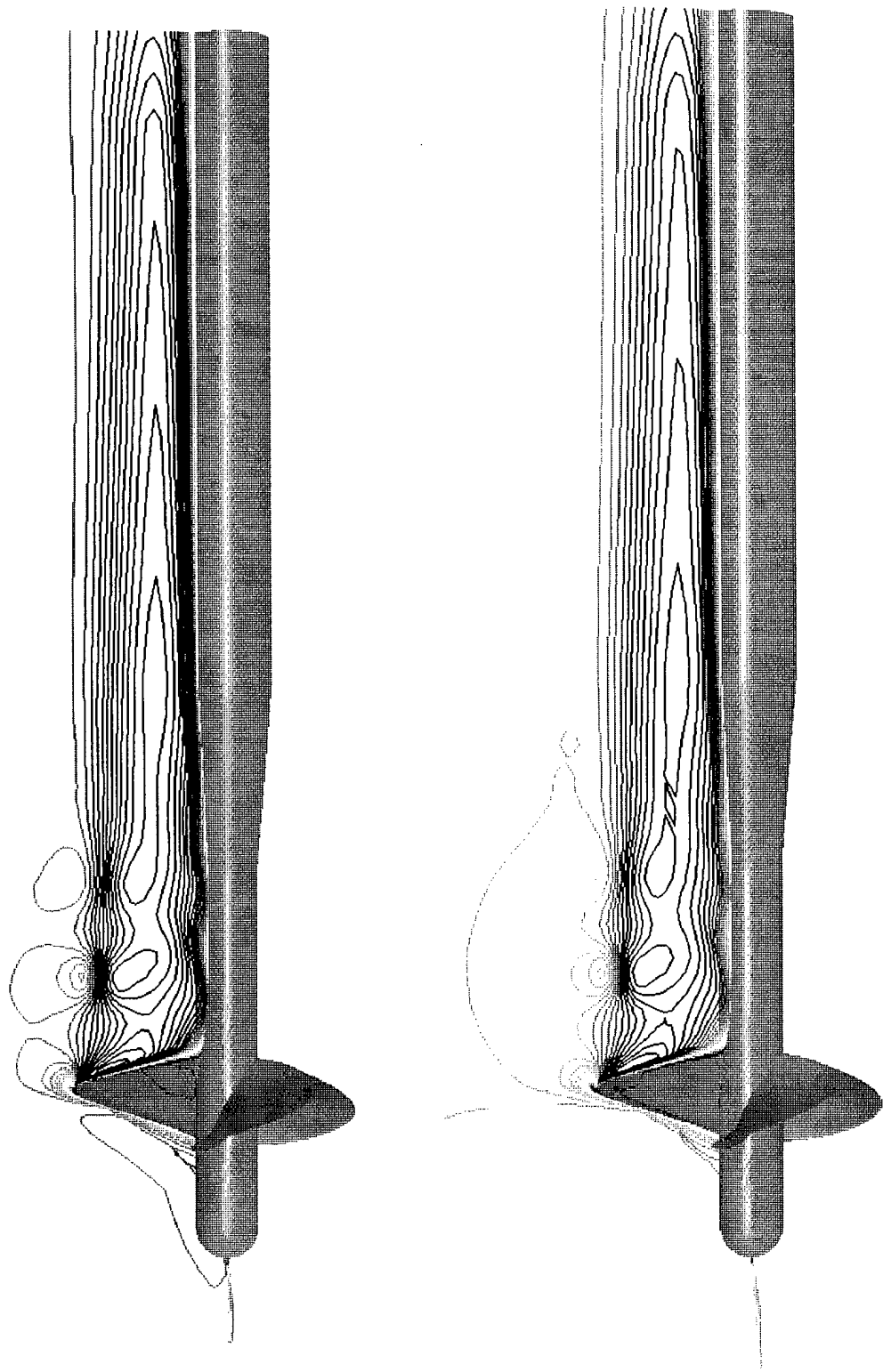


Figure 81.

Snapshots of the Computed Contours of the  $u$ -Component of Velocity at the Plane of Symmetry for the Prescribed 15° Pitch, 5° Yaw, and 5° Roll Maneuver of a Fully-Appended SUBOFF at  $Re=12,000,000$

Figure 82. 3-Block Grid for Marine Propeller 4119 Tested in a Uniform Freestream





Computed Contours of the  $u$ -Component of Velocity for Two Different Multigrid Cycles of Marine Propeller 4119 Tested in a Uniform Freestream at  $Re = 576,000$  (Where the Top Contour Plot Refers to One Multigrid Cycle Per Time Step and the Bottom Contour Plot Refers to Two Multigrid Cycles Per Time Step)

Figure 83.

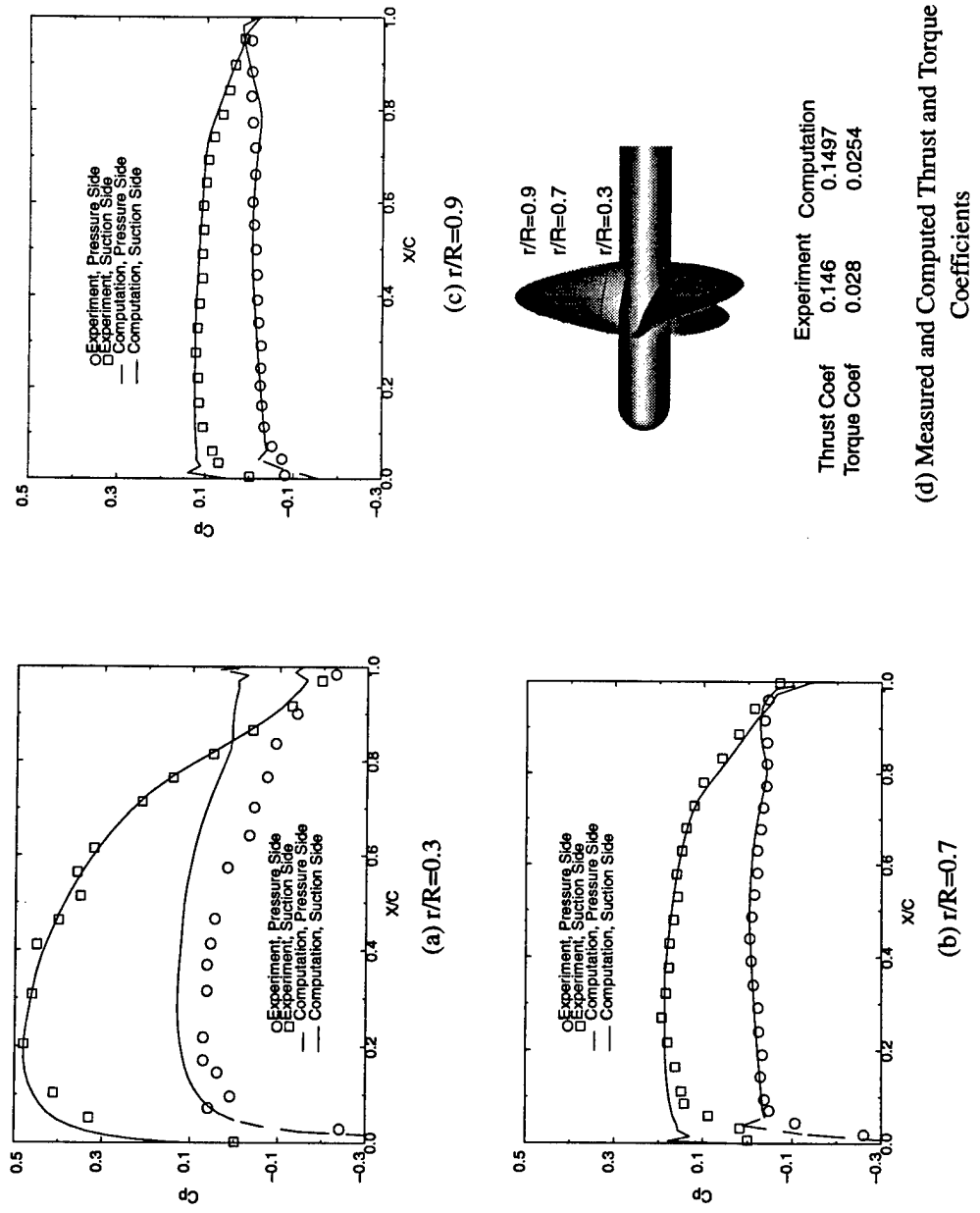


Figure 84. Computed and Measured Static-Pressure Distributions on the Blade Surfaces and Thrust and Torque Coefficients of Marine Propeller 4119 Tested in a Uniform Freestream at  $Re = 576,000$

193

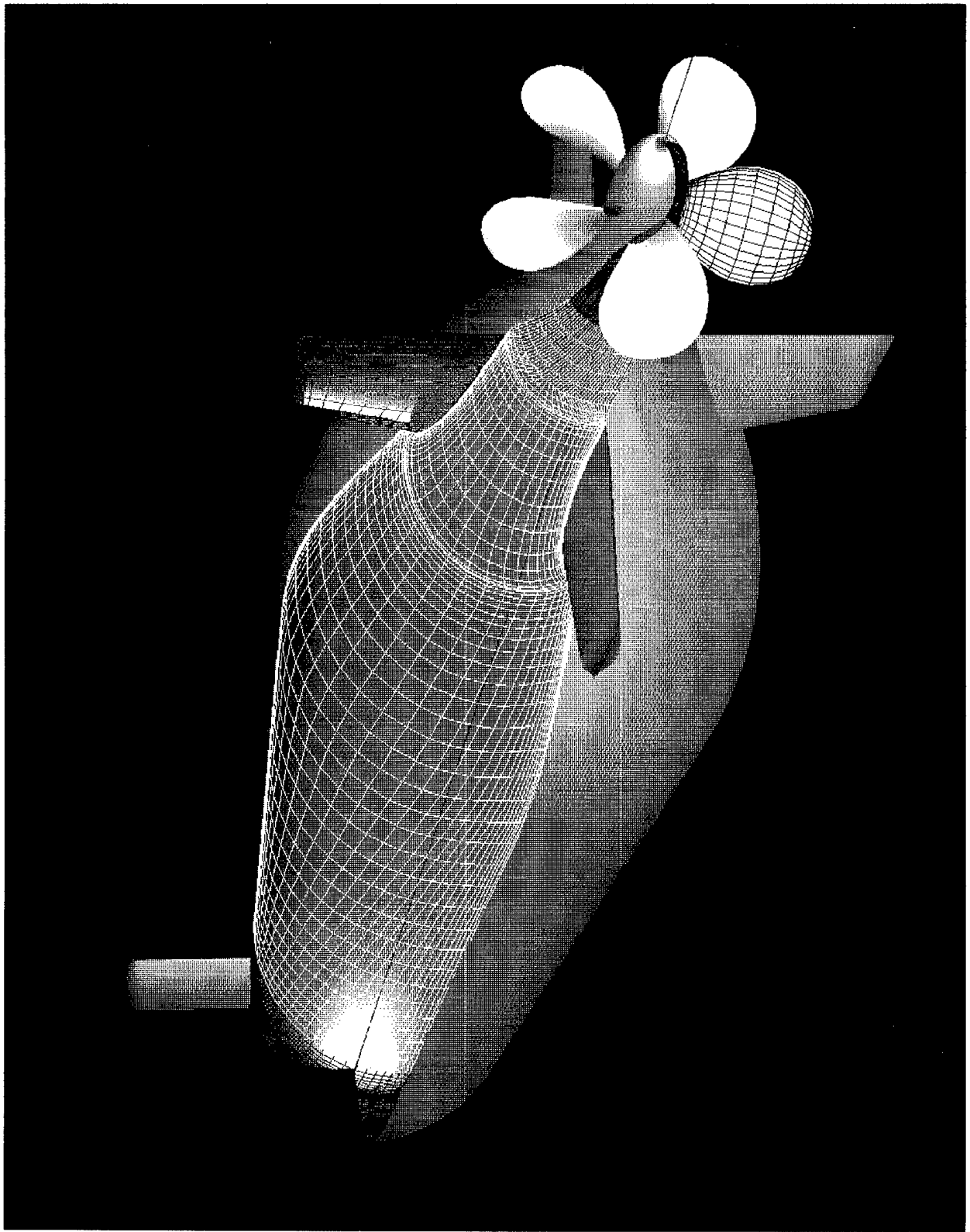


Figure 85. Solid-Body Model of the Appended SUBOFF with a Rotating Propeller, Including a Portion of the Surface Grid for the 13-Block Grid

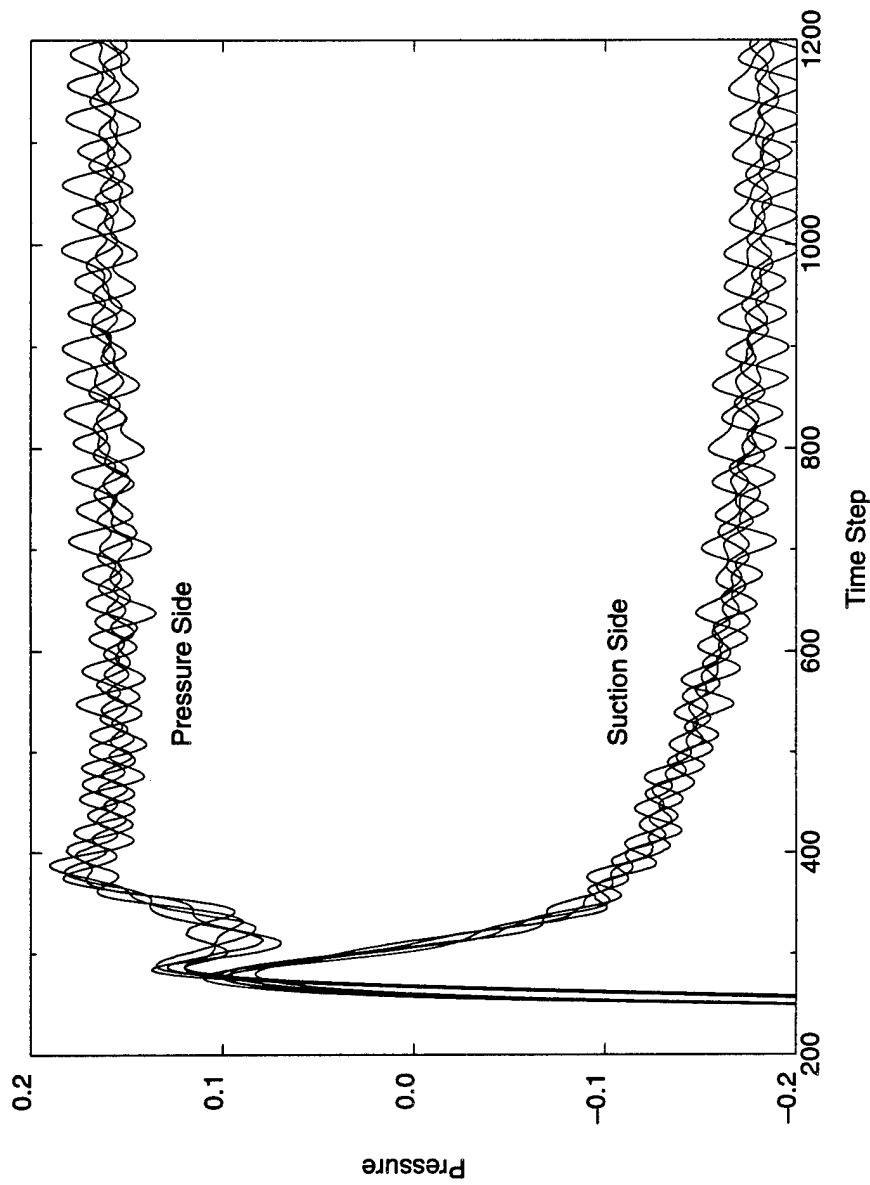


Figure 86.

Blade Pressure History, Using Local Time Stepping in the Beginning, for the Appended SUBOFF with a Rotating Propeller at 0° Angle of Attack and  $Re = 12,000,000$

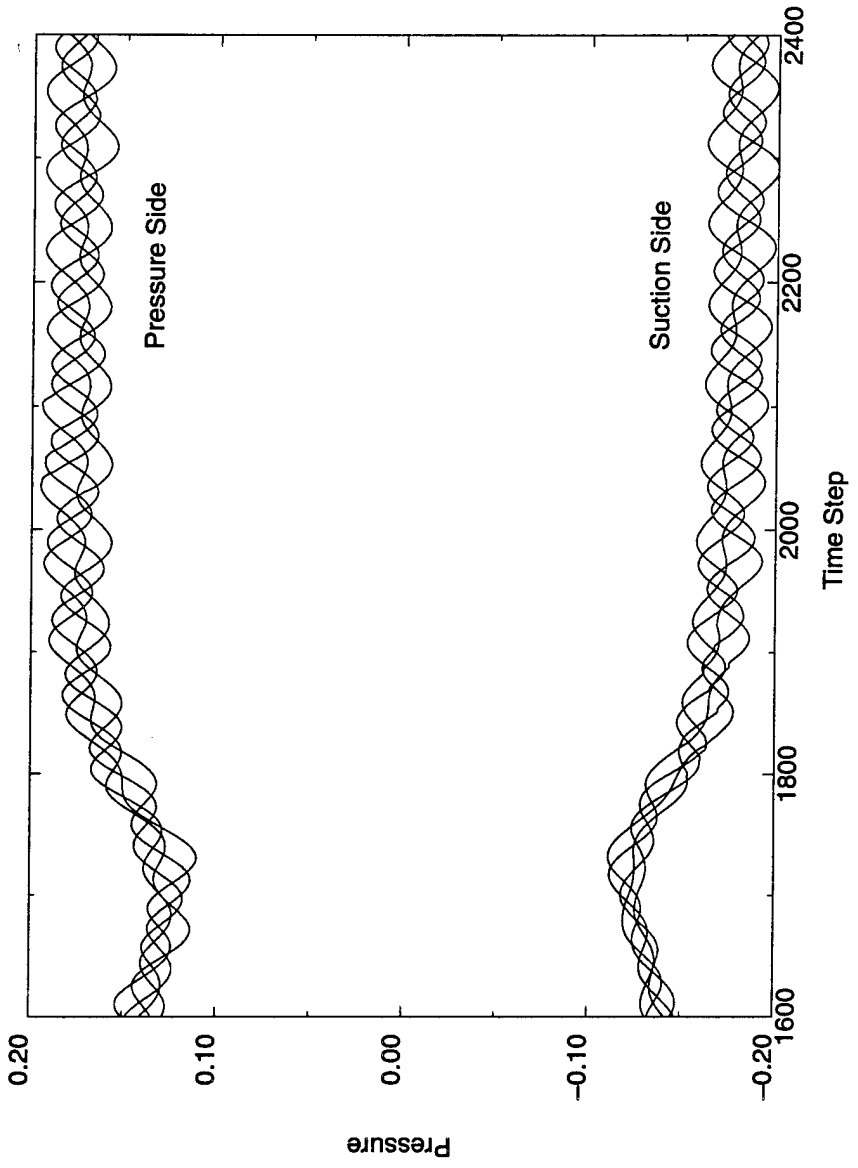


Figure 87. Blade Pressure History, Without Using Local Time Stepping in the Beginning, for the Appended SUBOFF with a Rotating Propeller at 0° Angle of Attack and  $Re = 12,000,000$

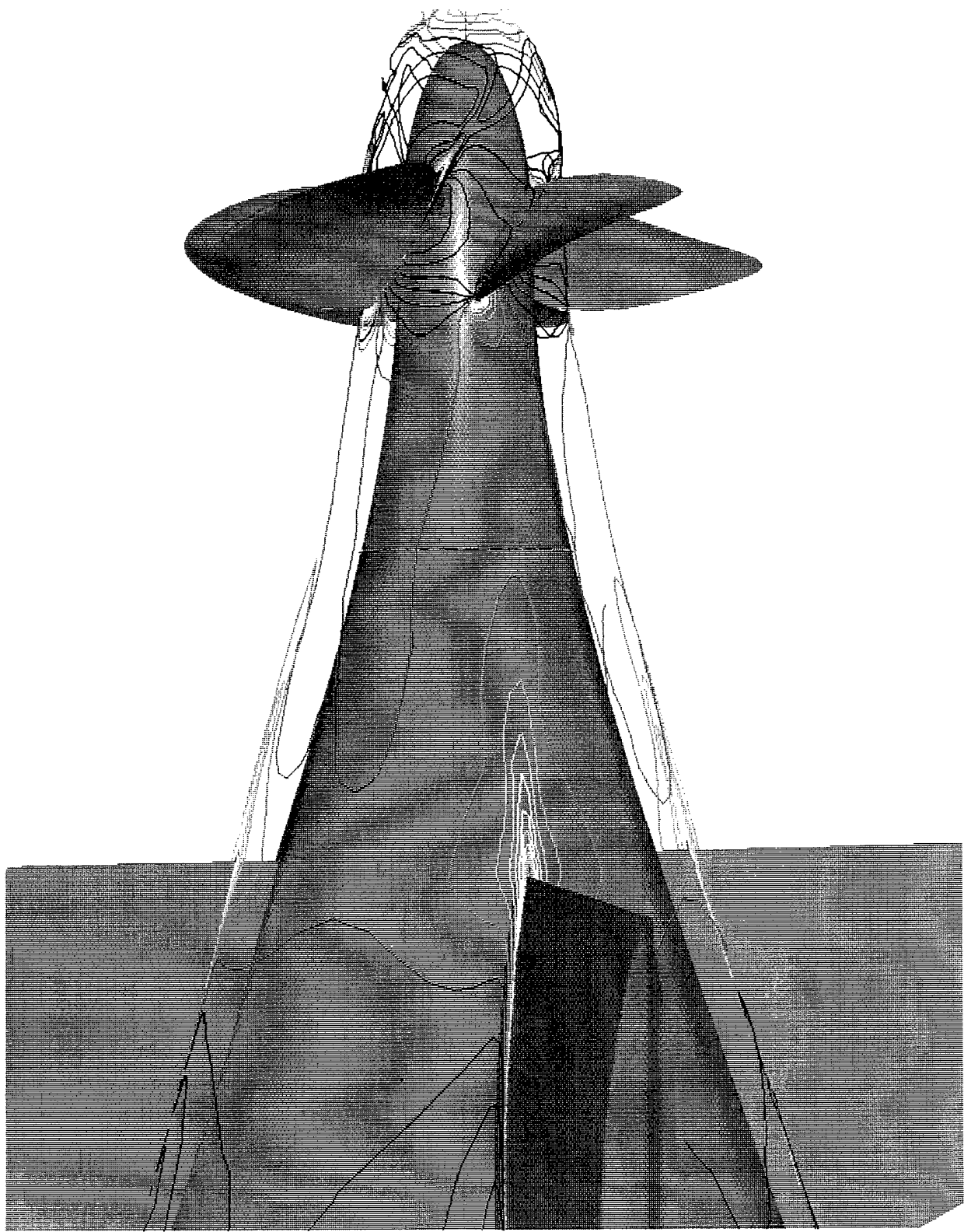


Figure 88.  
Computed Contours of the Axial Velocity in the Aft Region for the Periodic  
Solution of the Appended SUBOFF with a Rotating Propeller at  $0^\circ$  Angle of Attack  
and  $Re = 12,000,000$

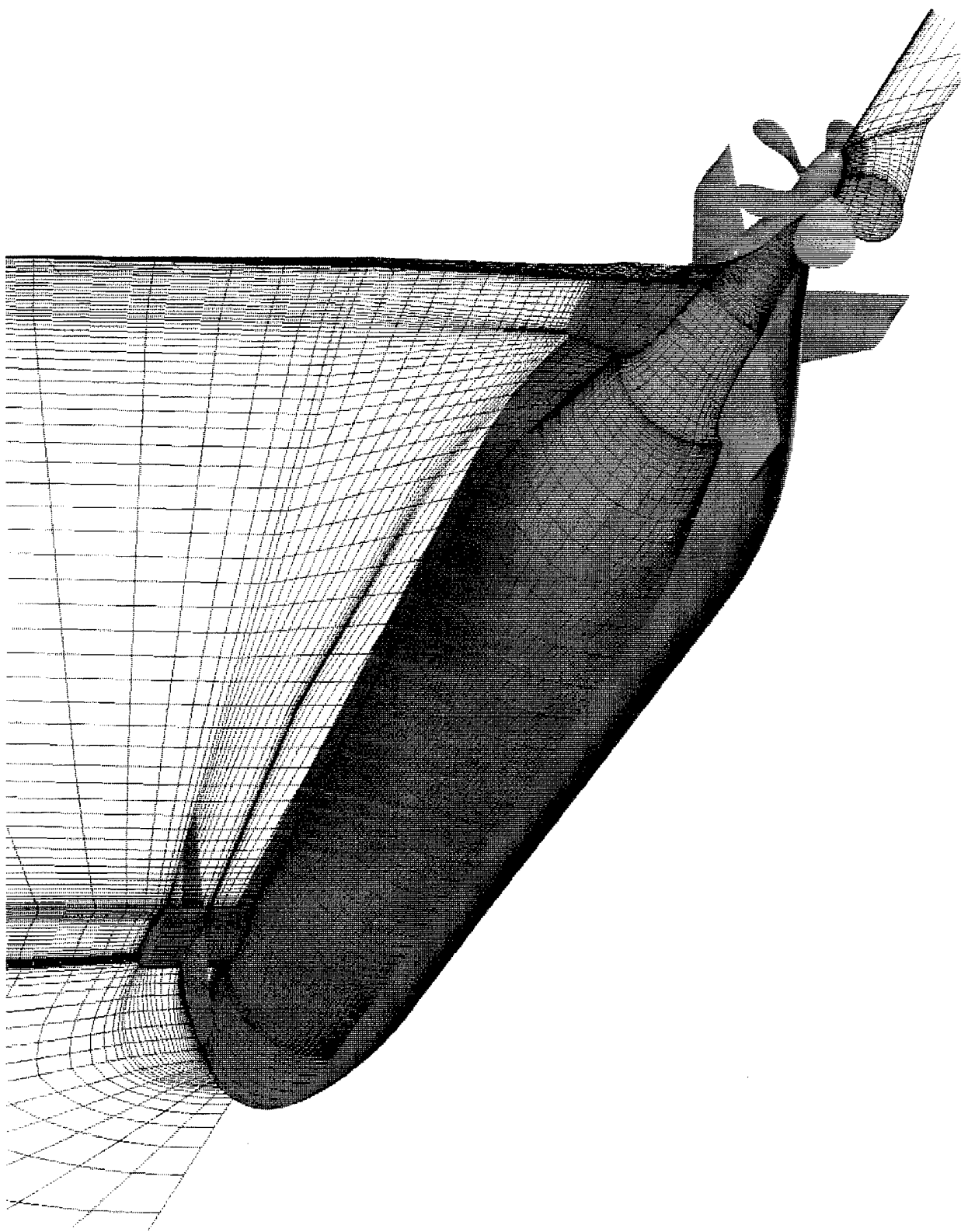


Figure 89. Solid-Body Model of the Fully-Appended SUBOFF with a Rotating Propeller,  
Including a Portion of the 51-Block Grid

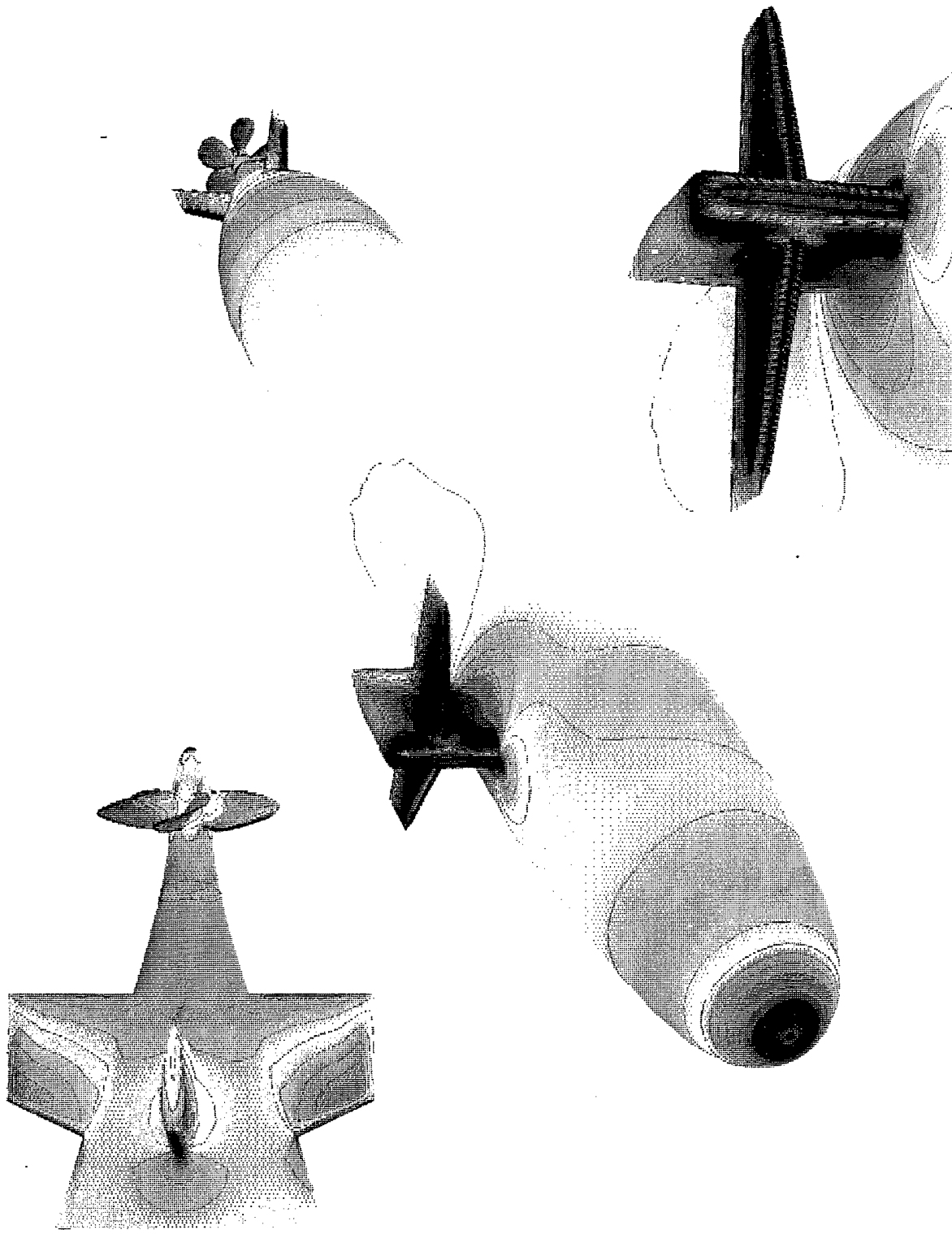
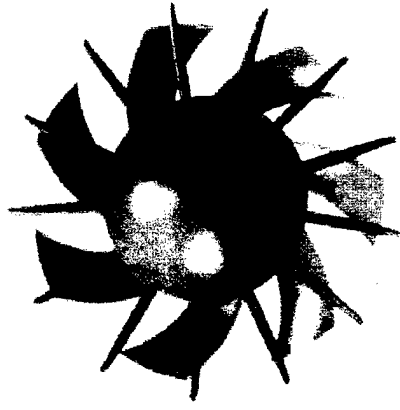
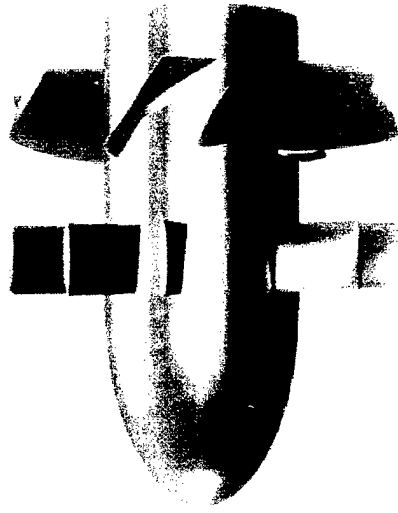


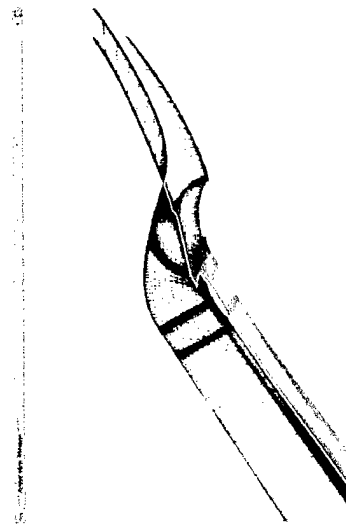
Figure 90. Computed Contours of Surface Pressure for the Periodic Solution of the Fully-Appended SUBOFF with a Rotating Propeller at  $0^\circ$  Angle of Attack and  $Re = 12,000,000$



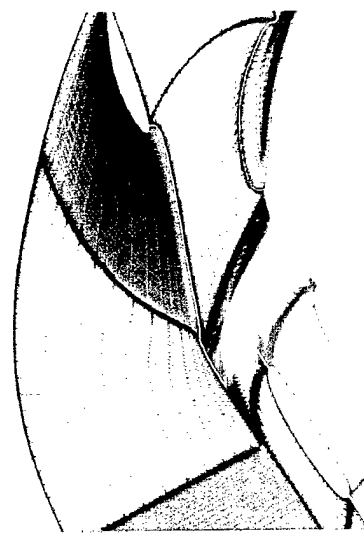
(a) Downstream View



(b) Inboard View



(c) Computational Grid



(d) Enlarged View of Interface

Figure 91. Solid-Body Model and Computational Grid for HIREP

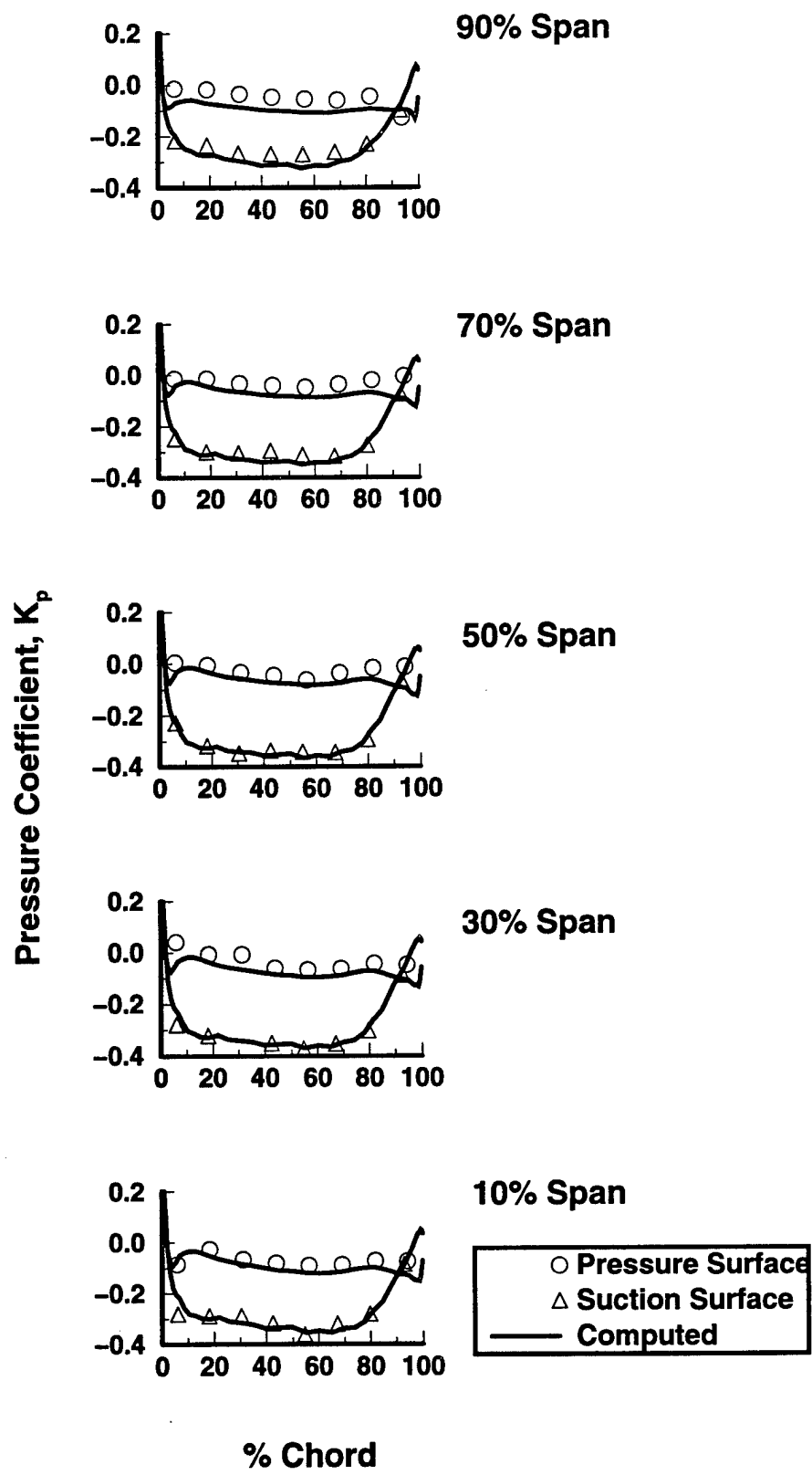
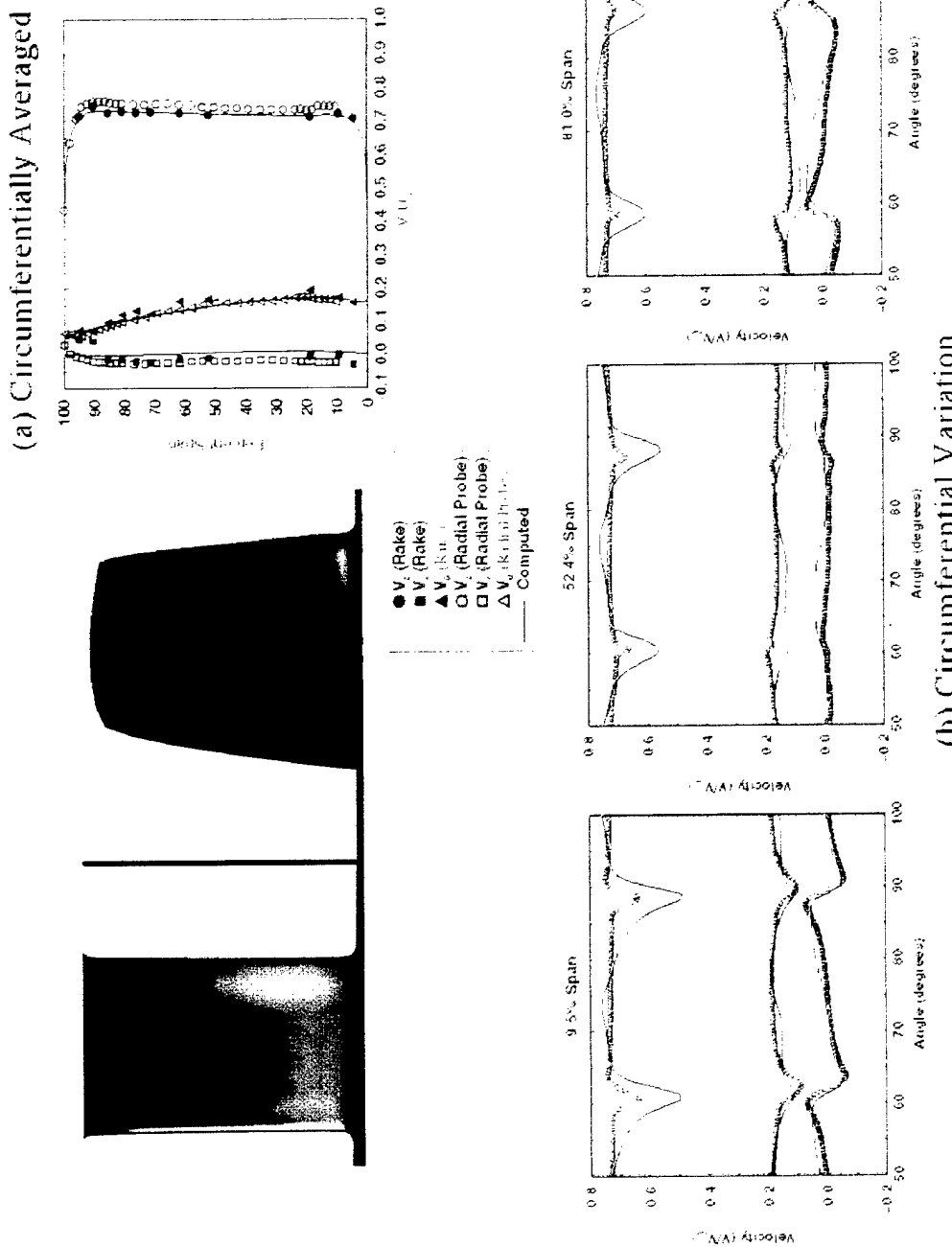


Figure 92.

Computed and Measured Static-Pressure Distributions on the Inlet Guide Vanes of HIREP at  $Re = 2,300,000$

Figure 93.

Computed and Measured Velocity Distributions Between the Inlet Guide Vanes and the Rotor Blades of HIREP at  $Re = 2,300,000$



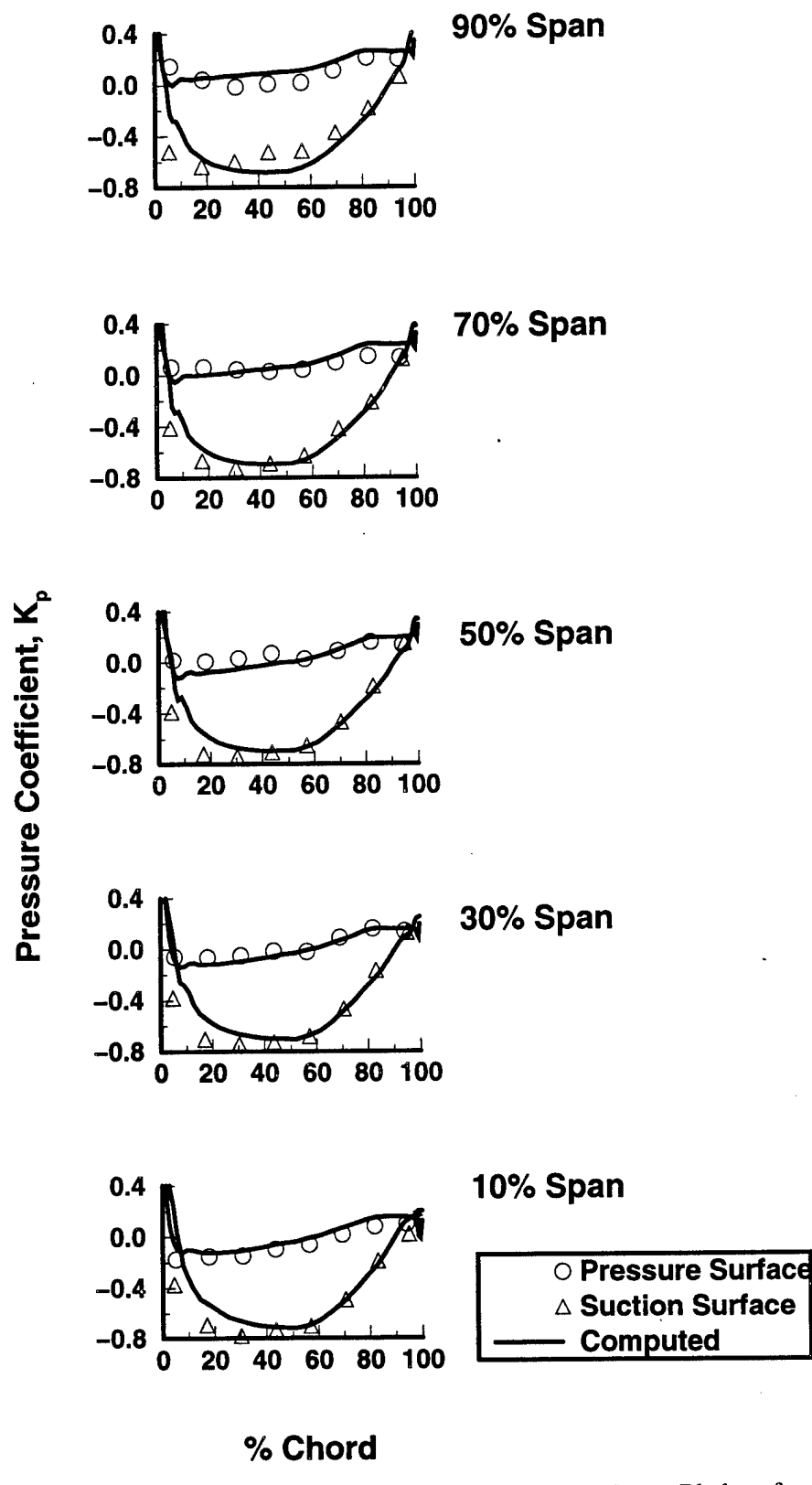


Figure 94.

Computed and Measured Static-Pressure Distributions on the Rotor Blades of HIREP at  $Re = 5,500,000$  (Using the Inlet Relative Velocity at 90% Span)

Figure 95. Experimentally Observed Skin-Friction Lines and Computed Particle Traces on the Rotor Blades of HIREP at  $Re = 5,500,000$  (Using the Inlet Relative Velocity at 90% Span)

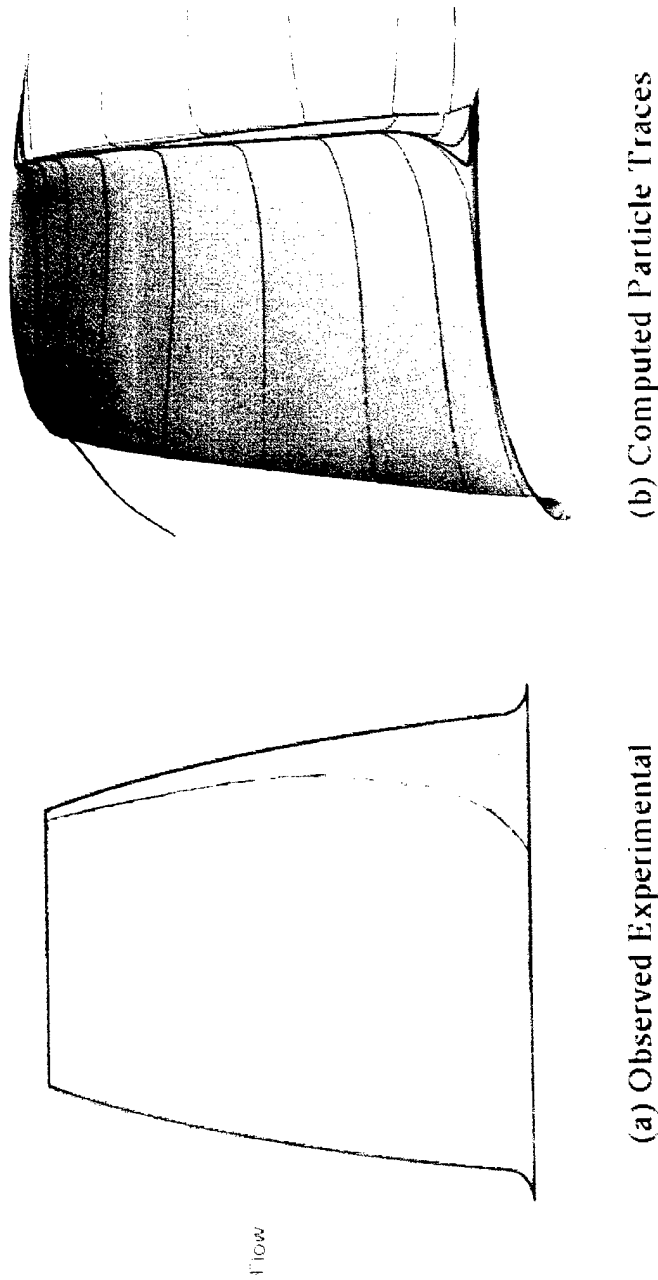
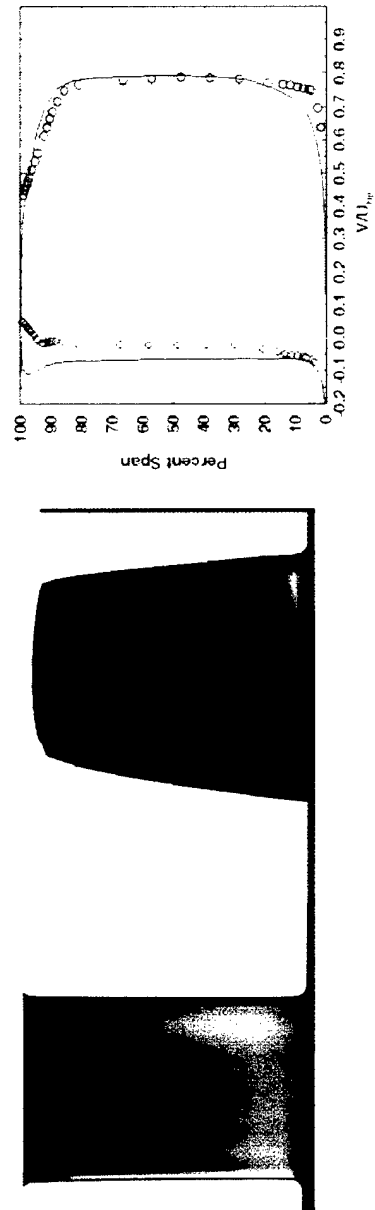


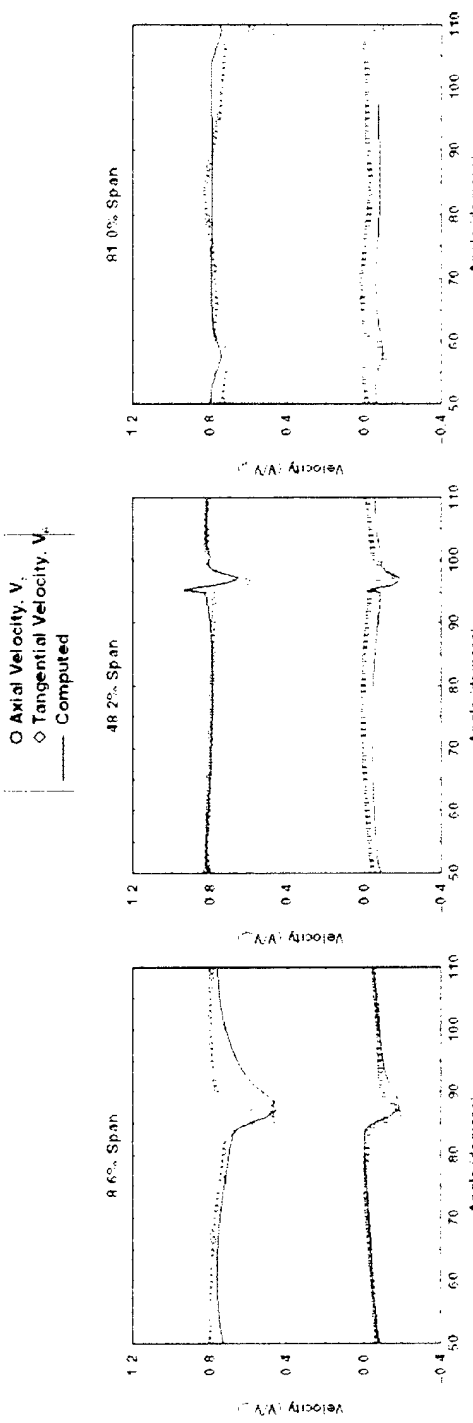
Figure 96.

Computed and Measured Velocity Distributions Downstream of the Rotor Blades of HIREP at  $Re = 5,500,000$  (Using the Inlet Relative Velocity at 90% Span)

(a) Circumferentially Averaged



(b) Circumferential Variation



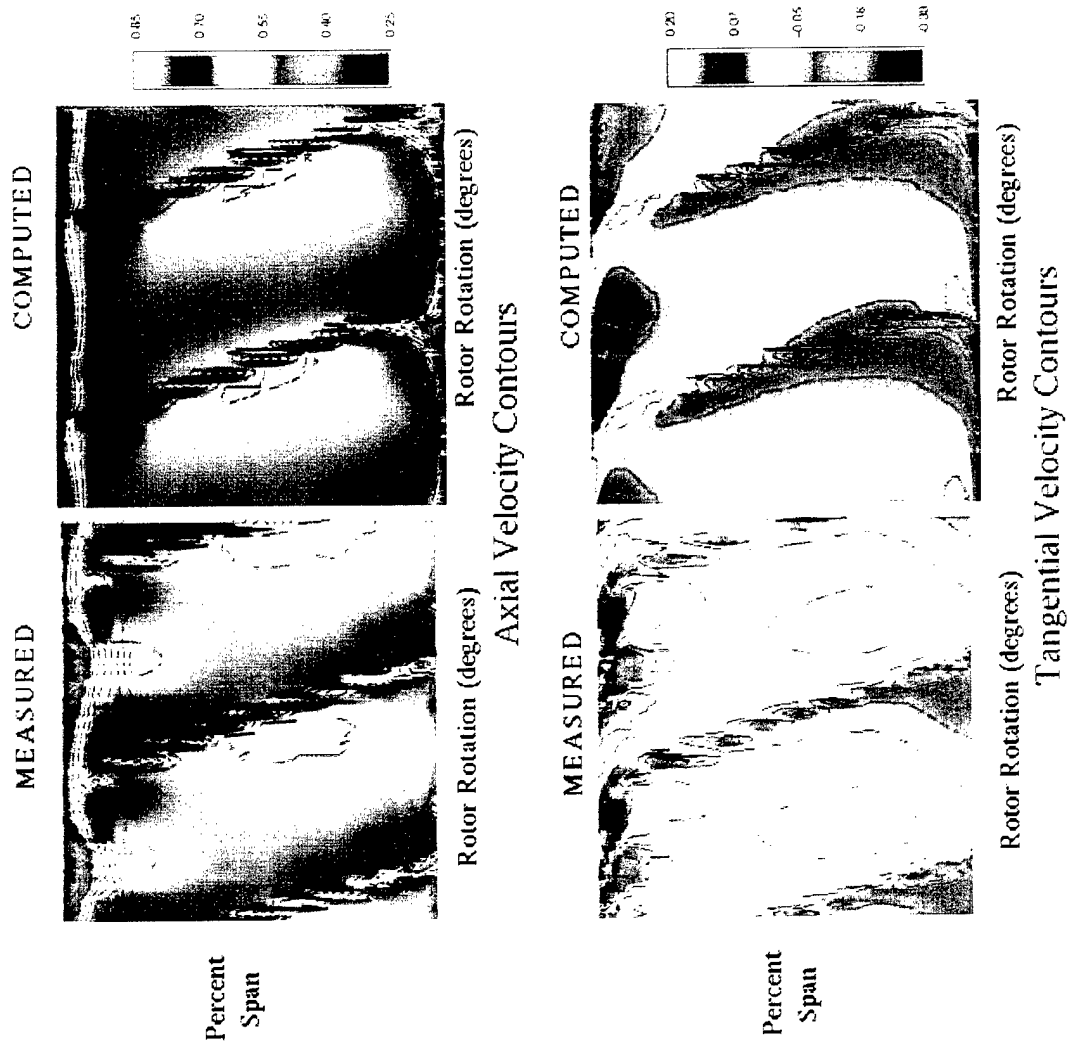


Figure 97.

Computed and Measured Velocity Contours Downstream of the Rotor Blades of HIREP at  $Re = 5,500,000$  (Using the Inlet Relative Velocity at 90% Span)

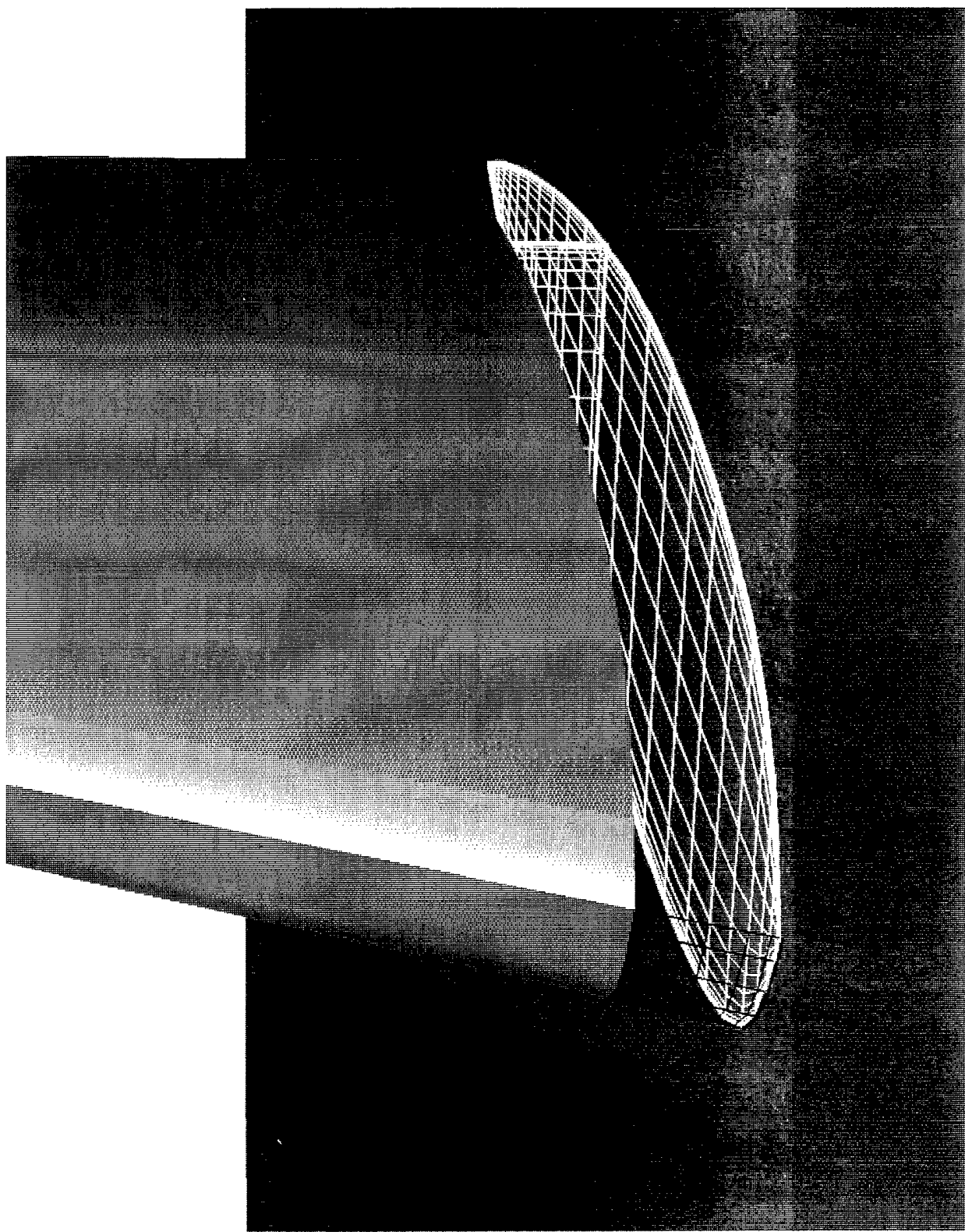


Figure 98. SUBOFF Stern Appendage on a Flat Plate, with a Small Gap and the Corresponding Grid Existing Between the Two Surfaces

U-Velocity Contours  
10 Degree Deflection

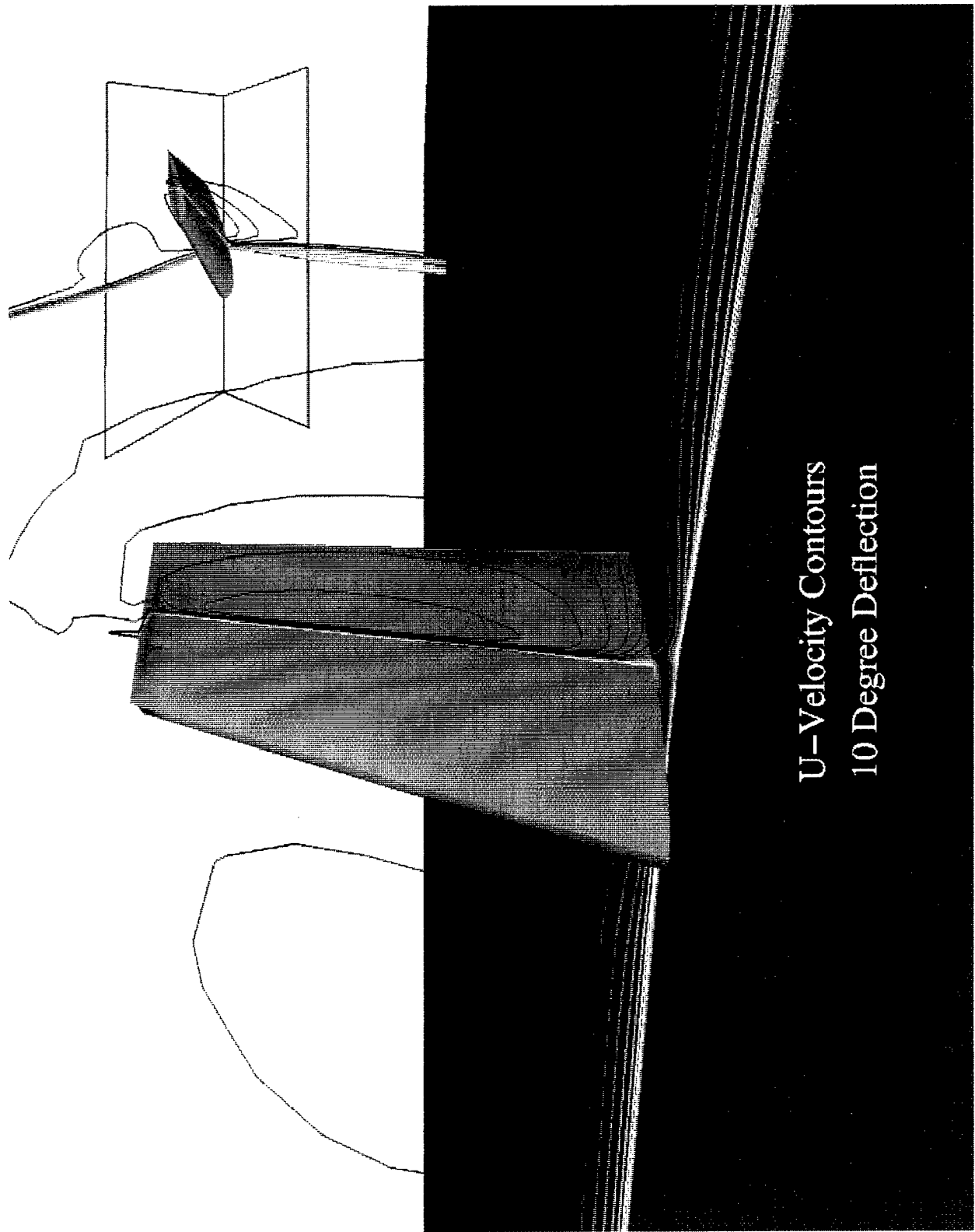


Figure 99. Snapshot of the Computed The u-Component of Velocity at  $10^\circ$  Deflection of a SUBOFF Stern Appendage Moving Over a Flat Plate at  $Re = 12,000,000$

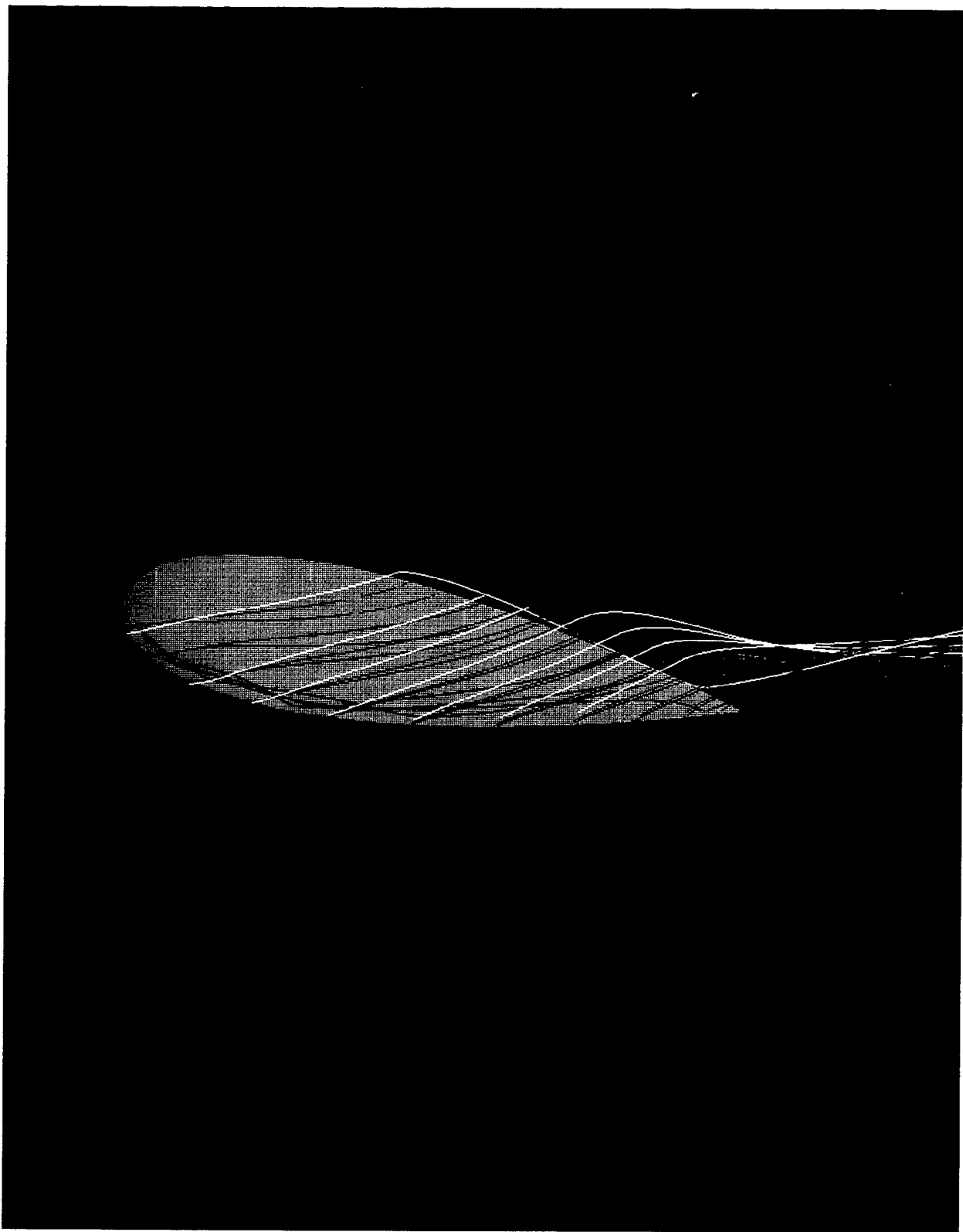


Figure 100. Snapshot of the Particle Traces Looking Up Towards the Bottom of the Appendage at 10° Deflection of a SUBOFF Stern Appendage Moving Over a Flat Plate at  $Re = 12,000,000$

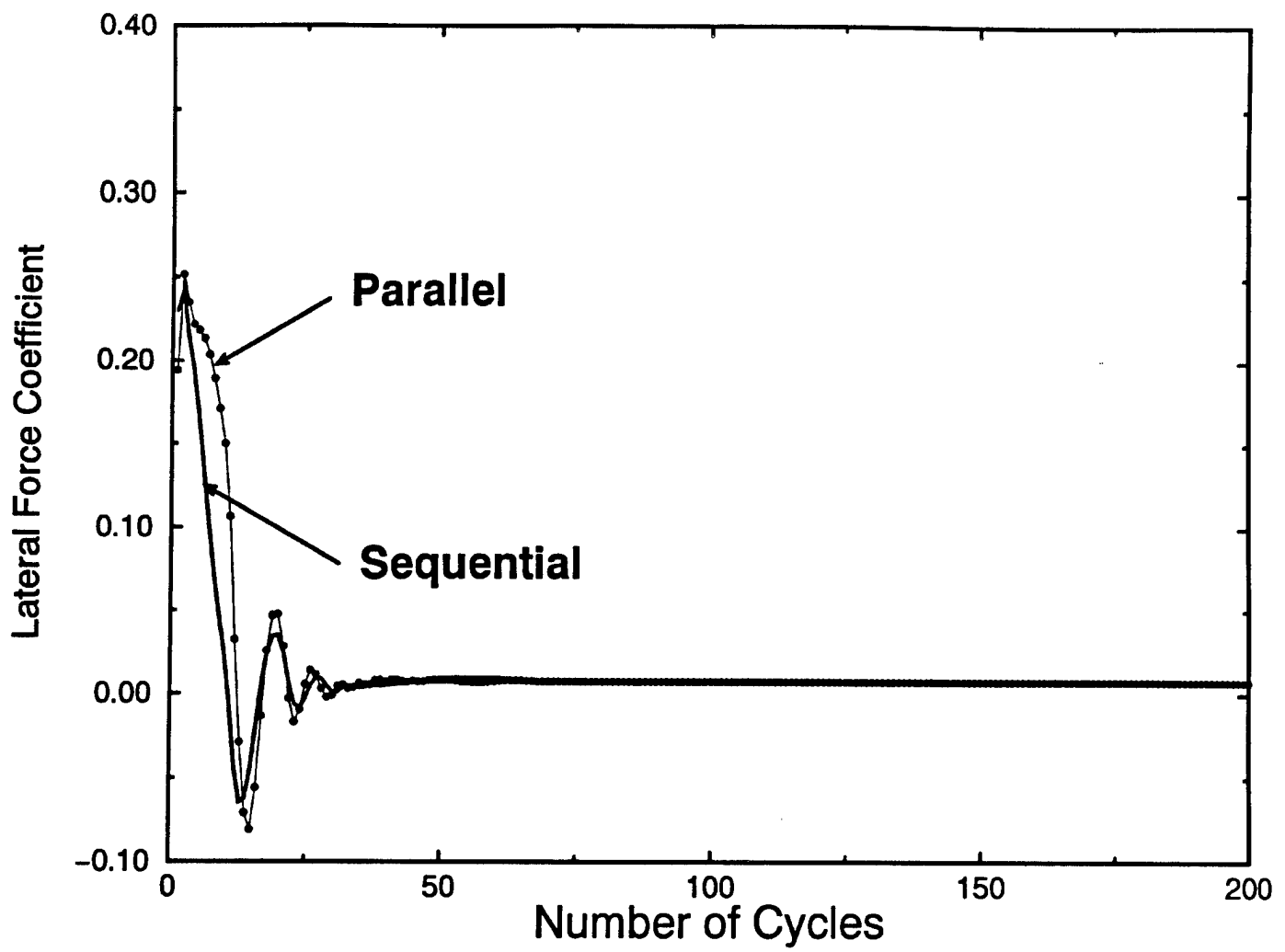


Figure 101. Convergence Behavior of the Parallel Algorithm for the Lateral Force Coefficient at an Angle of Drift of 18.11°

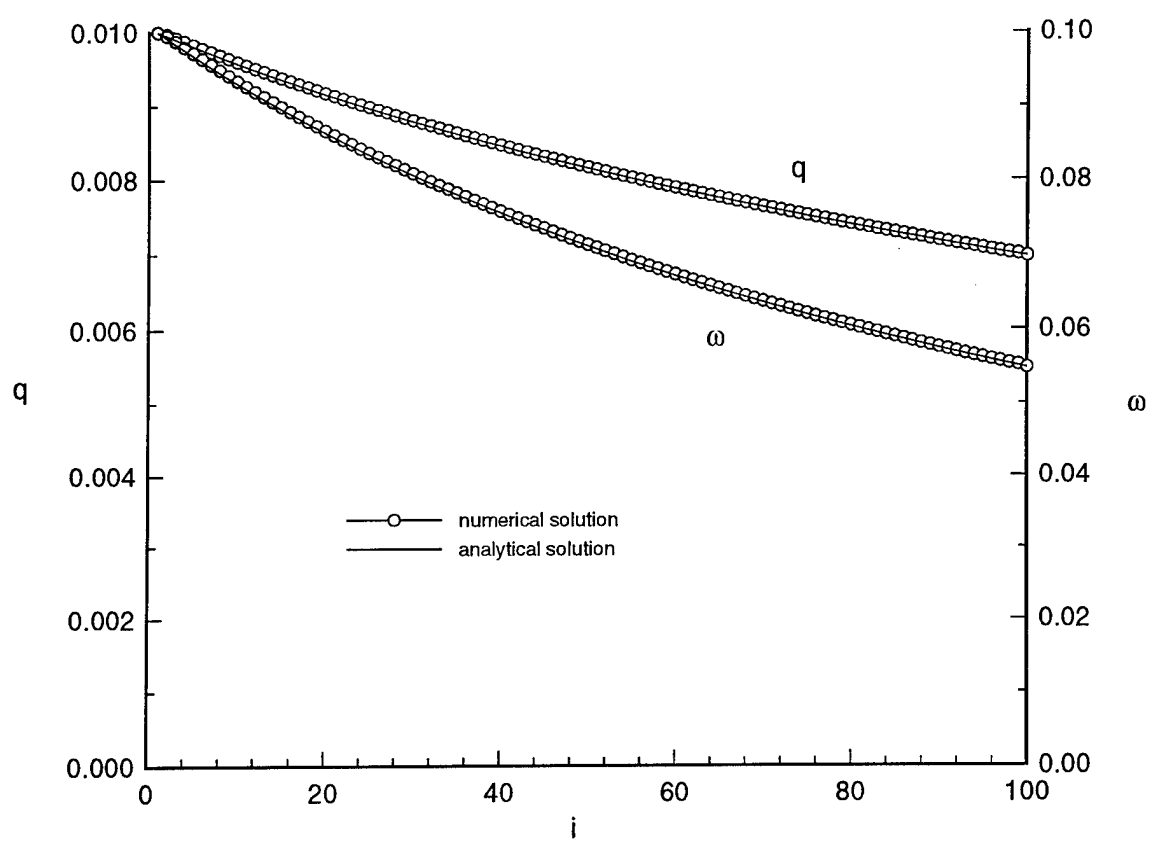


Figure 102. Spatial Decay of  $q$  and  $\omega$  in Homogeneous Turbulence

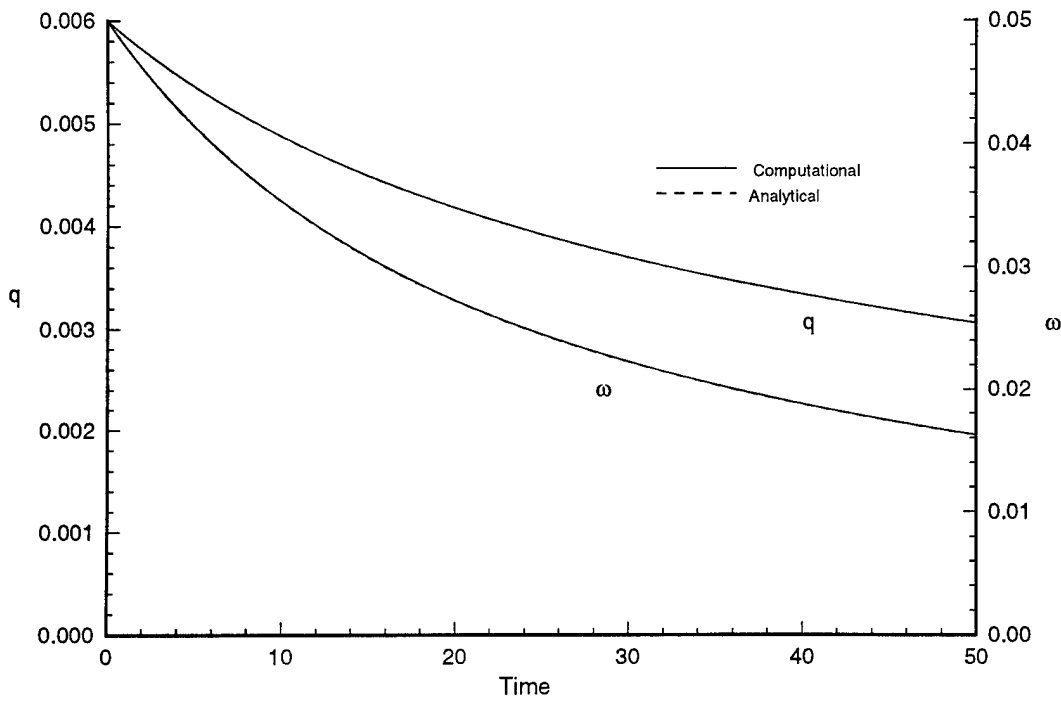


Figure 103. Unsteady Decay of  $q$  and  $\omega$  in Homogeneous Turbulence

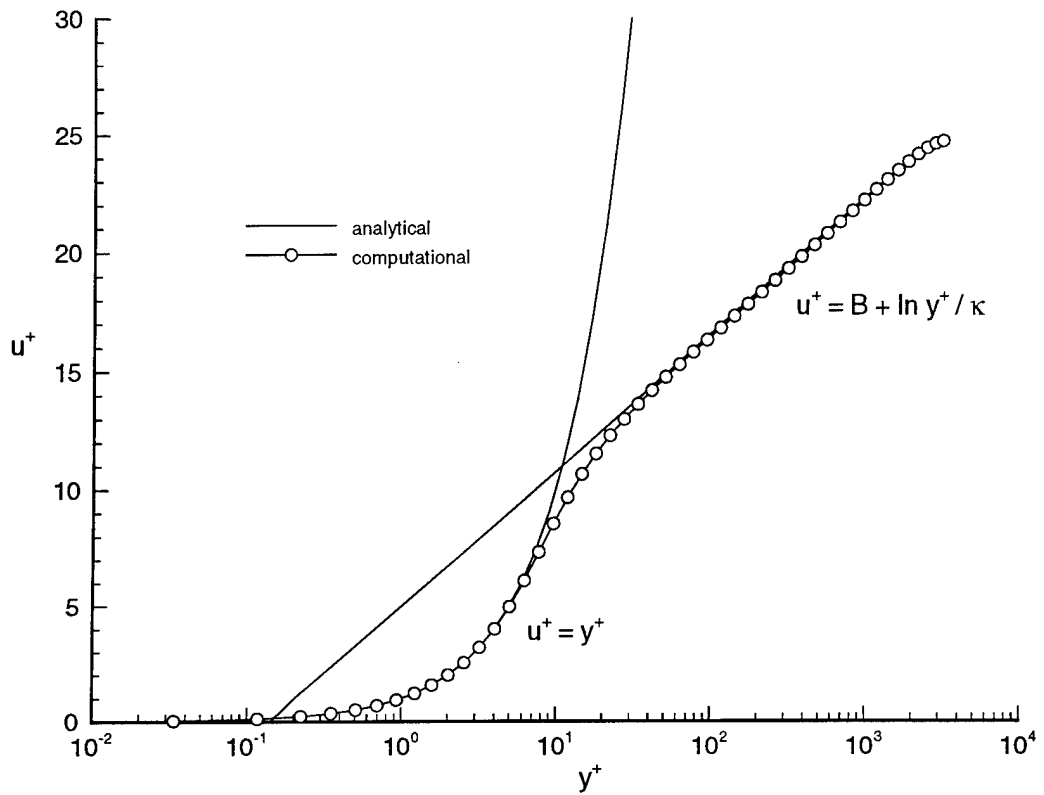


Figure 104. Velocity Profile in a Two-Dimensional Channel

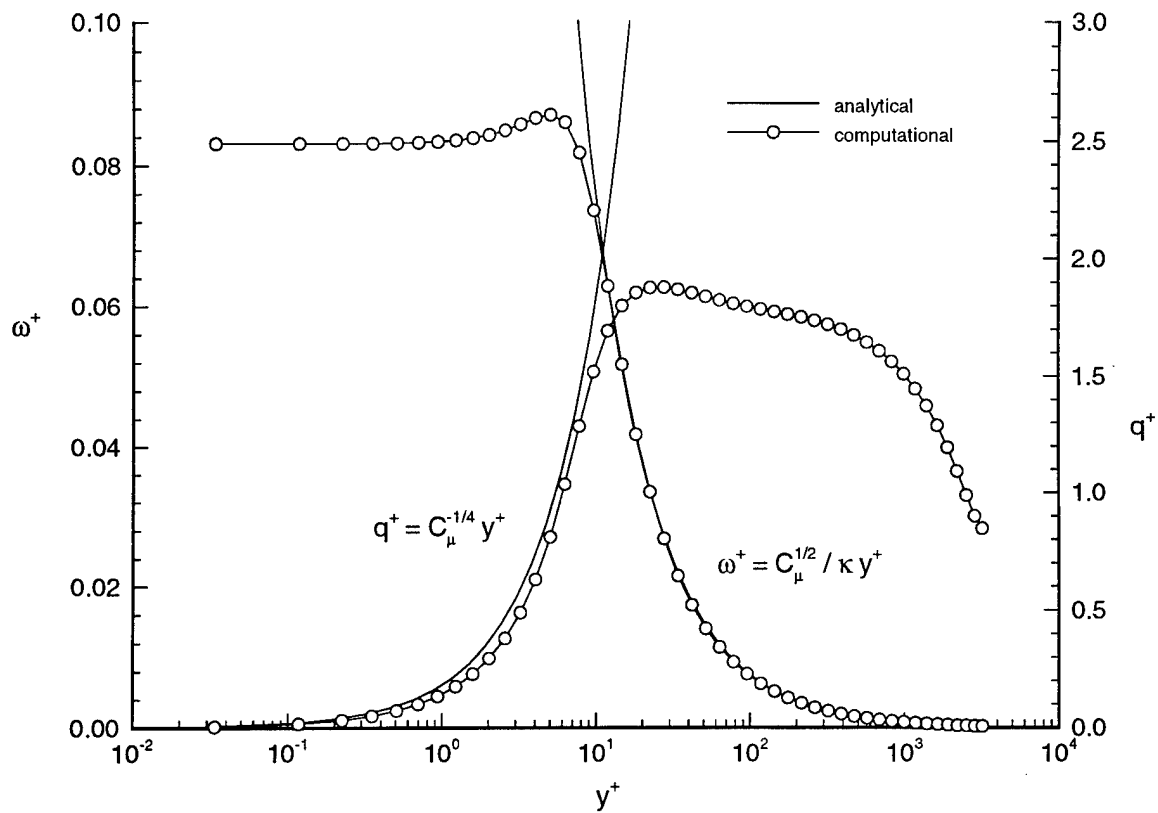


Figure 105. Turbulence Profiles in a Two-Dimensional Channel

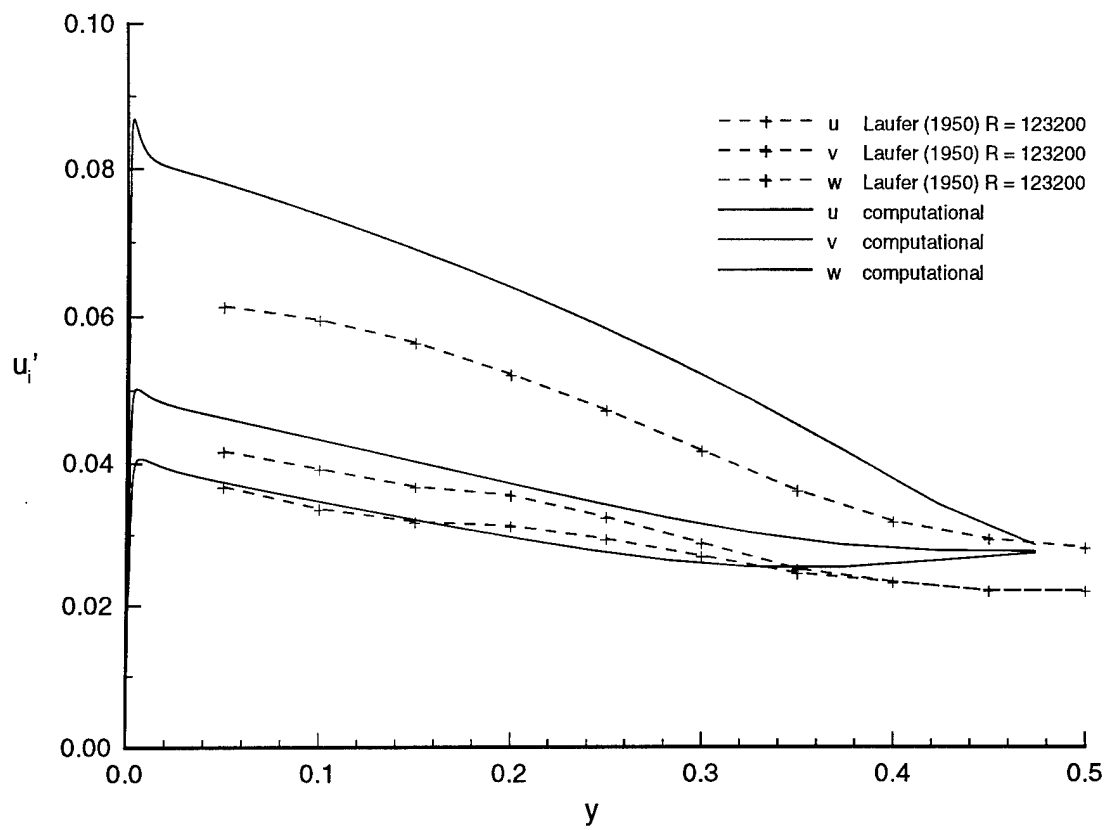


Figure 106. Average Velocity Fluctuations in a Two-Dimensional Channel

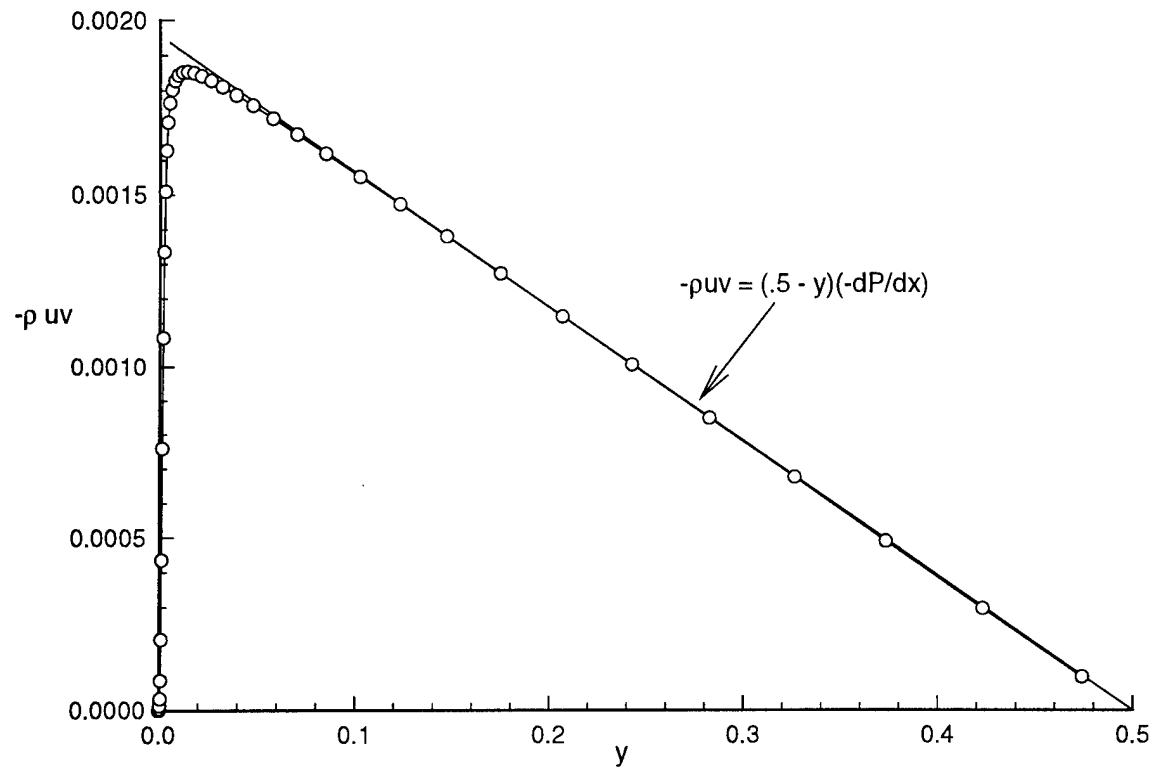


Figure 107. Shear Stress in a Two-Dimensional Channel

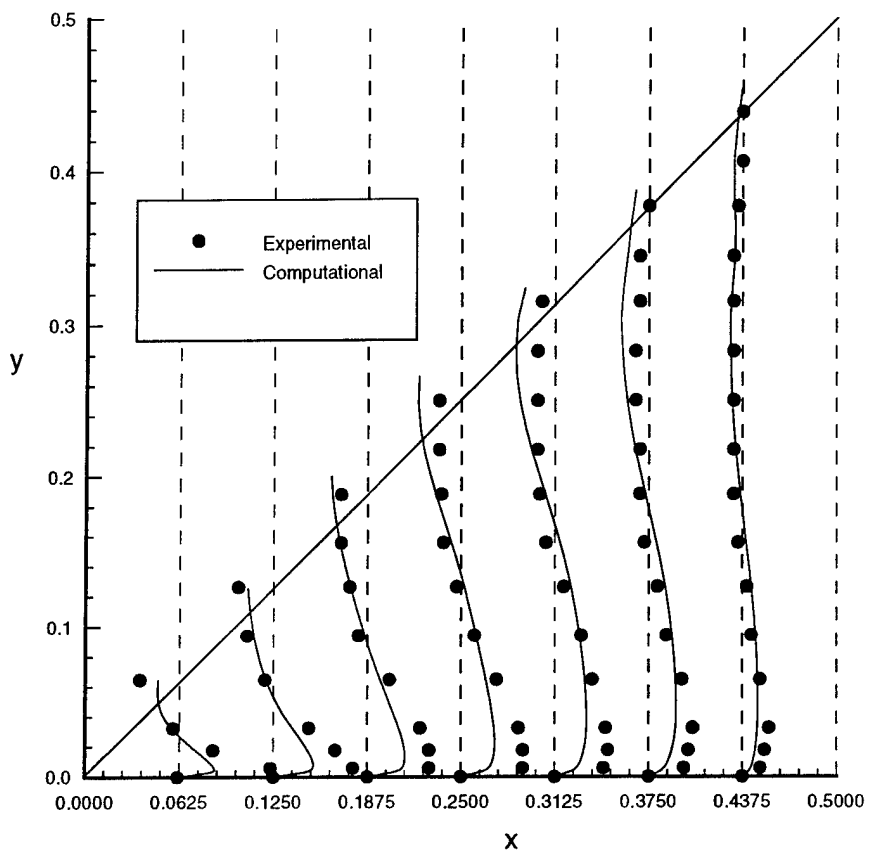


Figure 108. Secondary Velocity Profiles in a Square Duct

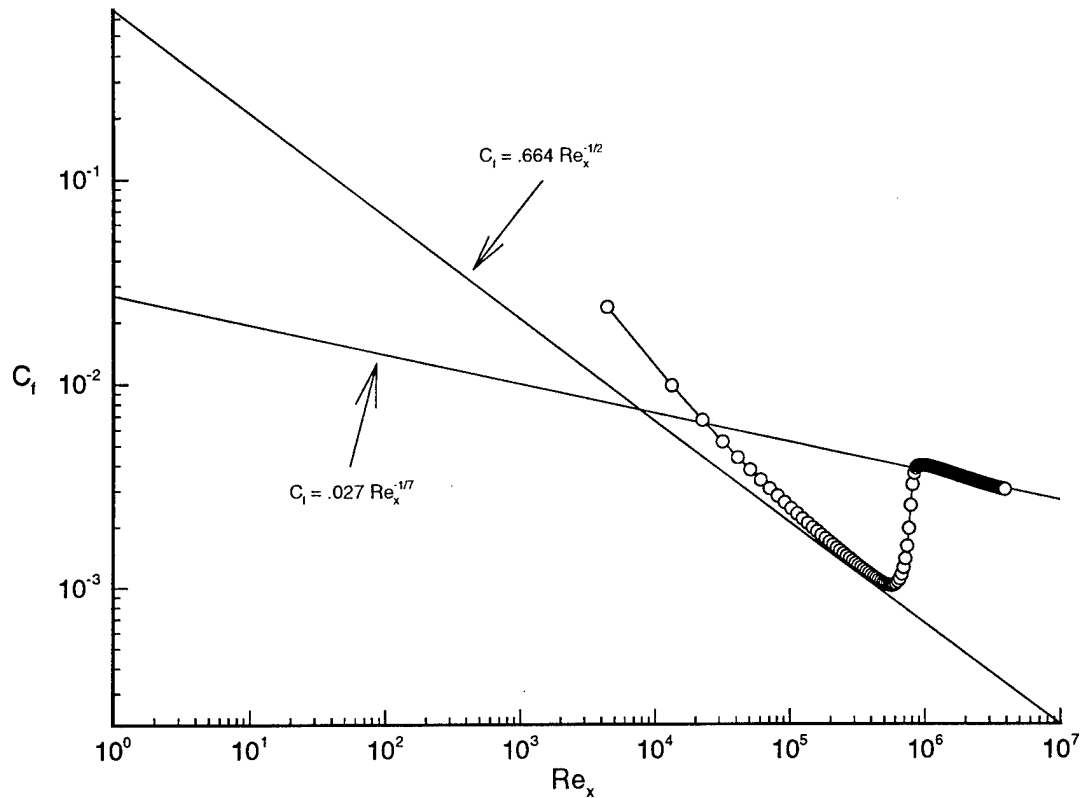


Figure 109. Skin-Friction Coefficient for a Turbulent Flat Plate Boundary Layer

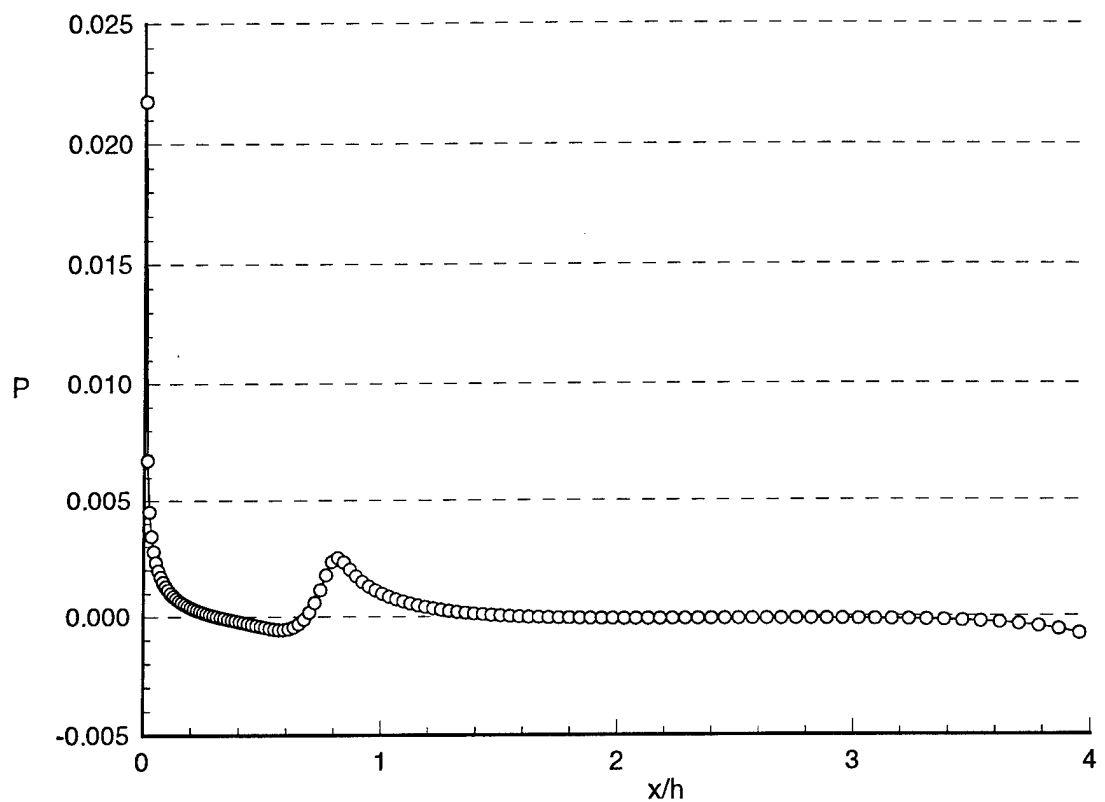


Figure 110. Surface Pressure for a Turbulent Flat Plate Boundary Layer

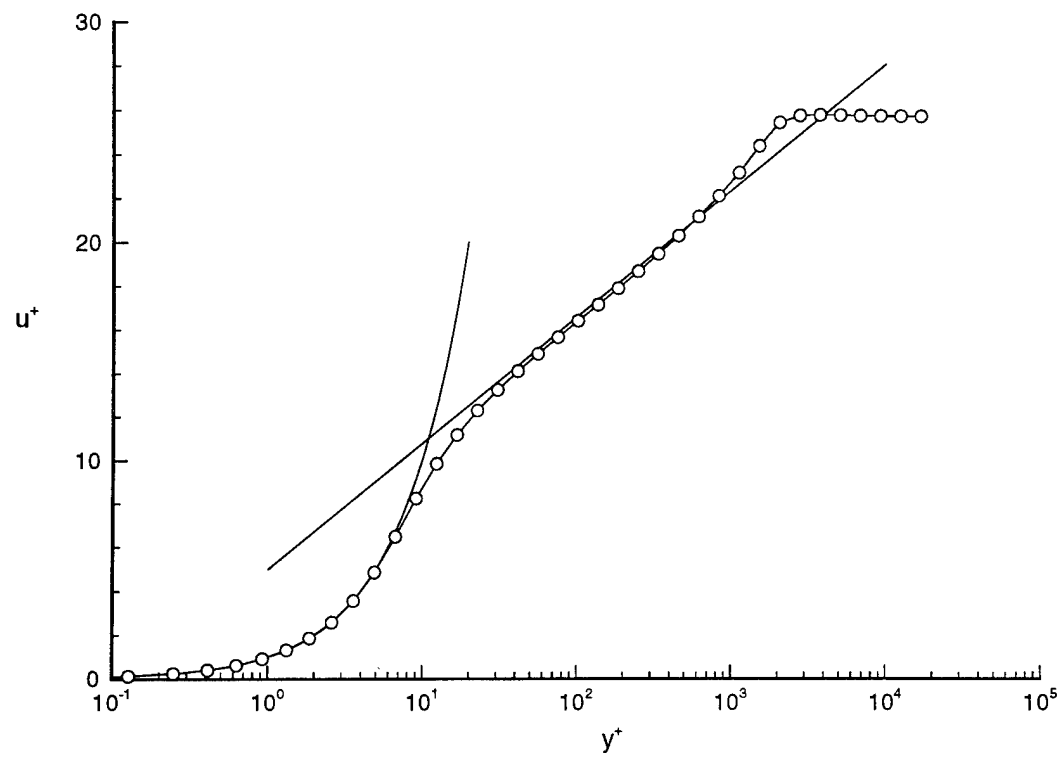


Figure 111. Velocity Profile for a Flat Plate Boundary Layer at  $Re_x = 4,000,000$

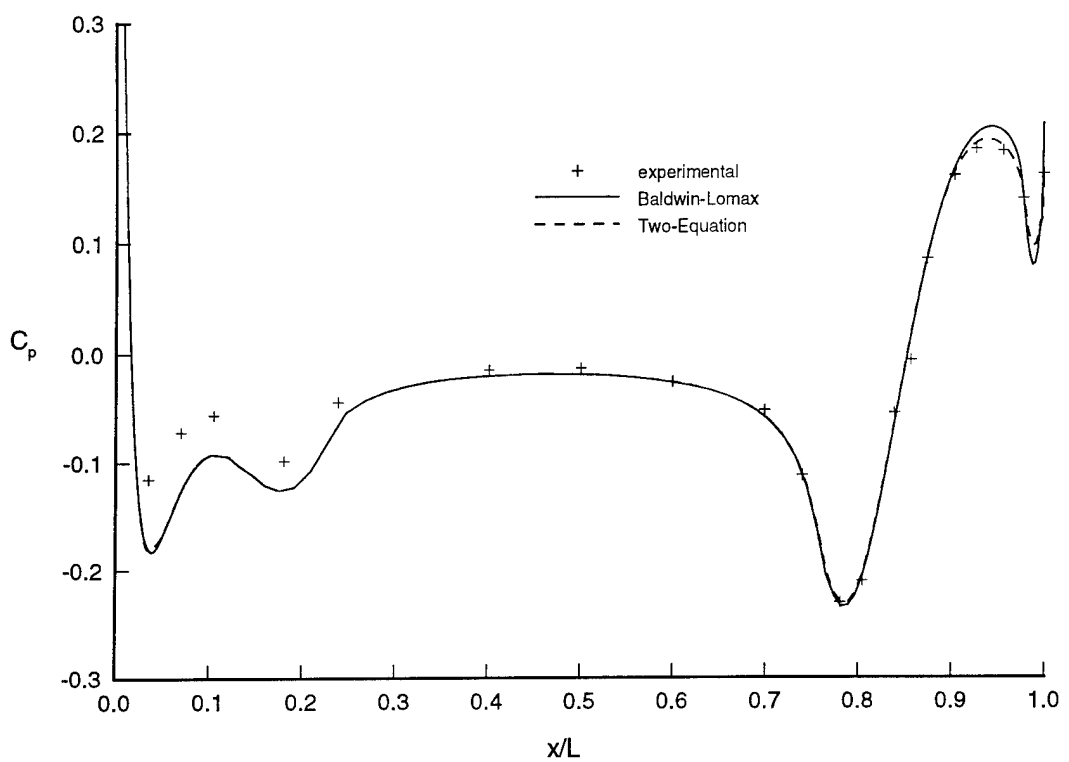


Figure 112. Pressure Distribution on the SUBOFF Barebody

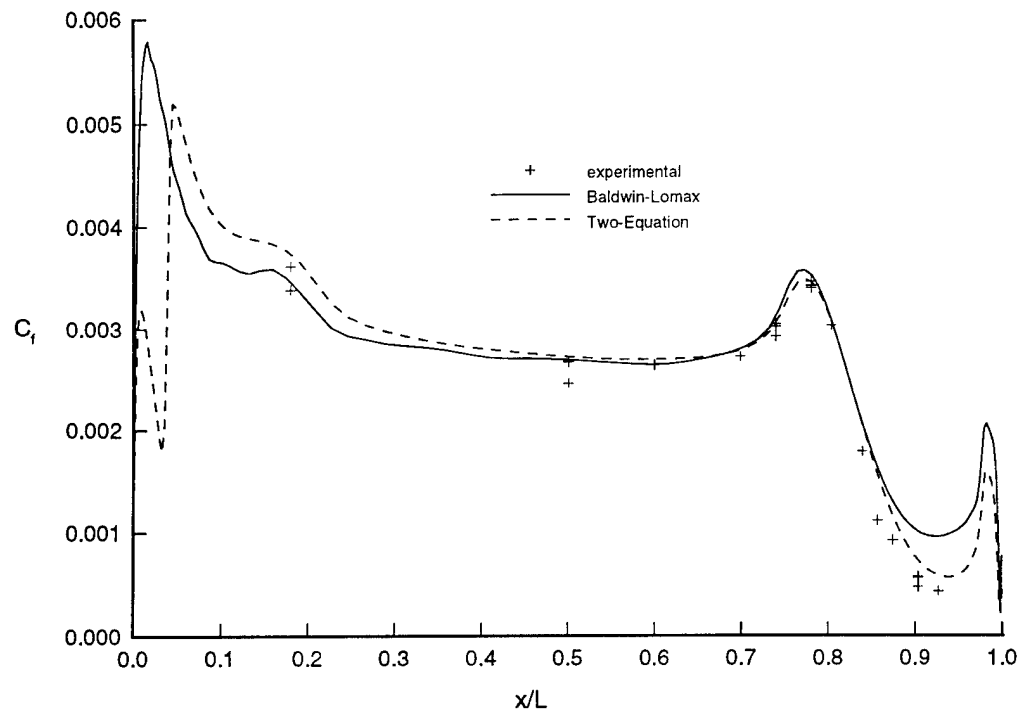


Figure 113. Skin-Friction Distribution on the SUBOFF Barebody

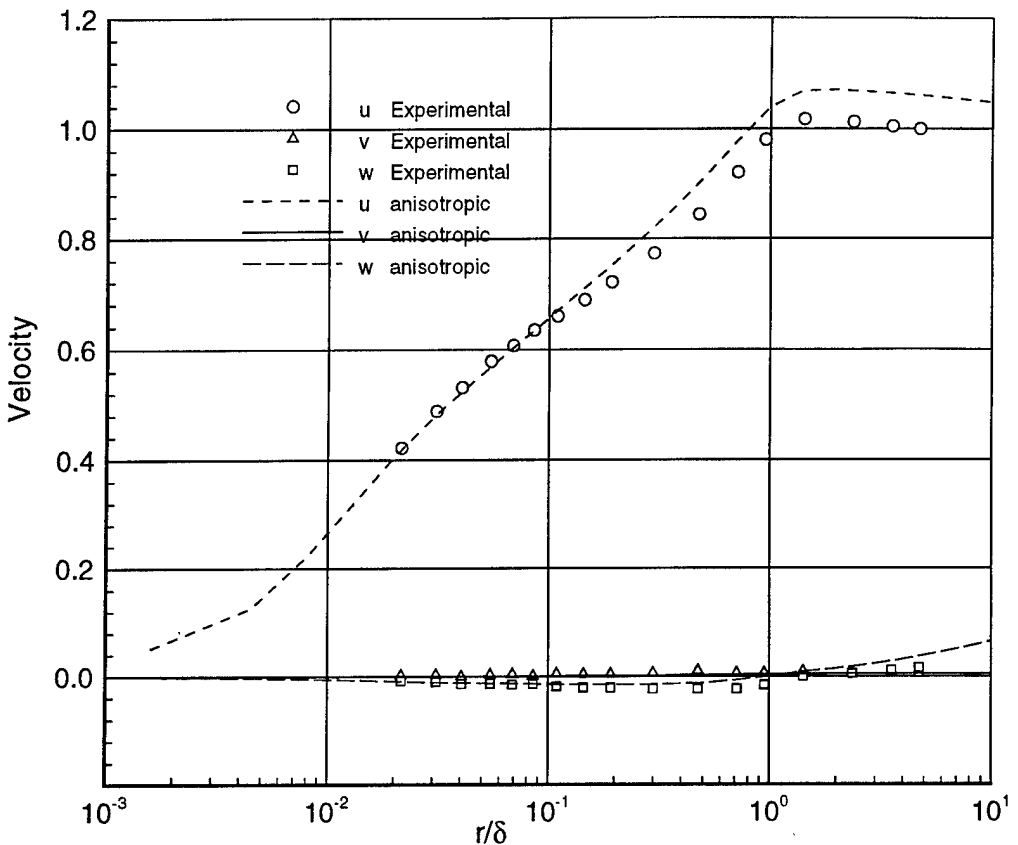


Figure 114. Boundary Layer Velocity Profiles on a 6:1 Prolate Spheroid Using the Anisotropic Turbulence Model ( $x/L = 0.4$ ,  $\phi = 100^\circ$ ,  $\alpha = 10^\circ$ , and  $Re = 4,200,000$ )

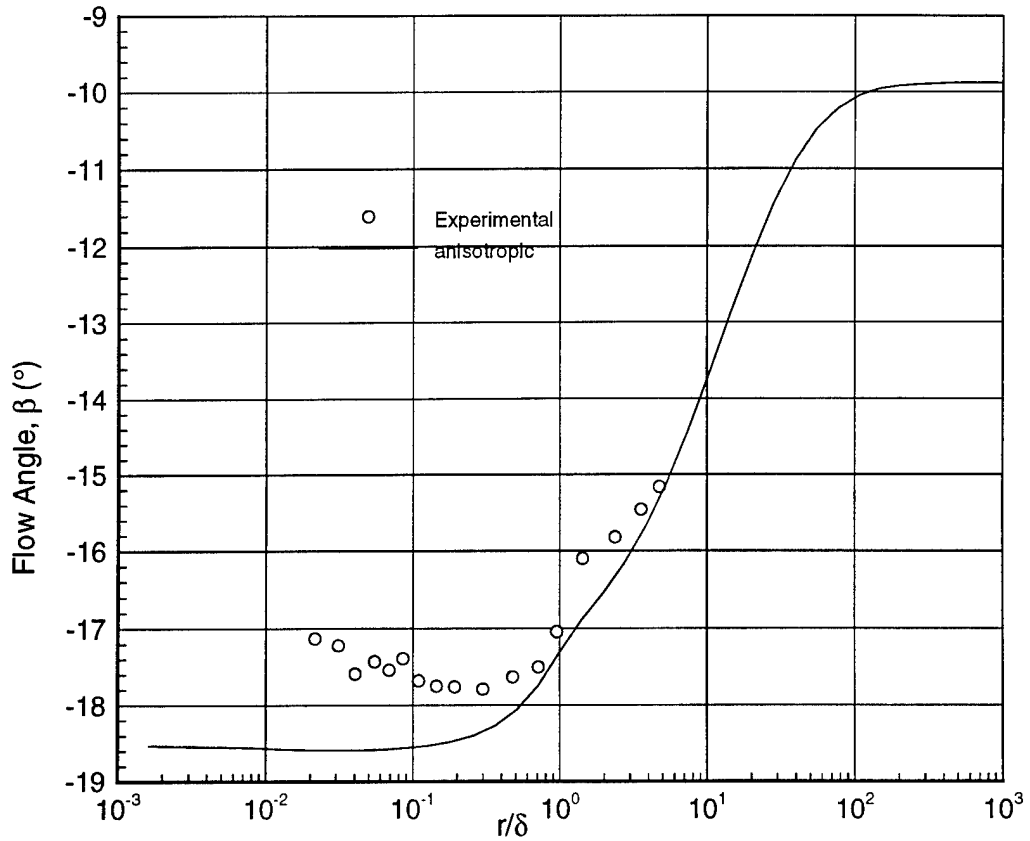


Figure 115. Surface Flow Angles on a 6:1 Prolate Spheroid Using the Anisotropic Turbulence Model ( $x/L = 0.4$ ,  $\phi = 100^{\circ}$ ,  $\alpha = 10^{\circ}$ , and  $Re = 4,200,000$ )

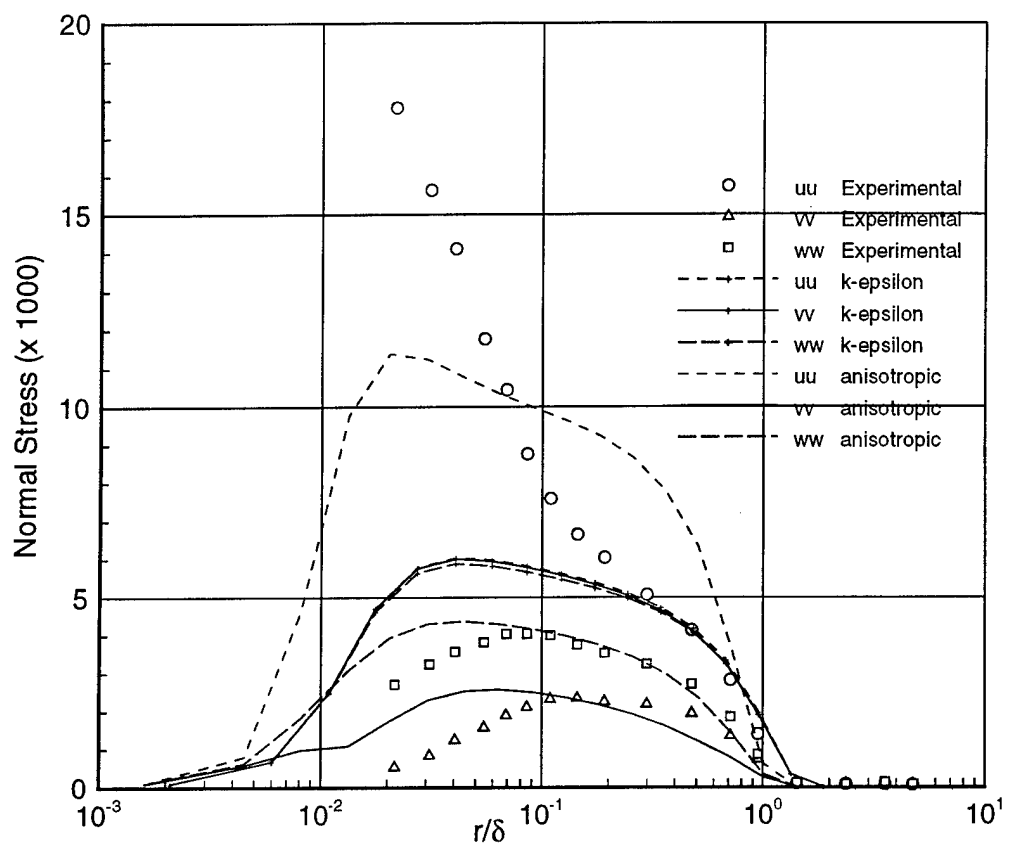


Figure 116. Boundary Layer Normal-Stress Profiles on a 6:1 Prolate Spheroid Using the Anisotropic Turbulence Model ( $x/L = 0.4$ ,  $\phi = 100^\circ$ ,  $\alpha = 10^\circ$ , and  $Re = 4,200,000$ )

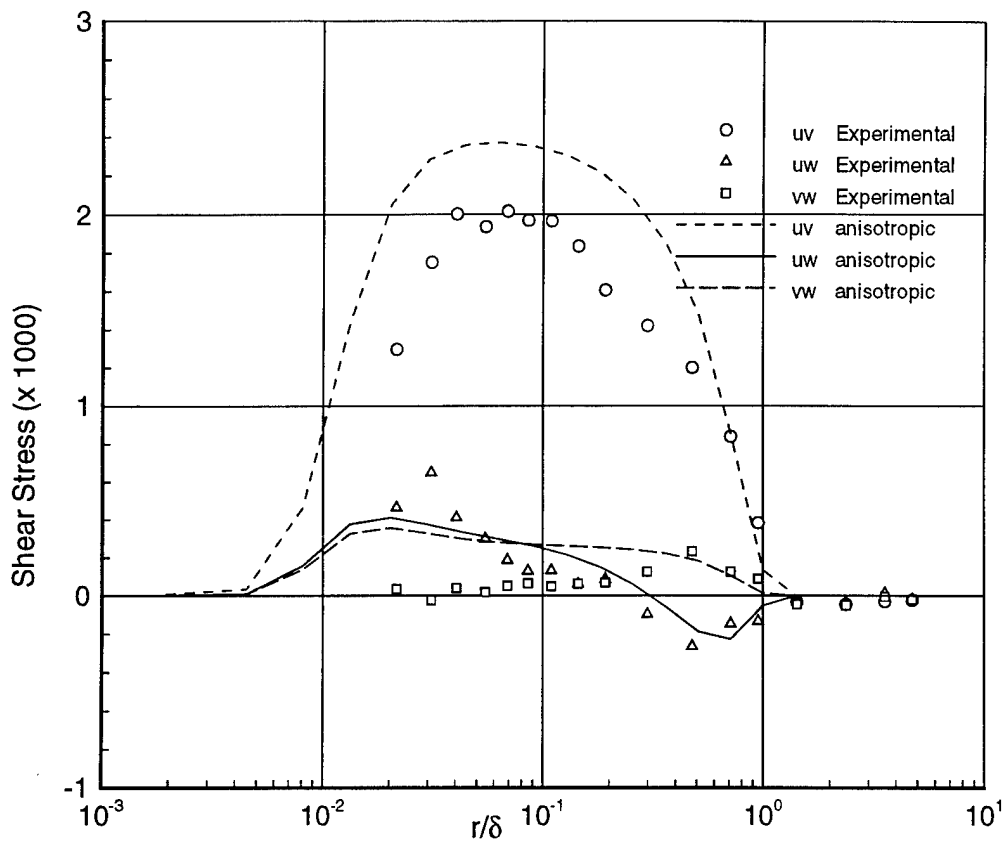
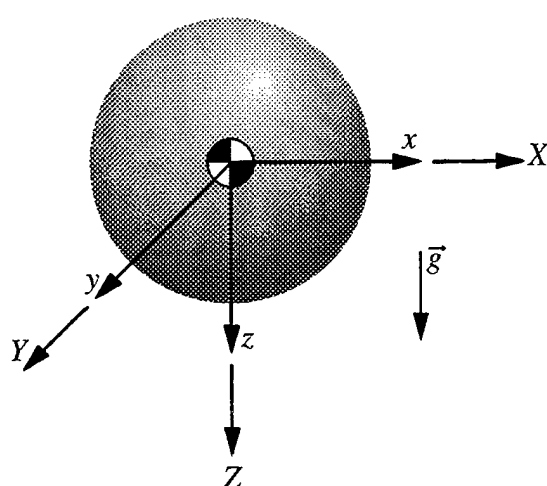


Figure 117. Boundary Layer Shear-Stress Profiles on a 6:1 Prolate Spheroid Using the Anisotropic Turbulence Model ( $x/L = 0.4$ ,  $\phi = 100^\circ$ ,  $\alpha = 10^\circ$ , and  $Re = 4,200,000$ )

**Initial  $t=0$**



**Later  $t > 0$**

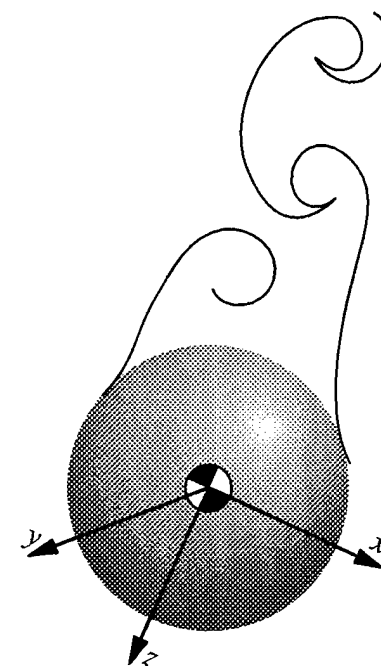
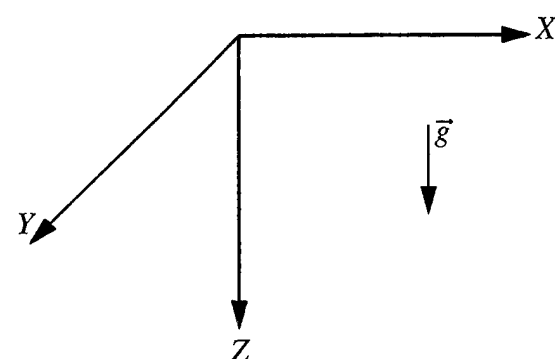


Figure 118. Schematic of the Free-Falling Sphere Calculation

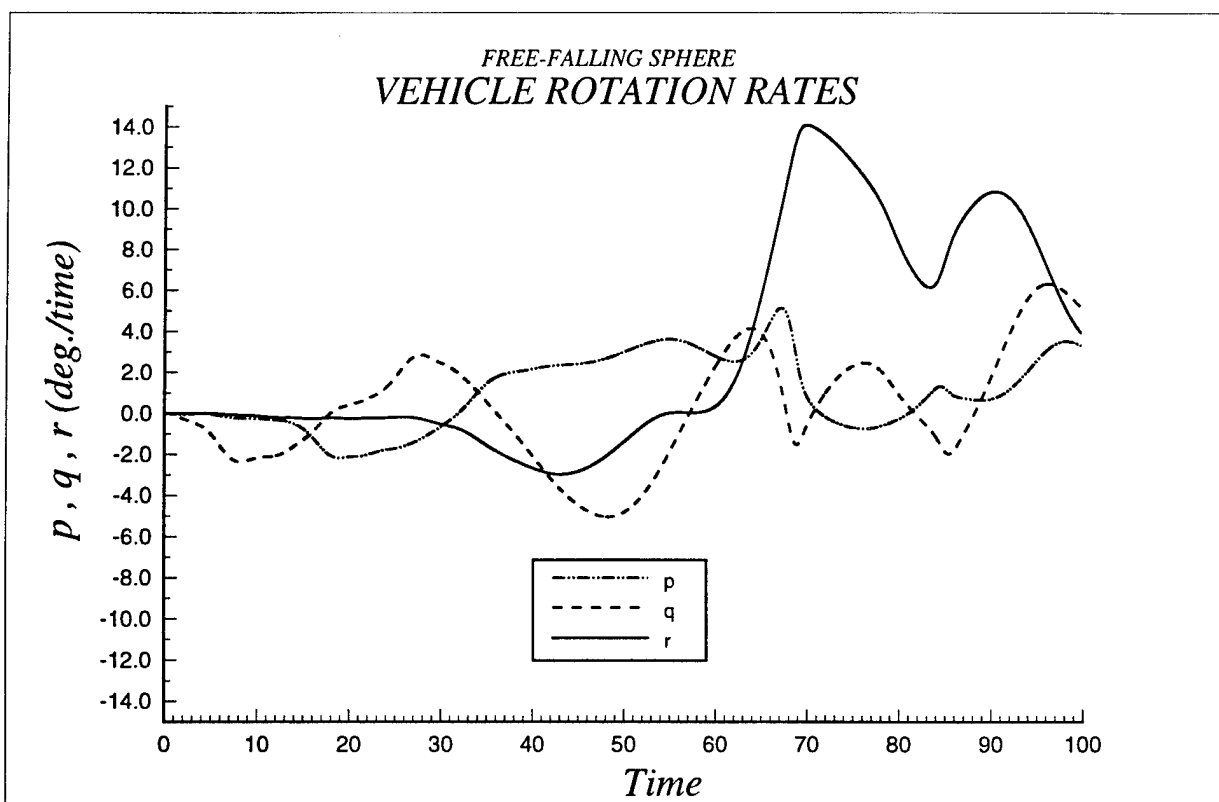
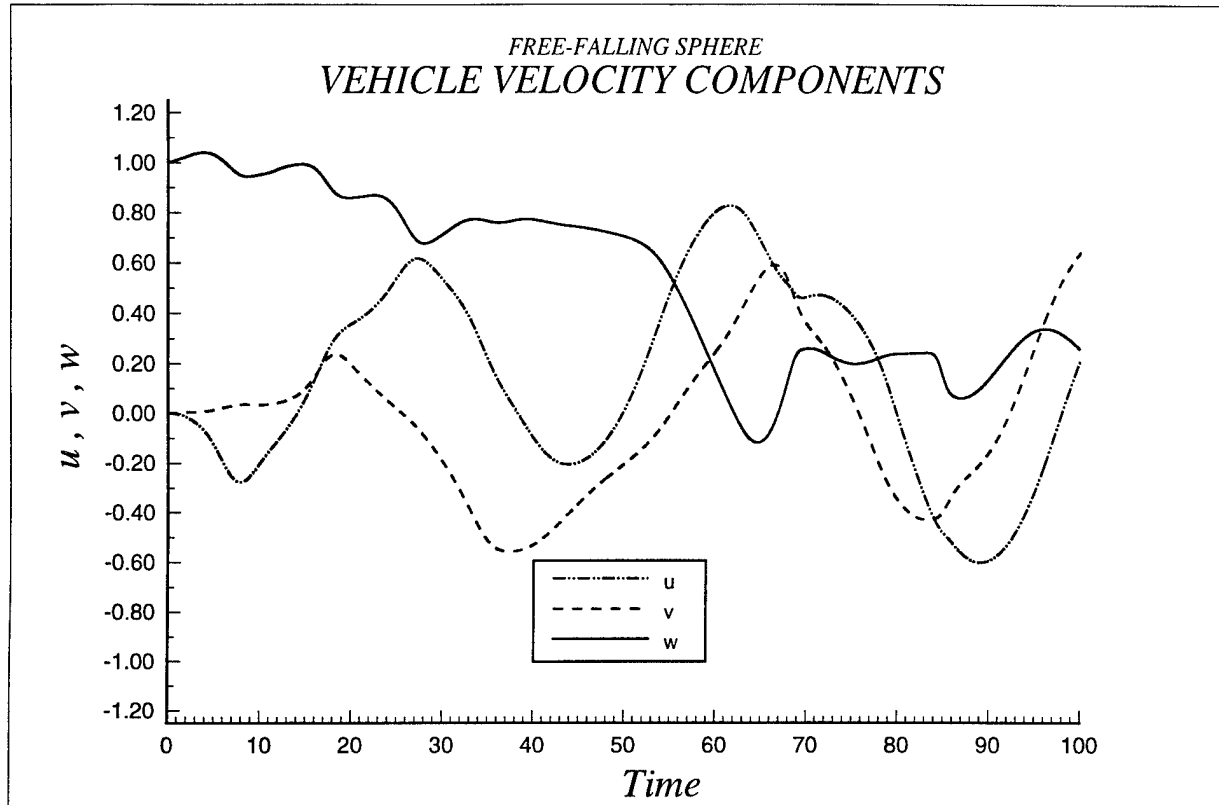


Figure 119. Body-Fixed Velocity and Rotation Rate Histories for the Free-Falling Sphere  
 Obtained from Integration of the 6DOF Equations:  
 (a) Velocities  
 (b) Rotation Rates

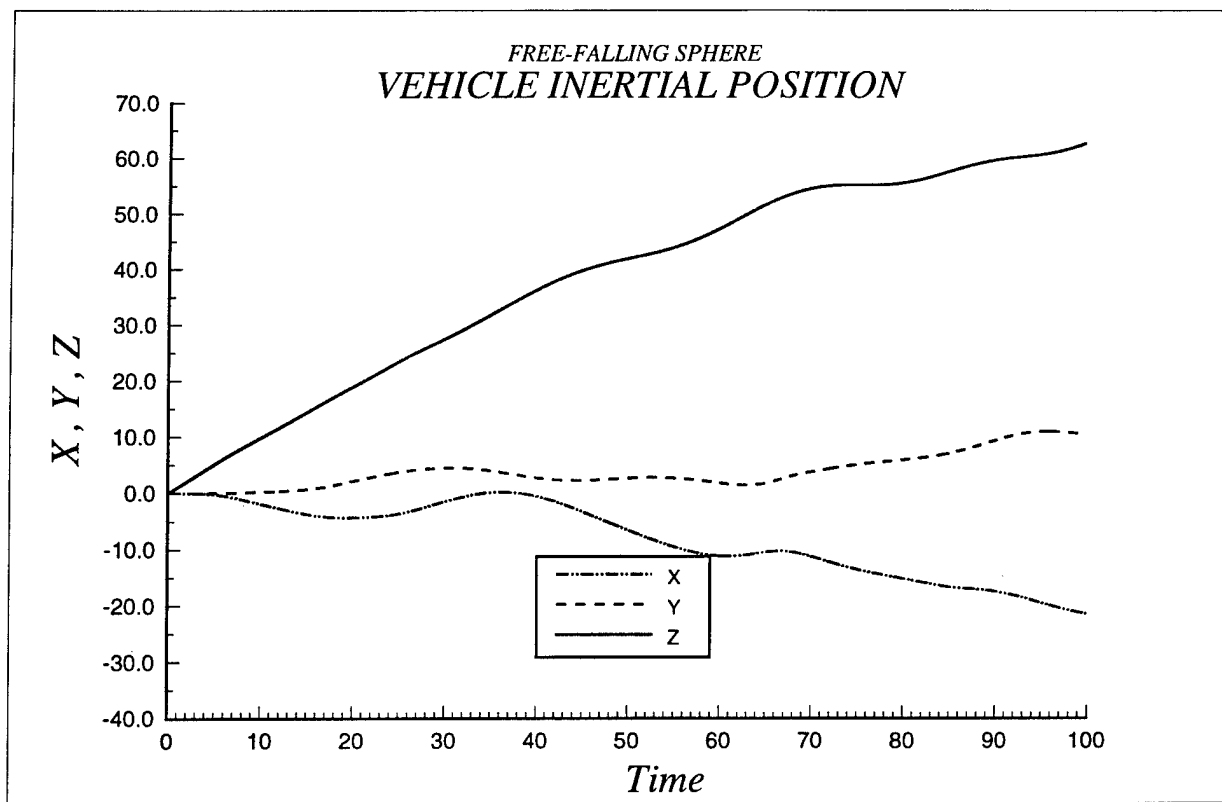
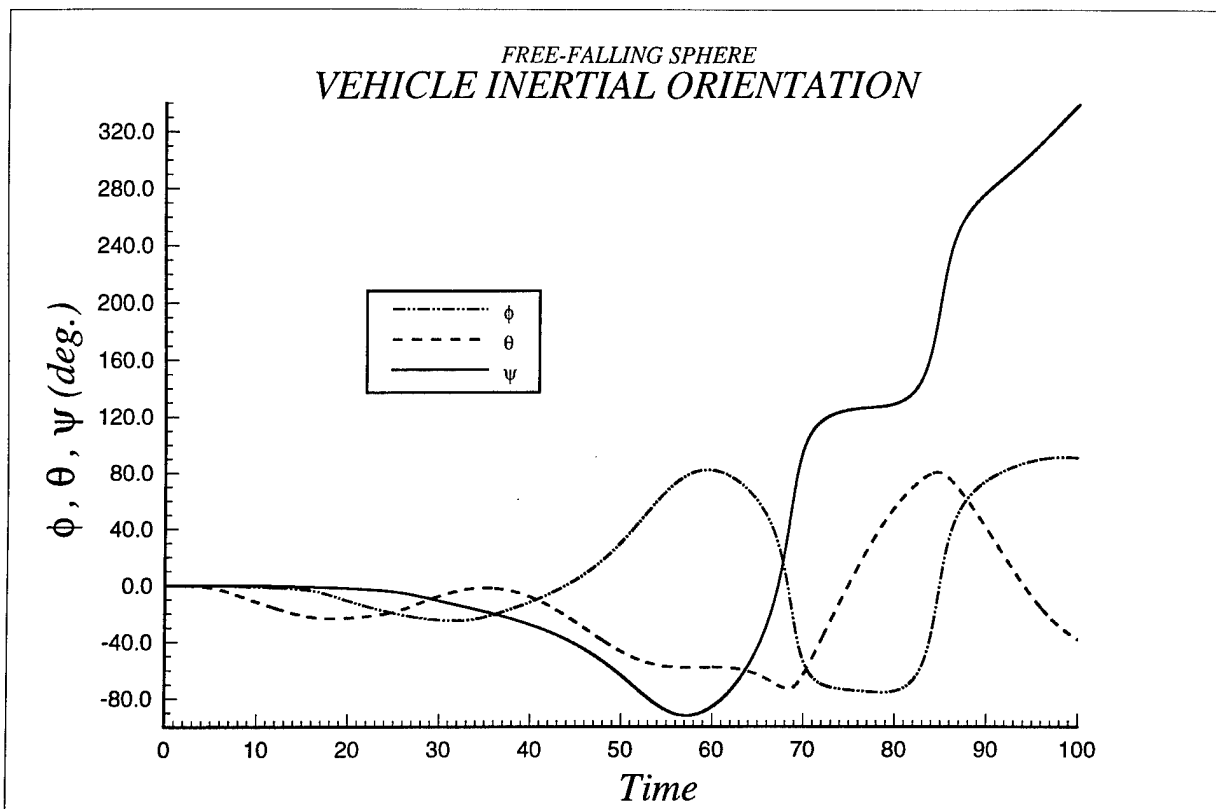


Figure 120. Inertial Trajectory for the Free-Falling Sphere Obtained from Integration of the Kinematic Equations:  
 (a) Orientation  
 (b) Position

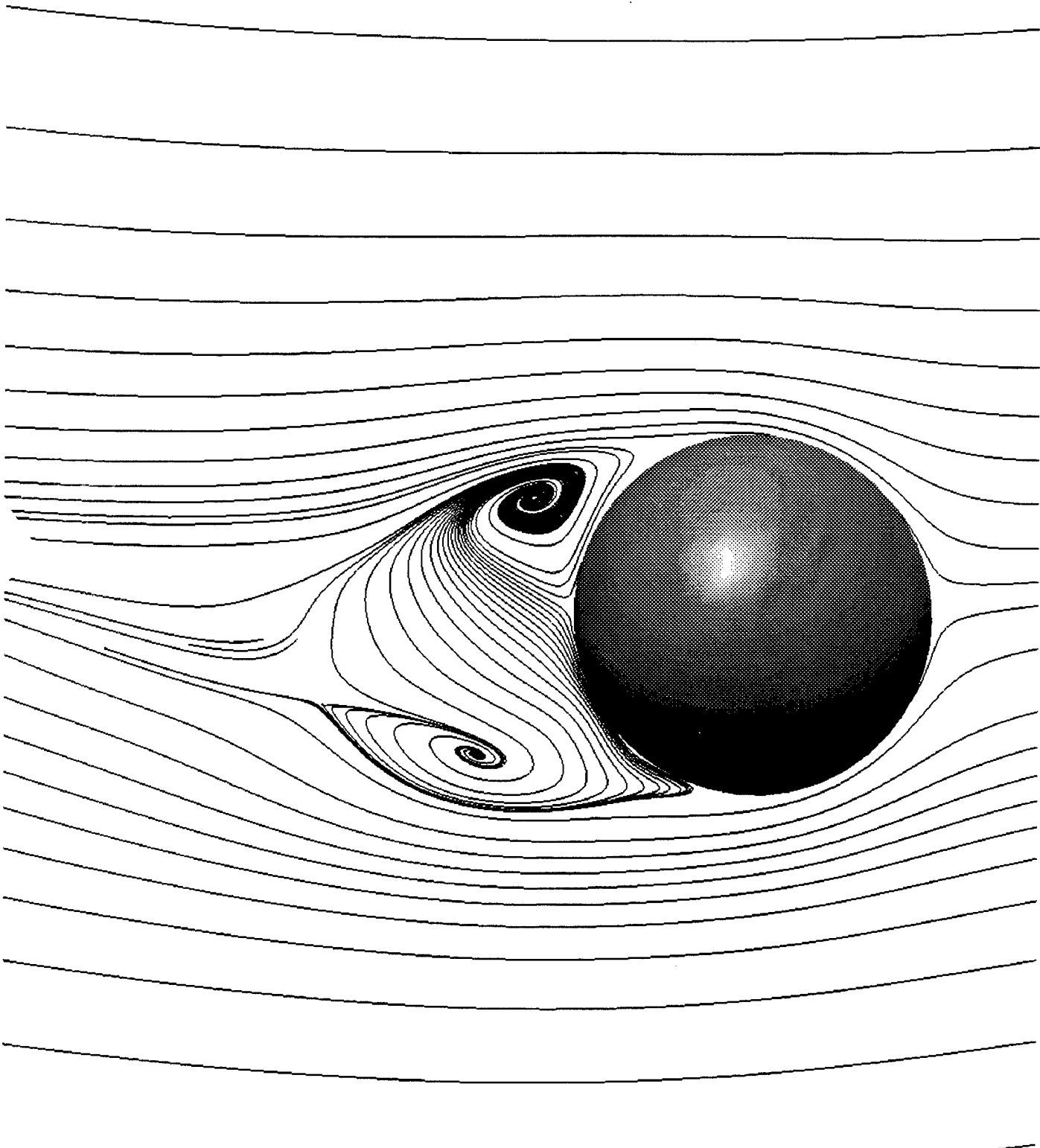
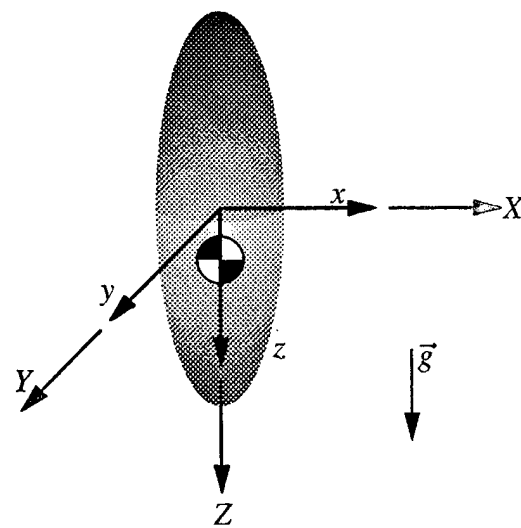


Figure 121. Particle Traces in the Relative Velocity Field for the Free-Falling Sphere Showing the Location of the Lee-Side Ring Vortex

**Initial  $t=0$**



**Later  $t > 0$**

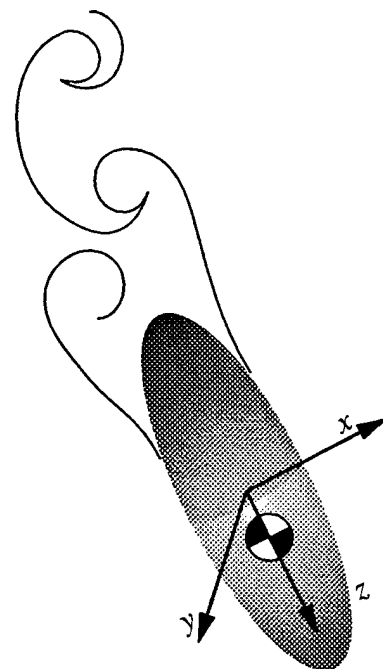
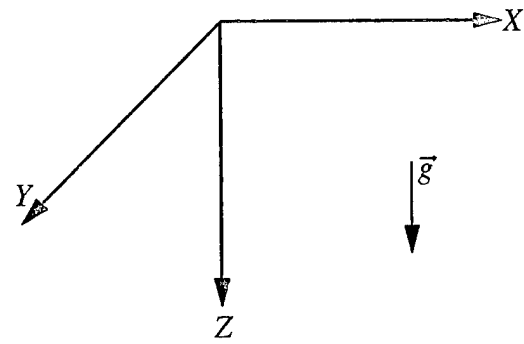


Figure 122. Schematic of the Free-Falling Ellipsoid Calculation

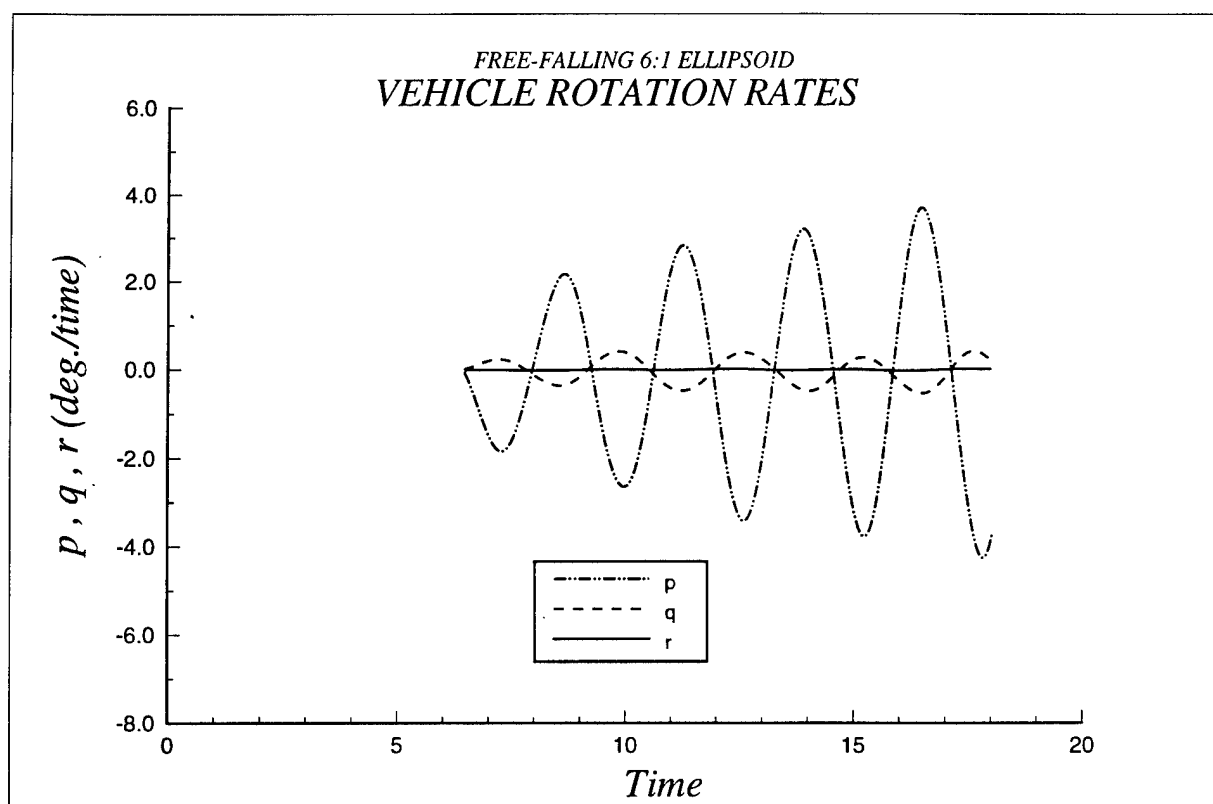
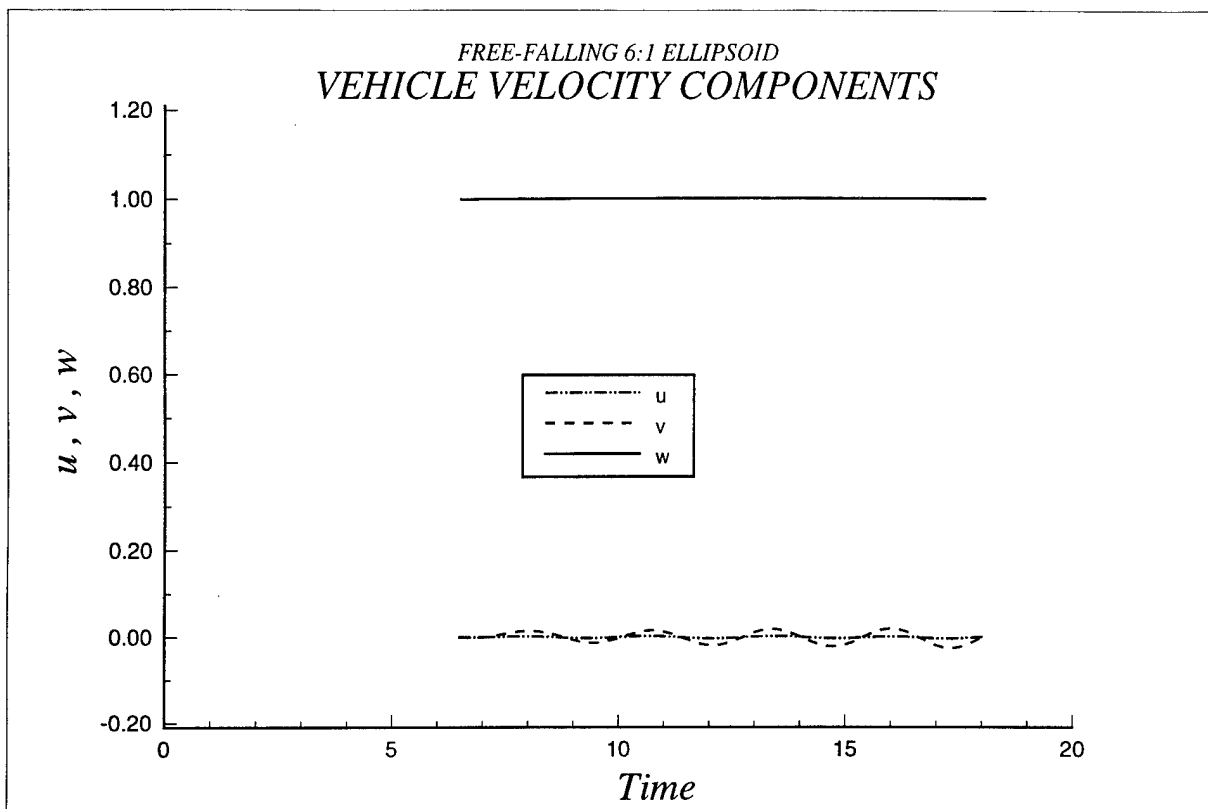


Figure 123.

Body-Fixed Velocity and Rotation Rate Histories for the Free-Falling 6:1 Prolate Spheroid Obtained from Integration of the 6DOF Equations:  
 (a) Velocities  
 (b) Rotation Rates

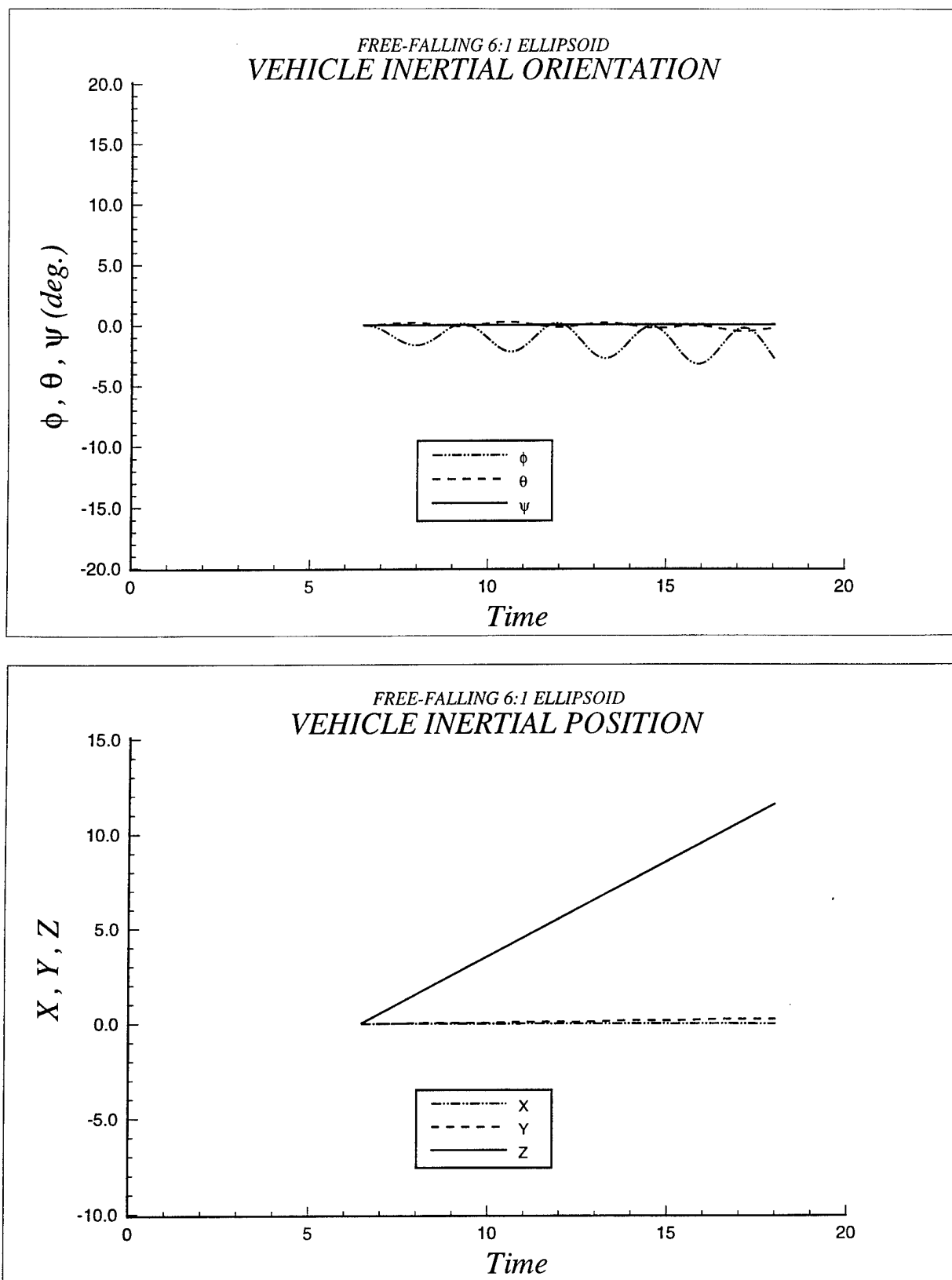


Figure 124.

Inertial Trajectory for the Free-Falling 6:1 Prolate Spheroid Obtained from Integration of the Kinematic Equations:  
 (a) Orientation  
 (b) Position

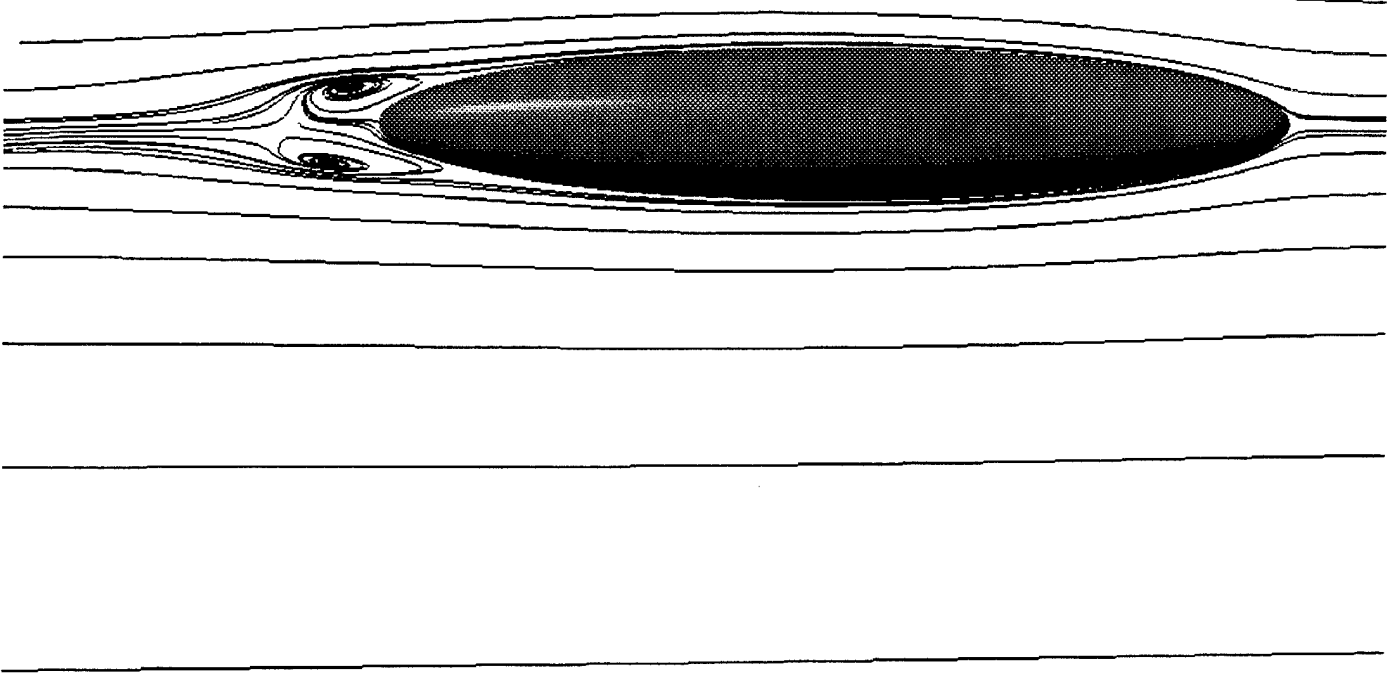


Figure 125. Particle Traces in the Relative Velocity Field for the Free-Falling 6:1 Prolate Spheroid Showing the Location of the Lee-Side Ring Vortex

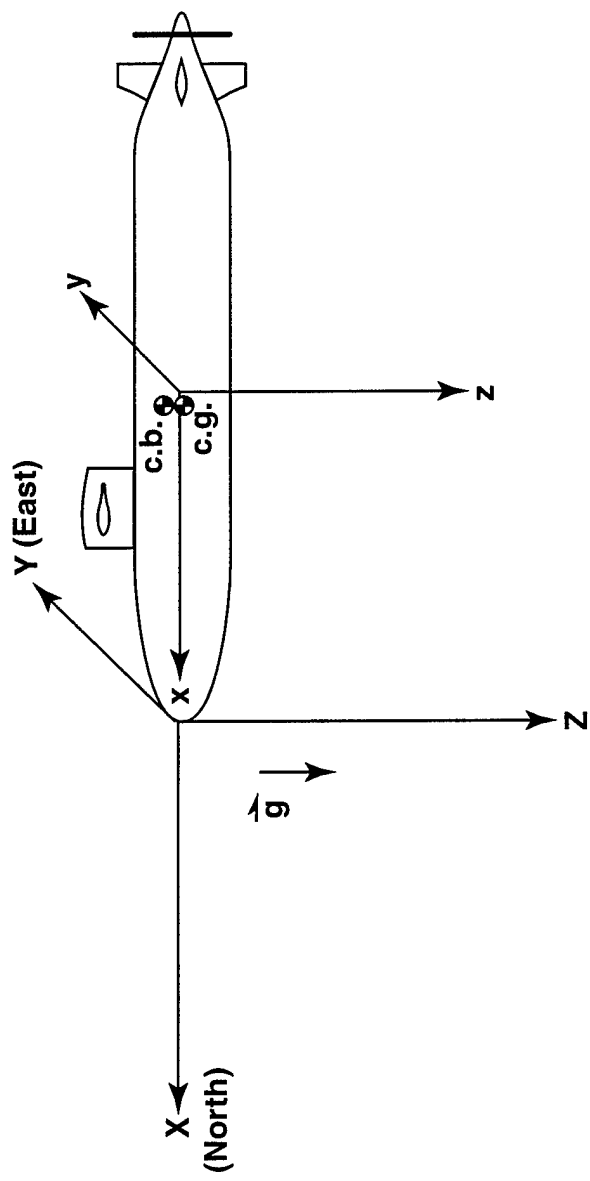


Figure 126. Schematic of the Initial Condition for the Actuator Disc-Propelled SUBOFF Calculation Showing the Relative Locations of the Inertial and Body-Fixed Coordinate Systems

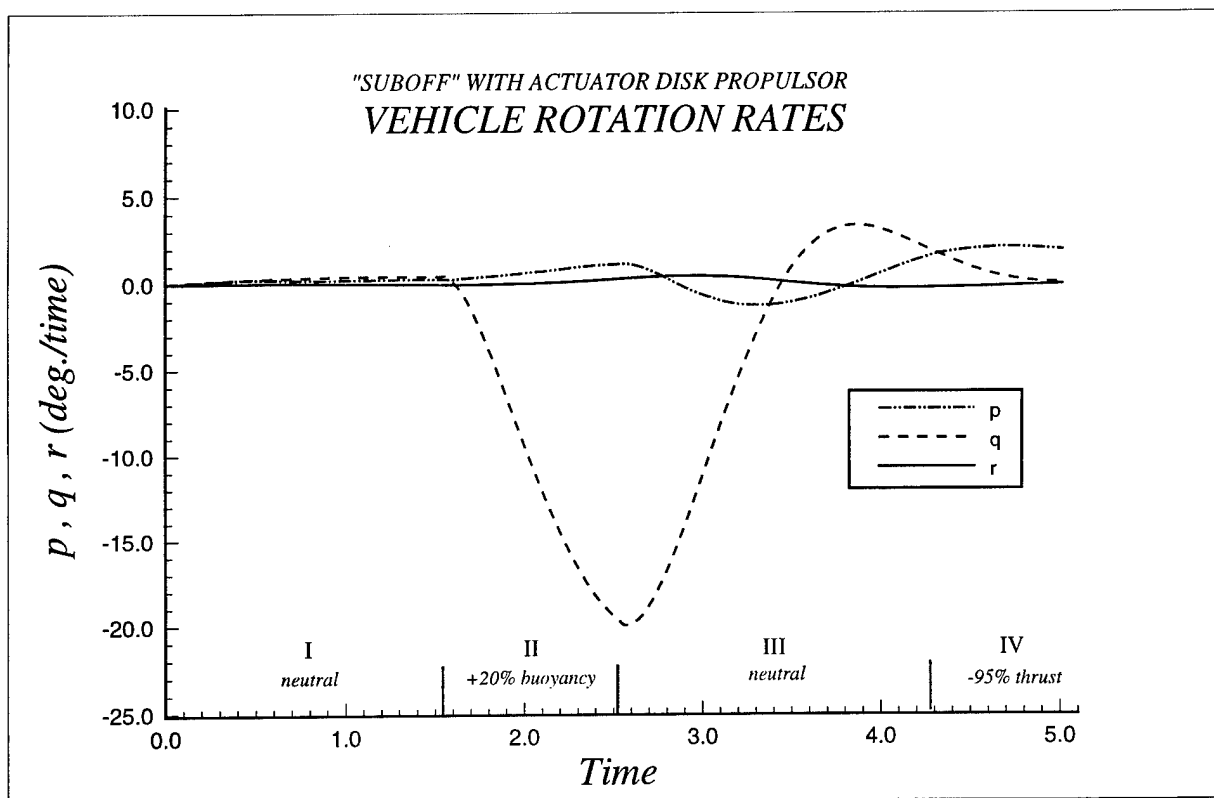
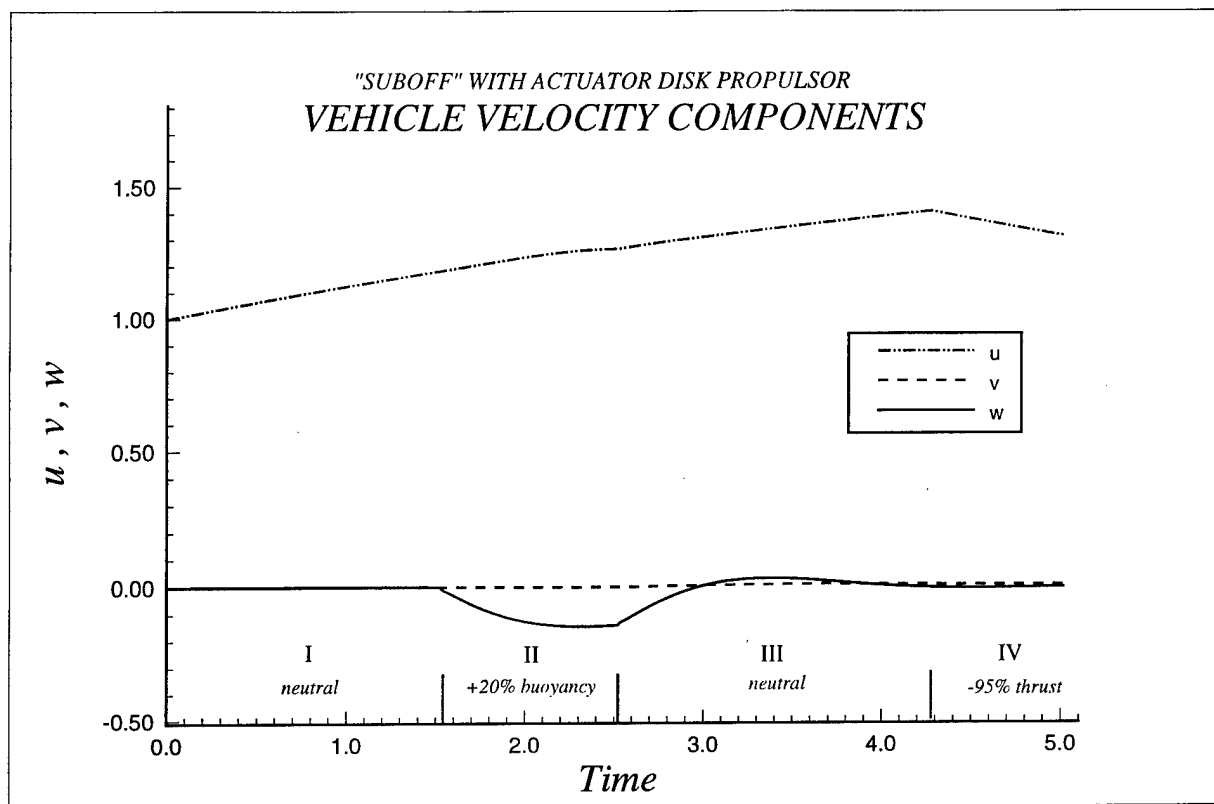


Figure 127. Body-Fixed Velocity and Rotation Rate Histories for the Propelled SUBOFF  
 Obtained from Integration of the 6DOF Equations:  
 (a) Velocities  
 (b) Rotation Rates

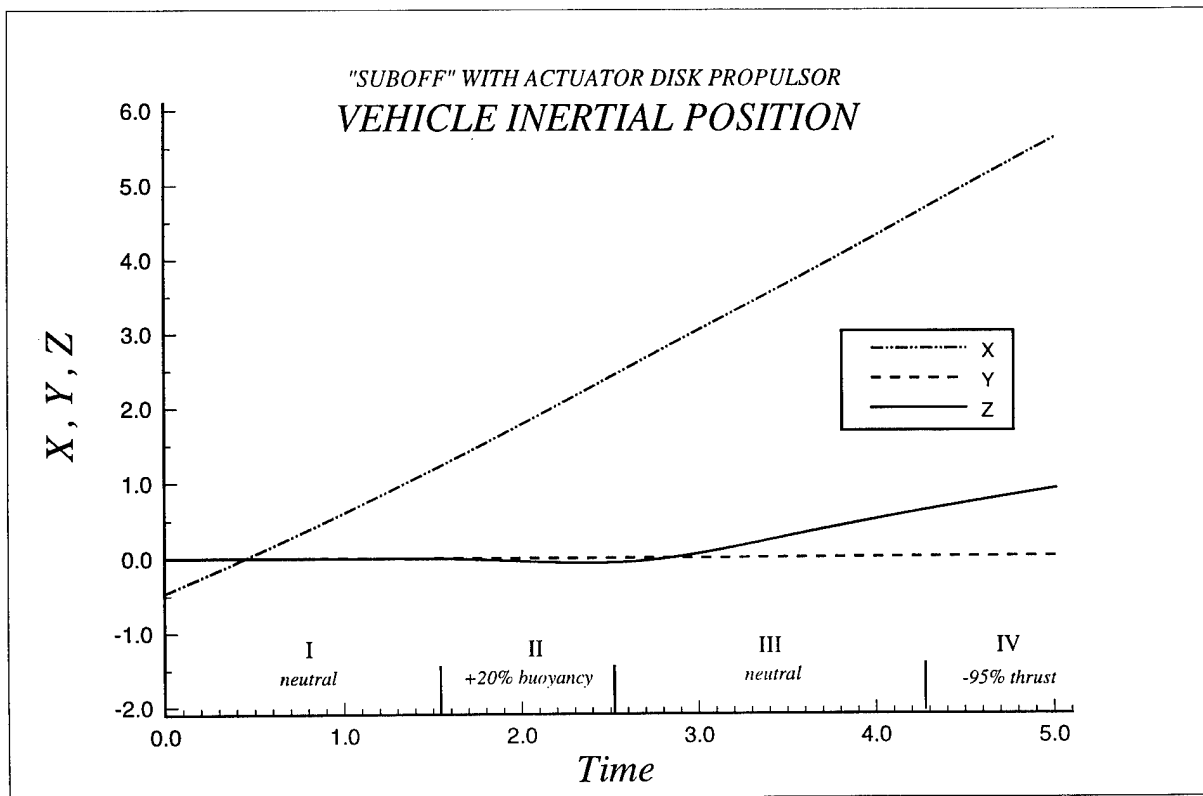
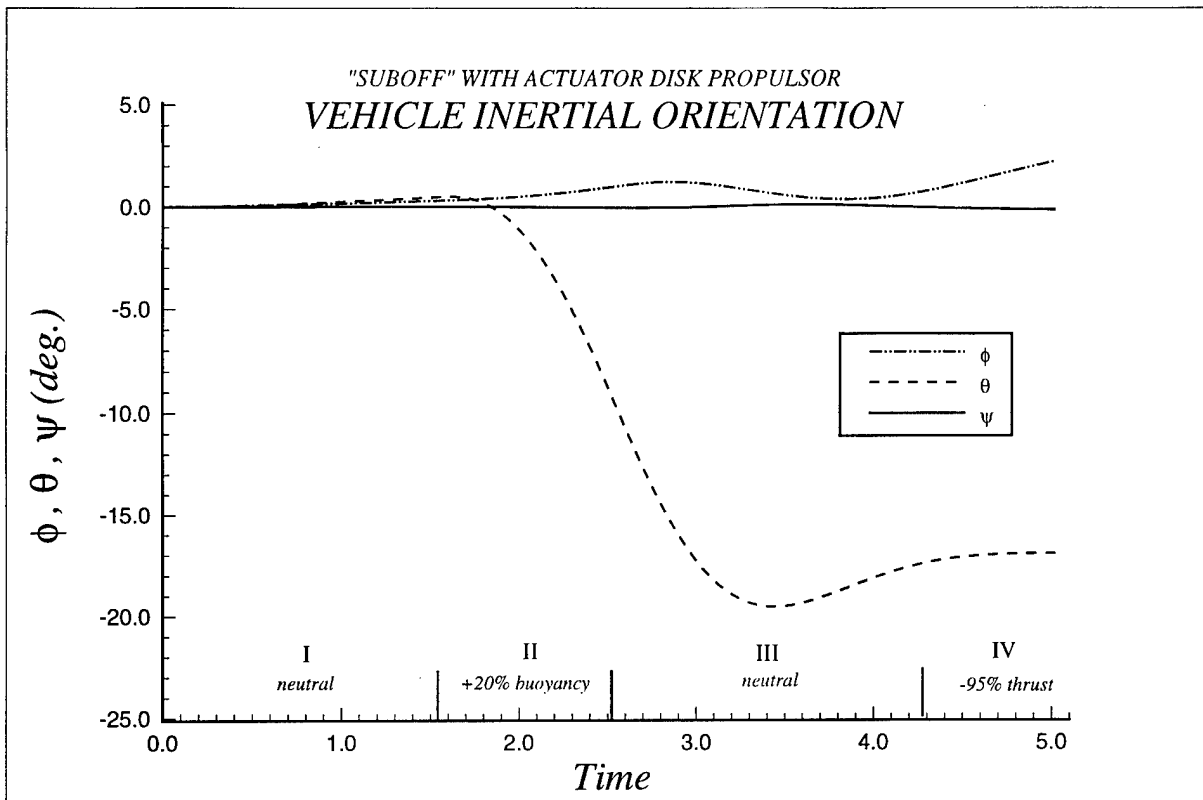


Figure 128. Inertial Trajectory for the Propelled SUBOFF Obtained from Integration of the Kinematic Equations:  
(a) Orientation  
(b) Position

$t = 0.02$

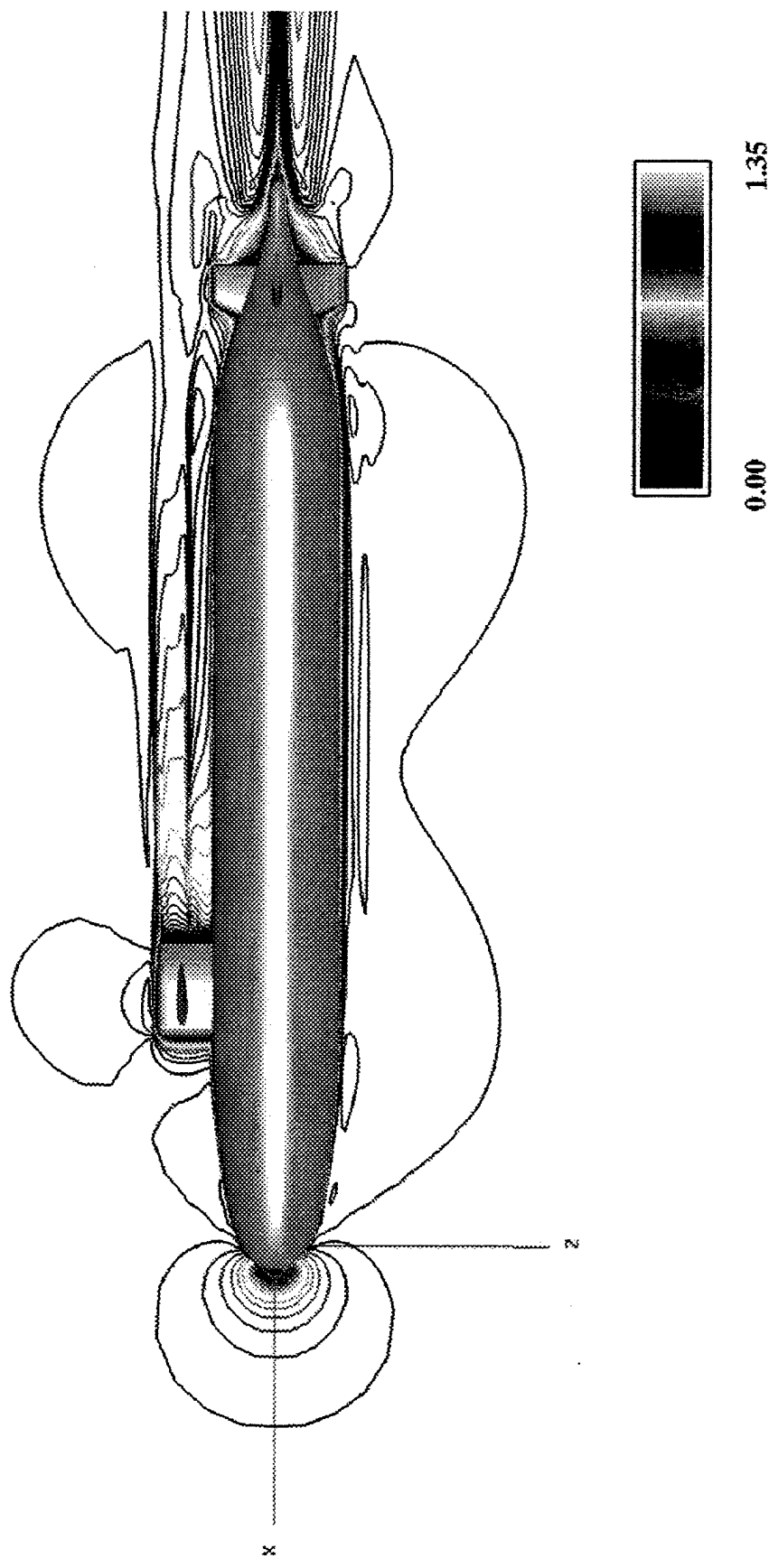


Figure 129.

Contours of Relative Velocity in the Geometric Symmetry Plane for the Propelled SUBOFF,  $t = 0.02$  (Beginning of Phase I)

$t = 2.52$

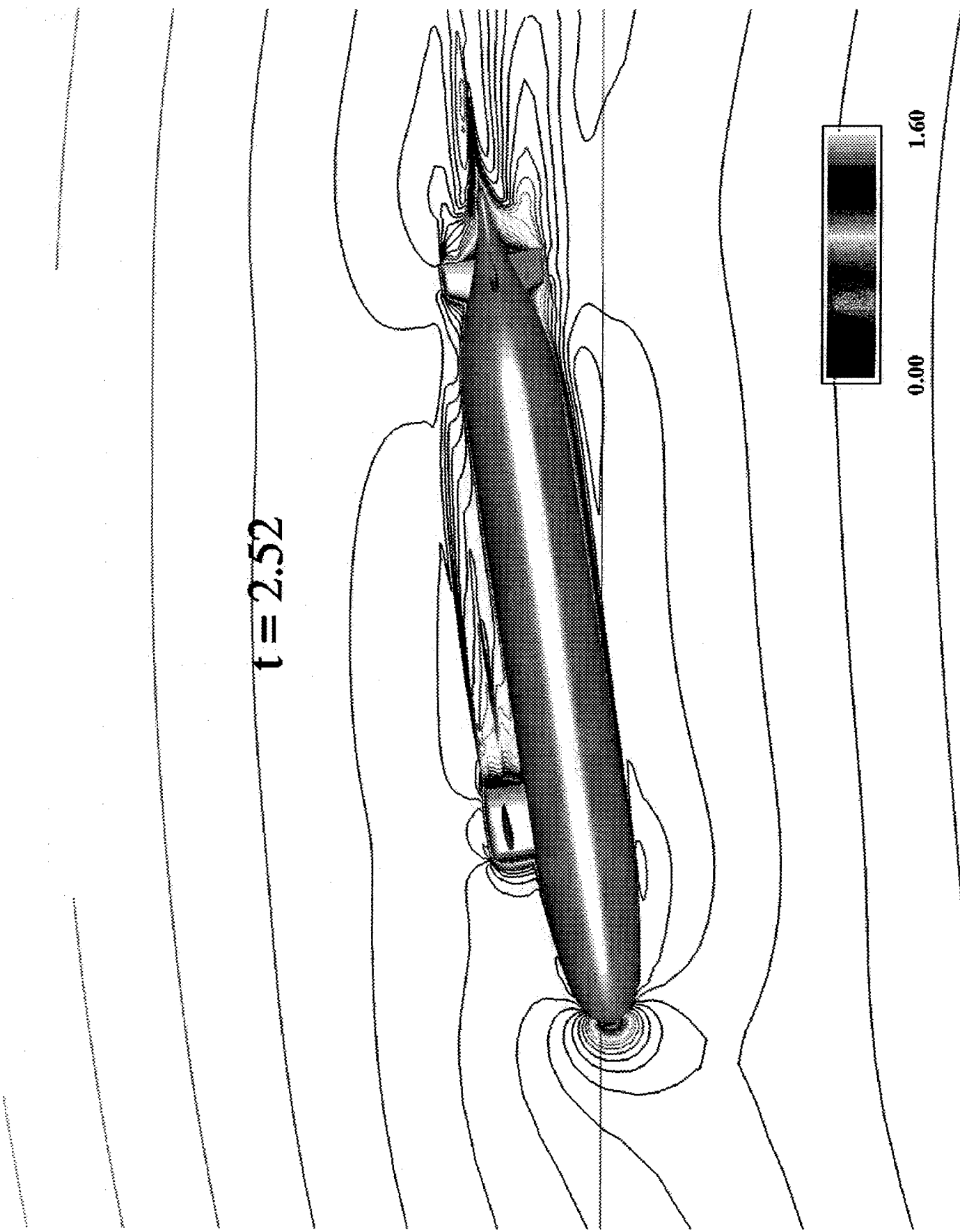


Figure 130. Contours of Relative Velocity in the Geometric Symmetry Plane for the Propelled SUBOFF,  $t = 2.52$  (Between Phases I and II)

$t = 5.02$

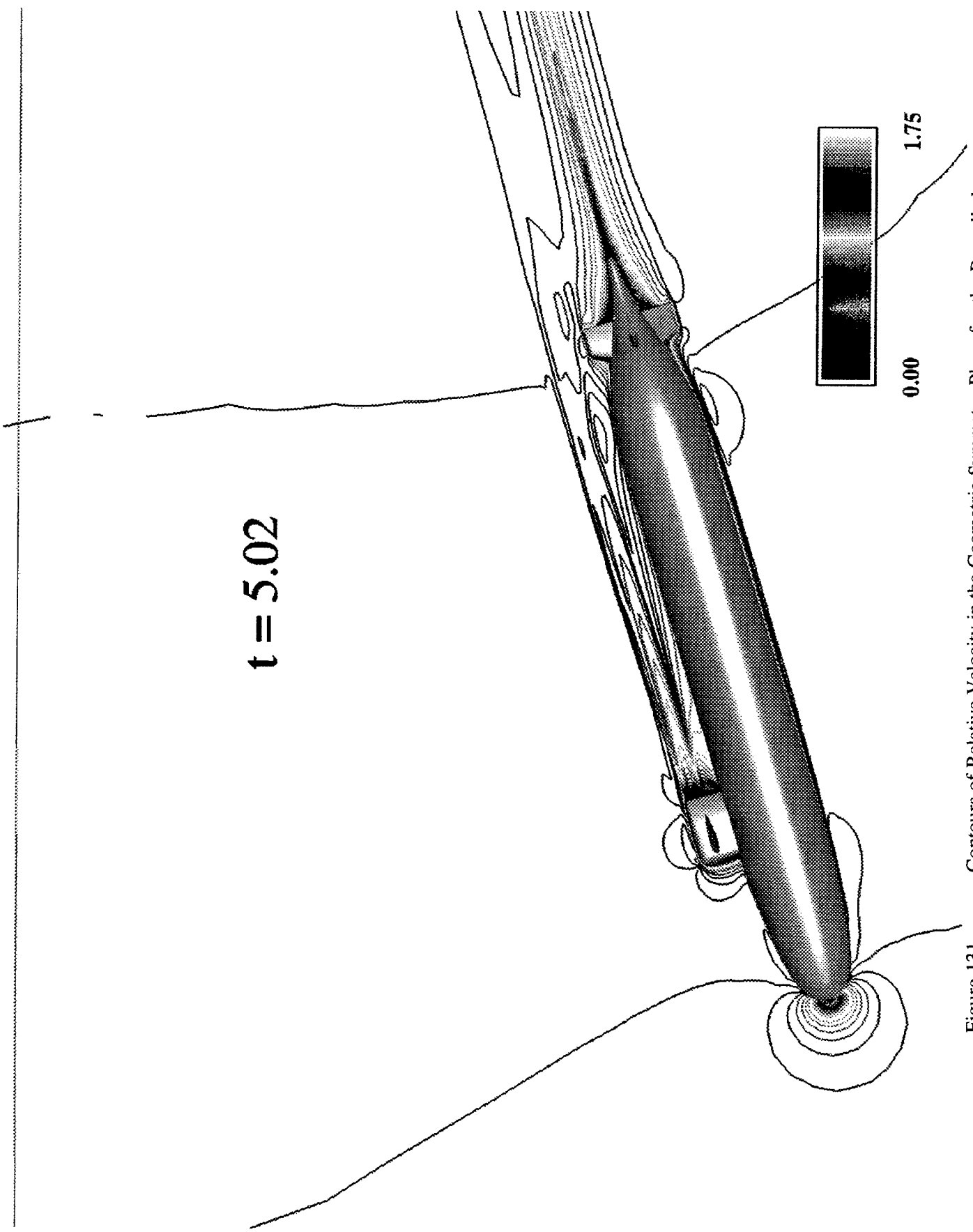


Figure 131. Contours of Relative Velocity in the Geometric Symmetry Plane for the Propelled SUBOFF,  $t = 5.02$  (End of the Simulation)

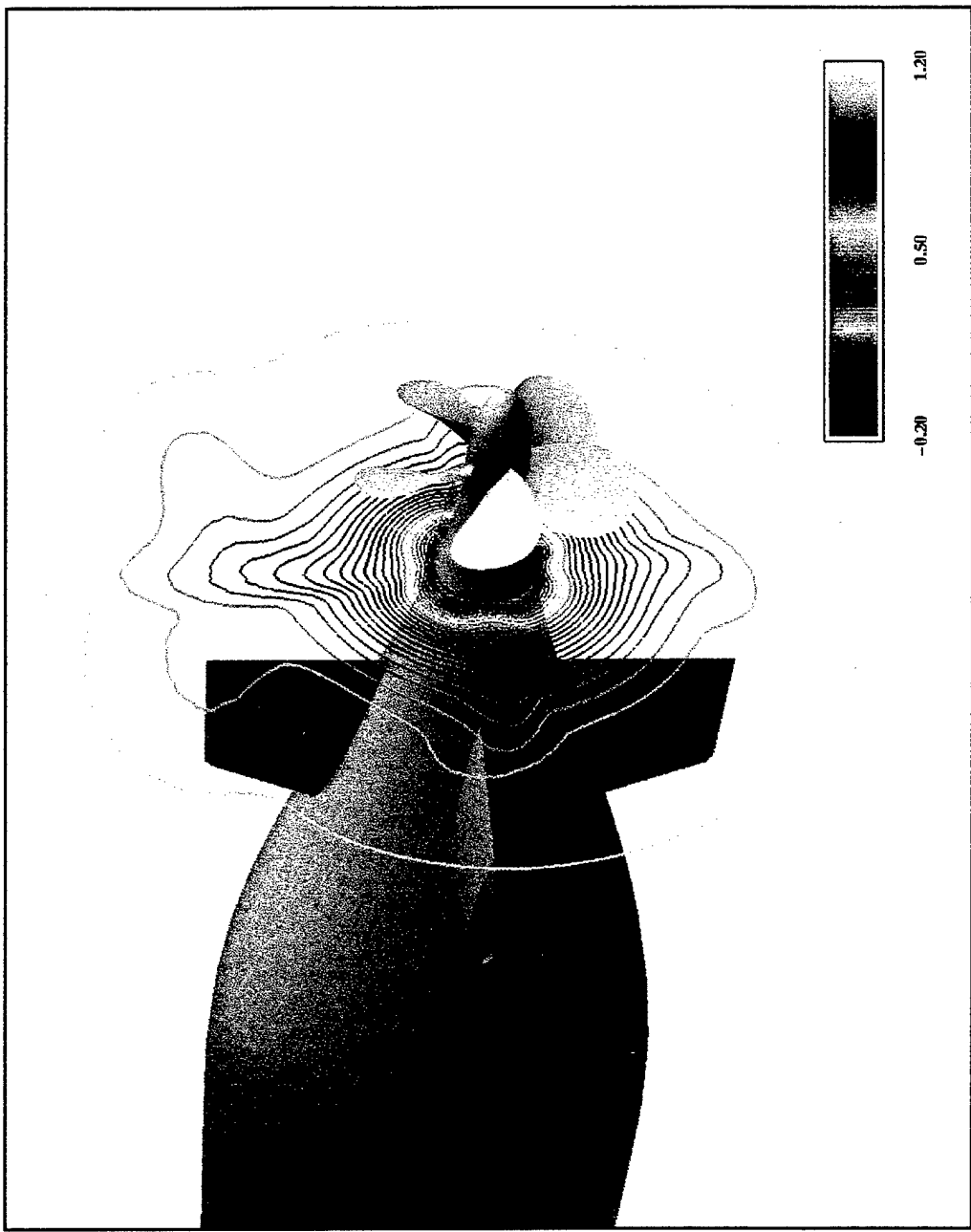


Figure 132. Contours of the  $u$ -Component of Velocity at  $t = 0.0$  for the Fully-Appended SUBOFF with a Rotating Propeller at  $Re = 12,800,000$

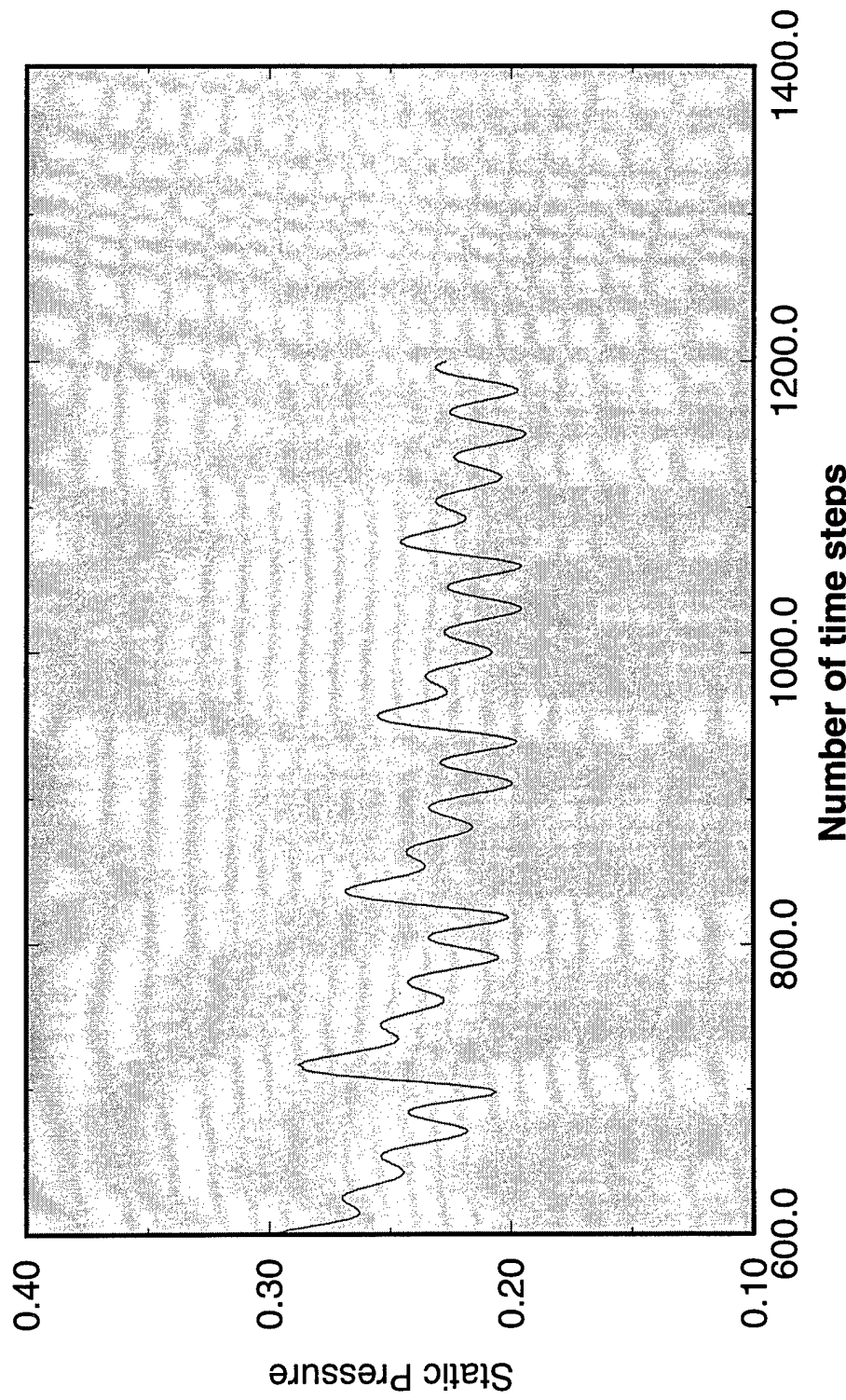


Figure 133. Unsteady Pressure Signature on a Blade at  $t = 0.0$  for the Fully-Appended SUBOFF with a Rotating Propeller at  $Re = 12,800,000$

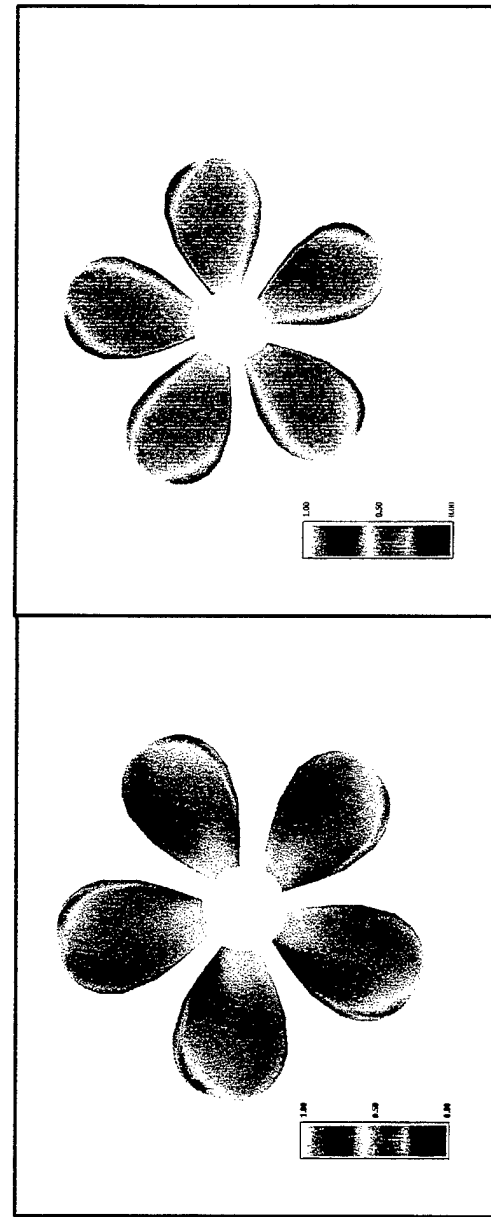
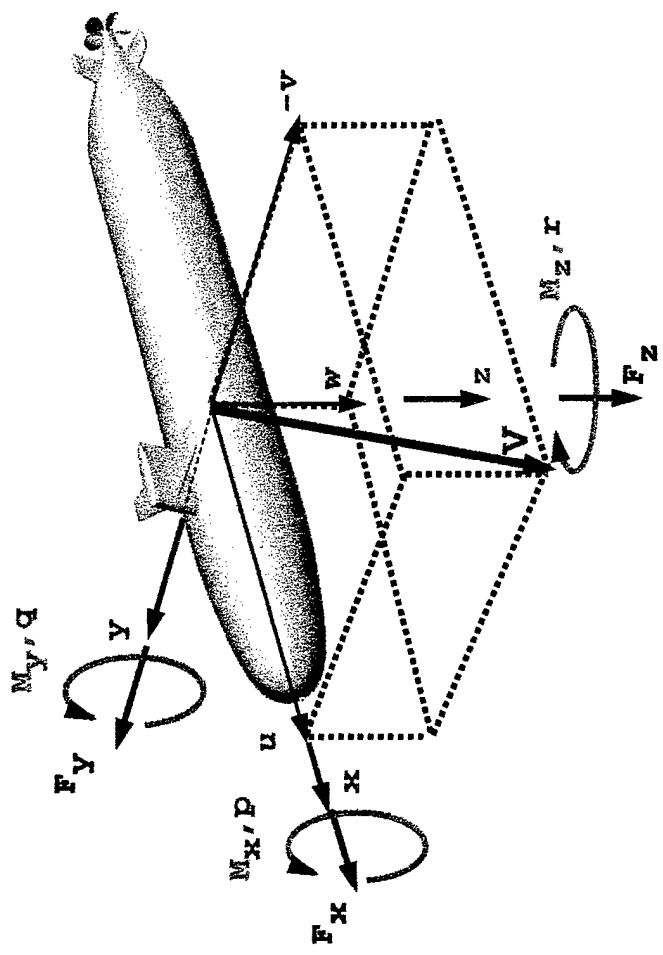


Figure 134. Surface Pressure Distribution on the Pressure Surface (Left) and Suction Surface (Right) of the Rotating Propeller Blades at  $t = 0.0$  for the Fully-Appended SUBOFF at  $Re = 12,800,000$



	Roll Axis x	Pitch Axis y	Yaw Axis z
Angular rates	p	q	r
Linear velocity components	u	v	w
Hydrodynamic force components	$F_x$	$F_y$	$F_z$
Hydrodynamic moment components	$M_x$	$M_y$	$M_z$

Figure 135. Definitions of the Force, Moment, and Velocity Components in the Body-Fixed Coordinate System

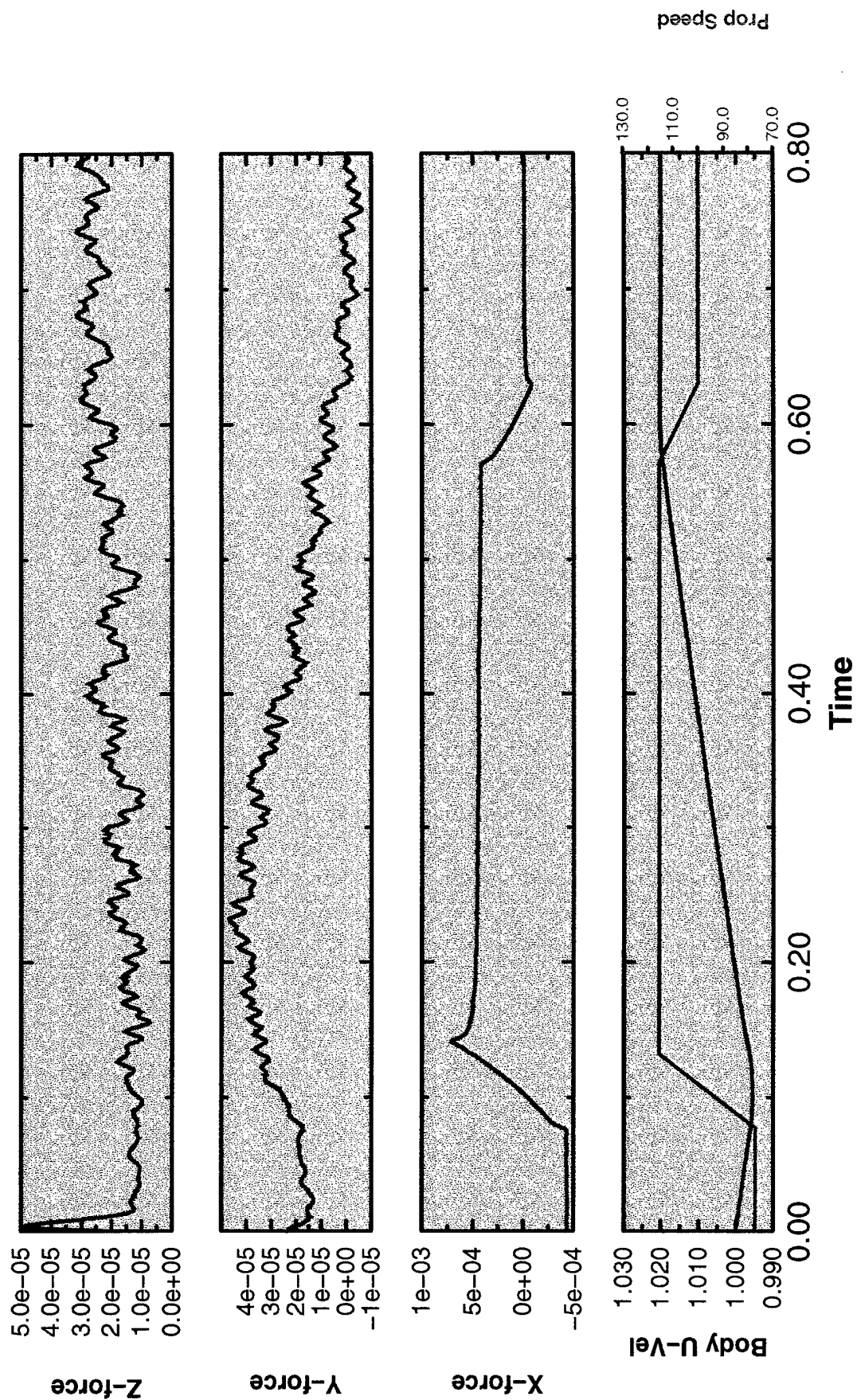


Figure 136. Time History of the Forces, the  $u$ -Component of the Vehicle Velocity, and the Propeller Angular Velocity for the Unconstrained Motion of the Fully-Appended SUBOFF with a Rotating Propeller

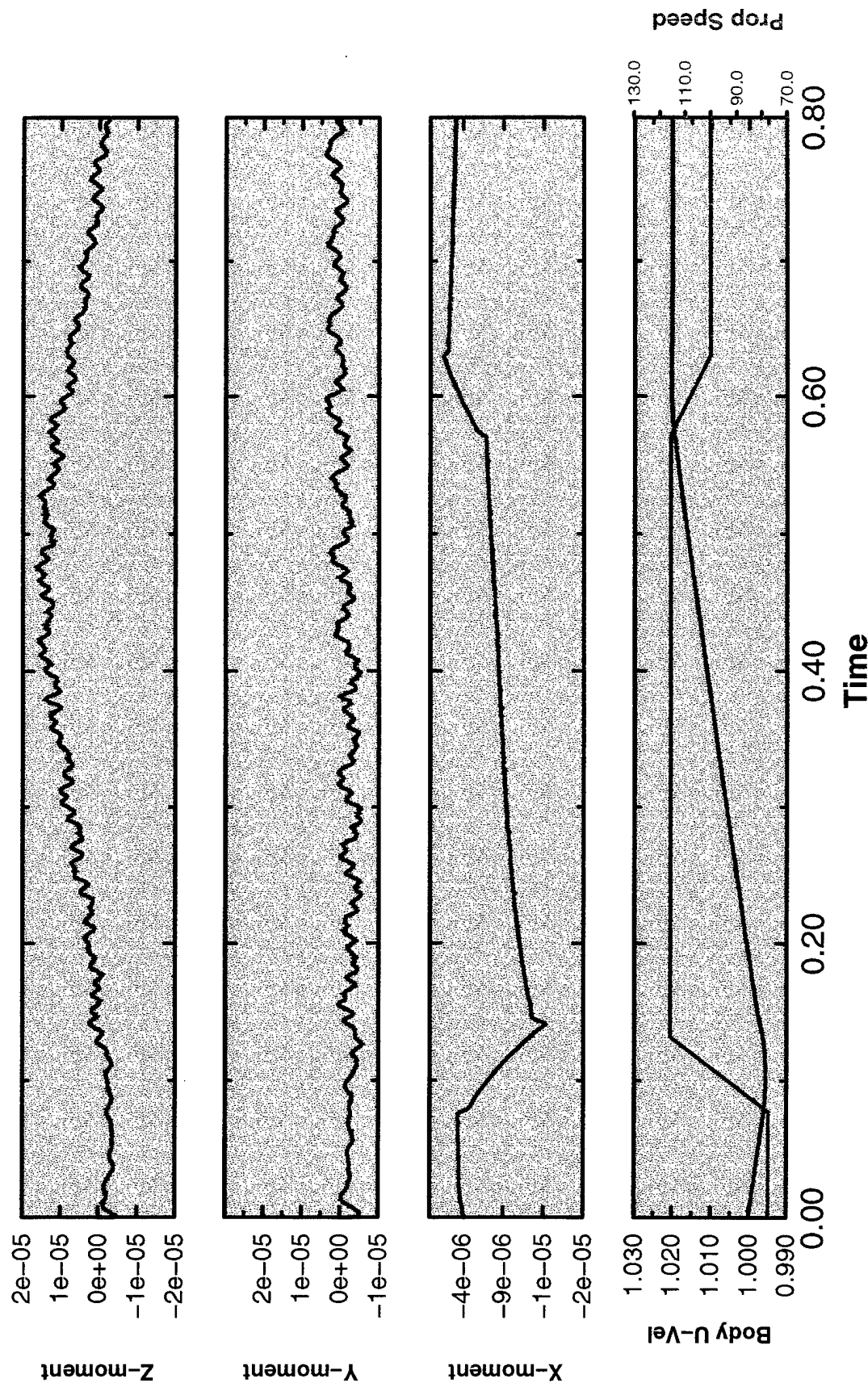


Figure 137.

Time History of the Moments, the  $u$ -Component of the Vehicle Velocity, and the Propeller Angular Velocity for the Unconstrained Motion of the Fully-Appended SUBOFF with a Rotating Propeller

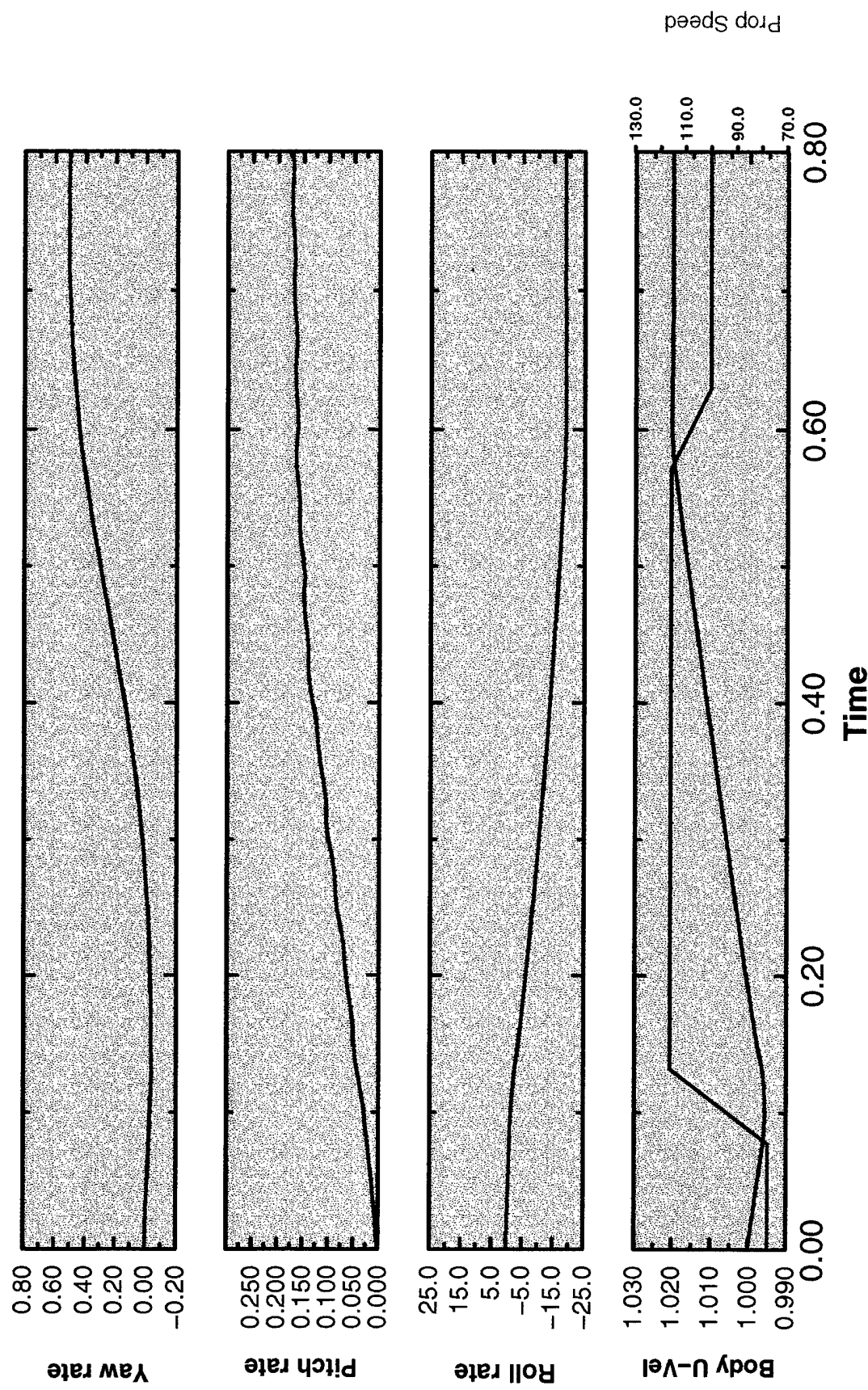


Figure 138.

Time History of the Angular Rates, the  $u$ -Component of the Vehicle Velocity, and the Propeller Angular Velocity for the Unconstrained Motion of the Fully-Appended SUBOFF with a Rotating Propeller

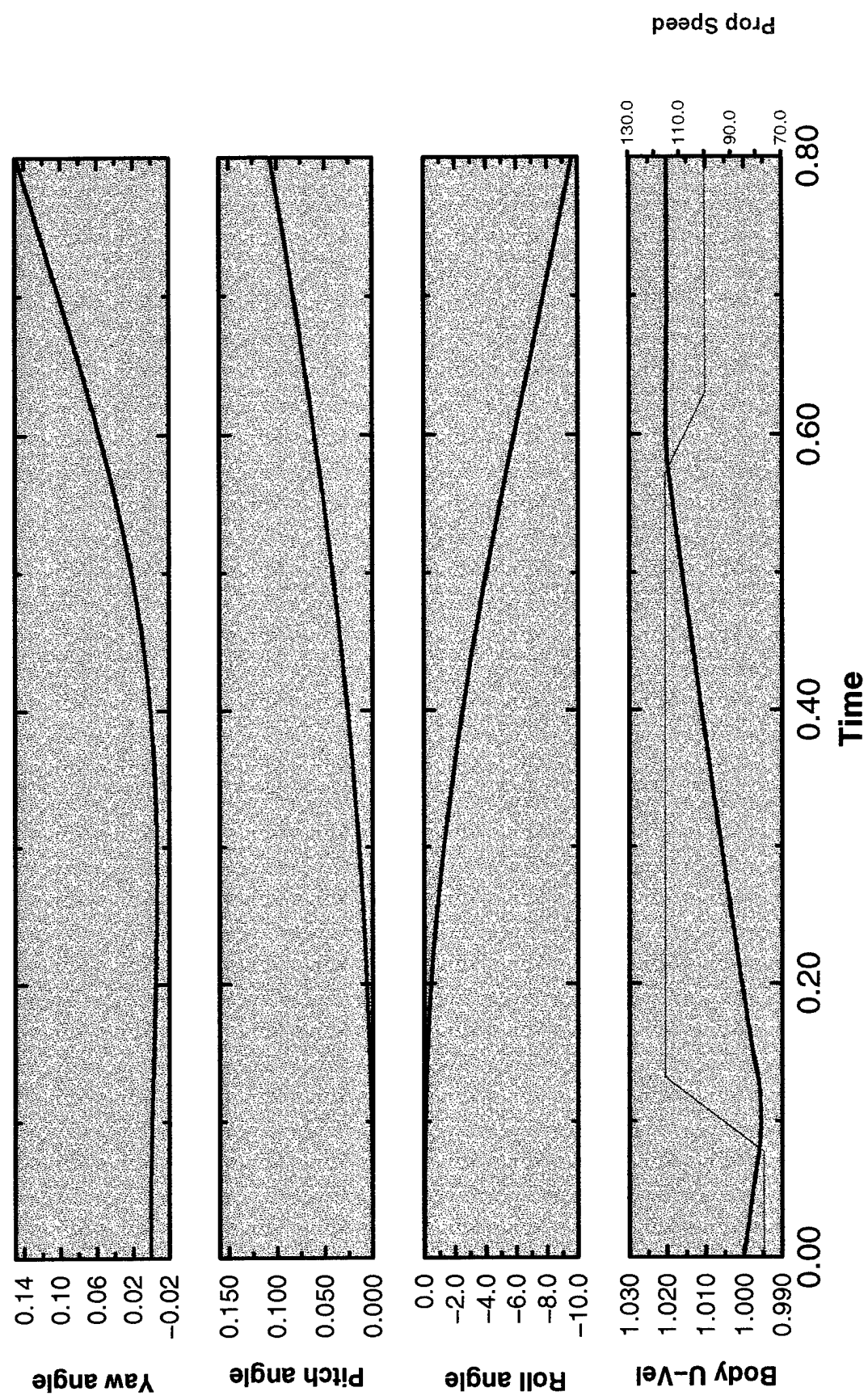


Figure 139.

Time History of the Vehicle's Orientation, the  $u$ -Component of the Vehicle Velocity, and the Propeller Angular Velocity for the Unconstrained Motion of the Fully-Appended SUBOFF with a Rotating Propeller

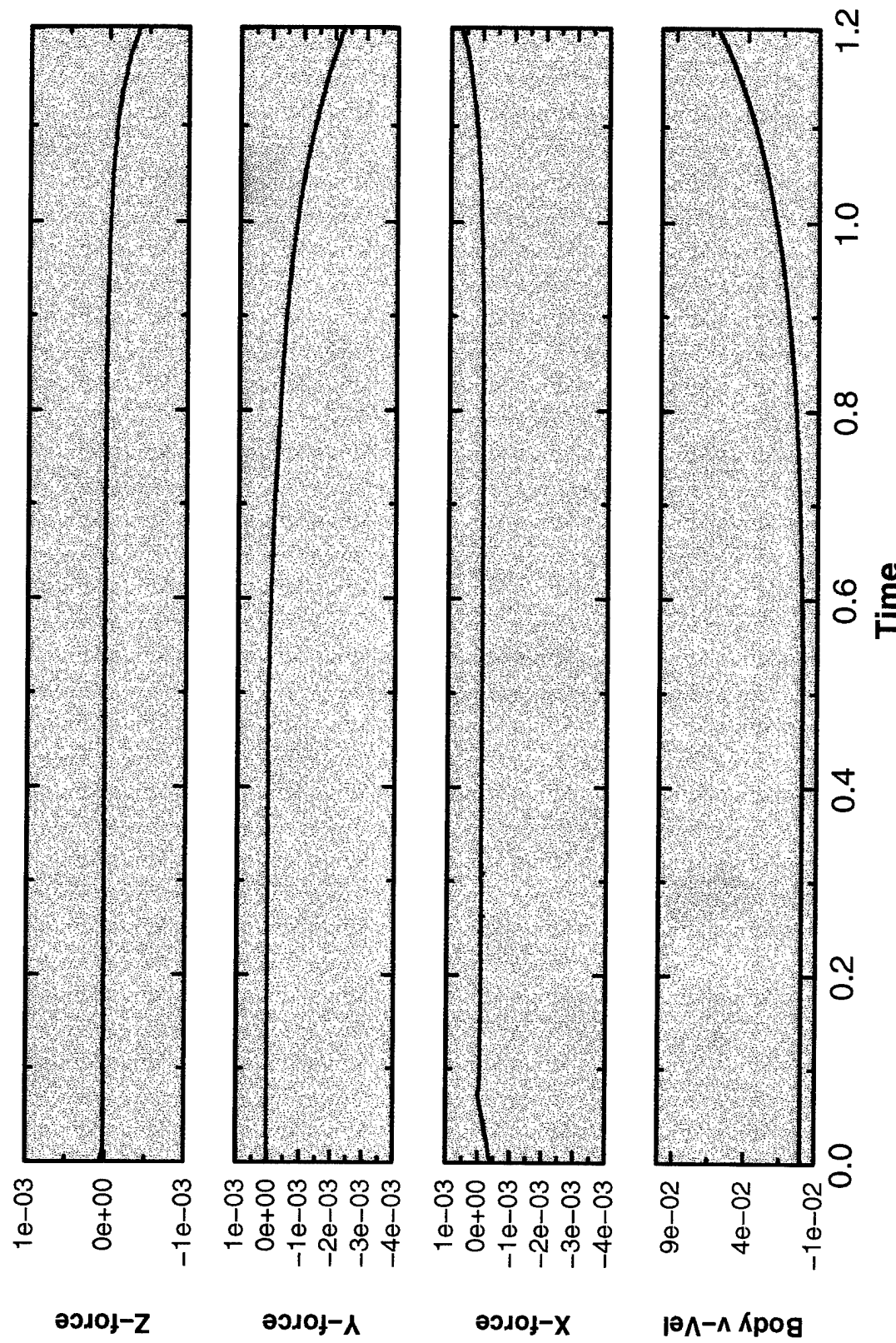


Figure 140.

Time History of the Forces and the  $v$ -Component of the Vehicle Velocity (Sideslip) for the Roll and Yaw Moments Applied to the Fully-Appended SUBOFF with a Rotating Propeller

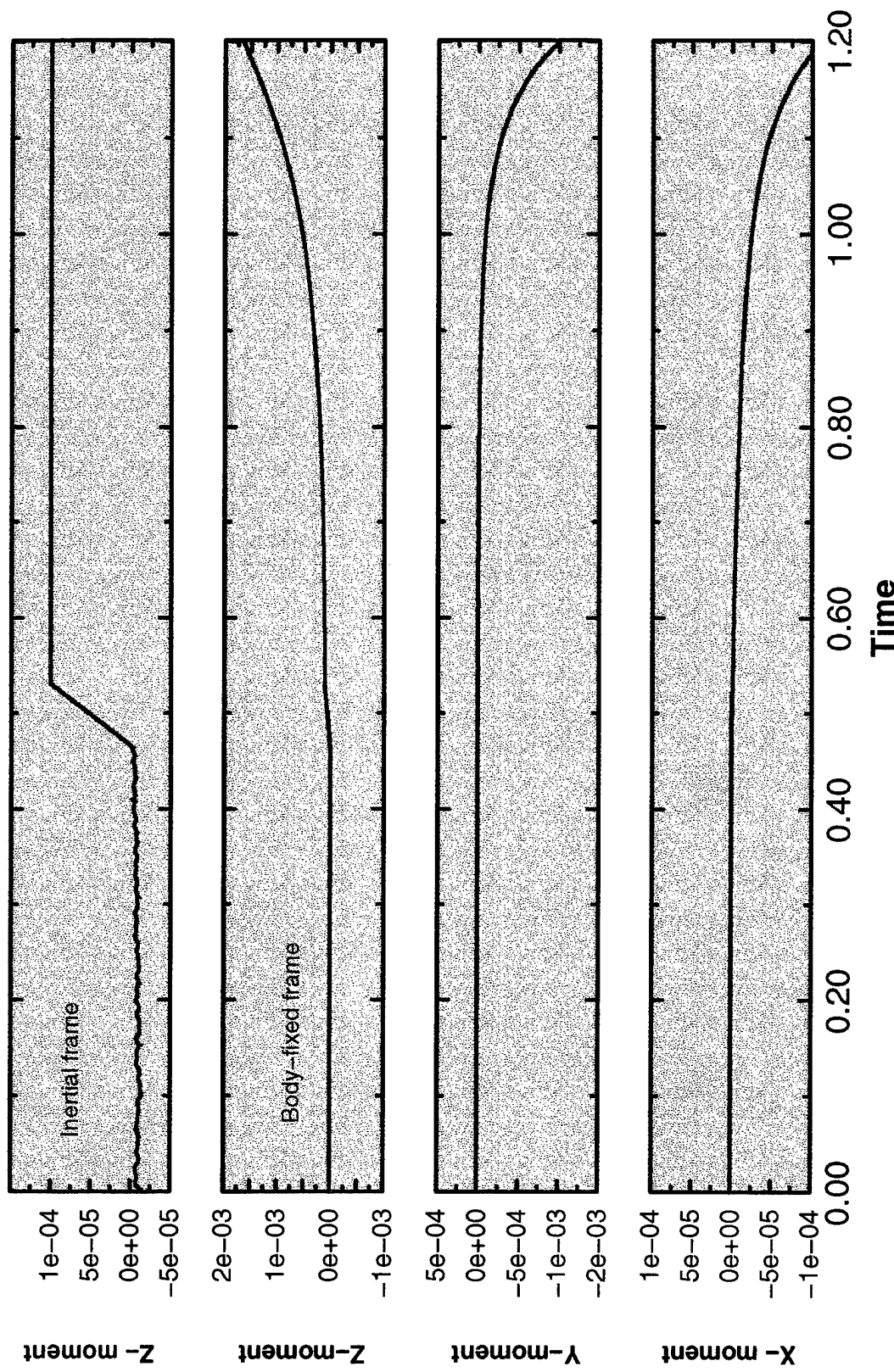


Figure 141.

Time History of the Moments for the Roll and Yaw Moments Applied to the Fully-Appended SUBOFF with a Rotating Propeller

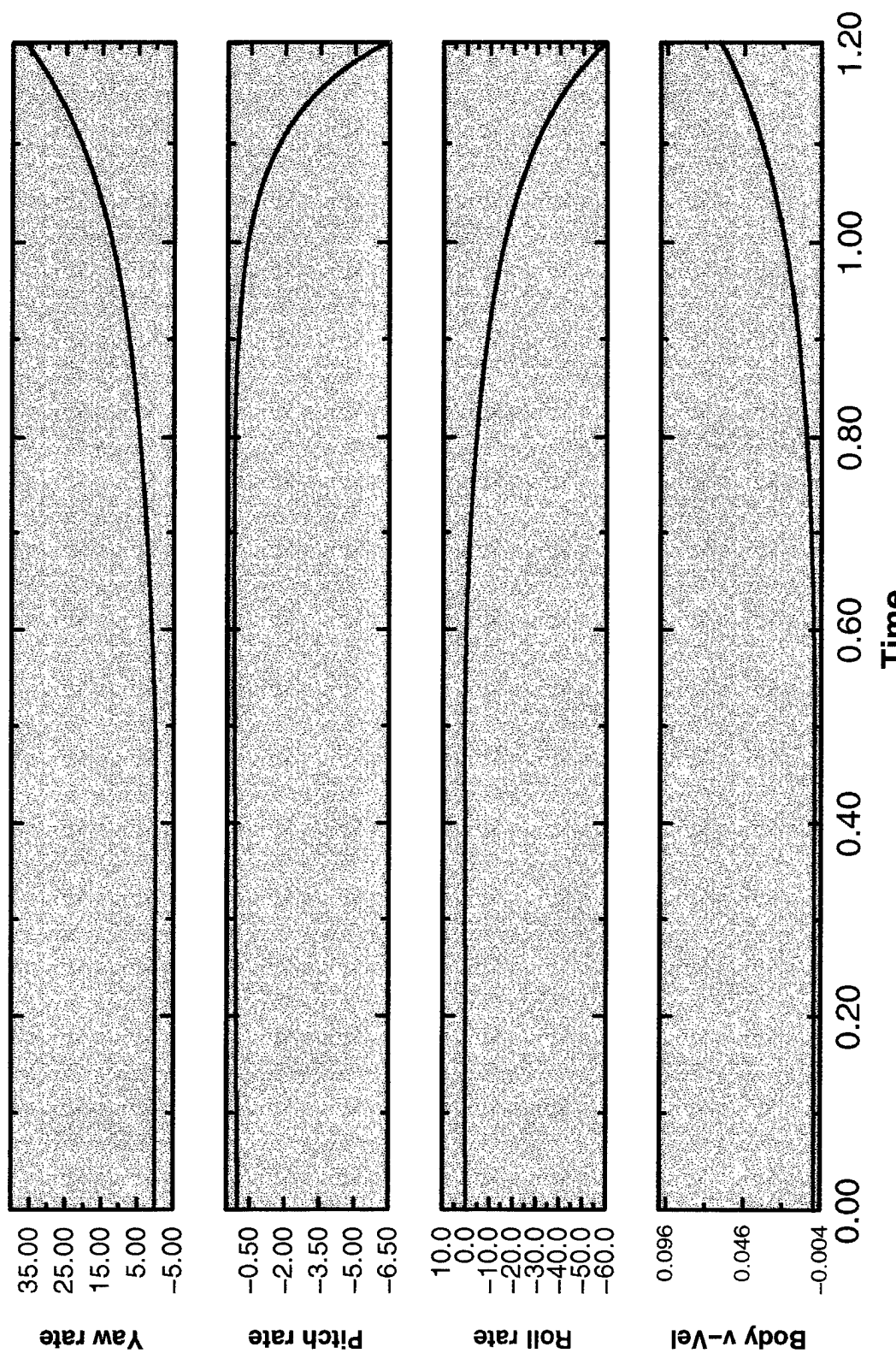


Figure 142.

Time History of the Angular Rates and the  $v$ -Component of the Vehicle Velocity (Sideslip) for the Roll and Yaw Moments Applied to the Fully-Appended SUBOFF with a Rotating Propeller

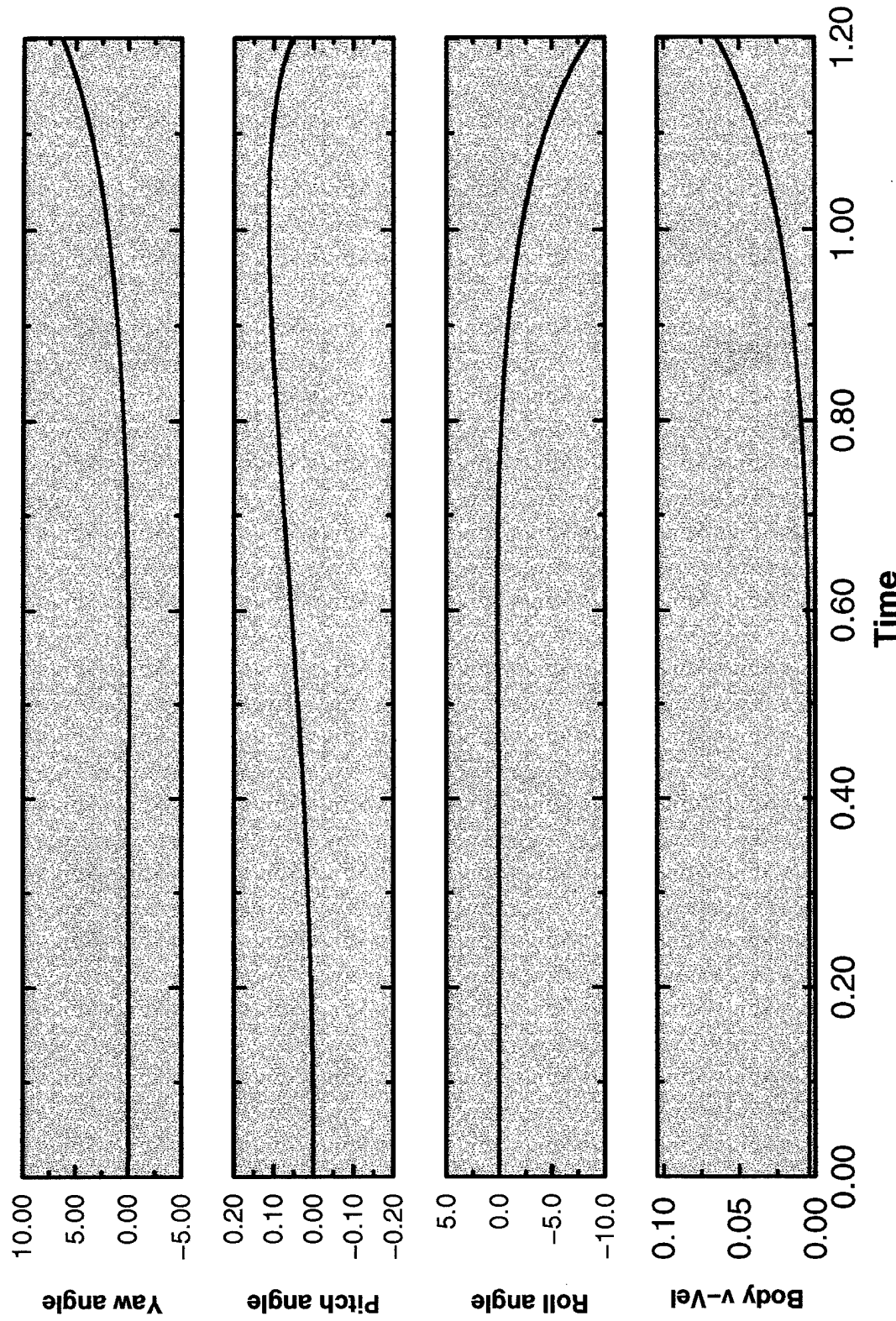


Figure 143. Time History of the Vehicle's Orientation and the  $v$ -Component of the Vehicle Velocity (Sideslip) for the Roll and Yaw Moments Applied to the Fully-Appended SUBOFF with a Rotating Propeller

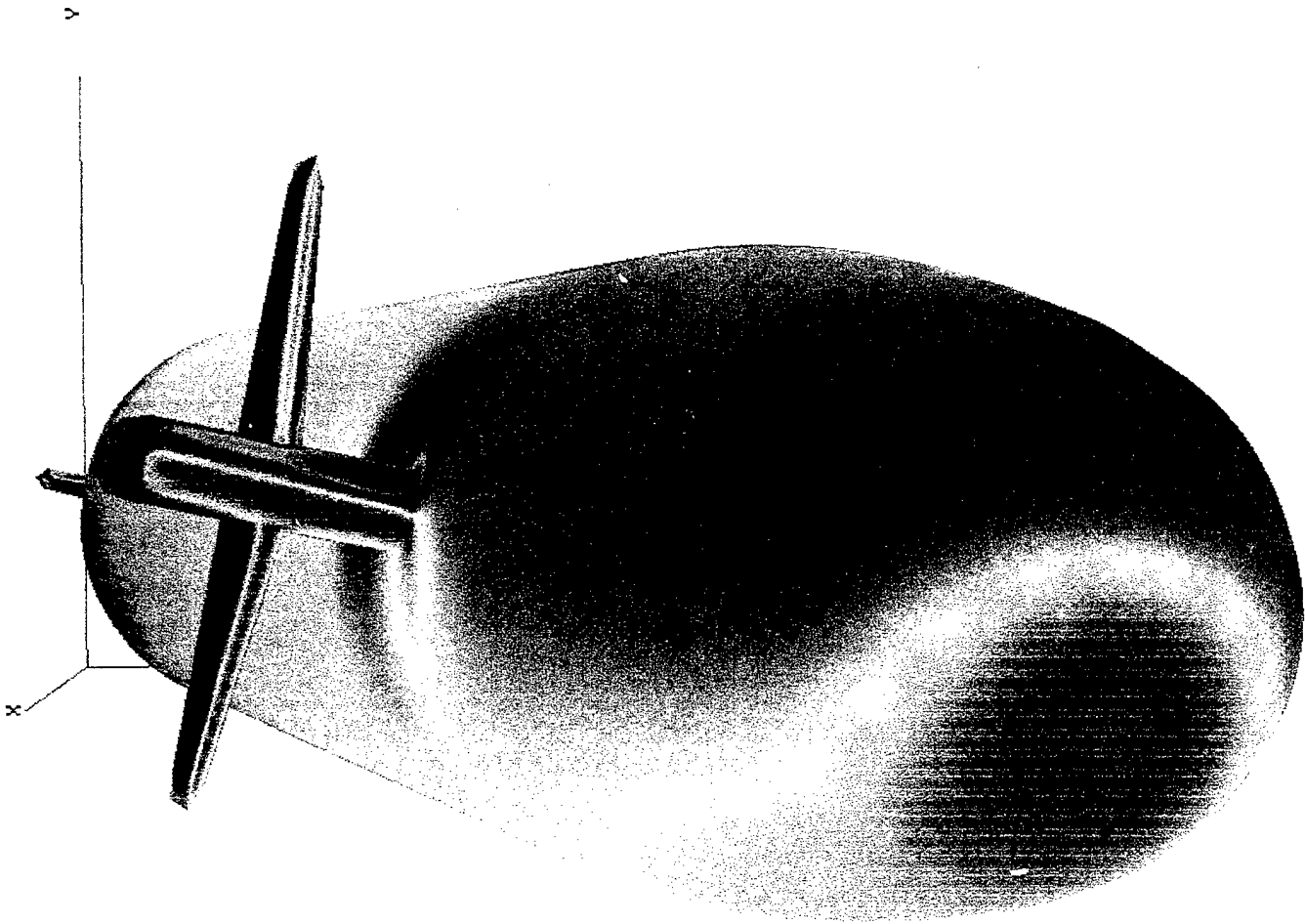
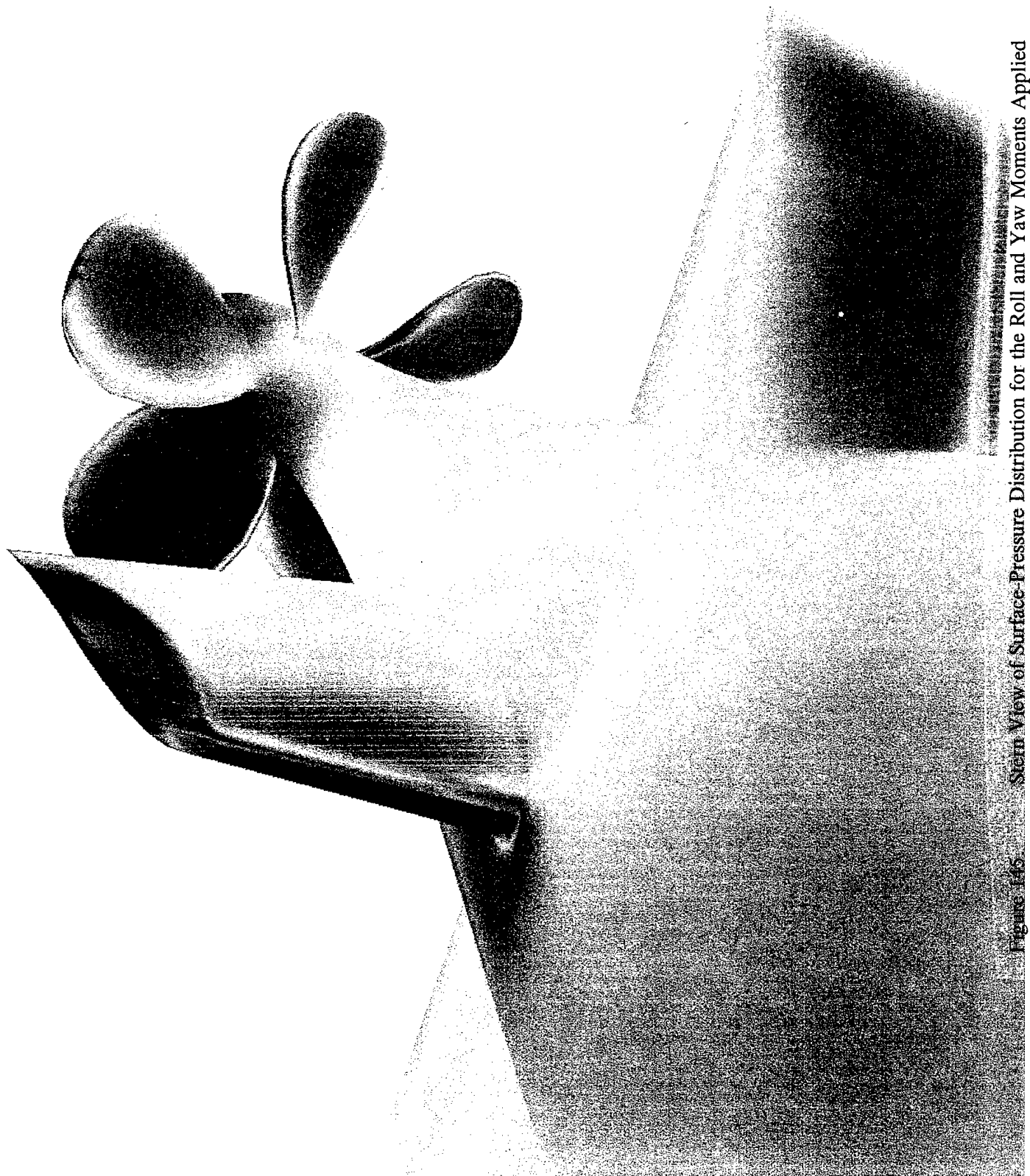


Figure 144.

Starboard View of Surface-Pressure Distribution for the Roll and Yaw Moments  
Applied to the Fully-Appended SUBOFF with a Rotating Propeller



Figures 254-256 Stern View of Surface-Pressure Distribution for the Roll and Yaw Moments Applied to the Fully-Appended SUBOFF with a Rotating Propeller

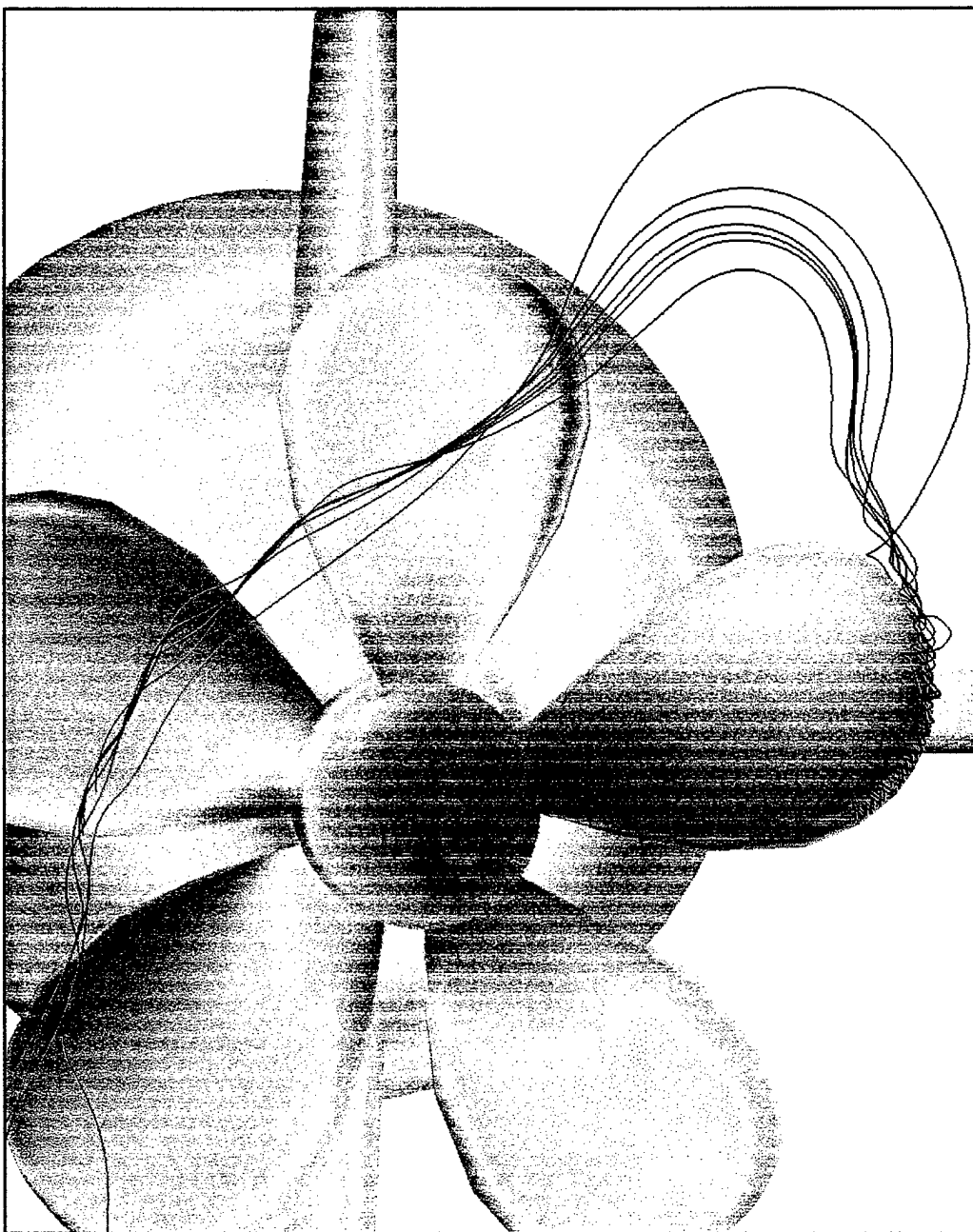


Figure 146. Particle Traces Showing a Rotor Blade Tip Vortex for the Roll and Yaw Moments Applied to the Fully-Appended SUBOFF with a Rotating Propeller

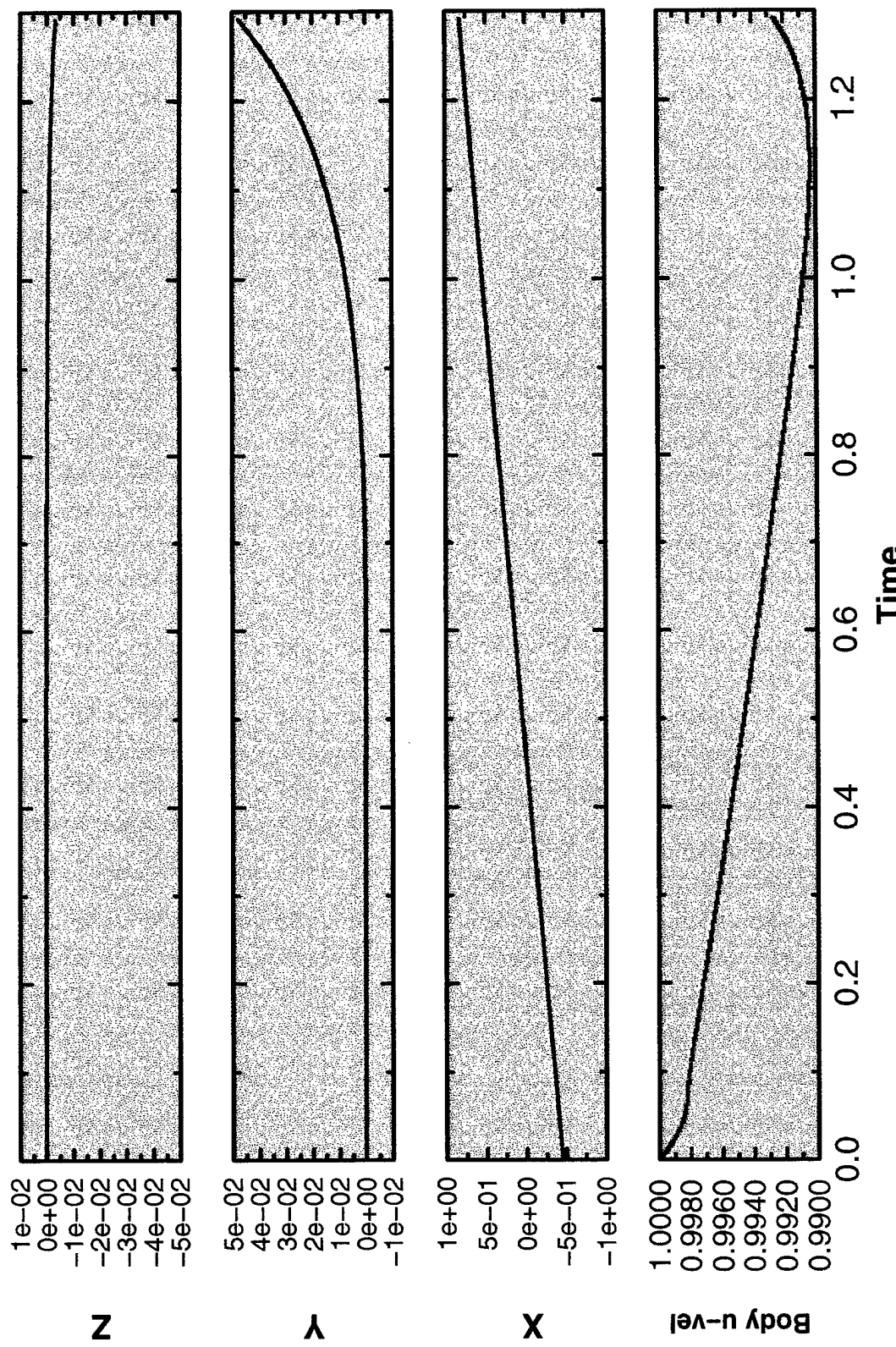


Figure 147. Time History of the Vehicle's Path and the  $u$ -Component of the Vehicle Velocity for the Roll and Yaw Moments Applied to the Fully-Appended SUBOFF with a Rotating Propeller

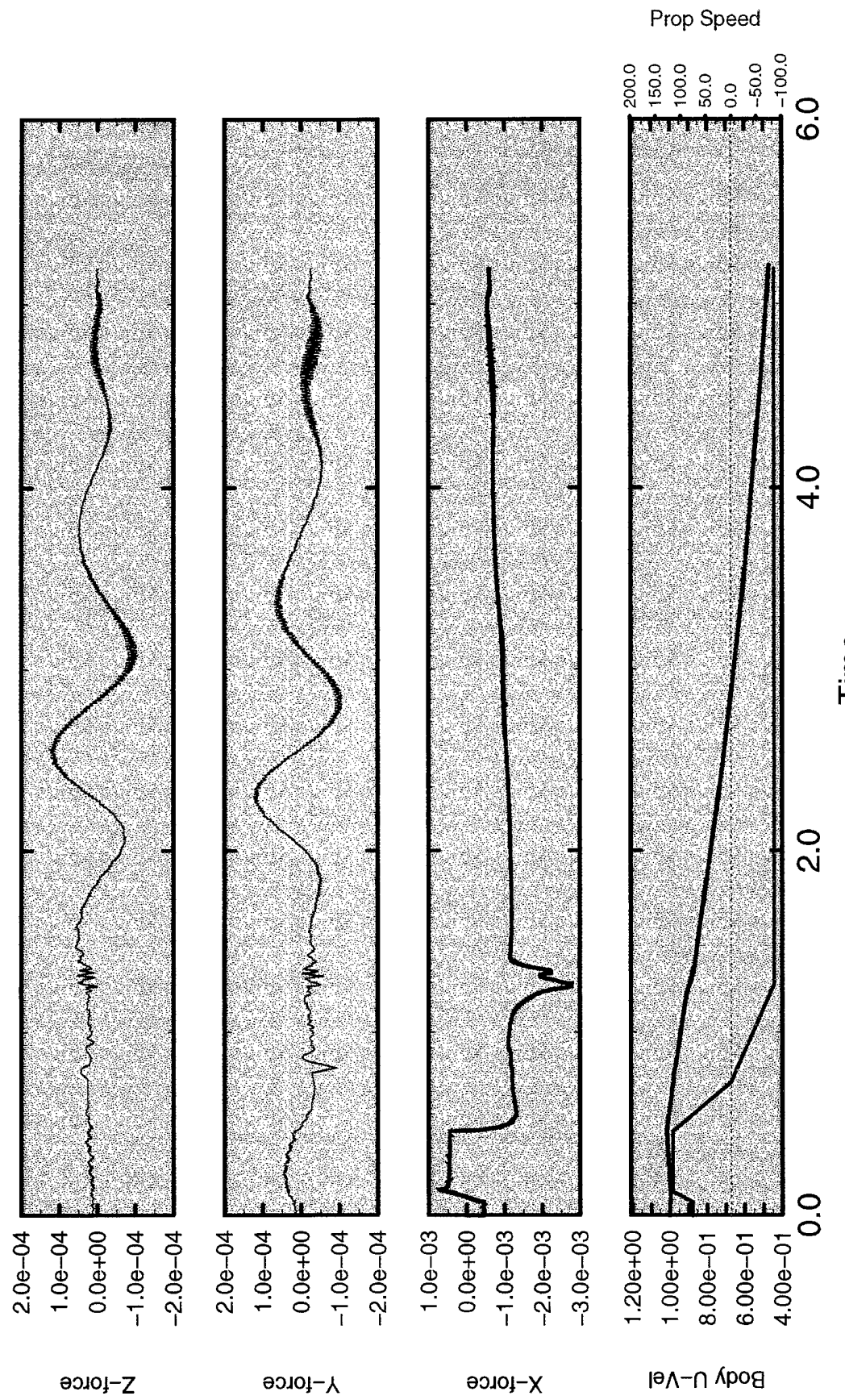


Figure 148. Time History of the Forces, the  $u$ -Component of the Vehicle Velocity, and the Propeller Angular Velocity for the Fully-Appended SUBOFF with a Propeller Rotating in Reverse

Figure 149. Ring Vortex Formation at  $t = 2.01$  (with the Propeller Colored by Surface Pressure and the Particle Traces Colored by the Velocity Magnitude)

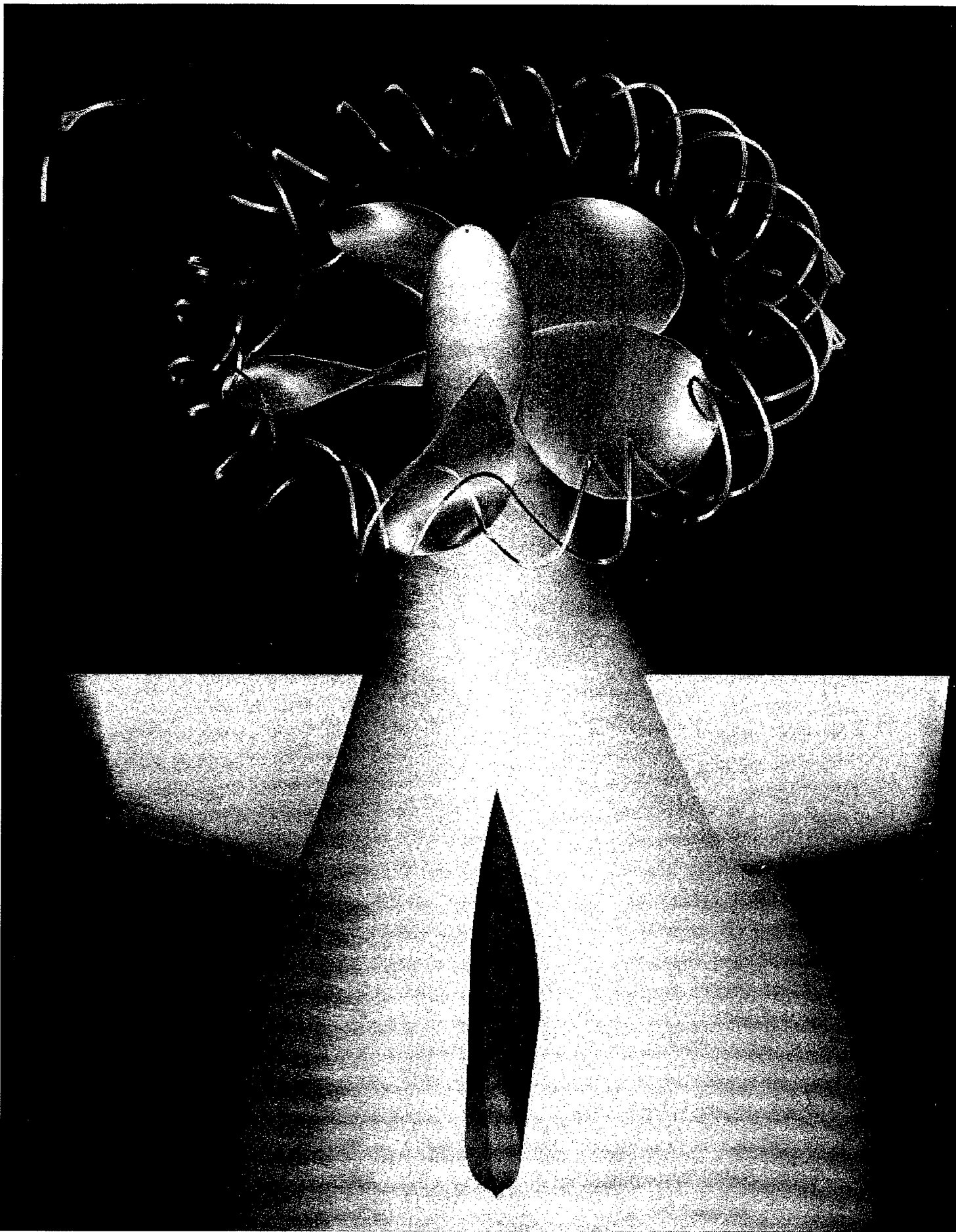
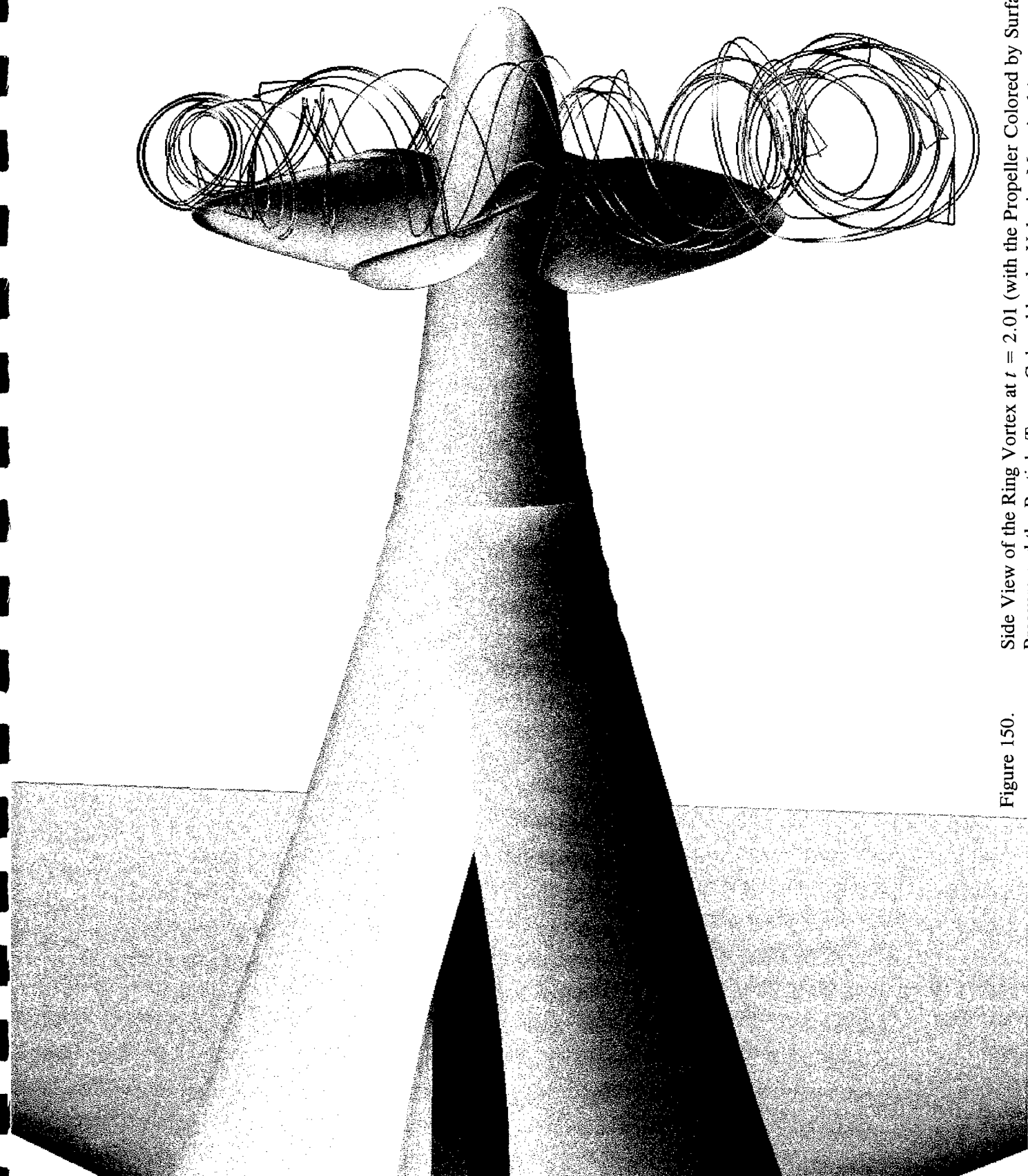
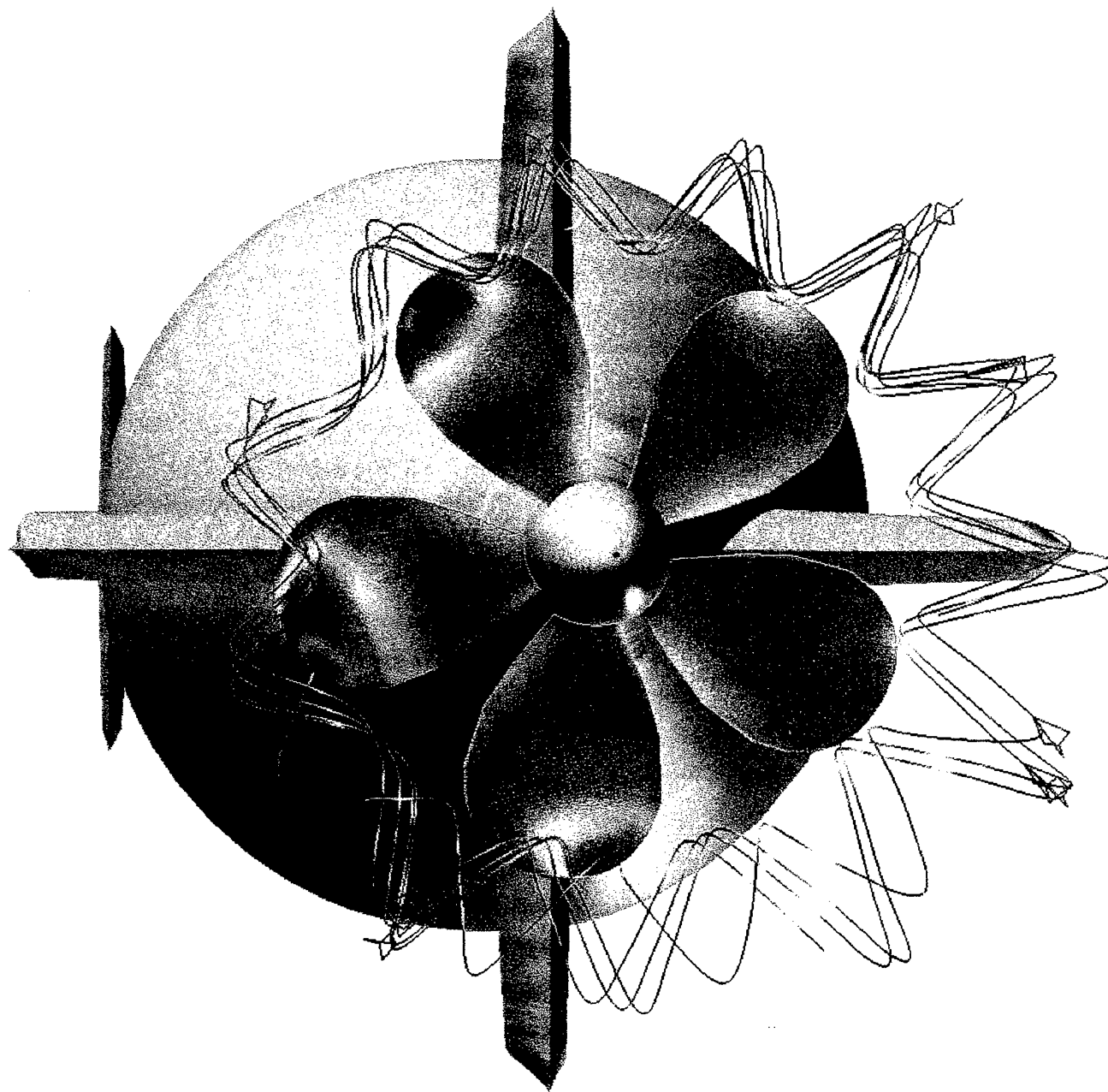


Figure 150.

Side View of the Ring Vortex at  $t = 2.01$  (with the Propeller Colored by Surface Pressure and the Particle Traces Colored by the Velocity Magnitude)





Asymmetric Structure of the Ring Vortex at  $t = 2.01$  (with the Propeller Colored by Surface Pressure and the Particle Traces Colored by the Velocity Magnitude)

Figure 151.

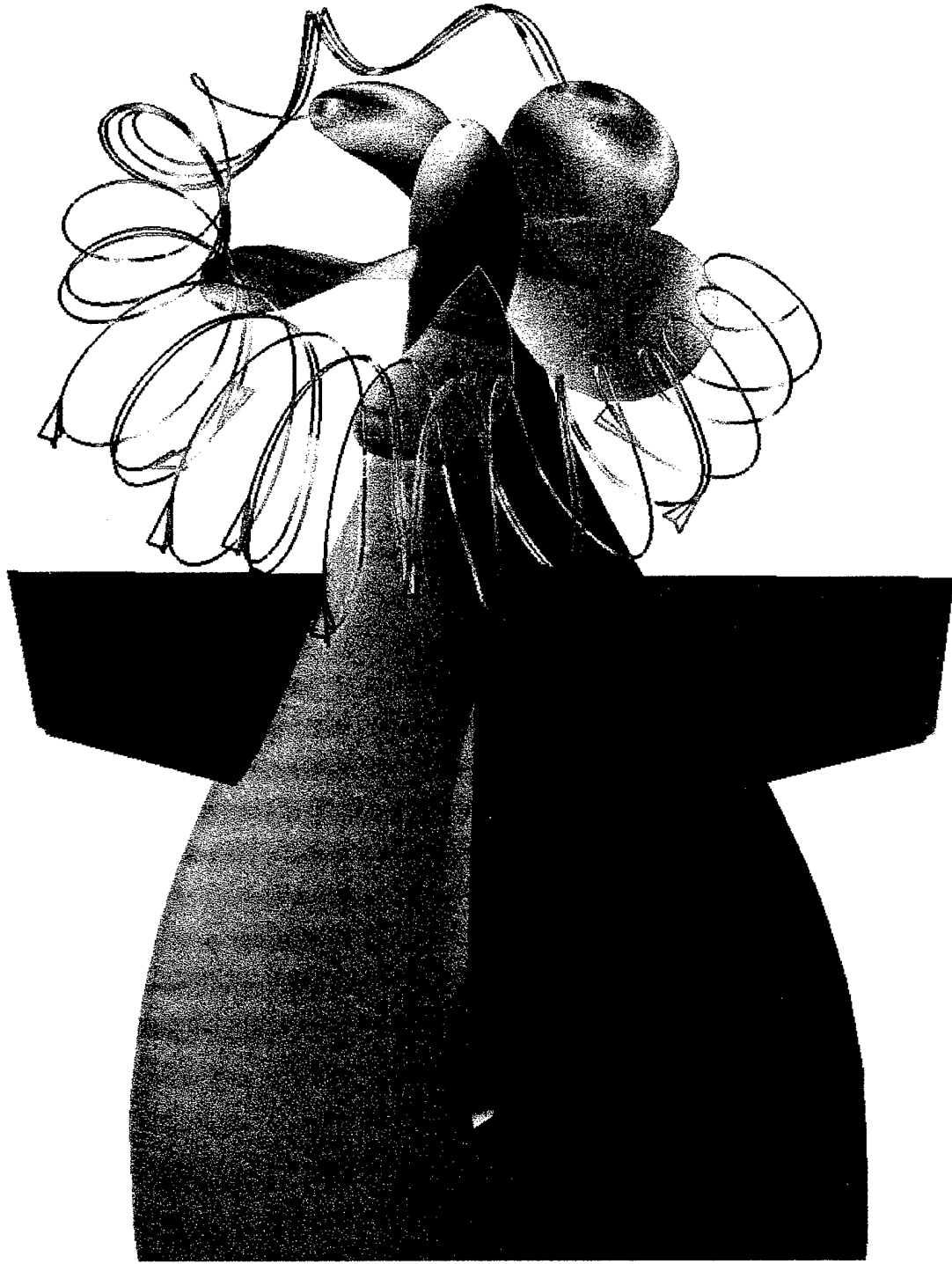


Figure 152. Ring Vortex Position at  $t = 2.33$  (with the Propeller Colored by Surface Pressure and the Particle Traces Colored by the Velocity Magnitude)

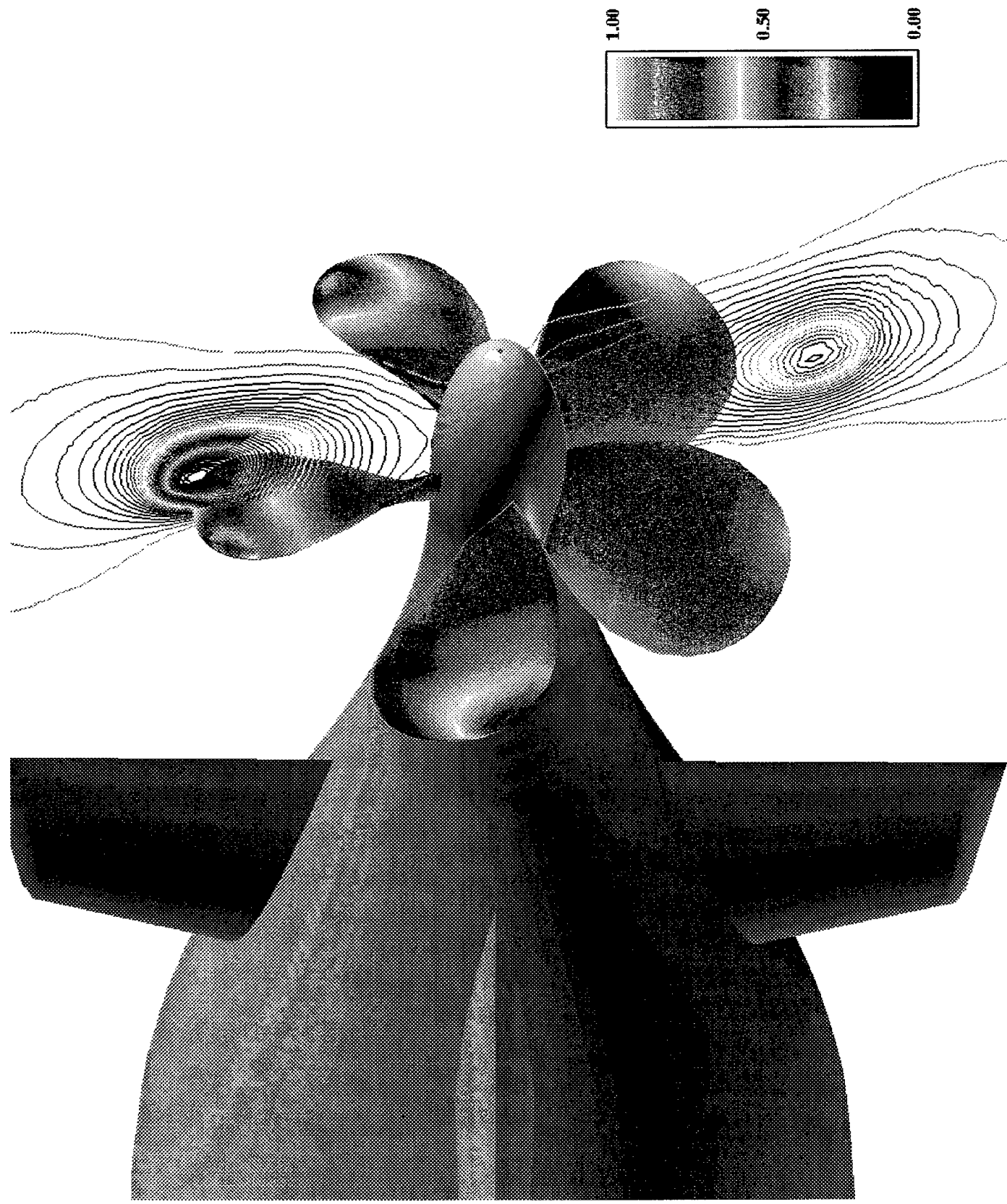


Figure 153. Contour Lines of Static Pressure Showing the Varying Strength of the Vortex Ring Along Its Core (with the Propeller Colored by the Surface Pressure)

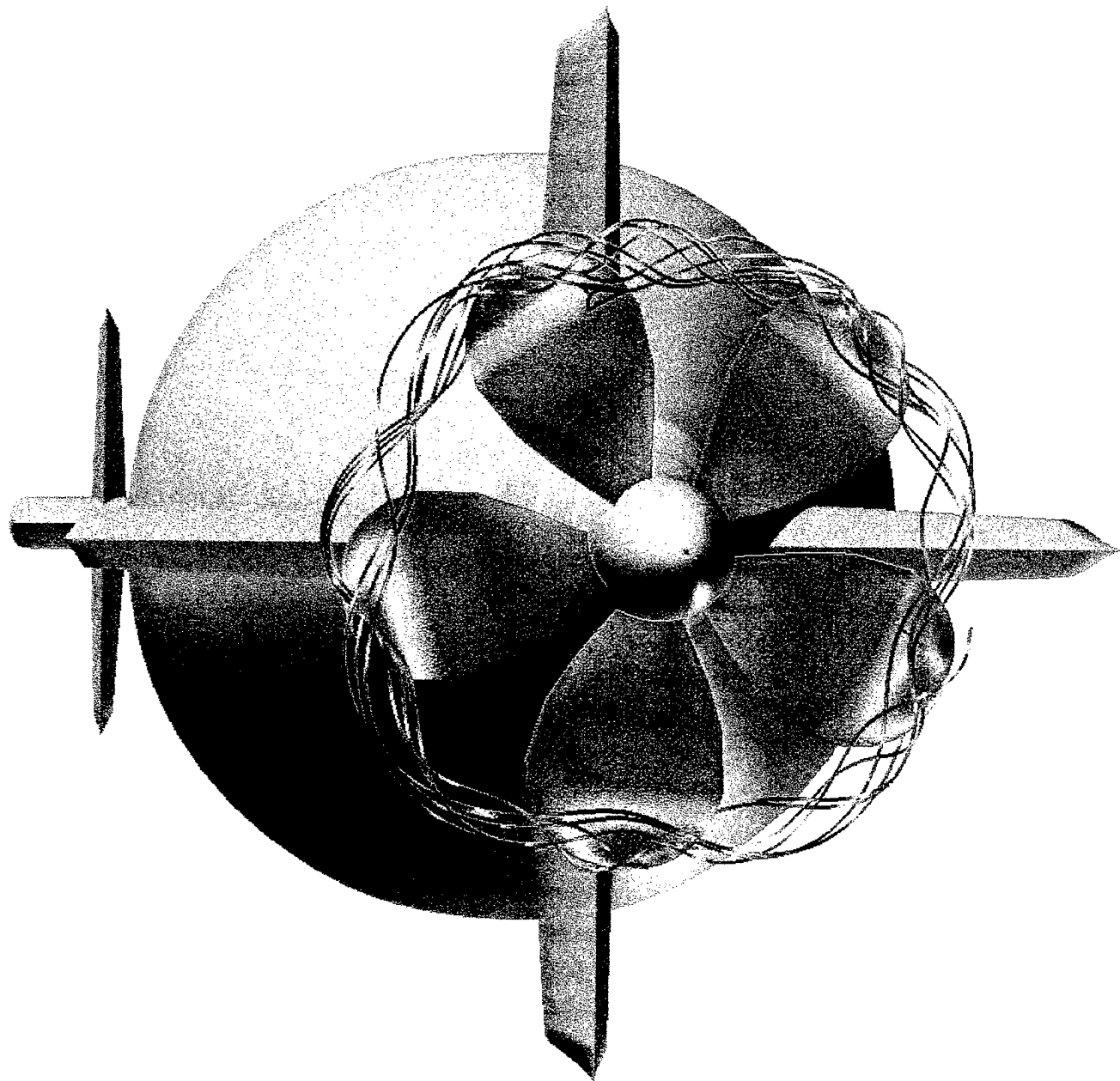


Figure 154. Ring Vortex Becoming Weaker and More Symmetric as Vehicle Decelerates to Time  $t = 5.15$  (with the Propeller Colored by Surface Pressure and the Particle Traces Colored by the Velocity Magnitude)

Figure 155. Side View of the Ring Vortex at  $t = 5.15$  (with the Propeller Colored by Surface Pressure and the Particle Traces Colored by the Velocity Magnitude)

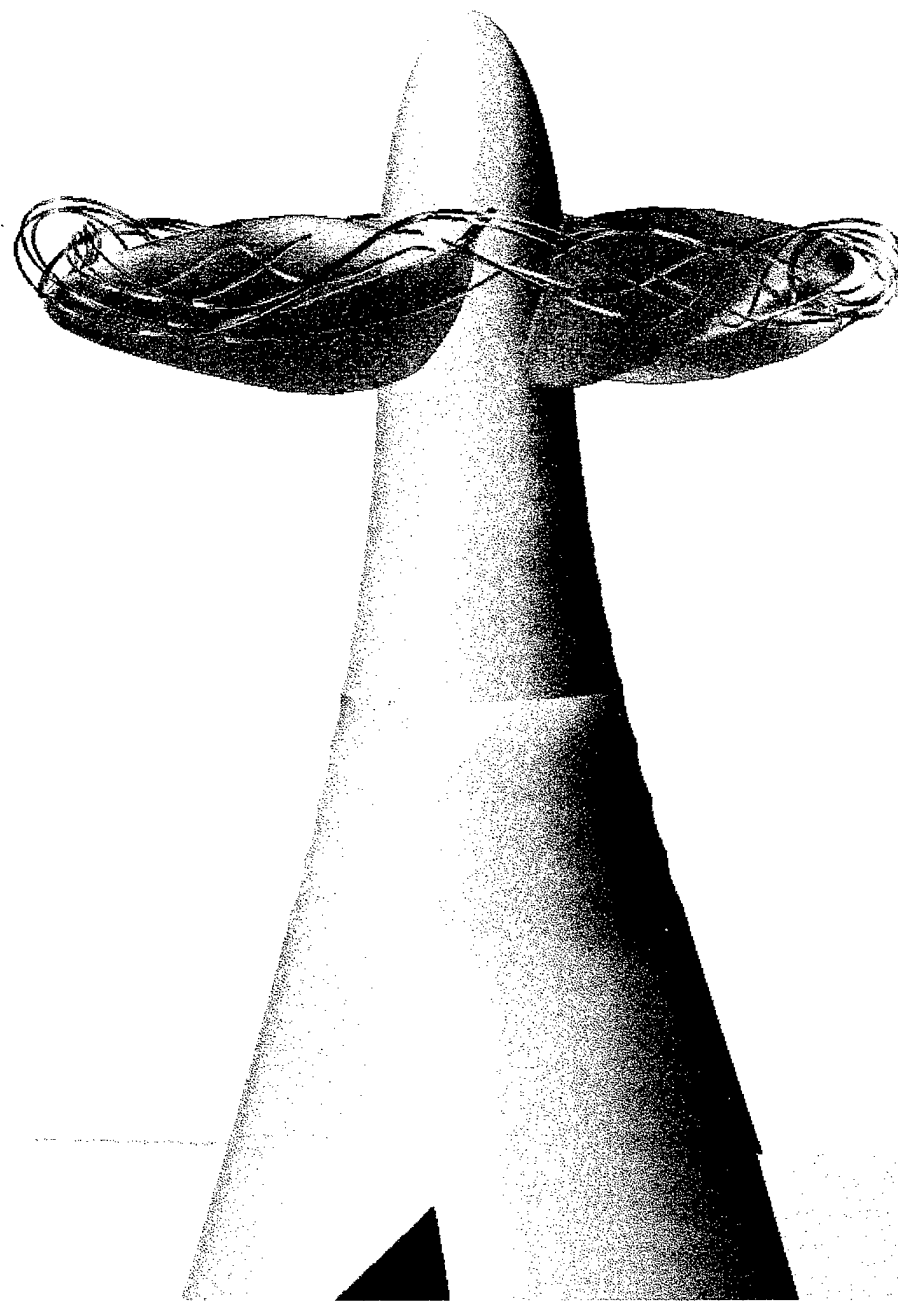
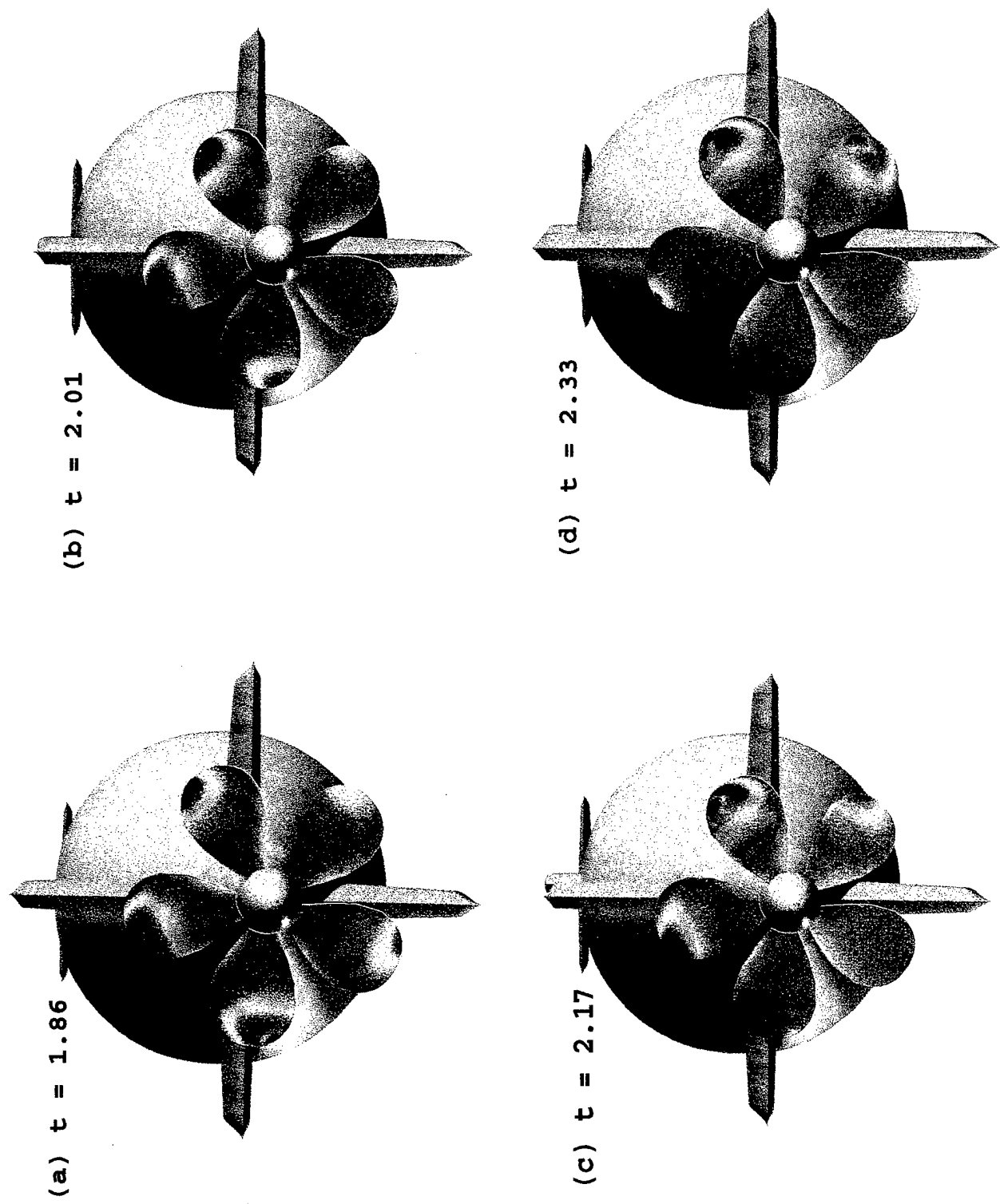


Figure 156. Low-Pressure Region of Ring Vortex Image Rotating in the Opposite Direction of Blade Rotation



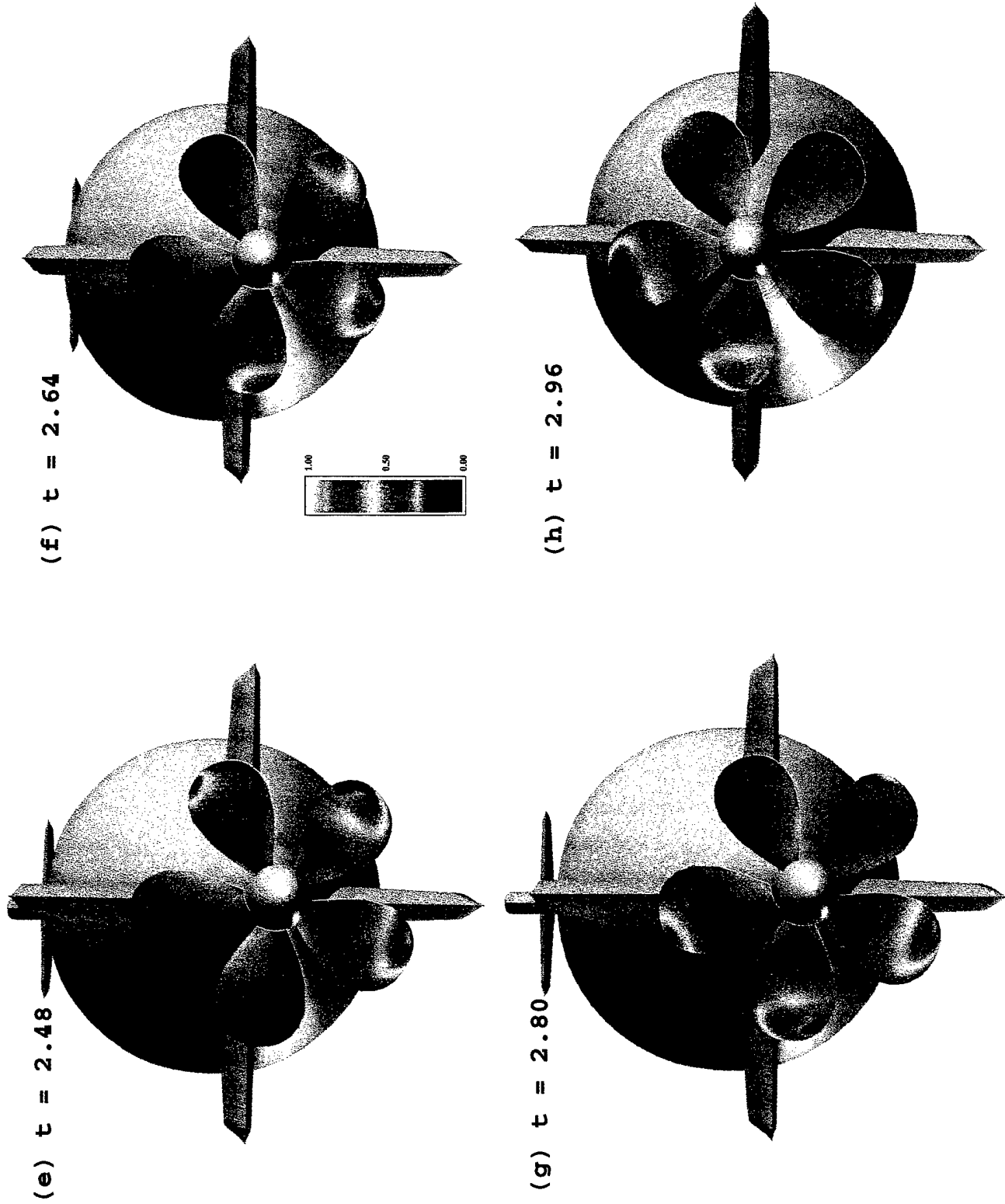


Figure 156. Low-Pressure Region of Ring Vortex Image Rotating in the Opposite Direction of Blade Rotation

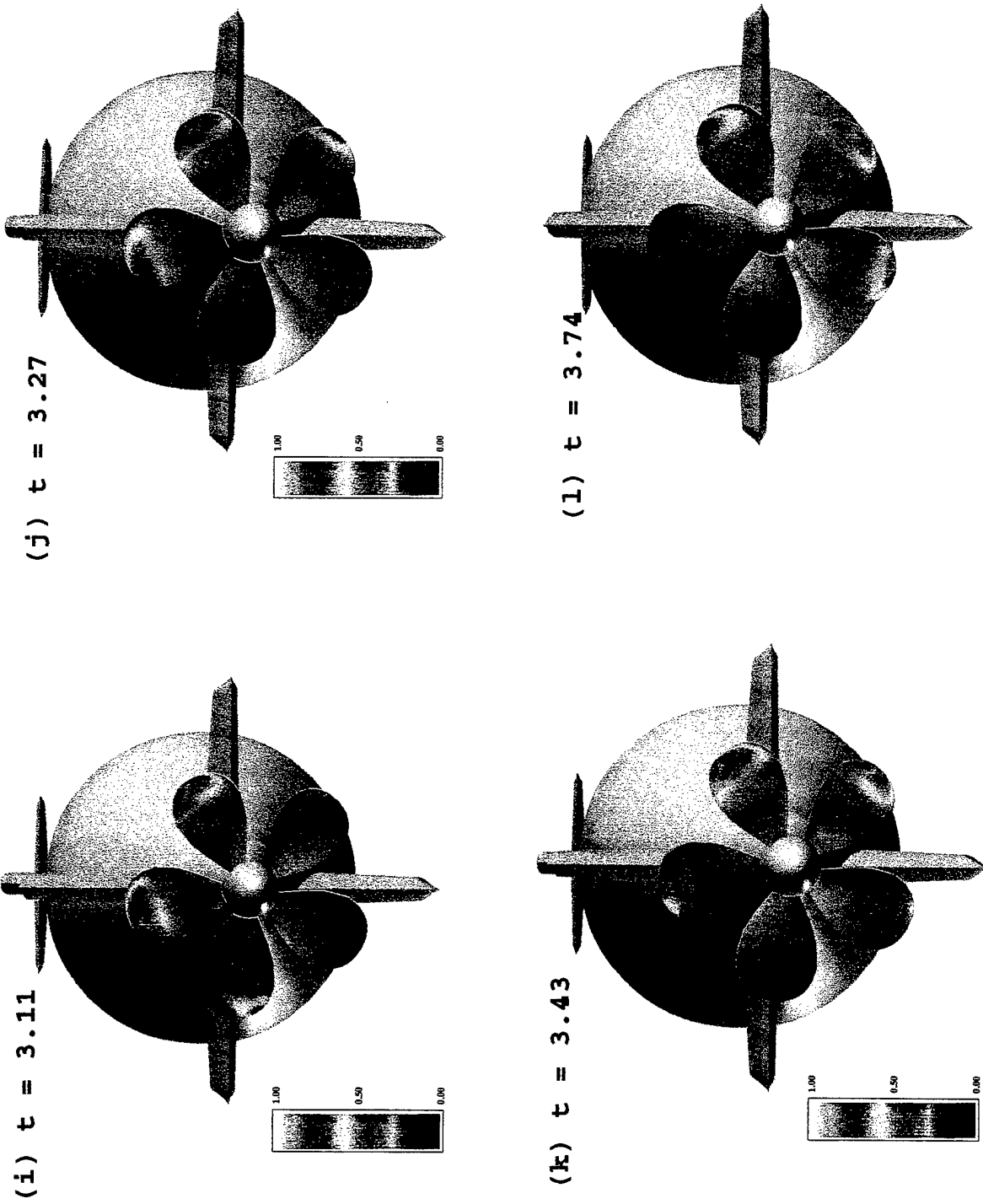


Figure 156. Low-Pressure Region of Ring Vortex Image Rotating in the Opposite Direction of Blade Rotation

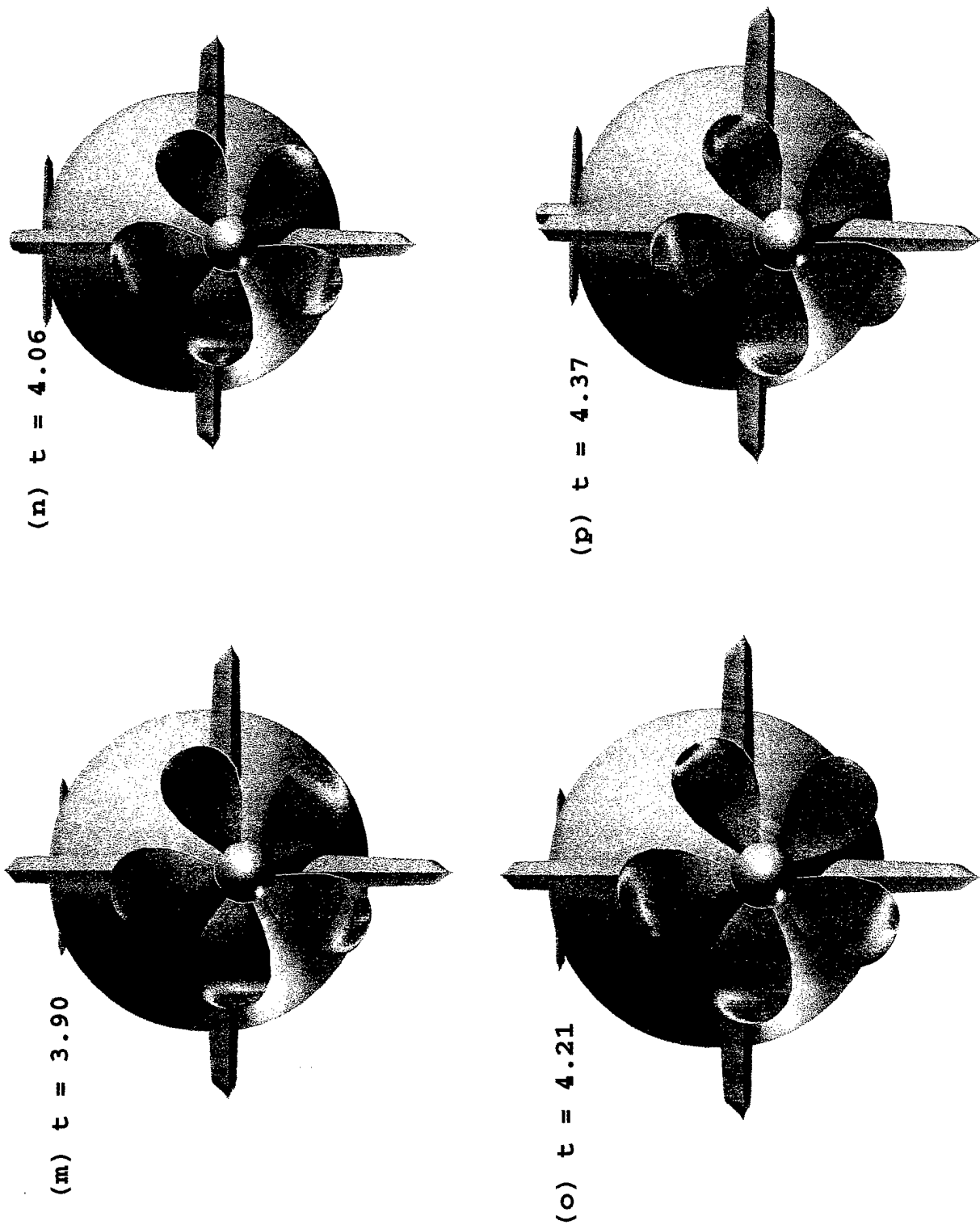


Figure 156. Low-Pressure Region of Ring Vortex Image Rotating in the Opposite Direction of Blade Rotation

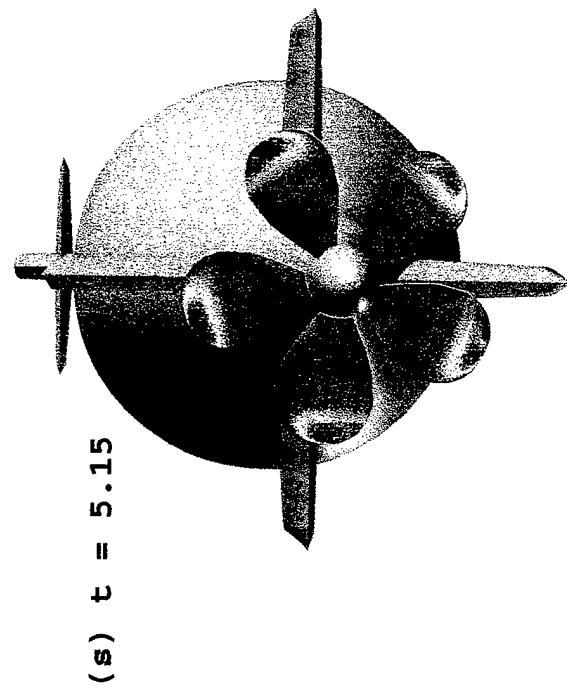
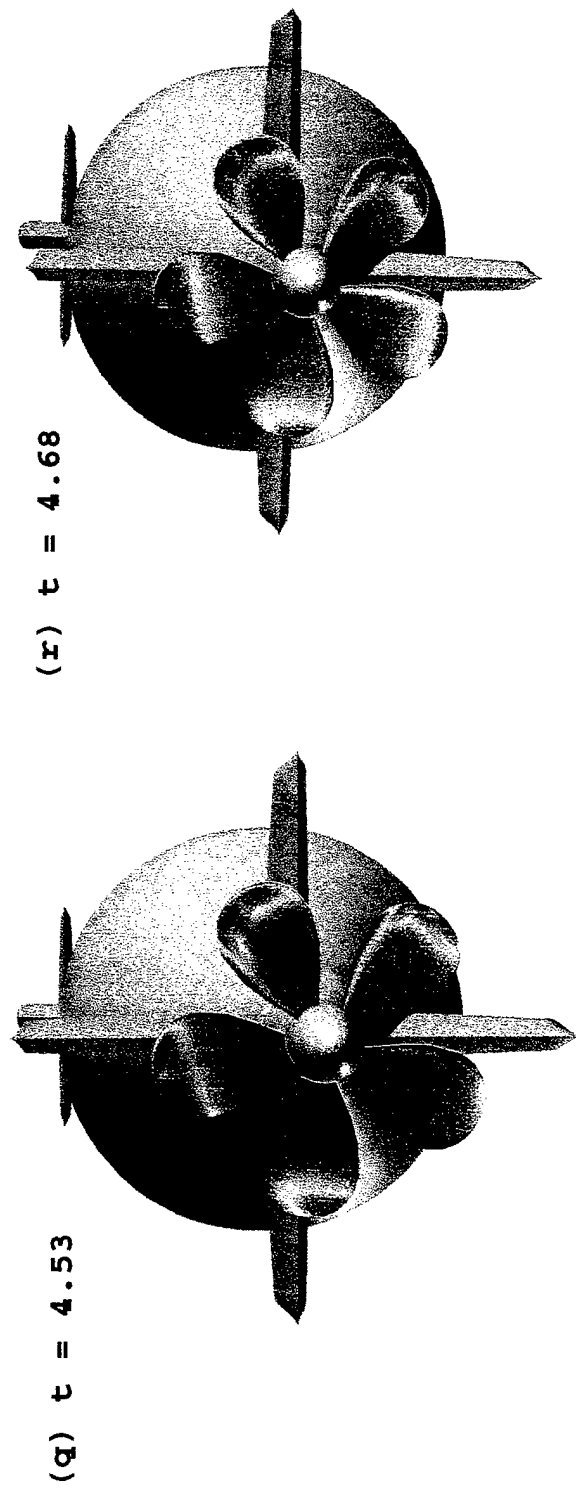


Figure 156. Low-Pressure Region of Ring Vortex Image Rotating in the Opposite Direction of Blade Rotation

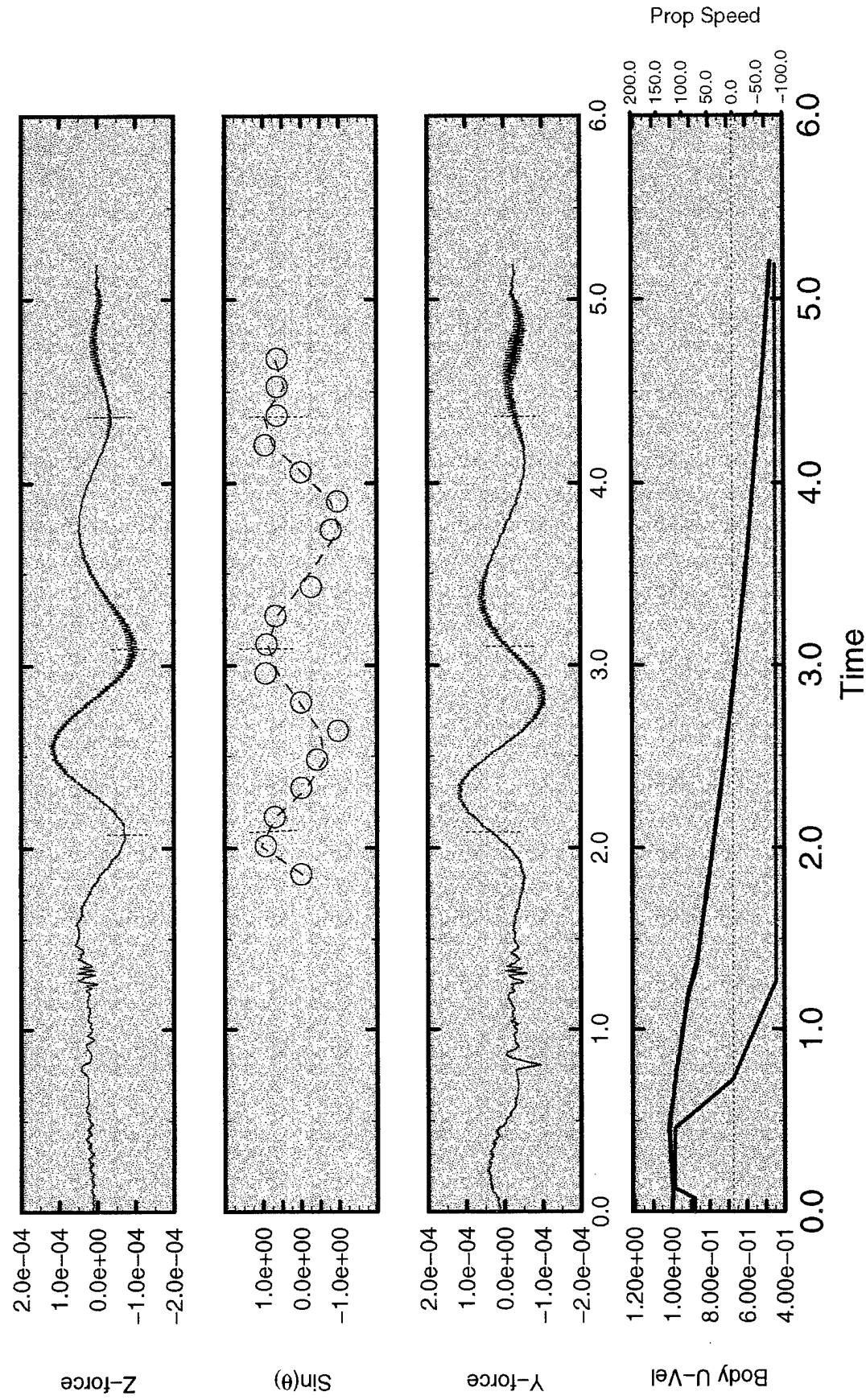


Figure 157.

Time History of the Forces, the Location of the Ring Vortex Image, the  $u$ -Component of the Vehicle Velocity, and the Propeller Angular Velocity for the Fully-Appended SUBOFF with a Propeller Rotating in Reverse

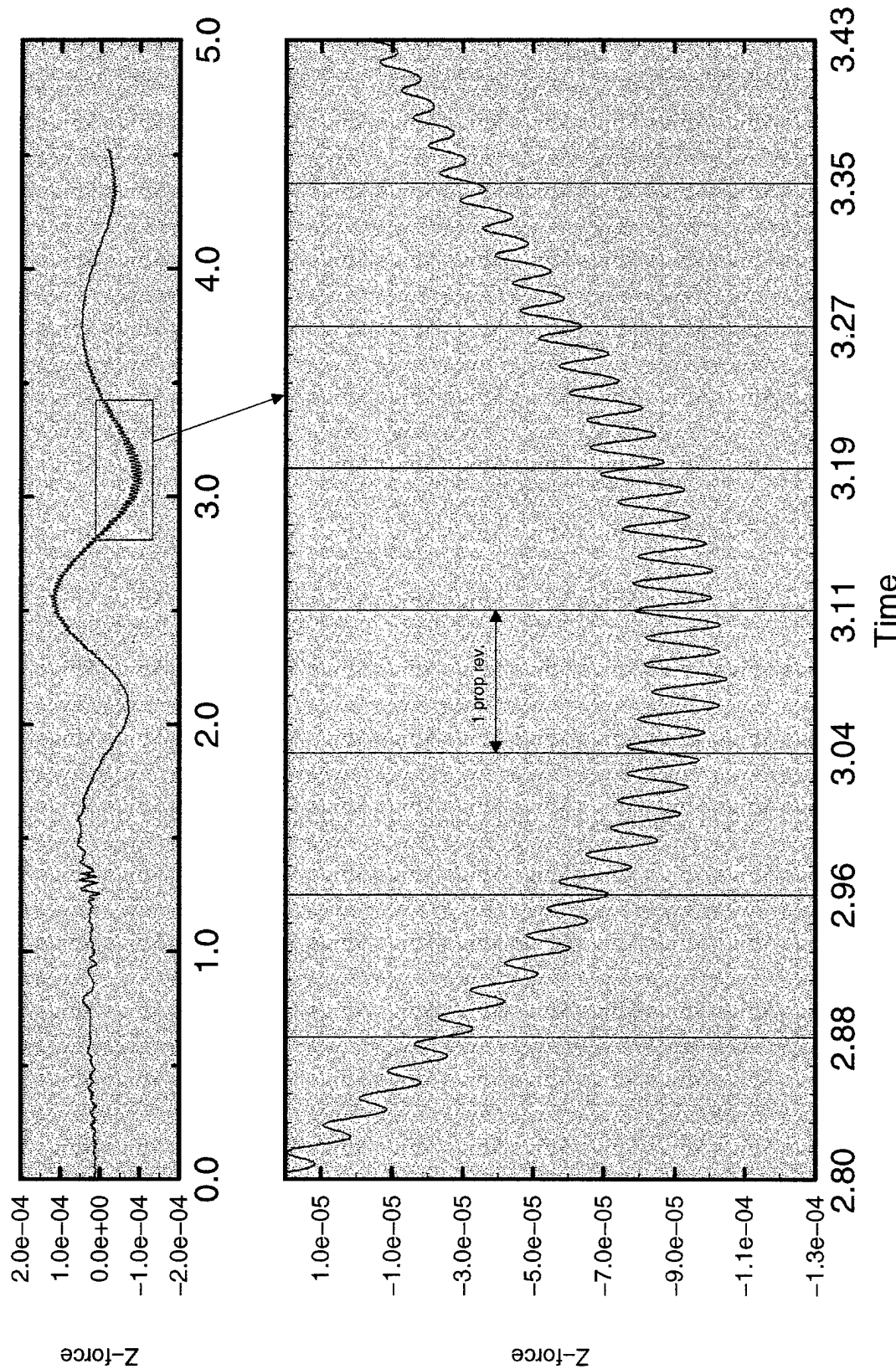


Figure 158. Large-Amplitude, Low-Frequency and Low-Amplitude, High-Frequency Force Oscillations for the Fully-Appended SUBOFF with a Propeller Rotating in Reverse

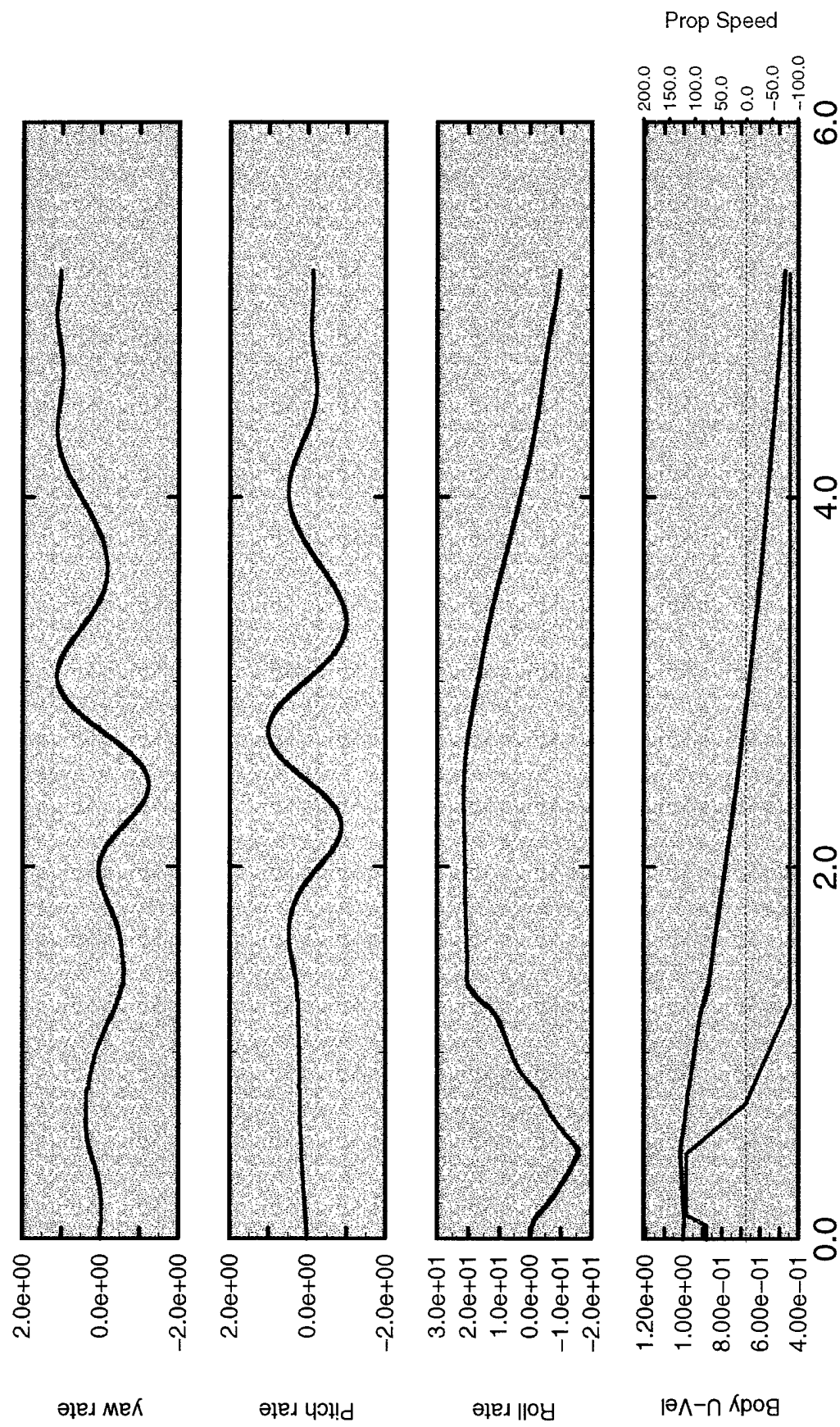


Figure 159.

Time History of the Angular Rates, the  $u$ -Component of the Vehicle Velocity, and the Propeller Angular Velocity for the Fully-Appended SUBOFF with a Propeller Rotating in Reverse

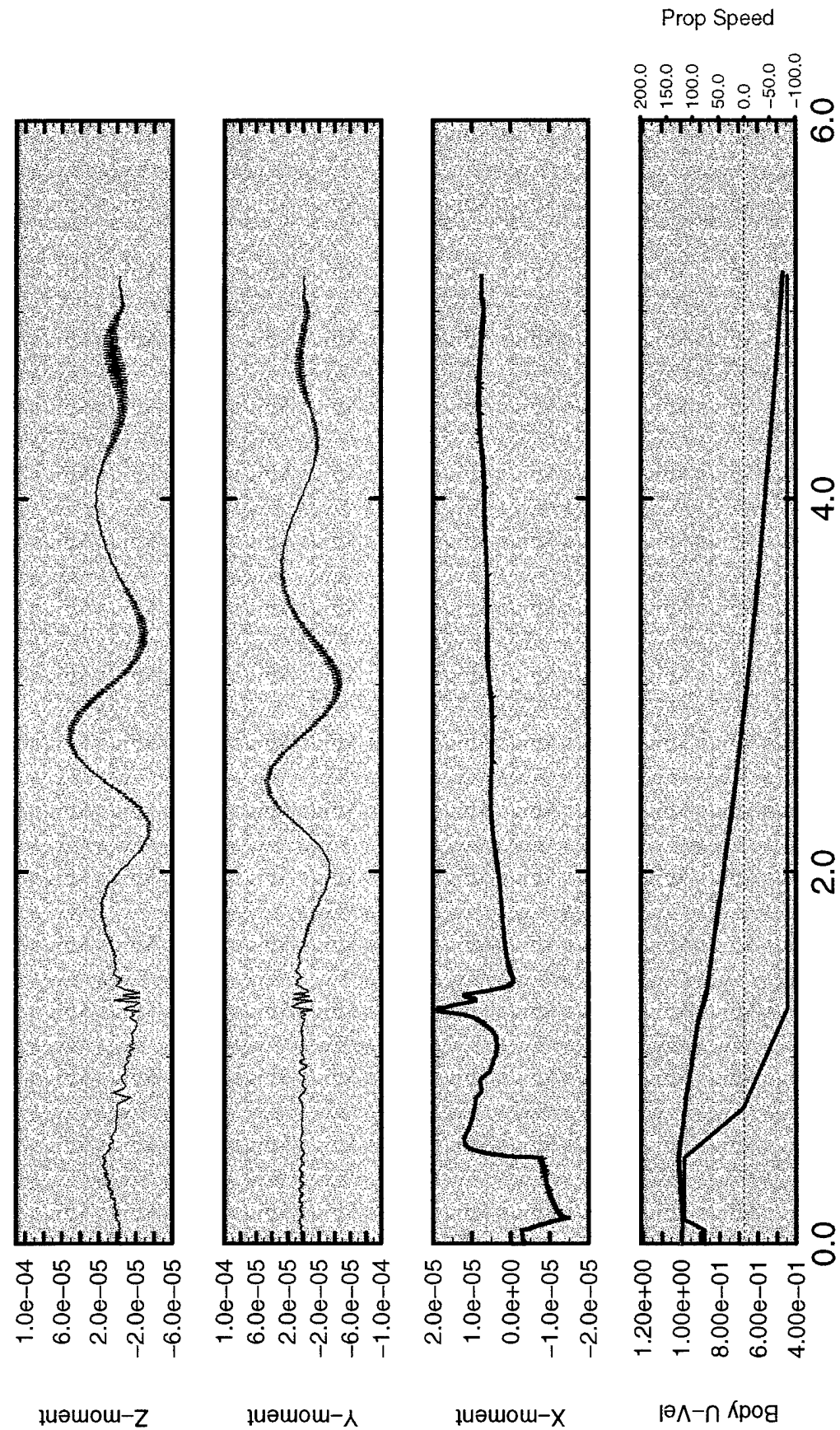


Figure 160.

Time History of the Moments, the  $u$ -Component of the Vehicle Velocity, and the Propeller Angular Velocity for the Fully-Appended SUBOFF with a Propeller Rotating in Reverse

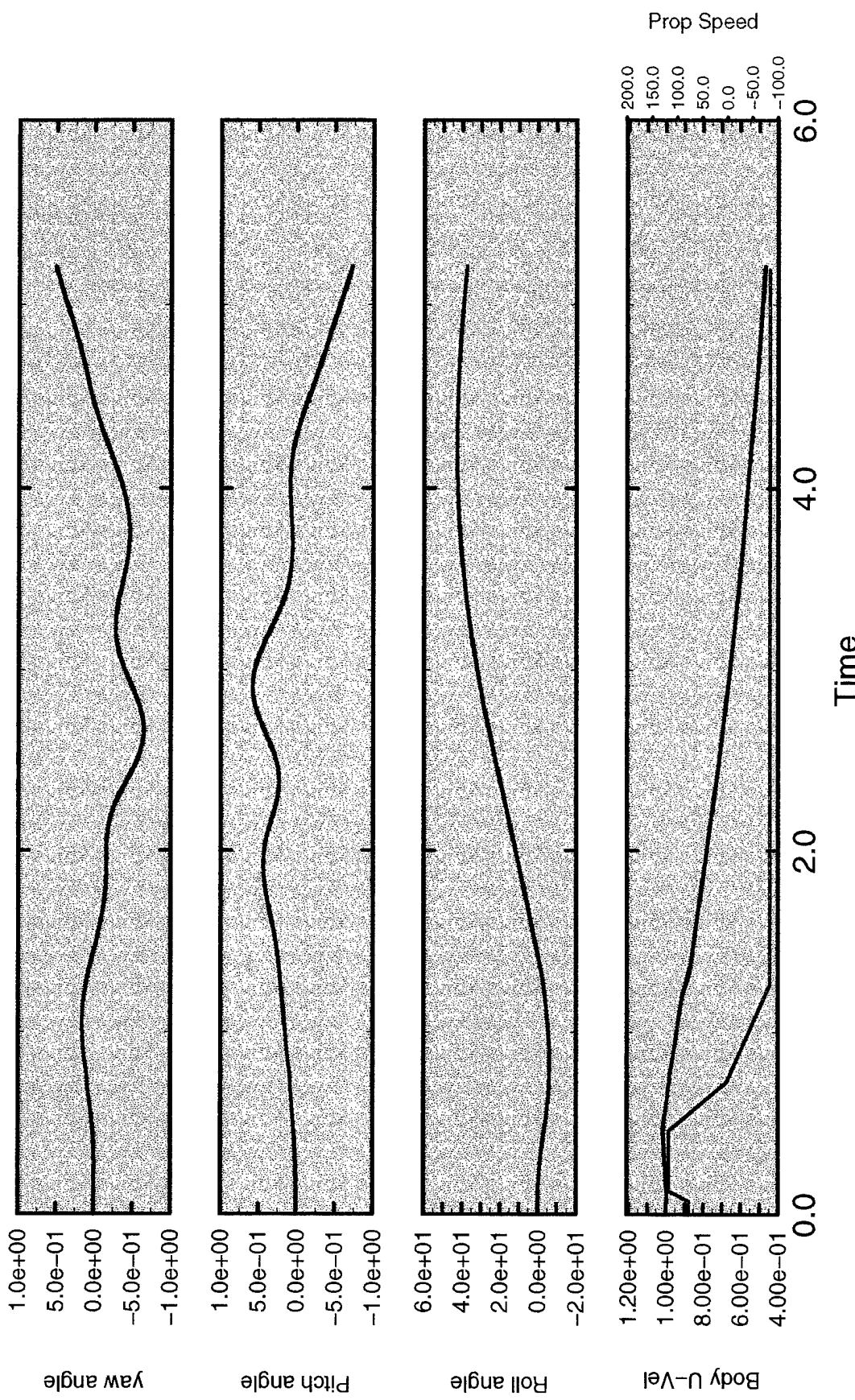


Figure 161.

Time History of the Vehicle's Orientation, the  $u$ -Component of the Vehicle Velocity, and the Propeller Angular Velocity for the Fully-Appended SUBOFF with a Propeller Rotating in Reverse

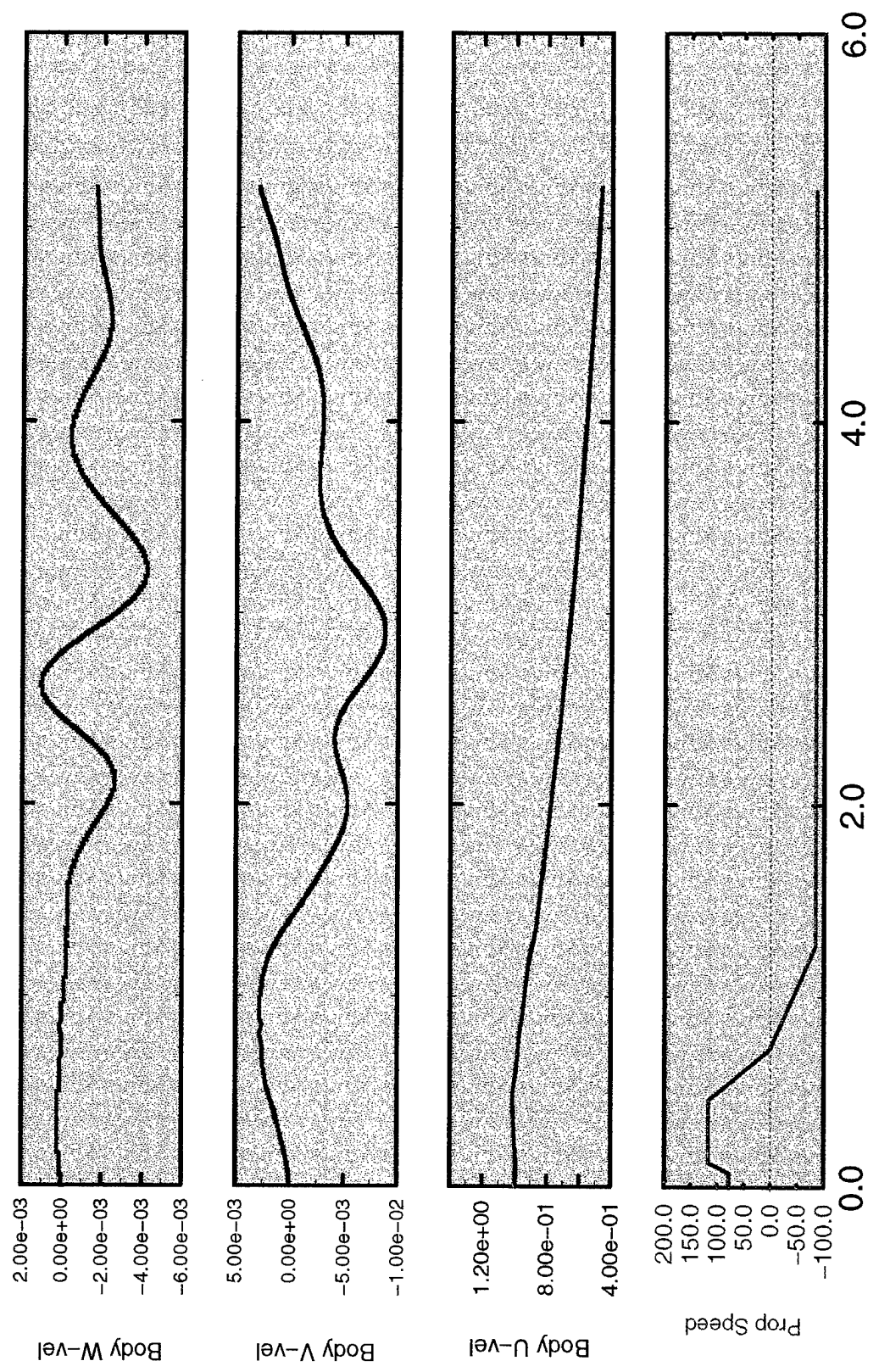


Figure 162. Time History of the Vehicle's Linear Velocity Components and the Propeller Angular Velocity for the Fully-Appended SUBOFF with a Propeller Rotating in Reverse

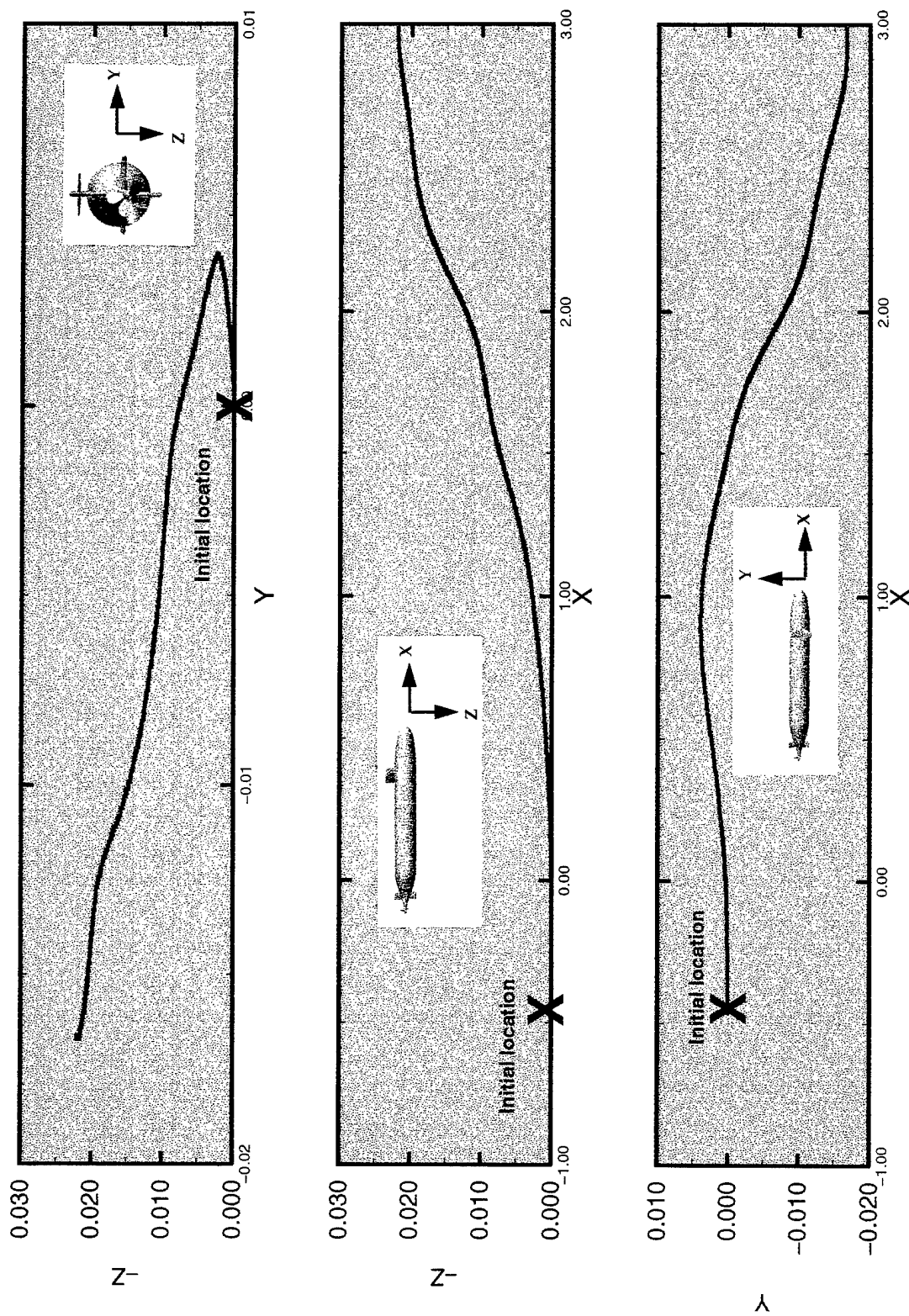


Figure 163.

Vehicle's Path for the Fully-Appended SUBOFF with a Propeller Rotating in Reverse